



UNIVERSITAT DE  
BARCELONA

## Electronic Structure Engineering for Enhanced Additive Performance in Robust Sulfur Cathodes

Chen Huang

**ADVERTIMENT.** La consulta d'aquesta tesi queda condicionada a l'acceptació de les següents condicions d'ús: La difusió d'aquesta tesi per mitjà del servei TDX ([www.tdx.cat](http://www.tdx.cat)) i a través del Dipòsit Digital de la UB ([diposit.ub.edu](http://diposit.ub.edu)) ha estat autoritzada pels titulars dels drets de propietat intel·lectual únicament per a usos privats emmarcats en activitats d'investigació i docència. No s'autoritza la seva reproducció amb finalitats de lucre ni la seva difusió i posada a disposició des d'un lloc aliè al servei TDX ni al Dipòsit Digital de la UB. No s'autoritza la presentació del seu contingut en una finestra o marc aliè a TDX o al Dipòsit Digital de la UB (framing). Aquesta reserva de drets afecta tant al resum de presentació de la tesi com als seus continguts. En la utilització o cita de parts de la tesi és obligat indicar el nom de la persona autora.

**ADVERTENCIA.** La consulta de esta tesis queda condicionada a la aceptación de las siguientes condiciones de uso: La difusión de esta tesis por medio del servicio TDR ([www.tdx.cat](http://www.tdx.cat)) y a través del Repositorio Digital de la UB ([diposit.ub.edu](http://diposit.ub.edu)) ha sido autorizada por los titulares de los derechos de propiedad intelectual únicamente para usos privados enmarcados en actividades de investigación y docencia. No se autoriza su reproducción con finalidades de lucro ni su difusión y puesta a disposición desde un sitio ajeno al servicio TDR o al Repositorio Digital de la UB. No se autoriza la presentación de su contenido en una ventana o marco ajeno a TDR o al Repositorio Digital de la UB (framing). Esta reserva de derechos afecta tanto al resumen de presentación de la tesis como a sus contenidos. En la utilización o cita de partes de la tesis es obligado indicar el nombre de la persona autora.

**WARNING.** On having consulted this thesis you're accepting the following use conditions: Spreading this thesis by the TDX ([www.tdx.cat](http://www.tdx.cat)) service and by the UB Digital Repository ([diposit.ub.edu](http://diposit.ub.edu)) has been authorized by the titular of the intellectual property rights only for private uses placed in investigation and teaching activities. Reproduction with lucrative aims is not authorized nor its spreading and availability from a site foreign to the TDX service or to the UB Digital Repository. Introducing its content in a window or frame foreign to the TDX service or to the UB Digital Repository is not authorized (framing). Those rights affect to the presentation summary of the thesis as well as to its contents. In the using or citation of parts of the thesis it's obliged to indicate the name of the author.



UNIVERSITAT<sub>DE</sub>  
BARCELONA

# **Electronic Structure Engineering for Enhanced Additive Performance in Robust Sulfur Cathodes**

Chen Huang



Doctoral Program: Electrochemistry. Science and Technology

**Electronic Structure Engineering for Enhanced Additive  
Performance in Robust Sulfur Cathodes**

Author

Chen Huang

Director

Andreu Cabot Codina

Tutor

Elvira Gómez Valentín

Barcelona, June 2025

Programa de Doctorat: Electroquímica. Ciència i Tecnologia

**Enginyeria d'estructures electròniques per a un rendiment additiu  
millorat en càtodes de sofre robusts**

Author

Chen Huang

Director

Andreu Cabot Codina

Tutor

Elvira Gómez Valentín

Barcelona, Juny de 2025

# Table of Contents

Acknowledgements.....	1
List of Publications .....	3
Authors' contributions .....	4
Preface .....	7
Results.....	8
Resultados.....	13
Acronyms.....	18
1. Introduction.....	21
1.1 Background.....	21
1.2 Reaction mechanism of LSBs.....	22
1.3 Reaction mechanism of RT-SSBs .....	24
1.4 The challenges for MSBs.....	25
1.4.1 Sulfur cathode.....	25
1.4.2 Metal anode.....	26
1.5 Technical modification.....	27
1.5.1 Modification of cathode materials .....	27
1.5.2 Morphology classification.....	32
1.6 Strategies to enhance the adsorption-catalysis of polysulfide conversion. ....	36
1.6.1 Heterojunction engineering.....	36
1.6.2 Defect engineering .....	37
1.6.3 Lattice distortion engineering .....	38
1.6.4 Doping engineering.....	38
1.6.5 Single atom strategy.....	39
1.7 Reference .....	39
2. Objectives .....	50
3. Experimental section.....	53
3.1 Chemicals or raw materials used in experiments.....	53
3.2 Material preparation method.....	54
3.2.1 Co-precipitation method .....	54
3.2.2 Solvothermal method.....	55
3.2.3 High-temperature carbonization method.....	55
3.3 Materials characterizations .....	57
3.3.1 X-ray diffraction (XRD, Miniflex 600).....	57
3.3.2 Raman laser spectrometer (LabRAM Odyssey).....	58
3.3.3 X-ray photoelectron spectrometer (XPS, Thermo Fisher Scientific, ESCALAB 250) .....	59
3.3.4 Scanning electron microscope (SEM, UniColore).....	60
3.3.5 Transmission electron microscope (TEM, UniColore) .....	62
3.3.6 Nitrogen adsorption-desorption test (BELSORP MAX II).....	63
3.3.7 Thermogravimetric analysis (TGA, NETZSCH, STA449-F5) .....	64
3.3.8 Electron paramagnetic resonance (EPR, JES-FA200) .....	64
3.3.9 UV-Vis absorption spectroscopy (Lambda 950 UV-Vis-NIR Spectrophotometer, Perkin Elmer) .....	65

3.3.10 X-ray absorption spectroscopy.....	66
3.4 Electrochemical methods .....	68
3.4.1 Cyclic voltammetry (CV).....	69
3.4.2 Galvanostatic charge-discharge (GCD) .....	69
3.4.3 Electrochemical impedance spectroscopy (EIS).....	70
4. Combined Defect and Heterojunction Engineering in ZnTe/CoTe <sub>2</sub> @NC Sulfur Hosts Toward Robust Lithium–Sulfur Batteries .....	73
5. Electronic Spin Alignment within Homologous NiS <sub>2</sub> /NiSe <sub>2</sub> Heterostructures to Promote Sulfur Redox Kinetics in Lithium-Sulfur Batteries.....	119
6. Anionic Doping in Layered Transition Metal Chalcogenides for Robust Lithium-Sulfur Batteries .....	171
7.Generation of Unpaired Electrons to Promote Electron Transfer at the Cathode of Room-Temperature Sodium Sulfur Batteries.....	225
8. Conclusions and future work .....	265
Resum .....	270
Curriculum vitae .....	274

## **Acknowledgements**

As time swiftly passes, I find myself reflecting on the whirlwind journey of the past three years of doctoral life. These years, spent far from the familiarity of home, have been a period of profound growth and transformation. They have not only bestowed upon me a wealth of knowledge but have also nurtured my scientific literacy, fostered independent thinking, and refined my practical skills.

### **Gratitude for guidance**

First and foremost, I extend my heartfelt gratitude to my supervisor, Professor Andreu Cabot, for granting me the invaluable opportunity to pursue my doctoral studies under his mentorship. Professor Cabot's unwavering support and guidance have been instrumental in shaping my academic and personal growth. Under his mentorship, I have been able to delineate my research trajectory and navigate the complexities of doctoral study with confidence. Beyond imparting academic knowledge, Professor Andreu Cabot has instilled in me essential qualities of empathy, compassion, and autonomy. His encouragement of independent thinking and emphasis on valuing student perspectives have been invaluable lessons that will endure throughout my academic journey.

### **Gratitude for instruction**

I am also deeply grateful to my colleagues within the research group, particularly the senior members in the laboratory, whose guidance and support have been indispensable. Their wealth of experience and willingness to offer guidance and advice have been a constant source of reassurance during moments of academic challenge. Their unwavering support has fortified me on my research journey, and I extend my sincerest wishes for their continued success and recognition in their respective fields.

### **Gratitude for companionship**

In addition to academic guidance, I am thankful for the camaraderie and collaboration shared with my fellow doctoral candidates. Together, we have formed a community of scholars bound

by a shared pursuit of knowledge and excellence. Through mutual support and collaboration, we have navigated the highs and lows of doctoral research, filling in each other's knowledge gaps and offering solace during moments of frustration. I am immensely grateful for their companionship and solidarity and am confident that we will all continue to shine brightly in our respective fields.

### **Gratitude for supporting**

Finally, I express my gratitude to all my colleagues at IREC for the joy they have brought into our research lives. Amidst the rigors of academic pursuit, their camaraderie and support have served as a beacon of light, illuminating even the most mundane of routines with moments of happiness and laughter. I extend my heartfelt thanks to each of them for their assistance and companionship, and I wish them all smooth sailing and a future filled with success and fulfillment.

Chen Huang

## List of publications

My doctoral research findings have been disseminated across four manuscripts (as first author), all of which have been either published or accepted in peer-reviewed journals. Below is the list of publications featured in this thesis:

1. **Chen Huang**, Jing Yu, Canhuang Li, Zhibiao Cui, Chaoqi Zhang, Chaoyue Zhang, Bingfei Nan, Junshan Li, Jordi Arbiol, and Andreu Cabot, Combined Defect and Heterojunction Engineering in ZnTe/CoTe<sub>2</sub>@NC Sulfur Hosts toward Robust Lithium-Sulfur Batteries. Adv. Funct. Mater. 2023, 33, 2305624.
2. **Chen Huang**, Jing Yu, Chao Yue Zhang, Zhibiao Cui, Jiakun Chen, Wei-Hong Lai, Yao-Jie Lei, Bingfei Nan, Xuan Lu, Ren He, Li Gong, Junshan Li, Canhuang Li, Xuede Qi, Qian Xue, Jin Yuan Zhou, Xueqiang Qi, Lluís Balcells, Jordi Arbiol, and Andreu Cabot Electronic Spin Alignment within Homologous NiS<sub>2</sub>/NiSe<sub>2</sub> Heterostructures to Promote Sulfur Redox Kinetics in Lithium-Sulfur Batteries. Adv. Mater. 2024, 36, 2400810.
3. **Chen Huang**, Jing Yu, Chao Yue Zhang, Zhibiao Cui, Ren He, Linlin Yang, Bingfei Nan, Canhuang Li, Xuede Qi, Xueqiang Qi, Junshan Li, Jin Yuan Zhou, Oleg Usoltsev, Laura Simonelli, Jordi Arbiol, Yao-Jie Lei, Qing Sun, Guoxiu Wang, Andreu Cabot, Anionic Doping in Layered Transition Metal Chalcogenides for Robust Lithium-Sulfur Batteries. Angew. Chem. Int. Ed. 2025, e202420488.
4. **Chen Huang**, Jing Yu, Yao-Jie Lei, Oleg Usoltsev, Li Gong, Zhibiao Cui, Junshan Li, Canhuang Li, Bingfei Nan, Xuan Lu, Ren He, Xuede Qi, Qian Xue, Jiali Chai, Yuchuan Ren, Xiaoyu Bi, Yapeng Cheng, Jin Yuan Zhou, Alina Skorynina, Aram Bugaev, Paulina R.Martínez-Alanis, Lluís Balcells, Jordi Arbiol, Chao Yue Zhang and Andreu Cabot, Generation of Unpaired Electrons to Promote Electron Transfer at the Cathode of Room-Temperature Sodium Sulfur Batteries. Chem. Eng. J. 2025, 506,160146.

## Authors' contributions

The entirety of the research conducted for this thesis was carried out within the Functional Materials Research Group at the Catalonia Institute for Energy Research. As a doctoral candidate, Chen Huang primarily focused on material design, data processing and analysis, and thesis writing. Four papers that have been published are included in this thesis, and any co-authors' contributions are delineated in the subsequent paragraphs. Furthermore, all published papers are indexed in the Science Citation Index and are categorized within the 1st quartile. None of the content presented in this thesis has been previously included in other theses. Professor Andreu Cabot provided valuable input by participating in the revision process of all published articles.

### Chaper 4:

Chen Huang, Jing Yu, Canhuang Li, Zhibiao Cui, Chaoqi Zhang, Chaoyue Zhang, Bingfei Nan, Junshan Li, Jordi Arbiol, and Andreu Cabot, *Combined Defect and Heterojunction Engineering in ZnTe/CoTe<sub>2</sub>@NC Sulfur Hosts toward Robust Lithium-Sulfur Batteries*.

In this study, Chen Huang spearheaded experiment design, experimental characterization, electrode material preparation, experimental data processing, and paper writing. Jing Yu and Jordi Arbiol primarily conducted high-resolution transmission electron microscopy (HRTEM) testing. Canhuang Li, Zhibiao Cui, Chaoqi Zhang, and Bingfei Nan contributed to data analysis, while Chaoyue Zhang focused on analyzing DFT theoretical calculation data. Junshan Li conducted X-ray photoelectron spectroscopy (XPS) testing. Andreu Cabot played a pivotal role in supervising the project and providing critical revisions and polishing of the paper.

### Chapter 5:

Chen Huang, Jing Yu, Chao Yue Zhang, Zhibiao Cui, Jiakun Chen, Wei-Hong Lai, Yao-Jie Lei, Bingfei Nan, Xuan Lu, Ren He, Li Gong, Junshan Li, Canhuang Li, Xuede Qi, Qian Xue, Jin Yuan Zhou, Xueqiang Qi, Lluís Balcells, Jordi Arbiol, and Andreu Cabot, *Electronic Spin Alignment within Homologous NiS<sub>2</sub>/NiSe<sub>2</sub> Heterostructures to Promote Sulfur Redox Kinetics in Lithium-Sulfur Batteries*.

In this study, Chen Huang played a central role in designing experiments, synthesizing



materials, conducting electrochemical testing, processing data, and drafting the paper. Jing Yu, Jiakun Chen, and Jordi Arbiol contributed to transmission electron microscopy and HRTEM testing, which provided crucial insights into the properties and composition of the materials. Chao Yue Zhang conducted theoretical calculations, while Wei-Hong Lai and Yao-Jie Lei oversaw synchrotron radiation and in situ X-ray diffraction (XRD) testing, including data analysis. Bingfei Nan, Xuan Lu, Ren He, Li Gong, Junshan Li, Canhuang Li, Xuede Qi, Qian Xue, and Jin Yuan Zhou participated in various aspects of data analysis. Lluís Balcells conducted magnetic testing of the electrode materials. Andreu Cabot played a pivotal role throughout the study, from evaluating the feasibility of the thesis proposal to providing ongoing feedback and revisions for the articles and the final thesis. This collaborative effort enabled the comprehensive exploration of the research topic and the synthesis of valuable insights into the materials' properties and performance.

#### Chapter 6:

Chen Huang, Jing Yu, Chao Yue Zhang, Zhibiao Cui, Ren He, Linlin Yang, Bingfei Nan, Canhuang Li, Xuede Qi, Xueqiang Qi, Junshan Li, Jin Yuan Zhou, Oleg Usoltsev, Laura Simonelli, Jordi Arbiol, Yao-Jie Lei, Qing Sun, Guoxiu Wang, Andreu Cabot, *Anionic Doping in Layered Transition Metal Chalcogenides for Robust Lithium-Sulfur Batteries*

In this study, Chen Huang was primarily responsible for designing experimental concepts, conducting experiments, processing data, drafting the manuscript, submitting the paper, and revising the manuscript. Jing Yu and Jordi Arbiol focused on characterizing the morphology of electrode materials using scanning electron microscopy (SEM) and transmission electron microscopy (TEM). Chao Yue Zhang contributed to the analysis of theoretical calculation data. Zhibiao Cui, Ren He, Linlin Yang, Bingfei Nan, Canhuang Li, Xuede Qi, Xueqiang Qi, Junshan Li, Jin Yuan Zhou, Oleg Usoltsev, and Laura Simonelli assisted in analyzing experimental data. Yao-Jie Lei conducted X-ray absorption spectroscopy (XAS) and ex situ XAS tests on host materials, while Qing Sun performed in situ XRD measurements. Guoxiu Wang and Andreu Cabot played a pivotal role in this work, contributing significantly to manuscript revision and securing funding support.

#### Chapter 7:

Chen Huang, Jing Yu, Yao-Jie Lei, Oleg Usoltsev, Li Gong, Zhibiao Cui, Junshan Li,

Canhuang Li, Bingfei Nan, Xuan Lu, Ren He, Xuede Qi, Qian Xue, Jiali Chai, Yuchuan Ren, Xiaoyu Bi, Yapeng Cheng, Jin Yuan Zhou, Alina Skorynina, Aram Bugaev, Paulina R.Martínez-Alanis, Lluís Balcells, Jordi Arbiol, Chao Yue Zhang and Andreu Cabot, *Generation of Unpaired Electrons to Promote Electron Transfer at the Cathode of Room-Temperature Sodium Sulfur Batteries*

In this study, Chen Huang played a leading role in constructing the experimental protocol, preparing materials, conducting physical characterization and electrochemical testing, processing data, and drafting the initial manuscript. Jing Yu and Jordi Arbiol made significant contributions through transmission electron microscopy (TEM) and HRTEM to analyze the morphology of the electrode materials. Chao Yue Zhang, Jin Yuan Zhou supervised the theoretical calculations, providing crucial insights. Oleg Usoltsev, Alina Skorynina, and Aram Bugaev were involved in synchrotron radiation testing and data analysis. Li Gong, Zhibiao Cui, Junshan Li, Canhuang Li, Bingfei Nan, Xuan Lu, Ren He, Xuede Qi, Qian Xue, Jiali Chai, Yuchuan Ren, Xiaoyu Bi, Yapeng Cheng and Paulina R.Martínez-Alanis participated comprehensively in all aspects of data analysis. Lluís Balcells conducted magnetic testing on the electrode materials. Andrew Cabot was instrumental throughout the research process, from evaluating the feasibility of the study proposal to offering continuous feedback and revisions on the final manuscript. This collaborative effort enabled a thorough exploration of the research topic and the synthesis of valuable insights into the characteristics and performance of the materials.

## Preface

The doctoral thesis was authored by PhD candidate Chen Huang at the Catalonia Institute for Energy research (IREC) between 2022 and 2025, with funding provided by the China Scholarship Council. The thesis primarily focuses on electron modulation engineering for optimizing active cathode host materials in high-performance metal-sulfur batteries (MSBs). Comprising eight main chapters, the paper begins with an overarching introduction to MSBs, highlighting the current challenges and the research efforts aimed at overcoming them. Chapter 2 outlines the objectives of the paper, while Chapter 3 details the experimental methods employed. Chapters 4 through 7 delve into the complexities of MSB, discussing in depth the various strategies devised to address common challenges. These strategies include: (i) Designing heterostructures and vacancies engineering (ii) Creating homologous heterogeneous structures (iii) Developing P-N heterogeneous engineering (iv) Preparing hollow structure (v) Introducing anion doping strategies. In Chapter 4, the thesis focuses on the synthesis of a ZnTe/CoTe<sub>2</sub> composite material with vacancies and heterostructures. The incorporation of vacancies enhances the conductivity of the electrode material, while the designed heterostructure facilitates Li<sup>+</sup> diffusion. In Chapter 5, the hollow homogeneous heterostructure NiS<sub>2</sub>/NiSe<sub>2</sub>@NC host material is employed in LSBs, promoting changes in the Ni<sup>3+</sup> spin state. Chapter 6 focuses on the generation of Se vacancies and lattice distortion in Bi<sub>2</sub>Se<sub>3</sub>@C via introduction doping strategies. Finally, Chapter 7 explores a P-N heterojunction strategy through the synthesis of Co<sub>3</sub>O<sub>4</sub>-NC@C<sub>3</sub>N<sub>4</sub> electrode materials, elucidating the electron transfer mechanism and the spin effect on Co<sup>3+</sup>.

## Results

As global energy demand continues to rise, the development of high-power and energy-density energy storage devices becomes increasingly imperative. Among the various options, MSBs stand out for their ability to store charge through the conversion between chemical and electrical energy. They offer advantages over traditional lithium-ion batteries, such as high specific capacity and energy density, as well as the abundance and affordability of elemental sulfur. However, despite these advantages, MSBs face significant challenges that hinder their practical application. **Poor Conductivity:** Elemental sulfur and discharge products like  $\text{Li}_2\text{S}/\text{Na}_2\text{S}$  exhibit poor conductivity, impeding electron migration and ion diffusion. **Volume Expansion:** During charge and discharge, sulfur experiences significant volume expansion, leading to reduced cycle life of the host material. **Polysulfide Shuttle:** Soluble polysulfides dissolve into the electrolyte, decreasing sulfur utilization efficiency. Addressing these challenges requires innovative approaches. One promising strategy involves designing effective catalysts, particularly transition metal compounds (TMCs), which offer high capacity and redox voltage. However, TMCs often suffer from poor conductivity and structural stability, limiting their practical application in batteries. To overcome these limitations, this research proposes several solutions: **Defect Engineering:** Introducing defects into TMCs can enhance their conductivity and stability, accelerating the diffusion rate of ions. **Heterogeneous Interfaces:** Creating interfaces between TMCs and other materials can improve their performance by regulating physical properties such as valence state and spin state, thereby promoting the kinetics of sulfur redox reactions (SRR). **Spin regulation:** Specifically, the transition metal ions from a low-spin to a high-spin state, increases the number of unpaired electrons in transition metal ions. This increase in unpaired electrons enhances the electrocatalytic activity of the catalysts, which in turn accelerates the redox reactions of sulfur and polysulfides, ultimately improving the overall performance of the battery. **Doping strategy:** Doping enhances the conductivity of cathode materials, facilitating the rapid transmission of electrons. This reduction in internal resistance leads to improved energy efficiency and better rate performance. Additionally, doping elements can form strong chemical

bonds with polysulfides, effectively anchoring them to the cathode material. This process helps to suppress the shuttle effect, minimizing capacity loss and extending the battery's cycle life.

**Lattice distortion:** Lattice distortion can introduce additional active sites, enhancing the electrocatalytic activity of electrode materials and thereby accelerating the redox reactions of sulfur and polysulfides. Furthermore, lattice distortion may alter the crystal structure, creating more favorable ion migration channels, reducing ion diffusion resistance, and consequently improving the battery's rate performance and ionic conductivity. By focusing on these strategies, this research aims to address the key challenges hindering the commercialization of MSBs. Through the development of effective catalysts and innovative design approaches, the goal is to unlock the full potential of MSBs paving the way for their widespread adoption in energy storage applications. The main research contents of this paper are as follows:

In Chapter 4, to enhance the performance of lithium-sulfur batteries (LSBs), the strategy proposed focused on integrating vacancies and heterojunction engineering into the design of ZnTe/CoTe<sub>2</sub>@NC host materials. A novel approach for designing sulfur host materials for LSBs was introduced, leveraging nitrogen-doped carbon (NC) as the base material, coated with a small amount of transition metal telluride (TMT) catalyst. The optimization of sulfur redox kinetics was achieved through the modulation of anion vacancy concentration and the design of ZnTe/CoTe<sub>2</sub> heterostructures. The incorporation of anion vacancies within the sulfur host at the cathode of LSBs serves a dual purpose. Firstly, it generally increases the number of carriers within the crystal and induces changes in the electronic structure near defect sites. Secondly, activated unpaired cations effectively capture polysulfides, mitigating the shuttle effect. Additionally, the formation of heterostructures facilitates the diffusion of ions and electrons, thereby accelerating the conversion reaction. Both theoretical calculations and experimental data corroborate the efficacy of this approach. Te vacancies were found to enhance the adsorption of lithium polysulfides (LiPSs), while the resultant TMT/TMT and TMT/C heterostructures significantly improved Li<sup>+</sup> diffusion and electron transport. Consequently, the v-ZnTe/CoTe<sub>2</sub>@NC/S composite exhibited remarkable performance metrics, including high specific capacity (up to 1608 mA·h·g<sup>-1</sup> at 0.1C) and extended cycle life (maintaining 890.8 mA·h·g<sup>-1</sup> after 100 cycles at 0.1C, even with a reduced electrolyte volume to 7.5 μL·mg<sup>-1</sup>). Notably, even under a high sulfur load of 5.4 mg·cm<sup>-2</sup>, a substantial capacity of 1273 mA·h·g<sup>-1</sup>

<sup>1</sup> was retained at 0.1C.

In Chapter 5, a homologous heterostructure composed of NiS<sub>2</sub> and NiSe<sub>2</sub>, encapsulated within a NC matrix (NiS<sub>2</sub>/NiSe<sub>2</sub>@NC), was designed to optimize electron spin arrangement and promote sulfur redox kinetics in LSBs. The synthesized NiS<sub>2</sub>/NiSe<sub>2</sub> heterostructure demonstrated superior catalytic activity when employed as an additive in sulfur cathodes. The key design feature of the NiS<sub>2</sub>/NiSe<sub>2</sub> heterostructure is its ability to induce spin splitting of 3d orbitals, facilitating the transition of Ni<sup>3+</sup> from low spin to high spin states. This transition generates additional unpaired electrons, thereby enhancing the electronic energy level and activating the electronic state. The spin configuration of NiS<sub>2</sub>/NiSe<sub>2</sub>@NC, coupled with its hollow structure, synergistically contributes to the promotion of sulfur redox kinetics. The LSBs utilizing NiS<sub>2</sub>/NiSe<sub>2</sub>@NC/S cathodes exhibited exceptional electrochemical performance. A specific capacity of 1458 mAh·g<sup>-1</sup> was achieved at a 0.1C low current rate. Even at a high current rate of 5C, a specific capacity of 572 mAh·g<sup>-1</sup> was maintained. The average capacity decay rate per cycle was only 0.025% after 500 cycles at 1C current rate. Moreover, the LSBs maintained impressive performance even under challenging conditions: At a high sulfur loading of 6.2 mg·cm<sup>-2</sup>, an initial capacity of up to 1173 mAh·g<sup>-1</sup> (equivalent to 7.27 mAh·cm<sup>-2</sup>) was achieved at 0.1C. After 300 cycles, a significant capacity of 1058 mAh·g<sup>-1</sup> was retained, highlighting the stability of the NiS<sub>2</sub>/NiSe<sub>2</sub>@NC/S cathode.

In Chapter 6, the robustness of LSBs was achieved through the generation of Se vacancies and induced lattice distortion in Te-doped Bi<sub>2</sub>Se<sub>3-x</sub>@C. The construction of Te-Bi<sub>2</sub>Se<sub>3-x</sub>@C with Se vacancies involved the uniform doping of Te atoms into the Bi<sub>2</sub>Se<sub>3</sub> lattice. Te doping induces lattice distortion and alters the local structure of the catalyst. This provides insights into the relationship between strain and catalytic performance, offering a deeper understanding of how structural changes impact the electrochemical properties. Te doping-induced vacancies modulate the electronic structure around atomic defect sites. This leads to an increase in the number of carriers within the crystal and activates unpaired cations to capture more polysulfides. These modifications enhance the adsorption capacity and intrinsic catalytic activity towards polysulfides. Both experimental results and theoretical calculations confirm that Te atom doping induces lattice distortion and generates ion vacancies. This process adjusts the coordination environment and electronic structure of Bi atoms, achieving a balance between

polysulfide adsorption and intrinsic catalysis. As a result of these advancements,  $\text{Te-Bi}_2\text{Se}_3\text{-x@C/S}$  demonstrates outstanding electrochemical performance: A specific capacity of  $1508 \text{ mAh}\cdot\text{g}^{-1}$  is achieved at a low current density of  $0.1\text{C}$ . The specific capacity remains high even at high current rates, ranging from  $1508 \text{ mAh}\cdot\text{g}^{-1}$  at  $0.1\text{C}$  to  $655.8 \text{ mAh}\cdot\text{g}^{-1}$  at  $5\text{C}$ . After 500 cycles, the material maintains a high specific capacity of  $998.7 \text{ mAh}\cdot\text{g}^{-1}$ , indicating long-term stability. Even under a high sulfur loading of  $6.4 \text{ mg}\cdot\text{cm}^{-2}$ , a specific capacity of  $1251 \text{ mAh}\cdot\text{g}^{-1}$  is achieved at a current rate of  $0.1\text{C}$ .

In Chapter 7, the electron transfer mechanism in the P-N heterostructure of the room temperature sodium-sulfur batteries (RT-SSBs)  $\text{Co}_3\text{O}_4\text{-NC@C}_3\text{N}_4$  was investigated. This study elucidated the intricate process of electron transfer within the P-N heterojunction, shedding light on its role in enhancing battery performance. The proposed  $\text{Co}_3\text{O}_4\text{-NC@C}_3\text{N}_4$  composite, comprising hollow tubular  $\text{C}_3\text{N}_4$  nanostructures loaded with  $\text{Co}_3\text{O}_4$  nanoparticles, serves as a sulfur host additive. Through theoretical calculations and experimental analyses, the electron transfer mechanism in the P-N heterojunction was thoroughly examined. The electron transfer mechanism unfolds as follows: Initially, the N atoms within the  $\text{C}_3\text{N}_4$  matrix act as electron donors, facilitating the transfer of spin electrons to Co within the  $\text{Co}_3\text{O}_4$  nanoparticles. This transfer of spin electrons induces a transition in the spin state of Co from low spin to high spin, resulting in the generation of additional unpaired electrons within the 3d orbitals for Co. Concurrently, the spin electrons transferred to  $\text{Co}_3\text{O}_4$  are subsequently transferred to the polysulfide species with a lower transfer kinetic barrier. This transfer process effectively reduces the redox reaction kinetic barrier during the SRR process, thereby enhancing the overall sulfur redox kinetics. As a consequence of this electron transfer mechanism, the  $\text{Co}_3\text{O}_4\text{-NC@C}_3\text{N}_4/\text{S}$  composite exhibits remarkable electrochemical performance: The specific capacity ranges from  $1143 \text{ mAh}\cdot\text{g}^{-1}$  at  $0.1\text{C}$  to  $575 \text{ mAh}\cdot\text{g}^{-1}$  at  $5\text{C}$ , demonstrating its ability to sustain high current densities. Even after 1000 cycles, the composite maintains a current retention rate of 81.3%, indicating its robust cycling stability.

In summary, the four studies presented above address key challenges in MSBs through the introduction of heterostructures, vacancy engineering, doping strategies, and P-N heterojunctions. These innovative approaches significantly enhance the adsorption and catalytic processes in MSBs. As a result, the host materials developed in these studies exhibit

outstanding electrochemical performance, characterized by high specific capacity and long cycle life. Notably, these materials maintain excellent stability even under high loading and lean electrolyte conditions, further demonstrating their practical applicability.



## Resultados

A medida que la demanda mundial de energía continúa aumentando, el desarrollo de dispositivos de almacenamiento de energía de alta potencia y densidad energética se vuelve cada vez más imperativo. Entre las diversas opciones, las baterías de metal-azufre (MSB) se destacan por su capacidad de almacenar carga a través de la conversión entre energía química y eléctrica. Ofrecen ventajas sobre las baterías tradicionales de iones de litio, como una alta capacidad específica y densidad energética, así como la abundancia y asequibilidad del azufre elemental. Sin embargo, a pesar de estas ventajas, las MSB enfrentan desafíos importantes que dificultan su aplicación práctica. Mala conductividad: el azufre elemental y los productos de descarga como  $\text{Li}_2\text{S}/\text{Na}_2\text{S}$  exhiben mala conductividad, lo que impide la migración de electrones y la difusión de iones. Expansión de volumen: durante la carga y descarga, el azufre experimenta una expansión de volumen significativa, lo que lleva a una reducción del ciclo de vida del material anfitrión. Lanzadera de polisulfuro: los polisulfuros solubles se disuelven en el electrolito, lo que disminuye la eficiencia de utilización del azufre. Abordar estos desafíos requiere enfoques innovadores. Una estrategia prometedora implica el diseño de catalizadores efectivos, en particular compuestos de metales de transición (TMC), que ofrecen alta capacidad y voltaje redox. Sin embargo, los TMC a menudo sufren de mala conductividad y estabilidad estructural, lo que limita su aplicación práctica en baterías. Para superar estas limitaciones, esta investigación propone varias soluciones: Ingeniería de defectos: la introducción de defectos en los TMC puede mejorar su conductividad y estabilidad, acelerando la tasa de difusión de iones. Interfaces heterogéneas: la creación de interfaces entre compuestos de metales de transición y otros materiales puede mejorar su rendimiento al regular las propiedades físicas como el estado de valencia y el espín, promoviendo así la cinética de las reacciones redox del azufre. Regulación del espín: específicamente, el cambio de los iones de metales de transición de un estado de espín bajo a uno de espín alto aumenta el número de electrones desapareados en los iones de metales de transición. Este aumento de electrones desapareados mejora la actividad electrocatalítica de los catalizadores, lo que a su vez acelera las reacciones redox del azufre y los polisulfuros, mejorando en última instancia el rendimiento general de la batería. Estrategia

de dopaje: el dopaje mejora la conductividad de los materiales del cátodo, facilitando la transmisión rápida de electrones. Esta reducción de la resistencia interna conduce a una mejor eficiencia energética y un mejor rendimiento de la velocidad. Además, los elementos dopantes pueden formar fuertes enlaces químicos con los polisulfuros, anclándolos eficazmente al material del cátodo. Este proceso ayuda a suprimir el efecto lanzadera, minimizando la pérdida de capacidad y extendiendo la vida útil de la batería. Distorsión reticular: La distorsión reticular puede introducir sitios activos adicionales, mejorando la actividad electrocatalítica de los materiales de los electrodos y acelerando así las reacciones redox del azufre y los polisulfuros. Además, la distorsión reticular puede alterar la estructura cristalina, creando canales de migración de iones más favorables, reduciendo la resistencia a la difusión de iones y, en consecuencia, mejorando el rendimiento de la batería y la conductividad iónica. Al centrarse en estas estrategias, esta investigación tiene como objetivo abordar los desafíos clave que obstaculizan la comercialización de los MSB. A través del desarrollo de catalizadores efectivos y enfoques de diseño innovadores, el objetivo es liberar todo el potencial de los MSB allanando el camino para su adopción generalizada en aplicaciones de almacenamiento de energía. Los principales contenidos de investigación de este artículo son los siguientes:

En el Capítulo 4, para mejorar el rendimiento de las baterías de litio y azufre (LSB), la estrategia propuesta se centró en integrar las vacantes y la ingeniería de heterojunción en el diseño de materiales hospedantes de  $\text{ZnTe/CoTe}_2@\text{NC}$ . Se introdujo un nuevo enfoque para diseñar materiales hospedantes de azufre para LSB, aprovechando el carbono dopado con nitrógeno (NC) como material base, recubierto con una pequeña cantidad de catalizador de telururo de metal de transición (TMT). La optimización de la cinética redox del azufre se logró mediante la modulación de la concentración de vacantes de aniones y el diseño de heteroestructuras de  $\text{ZnTe/CoTe}_2$ . La incorporación de vacantes de aniones dentro del hospedante de azufre en el cátodo de las LSB tiene un doble propósito. En primer lugar, generalmente aumenta el número de portadores dentro del cristal e induce cambios en la estructura electrónica cerca de los sitios de defectos. En segundo lugar, los cationes desapareados activados capturan eficazmente los polisulfuros, mitigando el efecto lanzadera. Además, la formación de heteroestructuras facilita la difusión de iones y electrones, acelerando así la reacción de conversión. Tanto los cálculos teóricos como los datos experimentales

corroboran la eficacia de este enfoque. Se descubrió que las vacantes de Te mejoran la adsorción de polisulfuros de litio (LiPSs), mientras que las heteroestructuras TMT/TMT y TMT/C resultantes mejoraron significativamente la difusión de  $\text{Li}^+$  y el transporte de electrones. En consecuencia, el compuesto  $v\text{-ZnTe/CoTe}_2\text{@NC/S}$  exhibió métricas de rendimiento notables, incluida una alta capacidad específica (hasta  $1608 \text{ mA}\cdot\text{h}\cdot\text{g}^{-1}$  a 0,1 C) y una vida útil prolongada (manteniendo  $890,8 \text{ mA}\cdot\text{h}\cdot\text{g}^{-1}$  después de 100 ciclos a 0,1 C, incluso con un volumen de electrolito reducido a  $7,5 \mu\text{L}\cdot\text{mg}^{-1}$ ). Cabe destacar que, incluso bajo una alta carga de azufre de  $5,4 \text{ mg}\cdot\text{cm}^{-2}$ , se mantuvo una capacidad sustancial de  $1273 \text{ mA}\cdot\text{h}\cdot\text{g}^{-1}$  a 0,1 C.

En el Capítulo 5, se diseñó una heteroestructura homóloga compuesta de  $\text{NiS}_2$  y  $\text{NiSe}_2$ , encapsulada dentro de una matriz de carbono dopada con nitrógeno ( $\text{NiS}_2/\text{NiSe}_2\text{@NC}$ ), para optimizar la disposición de espín de los electrones y promover la cinética redox del azufre en los LSB. La heteroestructura  $\text{NiS}_2/\text{NiSe}_2$  sintetizada demostró una actividad catalítica superior cuando se empleó como aditivo en cátodos de azufre. La característica clave del diseño de la heteroestructura  $\text{NiS}_2/\text{NiSe}_2$  es su capacidad para inducir la división de espín de los orbitales 3d, lo que facilita la transición de  $\text{Ni}^{3+}$  de estados de espín bajo a espín alto. Esta transición genera electrones desapareados adicionales, mejorando así el nivel de energía electrónica y activando el estado electrónico. La configuración de espín de  $\text{NiS}_2/\text{NiSe}_2\text{@NC}$ , junto con su estructura hueca, contribuye sinérgicamente a la promoción de la cinética redox del azufre. Los LSB que utilizan cátodos  $\text{NiS}_2/\text{NiSe}_2\text{@NC/S}$  exhibieron un rendimiento electroquímico excepcional. Se logró una capacidad específica de  $1458 \text{ mAh}\cdot\text{g}^{-1}$  a una tasa de corriente baja de 0,1 C. Incluso a una tasa de corriente alta de 5 C, se mantuvo una capacidad específica de  $572 \text{ mAh}\cdot\text{g}^{-1}$ . La tasa de disminución de capacidad promedio por ciclo fue solo del 0,025 % después de 500 ciclos a una tasa de corriente de 1 C. Además, los LSB mantuvieron un rendimiento impresionante incluso en condiciones difíciles: con una alta carga de azufre de  $6,2 \text{ mg}\cdot\text{cm}^{-2}$ , se logró una capacidad inicial de hasta  $1173 \text{ mAh}\cdot\text{g}^{-1}$  (equivalente a  $7,27 \text{ mAh}\cdot\text{cm}^{-2}$ ) a 0,1 C. Después de 300 ciclos, se mantuvo una capacidad significativa de  $1058 \text{ mAh}\cdot\text{g}^{-1}$ , lo que resalta la estabilidad del cátodo  $\text{NiS}_2/\text{NiSe}_2\text{@NC/S}$ .

En el Capítulo 6, la robustez de los LSB se logró a través de la generación de vacantes de Se y la distorsión de red inducida en  $\text{Bi}_2\text{Se}_3\text{@C}$  dopado con Te. La construcción de  $\text{Te-Bi}_2\text{Se}_{3-x}\text{@C}$  con vacantes de Se implicó el dopaje uniforme de átomos de Te en la red de  $\text{Bi}_2\text{Se}_3$ . El dopaje

con Te induce una distorsión de red y altera la estructura local del catalizador. Esto proporciona información sobre la relación entre la deformación y el rendimiento catalítico, ofreciendo una comprensión más profunda de cómo los cambios estructurales afectan las propiedades electroquímicas. Las vacantes inducidas por el dopaje con Te modulan la estructura electrónica alrededor de los sitios de defectos atómicos. Esto conduce a un aumento en el número de portadores dentro del cristal y activa cationes no apareados para capturar más polisulfuros. Estas modificaciones mejoran la capacidad de adsorción y la actividad catalítica intrínseca hacia los polisulfuros. Tanto los resultados experimentales como los cálculos teóricos confirman que el dopaje de átomos de Te induce una distorsión de red y genera vacantes iónicas. Este proceso ajusta el entorno de coordinación y la estructura electrónica de los átomos de Bi, logrando un equilibrio entre la adsorción de polisulfuro y la catálisis intrínseca. Como resultado de estos avances,  $\text{Te-Bi}_2\text{Se}_{3-x}\text{@C/S}$  demuestra un rendimiento electroquímico excepcional: se logra una capacidad específica de  $1508 \text{ mAh}\cdot\text{g}^{-1}$  a una baja densidad de corriente de 0,1 C. La capacidad específica se mantiene alta incluso a altas tasas de corriente, que van desde  $1508 \text{ mAh}\cdot\text{g}^{-1}$  a 0,1 C hasta  $655,8 \text{ mAh}\cdot\text{g}^{-1}$  a 5 C. Después de 500 ciclos, el material mantiene una alta capacidad específica de  $998,7 \text{ mAh}\cdot\text{g}^{-1}$ , lo que indica estabilidad a largo plazo. Incluso con una alta carga de azufre de  $6,4 \text{ mg}\cdot\text{cm}^{-2}$ , se logra una capacidad específica de  $1251 \text{ mAh}\cdot\text{g}^{-1}$  a una tasa de corriente de 0,1 C.

En el Capítulo 7, se investigó el mecanismo de transferencia de electrones en la heteroestructura P-N de las baterías de sodio-azufre a temperatura ambiente (RT-SSBs)  $\text{Co}_3\text{O}_4\text{-NC}@C_3\text{N}_4$ . Este estudio dilucidó el intrincado proceso de transferencia de electrones dentro de la heterojunción P-N, arrojando luz sobre su papel en la mejora del rendimiento de la batería. El compuesto  $\text{Co}_3\text{O}_4\text{-NC}@C_3\text{N}_4$  propuesto, que comprende nanoestructuras  $C_3N_4$  tubulares huecas cargadas con nanopartículas de  $\text{Co}_3\text{O}_4$ , sirve como un aditivo anfitrión de azufre. A través de cálculos teóricos y análisis experimentales, se examinó a fondo el mecanismo de transferencia de electrones en la heterojunción P-N. El mecanismo de transferencia de electrones se desarrolla de la siguiente manera: Inicialmente, los átomos de N dentro de la matriz  $C_3N_4$  actúan como donadores de electrones, facilitando la transferencia de electrones de espín a Co dentro de las nanopartículas de  $\text{Co}_3\text{O}_4$ . Esta transferencia de electrones de espín induce una transición en el estado de espín de Co de espín bajo a espín alto, lo que da como

resultado la generación de electrones desapareados adicionales dentro de los orbitales 3d para Co. Al mismo tiempo, los electrones de espín transferidos a  $\text{Co}_3\text{O}_4$  se transfieren posteriormente a las especies de polisulfuro con una barrera cinética de transferencia más baja. Este proceso de transferencia reduce eficazmente la barrera cinética de la reacción redox durante el proceso de reacción de reducción de azufre (SRR), mejorando así la cinética redox general del azufre. Como consecuencia de este mecanismo de transferencia de electrones, el compuesto  $\text{Co}_3\text{O}_4\text{-NC@C}_3\text{N}_4/\text{S}$  exhibe un rendimiento electroquímico notable: la capacidad específica varía de  $1143 \text{ mAh}\cdot\text{g}^{-1}$  a  $0,1 \text{ C}$  a  $575 \text{ mAh}\cdot\text{g}^{-1}$  a  $5 \text{ C}$ , lo que demuestra su capacidad para soportar altas densidades de corriente. Incluso después de 1000 ciclos, el compuesto mantiene una tasa de retención de corriente del 81,3 %, lo que indica su robusta estabilidad cíclica.

En resumen, los cuatro estudios presentados abordan desafíos clave en los MSB mediante la introducción de heteroestructuras, ingeniería de vacantes, estrategias de dopaje y heterojunciones P-N. Estos enfoques innovadores mejoran significativamente los procesos de adsorción y catalíticos en los MSB. Como resultado, los materiales huésped desarrollados en estos estudios exhiben un rendimiento electroquímico excepcional, caracterizado por una alta capacidad específica y una larga vida útil. Cabe destacar que estos materiales mantienen una excelente estabilidad incluso en condiciones de alta carga y electrolito pobre, lo que demuestra aún más su aplicabilidad práctica.

## Acronyms

Backscattered electrons (BSE)  
Cyclic voltammetry (CV)  
Extended x-ray absorption fine structure (EXAFS)  
Electrochemical impedance spectroscopy (EIS)  
Electron Paramagnetic Resonance (EPR)  
Galvanostatic charge-discharge (GCD)  
High-resolution scanning electron microscopy (HR-TEM)  
Lithium polysulfides (LiPSs)  
Lithium-sulfur batteries (LSBs)  
Metal-organic frameworks (MOFs)  
Metal-sulfur batteries (MSBs)  
Nitrogen-doped carbon (NC)  
One-dimensional (1D)  
Polyethylenimine functionalized carbon-carbon quantum dots (PEI-CDots)  
Room temperature sodium-sulfur batteries (RT-SSBs)  
Single-atom catalysts (SACs)  
Secondary electrons (SE)  
Solid electrolyte interface (SEI)  
Sodium polysulfides (SPSs)  
Sulfur reduction reaction (SRR)  
Thermogravimetric analysis (TGA)  
Two-dimensional (2D)  
Three-dimensional (3D)  
Transmission electron microscopy (TEM)  
Transition metal compounds (TMCs)  
Transition metal oxides (TMOs)  
Transition metal sulfides (TMSs)

Transition metal selenides (TMSes)

Transition metal telluride (TMT)

UV-Vis absorption spectroscopy (UV-vis)

X-ray absorption near edge structure (XANES)

X-ray absorption spectroscopy (XAS)

X-ray diffraction (XRD)

X-ray photoelectron spectroscopy (XPS)

Zero-dimensional (0D)

# **Chapter 1**

## **INTRODUCTION**



# 1. Introduction

## 1.1 Background

In recent years, amidst the growing global calls for carbon neutrality and peaking emissions, there has been a significant drive towards the development of multifunctional energy storage devices.<sup>1-4</sup> This surge in interest is primarily fueled by the imperative to reduce reliance on traditional energy sources to achieve carbon neutrality.<sup>5-6</sup> The urgent need for transitioning from conventional energy sources to renewable alternatives is underscored by this goal. Within the realm of renewable energy development, the advancement of energy storage technology has emerged as a critical focus.<sup>7-11</sup> This is because such technology not only mitigates the inherent intermittency and variability of renewable energy sources but also improves the overall efficiency of energy conversion systems.

Lithium-ion batteries have entrenched themselves as a dominant force in the energy storage market, boasting mature technology with high conversion efficiency and rapid response times.<sup>12-14</sup> However, as the demand for battery performance escalates alongside the surge in electric vehicles and next-generation energy systems, the limitations of lithium-ion batteries are becoming apparent.<sup>15-16</sup> Their energy density falls short of meeting the burgeoning market demands. In response, there is a pressing need to develop energy storage devices with higher energy density and specific capacity. MSBs have emerged as a promising candidate, garnering widespread attention from researchers for their remarkable energy density and specific capacity (Figure 1-1).<sup>17-22</sup> For instance, in LSBs, the theoretical specific capacity can reach up to 1675 mAh g<sup>-1</sup>, with an energy density as high as 2600 Wh kg<sup>-1</sup>.<sup>23-24</sup> Moreover, MSBs utilize sulfur as the positive electrode material, which offers the dual advantages of low cost and natural abundance.<sup>25</sup> This inherent characteristic further enhances the appeal of these batteries, driving intensive research and development efforts in the field.

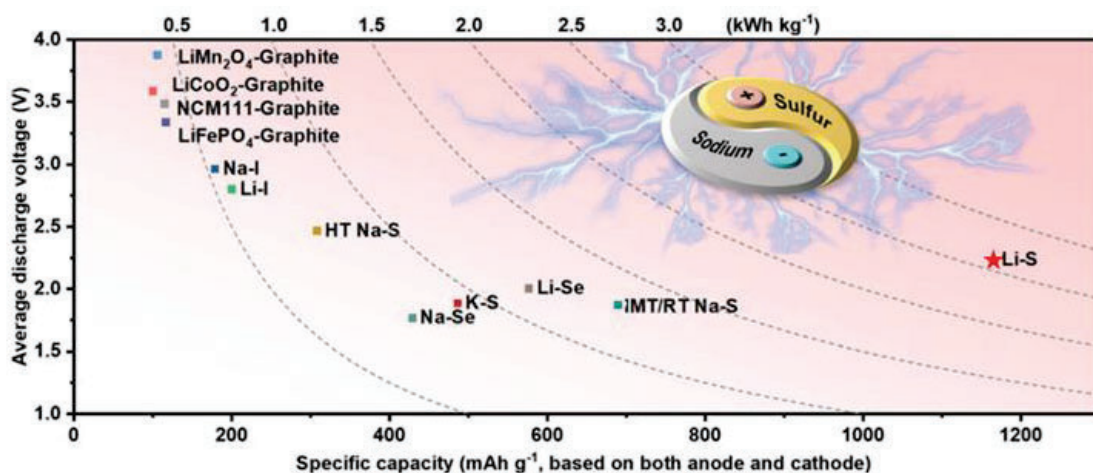
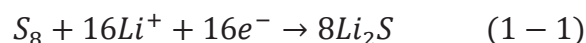


**Figure 1-1.** Comparison of energy density and capacity for different energy storage devices.<sup>26</sup> Reproduced with permission from Ref. [26]. Copyright 2020, Royal Society of Chemistry.

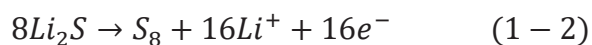
## 1.2 Reaction mechanism of LSBs

LSBs are rechargeable battery systems with sulfur as the cathode (1675 mAh g<sup>-1</sup>) and lithium metal as the anode (3860 mAh g<sup>-1</sup>).<sup>24, 27 28</sup> They typically use ether-based electrolytes (or solid-state electrolytes) and employ porous separators. During the initial charge and discharge processes, the main reaction involves the conversion of S<sub>8</sub> to Li<sub>2</sub>S. The chemical equations in the battery are as follows:<sup>29-32</sup>

Discharge process:



Charge process:



These reactions describe the conversion between S<sub>8</sub> and Li<sup>+</sup>, where Li<sup>+</sup> move between the electrolyte and electrode materials during charging and discharging processes.

In this high theoretical capacity reaction, with a theoretical capacity of 1675 mAh g<sup>-1</sup>, S<sub>8</sub> is reduced to Li<sub>2</sub>S during discharge, while during charging, Li<sub>2</sub>S is oxidized to S<sub>8</sub>. Compared to other energy storage devices, the reaction process of LSBs is more complex due to the necessity for each sulfur atom to undergo a complex two-electron oxidation-reduction reaction.<sup>33</sup>

During discharge, LSBs typically undergo two plateaus. Firstly, S<sub>8</sub> is reduced to soluble polysulfides S<sub>k</sub><sup>-2</sup> (4 ≤ k ≤ 8), and then these soluble polysulfides are further reduced to solid

$\text{Li}_2\text{S}$ . This process can be represented as a solid-liquid-solid transformation. Specifically, when the discharge voltage stabilizes at around 2.35 V, the obtained capacity represents 25% of the theoretical total capacity ( $\sim 419 \text{ mAh g}^{-1}$ ). The electrochemical reduction process in this part mainly involves two stages. Initially, solid  $\text{S}_8$  undergoes migration reactions with  $\text{Li}^+$  and electrons to form soluble long-chain  $\text{Li}_2\text{S}_8$ . Subsequently,  $\text{Li}_2\text{S}_8$  undergoes single-phase liquid-liquid reactions to be reduced to lower-order polysulfides ( $\text{S}_k^{-2}$ ,  $k > 4$ ). When the discharge plateau is  $< 2.1 \text{ V}$ , corresponding to the further reduction of lower-order polysulfides to solid products ( $\text{Li}_2\text{S}_2/\text{Li}_2\text{S}$ ), this portion of capacity constitutes 75 % of the theoretical total capacity ( $\sim 1256 \text{ mAh g}^{-1}$ ).

This process also undergoes two stages of electrochemical reduction. In the first stage, dissolved lower-order polysulfides are reduced to insoluble  $\text{Li}_2\text{S}_2$  or  $\text{Li}_2\text{S}$ , which involves a slow two-phase reaction between liquid and solid phases. In the final stage,  $\text{Li}_2\text{S}_2$  is ultimately reduced to  $\text{Li}_2\text{S}$ . These two low-electrical conductivity solid-phase transition processes can lead to significant polarization and slow sulfur reduction kinetics. During the charging stage, reversible solid-liquid-solid reactions occur, wherein  $\text{Li}_2\text{S}$  is converted to elemental  $\text{S}_8$  via dissolved intermediate polysulfides (Figure 1-2 a-b).

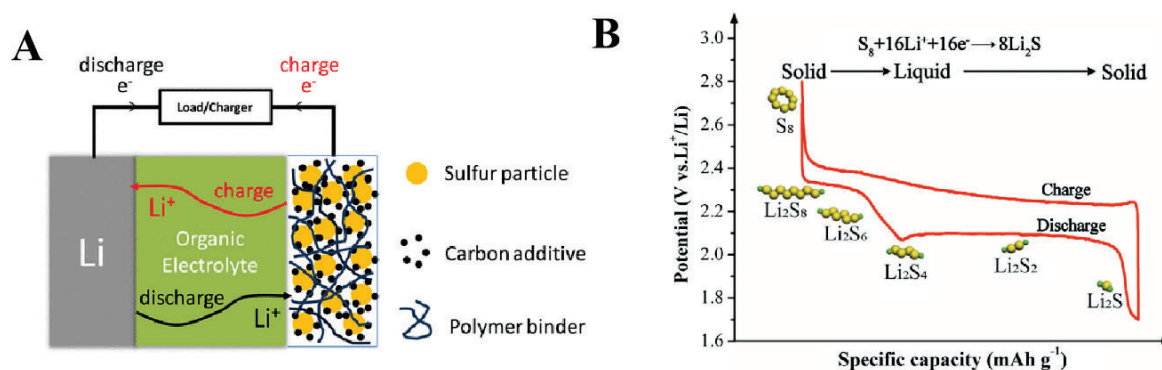
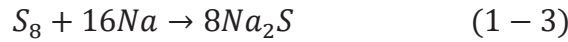


**Figure 1-2.** (a) Schematic configuration of Li-S battery.<sup>34</sup> Reproduced with permission from Ref.<sup>[34]</sup>. Copyright 2014, American Chemical Society. (b) Typical charge-discharge voltage profiles and corresponding reaction mechanism of Li-S battery.<sup>35</sup> Reproduced with permission from Ref.<sup>[35]</sup>. Copyright 2017, Wiley-VCH.

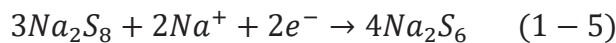
### 1.3 Reaction mechanism of RT-SSBs

The cathode of the RT-SSBs system undergoes a reversible double-electron reaction between  $\text{Na}^+$  and  $\text{S}_8$ . the RT-SSBs mainly consists of a sulfur positive electrode, a sodium negative electrode, a glass fiber separator, and an ester electrolyte. The sulfur cathode can provide a high theoretical specific capacity of  $1675 \text{ mA h g}^{-1}$ , primarily involving the conversion between  $\text{S}_8$  and  $\text{Na}_2\text{S}$ , as shown in the reaction equation:<sup>36-38</sup>

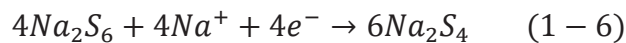


However, multiple complex chemical reactions typically occur on the cathode. The operating voltage of the RT-SSBs generally ranges from 0.8 to 2.8 V, mainly due to sulfur oxidation-reduction reactions within this voltage range. Normally, sulfur exists in the form of cyclical  $\text{S}_8$ . During discharge,  $\text{S}_8$  gradually reduces to form long-chain polysulfides ( $\text{Na}_2\text{S}_8$ ,  $\text{Na}_2\text{S}_6$ ), middle-chain polysulfides ( $\text{Na}_2\text{S}_4$ ,  $\text{Na}_2\text{S}_3$ ), and ultimately short-chain polysulfides ( $\text{Na}_2\text{S}_2$  and  $\text{Na}_2\text{S}$ ) at 0.8 V. During charging, short-chain polysulfides are continuously oxidized to form middle-chain polysulfides and finally long-chain polysulfides within the 0.8-2.8 V range.

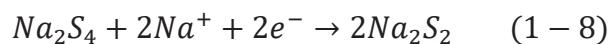
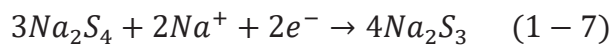
Using  $\text{S}_8$  as the initial cathode material, the primary reaction occurs at a voltage of 2.2 V, where  $\text{S}_8$  is reduced to form long-chain sodium polysulfides (SPSs) via a solid-liquid reaction:<sup>36, 39-40</sup> (Figure 1-2 a-b)



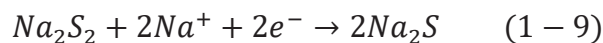
In the subsequent steps, the reactions involve voltages between 2.2 and 1.65 V, representing a liquid-liquid reaction from long-chain SPSs to middle-chain SPSs:



At a voltage of 1.65V, the main reaction involves a liquid-solid reaction of  $\text{Na}_2\text{S}_4$  to produce short-chain NPSs:



Finally, at voltages below 1.2V, a solid-solid reaction occurs:



In summary, the reactions involving SPSs are simultaneous, making the conversion reactions

relatively complex. Furthermore, during the reduction of long-chain SPSs to short-chain SPSs, SPSs dissolve into the electrolyte. Additionally, the poor conductivity of insoluble short-chain SPSs like  $\text{Na}_2\text{S}_2$  and  $\text{Na}_2\text{S}$  may lead to sluggish reaction kinetics.

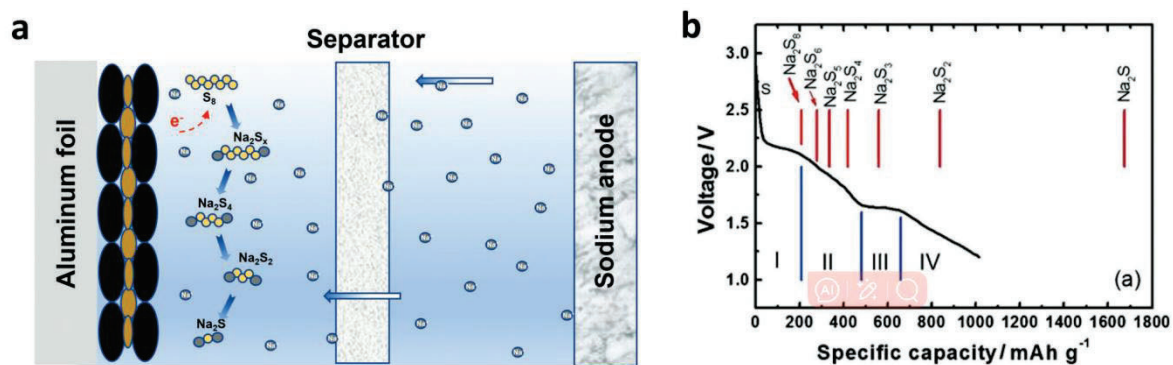


**Figure 1-2.** (a) Schematic diagram of the principle of the redox reaction of sulfur cathode for the RT-SSBs. (b) Theoretical versus practical discharge capacities.<sup>41</sup> Reproduced with permission. Reproduced with permission from Ref. <sup>[41]</sup> Copyright 2014, Wiley-VCH.

## 1.4 The challenges for MSBs

### 1.4.1 Sulfur cathode

In practical applications, MSBs face the following challenges for sulfur cathode.

- 1) During the cycling of batteries, dissolved reaction intermediates can result in the depletion of active materials. In particular, intermediate long-chain polysulfides (such as  $\text{Li}/\text{Na}_2\text{S}_4$  to  $\text{Li}/\text{Na}_2\text{S}_8$ ) tend to dissolve readily in the electrolyte, causing continuous dissolution of active materials into the electrolyte.<sup>42-43</sup> As a consequence, some active materials may remain in a dissolved state, hindering their effective participation in the charge and discharge processes. This, in turn, diminishes the energy density and power density of the battery.
- 2) The conductivity of the cathode material sulfur and its reaction product lithium/sodium sulfide is relatively low.<sup>44-45</sup> This characteristic impedes the mobility of ions within the electrode. Consequently, during the discharge process, lithium/sodium sulfide may precipitate on the cathode surface, forming an insulating layer. This insulating layer can lead to the development of an insulating interface on the cathode surface, thereby impacting the cycling performance of the cathode.

3) During the process of lithium/sodiumization, sulfur experiences considerable volume changes.<sup>46-47</sup> This is primarily because there exists a density disparity between sulfur and polysulfides. Consequently, a significant expansion in volume occurs when sulfur undergoes complete lithium/sodium conversion into lithium and sodium sulfide. Conversely, during the reverse process, the volume undergoes a sharp contraction. This change in volume can result in the collapse and damage of the electrode structure.

### **1.4.2 Metal anode**

In addition, MSBs also face some challenges at the anode.

1) The shuttle effect presents a significant challenge for MSBs. This phenomenon involves the dissolution of long-chain polysulfides in the electrolyte, which can migrate to the anode through chemical reduction and form low-valent compounds. These compounds are not constrained by polarity, allowing some of them to return to the sulfur cathode and undergo oxidation once again. The shuttle effect leads to a decrease in the charge and discharge capacity of the battery system and lowers the coulombic efficiency during cycling. Moreover, it results in severe self-discharge during standing periods, significantly diminishing the practical utility of MSBs.

2) Uneven deposition at the solid electrolyte interface (SEI) presents another challenge for MSBs. At the interface between the metal negative electrode and the electrolyte, a reaction occurs between the electrolyte and the negative electrode material, forming a SEI film. While this SEI membrane permits ion passage, it inhibits electron flow. However, in many instances, the SEI is not uniformly dense and contains various pores. These pores enable continued contact and reaction between the electrolyte and the negative electrode material, leading to the ongoing consumption of metal and electrolyte. Consequently, this results in reduced reversibility and a shortened service life of the battery.

3) Metal dendrite growth poses another significant challenge. Due to the non-uniformity of metal deposition, dendrite formation can occur. These dendrites can lead to extensive rupture of the SEI film, resulting in further consumption of metal and electrolyte, thereby impacting the battery's lifespan. Additionally, locally thickened SEI films can increase impedance,

consequently reducing coulombic efficiency.

## **1.5 Technical modification**

### **1.5.1 Modification of cathode materials**

#### **1.5.1.1 Carbon materials**

Carbon materials offer numerous advantages, including excellent electrical conductivity, high porosity, strong adsorption capacity, and cost-effectiveness.<sup>48-52</sup> By utilizing carbon materials to construct a conductive network, it is possible to address the insulation deficiencies of sulfur elements. The porosity of carbon materials facilitates the uniform distribution of sulfur into the interstices, thereby enhancing sulfur loading and providing additional active sites. Moreover, the intricate pore structure of carbon materials can physically constrain polysulfide locations, preventing their dissolution and diffusion, and thus mitigating the "shuttle effect". Additionally, the superior mechanical strength and porous structure of carbon materials can alleviate the volume expansion and contraction issues that occur during charging and discharging in MSBs. Currently, sulfur/carbon composites, including sulfur/porous carbon,<sup>53</sup> sulfur/carbon nanotube,<sup>54</sup> sulfur/graphene,<sup>55</sup> and sulfur/carbon fiber composites,<sup>56</sup> are extensively studied. Through systematic design and fabrication, these materials can effectively enhance the performance of MSBs, thereby opening up new possibilities for their application in energy storage.

#### **1.5.1.2 Transition metal oxides (TMOs)**

TMOs typically contain oxygen anions, giving them highly polar surfaces.<sup>57</sup> Due to the strong bonding between metal and oxygen in TMOs, they are less soluble in most organic solvents. In comparison, nano TMOs have more polar active sites than nano carbon materials, which can be utilized for adsorbing polysulfides.<sup>58</sup> Additionally, TMOs can significantly enhance the volumetric energy density of MSBs.



### 1.5.1.3 Transition metal sulfides (TMSs)

With the continuous advancement of synthetic methods for TMSs, researchers have begun to explore their application in the cathode materials of MSBs.<sup>59-61</sup> TMSs exhibit strong affinity with sulfur-containing substances, thereby effectively limiting the loss of active materials in the cathode.<sup>62</sup> This characteristic is crucial for MSBs as one of their main challenges is the dissolution and diffusion of sulfur, leading to a decrease in battery performance. By incorporating TMSs into the cathode material, the dissolution and diffusion of sulfur can be effectively suppressed, thereby improving the battery's cycle life and energy density.<sup>24</sup>

One potential advantage of TMSs as cathode materials for MSBs are their abundant controllability.<sup>63</sup> By adjusting the synthesis methods, material structure, and composition, precise design of TMSs materials can be achieved to meet the requirements of different battery applications. Additionally, TMSs possess high conductivity and chemical stability, which contribute to enhancing the performance of the battery.<sup>64-65</sup>

Although TMSs hold promising prospects for application in MSBs, they also face challenges such as improving material synthesis cost, cycle stability, and kinetic performance. Therefore, continuous in-depth research and development are needed in the future to realize the commercial application of TMSs in MSBs.

### 1.5.1.4 Transition metal selenides (TMSeS)

TMSeS are compounds composed of transition metals and selenium. They possess unique physical and chemical properties, including high electrical conductivity, excellent catalytic activity, and good chemical stability.<sup>66</sup> TMSeS include cobalt selenide (CoSe),<sup>67</sup> nickel selenide (NiSe),<sup>68</sup> molybdenum diselenide (MoSe<sub>2</sub>),<sup>69</sup> and tungsten diselenide (WSe<sub>2</sub>).<sup>46, 70</sup> Due to their abundant surface active sites and variable oxidation states, TMSeS are extensively researched and applied in fields such as electrochemical energy storage, catalysis, and sensing.

#### *Advantages in Electrochemical Energy Storage*

TMSeS exhibit significant advantages in the field of electrochemical energy storage, primarily in the following aspects:

#### 1. High Electrical Conductivity



TMSes typically have high electrical conductivity, which helps to improve the overall conductivity of electrode materials. This enhancement in conductivity boosts the efficiency of electrochemical reactions, which is crucial for the charge and discharge processes of batteries. Consequently, TMSes can effectively reduce resistance, increasing both energy density and power density of the batteries.

## 2. Multiple Oxidation States

The metal elements in TMSes can exist in various oxidation states, endowing them with high catalytic activity in electrochemical reactions. For instance, in LSBs, TMSes can effectively catalyze the conversion of polysulfides, increasing sulfur utilization and enhancing battery performance

## 3. Rich Active Sites

The surfaces of selenide materials are typically rich in active sites, which contribute to increasing the rate and efficiency of electrochemical reactions. This is particularly advantageous in electrocatalytic reactions

## 4. Corrosion Resistance

TMSes possess good corrosion resistance and chemical stability, allowing them to remain stable in the working environment of batteries and reducing the degradation of electrode materials

## 5. Stable Structure

These materials have stable crystal structures, which provide excellent long-term cycling stability, thereby improving the lifespan of batteries.

## 6. Tunable Physical and Chemical Properties

Through adjustments in synthesis methods, the morphology and structure of TMSes can be precisely controlled at the nanoscale. This optimization can enhance their physical and chemical properties. For example, altering the morphology of selenides can increase their surface area and the number of active sites.

### *Multifunctional Applications*

**Lithium-Ion Batteries:** TMSes used as electrode materials in lithium-ion batteries exhibit high capacity and long cycle life, significantly boosting the energy density of the batteries.

**Sodium-Ion Batteries:** Similarly, TMSes demonstrate good electrochemical performance in

sodium-ion batteries, making them a promising alternative to lithium-ion batteries.

Supercapacitors: In supercapacitors, TMSes provide high power density and energy density due to their high conductivity and large surface area.

LSBs: TMSes can effectively catalyze the conversion of sulfur compounds, increasing sulfur utilization and reducing polysulfide dissolution and loss, thus improving the performance of LSBs.

TMSes offer remarkable advantages in electrochemical energy storage, including high electrical conductivity, excellent catalytic activity, good chemical stability, and tunable physical and chemical properties. These features make TMSes highly promising materials for various energy storage devices. With further material design and engineering optimization, the application prospects of TMSes will become even broader.

#### **1.5.1.5 Transition metal tellurides (TMTs)**

TMTs are compounds composed of transition metals and tellurium. They exhibit unique physical and chemical properties, including high electrical conductivity, excellent catalytic activity, and good thermal stability. TMTs include nickel telluride ( $\text{NiTe}_2$ ),<sup>71</sup> cobalt telluride ( $\text{CoTe}_2$ ),<sup>72</sup> zinc telluride ( $\text{ZnTe}$ ),<sup>73</sup> and molybdenum telluride ( $\text{MoTe}_2$ ),<sup>74</sup>. Due to their diverse chemical compositions and unique crystal structures, these materials are widely used in electronic devices, optoelectronic devices, thermoelectric materials, and electrochemical energy storage.

TMTs exhibit several advantageous properties that make them highly suitable for use in MSBs, such as LSBs and RT-SSBs. These advantages include high electrical conductivity, strong catalytic activity, and excellent stability, which are crucial for enhancing the performance of MSBs.

##### **1. High Electrical Conductivity**

TMTs generally have high electrical conductivity, which is essential for improving the overall conductivity of the electrode materials in MSBs. This enhanced conductivity facilitates efficient charge transfer and reduces the internal resistance of the battery, thereby improving its energy density and power output.

## 2. Strong Catalytic Activity

TMTs possess excellent catalytic properties that can significantly enhance the redox reactions of sulfur species. Their catalytic activity helps in the effective conversion of polysulfides during the charge and discharge cycles, mitigating the shuttle effect (the migration of polysulfides between the cathode and anode) and improving the utilization of sulfur. This leads to higher specific capacities and better cycling stability.

## 3. Enhanced Polysulfide Adsorption

The surface of TMTs provides abundant active sites that can strongly adsorb polysulfide intermediates. This adsorption capability helps in retaining the polysulfides within the cathode region, reducing their dissolution and preventing capacity loss. This property is particularly beneficial for maintaining the long-term stability of MSBs.

## 4. Structural Stability

TMTs exhibit excellent structural stability, which is crucial for the longevity and durability of MSBs. Their robust structure can withstand the volume changes associated with the repeated formation and dissolution of sulfur species during cycling, thereby preventing electrode degradation and extending the battery's lifespan.

## 5. Tunable Properties

The physical and chemical properties of TMTs can be finely tuned through various synthesis methods. By adjusting parameters such as particle size, morphology, and composition, it is possible to optimize the performance of TMTs for specific applications in MSBs. For instance, increasing the specific surface area can enhance the active sites available for sulfur reactions, while modifying the electronic structure can improve catalytic efficiency.

## 6. Formation of Heterostructures

TMTs can form heterostructures with other materials, which can further enhance their performance in MSBs. These heterostructures can create synergistic effects that improve ionic and electronic conductivity, enhance catalytic activity, and provide better structural integrity. The combination of different materials in a heterostructure can also introduce built-in electric fields, promoting faster ion diffusion and charge transfer.

## 7. Multi-Valent States

Transition metal elements in tellurides can exist in multiple valence states, enabling them to

participate in various redox reactions. This multivalence provides additional pathways for electron transfer, enhancing the overall electrochemical performance of the battery. It also contributes to better charge storage capacity and improved cycling stability.

TMTs offer a range of advantages that make them highly effective for use in MSBs. Their high electrical conductivity, strong catalytic activity, excellent polysulfide adsorption capabilities, structural stability, and tunable properties contribute to enhanced battery performance. By leveraging these unique properties, TMTs can significantly improve the energy density, efficiency, and longevity of MSBs, making them a promising material for next-generation energy storage solutions.

#### **1.5.1.6 Sulfur/conductive polymer**

Sulfur/conductive polymer composite materials combine the advantages of sulfur and conductive polymers. Conductive polymers exhibit good conductivity, promoting electron transfer efficiency, and possess good toughness, which can alleviate sulfur volume changes during cycling.<sup>75-76</sup> In the early stages of research, researchers primarily used polymers as coating materials for the cathode of MSBs.

As understanding of MSBs deepens, sulfur/conductive polymer composite materials have gradually become important components of MSBs for cathode.<sup>76-78</sup> These composites not only provide good conductivity and mechanical support but also effectively limit sulfur dissolution and diffusion, thereby improving the battery's cycle life and energy density.

Furthermore, sulfur/conductive polymer composites offer design flexibility, allowing precise control of battery performance by adjusting the composition and structure of the materials. For example, variations in the type and content of conductive polymers, as well as the dispersion state and loading of sulfur, can meet the requirements of different battery applications.

Therefore, sulfur/conductive polymer composite materials hold broad prospects in the field of MSBs, offering new solutions to address the challenges faced by MSBs.

### **1.5.2 Morphology classification**

Due to the poor ionic conductivity and electrolyte wettability of sulfur, metal ions (such as  $\text{Li}^+$ ,

Na<sup>+</sup>, etc.) exhibit significant energy barriers for migration throughout the cathode. To accelerate the kinetics of sulfur oxidation-reduction, the morphology of host materials can be modified to enhance the migration rate of metal ions within the cathode. Host materials for sulfur can be classified based on dimensions into zero-dimensional (0D), one-dimensional (1D), (two-dimensional (2D), and three-dimensional (3D) structures.

### 1.5.2.1 Zero-dimensional structures (0D)

In 0D structures, nanoparticles and nanoclusters are predominantly found.<sup>79-80</sup> This architecture boasts a high surface area and short ion transport pathways, which facilitate an increase in the electrochemical reaction rate. Quantum dots and clusters represent examples of 0D materials. However, due to the tendency of 0D materials to aggregate, they are not suitable for standalone use as sulfur host materials. To address the challenges associated with 0D materials in practical applications, a combination of 0D materials and carbon is often employed. This combination leads to composite materials with close to 100 % exposed sites, significantly enhancing performance in the realm of energy storage. For instance, Xiong et al. devised a composite cathode incorporating polyethylenimine functionalized carbon-carbon quantum dots (PEI-CDots) for sulfur-based batteries.<sup>81</sup> This composite exhibited notable cycling stability and high areal sulfur loading, primarily attributed to the enhancement of ionic conductivity around the solid-electrolyte interface facilitated by the carbon quantum dots (Figure 1-3).

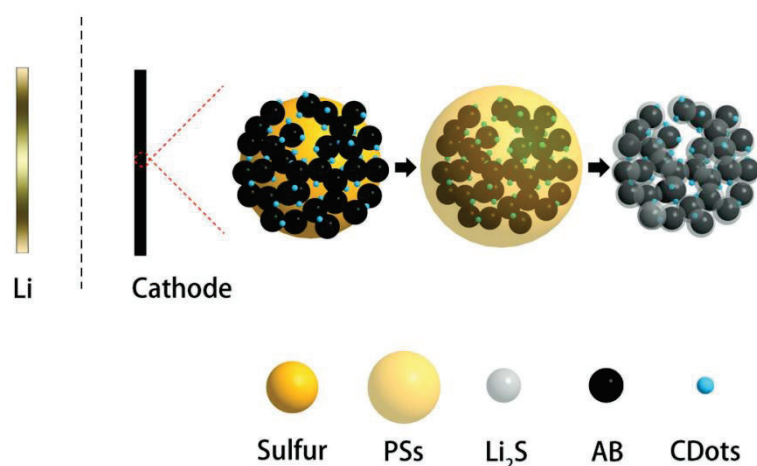


**Figure 1-3.** Synthesis process of PEI-CDots@AB/S cathode.<sup>81</sup> Reproduced with permission.<sup>[81]</sup>

Copyright 2019, Wiley-VCH.

### 1.5.2.2 One-dimensional structures (1D)

In 1D structures, materials are typically arranged in lines or fibers, such as nanowires<sup>82</sup> and nanorods.<sup>83-84</sup> The longitudinal orientation of this structure provides rapid ion diffusion pathways, thereby enhancing the reaction rate. Initially, carbon nanotubes and carbon fibers were recognized as effective carriers for sulfur immobilization in MSBs,<sup>54, 85-87</sup> owing to their high specific surface area, pore volume, and robust physical confinement capabilities against polysulfides. Electrospinning, compared to traditional gas/liquid phase growth synthesis methods, holds significant promise for fabricating one-dimensional inorganic compounds with adjustable porosity and structure.<sup>88-89</sup>

For instance, Yao et al. synthesized a dual-functional flexible free-standing carbon nanofiber conductive framework in situ embedded with TiN-VN heterostructures (TiN-VN@CNFs) as an advanced host simultaneously for both the sulfur cathode (S/TiN-VN@CNFs) and the lithium anode (Li/TiN-VN@CNFs) is designed (Figure 1-4). The synergistic effects of TiN-VN and one-dimensional carbon fibers endow the host material with exceptional catalytic and adsorption properties in LSBs.<sup>90</sup>

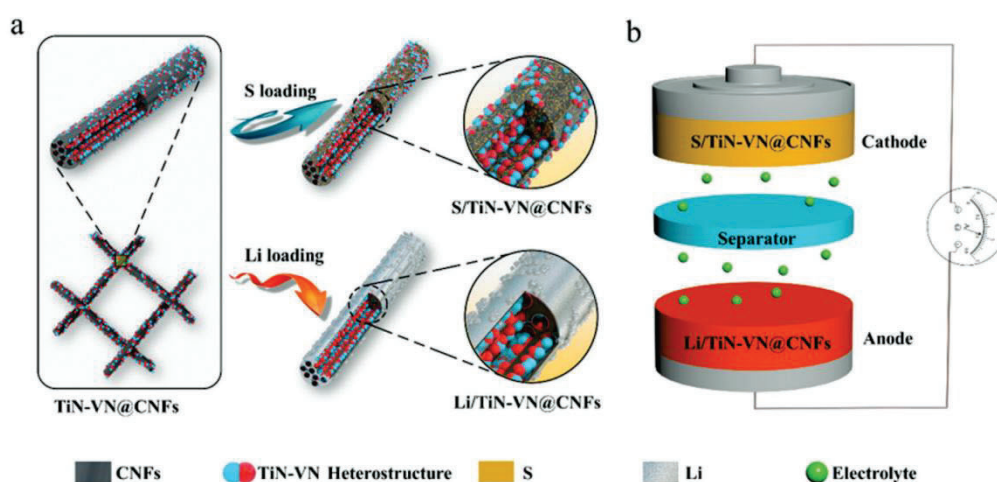


**Figure 1-4.** (a) Synthesis schematic for the S/TiN-VN@CNFs cathode and the Li/TiN-VN@CNFs anode. (b) Schematic diagram of the S/TiN-VN@CNFs|| Li/TiN-VN@CNFs full battery configuration.<sup>90</sup> Reproduced with permission. <sup>[90]</sup> Copyright 2020, Wiley-VCH.

### 1.5.2.3 Two-dimensional structures (2D)

2D materials are proving to be valuable as emerging cathode hosts due to their infinite lateral dimensions (Figure 1-5).<sup>91</sup> These materials are studied based on differences in anisotropy and the crystal planes exposing catalytically active sites, with a focus on carbon materials, sheet metal oxides/selenides/nitrides,<sup>92</sup> layered metal hydroxides,<sup>93</sup> and metal-organic frameworks (MOFs).<sup>94</sup> The relatively weak van der Waals force between atoms in 2D layered materials allows for the acceleration of metal ion diffusion by increasing the interlayer spacing.

For example, Xiong et al. designed layered silicate materials with larger interlayer spacing, effectively reducing the diffusion barrier for  $\text{Li}^+$ . This approach enhances the performance of the cathode by facilitating faster ion diffusion.<sup>95</sup>

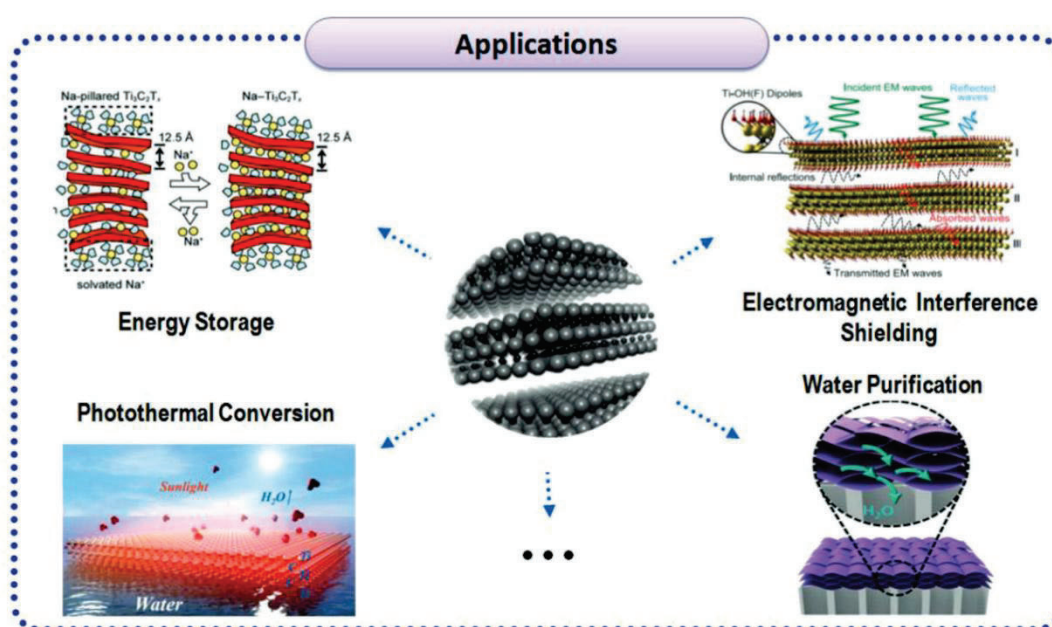


**Figure 1-5.** Applications of  $\text{Ti}_3\text{C}_2\text{T}_x$  MXene. Reproduced with permission.<sup>[96]</sup> Copyright 2018, Wiley-VCH.

### 1.5.2.4 Three-dimensional structures (3D)

3D electrode materials are extensively employed in MSBs owing to their diverse morphology. Research on three-dimensional materials primarily explores hollow,<sup>96</sup> core-shell,<sup>97</sup> and multi-shell<sup>98</sup> structures. These structures serve dual purposes: they mitigate volume expansion of



electrode materials during charge and discharge processes, and they provide ample space to confine active sulfur material.

For instance, Li et al. developed a new physical and chemical entrapment strategy is based on a highly efficient sulfur host, namely hollow carbon nanofibers (HCFs) filled with  $\text{MnO}_2$  nanosheets. Benefiting from both the HCFs and birnessite-type  $\text{MnO}_2$  nanosheets, the  $\text{MnO}_2@\text{HCF}$  hybrid host not only facilitates electron and ion transfer during the redox reactions, but also efficiently prevents polysulfide dissolution.<sup>99</sup>

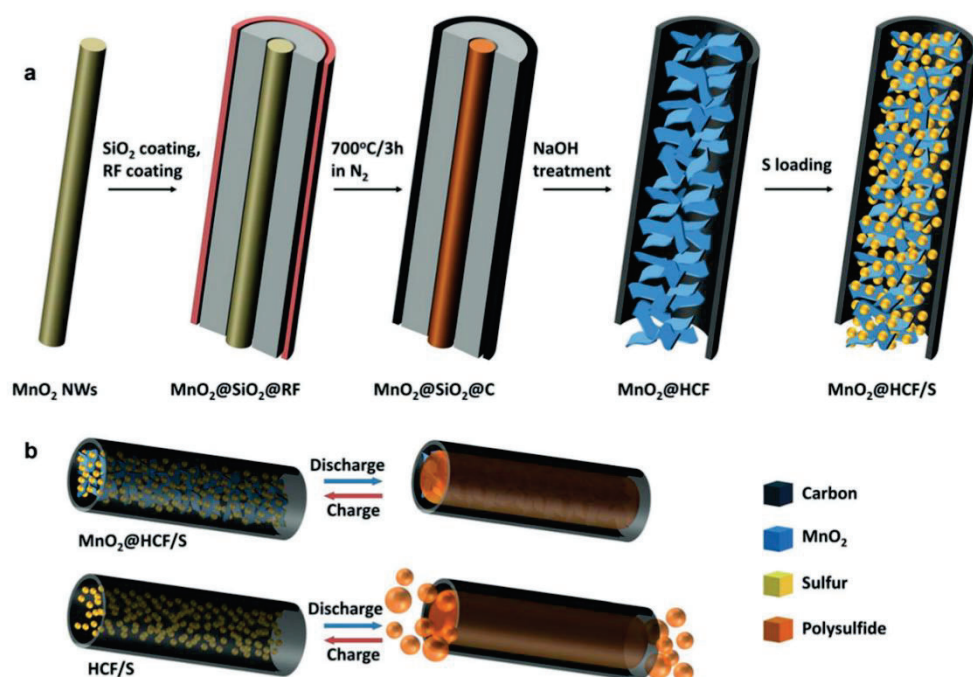


**Figure 1-6.** (a) Synthesis of the  $\text{MnO}_2@\text{HCF}/\text{S}$  composite. (b) Advantages of the  $\text{MnO}_2@\text{HCF}/\text{S}$  composite over HCF/S.<sup>99</sup> Reproduced with permission.<sup>[100]</sup> Copyright 2015, Wiley-VCH.

## 1.6 Strategies to enhance the adsorption-catalysis of polysulfide conversion.

### 1.6.1 Heterojunction engineering

To maximize the catalytic effects in MSBs, it is imperative to design composite materials. The catalytic activity is intimately linked with the electronic band structure, thus necessitating strategies to finely tune the electronic properties of active sites within composite materials. At



the material structure level, interface engineering offers a potent approach to tailor the electronic properties of active sites, thereby enhancing catalytic performance.<sup>100-102</sup> By strategically manipulating the interfaces between different components within composite materials, it is possible to adjust charge transfer processes, electronic band alignments, and surface reactivity, ultimately improving electrocatalytic activity and selectivity.

In the field of electrochemistry, heterogeneous structures formed by semiconductors with different band gaps find broad applications, such as in electrocatalysis,<sup>103-105</sup> batteries,<sup>106-107</sup> and supercapacitors.<sup>108-109</sup> At the interfaces of two different semiconductors, phenomena like abundant phase boundaries, charge accumulation/depletion, electric fields, and band bending are observed.<sup>110</sup> These peculiar regions play a crucial role in facilitating the diffusion of ions and electrons, thereby accelerating the conversion reactions of polysulfides in MSBs.

Li et al. successfully synthesized a multi-level host material with rich defects,  $\text{Co}_3\text{O}_4\text{-TiO}_2$  p-n heterojunction structure, for MSBs. The heterojunction structure formed by  $\text{Co}_3\text{O}_4$  and  $\text{TiO}_2$  induces an intrinsic electric field at the interface, thereby enhancing the adsorption and catalytic performance towards polysulfides.<sup>111</sup>

### 1.6.2 Defect engineering

At the atomic level, vacancy engineering, particularly anion vacancies, has been demonstrated as a successful method to significantly enhance material performance by altering the stoichiometry of compounds.<sup>112-113</sup> For the cathode of MSBs, introducing anion vacancies into the sulfur host not only increases the number of charge carriers within the crystal and changes the electronic structure near defect sites, but also effectively activates unpaired cations to capture polysulfides,<sup>114-116</sup> thereby improving sulfur utilization.

For example, Wang et al. employed an acid-etching method to fabricate  $\text{ZnS}$  nanotubes with abundant sulfur vacancies, which were then supported on separate carbon cloth to serve as LSB electrodes.<sup>117</sup> The generation of sulfur vacancies in  $\text{ZnS}$  effectively adjusts its electronic structure, enhances its interaction with active sulfur, promotes ion/electron transfer, and ultimately enhances LSB performance.

### 1.6.3 Lattice distortion engineering

Inducing lattice distortion by adjusting the d-spacing within the lattice has been considered as an alternative strategy to optimize the catalytic performance of host materials in MSBs.<sup>118</sup> Theoretically, this change in the symmetry of the crystal structure causes a displacement of the positive/negative charge centers within the unit cell, creating a built-in electric field that promotes charge transfer.<sup>119-120</sup>

Wang et al. prepared  $\text{Co}_{0.9}\text{Zn}_{0.1}\text{Te}_2@\text{NC}$  by uniformly doping zinc atoms into the  $\text{CoTe}_2$  lattice. Experimental and theoretical results show that lattice strain changes the coordination environment of cobalt atoms and adjusts the d-band center of the catalyst. This adjustment, in turn, promotes the adsorption and catalysis of polysulfides by host materials.<sup>120</sup>

### 1.6.4 Doping engineering

Doping strategies are recognized as effective means to enhance the conductivity,<sup>121</sup> electronic configuration,<sup>122</sup> and surface properties<sup>28</sup> of host materials. In the realm of carbon materials, the incorporation of various elements such as boron (B), nitrogen (N), and S has garnered significant attention.<sup>123</sup> Anionic doping, for instance, serves to modulate the d-band center of doped metal compounds, thereby augmenting the polysulfide affinity and improving sulfur utilization efficiency.<sup>124-125</sup> For instance, Zhang et.al synthesized boron-doped  $\text{MoS}_2$ , which demonstrated prolonged cycle life in LSBs.<sup>126</sup> This enhancement can be primarily attributed to the favorable orbital orientation of boron atoms and the presence of a perpendicular vacancy  $\sigma$  orbital, maximizing overlap with sulfur's frontal orbital, thereby ensuring full activation and facilitating improved kinetics in the formation and dissolution of  $\text{Li}_2\text{S}$ .

Conversely, cation-doped compounds offer a broader spectrum of functionalities. For example, Zhang et al. introduced cobalt doping into  $\text{Ni}_2\text{P}$ , yielding  $\text{Ni}_2\text{Co}_4\text{P}_3$ . In comparison to pure  $\text{Ni}_2\text{P}$ ,  $\text{Ni}_2\text{Co}_4\text{P}_3$  boasts a higher d-band center, enhancing the adsorption of LiPSs and reducing the potential energy barrier for S-S bond cleavage.<sup>127</sup> This modification effectively accelerates the subsequent lithiation process.

### 1.6.5 Single atom strategy

Single-atom materials have demonstrated exceptional capabilities in enhancing the kinetics of host materials transformation, owing to their high atom utilization efficiency.<sup>128-129</sup> Ever since Wan's group<sup>130</sup> pioneered the incorporation of single-atom cobalt into graphene as a sulfur host, single-atom catalysts (SACs) have gained widespread adoption in sulfur hosting applications.<sup>131-134</sup> Precisely selecting the types of metal centers and fine-tuning their coordination environments are recognized as two effective strategies for optimizing catalytic performance. Cheng et.al synthesized a series of SACs (with metals including Mn, Cu, Cr, and Ti) embedded within three-dimensional carbon foam to elucidate the influence of metal centers on improving the reaction kinetics of LiPSs in LSBs.<sup>133</sup> Furthermore, the catalytic activity of SACs can be further enhanced by adjusting their unique coordination structures. Yang investigated the correlation between Co SACs with varying N coordination numbers and the corresponding catalytic efficiencies towards LiPSs.<sup>134</sup>

### 1.7 References

1. Tan, K. M.; Babu, T. S.; Ramachandaramurthy, V. K.; Kasinathan, P.; Solanki, S. G.; Raveendran, S. K., Empowering Smart Grid: A Comprehensive Review of Energy Storage Technology and Application with Renewable Energy Integration. *Journal of Energy Storage* **2021**, *39*, 102591.
2. Chakraborty, M. R.; Dawn, S.; Saha, P. K.; Basu, J. B.; Ustun, T. S. A Comparative Review on Energy Storage Systems and Their Application in Deregulated Systems *Batteries* [Online], 2022.
3. Ma, J.; Yang, L.; Wang, D.; Li, Y.; Xie, Z.; Lv, H.; Woo, D., Digitalization in Response to Carbon Neutrality: Mechanisms, Effects and Prospects. *Renewable and Sustainable Energy Reviews* **2024**, *191*, 114138.
4. Chen, S.; Zhang, C.; Lu, X., Energy Conversion from Fossil Fuel to Renewable Energy. In *Handbook of Air Quality and Climate Change*, Akimoto, H.; Tanimoto, H., Eds. Springer Nature Singapore: Singapore, 2020; pp 1-44.
5. Woon, K. S.; Phuang, Z. X.; Taler, J.; Varbanov, P. S.; Chong, C. T.; Klemeš, J. J.; Lee, C. T., Recent Advances in Urban Green Energy Development towards Carbon Emissions Neutrality. *Energy* **2023**, *267*, 126502.
6. Zhang, Z.; Hu, G.; Mu, X.; Kong, L., From Low Carbon to Carbon Neutrality: A Bibliometric Analysis of the Status, Evolution and Development Trend. *Journal of Environmental Management* **2022**, *322*, 116087.
7. Arsad, A. Z.; Hannan, M. A.; Al-Shetwi, A. Q.; Mansur, M.; Muttaqi, K. M.; Dong, Z. Y.; Blaabjerg, F., Hydrogen Energy Storage Integrated Hybrid Renewable Energy Systems: A Review Analysis for Future Research Directions. *International Journal of Hydrogen Energy* **2022**, *47* (39), 17285-17312.
8. Vlad, A.; Singh, N.; Galande, C.; Ajayan, P. M., Design Considerations for Unconventional Electrochemical Energy Storage Architectures. *Advanced Energy Materials* **2015**, *5* (19), 1402115.

9. Smdani, G.; Islam, M. R.; Ahmad Yahaya, A. N.; Bin Safie, S. I., Performance Evaluation of Advanced Energy Storage Systems: A Review. *Energy & Environment* **2022**, *34* (4), 1094-1141.
10. Zhao, X.; Sánchez, B. M.; Dobson, P. J.; Grant, P. S., The Role of Nanomaterials in Redox-Based Supercapacitors for Next Generation Energy Storage Devices. *Nanoscale* **2011**, *3* (3), 839-855.
11. Palomares, V.; Serras, P.; Villaluenga, I.; Hueso, K. B.; Carretero-González, J.; Rojo, T., Na-ion Batteries, Recent Advances and Present Challenges to Become Low Cost Energy Storage Systems. *Energy & Environmental Science* **2012**, *5* (3), 5884-5901.
12. Wang, J.; Ma, J.; Zhuang, Z.; Liang, Z.; Jia, K.; Ji, G.; Zhou, G.; Cheng, H.-M., Toward Direct Regeneration of Spent Lithium-Ion Batteries: A Next-Generation Recycling Method. *Chemical Reviews* **2024**, *124* (5), 2839-2887.
13. Alkhedher, M.; Al Tahhan, A. B.; Yousaf, J.; Ghazal, M.; Shahbazian-Yassar, R.; Ramadan, M., Electrochemical and Thermal Modeling of Lithium-Ion Batteries: A Review of Coupled Approaches for Improved Thermal Performance and Safety Lithium-Ion Batteries. *Journal of Energy Storage* **2024**, *86*, 111172.
14. Lv, C.; Zhou, X.; Zhong, L.; Yan, C.; Srinivasan, M.; Seh, Z. W.; Liu, C.; Pan, H.; Li, S.; Wen, Y.; Yan, Q., Machine Learning: An Advanced Platform for Materials Development and State Prediction in Lithium-Ion Batteries. *Advanced Materials* **2022**, *34* (25), 2101474.
15. Zheng, Y.; Che, Y.; Hu, X.; Sui, X.; Stroe, D.-I.; Teodorescu, R., Thermal State Monitoring of Lithium-Ion Batteries: Progress, Challenges, and Opportunities. *Progress in Energy and Combustion Science* **2024**, *100*, 101120.
16. Wang, Y.; Lai, X.; Chen, Q.; Han, X.; Lu, L.; Ouyang, M.; Zheng, Y., Progress and challenges in Ultrasonic Technology for State Estimation and Defect Detection of Lithium-Ion Batteries. *Energy Storage Materials* **2024**, *69*, 103430.
17. Zhao, M.; Li, B.-Q.; Zhang, X.-Q.; Huang, J.-Q.; Zhang, Q., A Perspective toward Practical Lithium–Sulfur Batteries. *ACS Central Science* **2020**, *6* (7), 1095-1104.
18. Chen, Y.; Wang, T.; Tian, H.; Su, D.; Zhang, Q.; Wang, G., Advances in Lithium–Sulfur Batteries: From Academic Research to Commercial Viability. *Advanced Materials* **2021**, *33* (29), 2003666.
19. Wang, M.; Bai, Z.; Yang, T.; Nie, C.; Xu, X.; Wang, Y.; Yang, J.; Dou, S.; Wang, N., Advances in High Sulfur Loading Cathodes for Practical Lithium-Sulfur Batteries. *Advanced Energy Materials* **2022**, *12* (39), 2201585.
20. Wang, Y.-X.; Zhang, B.; Lai, W.; Xu, Y.; Chou, S.-L.; Liu, H.-K.; Dou, S.-X., Room-Temperature Sodium-Sulfur Batteries: A Comprehensive Review on Research Progress and Cell Chemistry. *Advanced Energy Materials* **2017**, *7* (24), 1602829.
21. Wang, N.; Wang, Y.; Bai, Z.; Fang, Z.; Zhang, X.; Xu, Z.; Ding, Y.; Xu, X.; Du, Y.; Dou, S.; Yu, G., High-Performance Room-Temperature Sodium–Sulfur Battery Enabled by Electrocatalytic Sodium Polysulfides Full Conversion. *Energy & Environmental Science* **2020**, *13* (2), 562-570.
22. Fang, R.; Xu, J.; Wang, D.-W., Covalent Fixing of Sulfur in Metal–Sulfur Batteries. *Energy & Environmental Science* **2020**, *13* (2), 432-471.
23. Kong, Y.; Wang, L.; Mamoor, M.; Wang, B.; Qu, G.; Jing, Z.; Pang, Y.; Wang, F.; Yang, X.; Wang, D.; Xu, L., Co/Mon Invigorated Bilateral Kinetics Modulation for Advanced Lithium–Sulfur Batteries. *Advanced Materials* **2024**, *36* (13), 2310143.
24. Yao, W.; Zheng, W.; Xu, J.; Tian, C.; Han, K.; Sun, W.; Xiao, S., ZnS-SnS@NC Heterostructure as Robust Lithiophilicity and Sulfiphilicity Mediator toward High-Rate and Long-Life Lithium–Sulfur Batteries. *ACS Nano* **2021**, *15* (4), 7114-7130.

25. Sungjemmenla; Soni, C. B.; Vineeth, S. K.; Kumar, V., Exploration of the Unique Structural Chemistry of Sulfur Cathode for High-Energy Rechargeable Beyond-Li Batteries. *Advanced Energy and Sustainability Research* **2022**, *3* (5), 2100157.
26. Wang, Y.; Zhou, D.; Palomares, V.; Shanmukaraj, D.; Sun, B.; Tang, X.; Wang, C.; Armand, M.; Rojo, T.; Wang, G., Revitalising Sodium–Sulfur Batteries for Non-High-Temperature Operation: a Crucial Review. *Energy & Environmental Science* **2020**, *13* (11), 3848-3879.
27. Lin, H.; Zhang, S.; Zhang, T.; Cao, S.; Ye, H.; Yao, Q.; Zheng, G. W.; Lee, J. Y., A Cathode-Integrated Sulfur-Deficient Co<sub>9</sub>S<sub>8</sub> Catalytic Interlayer for the Reutilization of “Lost” Polysulfides in Lithium–Sulfur Batteries. *ACS Nano* **2019**, *13* (6), 7073-7082.
28. Liu, W.; Luo, C.; Zhang, S.; Zhang, B.; Ma, J.; Wang, X.; Liu, W.; Li, Z.; Yang, Q.-H.; Lv, W., Cobalt-Doping of Molybdenum Disulfide for Enhanced Catalytic Polysulfide Conversion in Lithium–Sulfur Batteries. *ACS Nano* **2021**, *15* (4), 7491-7499.
29. Wang, L.; Zhang, T.; Yang, S.; Cheng, F.; Liang, J.; Chen, J., A Quantum-Chemical Study on the Discharge Reaction Mechanism of Lithium-Sulfur Batteries. *Journal of Energy Chemistry* **2013**, *22* (1), 72-77.
30. Wild, M.; O'Neill, L.; Zhang, T.; Purkayastha, R.; Minton, G.; Marinescu, M.; Offer, G. J., Lithium Sulfur Batteries, A Mechanistic Review. *Energy & Environmental Science* **2015**, *8* (12), 3477-3494.
31. Li, T.; Bai, X.; Gulzar, U.; Bai, Y.-J.; Capiglia, C.; Deng, W.; Zhou, X.; Liu, Z.; Feng, Z.; Proietti Zaccaria, R., A Comprehensive Understanding of Lithium–Sulfur Battery Technology. *Advanced Functional Materials* **2019**, *29* (32), 1901730.
32. Kang, W.; Deng, N.; Ju, J.; Li, Q.; Wu, D.; Ma, X.; Li, L.; Naebe, M.; Cheng, B., A Review of Recent Developments in Rechargeable Lithium–Sulfur Batteries. *Nanoscale* **2016**, *8* (37), 16541-16588.
33. Shao, Q.; Zhu, S.; Chen, J., A Review on Lithium-Sulfur Batteries: Challenge, Development, and Perspective. *Nano Research* **2023**, *16* (6), 8097-8138.
34. Manthiram, A.; Fu, Y.; Chung, S.-H.; Zu, C.; Su, Y.-S., Rechargeable Lithium–Sulfur Batteries. *Chemical Reviews* **2014**, *114* (23), 11751-11787.
35. Fang, R.; Zhao, S.; Sun, Z.; Wang, D.-W.; Cheng, H.-M.; Li, F., More Reliable Lithium-Sulfur Batteries: Status, Solutions and Prospects. *Advanced Materials* **2017**, *29* (48), 1606823.
36. Wang, Y.; Huang, X. L.; Liu, H.; Qiu, W.; Feng, C.; Li, C.; Zhang, S.; Liu, H. K.; Dou, S. X.; Wang, Z. M., Nanostructure Engineering Strategies of Cathode Materials for Room-Temperature Na–S Batteries. *ACS Nano* **2022**, *16* (4), 5103-5130.
37. Zhang, J.-Y.; Zhang, X.-Y.; Wang, J.; Feng, Y.; Fan, L.-L.; Cao, Y.-D.; Liu, H.; Lv, C.-L.; Gao, G.-G., The Explicit Multi-Electron Catalytic Mechanism of Heteropolyvanadotungstate Dominating Ultra-Durable Room-Temperature Na-S Batteries. *Advanced Functional Materials* **2024**, *34*, 2400170.
38. Marangon, V.; Barcaro, E.; De Boni, F.; Prato, M.; Bresser, D.; Hassoun, J., Effective Liquid Electrolytes for Enabling Room-Temperature Sodium–Sulfur Batteries. *Advanced Sustainable Systems* **2024**, *8*, 2400268.
39. Zhao, L.; Tao, Y.; Zhang, Y.; Lei, Y.; Lai, W.-H.; Chou, S.; Liu, H.-K.; Dou, S.-X.; Wang, Y.-X., A Critical Review on Room-Temperature Sodium-Sulfur Batteries: From Research Advances to Practical Perspectives. *Advanced Materials* **2024**, *36* (25), 2402337.
40. Lei, Y.-J.; Liu, H.-W.; Yang, Z.; Zhao, L.-F.; Lai, W.-H.; Chen, M.; Liu, H.; Dou, S.; Wang, Y.-X., A Review on the Status and Challenges of Cathodes in Room-Temperature Na-S Batteries. *Advanced Functional Materials* **2023**, *33* (11), 2212600.
41. Yu, X.; Manthiram, A., Capacity Enhancement and Discharge Mechanisms of Room-Temperature Sodium–Sulfur Batteries. *ChemElectroChem* **2014**, *1* (8), 1275-1280.

42. Huang, C.; Yu, J.; Li, C.; Cui, Z.; Zhang, C.; Zhang, C.; Nan, B.; Li, J.; Arbiol, J.; Cabot, A., Combined Defect and Heterojunction Engineering in ZnTe/CoTe<sub>2</sub>@NC Sulfur Hosts Toward Robust Lithium–Sulfur Batteries. *Advanced Functional Materials* **2023**, *33* (46), 2305624.
43. Ruan, J.; Lei, Y.-J.; Fan, Y.; Borrás, M. C.; Luo, Z.; Yan, Z.; Johannessen, B.; Gu, Q.; Konstantinov, K.; Pang, W. K.; Sun, W.; Wang, J.-Z.; Liu, H.-K.; Lai, W.-H.; Wang, Y.-X.; Dou, S.-X., Linearly Interlinked Fe-N<sub>x</sub>-Fe Single Atoms Catalyze High-Rate Sodium-Sulfur Batteries. *Advanced Materials* **2024**, *36* (21), 2312207.
44. Huang, C.; Yu, J.; Zhang, C. Y.; Cui, Z.; Chen, J.; Lai, W.-H.; Lei, Y.-J.; Nan, B.; Lu, X.; He, R.; Gong, L.; Li, J.; Li, C.; Qi, X.; Xue, Q.; Zhou, J. Y.; Qi, X.; Balcells, L.; Arbiol, J.; Cabot, A., Electronic Spin Alignment within Homologous NiS<sub>2</sub>/NiSe<sub>2</sub> Heterostructures to Promote Sulfur Redox Kinetics in Lithium-Sulfur Batteries. *Advanced Materials* **2024**, *36* (25), 2400810.
45. Li, Z.; Chen, X.; Yao, G.; Wei, L.; Chen, Q.; Luo, Q.; Zheng, F.; Wang, H., Strengthening d-p Orbital-Hybridization via Coordination Number Regulation of Manganese Single-Atom Catalysts Toward Fast Kinetic and Long-Life Sodium–Sulfur Batteries. *Advanced Functional Materials* **2024**, *n/a* (n/a), 2400859.
46. Zhang, C.; Fei, B.; Yang, D.; Zhan, H.; Wang, J.; Diao, J.; Li, J.; Henkelman, G.; Cai, D.; Biendicho, J. J.; Morante, J. R.; Cabot, A., Robust Lithium–Sulfur Batteries Enabled by Highly Conductive WSe<sub>2</sub>-Based Superlattices with Tunable Interlayer Space. *Advanced Functional Materials* **2022**, *32* (24), 2201322.
47. Yang, H.; Zhou, S.; Zhang, B.-W.; Chu, S.-Q.; Guo, H.; Gu, Q.-F.; Liu, H.; Lei, Y.; Konstantinov, K.; Wang, Y.-X.; Chou, S.-L.; Liu, H.-K.; Dou, S.-X., Architecting Freestanding Sulfur Cathodes for Superior Room-Temperature Na–S Batteries. *Advanced Functional Materials* **2021**, *31* (32), 2102280.
48. Guan, L.; Hu, H.; Li, L.; Pan, Y.; Zhu, Y.; Li, Q.; Guo, H.; Wang, K.; Huang, Y.; Zhang, M.; Yan, Y.; Li, Z.; Teng, X.; Yang, J.; Xiao, J.; Zhang, Y.; Wang, X.; Wu, M., Intrinsic Defect-Rich Hierarchically Porous Carbon Architectures Enabling Enhanced Capture and Catalytic Conversion of Polysulfides. *ACS Nano* **2020**, *14* (5), 6222-6231.
49. Li, J.; Chen, C.; Chen, Y.; Li, Z.; Xie, W.; Zhang, X.; Shao, M.; Wei, M., Polysulfide Confinement and Highly Efficient Conversion on Hierarchical Mesoporous Carbon Nanosheets for Li–S Batteries. *Advanced Energy Materials* **2019**, *9* (42), 1901935.
50. Yang, J.-y.; Han, H.-j.; Repich, H.; Zhi, R.-c.; Qu, C.-z.; Kong, L.; Kaskel, S.; Wang, H.-q.; Xu, F.; Li, H.-j., Recent Progress on the Design of Hollow Carbon Spheres to Host Sulfur in Room-Temperature Sodium–Sulfur Batteries. *New Carbon Materials* **2020**, *35* (6), 630-645.
51. Li, S.; Jin, B.; Zhai, X.; Li, H.; Jiang, Q., Review of Carbon Materials for Lithium-Sulfur Batteries. *ChemistrySelect* **2018**, *3* (8), 2245-2260.
52. Carter, R.; Oakes, L.; Douglas, A.; Muralidharan, N.; Cohn, A. P.; Pint, C. L., A Sugar-Derived Room-Temperature Sodium Sulfur Battery with Long Term Cycling Stability. *Nano Letters* **2017**, *17* (3), 1863-1869.
53. Wang, M.; Xia, X.; Zhong, Y.; Wu, J.; Xu, R.; Yao, Z.; Wang, D.; Tang, W.; Wang, X.; Tu, J., Porous Carbon Hosts for Lithium–Sulfur Batteries. *Chemistry – A European Journal* **2019**, *25* (15), 3710-3725.
54. Zheng, M.; Chi, Y.; Hu, Q.; Tang, H.; Jiang, X.; Zhang, L.; Zhang, S.; Pang, H.; Xu, Q., Carbon Nanotube-Based Materials For Lithium–Sulfur Batteries. *Journal of Materials Chemistry A* **2019**, *7* (29), 17204-17241.
55. Yu, M.; Li, R.; Wu, M.; Shi, G., Graphene Materials for Lithium–Sulfur Batteries. *Energy Storage Materials* **2015**, *1*, 51-73.
56. Zhong, Y.; Chao, D.; Deng, S.; Zhan, J.; Fang, R.; Xia, Y.; Wang, Y.; Wang, X.; Xia, X.; Tu, J., Confining Sulfur in Integrated Composite Scaffold with Highly Porous Carbon Fibers/Vanadium Nitride Arrays for High-Performance Lithium–Sulfur Batteries. *Advanced Functional Materials* **2018**, *28* (38), 1706391.



57. Wang, B.; Ren, Y.; Zhu, Y.; Chen, S.; Chang, S.; Zhou, X.; Wang, P.; Sun, H.; Meng, X.; Tang, S., Construction of  $\text{Co}_3\text{O}_4/\text{ZnO}$  Heterojunctions in Hollow N-Doped Carbon Nanocages as Microreactors for Lithium–Sulfur Full Batteries. *Advanced Science* **2023**, *10* (19), 2300860.
58. Zhang, C. Y.; Lu, X.; Han, X.; Yu, J.; Zhang, C.; Huang, C.; Balcells, L.; Manjón, A. G.; Jacas Biendicho, J.; Li, J.; Arbiol, J.; Sun, G.; Zhou, J. Y.; Cabot, A., Identifying the Role of the Cationic Geometric Configuration in Spinel Catalysts for Polysulfide Conversion in Sodium–Sulfur Batteries. *Journal of the American Chemical Society* **2023**, *145* (34), 18992-19004.
59. Yu, Z.; Zhang, N.; Zhang, X.; Li, Y.; Xie, G.; Ge, W.; Zhang, L.; Zhang, T., Synthesis and Research of Layered  $\text{CoS}/\text{Graphene}$  Nanoflakes as Sulfur Cathode for High-Energy Lithium Sulfur Batteries. *Journal of Electroanalytical Chemistry* **2019**, *854*, 113524.
60. Zhang, Y.; Liu, X.; Jin, Q.; Han, F.; Zhang, Z.; Zhang, X.; Wu, L.,  $\text{CoS}_2@\text{C}$  Catalyzes Polysulfide Conversion to Promote the Rate and Cycling Performances of Lithium–Sulfur Batteries. *Dalton Transactions* **2023**, *52* (44), 16167-16172.
61. Lei, Y.; Wu, C.; Lu, X.; Hua, W.; Li, S.; Liang, Y.; Liu, H.; Lai, W.-H.; Gu, Q.; Cai, X.; Wang, N.; Wang, Y.-X.; Chou, S.-L.; Liu, H.-K.; Wang, G.; Dou, S.-X., Streamline Sulfur Redox Reactions to Achieve Efficient Room-Temperature Sodium–Sulfur Batteries. *Angewandte Chemie International Edition* **2022**, *61* (16), e202200384.
62. Shen, Z.; Jin, X.; Tian, J.; Li, M.; Yuan, Y.; Zhang, S.; Fang, S.; Fan, X.; Xu, W.; Lu, H.; Lu, J.; Zhang, H., Cation-Doped  $\text{ZnS}$  Catalysts for Polysulfide Conversion in Lithium–Sulfur Batteries. *Nature Catalysis* **2022**, *5* (6), 555-563.
63. Ye, C.; Zhang, L.; Guo, C.; Li, D.; Vasileff, A.; Wang, H.; Qiao, S.-Z., A 3D Hybrid of Chemically Coupled Nickel Sulfide and Hollow Carbon Spheres for High Performance Lithium–Sulfur Batteries. *Advanced Functional Materials* **2017**, *27* (33), 1702524.
64. Kumar, M.; Padhan, A. K.; Mandal, D.; Nagaiah, T. C., An Elemental Sulfur/ $\text{CoS}_2$ - Ionic Liquid Based Anode for High-Performance Aqueous Sodium-Ion Batteries. *Energy Storage Materials* **2022**, *45*, 1052-1061.
65. Zhang, R.; Esposito, A. M.; Thornburg, E. S.; Chen, X.; Zhang, X.; Philip, M. A.; Magana, A.; Gewirth, A. A., Conversion of  $\text{Co}$  Nanoparticles to  $\text{CoS}$  in Metal–Organic Framework-Derived Porous Carbon during Cycling Facilitates  $\text{Na}_2\text{S}$  Reactivity in a  $\text{Na-S}$  Battery. *ACS Applied Materials & Interfaces* **2020**, *12* (26), 29285-29295.
66. Yang, D.; Zhang, C.; Biendicho, J. J.; Han, X.; Liang, Z.; Du, R.; Li, M.; Li, J.; Arbiol, J.; Llorca, J.; Zhou, Y.; Morante, J. R.; Cabot, A.,  $\text{ZnSe}/\text{N}$ -Doped Carbon Nanoreactor with Multiple Adsorption Sites for Stable Lithium–Sulfur Batteries. *ACS Nano* **2020**, *14* (11), 15492-15504.
67. Ye, Z.; Jiang, Y.; Li, L.; Wu, F.; Chen, R., A High-Efficiency  $\text{CoSe}$  Electrocatalyst with Hierarchical Porous Polyhedron Nanoarchitecture for Accelerating Polysulfides Conversion in  $\text{Li-S}$  Batteries. *Advanced Materials* **2020**, *32* (32), 2002168.
68. Yan, T.; Feng, J.; Zeng, P.; Zhao, G.; Wang, L.; Yuan, C.; Cheng, C.; Li, Y.; Zhang, L., Modulating  $e_g$  Orbitals Through Ligand Engineering to Boost the Electrocatalytic Activity of  $\text{NiSe}$  for Advanced Lithium-Sulfur Batteries. *Journal of Energy Chemistry* **2022**, *74*, 317-323.
69. Wong, H.; Ou, X.; Zhuang, M.; Liu, Z.; Hossain, M. D.; Cai, Y.; Liu, H.; Lee, H.; Wang, C.-Z.; Luo, Z., Selenium Edge as a Selective Anchoring Site for Lithium–Sulfur Batteries with  $\text{MoSe}_2/\text{Graphene}$ -Based Cathodes. *ACS Applied Materials & Interfaces* **2019**, *11* (22), 19986-19993.
70. Li, H.-J.; Xi, K.; Wang, W.; Liu, S.; Li, G.-R.; Gao, X.-P., Quantitatively Regulating Defects of 2D Tungsten Selenide to Enhance Catalytic Ability for Polysulfide Conversion in A Lithium Sulfur Battery. *Energy Storage Materials* **2022**, *45*, 1229-1237.

71. Yao, W.; Tian, C.; Yang, C.; Xu, J.; Meng, Y.; Manke, I.; Chen, N.; Wu, Z.; Zhan, L.; Wang, Y.; Chen, R., P-Doped NiTe<sub>2</sub> with Te-Vacancies in Lithium–Sulfur Batteries Prevents Shuttling and Promotes Polysulfide Conversion. *Advanced Materials* **2022**, *34* (11), 2106370.
72. Cheng, Z.; Wang, M.; Dong, Y.; Han, Y.; Yan, X.; Xie, L.; Zheng, X.; Han, L.; Zhang, J., Two-Birds with One Stone: Improving both Cathode and Anode Electrochemical Performances via Two-dimensional Te-CoTe<sub>2</sub>/rGO Ultrathin Nanosheets as Sulfur Hosts in Lithium–Sulfur Batteries. *Journal of Colloid and Interface Science* **2023**, *649*, 86-96.
73. Tian, K.; Wei, C.; Wang, Z.; Li, Y.; Xi, B.; Xiong, S.; Feng, J., Heterogenization-Activated Zinc Telluride via Rectifying Interfacial Contact to Afford Synergistic Confinement-Adsorption-Catalysis for High-Performance Lithium–Sulfur Batteries. *Small* **2024**, *20* (23), 2309422.
74. He, J.; Bhargava, A.; Manthiram, A., In Situ Grown 1T'-MoTe<sub>2</sub> Nanosheets on Carbon Nanotubes as an Efficient Electrocatalyst and Lithium Regulator for Stable Lithium–Sulfur Full Cells. *Advanced Energy Materials* **2022**, *12* (1), 2103204.
75. Zeng, S.; Li, L.; Xie, L.; Zhao, D.; Wang, N.; Chen, S., Conducting Polymers Crosslinked with Sulfur as Cathode Materials for High-Rate, Ultralong-Life Lithium–Sulfur Batteries. *ChemSusChem* **2017**, *10* (17), 3378-3386.
76. Zhu, J.; Zhu, P.; Yan, C.; Dong, X.; Zhang, X., Recent Progress in Polymer Materials for Advanced Lithium–Sulfur Batteries. *Progress in Polymer Science* **2019**, *90*, 118-163.
77. Zhang, Y.; Peng, Y.; Wang, Y.; Li, J.; Li, H.; Zeng, J.; Wang, J.; Hwang, B. J.; Zhao, J., High Sulfur-Containing Carbon Polysulfide Polymer as A Novel Cathode Material for Lithium-Sulfur Battery. *Scientific Reports* **2017**, *7* (1), 11386.
78. Hencz, L.; Chen, H.; Ling, H. Y.; Wang, Y.; Lai, C.; Zhao, H.; Zhang, S., Housing Sulfur in Polymer Composite Frameworks for Li–S Batteries. *Nano-Micro Letters* **2019**, *11* (1), 17.
79. Hussain, S.; Liu, T.; Javed, M. S.; Aslam, N.; Zeng, W., Highly Reactive 0D ZnS Nanospheres and Nanoparticles for Formaldehyde Gas-Sensing Properties. *Sensors and Actuators B: Chemical* **2017**, *239*, 1243-1250.
80. Wei, X.; Kang, X.; Zuo, Z.; Song, F.; Wang, S.; Zhu, M., Hierarchical Structural Complexity in Atomically Precise Nanocluster Frameworks. *National Science Review* **2020**, *8* (3).
81. Hu, Y.; Chen, W.; Lei, T.; Zhou, B.; Jiao, Y.; Yan, Y.; Du, X.; Huang, J.; Wu, C.; Wang, X.; Wang, Y.; Chen, B.; Xu, J.; Wang, C.; Xiong, J., Carbon Quantum Dots–Modified Interfacial Interactions and Ion Conductivity for Enhanced High Current Density Performance in Lithium–Sulfur Batteries. *Advanced Energy Materials* **2019**, *9* (7), 1802955.
82. Li, X.; Ding, K.; Gao, B.; Li, Q.; Li, Y.; Fu, J.; Zhang, X.; Chu, P. K.; Huo, K., Freestanding Carbon Encapsulated Mesoporous Vanadium Nitride Nanowires Enable Highly Stable Sulfur Cathodes for Lithium–Sulfur Batteries. *Nano Energy* **2017**, *40*, 655-662.
83. Chen, S.; Huang, X.; Liu, H.; Sun, B.; Yeoh, W.; Li, K.; Zhang, J.; Wang, G., 3D Hyperbranched Hollow Carbon Nanorod Architectures for High-Performance Lithium–Sulfur Batteries. *Advanced Energy Materials* **2014**, *4* (8), 1301761.
84. Zhang, M.; Yu, C.; Zhao, C.; Song, X.; Han, X.; Liu, S.; Hao, C.; Qiu, J., Cobalt-Embedded Nitrogen-Doped Hollow Carbon Nanorods for Synergistically Immobilizing the Discharge Products in Lithium–Sulfur Battery. *Energy Storage Materials* **2016**, *5*, 223-229.
85. Hao, H.; Wang, Y.; Katyal, N.; Yang, G.; Dong, H.; Liu, P.; Hwang, S.; Mantha, J.; Henkelman, G.; Xu, Y.; Boscoboinik, J. A.; Nanda, J.; Mitlin, D., Molybdenum Carbide Electrocatalyst In Situ Embedded in Porous



Nitrogen-Rich Carbon Nanotubes Promotes Rapid Kinetics in Sodium-Metal–Sulfur Batteries. *Advanced Materials* **2022**, *34* (26), 2106572.

86. Wang, H.; Zhang, C.; Chen, Z.; Liu, H. K.; Guo, Z., Large-Scale Synthesis of Ordered Mesoporous Carbon Fiber and its Application as Cathode Material for Lithium-Sulfur Batteries. *Carbon* **2015**, *81*, 782-787.

87. Lu, Q.; Wang, X.; Cao, J.; Chen, C.; Chen, K.; Zhao, Z.; Niu, Z.; Chen, J., Freestanding Carbon Fiber Cloth/Sulfur Composites for Flexible Room-Temperature Sodium-Sulfur Batteries. *Energy Storage Materials* **2017**, *8*, 77-84.

88. Chen, W.; Liu, X.; Wu, J.; Wang, Q.; Zhang, Y.; Yan, S.; Hou, P.; Luo, S., Electrospun Fe<sub>1-x</sub>S@Nitrogen-Doped Carbon Fibers as Anode Material for Sodium-Ion Batteries. *Journal of Electroanalytical Chemistry* **2023**, *929*, 117095.

89. Li, C.; Qiu, M.; Li, R.; Li, X.; Wang, M.; He, J.; Lin, G.; Xiao, L.; Qian, Q.; Chen, Q.; Wu, J.; Li, X.; Mai, Y.-W.; Chen, Y., Electrospinning Engineering Enables High-Performance Sodium-Ion Batteries. *Advanced Fiber Materials* **2022**, *4* (1), 43-65.

90. Yao, Y.; Wang, H.; Yang, H.; Zeng, S.; Xu, R.; Liu, F.; Shi, P.; Feng, Y.; Wang, K.; Yang, W.; Wu, X.; Luo, W.; Yu, Y., A Dual-Functional Conductive Framework Embedded with TiN-VN Heterostructures for Highly Efficient Polysulfide and Lithium Regulation toward Stable Li–S Full Batteries. *Advanced Materials* **2020**, *32* (6), 1905658.

91. Ali, T.; Yan, C., 2D Materials for Inhibiting the Shuttle Effect in Advanced Lithium–Sulfur Batteries. *ChemSusChem* **2020**, *13* (6), 1447-1479.

92. Ye, C.; Jiao, Y.; Jin, H.; Slattery, A. D.; Davey, K.; Wang, H.; Qiao, S.-Z., 2D MoN-VN Heterostructure To Regulate Polysulfides for Highly Efficient Lithium-Sulfur Batteries. *Angewandte Chemie International Edition* **2018**, *57* (51), 16703-16707.

93. Yu, W.; Deng, N.; Cheng, K.; Yan, J.; Cheng, B.; Kang, W., Advances in Preparation Methods and Mechanism Analysis of Layered Double Hydroxide for Lithium-Ion Batteries and Lithium-Sulfur Batteries. *Journal of Energy Chemistry* **2021**, *58*, 472-499.

94. Dhakshinamoorthy, A.; Asiri, A. M.; Garcia, H., 2D Metal–Organic Frameworks as Multifunctional Materials in Heterogeneous Catalysis and Electro/Photocatalysis. *Advanced Materials* **2019**, *31* (41), 1900617.

95. Xiong, D.; Li, X.; Bai, Z.; Lu, S., Recent Advances in Layered Ti<sub>3</sub>C<sub>2</sub>T<sub>x</sub> MXene for Electrochemical Energy Storage. *Small* **2018**, *14* (17), 1703419.

96. Fu, A.; Wang, C.; Pei, F.; Cui, J.; Fang, X.; Zheng, N., Recent Advances in Hollow Porous Carbon Materials for Lithium–Sulfur Batteries. *Small* **2019**, *15* (10), 1804786.

97. Yu, R.; Chung, S.-H.; Chen, C.-H.; Manthiram, A., A Core–Shell Cathode Substrate for Developing High-Loading, High-Performance Lithium–Sulfur Batteries. *Journal of Materials Chemistry A* **2018**, *6* (48), 24841-24847.

98. Xie, F.; Zhang, L.; Gu, Q.; Chao, D.; Jaroniec, M.; Qiao, S.-Z., Multi-Shell Hollow Structured Sb<sub>2</sub>S<sub>3</sub> for Sodium-ion Batteries with Enhanced Energy Density. *Nano Energy* **2019**, *60*, 591-599.

99. Li, Z.; Zhang, J.; Lou, X. W., Hollow Carbon Nanofibers Filled with MnO<sub>2</sub> Nanosheets as Efficient Sulfur Hosts for Lithium–Sulfur Batteries. *Angewandte Chemie International Edition* **2015**, *54* (44), 12886-12890.

100. Xiao, Y.; Guo, S.; Ouyang, Y.; Li, D.; Li, X.; He, W.; Deng, H.; Gong, W.; Tan, C.; Zeng, Q.; Zhang, Q.; Huang, S., Constructing Heterogeneous Structure in Metal–Organic Framework-Derived Hierarchical Sulfur Hosts for Capturing Polysulfides and Promoting Conversion Kinetics. *ACS Nano* **2021**, *15* (11), 18363-18373.

101. Zhang, D.; Luo, Y.; Wu, B.; Zeng, P.; Xiang, C.; Zhao, C.; Sofer, Z.; Chen, M.; Wang, X., A Heterogeneous FeP-CoP Electrocatalyst for Expediting Sulfur Redox in High-Specific-Energy Lithium-Sulfur Batteries. *Electrochimica Acta* **2021**, *397*, 139275.

102. Bai, Y.; Nguyen, T. T.; Chu, R.; Song, H.; Kim, N. H.; Lee, J. H., Heterostructured TiN/TiO<sub>2</sub> on the Hierarchical N-doped Carbon for Enhancing the Polysulfide Immobilization and Sulfur Reduction in Lithium-Sulfur Battery. *Chemical Engineering Journal* **2023**, *476*, 146581.
103. Xue, J.-Y.; Li, F.-L.; Chen, B.; Geng, H.; Zhang, W.; Xu, W.-Y.; Gu, H.; Braunstein, P.; Lang, J.-P., Engineering Multiphase MoSe<sub>2</sub>/NiSe Heterostructure Interfaces for Superior Hydrogen Production Electrocatalysis. *Applied Catalysis B: Environmental* **2022**, *312*, 121434.
104. Jiang, L.; Duan, J.; Zhu, J.; Chen, S.; Antonietti, M., Iron-Cluster-Directed Synthesis of 2D/2D Fe–N–C/MXene Superlattice-like Heterostructure with Enhanced Oxygen Reduction Electrocatalysis. *ACS Nano* **2020**, *14* (2), 2436-2444.
105. Wang, X.; Han, X.; Du, R.; Xing, C.; Qi, X.; Liang, Z.; Guardia, P.; Arbiol, J.; Cabot, A.; Li, J., Cobalt Molybdenum Nitride-Based Nanosheets for Seawater Splitting. *ACS Applied Materials & Interfaces* **2022**, *14* (37), 41924-41933.
106. Zhang, L.; Bi, J.; Liu, T.; Chu, X.; Lv, H.; Mu, D.; Wu, B.; Wu, F., TiN/TiC Heterostructures Embedded with Single Tungsten Atoms Enhance Polysulfide Entrapment and Conversion for High-Capacity Lithium-Sulfur Battery Applications. *Energy Storage Materials* **2023**, *54*, 410-420.
107. Wang, J.; Wang, B.; Sun, H.; Wang, G.; Bai, J.; Wang, H., Heterogeneous Interface Containing Selenium Vacancies Space-Confined in Double Carbon to Induce Superior Electronic/Ionic Transport Dynamics for Sodium/Potassium-Ion Half/Full Batteries. *Energy Storage Materials* **2022**, *46*, 394-405.
108. Luo, L.; Wang, X.; Yang, S.; Dai, J.; Li, D.; Xia, L.; Chi, C.; Cabot, A.; Xu, Y.; Dai, L., PPy/PANI@MoS<sub>2</sub> Composites with a Dual-Channel Architecture for Advanced Asymmetric Supercapacitors. *ACS Applied Energy Materials* **2023**, *6* (11), 5940-5951.
109. K. A, S. R.; Barman, N.; Radhakrishnan, S.; Thapa, R.; Rout, C. S., Hierarchical Architecture of the Metallic VTe<sub>2</sub>/Ti<sub>3</sub>C<sub>2</sub>T<sub>x</sub> MXene Heterostructure for Supercapacitor Applications. *Journal of Materials Chemistry A* **2022**, *10* (44), 23590-23602.
110. Li, Y.; Zhang, J.; Chen, Q.; Xia, X.; Chen, M., Emerging of Heterostructure Materials in Energy Storage: A Review. *Advanced Materials* **2021**, *33* (27), 2100855.
111. Li, Q.; Zhang, M.; Xu, Y.; Quan, X.; Xu, Y.; Liu, W.; Wang, L., Constructing Heterojunction Interface of Co<sub>3</sub>O<sub>4</sub>/TiO<sub>2</sub> for Efficiently Accelerating Acetaminophen Degradation via Photocatalytic Activation of Sulfite. *Chinese Chemical Letters* **2023**, *34* (3), 107530.
112. Dai, J.; Qi, X.; Xia, L.; Xue, Q.; Luo, L.; Wang, X.; Yang, C.; Li, D.; Xie, H.; Cabot, A.; Dai, L.; Xu, Y., Aqueous Ammonium-Ion Supercapacitors with Unprecedented Energy Density and Stability Enabled by Oxygen Vacancy-Enriched MoO<sub>3</sub>@C. *Advanced Functional Materials* **2023**, *33* (10), 2212440.
113. Zhang, Y.; Xing, C.; Liu, Y.; Spadaro, M. C.; Wang, X.; Li, M.; Xiao, K.; Zhang, T.; Guardia, P.; Lim, K. H.; Moghaddam, A. O.; Llorca, J.; Arbiol, J.; Ibáñez, M.; Cabot, A., Doping-Mediated Stabilization of Copper Vacancies to Promote Thermoelectric Properties of Cu<sub>2-x</sub>S. *Nano Energy* **2021**, *85*, 105991.
114. Hu, S.; Huang, X.; Zhang, L.; Li, G.; Chen, S.; Zhang, J.; Liu, X., Vacancy-Defect Topological Insulators Bi<sub>2</sub>Te<sub>3-x</sub> Embedded in N and B Co-Doped 1D Carbon Nanorods Using Ionic Liquid Dopants for Kinetics-Enhanced Li–S Batteries. *Advanced Functional Materials* **2023**, *33* (20), 2214161.
115. Li, W.; Ma, Y.; Li, P.; Jing, X.; Jiang, K.; Wang, D., Electrochemically Activated Cu<sub>2-x</sub>Te as an Ultraflat Discharge Plateau, Low Reaction Potential, and Stable Anode Material for Aqueous Zn-Ion Half and Full Batteries. *Advanced Energy Materials* **2021**, *11* (42), 2102607.
116. Hou, W.; Feng, P.; Guo, X.; Wang, Z.; Bai, Z.; Bai, Y.; Wang, G.; Sun, K., Catalytic Mechanism of Oxygen Vacancies in Perovskite Oxides for Lithium–Sulfur Batteries. *Advanced Materials* **2022**, *34* (26), 2202222.

117. Wang, J.; Zhao, Y.; Li, G.; Luo, D.; Liu, J.; Zhang, Y.; Wang, X.; Shui, L.; Chen, Z., Aligned Sulfur-Deficient  $\text{ZnS}_{1-x}$  Nanotube Arrays as Efficient Catalyzer for High-Performance Lithium/Sulfur Batteries. *Nano Energy* **2021**, *84*, 105891.
118. Li, H.-J.; Song, Y.-H.; Xi, K.; Wang, W.; Liu, S.; Li, G.-R.; Gao, X.-P., Sulfur Vacancies in  $\text{Co}_9\text{S}_8-x/\text{N}$ -Doped Graphene Enhancing the Electrochemical Kinetics for High-Performance Lithium–Sulfur Batteries. *Journal of Materials Chemistry A* **2021**, *9* (17), 10704-10713.
119. Zhang, K.; Zhang, G.; Qu, J.; Liu, H., Zinc Substitution-Induced Subtle Lattice Distortion Mediates the Active Center of Cobalt Diselenide Electrocatalysts for Enhanced Oxygen Evolution. *Small* **2020**, *16* (11), 1907001.
120. Wang, B.; Wang, L.; Ding, D.; Zhai, Y.; Wang, F.; Jing, Z.; Yang, X.; Kong, Y.; Qian, Y.; Xu, L., Zinc-Assisted Cobalt Ditetelluride Polyhedra Inducing Lattice Strain to Endow Efficient Adsorption-Catalysis for High-Energy Lithium–Sulfur Batteries. *Advanced Materials* **2022**, *34* (50), 2204403.
121. Luo, D.; Li, G.; Deng, Y.-P.; Zhang, Z.; Li, J.; Liang, R.; Li, M.; Jiang, Y.; Zhang, W.; Liu, Y.; Lei, W.; Yu, A.; Chen, Z., Synergistic Engineering of Defects and Architecture in Binary Metal Chalcogenide toward Fast and Reliable Lithium–Sulfur Batteries. *Advanced Energy Materials* **2019**, *9* (18), 1900228.
122. Shang, C.; Li, G.; Wei, B.; Wang, J.; Gao, R.; Tian, Y.; Chen, Q.; Zhang, Y.; Shui, L.; Zhou, G.; Hu, Y.; Chen, Z.; Wang, X., Dissolving Vanadium into Titanium Nitride Lattice Framework for Rational Polysulfide Regulation in Li–S Batteries. *Advanced Energy Materials* **2021**, *11* (3), 2003020.
123. Peng, L.; Wei, Z.; Wan, C.; Li, J.; Chen, Z.; Zhu, D.; Baumann, D.; Liu, H.; Allen, C. S.; Xu, X.; Kirkland, A. I.; Shakir, I.; Almutairi, Z.; Tolbert, S.; Dunn, B.; Huang, Y.; Sautet, P.; Duan, X., A Fundamental Look at Electrocatalytic Sulfur Reduction Reaction. *Nature Catalysis* **2020**, *3* (9), 762-770.
124. Liu, Y.; Ma, S.; Liu, L.; Koch, J.; Rosebrock, M.; Li, T.; Bettels, F.; He, T.; Pfnür, H.; Bigall, N. C.; Feldhoff, A.; Ding, F.; Zhang, L., Nitrogen Doping Improves the Immobilization and Catalytic Effects of  $\text{Co}_9\text{S}_8$  in Li-S Batteries. *Advanced Functional Materials* **2020**, *30* (32), 2002462.
125. Song, Y.; Sun, Z.; Fan, Z.; Cai, W.; Shao, Y.; Sheng, G.; Wang, M.; Song, L.; Liu, Z.; Zhang, Q.; Sun, J., Rational Design of Porous Nitrogen-Doped  $\text{Ti}_3\text{C}_2$  MXene as a Multifunctional Electrocatalyst for Li–S Chemistry. *Nano Energy* **2020**, *70*, 104555.
126. Tian, D.; Song, X.; Qiu, Y.; Sun, X.; Jiang, B.; Zhao, C.; Zhang, Y.; Xu, X.; Fan, L.; Zhang, N., Basal-Plane-Activated Molybdenum Sulfide Nanosheets with Suitable Orbital Orientation as Efficient Electrocatalysts for Lithium–Sulfur Batteries. *ACS Nano* **2021**, *15* (10), 16515-16524.
127. Shen, Z.; Cao, M.; Zhang, Z.; Pu, J.; Zhong, C.; Li, J.; Ma, H.; Li, F.; Zhu, J.; Pan, F.; Zhang, H., Efficient  $\text{Ni}_2\text{Co}_4\text{P}_3$  Nanowires Catalysts Enhance Ultrahigh-Loading Lithium–Sulfur Conversion in a Microreactor-Like Battery. *Advanced Functional Materials* **2020**, *30* (3), 1906661.
128. Cheng, N.; Zhang, L.; Doyle-Davis, K.; Sun, X., Single-Atom Catalysts: From Design to Application. *Electrochemical Energy Reviews* **2019**, *2* (4), 539-573.
129. Song, P.; Luo, M.; Liu, X.; Xing, W.; Xu, W.; Jiang, Z.; Gu, L., Zn Single Atom Catalyst for Highly Efficient Oxygen Reduction Reaction. *Advanced Functional Materials* **2017**, *27* (28), 1700802.
130. Du, Z.; Chen, X.; Hu, W.; Chuang, C.; Xie, S.; Hu, A.; Yan, W.; Kong, X.; Wu, X.; Ji, H.; Wan, L.-J., Cobalt in Nitrogen-Doped Graphene as Single-Atom Catalyst for High-Sulfur Content Lithium–Sulfur Batteries. *Journal of the American Chemical Society* **2019**, *141* (9), 3977-3985.
131. Zhang, S.; Ao, X.; Huang, J.; Wei, B.; Zhai, Y.; Zhai, D.; Deng, W.; Su, C.; Wang, D.; Li, Y., Isolated Single-Atom Ni–N<sub>5</sub> Catalytic Site in Hollow Porous Carbon Capsules for Efficient Lithium–Sulfur Batteries. *Nano Letters* **2021**, *21* (22), 9691-9698.

132. Zhang, D.; Wang, S.; Hu, R.; Gu, J.; Cui, Y.; Li, B.; Chen, W.; Liu, C.; Shang, J.; Yang, S., Catalytic Conversion of Polysulfides on Single Atom Zinc Implanted MXene toward High-Rate Lithium–Sulfur Batteries. *Advanced Functional Materials* **2020**, *30* (30), 2002471.
133. Han, Z.; Zhao, S.; Xiao, J.; Zhong, X.; Sheng, J.; Lv, W.; Zhang, Q.; Zhou, G.; Cheng, H.-M., Engineering d-p Orbital Hybridization in Single-Atom Metal-Embedded Three-Dimensional Electrodes for Li–S Batteries. *Advanced Materials* **2021**, *33* (44), 2105947.
134. Fang, D.; Sun, P.; Huang, S.; Shang, Y.; Li, X.; Yan, D.; Lim, Y. V.; Su, C.-Y.; Su, B.-J.; Juang, J.-Y.; Yang, H. Y., An Exfoliation–Evaporation Strategy To Regulate N Coordination Number of Co Single-Atom Catalysts for High-Performance Lithium–Sulfur Batteries. *ACS Materials Letters* **2022**, *4* (1), 1-10.

# **Chapter 2**

## **Objectives**

## 2. Objectives

The primary goal of this thesis is to address the challenges encountered in the practical application of MSBs by electronically regulating the sulfur host cathode material. This study aims to resolve critical issues such as the polysulfide shuttle effect, poor conductivity, and volume expansion, thereby enabling the development of high energy and power density energy storage devices. The specific objectives of this thesis are as follows:

### 1. Design and synthesize advanced sulfur host materials:

Develop novel sulfur host materials with improved electronic conductivity, stability, and affinity for sulfur species.

In Chapters 4 to 7, we designed a series of polar host materials-including v-ZnTe/CoTe<sub>2</sub>@NC, NiS<sub>2</sub>/NiSe<sub>2</sub>@NC, Te-Bi<sub>2</sub>Se<sub>3-x</sub>@C, and Co<sub>3</sub>O<sub>4</sub>-NC@C<sub>3</sub>N<sub>4</sub>-to enhance the electrode's reactivity toward polysulfides and to accelerate the conversion between polysulfides and S<sub>8</sub>.

### 2. Optimize structural and compositional properties:

Optimize structural characteristics such as porosity, surface area, and pore size distribution of sulfur host materials to achieve maximum sulfur loading and retention.

In Chapter 4, we synthesized a dodecahedral structure. In Chapter 5, a hollow architecture was developed to mitigate the volume expansion of the electrode material during charge–discharge cycles. In Chapters 6 and 7, 1D structures were designed to facilitate ion diffusion and enhance electrochemical kinetics.

### 3. Comprehensive electrochemical performance evaluation:

In Chapters 4 to 7, we conduct extensive electrochemical tests, including cyclic voltammetry (CV), galvanostatic charge-discharge (GCD) measurements, and electrochemical impedance spectroscopy (EIS) to assess the performance of developed sulfur host materials.

Evaluate the long-term cycling stability, rate capability, and energy density of MSBs incorporating these new host materials.

### 4. Gain insight into degradation mechanisms:

In Chapters 4 to 7, we investigate the degradation mechanisms of sulfur host materials during battery operation through SEM.

Develop strategies to mitigate degradation and enhance the lifespan of sulfur host materials.

#### **5. Integration into practical battery systems:**

To evaluate the practical applicability of the electrode materials, we systematically analyzed their electrochemical performance under high mass loading and lean electrolyte conditions from Chapters 4 to 7. Remarkably, the designed electrodes maintained high specific capacity and long cycle life even under these demanding conditions. Furthermore, they were successfully assembled into pouch batteries capable of powering devices such as LEDs, demonstrating their strong potential for practical applications.

#### **6. Developing advanced electronic control mechanisms:**

In Chapter 4, heterostructure and vacancy engineering were employed to modulate the electronic structure of the host materials. In Chapter 5, homologous heterostructures were designed to enhance the electrical conductivity of the electrode materials and to investigate the relationship between electron transfer and spin states. In Chapter 6, doping strategies were utilized to further optimize the electronic structure of the host materials. In Chapter 7, P-N heterostructures were constructed to systematically explore the interplay between heterostructure interfaces and spin states.

# **Chapter 3**

## **Experimental section**



### 3. Experimental section

This chapter focuses on the experimental procedures, detailing the preparation and characterization methods of the materials. The prepared electrode materials are utilized for electrochemical testing and characterization in MSBs. All the chemical reagents and instruments employed in the preparation of electrode materials are systematically presented in table format.

#### 3.1 Chemicals or raw materials used in experiments.

**Table 3.1.** List of chemicals used in experiments (all acquired at Sigma Aldrich)

Chemical Name	Molecular Formula/Purity	Manufacturer
Cobalt(II) nitrate hexahydrate	Co(NO <sub>3</sub> ) <sub>2</sub> ·6H <sub>2</sub> O, 98%	Sigma Aldrich
Zinc nitrate hexahydrate	Zn(NO <sub>3</sub> ) <sub>2</sub> ·6H <sub>2</sub> O, 98%	Sigma Aldrich
2-Methylimidazole	C <sub>4</sub> H <sub>6</sub> N <sub>2</sub> , 99.7%	Sigma Aldrich
Methanol	CH <sub>3</sub> OH, 98%	Sigma Aldrich
Polyvinylidene fluoride	PVDF, ≥99.9%	Sigma Aldrich
N-methylpyrrolidone	NMP, ≥99.5%	Sigma Aldrich
1,3- dioxolane	DOL, ≥99.9%	Sigma Aldrich
1,2-dimethoxyethane	DME, ≥99.9%	Sigma Aldrich
Dopamine hydrochloride	DA·HCl, ≥98%	Sigma Aldrich
Nickel Nitrate hexahydrate	Ni(NO <sub>3</sub> ) <sub>2</sub> 6H <sub>2</sub> O, 98%	Sigma Aldrich
Trimestic acid	H <sub>3</sub> BTC ≥98%	Sigma Aldrich
Bismuth nitrate pentahydrate	Bi(NO <sub>3</sub> ) <sub>3</sub> ·5H <sub>2</sub> O, 98%	Sigma Aldrich
Selenium powder	Se, ≥99%	Sigma Aldrich
Tellurium powder	Te, ≥99%	Sigma Aldrich
Urea	CH <sub>4</sub> N <sub>2</sub> O, ≥99.9%	Sigma Aldrich
Melamine	C <sub>3</sub> H <sub>6</sub> N <sub>6</sub> , ≥99.9%	Sigma Aldrich
Dimethyl carbonate	DEC, ≥99.9%	Sigma Aldrich
Ethylene carbonate	EC, ≥99.9%	Sigma Aldrich
Fluoroethylene carbonate	FEC, ≥99.9%	Sigma Aldrich
N,N-dimethylformamide	DMF, ≥99.8%	Sigma Aldrich

## **3.2 Material preparation methods**

### **3.2.1 Co-precipitation method**

The co-precipitation method is a chemical synthesis technique used to prepare uniformly dispersed multi-component transition metal compounds, composite materials, and nanomaterials. This method achieves solid materials with uniform composition and structure by simultaneously precipitating multiple ions in solution. In Chapter 4, the co-precipitation method is used to prepare electrode materials. The specific steps involved in the co-precipitation method are as follows:

**Dissolution and Mixing:** Different metal salts are dissolved in water or suitable solvents to form a homogeneous metal ion solution. **Precipitant Addition:** Precipitants such as hydroxides, carbonates, or sulfides are added to the solution. These precipitants react with the metal ions to form insoluble compounds, which gradually precipitate out of the solution. **Precipitation Process Control:** The precipitation process is carefully controlled by adjusting parameters such as pH value, temperature, concentration of the precipitant, and stirring rate. This ensures the simultaneous and uniform co-precipitation of each component. **Solid-Liquid Separation and Washing:** The solid precipitate is separated from the liquid phase using techniques like filtration or centrifugation. The precipitate is then thoroughly washed with pure water or an appropriate solvent to remove any residual impurities or soluble salts. **Drying and Heat Treatment:** After washing, the precipitate is dried to remove any remaining solvent. Subsequently, heat treatment processes such as calcination are employed to transform the precipitate into the desired compound or composite material with enhanced properties.

Compared to other synthesis methods, the co-precipitation strategy offers advantages such as excellent uniformity and high purity of the resulting materials. However, several critical considerations must be taken into account during operation: **Precipitant Selection:** choosing an appropriate precipitant is crucial to ensure complete precipitation of the target metal ions and to prevent interference from coexisting ions. **pH Control:** maintaining strict control over the pH of the solution is essential. It ensures that all components precipitate simultaneously and prevents separation of individual components during precipitation. **Stirring Rate:** Controlling

the stirring rate helps in achieving uniform formation of precipitation and prevents agglomeration of particles, ensuring homogeneous material synthesis. Washing and Purification: Thorough washing of the precipitate is necessary to eliminate impurities, ensuring the purity and optimal performance of the final material.

### **3.2.2 Solvothermal method**

The solvothermal method is a chemical synthesis technique that involves increasing the reaction temperature and pressure by heating the solvent in a closed container, such as an autoclave. This process promotes the dissolution, diffusion, and crystallization of the reactants. By achieving high temperature and pressure conditions at relatively lower temperatures, the solvothermal method aids in controlling the morphology and size of materials, making it particularly useful for preparing uniform nanomaterials and complex crystal structures. In this context, the solvothermal method is employed to synthesize nanomaterials, as discussed in Chapters 5 and 6.

When utilizing the solvothermal method, several critical factors need attention:

**Solvent Selection:** Choose solvents that can dissolve the reactants and remain stable under high-temperature and high-pressure conditions. **Temperature, pressure, and time control:** Carefully regulate these parameters to optimize the reaction conditions and achieve the desired material properties. **Reaction Vessel:** Use appropriate reaction vessels, such as autoclaves, ensuring they can withstand the required temperature and pressure. **Airtightness and Safety:** Ensure the equipment is well-sealed and equipped with a pressure relief valve to prevent accidents. The solvent should fill 60-80% of the volume of the liner to allow for expansion. **Pre- and Post-Reaction Procedures:** Before starting the reaction, securely tighten the lid of the container. After the reaction, wait for the stainless steel shell to cool completely to room temperature before proceeding with subsequent experiments.

### **3.2.3 High-temperature carbonization method**

High-temperature carbonization method (HTC) is a commonly used technique for preparing carbon materials by converting carbon-containing precursors into carbon materials at high

temperatures. This method is widely applied in the preparation of various forms and structures of carbon materials, including activated carbon, carbon fibers, graphene, and carbon nanotubes. In the preparation of electrode materials using the HTC, suitable carbon-containing precursor materials are first selected. These precursors can be organic polymers, natural materials (such as wood or cellulose), organometallic compounds, pitch, and more. In some cases, the precursors may require pretreatment, such as drying, impregnation, or chemical modification, to enhance the quality and performance of the carbonized product.

The precursor is then placed in a high-temperature furnace and heated to high temperatures (typically between 600°C and 2000°C) under an inert atmosphere (such as argon or nitrogen). During this process, the precursor undergoes pyrolysis and dehydration, volatilizing low molecular weight components (such as water, carbon dioxide, methane, etc.) and rearranging its carbon skeleton structure, ultimately forming carbon materials.

After the carbonization process is complete, the sample is cooled to room temperature, extracted, and subjected to further post-treatment (such as washing, additional heat treatment, or surface modification) to obtain the desired carbon material.

Compared to other thermal treatment methods, the HTC has the following advantages:

High-temperature treatment can remove most impurities, resulting in high-purity carbon materials.

By adjusting the carbonization temperature, time, and atmosphere, the microstructure and performance of the final product can be controlled.

It is suitable for a variety of precursor materials and can produce carbon materials in various forms, such as powders, fibers, and films.

In summary, the HTC is a crucial technique for preparing carbon materials. Through high-temperature treatment, various carbon-containing precursors can be converted into high-performance carbon materials, offering significant industrial and research applications.

### 3.3 Materials characterizations

#### 3.3.1 X-ray diffraction (XRD, Miniflex 600)

XRD is a widely used material analysis technique employed to determine the crystal structure, crystallographic parameters, and crystalline properties of substances. This method is based on the interaction of X-rays with the crystal structure of materials, resulting in diffraction phenomena.

XRD typically utilizes X-ray sources such as tungsten or copper X-ray tubes, which emit X-rays of specific wavelengths, commonly molybdenum K $\alpha$  line ( $\lambda=0.71$  Å) or copper K $\alpha$  line ( $\lambda=1.54$  Å). When the wavelength of incident X-rays is close to the lattice spacing of a crystal, diffraction occurs as the X-rays interact with the sample. According to the Bragg's law, the crystal structure within the sample diffracts the incident X-rays into a series of diffraction peaks with specific angles and intensities. The typical form of the Bragg equation is:

$$2d\sin\theta = n\lambda \quad (3 - 1)$$

Here,  $d$  represents the lattice spacing of the material,  $\lambda$  is the wavelength of the incident ray, and  $\theta$  denotes the angle of incidence.

By rotating the sample or detector and recording changes in diffraction angle and intensity, an XRD diffraction pattern is obtained. The positions and intensities of the diffraction peaks in the pattern provide crucial information about the crystal structure and lattice parameters.

Analysis of the diffraction pattern allows determination of various aspects of the crystal, including lattice parameters, unit cell volume, crystal structure type, crystal orientation, and relative content. XRD finds extensive applications in fields such as materials science, solid-state physics, geology, chemistry, and biology. It is used to analyze the structure, crystal orientation, unit cell parameters, and grain boundary properties of crystalline materials. Additionally, XRD can determine the phase composition of materials, crystal purity, stress state, and structural changes within crystals.

XRD patterns were recorded using a Rigaku MiniFlex 600 diffractometer with Cu K $\alpha$  radiation ( $\lambda = 1.5406$  Å), operated at 40 kV and 15 mA. Data were collected over a  $2\theta$  range of  $5^\circ$ – $80^\circ$  with a step size of  $0.02^\circ$  and a scan rate of  $2^\circ/\text{min}$ .

### 3.3.2 Raman laser spectrometer (LabRAM Odyssey)

The Raman laser spectrometer is an advanced optical instrument utilized for analyzing the molecular structure and chemical composition of materials. It operates based on the principle of Raman scattering, which provides a characteristic spectrum revealing molecular vibrations and lattice information of the sample.

#### Working Principle:

The Raman spectrometer employs a monochromatic laser light source, typically a laser diode with wavelengths like 785 nm or 532 nm. These lasers emit a single wavelength beam that illuminates the sample surface. When the laser light interacts with the sample, most photons undergo elastic scattering known as Rayleigh scattering, maintaining their original frequency and energy. However, a small fraction of photons undergo inelastic scattering—Raman scattering—where the frequency of some photons changes. This frequency shift, known as Raman frequency shift, is unique to each material and provides valuable molecular information. The scattered light from the sample is collected by an efficient optical system, including objective lenses, focusing lenses, and optical fibers, to maximize the collection of Raman scattered photons. This collected light is then directed to a spectrometer.

#### Components:

**Laser Source:** Provides monochromatic light to interact with the sample.

**Sample Holder:** Positions the sample for accurate laser irradiation.

**Scattering Collection System:** Collects scattered light efficiently.

**Spectrometer:** Separates and analyzes Raman scattered light using a grating or interferometer to distinguish different wavelengths.

**Detector:** Converts optical signals into electrical signals for further processing.

**Data Processing System:** Controls the instrument, collects Raman spectra, and analyzes data using computer software for real-time display, peak identification, and spectral line fitting.

#### Output:

The spectrometer converts the collected Raman scattering spectrum into a graph showing the relationship between wave number or Raman frequency shift and the intensity of scattered light. This Raman spectrum serves as a fingerprint of the sample's molecular composition and

structure.

Raman spectra were recorded using a LabRAM Odyssey Raman spectrometer (Horiba) equipped with a 532 nm laser as the excitation source. The laser power was set to 1–5 mW to avoid sample damage. A 50× objective lens was used for focusing, and the spectral resolution was  $\sim 1 \text{ cm}^{-1}$ . Each spectrum was acquired with an integration time of 10 s and averaged over 2–3 accumulations.

### **3.3.3 X-ray photoelectron spectroscopy (XPS, Thermo Fisher Scientific, ESCALAB 250)**

XPS is an advanced characterization technique used for analyzing the chemical composition and electronic structure of material surfaces. We use XPS technology to obtain information about the elemental composition, chemical state, and electronic state of material surfaces by measuring the energy of photoelectrons emitted from the sample surface.

The working principle involves irradiating the sample surface with a monochromatic X-ray beam (usually Al  $K_{\alpha}$  line with an energy of approximately 1486.6 eV). When the X-rays strike the sample, the atoms on the sample surface absorb the X-ray energy, causing the inner-shell electrons (typically 1s, 2s, or 2p electrons) to be excited and emitted from the sample—a process known as the photoelectric effect. The kinetic energy of the emitted photoelectrons is measured by an electron energy analyzer. The binding energy of the photoelectrons can be calculated using the known X-ray energy and the measured kinetic energy, based on the following relationship:

$$E_b = h\nu - E_k - \varphi \quad (3 - 2)$$

$E_b$  is the binding energy of the photoelectrons

$h\nu$  is the energy of the X-rays

$E_k$  is the kinetic energy of the photoelectrons

$\varphi$  is the work function of the spectrometer.

The distribution of binding energies forms an XPS spectrum, where each peak represents the binding energy of different elements or the same element in different chemical environments. By analyzing the position, intensity, and shape of these peaks, the elemental composition,

chemical state, and electronic structure of the sample surface can be determined.

An XPS mainly consists of the following components:

X-ray source: Typically uses aluminum (Al K $\alpha$ ) or magnesium (Mg K $\alpha$ ) as the X-ray source to produce high-intensity, monochromatic X-rays.

Sample chamber: The sample is placed in a vacuum environment within the sample chamber to prevent air molecules from interfering with the emission and detection of photoelectrons.

Electron energy analyzer: Precisely measures the kinetic energy of emitted photoelectrons.

Common types of energy analyzers include spherical and cylindrical analyzers.

Detector: Detects and counts the photoelectron signals transmitted from the analyzer and converts them into processable data.

Data processing system: Computer software collects, processes, and analyzes the photoelectron spectroscopy data, generates spectra, and performs peak analysis, quantitative composition, and chemical state identification.

XPS are widely used in material science, surface chemistry, semiconductor industry, corrosion research, catalyst development, biomaterials, and nanotechnology. They play a crucial role in studying the surface composition, chemical state changes, interface reactions, and thin film thickness measurements. In summary, XPS provide detailed chemical information about the sample surface by measuring the energy distribution of photoelectrons, making them an essential tool for researching material surface properties and chemical reactions.

XPS measurements were performed using a Thermo Fisher Scientific ESCALAB 250 spectrometer equipped with a monochromatic Al K $\alpha$  radiation source ( $h\nu = 1486.6$  eV). The pass energy was set to 100 eV for survey scans and 20 eV for high-resolution spectra. The base pressure in the analysis chamber was maintained at  $\sim 10^{-9}$  mbar. All binding energies were calibrated using the C 1s peak at 284.8 eV as the reference.

### **3.3.4 Scanning electron microscopy (SEM, UniColore)**

SEM is a high-resolution microscopy technique that obtains surface morphology and compositional information of samples through signals generated by the interaction of an electron beam with the sample. Compared to optical microscopes, SEM offers higher resolution



and greater depth of focus, allowing for the observation of smaller and more detailed sample features. Therefore, SEM is widely used in fields such as materials science, biology, geology, and nanotechnology. SEM can observe and analyze various samples, including metals, ceramics, polymers, biological tissues, and nanomaterials.

SEM uses a thermionic or field emission electron gun to generate a high-energy electron beam. A thermionic gun produces electrons by heating a tungsten filament or lanthanum hexaboride ( $\text{LaB}_6$ ), while a field emission gun uses a strong electric field to emit electrons from a sharp tip. The generated electron beam is accelerated and focused by an electromagnetic lens system, forming a fine probe. The acceleration voltage typically ranges from several kilovolts to tens of kilovolts, and the diameter of the electron beam can be reduced to a few nanometers.

Samples typically require appropriate preparation, including fixation, dehydration, drying, and metal coating (such as gold sputtering). Metal coating aims to enhance the sample's conductivity, facilitating electron beam scanning and signal detection in the SEM. The focused electron beam scans the sample surface line by line. When the electron beam hits the sample surface, it interacts with the atoms in the sample, generating various signals, including secondary electrons (SE), backscattered electrons (BSE), transmitted electrons, characteristic X-rays, and other radiation.

These signals are detected and converted into electrical signals. SE are used to form high-resolution surface morphology images, while BSE provide information on the composition and relative density of the sample. The electrical signals received by the detector are amplified and processed to generate image data. The images can be observed on a display screen or recorded as digital images. Image analysis software can be used to measure the sample's size, shape, and surface morphology, as well as to perform spectral analysis (EDS or EDX) to obtain the elemental composition and chemical information of the sample.

In summary, SEM is a powerful microscopy technique that provides high-resolution and high-depth-of-focus surface morphology and compositional information of samples. SEM images were acquired using a UniColore SEM system operated at an accelerating voltage of 5-15 kV. Samples were sputter-coated with a thin layer of gold to enhance conductivity. Both secondary electron and backscattered electron modes were used to observe the surface morphology and elemental contrast.

### **3.3.5 Transmission electron microscopy (TEM, UniColore)**

TEM is a high-resolution microscopy tool primarily employed to observe the internal microstructure and atomic-level details of samples. Unlike the SEM, which captures surface images, TEM operates by transmitting electrons through the sample, allowing for superior resolution compared to SEM. TEM utilizes either a thermionic or field emission electron gun to generate a high-energy electron beam. The thermionic source heats a tungsten filament or lanthanum hexaboride (LaB<sub>6</sub>) to emit electrons, whereas the field emission gun emits electrons from a sharp tip using a strong electric field. The resulting electron beam is accelerated to tens to hundreds of kilovolts and focused through an array of electromagnetic lenses. The beam diameter can be reduced to a nanometer scale, enabling it to pass through the sample and produce detailed, high-resolution images.

Samples for TEM analysis are typically prepared as extremely thin slices, ranging from hundreds of nanometers to a few micrometers in thickness. These slices are commonly prepared using specialized techniques such as focused ion beam (FIB) milling or mechanical sectioning to ensure they are suitable for electron transmission. As the electron beam passes through the thin sample slice, the intensity of transmitted electrons varies according to the sample's internal structure. During transmission, the electron beam interacts with sample atoms through scattering, absorption, and transmission, creating intricate transmission patterns.

Adjusting the electron lens system allows TEM to capture images at different depths and focal points, revealing comprehensive details of the sample's internal structure. Detectors collect the signals of transmitted electrons, which are then converted into electrical signals, amplified, and processed. The final images can be observed on a screen or digitally recorded, facilitating further analysis using specialized image processing software.

TEM is extensively used in diverse fields such as materials science, biology, nanotechnology, and electronics, facilitating the observation and analysis of complex structures including crystal structures, nanoparticles, biomolecules, and material interfaces. TEM was performed using a UniColore TEM system operated at an accelerating voltage of 200 kV. High-resolution TEM (HRTEM) images and selected area electron diffraction (SAED) patterns were obtained to analyze the crystal structure and lattice fringes. Samples were ultrasonically dispersed in

ethanol and drop-cast onto a carbon-coated copper grid.

### **3.3.6 Nitrogen adsorption-desorption test (BELSORP MAX II)**

Nitrogen adsorption-desorption testing (or nitrogen adsorption method) is a widely employed technique for characterizing material pore structure and specific surface area. This method revolves around measuring the adsorption and desorption of gas molecules on the surface of solids across varying pressures. Initially, samples undergo pretreatment to remove surface adsorbates and moisture, ensuring the accuracy of subsequent test results.

Typically conducted at low temperatures (often below the temperature of liquid nitrogen), nitrogen adsorption tests ensure sufficient adsorption of gas molecules onto the sample's surface and pores. Samples are placed within an adsorption apparatus where nitrogen is introduced while pressure and temperature are adjusted, facilitating gradual adsorption onto the sample's surface and pores. Throughout the adsorption process, measurements of nitrogen adsorption at different pressures are recorded.

Data gathered during both adsorption and desorption phases enable calculation of critical parameters such as specific surface area, pore volume, and pore size distribution using various adsorption isotherms (e.g., BET isotherm) and desorption isotherms. Common analytical methods include the Brunauer-Emmett-Teller method, Barrett-Joyner-Halenda method (BJH), among others.

Nitrogen adsorption-desorption tests find extensive applications in fields like materials science, chemical engineering, and catalyst research. They serve to evaluate and compare pore structure characteristics among different materials. Nitrogen adsorption-desorption isotherms were measured at 77 K using a BELSORP MAX II surface area and porosity analyzer. Prior to measurements, samples were degassed under vacuum at 150 °C for 6 hours to remove adsorbed gases and moisture. The specific surface area was calculated using the BET method, and the pore size distribution was determined by the BJH method based on the desorption branch of the isotherm.

### **3.3.7 Thermogravimetric analysis (TGA, NETZSCH, STA449-F5)**

TGA is an important thermal analysis technique used to study the mass change of substances under controlled temperature conditions, either during heating or at constant temperatures. It involves recording the variation in sample mass over time to analyze properties such as thermal stability and decomposition behavior at different temperatures. Samples are typically prepared in powder or small block form and placed in precise sample boats for accurate mass measurement. These boats are placed in a TGA instrument, often in an inert gas environment like nitrogen or argon, to prevent interference from air during the experiment.

The temperature is gradually increased or held constant at the beginning of the experiment. Throughout the process, the TGA instrument continuously records the changes in sample boat mass. As the temperature changes, the sample may undergo various processes such as thermal decomposition, physical adsorption, or chemical reactions, resulting in mass changes. These changes are detected and recorded by the instrument's sensitive balance, ultimately generating a thermogravimetric curve (TG curve).

TGA, as a powerful thermal analysis technique, provides researchers with a crucial tool to deeply understand the thermal properties and reaction behaviors of samples. Thermogravimetric analysis was used to measure the S content in the cathode from 50 °C to 400 °C at a heating rate of 5°C/min in an N<sub>2</sub> atmosphere

### **3.3.8 Electron paramagnetic resonance (EPR, JES-FA200)**

EPR, also known as Electron Spin Resonance, is a technique used to study materials with unpaired electrons by examining their electron magnetic resonance. EPR is primarily used to detect and analyze samples with unpaired electrons, such as free radicals, transition metal ions, and defect centers.

Principle of Operation:

Paramagnetic materials contain unpaired electrons, which have spin and magnetic moments. In the absence of an external magnetic field, these spin magnetic moments are randomly oriented. When the paramagnetic material is placed in an external magnetic field, the spin

magnetic moments of the unpaired electrons interact with the field, causing a splitting of the spin states. This energy level splitting is known as the Zeeman effect.

At a specific frequency, typically in the microwave range, when the strength of the external magnetic field meets a particular condition, the electron spins can absorb microwave energy and transition from a lower energy level to a higher one. This specific condition is known as the resonance condition.

Under resonance conditions, the absorption of microwave energy by the electrons causes a change in magnetization, which is detected and recorded. By measuring the absorbed microwave energy, an EPR spectrum is obtained.

An EPR spectrum contains information about the unpaired electrons in the sample, including:  
g-factor: Indicates the magnetic characteristics of the electron. It is a dimensionless value that helps identify different paramagnetic species.

Hyperfine structure: Caused by interactions between the electrons and nearby atomic nuclei, providing detailed information about the electronic environment.

Line width and shape: Provide information about electron relaxation times and dynamic processes.

EPR is a powerful analytical tool that provides crucial information about the chemical and physical properties of samples by detecting the magnetic resonance of unpaired electrons. EPR measurements were conducted at a temperature of 300 K and across a magnetic field strength range of 0.3 to 1.5 Tesla (T).

### **3.3.9 UV-Vis absorption spectroscopy (Lambda 950 UV-Vis-NIR Spectrophotometer, Perkin Elmer)**

UV-Vis Absorption Spectroscopy is a technique used to analyze the optical properties and chemical composition of molecules and materials. It is based on the ability of substances to absorb ultraviolet and visible light. By measuring the absorption intensity of a sample at different wavelengths, information about its molecular structure and concentration can be obtained.

UV-Vis absorption spectroscopy involves illuminating a sample with ultraviolet and visible

light (typically in the wavelength range of 200-800 nm from a light source and measuring the sample's absorption of light at different wavelengths. When light is directed at the sample, molecules within the sample absorb light at specific wavelengths, causing electrons to transition from the ground state to an excited state. By detecting the change in light intensity after passing through the sample, an absorption spectrum is obtained.

The absorption spectrum is typically presented as a plot of absorbance (A) versus wavelength ( $\lambda$ ). Absorbance is defined as:

$$A = -\log\left(\frac{I}{I_0}\right) \quad (3 - 3)$$

where  $I_0$  is the incident light intensity and  $I$  is the transmitted light intensity.

Key Features and Applications:

Qualitative Analysis: By comparing the absorption spectrum of a sample with standard spectra of known substances, specific molecules or groups within the sample can be identified.

Quantitative Analysis: According to the Beer-Lambert Law, absorbance is directly proportional to the concentration of the absorbing species in the solution and the path length of the light. By measuring absorbance, the concentration of the target substance in the sample can be calculated.

The Beer-Lambert Law is expressed as:

$$A = \epsilon lc \quad (3 - 4)$$

where A is absorbance,  $\epsilon$  is the molar absorptivity, c is the concentration of the absorbing species, and l is the path length.

Structural Analysis: Different molecules or groups absorb light at specific wavelengths with varying peak positions and intensities. The absorption spectrum can provide information about molecular structure, such as conjugated systems, functional groups, and types of electronic transitions.

UV-Vis absorption spectroscopy is a crucial spectroscopic technique that provides valuable information about the molecular structure and concentration of samples by measuring their absorbance in the ultraviolet and visible light ranges.

### 3.3.10 X-ray absorption spectroscopy

X-ray absorption spectroscopy (XAS) measurements were conducted to analyze the local

electronic structure and oxidation states of the active species. Bi and Te K-edge XAS spectra were collected at the XAS beamline of the Australian Synchrotron (Clayton, VIC) using a Si(111) double-crystal monochromator in fluorescence mode at room temperature. Co K-edge XAS spectra were acquired at the CLAEISS beamline of the ALBA Synchrotron Light Facility (Barcelona, Spain).

XAS is an analytical technique that uses X-rays to study the structural, electronic, and chemical environment of materials. XAS is divided into two main parts: X-ray Absorption Near Edge Structure (XANES) and Extended X-ray Absorption Fine Structure (EXAFS).

When X-rays irradiate a sample and their energy exceeds the binding energy of an inner-shell electron of an atom in the sample, the X-rays are absorbed, and the electron is excited to unoccupied energy levels or completely ejected from the atom, a process known as the photoelectric effect. By measuring the absorption coefficient at different X-ray energies, an X-ray absorption spectrum is obtained.

#### **Main Components of XAS Spectrum:**

**XANES:** This is the region near the absorption edge (typically within about 50 eV) where there is a sharp change in the absorption coefficient. XANES provides information about the electronic structure, oxidation state, and local symmetry of the absorbing atom.

**EXAFS:** This region extends beyond the absorption edge (up to over 1000 eV) and consists of oscillations caused by the interference of the ejected electron wave with neighboring atoms. EXAFS provides information about interatomic distances, coordination numbers, and local structural details.

#### **Key Features and Applications:**

**Elemental Selectivity:** XAS can selectively probe the local structure and chemical state of specific elements because each element has its unique X-ray absorption edge.

**Non-destructive:** The technique is generally non-destructive, allowing measurements to be made without damaging the sample.

**Versatility:** XAS is applicable to various sample forms, including solids, liquids, gases, thin films, and powders.

**Rich Information:** XANES provides insights into the electronic structure, oxidation states, and local symmetry, while EXAFS can reveal local structural information such as interatomic

distances and coordination numbers.

Wide Applications: XAS is widely used in materials science, chemistry, physics, biology, and environmental science. Applications include studying active centers in catalysts, local structures in metal oxides, metal binding sites in biomolecules, and speciation of pollutants in environmental samples.

XAS is a powerful technique that provides detailed information about the local structure, electronic states, and chemical environment of materials, with broad applications across many scientific fields.

### 3.4 Electrochemical methods

In this thesis, electrochemical testing serves as the key method for characterizing the electrochemical performance of MSBs. We utilized an electrochemical workstation provided by CorrTest from Wuhan, along with instruments from LAND in Wuhan and NEWARE in Shenzhen for constant current charge-discharge experiments. The main testing techniques employed include cyclic voltammetry (CV), galvanostatic charge/discharge (GCD), and electrochemical impedance spectroscopy (EIS). These methods were essential for in-depth analysis of the MSBs performance characteristics.

The prepared electrode material, Super P, and PVDF binder were mixed and ground according to 8:1:1, and NMP as added during the grinding process to prepare slurry. Then it was evenly coated on the current collector on the aluminum foil, and finally dried at 60 °C for 12 h and cut into 12 mm circular pieces to obtain the working electrode. The sulfur content of the cathode was 1.2 mg cm<sup>-2</sup>. For each coin cell, 20 μL of electrolyte was used. To further highlight the practical application of the electrode, the high loading cathode was prepared by the same method. The prepared sulfur electrode was used as the cathode, the lithium foil was used as the anode, and Celgard 2400/glass fiber and 1.0 M Lithium Bis(trifluoromethanesulfonyl)imide (LiTFSI) and 0.1 M LiNO<sub>3</sub> were dissolved in DOL/DME (v:v, 1:1)/ 1 M NaClO<sub>4</sub> in a 1:1 mixture of DEC and EC, with 5 wt% FEC as the electrolyte additive as the separator and electrolyte, respectively, to assemble a 2023 coin battery in argon-filled in the airy glove box. The prepared battery is subjected to CV and GCD tests at a voltage window of 1.7-2.8 V/0.8-



2.8 V, and an EIS test is performed at a frequency of 0.01 Hz-100 KHz.

### **3.4.1 Cyclic voltammetry (CV)**

CV is a widely utilized electrochemical testing method employed to investigate the behavior and reaction mechanisms of electrochemical systems. It operates on the fundamental relationship between current and voltage, achieved by applying a sinusoidal potential signal to an electrode to regulate and monitor electrochemical processes. CV entails the application of a sinusoidal waveform potential signal to the working electrode, with the rate of potential change referred to as the scan rate. Typically, measurements are conducted during a linear change in potential over time in electrochemical experiments. Variations in the potential applied to the working electrode induce electrochemical reactions on its surface, facilitating charge transfer and resulting in a measurable current response. CV test quantifies the changes in current during the application of potential.

CV curves graphically depict the relationship between current response and potential change, conventionally plotted with current (y-axis) against potential (x-axis). These curves furnish valuable insights into electrochemical reaction rates, reaction reversibility, peak potentials, and peak currents. CV is instrumental in probing the kinetic properties of electrochemical reactions, such as reaction rate constants and electron transfer processes. Furthermore, the morphology and features of CV curves facilitate analysis of the electrochemical characteristics of electrode surfaces, encompassing the identification of active sites and assessment of catalytic activity. CV also serves as a valuable tool for assessing the stability of electrolytes and the ion transport properties within electrochemical solutions.

In essence, CV stands as a versatile and extensively applied electrochemical testing technique pivotal for comprehending and refining the performance of electrochemical systems.

### **3.4.2 Galvanostatic charge-discharge (GCD)**

GCD is a commonly used electrochemical testing method for assessing the performance and characteristics of electrochemical energy storage systems, such as batteries. It primarily controls the charging and discharging processes by applying a constant electric current to

monitor and record the voltage changes of the battery under specific current conditions.

During galvanostatic charging, a constant current is applied, determining the rate at which the battery charges. The battery absorbs charge during this process, and the current magnitude depends on the battery's internal resistance and charging rate. The voltage of the battery varies over time when a constant current is applied, and this variation is plotted as the galvanostatic charge-discharge curve. By recording these changes, one can evaluate the electrochemical performance of the battery, including factors like charging capacity, efficiency, and the impact of charging rates.

After charging is complete, the battery can be discharged using the same or a different constant current. During discharge, the battery releases stored charge, with the current direction reversed compared to charging, causing the voltage to gradually decrease as discharge progresses. Analyzing the slope and shape of the galvanostatic charge-discharge curve provides insights into the battery's internal resistance, electrochemical reaction kinetics, and the efficiency of energy storage and release processes.

GCD is a critical method for evaluating the electrochemical performance of batteries, offering essential data on capacity, efficiency, and cycling stability. Moreover, these curves can be utilized to study electrochemical reaction mechanisms and kinetic properties within batteries, such as solute diffusion and electron transfer processes.

In summary, GCD is a straightforward yet effective electrochemical testing method applicable to various electrochemical energy storage systems. It provides crucial experimental data supporting the advancement and application of battery technology.

### **3.4.3 Electrochemical impedance spectroscopy (EIS)**

EIS is an advanced technique widely used for studying the complex impedance characteristics and interface processes in electrochemical systems. It involves applying small-amplitude alternating current signals of varying frequencies to electrodes or batteries within the electrochemical system to obtain impedance spectra. EIS operates by applying small-amplitude AC signals across a range of frequencies typically spanning from a few hertz to several hundred kilohertz, covering a wide spectrum from low to high frequencies. The amplitude of the

electrical signal is usually kept small enough to avoid significant electrochemical reactions, thereby maintaining the system in a steady-state response.

After applying the AC signal, the voltage response of the system is measured. This response includes components such as resistance (the real part of impedance) and capacitance (the imaginary part of impedance), providing detailed information about electrode/electrolyte interfaces, charge transfer processes, and electrochemical reaction kinetics. Complex mathematical and statistical analyses of the measurement data yield impedance spectra, which depict the relationship between frequency and impedance complex numbers. Impedance spectra are typically presented in forms such as Nyquist plots and Bode plots, which intuitively illustrate the complex characteristics of electrochemical systems.

EIS enables in-depth analysis of electrode/electrolyte interface properties, such as charge transfer resistance, double-layer capacitance, and electrolyte diffusion processes. By measuring impedance spectra of different electrode materials, their performance and stability can be evaluated, aiding in electrode design and optimization. EIS is also used to assess the conductivity and stability of electrolytes, which is crucial for developing efficient electrolyte systems.

EIS is a powerful electrochemical testing technique that provides critical interface and dynamic information essential for understanding and optimizing electrochemical system.

# **Chapter 4**

## **Combined Defect and Heterojunction Engineering in ZnTe/CoTe<sub>2</sub>@NC Sulfur Hosts Toward Robust Lithium–Sulfur Batteries**

## **4. Combined Defect and Heterojunction Engineering in ZnTe/CoTe<sub>2</sub>@NC Sulfur Hosts Toward Robust Lithium–Sulfur Batteries**

### **Key findings**

1. The sulfur redox catalyst was significantly optimized by adjusting the anion (Te) vacancy concentration and engineering ZnTe/CoTe<sub>2</sub> heterostructures.
2. Experimental results confirmed that tellurium vacancies enhance the adsorption of LiPSs, facilitating improved sulfur utilization.
3. The introduction of TMT/TMT and TMT/C heterostructures, together with the NC coating, promoted both rapid lithium-ion diffusion and electron transport.
4. The resulting v-ZnTe/CoTe<sub>2</sub>@NC/S composite sulfur cathode delivered an excellent initial capacity of 1608 mAh g<sup>-1</sup> at 0.1C, with long-term cycling stability showing an average capacity decay rate as low as 0.022% per cycle over 500 cycles at 1C.

### **Introduction**

The development of efficient sulfur cathode materials is crucial for advancing LSBs, which are promising next-generation energy storage systems due to their high theoretical capacity and energy density. However, several intrinsic limitations, including poor conductivity of sulfur and dissolution of LiPSs, severely hinder their practical application.

To address these challenges, advanced sulfur host materials that integrate strong polysulfide adsorption, high conductivity, and catalytic activity are necessary. In this chapter, we focus on the rational design of a composite sulfur host featuring engineered heterostructures and vacancy defects, aiming to simultaneously enhance electrochemical performance and cycling stability.

### **Purpose and background**

The core of this study lies in the design and modification of TMTs as efficient sulfur

hosts. TMTs exhibit several advantages:

Rich electronic structures and tunable band gaps contribute to superior electrical and optical behavior.

Some TMTs, such as  $\text{WTe}_2$ , possess topologically protected surface states, offering potential in quantum technologies.

$\text{ZnTe}$ , in particular, demonstrates high electron mobility, making it a candidate material for high-speed electronic and electrochemical applications.

Initially,  $\text{ZnTe@NC}$  was synthesized and tested as a sulfur host. Despite its promising properties, the material exhibited subpar electrochemical performance, prompting further exploration. Through literature reviews and preliminary experiments, we identified that heterostructure engineering and defect (vacancy) engineering could significantly enhance the catalytic properties and electronic structure of host materials.

### **Experimental strategy**

To improve performance, we designed a  $\text{ZnTe/CoTe}_2$  heterostructure, leveraging their structural compatibility to ensure efficient electronic integration. Though this approach improved the specific capacity of the composite, the cycle stability gains were limited. To resolve this issue, we introduced Te vacancies via hydrogen reduction treatment, producing  $v\text{-ZnTe/CoTe}_2\text{@NC}$ . Defects like vacancies are known to:

Provide additional active sites.

Adjust the surface adsorption energy of LiPSs.

Enhance overall conductivity by altering carrier concentration.

Induce localized electronic structure variations that favor charge transfer.

Furthermore, the heterostructure between  $\text{ZnTe}$  and  $\text{CoTe}_2$  generates a built-in electric field, which facilitates fast ion migration and promotes  $\text{Li}^+$  diffusion through the electrode.

### **Conclusion**

This work demonstrates that the combined strategy of heterostructure formation and vacancy engineering is a powerful route to enhance the electrochemical performance of TMT-based sulfur hosts in LSBs. The insights gained here offer valuable guidelines for the rational design of future electrode materials in sulfur-based energy storage

systems.

## RESEARCH ARTICLE

# Combined Defect and Heterojunction Engineering in ZnTe/CoTe<sub>2</sub>@NC Sulfur Hosts Toward Robust Lithium–Sulfur Batteries

Chen Huang, Jing Yu, Canhuang Li, Zhibiao Cui, Chaoqi Zhang,\* Chaoyue Zhang,\* Bingfei Nan, Junshan Li, Jordi Arbiol, and Andreu Cabot\*

Lithium–sulfur batteries (LSBs) are feasible candidates for the next generation of energy storage devices, but the shuttle effect of lithium polysulfides (LiPSs) and the poor electrical conductivity of sulfur and lithium sulfides limit their application. Herein, a sulfur host based on nitrogen-doped carbon (NC) coated with small amount of a transition metal telluride (TMT) catalyst is proposed to overcome these limitations. The properties of the sulfur redox catalyst are tuned by adjusting the anion vacancy concentration and engineering a ZnTe/CoTe<sub>2</sub> heterostructures. Theoretical calculations and experimental data demonstrate that tellurium vacancies enhance the adsorption of LiPSs, while the formed TMT/TMT and TMT/C heterostructures as well as the overall architecture of the composite simultaneously provide high Li<sup>+</sup> diffusion and fast electron transport. As a result, v-ZnTe/CoTe<sub>2</sub>@NC/S sulfur cathodes show excellent initial capacities up to 1608 mA h g<sup>−1</sup> at 0.1C and stable cycling with an average capacity decay rate of 0.022% per cycle at 1C during 500 cycles. Even at a high sulfur loading of 5.4 mg cm<sup>−2</sup>, a high capacity of 1273 mA h g<sup>−1</sup> at 0.1C is retained, and when reducing the electrolyte to 7.5 μL mg<sup>−1</sup>, v-ZnTe/CoTe<sub>2</sub>@NC/S still maintains a capacity of 890.8 mA h g<sup>−1</sup> after 100 cycles at 0.1C.

## 1. Introduction

Sulfur cathodes are regarded as a viable and advantageous alternative for the forthcoming generation of energy storage devices due to their high energy density (2600 Wh kg<sup>−1</sup>) and specific capacity (1675 mAh g<sup>−1</sup>) as well as the large sulfur abundance and low cost.<sup>[1]</sup> However, sulfur-related limitations such as the shutting of lithium polysulfides (LiPSs), poor conductivity of the charged and discharged cathode active material (S<sub>8</sub>/Li<sub>2</sub>S), inefficient sulfur usage, and huge volume expansion during charging and discharging restrain the practical application of lithium–sulfur batteries (LSBs).<sup>[2]</sup> To solve these shortcomings, various approaches have been considered, including the development of sulfur hosts<sup>[3]</sup> and the engineering of functional separators and binders able to trap the polysulfides.<sup>[4]</sup> Particularly, the use of catalytically active sulfur hosts has been

C. Huang, J. Yu, C. Li, C. Zhang, B. Nan, A. Cabot  
Catalonia Institute for Energy Research-IREC  
Sant Adrià de Besòs, 08930 Barcelona, Spain  
E-mail: czhang@irec.cat; acabot@irec.cat

C. Huang, C. Li  
Department of Chemistry  
Universitat de Barcelona  
08028 Barcelona, Spain

J. Yu, J. Arbiol  
Catalan Institute of Nanoscience and Nanotechnology (ICN2)  
CSIC and BIST  
Campus UAB, Bellaterra, 08193 Barcelona, Catalonia, Spain

Z. Cui  
School of Chemistry  
South China Normal University  
Guangzhou 510006, China

C. Zhang  
College of Materials Science and Engineering  
Fuzhou University  
No. 2, Xueyuan Road, Minhou County, Fuzhou City, Fujian  
Province 350108, China

C. Zhang  
Key Laboratory for Magnetism and Magnetic Materials of the Ministry of Education & School of Physical Science & Technology  
Lanzhou University  
Lanzhou 730000, China  
E-mail: czhang@irec-edu.cat

J. Li  
Institute for Advanced Study  
Chengdu University  
Chengdu 610106, China

J. Arbiol, A. Cabot  
ICREA Pg. Lluis Companys  
08010 Barcelona, Catalonia, Spain

 The ORCID identification number(s) for the author(s) of this article can be found under <https://doi.org/10.1002/adfm.202305624>

DOI: 10.1002/adfm.202305624



shown to accelerate sulfur reduction and oxidation reactions and has thus received considerable attention in recent years.<sup>[1a,5]</sup>

While porous and high surface area carbon materials (e.g., graphene, carbon nanotubes, and carbon fibers) are frequently used as sulfur hosts,<sup>[6]</sup> the weak interaction between nonpolar carbon materials and polar polysulfides is unable to inhibit the dissolution and shuttling effect of LiPSs.<sup>[7]</sup> Nitrogen<sup>[8]</sup> and supplementary metal additives can be introduced to capture the LiPS and accelerate their conversion.<sup>[9]</sup> Transition metal compounds (oxides, phosphides, carbides, and chalcogenides) have been shown particularly effective as polar catalytic additives in sulfur cathodes.<sup>[10]</sup> Among them, transition metal tellurides (TMTs) have been systematically ignored due to their high density as well as the low abundance and high cost of tellurium. Nevertheless, TMTs offer several patent advantages over the wide variety of tested compounds that, if used in very small quantities, could help balance and potentially overcome their drawbacks. These advantages include i) much higher electrical conductivities (e.g.,  $1.15 \times 10^6 \text{ S m}^{-1}$  for  $\text{NiTe}_2$ ) compared with oxides, sulfides, and selenides counterparts (e.g.,  $0.55 \text{ S m}^{-1}$  for  $\text{NiS}_2$ ),<sup>[11]</sup> and ii) high catalytic activities related to the metal cation ( $\text{Co}^{2+}$ ,  $\text{Zn}^{2+}$ , and  $\text{Ni}^{2+}$ ) forming an octahedral complex with  $\text{Te}_2^{2-}$  in a low-spin state, while the metal 3d orbital splits into two subordinate orbitals,  $t_{2g}$  and  $e_g$ . In TMTs, the metal ions adopt different spin modes in the 3D electronic configuration, which can promote the rapid charge transfer of the electrode and the LiPS conversion.<sup>[12]</sup>

To minimize the amount of TMT additive, suitable composite designs must be built, incorporating effective heterostructures and assuring a large TMT dispersion. Besides, given the close correlation between catalytic activity and electronic band structure, to optimize the electrocatalytic performance of the host, it is necessary to adjust the electronic properties of the active sites. At the material architecture level, these electronic properties can be adjusted through interface engineering. Additionally, at the atomic level, electronic characteristics can be tuned by regulating the coordination environment of the active site.

At the material architecture level, heterostructures composed of materials with different bandgaps have been widely used to optimize electronic parameters in electrode materials for photo/electrocatalysis,<sup>[13]</sup> batteries,<sup>[14]</sup> and supercapacitors.<sup>[15]</sup> At the interface of two different semiconductors, rich phase boundaries, charge accumulation/depletion, an electric field, and electronic band bending are encountered.<sup>[16]</sup> These singular regions can promote the diffusion of ions/electrons and thus accelerate the conversion reaction. For example, Zhang et al. prepared heterostructured  $\text{Fe}_3\text{C}/\text{FeN}$  nanoparticles in a 3D-ordered nitrogen-doped carbon and demonstrated the  $\text{Fe}_3\text{C}/\text{FeN}$  heterointerface to exhibit high sulfiphilicity.<sup>[17]</sup>

At the atomic level, vacancy engineering, particularly anionic vacancies, has been demonstrated as a successful approach to significantly improve material properties by just modifying the compound stoichiometry.<sup>[15d,18]</sup> Within sulfur hosts for LSB cathodes, introducing an anion vacancy not only generally increases the number of carriers within the crystal and changes the electronic structure near the defect sites, but the activated unpaired cations can also capture polysulfides efficiently,<sup>[19]</sup> thus improving the sulfur utilization rate. As an example in this direction, Wang et al. used an acid etching approach to produce  $\text{ZnS}$  nanotubes with abundant sulfur vacancies, which they then supported on free-

standing carbon cloth to use as LSB electrode. They showed the combination of architectural and sulfur-vacancy engineering to effectively modulate the electronic structure of  $\text{ZnS}$ , enhance its interactions with active sulfur, facilitate ion/electron transfer, and ultimately improve the LSB performance.<sup>[19b]</sup> Numerous other previous works have explored the effects of oxygen and sulfur vacancies on the performance of LSBs, however, the chemical affinity and catalytic activity of Te vacancies as LiPSs have been very rarely considered.<sup>[11b,20]</sup>

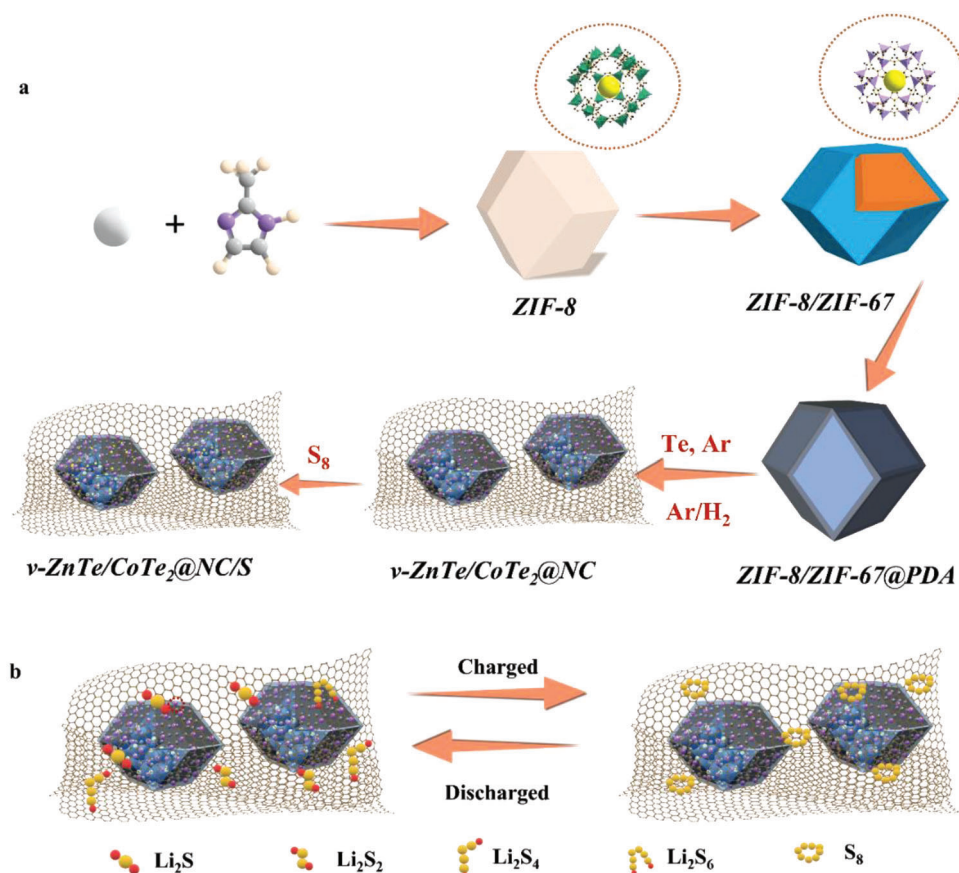
Defect and heterojunction engineering strategies have been validated separately in the context of LSBs, but no catalysts that simultaneously use both of these two electronic modification strategies to test their compatibility and potential synergy have been reported. Given the intricate nature of the Li-S reaction system, a single approach is unlikely to effectively meet the multiple challenges posed by LSBs.

The present study employs a dual engineering approach, manipulating vacancies and heterointerfaces, to develop an optimized TMT-based catalytic additive. More precisely, N-doped carbon-coated bimetallic telluride heterostructures containing Te vacancies ( $v\text{-ZnTe}/\text{CoTe}_2@\text{NC}$ ) are used as sulfur hosts in LSBs. We showcase here the exceptional specific capacity, stable cycling, and superior rate capability of  $v\text{-ZnTe}/\text{CoTe}_2@\text{NC}$  as sulfur host, which can be attributed to the synergistic effects and functionality of vacancies and heterointerface. These effects are observed even at high loading and in lean electrolyte conditions, thereby highlighting the remarkable potential of this system.

## 2. Results and Discussions

**Scheme 1a** illustrates the synthesis steps used to prepare  $v\text{-ZnTe}/\text{CoTe}_2@\text{NC}/\text{S}$  cathode materials and **Scheme 1b** the conversion between  $\text{S}_8$  and  $\text{Li}_2\text{S}$  involved in the LSB charging and discharging process. The synthesis details can be found in the Supporting Information (SI). Briefly, first, a zeolitic imidazole framework (ZIF), particularly the zinc-based ZIF-8, was synthesized by a self-assembly method at room temperature.<sup>[21]</sup> Afterward, a second metal-organic framework (MOF), cobalt-based ZIF-67, with the same crystal structure as ZIF-8, was coprecipitated on the surface of the preformed ZIF-8 to produce ZIF-8/ZIF-67 core-shell structures.<sup>[22]</sup> Afterward, ZIF-8/ZIF-67 particles were uniformly coated with polydopamine (PDA) using a tris-buffer solution (ZIF-8/ZIF-67@PDA). Then, tellurium powder was reacted at  $600^\circ\text{C}$  with the Co and Zn cationic nodes of the ZIF-8/ZIF-67@PDA precursor to obtain a zinc telluride/cobalt telluride heterostructure. Meanwhile, PDA organic molecules shrank to form a porous structure and were carbonized to form N-doped carbon (NC). Subsequently, Te vacancies were generated by annealing  $\text{ZnTe}/\text{CoTe}_2@\text{NC}$  under a reducing atmosphere ( $\text{Ar}/\text{H}_2$ ). Finally, the sulfur-containing  $v\text{-ZnTe}/\text{CoTe}_2@\text{NC}/\text{S}$  composite was produced using a melt-infiltration process.

The morphology of the as-prepared electrode materials was monitored by scanning electron microscopy (SEM) and transmission electron microscopy (TEM). Representative SEM images of the precursor are shown in **Figure 1a** and **Figure S1** (Supporting Information). ZIF-8, ZIF-8/ZIF-67, and ZIF-8/ZIF-67@PDA all show the conventional dodecahedral particle morphology with a regular and smooth surface.<sup>[21b,22b,23]</sup>



**Scheme 1.** a) Schematic illustration of the synthesis procedure used to produce v-ZnTe/CoTe<sub>2</sub>@NC/S composites. b) Scheme of the LSB charging and discharging process.

Due to the growth/coating of the additional layer, the ZIF-8/ZIF-67@PDA particle size is larger than that of ZIF-8, at 550 and 500 nm, respectively. ZnTe/CoTe<sub>2</sub>@NC obtained by reacting ZIF-8/ZIF-67@PDA with Te inherited the dodecahedral particle morphology (Figure 1b). However, the pyrolysis process resulted in a notable agglomeration and shrinkage of the ZnTe/CoTe<sub>2</sub>@NC particles, down to 200 nm. After annealing under a reducing atmosphere to generate Te vacancies, the produced v-ZnTe/CoTe<sub>2</sub>@NC material maintained the aggregation, particle size, and morphology of ZnTe/CoTe<sub>2</sub>@NC (Figure 1c). Representative TEM images of the final sulfur host material, v-ZnTe/CoTe<sub>2</sub>@NC, are shown in Figure 1d and Figure S2 (Supporting Information). v-ZnTe/CoTe<sub>2</sub>@NC is formed by ≈200 nm hollow polycrystalline particles with a crystal domain size of about 10 nm. Electron energy loss spectroscopy (EELS) chemical composition maps display an uneven distribution of N, Te, Zn, Co, C within the v-ZnTe/CoTe<sub>2</sub>@NC nanostructured dodecahedral particles (Figure 1e and Figure S3, Supporting Information). We observe multiple nanodomains of ZnTe and CoTe<sub>2</sub>, while N is mainly distributed on the material surface provided by the initial PDA coating. Results from the SEM-energy dispersive x-ray spectroscopy (EDX) spectra of ZnTe/CoTe<sub>2</sub>@NC, v-ZnTe/CoTe<sub>2</sub>@NC and the reference CoTe<sub>2</sub>@NC and ZnTe@NC materials are displayed in Figure S4 (Supporting Information). EDX analysis shows the amount of Te in v-ZnTe/CoTe<sub>2</sub>@NC to

be ≈10% lower than in ZnTe/CoTe<sub>2</sub>@NC (Figure S4, Supporting Information).

The high-resolution TEM (HRTEM) image of v-ZnTe/CoTe<sub>2</sub>@NC in Figure 1f shows that the lattice fringes displayed in the red squared magnified detail correspond to the (022), (210), and (2-1-2) crystal planes of ZnTe visualized along the [1-22] zone axis, while the lattice spacings shown in the orange squared detail correspond to the (220) and (1-20) crystal planes of CoTe<sub>2</sub> visualized along its [001] zone axis. In addition, a distinct ZnTe/CoTe<sub>2</sub> interface can be observed in Figure 1g.

The XRD patterns of v-ZnTe/CoTe<sub>2</sub>@NC and ZnTe/CoTe<sub>2</sub>@NC show the fingerprints of both the cubic ZnTe phase (F-43m, peaks at 25.3°(111), 41.8°(220), and 49.5°(311), JCPDS PDF#15-0746), and the orthorhombic phase of CoTe<sub>2</sub> (Pnn2, peaks at 31.7°(111), 32.9°(120), 43.5°(211), JCPDS PDF#89-2091) as shown in Figure 2a.<sup>[24]</sup> The absence of discernible XRD peaks from the carbon shell is ascribed to the strong crystallinity of the metal tellurides (ZnTe/CoTe<sub>2</sub>). To analyze the graphitization degree of carbon, we compared the intensities of the D (1350 cm<sup>-1</sup>) and G (1590 cm<sup>-1</sup>) Raman vibrational modes associated with the disordered structure and bond stretching motion of sp<sup>2</sup> hybridized carbon, respectively (Figure S5 and Table S1, Supporting Information).<sup>[25]</sup> While amorphous carbon provides more electrochemically active sites, graphitized carbon improves catalyst conductivity and



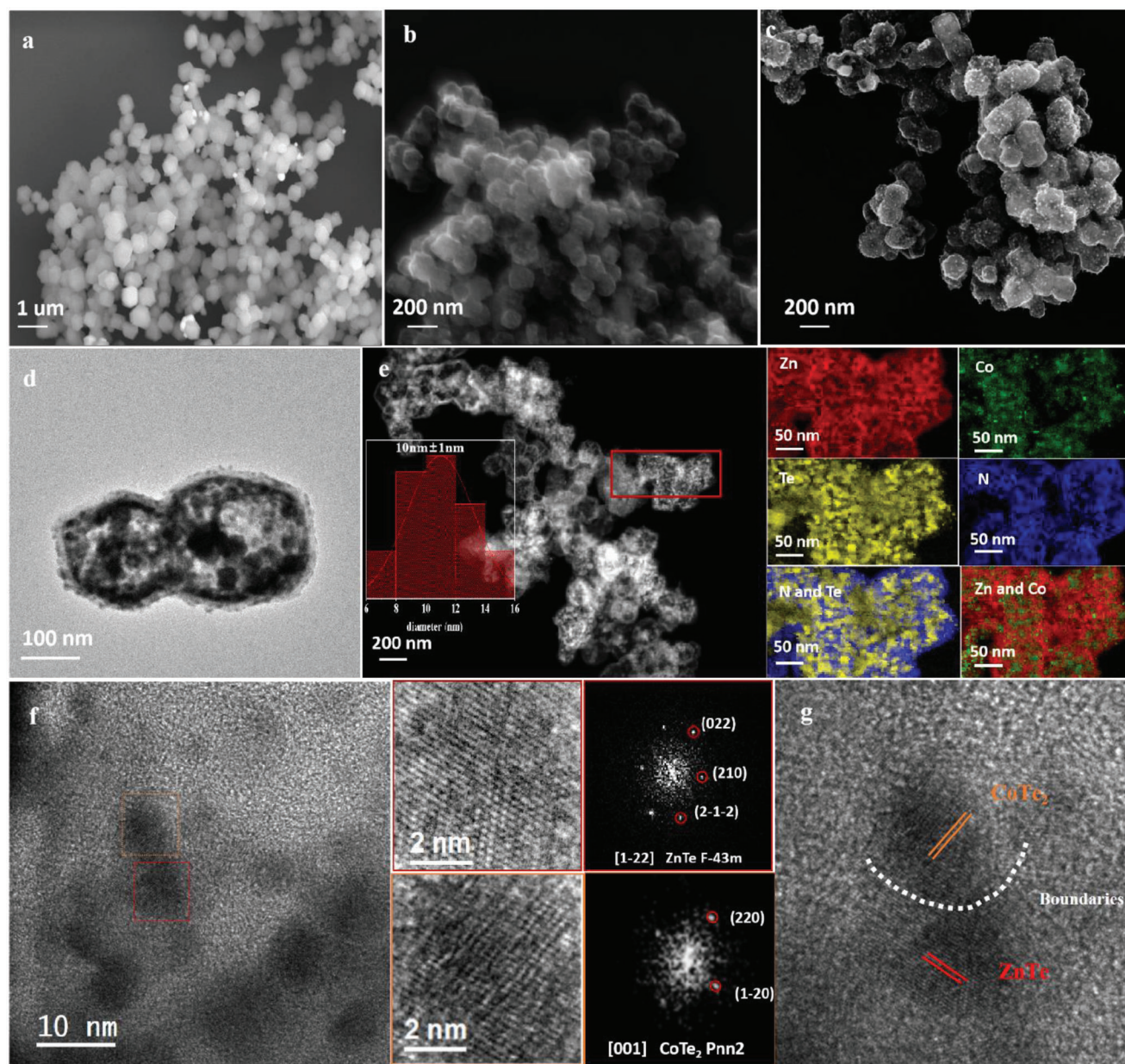


**Figure 1.** a–c) SEM images of ZIF-8/ZIF-67@PDA, ZnTe/CoTe<sub>2</sub>@NC, and v-ZnTe/CoTe<sub>2</sub>@NC. d) Low-magnification HAADF-STEM image of v-ZnTe/CoTe<sub>2</sub>@NC. e) EELS chemical composition maps of v-ZnTe/CoTe<sub>2</sub>@NC obtained from the red squared area in the STEM micrograph. f, g) HRTEM micrographs from the v-ZnTe/CoTe<sub>2</sub>@NC sample showing ZnTe and CoTe<sub>2</sub> crystal domains and a ZnTe/CoTe<sub>2</sub> interphase, and their corresponding power spectrum.

promotes charge transfer. However, no significant variations were observed among the various samples. The  $I_D/I_G$  peak intensity ratio was less than 1 in all the carbon-containing samples (v-ZnTe/CoTe<sub>2</sub>@NC, ZnTe/CoTe<sub>2</sub>@NC, CoTe<sub>2</sub>@NC, and ZnTe@NC), indicating that the carbonization process was highly effective in forming graphitized carbon from PDA.

The specific surface area and pore volume of v-ZnTe/CoTe<sub>2</sub>@NC, ZnTe/CoTe<sub>2</sub>@NC, CoTe<sub>2</sub>@NC, and ZnTe@NC were investigated using N<sub>2</sub> adsorption/desorption isotherms (Figure S6a, Supporting Information). The Brunauer–Emmett–Teller (BET) specific surface area of

v-ZnTe/CoTe<sub>2</sub>@NC, ZnTe/CoTe<sub>2</sub>@NC, CoTe<sub>2</sub>@NC, and ZnTe@NC was 589, 537.2, 518.9, and 485.6 m<sup>2</sup> g<sup>−1</sup>. In addition, the pore sizes of the four sulfur host cathode materials were concentrated in the range of 0–50 nm (Figure S6b, Supporting Information). The huge specific surface areas and small pores characterizing the produced materials are suitable to accommodate and disperse sulfur, preventing the dissolution and shuttling of sulfur during the electrochemical reaction, and further improving the utilization of active materials.<sup>[1c]</sup>

While no significant electron paramagnetic resonance (EPR) peak was obtained from ZnTe/CoTe<sub>2</sub>@NC, the



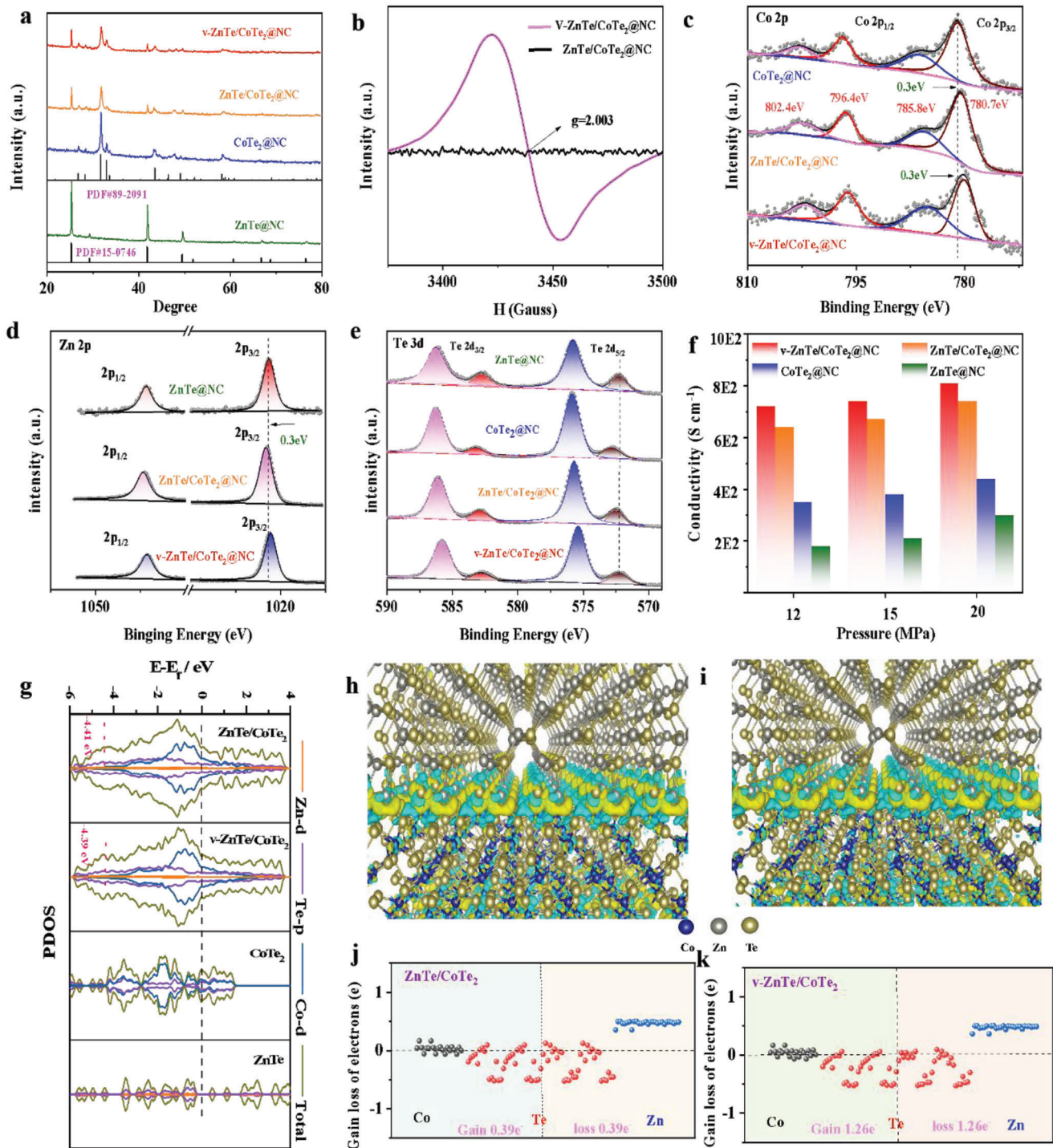


**Figure 2.** a) XRD patterns of v-ZnTe/CoTe<sub>2</sub>@NC, ZnTe/CoTe<sub>2</sub>@NC, CoTe<sub>2</sub>@NC, and ZnTe@NC. b) EPR images of the v-ZnTe/CoTe<sub>2</sub>@NC and ZnTe/CoTe<sub>2</sub>@NC. c) XPS Co 2p core-level spectrum. d) Zn 2p core-level spectrum. e) Te 3d core-level spectrum. f) Electrical conductivity of v-ZnTe/CoTe<sub>2</sub>@NC, ZnTe/CoTe<sub>2</sub>@NC, CoTe<sub>2</sub>@NC, and ZnTe@NC tested by the four-point probe method at different pressures. g) Density of states (DOS) of v-ZnTe/CoTe<sub>2</sub>, ZnTe/CoTe<sub>2</sub>, CoTe<sub>2</sub>, and ZnTe. The d band center is marked with a blue dotted line. h–k) Electron gain/loss of different atoms calculated by Bader charge analysis. In panels h and i, yellow represents the gain of electrons and blue represents the loss of electrons.

v-ZnTe/CoTe<sub>2</sub>@NC sample displayed a sharp signal at  $g = 2.003$  that can be assigned to the existence of unpaired electrons and associated with the Te vacancies generated during the thermal process under reducing (Ar/H<sub>2</sub>) atmosphere (Figure 2b).

The Co 2p X-ray photoelectron spectroscopy (XPS) spectrum of ZnTe/CoTe<sub>2</sub>@NC displays one doublet assigned to Co<sup>2+</sup> at 780.7 eV (Co 2p<sub>3/2</sub>) and 796.4 eV (Co 2p<sub>1/2</sub>) (Figure 2c). These binding energies are redshifted compared with CoTe<sub>2</sub>@NC (781.0 and 796.7 eV),<sup>[24]</sup> indicating an electronic influence of the ZnTe within the ZnTe/CoTe<sub>2</sub>@NC. The Zn 2p XPS spectrum also displays a doublet at 1021.6 eV (Zn 2p<sub>3/2</sub>) and 1044.7 eV (Zn 2p<sub>1/2</sub>) assigned to Zn<sup>2+</sup> (Figure 2d). This doublet is blueshifted with respect to ZnTe@NC.<sup>[26]</sup> The simultaneous blueshift of the Zn 2p spectrum and redshift of the Co 2p spectrum in ZnTe/CoTe<sub>2</sub>@NC points towards a decrease in the electronic density of Zn<sup>2+</sup> within ZnTe and an increase in Co<sup>2+</sup> within CoTe<sub>2</sub>, which is consistent with an electronic injection from ZnTe to CoTe<sub>2</sub>. The Te 3d XPS spectra show two doublets at 572.3 eV/583.1 eV and 575.2 eV/586.1 eV assigned with metal-Te bonds and tellurium oxide formed by surface oxidation of the ZnTe/CoTe<sub>2</sub> (Figure 2e).<sup>[24]</sup> A slight positive shift of the binding energy is also observed for the Te<sup>2-</sup> component of CoTe<sub>2</sub>@NC compared with ZnTe<sub>2</sub>@NC, while the Te 3d spectrum of the ZnTe/CoTe<sub>2</sub>@NC appears in between those of CoTe<sub>2</sub>@NC and ZnTe<sub>2</sub>@NC. Compared with ZnTe/CoTe<sub>2</sub>@NC, the Co 2p, Zn 2p, and Te 3d XPS spectra of v-ZnTe/CoTe<sub>2</sub>@NC are negatively shifted. This is consistent with the presence of Te vacancies increasing the electronic density at anionic sites.<sup>[19a]</sup> The C1s XPS spectra display peaks at 284.6, 286.2, and 288.4 eV attributed to C=C, C—O, and C=O respectively (Figure S7a, Supporting Information).<sup>[1c]</sup> The N 1s spectra show strong bands demonstrating the presence of N within the carbon (Figure S7b, Supporting Information). Three peaks at binding energies of 398.4, 399.8, and 402.1 eV, corresponding to pyridinic-N, pyrrolic-N, and graphitic-N were fitted. According to previous reports, N, especially pyridinic-N, can efficiently increase electron density and interaction with sulfur/polysulfides. It was also reported that the pyridinic-N and pyrrolic -N could effectively improve the affinity and binding energy of polar atoms with elemental sulfur (S<sub>8</sub>) and polar polysulfides (Li<sub>2</sub>S<sub>n</sub>, 4 ≤ n ≤ 8) by the strong Lewis acid–base interaction.<sup>[27]</sup>

Four-point probe conductivity tests (Figure 2f) showed v-ZnTe/CoTe<sub>2</sub>@NC to have a slightly higher electrical conductivity,  $7.2 \times 10^2 \text{ S cm}^{-1}$ , than ZnTe/CoTe<sub>2</sub>@NC ( $6.4 \times 10^2 \text{ S cm}^{-1}$ ), CoTe<sub>2</sub>@NC ( $3.5 \times 10^2 \text{ S cm}^{-1}$ ), and ZnTe@NC ( $1.8 \times 10^2 \text{ S cm}^{-1}$ ). The moderate electrical conductivity differences are related to the dominant role played by NC in the charge transport properties of the overall layer. Still, the larger conductivities obtained for v-ZnTe/CoTe<sub>2</sub>@NC are explained by the additional carriers contributed by the presence of vacancies. Besides, both heterostructured materials, v-ZnTe/CoTe<sub>2</sub>@NC and ZnTe/CoTe<sub>2</sub>@NC, show much larger electrical conductivities than the single telluride materials, ZnTe@NC and CoTe<sub>2</sub>@NC, which demonstrate the formed heterostructure to significantly contribute to improving charge transport.

DFT calculations were used to gain insight into the heterostructure electronic properties and effects (Figure 2g). DFT calculations of the total density of states (TDOS) of ZnTe were able to reproduce the discontinuous bandgap at the Fermi level

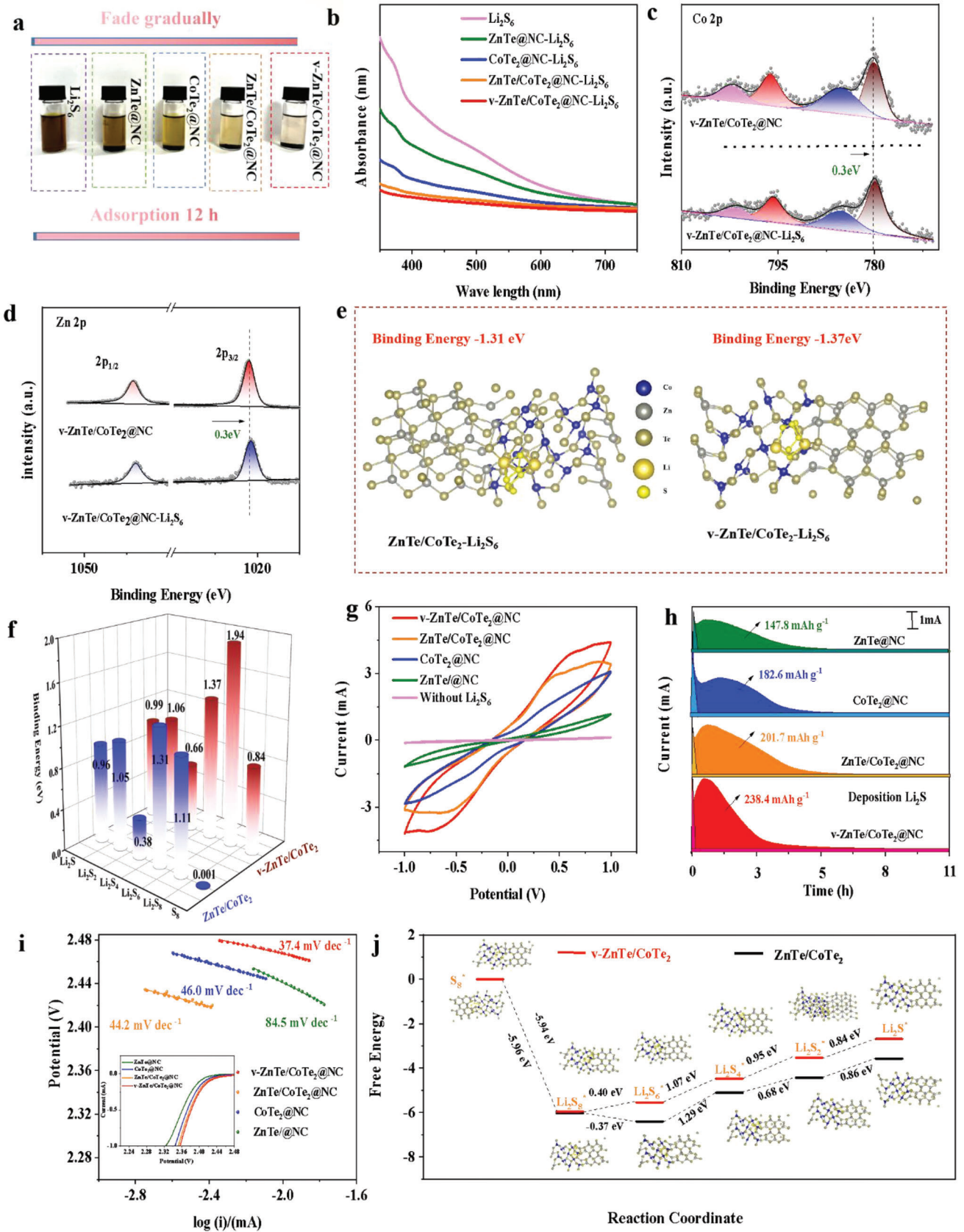
providing the semiconductor behavior. In contrast, we found the conduction band of ZnTe/CoTe<sub>2</sub> contains prominent hybridization bands that introduce a large TDOS at the Fermi level. While the TDOS of both v-ZnTe/CoTe<sub>2</sub> and ZnTe/CoTe<sub>2</sub> are continuous, the d band center of the two materials is compared by PDOS, showing that the d band center of the heterostructure electrode material with Te vacancies is slightly closer to the Fermi level. According to d-band theory, the shift of the d-band center of a metal toward the Fermi level increases the probability of electrons filling the antibonding orbital between the metal and adsorbed molecules, which boosts the ability to adsorb sulfur species.<sup>[28]</sup> Therefore, for v-ZnTe/CoTe<sub>2</sub>@NC, the d-band shift caused by vacancies is expected to enhance the adsorption capacity of LiPSs and promote the deposition of Li<sub>2</sub>S in subsequent battery tests.

DFT calculations of a theoretical slab model based on ZnTe and CoTe<sub>2</sub> were used to determine the electron gain and loss of atoms near the contact interface (see details in the Supporting Information). As shown in Figure 2h,i, the differential charge distribution demonstrates that electron transfer occurs at the heterointerface between ZnTe and CoTe<sub>2</sub>. To quantitatively determine the charge redistribution at the v-ZnTe/CoTe<sub>2</sub> interface and quantify the electron transfer between different atoms at the interface, a Bader charge analysis was performed (Figure 2j,k). From the Bader charge analysis, the acquisition of 1.26 electrons by the CoTe<sub>2</sub> unit from the ZnTe layer was calculated for v-ZnTe/CoTe<sub>2</sub>. On the other hand, for ZnTe/CoTe<sub>2</sub>, the CoTe<sub>2</sub> unit obtains 0.39 electrons from the ZnTe layer. Thus, in v-ZnTe/CoTe<sub>2</sub> the CoTe<sub>2</sub> obtains a significantly large amount of charge (0.87 additional electrons) from the ZnTe layer, than in ZnTe/CoTe<sub>2</sub>, indicating that vacancies have a very strong effect on the interphase charge redistribution. The gain of electrons by CoTe<sub>2</sub> coming from ZnTe is consistent with XPS results.

Li<sub>2</sub>S<sub>6</sub> adsorption experiments were performed to determine the LiPS adsorption ability of the different compounds. Equal amounts of v-ZnTe/CoTe<sub>2</sub>@NC, ZnTe/CoTe<sub>2</sub>@NC, CoTe<sub>2</sub>@NC, and ZnTe@NC were introduced into  $8 \times 10^{-3} \text{ M}$  Li<sub>2</sub>S<sub>6</sub> solutions and left undisturbed overnight (see details in the Supporting Information). As observed from the optical images shown in Figure 3a, while the initial Li<sub>2</sub>S<sub>6</sub> solution was dark brown, after overnight absorption, the supernatant of the solution containing ZnTe/CoTe<sub>2</sub>@NC shows a significantly lighter color than that of the solutions containing ZnTe@NC and CoTe<sub>2</sub>@NC, indicating that the formation of heterostructures is beneficial to the adsorption of polysulfides. Besides, the supernatant of the solution containing v-ZnTe/CoTe<sub>2</sub>@NC was even more decolorized, demonstrating that v-ZnTe/CoTe<sub>2</sub>@NC has an even stronger affinity towards Li<sub>2</sub>S<sub>6</sub>, which must be associated with the presence of Te vacancies. The LiPS adsorption was further analyzed by UV–vis spectroscopy (Figure 3b). Li<sub>2</sub>S<sub>6</sub> shows an obvious absorption band in the range of 350–400 nm, which gradually decreases in the presence of adsorbent materials. Particularly, no UV–vis absorption peak is observed in the solution containing v-ZnTe/CoTe<sub>2</sub>@NC.

After the LiPSs adsorption tests, v-ZnTe/CoTe<sub>2</sub>@NC was dried and characterized by XPS (Figure 3c,d). The high-resolution Co 2p and Zn 2p spectra of the sample after LiPS adsorption appeared slightly shifted toward lower binding energies compared with fresh v-ZnTe/CoTe<sub>2</sub>@NC. This shift is attributed to the





Co/Zn active sites chemically bonding with the more electronegative S atoms in LiPSs.

DFT calculations were performed to further analyze the interaction between host materials and LiPSs. The surface adsorption configuration of six different sulfur-containing species ( $\text{Li}_2\text{S}$ ,  $\text{Li}_2\text{S}_2$ ,  $\text{Li}_2\text{S}_4$ ,  $\text{Li}_2\text{S}_6$ ,  $\text{Li}_2\text{S}_8$ , and  $\text{S}_8$ ) in v-ZnTe/CoTe<sub>2</sub> and ZnTe/CoTe<sub>2</sub> were optimized as shown in Figures S8 and S9 (Supporting Information). DFT results show that the LiPSs binding energy of v-ZnTe/CoTe<sub>2</sub> is higher than that of ZnTe/CoTe<sub>2</sub> at the six stages of the lithiation process. Figure 3e,f shows the  $\text{Li}_2\text{S}_6$  adsorption configuration on v-ZnTe/CoTe<sub>2</sub> and ZnTe/CoTe<sub>2</sub>. The adsorption energies of  $\text{Li}_2\text{S}_6$  on the surfaces of v-ZnTe/CoTe<sub>2</sub> and ZnTe/CoTe<sub>2</sub> are  $-1.37$  and  $-1.31$  eV, respectively. The bond length of Li–S on the v-ZnTe/CoTe<sub>2</sub> ( $3.48$  Å) is longer than on ZnTe/CoTe<sub>2</sub> ( $3.03$  Å), which reveals that v-ZnTe/CoTe<sub>2</sub> can facilitate the decomposition of  $\text{Li}_2\text{S}$ . These results are consistent with Te vacancies within ZnTe/CoTe<sub>2</sub> effectively promoting the adsorption of polysulfides.

To evaluate the LiPSs conversion ability in the presence of different catalysts, symmetrical cells with different host materials in  $0.5$  M  $\text{Li}_2\text{S}_6$  electrolyte were assembled and tested using cyclic voltammetry, CV, Figure 3g). Compared with ZnTe/CoTe<sub>2</sub>@NC, CoTe<sub>2</sub>@NC, and ZnTe@NC cells, the v-ZnTe/CoTe<sub>2</sub>@NC symmetric cells show the highest current density, which points to an enhanced catalytic ability. Notice that the CV curve obtained in a  $\text{Li}_2\text{S}_6$ -free electrolyte shows a low current response, which demonstrates that lithiation/delithiation reactions dominate the current response.

The kinetics of the  $\text{Li}_2\text{S}$  nucleation process on the surfaces of v-ZnTe/CoTe<sub>2</sub>@NC, ZnTe/CoTe<sub>2</sub>@NC, CoTe<sub>2</sub>@NC, and ZnTe@NC were studied to evaluate the catalytic activity of the sulfur hosts. The v-ZnTe/CoTe<sub>2</sub>@NC cathode exhibited faster nucleation time and higher current response in the potentiostatic test at  $2.05$  V compared to ZnTe/CoTe<sub>2</sub>@NC, CoTe<sub>2</sub>@NC, and ZnTe@NC (Figure 3h). According to Faraday's theory ( $Q = It$ , where  $Q$ ,  $I$ , and  $t$  represent capacity, discharge current, and time respectively), the capacity of v-ZnTe/CoTe<sub>2</sub>@NC is  $238.4$  mAh  $\text{g}^{-1}$ , which is much higher than that of ZnTe/CoTe<sub>2</sub>@NC ( $201.7$  mAh  $\text{g}^{-1}$ ), CoTe<sub>2</sub>@NC ( $182.6$  mAh  $\text{g}^{-1}$ ) and ZnTe@NC ( $147.8$  mAh  $\text{g}^{-1}$ ). Overall, these experimental results show that the v-ZnTe/CoTe<sub>2</sub>@NC electrode can effectively reduce the Li–S redox reaction overpotential, restrain the LiPSs shuttle effect, and promote the nucleation reaction of  $\text{Li}_2\text{S}$ .

The Tafel curves of different sulfur host cathodes are shown in Figure 3i. Compared with ZnTe/CoTe<sub>2</sub>@NC, CoTe<sub>2</sub>@NC, and ZnTe@NC, v-ZnTe/CoTe<sub>2</sub>@NC is characterized by the smallest Tafel slope, which further indicates that v-ZnTe/CoTe<sub>2</sub>@NC can promote the formation of  $\text{Li}_2\text{S}$  and accelerate the oxidation reaction kinetics.

DFT calculations were further used to determine the Gibbs free energies of the v-ZnTe/CoTe<sub>2</sub> and ZnTe/CoTe<sub>2</sub> reduction pathways. The lithiation pathway for the  $\text{Li}_2\text{S}$  formation from  $\text{S}_8$

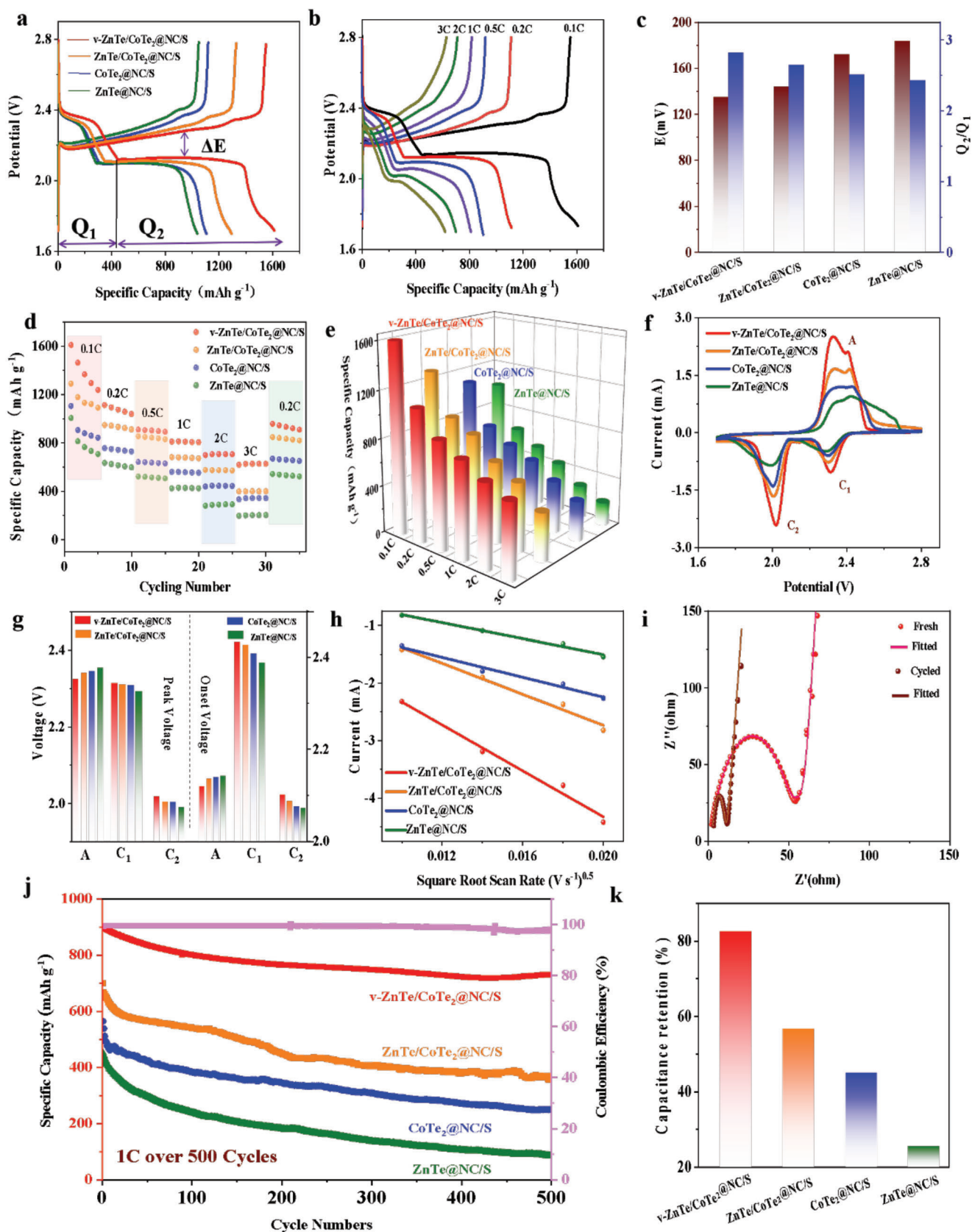
was studied. The optimized model and free energy distribution of polysulfide intermediates are shown in Figure 3j). The first step is the reaction of two  $\text{Li}^+$  with  $\text{S}_8$  to form  $\text{Li}_2\text{S}_8$ . Subsequently,  $\text{Li}_2\text{S}_8$  is further reduced to  $\text{Li}_2\text{S}_6$ ,  $\text{Li}_2\text{S}_4$ ,  $\text{Li}_2\text{S}_2$ , and finally,  $\text{Li}_2\text{S}$ . For both v-ZnTe/CoTe<sub>2</sub> and ZnTe/CoTe<sub>2</sub>, the maximum Gibbs free energy increase was obtained for the transformation of  $\text{Li}_2\text{S}_6$  to  $\text{Li}_2\text{S}_4$ , being the Gibbs free energy change for the v-ZnTe/CoTe<sub>2</sub> sample lower than that of ZnTe/CoTe<sub>2</sub>. This result shows that the reaction thermodynamics of S is more favorable on v-ZnTe/CoTe<sub>2</sub> than on ZnTe/CoTe<sub>2</sub>.

To study the electrochemical performance of the different materials as sulfur hosts, they were infiltrated with S to obtain v-ZnTe/CoTe<sub>2</sub>@NC/S, ZnTe/CoTe<sub>2</sub>@NC/S, CoTe<sub>2</sub>@NC/S, and ZnTe@NC/S composites. Upon sulfur incorporation, with no sulfur agglomerates observed on the surface of the host material (Figures S10–S12, Supporting Information). EELS chemical composition maps show S to be relatively evenly distributed across v-ZnTe/CoTe<sub>2</sub>@NC/S (Figure S13, Supporting Information). Compared to v-ZnTe/CoTe<sub>2</sub>@NC ( $589$  m<sup>2</sup> g<sup>−1</sup>), upon the introduction of sulfur, a dramatic decrease in surface area was measured for v-ZnTe/CoTe<sub>2</sub>@NC/S ( $32.9$  m<sup>2</sup> g<sup>−1</sup>), suggesting that S infiltrates throughout most of the host material pores (Figure S14, Supporting Information). Besides, X-ray powder diffraction (XRD) patterns further confirm the presence of S within the final electrode material (Figure S15a, Supporting Information). Thermogravimetry analysis (TGA) shows that the sulfur loading of v-ZnTe/CoTe<sub>2</sub>@NC/S is about 68% (Figure S15b, Supporting Information).

Coin cells were assembled using the sulfur cathodes, lithium foil as anode, and a solution of  $1.0$  M lithium bis(trifluoromethanesulfonyl)imide and  $0.2$  M  $\text{LiNO}_3$  in a mixture of 1,3-dioxolane (DOL) and 1,2-dimethoxyethane (DME) with a volume ratio of 1:1 as electrolyte (see details in the Supporting Information). The galvanostatic charge/discharge (GCD) curves of the different cathode materials (v-ZnTe/CoTe<sub>2</sub>@NC/S, ZnTe/CoTe<sub>2</sub>@NC/S, CoTe<sub>2</sub>@NC/S, and ZnTe@NC/S) at a current rate  $0.1$  C are shown in Figure 4a and Table S2 (Supporting Information). As generally observed in LSBs,<sup>[29]</sup> two distinct voltage plateaus are obtained during the cell discharge. The first voltage plateau at  $2.4$ – $2.1$  V is mainly attributed to the conversion of  $\text{S}_8$  to long-chain LiPSs ( $\text{S}_8$  to  $\text{Li}_2\text{S}_4$ ). The second voltage plateau in the voltage window of  $2.1$ – $1.7$  V corresponds to the liquid-solid reaction of polysulfides gaining electrons and reducing to insoluble  $\text{Li}_2\text{S}_2$  ( $\text{Li}_2\text{S}_4$  to  $\text{Li}_2\text{S}_2$ ) and the solid-solid reaction of  $\text{Li}_2\text{S}_2$  to  $\text{Li}_2\text{S}$ . Compared with other sulfur cathodes, v-ZnTe/CoTe<sub>2</sub>@NC/S exhibits the highest initial specific capacitance ( $1608$  mAh  $\text{g}^{-1}$ ), well above that of ZnTe/CoTe<sub>2</sub>@NC/S ( $1290$  mAh  $\text{g}^{-1}$ ), CoTe<sub>2</sub>@NC/S ( $1105$  mAh  $\text{g}^{-1}$ ), and ZnTe@NC/S ( $1005$  mAh  $\text{g}^{-1}$ ).

The GCD curves of the v-ZnTe/CoTe<sub>2</sub>@NC/S, ZnTe/CoTe<sub>2</sub>@NC/S, CoTe<sub>2</sub>@NC/S, ZnTe@NC/S, and NC/S cathodes at various current rates are shown in Figure 4b and

**Figure 3.** Photographs a) and absorbance curves b) of the static  $\text{Li}_2\text{S}_6$  adsorption experiment. c) Co 2p XPS spectra of v-ZnTe/CoTe<sub>2</sub>@NC and v-ZnTe/CoTe<sub>2</sub>@NC- $\text{Li}_2\text{S}_6$ . d) Zn 2p XPS spectra of v-ZnTe/CoTe<sub>2</sub>@NC and v-ZnTe/CoTe<sub>2</sub>@NC- $\text{Li}_2\text{S}_6$ . e) Model of the binding energy to  $\text{Li}_2\text{S}_6$  to v-ZnTe/CoTe<sub>2</sub> and ZnTe/CoTe. f) Binding energies of different polysulfides ( $\text{S}_8$ ,  $\text{Li}_2\text{S}_8$ ,  $\text{Li}_2\text{S}_6$ ,  $\text{Li}_2\text{S}_4$ ,  $\text{Li}_2\text{S}_2$ , and  $\text{Li}_2\text{S}$ ) to v-ZnTe/CoTe<sub>2</sub> and ZnTe/CoTe<sub>2</sub>. g) CV curves of symmetric cells with different electrode compositions (v-ZnTe/CoTe<sub>2</sub>@NC, ZnTe/CoTe<sub>2</sub>@NC, CoTe<sub>2</sub>@NC, and ZnTe@NC) at the scan rate of  $5$  mV  $\text{s}^{-1}$ . h) Potentiostatic discharge curves on different electrodes for studying the nucleation kinetics of  $\text{Li}_2\text{S}$ . i) Tafel plots and LSV polarization curves (insert) of v-ZnTe/CoTe<sub>2</sub>@NC, ZnTe/CoTe<sub>2</sub>@NC, CoTe<sub>2</sub>@NC, and ZnTe@NC j) Gibbs free energy profiles and optimized adsorption model of LiPS species on v-ZnTe/CoTe<sub>2</sub> and ZnTe/CoTe<sub>2</sub>.





Figures S16 and S17 (Supporting Information). As the current rate increased from 0.1C to 0.2C, 0.5C, 1C, 2C, and 3C, the specific capacitances of the v-ZnTe/CoTe<sub>2</sub>@NC/S cathode decreased from 1608.8 to 1112.2, 908.9, 811.1, 698.7, and 618.2 mA h g<sup>-1</sup>, respectively. A clear voltage plateau can be observed even at the highest current rate of 3C, indicating that the v-ZnTe/CoTe<sub>2</sub>@NC host could effectively catalyze the conversion of LiPS. When the current rate returns to 0.2C, the specific capacity of the v-ZnTe/CoTe<sub>2</sub>@NC/S electrode recovers to 1040 mA h g<sup>-1</sup>, demonstrating notable stability after high-rate charge–discharge processes. The performance of the v-ZnTe/CoTe<sub>2</sub>@NC/S electrode was well above that of all the other electrodes, particularly ZnTe/CoTe<sub>2</sub>@NC/S, demonstrating the positive effect played by the TMT catalyst, the Te vacancies and the heterojunctions.

The electrochemical performance of electrodes based on v-ZnTe/CoTe<sub>2</sub>@NC composites annealed under Ar/H<sub>2</sub> for different times, thus containing different amounts of vacancies, is shown in Figure S18 (Supporting Information). We observe the electrode based on the composite annealed for just 1 h (v-ZnTe/CoTe<sub>2</sub>@NC/S-1 h) to be characterized by clearly lower specific capacities associated with a too-low content of Te vacancies. Besides, the electrode based on the composite annealed for 5 h (v-ZnTe/CoTe<sub>2</sub>@NC/S-5 h) also displayed a lower performance than that annealed for 3 h (v-ZnTe/CoTe<sub>2</sub>@NC/S-3 h). Thus, an optimum amount of Te vacancies exist. While too-short annealing times do not introduce enough Te vacancies, too-long times strongly reduce the material changing its electronic band structure and overall properties. Previous works have also shown the existence of an optimal vacancy concentration to maximize the performance of catalytic systems and energy storage devices<sup>[25,30]</sup>

The voltage difference  $\Delta E$  between the oxidation platform and the second reduction platform is generally regarded as the polarization potential of the Li–S reaction (Figure 4c).<sup>[7]</sup> The polarization voltage of the v-ZnTe/CoTe<sub>2</sub>@NC (135 mV) electrode was significantly lower than that of ZnTe/CoTe<sub>2</sub>@NC (144 mV), CoTe<sub>2</sub>@NC (172 mV), and ZnTe@NC (184 mV). Thus, while both heterostructured tellurides showed an effective promotion of the LiPSs reaction kinetics compared with the single tellurides, the presence of vacancies further enhanced the reaction kinetics.

The capacity ratio of the first discharge platform ( $Q_1$ ) to the second discharge platform ( $Q_2$ ) can be used as a quantitative representation of the catalytic activity of the host material for LiPS conversion.<sup>[1a]</sup> Since the first platform involves 4 electrons and the second platform involves 12 electrons of the full 16-electron S<sub>8</sub> lithiation process, the theoretical ratio of  $Q_2/Q_1$  is 3. In practice, this ratio is always lower than 3 due to the dissolution of polysulfides that do not participate further in the reaction and the incomplete reduction from Li<sub>2</sub>S<sub>4</sub> to Li<sub>2</sub>S at the second discharge plateau. Thus  $Q_2/Q_1$  values reflect the degree of completion of the reduction reaction, which is mainly related to the ability of the host material to catalyze it and inhibit the shuttling effect. The  $Q_2/Q_1$  value of the four cathode materials (v-ZnTe/CoTe<sub>2</sub>@NC/S, ZnTe/CoTe<sub>2</sub>@NC/S, CoTe<sub>2</sub>@NC/S, and ZnTe@NC/S) are shown in Figure 4c. Consistently with pre-

vious results, the v-ZnTe/CoTe<sub>2</sub>@NC/S electrode exhibits the highest  $Q_2/Q_1$  ratio at 2.82, close to the theoretical value and well above that of ZnTe/CoTe<sub>2</sub>@NC (2.65), CoTe<sub>2</sub>@NC (2.51), and ZnTe@NC (2.43). Again, the two heterostructured tellurides showed improved performance over the single tellurides and the presence of vacancies further boosted the catalytic performance of the heterostructured materials.

The rate performance curves of the different sulfur cathodes are shown in Figure 4d,e. The specific capacity of all electrodes gradually decreases with the increase of the current rate. The v-ZnTe/CoTe<sub>2</sub>@NC/S electrode shows the highest specific capacities at all current rates, further demonstrating that the formation of vacancies and heterojunctions effectively promote polysulfide adsorption and charge transfer.

CV curves of the different cells at a scan rate of 0.1 mV<sup>-1</sup> are shown in Figure 4f. All curves show two cathodic peaks ( $C_1$  and  $C_2$ ) and one anodic peak (A), which is consistent with the measured charge/discharge plateaus. The two cathodic peaks and the anodic peak represent the reduction of sulfur to polysulfides (S<sub>8</sub>/Li<sub>2</sub>S<sub>8</sub> → Li<sub>2</sub>S<sub>6</sub>/Li<sub>2</sub>S<sub>4</sub>) followed by their reduction to Li<sub>2</sub>S<sub>2</sub>/Li<sub>2</sub>S (Li<sub>2</sub>S<sub>6</sub>/Li<sub>2</sub>S<sub>4</sub> → Li<sub>2</sub>S<sub>2</sub>/Li<sub>2</sub>S), and the oxidation of polysulfides to sulfur (Li<sub>2</sub>S<sub>2</sub>/Li<sub>2</sub>S → Li<sub>2</sub>S<sub>8</sub>/S<sub>8</sub>), respectively. Among the different cathode materials, v-ZnTe/CoTe<sub>2</sub>@NC/S exhibits the highest current densities, showing the most effective conversion of polysulfides, and the lowest polarization voltages. The cathodic peaks of the v-ZnTe/CoTe<sub>2</sub>@NC/S cathode show a much larger current density and are slightly shifted to higher potentials compared with the other cathodes, suggesting a promoted conversion of LiPSs to insoluble Li<sub>2</sub>S<sub>2</sub>/Li<sub>2</sub>S within the v-ZnTe/CoTe<sub>2</sub>@NC/S cathode. Besides, the oxidation peak of v-ZnTe/CoTe<sub>2</sub>@NC/S is shifted to a lower potential, indicating an enhanced Li<sub>2</sub>S decomposition.

The onset potentials at a current density of 10  $\mu$ A cm<sup>-2</sup> beyond the baseline current were used to quantitatively estimate the electrocatalytic activity (Figure 4g and Figure S19, Supporting Information). Cells based on v-ZnTe/CoTe<sub>2</sub>@NC/S cathodes showed the highest cathodic peak onset potentials and the lowest anodic peak onset potentials, which further demonstrated that the presence of vacancies and heterostructures accelerates the redox reaction kinetics.

CV curves at different scan rates, 0.1–0.4 mV s<sup>-1</sup>, within a voltage window of 1.7–2.8 V were used to study the reaction kinetics and the lithium-ion diffusion (Figure S20, Supporting Information). For all the cathode materials, as the scan rate increases, there is a gradual increase in the peak current intensity while the peak shape remains unaltered, which indicates excellent electrochemical properties. The CV curves show a linear relationship between the peak current ( $I_p$ ) and the square root of the scan rate ( $\nu$ ), as shown in Figure 4h and Figure S21a,b (Supporting Information). According to the Randles–Sevcik equation

$$I_p = 2.69 \times 10^5 n^{1.5} A D_{Li}^{+0.5} C_{Li}^{+} \nu^{0.5} \quad (1)$$

**Figure 4.** a) GCD curves of the different cathodes (v-ZnTe/CoTe<sub>2</sub>@NC/S, ZnTe/CoTe<sub>2</sub>@NC/S, CoTe<sub>2</sub>@NC/S, and ZnTe@NC/S) at a current rate of 0.1C. b) GCD curve of v-ZnTe/CoTe<sub>2</sub>@NC/S at a current density of 0.1C–C. c)  $\Delta E$  and  $Q_2/Q_1$  values of the as-prepared electrode during the charge–discharge process. d,e) Rate performance of the different electrodes. f) CV curves of different electrodes at a scan rate of 0.1 mV<sup>-1</sup>. g) Peak and onset potentials of the different electrodes. h) Peak current versus square root curve of scan rate. i) Nyquist plot of the EIS spectra of the v-ZnTe/CoTe<sub>2</sub>@NC/S. j) Long cycle test of different electrodes at 1C for 500 cycles and coulombic efficiency (v-ZnTe/CoTe<sub>2</sub>@NC). k) Capacitance retention after 500 cycles.

where  $n$  is the number of charges,  $A$  is the geometric area of the electrode, and  $C_{\text{Li}^+}$  represents the concentration of  $\text{Li}^+$ . Thus, the diffusion coefficient of  $\text{Li}^+$  ( $D_{\text{Li}^+}$ ) can be calculated from the linear fitting of  $I_p$  versus  $v^{0.5}$ .

$v\text{-ZnTe/CoTe}_2\text{@NC/S}$  electrodes displayed the sharpest slopes, corresponding to the highest  $D_{\text{Li}^+}$  values at the two cathodic peaks and the anodic peak (taken as whole despite its broadness),  $2.1 \times 10^{-7}$ ,  $3.5 \times 10^{-7}$ , and  $5.7 \times 10^{-7} \text{ cm}^2 \text{ s}^{-1}$ , respectively. The  $\text{ZnTe/CoTe}_2\text{@NC/S}$  electrode exhibited similar slopes and thus  $D_{\text{Li}^+}$  values, which were well above those of  $\text{CoTe}_2\text{@NC/S}$  and  $\text{ZnTe@NC/S}$  (Figure S21c, Supporting Information). These results indicate that the heterojunction accelerates the diffusion of  $\text{Li}^+$  during the redox reaction, while vacancies played a minor role in this parameter.

To study the interfacial charge transfer kinetics, electrochemical impedance spectroscopy (EIS) measurements were performed. The Nyquist plots of the EIS spectra obtained from the  $v\text{-ZnTe/CoTe}_2\text{@NC/S}$ ,  $\text{ZnTe/CoTe}_2\text{@NC/S}$ ,  $\text{CoTe}_2\text{@NC/S}$ , and  $\text{ZnTe@NC/S}$  coin cells before and after cycling and the equivalent circuit are shown in Figure 4i and Figure S22–S23 (Supporting Information). All the electrodes show a semi-circle in the high-frequency region related to the charge transfer resistance ( $R_{\text{ct}}$  in the equivalent circuit) and then a straight line in the low-frequency region whose slope is related to the  $\text{Li}$ -ion diffusion resistance.<sup>[31]</sup> In particular, the  $v\text{-ZnTe/CoTe}_2\text{@NC/S}$  fresh electrode showed the lowest  $R_{\text{ct}}$  (48.6  $\Omega$ ) compared with  $\text{ZnTe/CoTe}_2\text{@NC/S}$  (61.8  $\Omega$ ),  $\text{CoTe}_2\text{@NC/S}$  (88.6  $\Omega$ ) and  $\text{ZnTe@NC/S}$  (97.6  $\Omega$ ) electrodes. Electrodes  $v\text{-ZnTe/CoTe}_2\text{@NC/S}$  and  $\text{ZnTe/CoTe}_2\text{@NC/S}$  show approximately equal slopes in the low-frequency region, but well larger than  $\text{CoTe}_2\text{@NC/S}$  and  $\text{ZnTe@NC/S}$ , indicating that the heterojunction facilitates the diffusion of  $\text{Li}^+$ , which is consistent with the  $\text{Li}^+$  diffusion coefficients calculated from the CV curves. After the charge–discharge cycle, an additional R–C element, i.e., an additional interphase, was required to fit the high-frequency range of the EIS spectra ( $R_p$  in the equivalent circuit). This additional element was related to the deposition of insulating discharge products of  $\text{Li}_2\text{S}$  on the electrode surface during the cycle. The  $v\text{-ZnTe/CoTe}_2\text{@NC/S}$  electrode showed considerably lower  $R_p$  and  $R_{\text{ct}}$  compared to  $\text{ZnTe/CoTe}_2\text{@NC/S}$ ,  $\text{CoTe}_2\text{@NC/S}$ , and  $\text{ZnTe@NC/S}$  electrodes (Figure S24, Supporting Information). These lower resistances are consistent with faster polysulfide conversion reactions and faster charge transfer kinetics during lithiation/delithiation reactions. A lower  $R_{\text{ct}}$  was obtained after cycling associated with the chemical activation process of dissolution and redistribution of the active material.<sup>[32]</sup>

The cycle stability curves of the different electrodes ( $v\text{-ZnTe/CoTe}_2\text{@NC/S}$ ,  $\text{ZnTe/CoTe}_2\text{@NC/S}$ ,  $\text{CoTe}_2\text{@NC/S}$ , and  $\text{ZnTe@NC/S}$ ) at a current rate of 1C for 500 cycles are shown in Figure 4j. The  $v\text{-ZnTe/CoTe}_2\text{@NC/S}$ -based cell exhibits the highest initial specific capacity, followed by the  $\text{ZnTe/CoTe}_2\text{@NC/S}$ . Besides, after 500 cycles, these two electrodes also showed the highest capacity retention at 82.5% and 56.7%, above that of  $\text{CoTe}_2\text{@NC/S}$ , and  $\text{ZnTe@NC/S}$  at 45.1%, and 25.6%, respectively (Figure 4k). These results are again consistent with the formation of vacancies and heterostructures favoring the conversion of polysulfides, preventing more polysulfides from dissolving into the electrolyte.

After 500 cycles, the coin cells were disassembled and analyzed (Figure S25, Supporting Information). Compared with  $\text{ZnTe/CoTe}_2\text{@NC/S}$ ,  $\text{CoTe}_2\text{@NC/S}$ , and  $\text{ZnTe@NC/S}$ , the membrane of  $v\text{-ZnTe/CoTe}_2\text{@NC/S}$  was almost transparent, indicating a lower amount of LiPS reaching the membrane. Besides, the lithium anode of the cycled  $v\text{-ZnTe/CoTe}_2\text{@NC/S}$  coin cell shows much lower corrosion (Figure S26, Supporting Information) and a low concentration of S (Figure S27, Supporting Information), further confirming the effective trapping of LiPs at this cathode.

To determine the stability of the vacancies of the sulfur host material during cycling, the EPR spectrum of the cycled electrode material was analyzed and it is shown in Figure S28 (Supporting Information). A strong signal related to unpaired electrons and associated with the Te vacancies can be observed, showing that Te vacancies are maintained in the electrode material after cycling. However, the signal intensity decreased and its center position shifted from 2.003 to 1.98, which indicates the interaction of the Te vacancies with sulfur/polysulfides. Part of the original Te vacancies sites, particularly those at the material surface, may contain sulfur-based ions that the unpaired electrons thus not contributing to the EPR signal.

The performance dependence on the sulfur mass loading and the amount of electrolyte are important parameters to evaluate the practical application of LSB. The GCD curves of a high sulfur loading cell,  $5.4 \text{ mg cm}^{-2}$ , based on the  $v\text{-ZnTe/CoTe}_2\text{@NC/S}$  cathode are shown in Figure 5a. All the curves show a charging platform and two discharging platforms, denoting a proper performance. When the current rate is 0.1C, 0.2C, 0.5C, 1C, 2C, and 3C, the specific capacitances are 1273, 1104, 904.8, 808.3, 728.6, and 636.8  $\text{mA h g}^{-1}$ , respectively (Figure 5b). When the current rate returns to 0.1C, the specific capacity of the  $v\text{-ZnTe/CoTe}_2\text{@NC/S}$  electrode recovers to 1158  $\text{mAh g}^{-1}$ . The moderate decrease in specific capacitance with the increasing current rate indicates that the  $v\text{-ZnTe/CoTe}_2\text{@NC/S}$  has an excellent rate performance even at this relatively high sulfur loading because of its better electron transfer properties.

At high sulfur loading ( $5.4 \text{ mg cm}^{-2}$ ), when the electrolyte amount was decreased to  $12.3 \mu\text{L mg}^{-1}$ , the  $v\text{-ZnTe/CoTe}_2\text{@NC/S}$  cathode maintained a capacity above 1050  $\text{mAh g}^{-1}$  for at least 100 cycles, which corresponds to a slow capacity fade of 0.18% per cycle (Figure 5c). When further reducing the electrolyte amount to  $7.5 \mu\text{L mg}^{-1}$ ,  $v\text{-ZnTe/CoTe}_2\text{@NC/S}$  still maintained a capacity of 890.8  $\text{mA h g}^{-1}$  after 100 cycles (Figure 5d). These excellent results demonstrate that  $v\text{-ZnTe/CoTe}_2\text{@NC}$  effectively promotes the conversion of polysulfides, prevents the shuttling of polysulfides, and further improves the utilization of sulfur even at high loading and lean electrolyte conditions. By comparing with the other tested cathodes, this excellent performance must be associated with the formed heterostructures and the presence of tellurium vacancies. In addition,  $v\text{-ZnTe/CoTe}_2\text{@NC/S}$  cathodes stand out when compared with previous reports on sulfur host materials based on heterostructures or incorporating vacancies (Figure S29 and Tables S3 and S4, Supporting Information).<sup>[33]</sup>

Pouch cells based on  $v\text{-ZnTe/CoTe}_2\text{@NC/S}$  cathodes were further assembled and their cycle stability was tested (Figure S30, Supporting Information). At a current rate of 0.1C, the pouch cells containing a sulfur loading of  $5.6 \text{ mg cm}^{-2}$  and 11.2 mL  $\text{g}^{-1}$  electrolyte retained 86.78% of their capacity after 150 cycles.

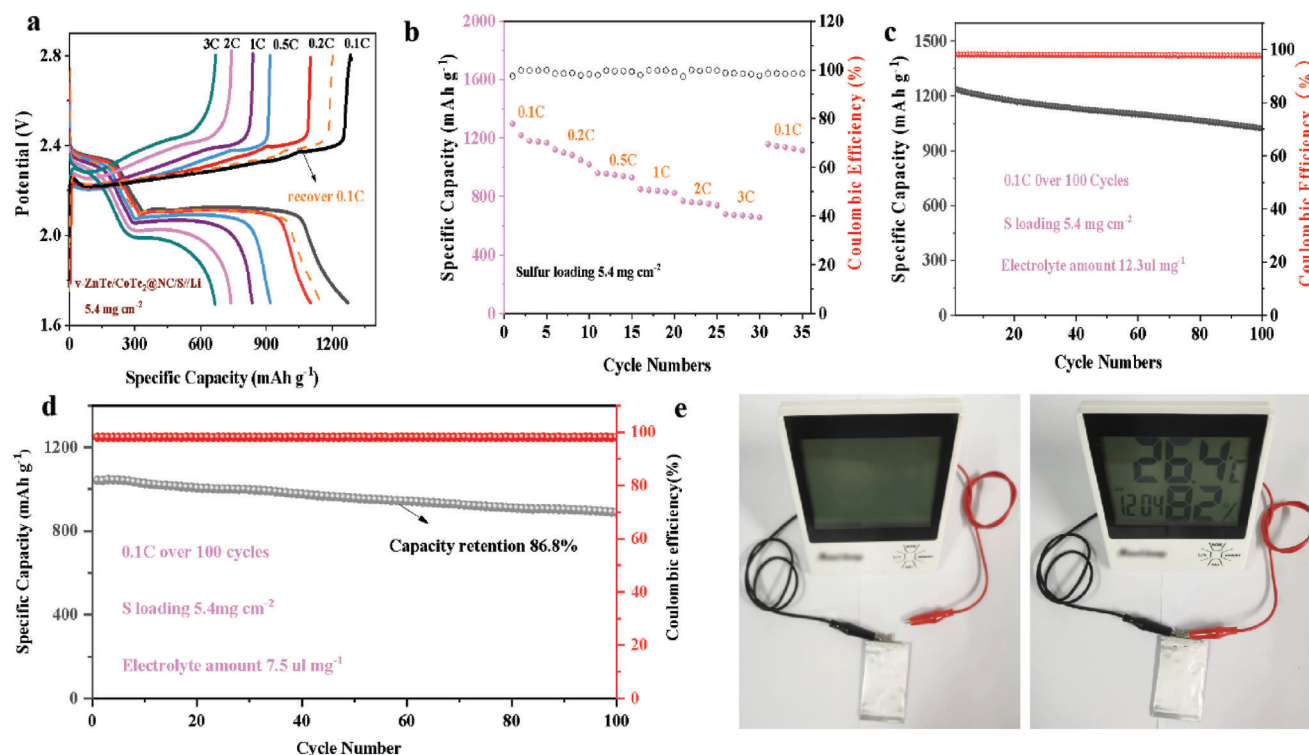


**Figure 5.** a) GCD curve of electrode v-ZnTe/CoTe<sub>2</sub>@NC/S under high loading (5.4 mg cm<sup>-2</sup>). b) Rate performance curve. c,d) Cycling stability of v-ZnTe/CoTe<sub>2</sub>@NC/S at 0.1C after 100 cycles at different electrolyte contents. e) Two v-ZnTe/CoTe<sub>2</sub>@NC/S-based pouch cells powering a commercial temperature and humidity monitoring clock.

Figure 5e displays how v-ZnTe/CoTe<sub>2</sub>@NC/S-based pouch cells can power a temperature and humidity monitoring clock, showing that the prepared electrodes have practical applications. Additionally, the electrochemical performance of pouch cells with higher sulfur loading and lower electrolyte composition were assembled and tested (Figure S31, Supporting Information). As observed in Figure S31a,c (Supporting Information), when the sulfur load was increased to 6.4 and 8.2 mg cm<sup>-2</sup>, the capacitance retention rates were 77.6% and 75.4% after 100 cycles at a current rate 3C. Besides, when reducing the electrolyte content to 6.3 and 4.8 mL g<sup>-1</sup>, the capacitance retention rates were 85.9% and 83.3% after 100 cycles at a current rate 3C (Figure S31b,c, Supporting Information).

### 3. Conclusions

In summary, a NC-based composite containing small amounts of ZnTe/CoTe<sub>2</sub> heterostructures with Te-vacancies as sulfur redox catalyst has been developed. As shown using both DFT calculations and experimental results, the presence of Te vacancies enhances the adsorption of LiPSs and promotes catalytic activity. The heterostructured TMT promotes the diffusion of ions and increases the electrical conductivity of the material. Benefiting from the optimized structure and composition, v-ZnTe/CoTe<sub>2</sub>@NC/S exhibits high initial capacity (1608 mA h<sup>-1</sup> at 0.1C), excellent rate capability, and long cycle life, even at high sulfur loading and in lean electrolyte conditions. Overall, this work demonstrates the combination of defect and interface engi-

neering to be an effective strategy to optimize the electrochemical performance of LSB cathode materials.

### Supporting Information

Supporting Information is available from the Wiley Online Library or from the author.

### Acknowledgements

The authors thank the support from the projects ENE2016-77798-C43-R and NANOGEN (PID2020-116093RB-C43), funded by MCIN/AEI/10.13039/501100011033/ and by "ERDF A way of making Europe," by the "European Union." C.H., J.Y., C.H.L., C.Q.Z., C.Y.Z., and B.F.N. thank the China Scholarship Council for the scholarship support. ICN2 acknowledges the support from the Severo Ochoa Programme (CEX2021-001214-S). IREC and ICN2 are both funded by the CERCA Program/Generalitat de Catalunya (2021SGR00457, 2021SGR01581). This project has received funding from the Advanced Materials program and was supported by MCIN with funding from European Union Next Generation EU (PRTR-C17.11).

### Conflict of Interest

The authors declare no conflict of interest.

### Data Availability Statement

The data that support the findings of this study are available from the corresponding author upon reasonable request.



## Keywords

heterostructures, lithium–sulfur batteries, lithium polysulfides, transition metal telluride, tellurium vacancies

Received: May 20, 2023

Revised: June 16, 2023

Published online: July 7, 2023

- [1] a) D. Yang, M. Li, X. Zheng, X. Han, C. Zhang, J. Jacas Biendicho, J. Llorca, J. Wang, H. Hao, J. Li, G. Henkelman, J. Arbiol, J. R. Morante, D. Mitlin, S. Chou, A. Cabot, *ACS Nano* **2022**, *16*, 11102; b) R. Xiao, D. Luo, J. Wang, H. Lu, H. Ma, E. M. Akinoglu, M. Jin, X. Wang, Y. Zhang, Z. Chen, *Adv. Sci.* **2022**, *9*, 2202352; c) W. Zhao, W. Zhang, Y. Lei, L. Wang, G. Wang, J. Wu, W. Fan, S. Huang, *ACS Appl. Mater. Interfaces* **2022**, *14*, 6801.
- [2] a) M. Li, D. Yang, J. J. Biendicho, X. Han, C. Zhang, K. Liu, J. Diao, J. Li, J. Wang, M. Heggen, R. E. Dunin-Borkowski, J. Wang, G. Henkelman, J. R. Morante, J. Arbiol, S.-L. Chou, A. Cabot, *Adv. Funct. Mater.* **2022**, *32*, 2200529; b) B. Jiang, Y. Qiu, D. Tian, Y. Zhang, X. Song, C. Zhao, M. Wang, X. Sun, H. Huang, C. Zhao, H. Zhou, A. Chen, L. Fan, N. Zhang, *Adv. Energy Mater.* **2021**, *11*, 2102995; c) E. Jung, S.-J. Kim, J. Kim, S. Koo, J. Lee, S.-Y. Kim, V. K. Paidi, W. Ko, J. Moon, K.-S. Lee, S.-P. Cho, D. Kim, S.-H. Yu, Y.-E. Sung, T. Hyeon, *ACS Energy Lett.* **2022**, *7*, 2646.
- [3] a) C. Wang, N. Sakai, Y. Ebina, T. Kikuchi, M. R. Snowdon, D. Tang, R. Ma, T. Sasaki, *J. Mater. Chem. A* **2021**, *9*, 9952; b) X. Zhang, T. Yang, Y. Zhang, X. Wang, J. Wang, Y. Li, A. Yu, X. Wang, Z. Chen, *Adv. Mater.* **2023**, *35*, 2208470; c) C. Y. Zhang, C. Zhang, G. W. Sun, J. L. Pan, L. Gong, G. Z. Sun, J. J. Biendicho, L. Balcells, X. L. Fan, J. R. Morante, J. Y. Zhou, A. Cabot, *Angew. Chem.* **2022**, *61*, e202211570; d) X. Sun, D. Tian, X. Song, B. Jiang, C. Zhao, Y. Zhang, L. Yang, L. Fan, X. Yin, N. Zhang, *Nano Energy* **2022**, *95*, 106979.
- [4] a) X. Lv, T. Lei, B. Wang, W. Chen, Y. Jiao, Y. Hu, Y. Yan, J. Huang, J. Chu, C. Yan, C. Wu, J. Wang, X. Niu, J. Xiong, *Adv. Energy Mater.* **2019**, *9*, 1901800; b) Y. Gong, Y. Wang, Z. Fang, S. Zhao, Y.-s. He, W. Zhang, J. Mu, L. Zhang, Z.-F. Ma, *Chem. Eng. J.* **2022**, *446*, 136943.
- [5] a) S. Hu, M. Yi, H. Wu, T. Wang, X. Ma, X. Liu, J. Zhang, *Adv. Funct. Mater.* **2022**, *32*, 2111084; b) D. Yang, Z. Liang, C. Zhang, J. J. Biendicho, M. Botifoll, M. C. Spadaro, Q. Chen, M. Li, A. Ramon, A. O. Moghaddam, J. Llorca, J. Wang, J. R. Morante, J. Arbiol, S.-L. Chou, A. Cabot, *Adv. Energy Mater.* **2021**, *11*, 2101250; c) Z. Liang, D. Yang, P. Tang, C. Zhang, J. J. Biendicho, Y. Zhang, J. Llorca, X. Wang, J. Li, M. Heggen, J. David, R. E. Dunin-Borkowski, Y. Zhou, J. R. Morante, A. Cabot, J. Arbiol, *Adv. Energy Mater.* **2021**, *11*, 2170022.
- [6] a) L. Guan, H. Hu, L. Li, Y. Pan, Y. Zhu, Q. Li, H. Guo, K. Wang, Y. Huang, M. Zhang, Y. Yan, Z. Li, X. Teng, J. Yang, J. Xiao, Y. Zhang, X. Wang, M. Wu, *ACS Nano* **2020**, *14*, 6222; b) J. Li, C. Chen, Y. Chen, Z. Li, W. Xie, X. Zhang, M. Shao, M. Wei, *Adv. Energy Mater.* **2019**, *9*, 1901935.
- [7] J. Wang, Y. Zhao, G. Li, D. Luo, J. Liu, Y. Zhang, X. Wang, L. Shui, Z. Chen, *Nano Energy* **2021**, *84*, 105891.
- [8] C. Zhang, R. Du, S. Martí-Sánchez, K. Xiao, D. Yang, C. Zhang, C. Li, G. Zeng, X. Chang, R. He, J. Arbiol, J. Li, J. J. Biendicho, A. Cabot, *Energies* **2023**, *16*, 4545.
- [9] a) D. Yang, Z. Liang, P. Tang, C. Zhang, M. Tang, Q. Li, J. J. Biendicho, J. Li, M. Heggen, R. E. Dunin-Borkowski, M. Xu, J. Llorca, J. Arbiol, J. R. Morante, S.-L. Chou, A. Cabot, *Adv. Mater.* **2022**, *34*, 2108835; b) C. Zhang, B. Fei, D. Yang, H. Zhan, J. Wang, J. Diao, J. Li, G. Henkelman, D. Cai, J. J. Biendicho, J. R. Morante, A. Cabot, *Adv. Funct. Mater.* **2022**, *32*, 2201322.
- [10] a) R. Sun, Y. Bai, M. Luo, M. Qu, Z. Wang, W. Sun, K. Sun, *ACS Nano* **2021**, *15*, 739; b) Y. Lu, J.-L. Qin, T. Shen, Y.-F. Yu, K. Chen, Y.-Z. Hu, J.-N. Liang, M.-X. Gong, J.-J. Zhang, D.-L. Wang, *Adv. Energy Mater.* **2021**, *11*, 2101780; c) W. Zhao, Y. Lei, Y. Zhu, Q. Wang, F. Zhang, X. Dong, H. N. Alshareef, *Nano Energy* **2021**, *86*, 106120; d) Z. Ye, Y. Jiang, L. Li, F. Wu, R. Chen, *Adv. Mater.* **2020**, *32*, 2002168; e) T. Chen, Z. Zhang, B. Cheng, R. Chen, Y. Hu, L. Ma, G. Zhu, J. Liu, Z. Jin, J. Am. Chem. Soc. **2017**, *139*, 12710; f) Y. Lu, J. L. Qin, T. Shen, Y. F. Yu, K. Chen, Y. Z. Hu, J. N. Liang, M. X. Gong, J. J. Zhang, D. L. Wang, *Adv. Energy Mater.* **2021**, *11*, 2101780.
- [11] a) C. Xing, Y. Zhang, K. Xiao, X. Han, Y. Liu, B. Nan, M. G. Ramon, K. H. Lim, J. Li, J. Arbiol, B. Poudel, A. Nozariasbmarz, W. Li, M. Ibáñez, A. Cabot, *ACS Nano* **2023**, *17*, 8442; b) W. Yao, C. Tian, C. Yang, J. Xu, Y. Meng, I. Manke, N. Chen, Z. Wu, L. Zhan, Y. Wang, R. Chen, *Adv. Mater.* **2022**, *34*, 2106370.
- [12] B. Wang, L. Wang, D. Ding, Y. Zhai, F. Wang, Z. Jing, X. Yang, Y. Kong, Y. Qian, L. Xu, *Adv. Mater.* **2022**, *34*, 2204403.
- [13] a) J.-Y. Xue, F.-L. Li, B. Chen, H. Geng, W. Zhang, W.-Y. Xu, H. Gu, P. Braunstein, J.-P. Lang, *Appl. Catal. B* **2022**, *312*, 121434; b) L. Jiang, J. Duan, J. Zhu, S. Chen, M. Antonietti, *ACS Nano* **2020**, *14*, 2436; c) X. Wang, X. Han, R. Du, C. Xing, X. Qi, Z. Liang, P. Guardia, J. Arbiol, A. Cabot, J. Li, *ACS Appl. Mater. Interfaces* **2022**, *14*, 41924; d) R. Du, K. Xiao, B. Li, X. Han, C. Zhang, X. Wang, Y. Zuo, P. Guardia, J. Li, J. Chen, J. Arbiol, A. Cabot, *Chem. Eng. J.* **2022**, *441*, 135999.
- [14] a) L. Zhang, J. Bi, T. Liu, X. Chu, H. Lv, D. Mu, B. Wu, F. Wu, *Energy Storage Mater.* **2023**, *54*, 410; b) J. Wang, B. Wang, H. Sun, G. Wang, J. Bai, H. Wang, *Energy Storage Mater.* **2022**, *46*, 394.
- [15] a) J.-Y. Xue, F.-L. Li, B. Chen, H. Geng, W. Zhang, W.-Y. Xu, H. Gu, P. Braunstein, J.-P. Lang, *Appl. Catal. B* **2022**, *312*; b) S. R. K. A., N. Barman, S. Radhakrishnan, R. Thapa, C. S. Rout, *J. Mater. Chem. A* **2022**, *10*, 23590; c) L. Luo, X. Wang, S. Yang, J. Dai, D. Li, L. Xia, C. Chi, A. Cabot, Y. Xu, L. Dai, *ACS Appl. Energy Mater.* **2023**, *6*, 5940; d) J. Dai, X. Qi, L. Xia, Q. Xue, L. Luo, X. Wang, C. Yang, D. Li, H. Xie, A. Cabot, L. Dai, Y. Xu, *Adv. Funct. Mater.* **2023**, *33*, 2212440.
- [16] Y. Li, J. Zhang, Q. Chen, X. Xia, M. Chen, *Adv. Mater.* **2021**, *33*, 2100855.
- [17] M. Zhang, J. Mu, Y. Li, Y. Pan, Z. Dong, B. Chen, S. Guo, W. Yuan, H. Fang, H. Hu, M. Wu, *J. Energy Chem.* **2023**, *78*, 105.
- [18] Y. Zhang, C. Xing, Y. Liu, M. C. Spadaro, X. Wang, M. Li, K. Xiao, T. Zhang, P. Guardia, K. H. Lim, A. O. Moghaddam, J. Llorca, J. Arbiol, M. Ibáñez, A. Cabot, *Nano Energy* **2021**, *85*, 105991.
- [19] a) S. Hu, X. Huang, L. Zhang, G. Li, S. Chen, J. Zhang, X. Liu, *Adv. Funct. Mater.* **2023**, *33*, 2214161; b) W. Li, Y. Ma, P. Li, X. Jing, K. Jiang, D. Wang, *Adv. Energy Mater.* **2021**, *11*, 2102607; c) W. Hou, P. Feng, X. Guo, Z. Wang, Z. Bai, Y. Bai, G. Wang, K. Sun, *Adv. Mater.* **2022**, *34*, 2202222.
- [20] S. Hu, X. Huang, L. Zhang, G. Li, S. Chen, J. Zhang, X. Liu, *Adv. Funct. Mater.* **2023**, *33*, 2214161.
- [21] a) D. Yang, C. Zhang, J. J. Biendicho, X. Han, Z. Liang, R. Du, M. Li, J. Li, J. Arbiol, J. Llorca, Y. Zhou, J. R. Morante, A. Cabot, *ACS Nano* **2020**, *14*, 15492; b) X. Wang, X. Han, R. Du, Z. Liang, Y. Zuo, P. Guardia, J. Li, J. Llorca, J. Arbiol, R. Zheng, A. Cabot, *Appl. Catal. B* **2023**, *320*, 121988.
- [22] a) S. Liu, Z. Wang, S. Zhou, F. Yu, M. Yu, C.-Y. Chiang, W. Zhou, J. Zhao, J. Qiu, *Adv. Mater.* **2017**, *29*, 1700874; b) X. Wang, J. Li, Q. Xue, X. Han, C. Xing, Z. Liang, P. Guardia, Y. Zuo, R. Du, L. Balcells, J. Arbiol, J. Llorca, X. Qi, A. Cabot, *ACS Nano* **2023**, *17*, 825.
- [23] a) X. Wang, C. Xing, Z. Liang, P. Guardia, X. Han, Y. Zuo, J. Llorca, J. Arbiol, J. Li, A. Cabot, *J. Mater. Chem. A* **2022**, *10*, 3659; b) C. Fu, X. Qi, L. Zhao, T. Yang, Q. Xue, Z. Zhu, P. Xiong, J. Jiang, X. An, H. Chen, J. S. Chen, A. Cabot, R. Wu, *Appl. Catal. B* **2023**, *335*, 122875; c) X. Wang, L. Yang, C. Xing, X. Han, R. Du, R. He, P. Guardia, J. Arbiol, A. Cabot, *Nanomaterials*, **2022**, *12*, 1098.

- [24] Y. Jiang, F. Wu, Z. Ye, Y. Zhou, Y. Chen, Y. Zhang, Z. Lv, L. Li, M. Xie, R. Chen, *Chem. Eng. J.* **2023**, 451, 138430.
- [25] C. Huang, A. Gao, F. Yi, Y. Wang, D. Shu, Y. Liang, Z. Zhu, J. Ling, J. Hao, *Chem. Eng. J.* **2021**, 419, 129643.
- [26] C. Zhang, H. Li, X. Zeng, R. Wang, L. Zhang, G. Liang, K. Davey, Y. Liu, L. Zhang, S. Zhang, Z. Guo, *Adv. Energy Mater.* **2022**, 12, 2202577.
- [27] W. Bao, L. Liu, C. Wang, S. Choi, D. Wang, G. Wang, *Adv. Energy Mater.* **2018**, 8, 1702485.
- [28] S. Feng, Z.-H. Fu, X. Chen, Q. Zhang, *InfoMat* **2022**, 4, e12304.
- [29] R. Zou, W. Liu, F. Ran, *InfoMat* **2022**, 4, e12319.
- [30] a) D. Yan, W. Wang, X. Luo, C. Chen, Y. Zeng, Z. Zhu, *Chem. Eng. J.* **2018**, 334, 864; b) F. Lu, M. Zhou, W. Li, Q. Weng, C. Li, Y. Xue, X. Jiang, X. Zeng, Y. Bando, D. Golberg, *Nano Energy* **2016**, 26, 313.
- [31] C. Zhang, J. J. Biendicho, T. Zhang, R. Du, J. Li, X. Yang, J. Arbiol, Y. Zhou, J. R. Morante, A. Cabot, *Adv. Funct. Mater.* **2019**, 29, 1903842.
- [32] C. Zhang, R. Du, J. J. Biendicho, M. Yi, K. Xiao, D. Yang, T. Zhang, X. Wang, J. Arbiol, J. Llorca, Y. Zhou, J. R. Morante, A. Cabot, *Adv. Energy Mater.* **2021**, 11.
- [33] a) H.-J. Li, K. Xi, W. Wang, S. Liu, G.-R. Li, X.-P. Gao, *Energy Storage Mater.* **2022**, 45, 1229; b) H. Song, T. Li, T. He, Z. Wang, D. Fang, Y. Wang, X. L. Li, D. Zhang, J. Hu, S. Huang, *Chem. Eng. J.* **2022**, 450, 138115; c) G. Liu, Q. Zeng, Z. Fan, S. Tian, X. Li, X. Lv, W. Zhang, K. Tao, E. Xie, Z. Zhang, *Chem. Eng. J.* **2022**, 448, 137683; d) L. Wu, J. Hu, X. Yang, Z. Liang, S. Chen, L. Liu, H. Hou, J. Yang, *J. Mater. Chem. A* **2022**, 10, 23811; e) Z. Wu, S. Chen, L. Wang, Q. Deng, Z. Zeng, J. Wang, S. Deng, *Energy Storage Mater.* **2021**, 38, 381; f) D. Cai, B. Liu, D. Zhu, D. Chen, M. Lu, J. Cao, Y. Wang, W. Huang, Y. Shao, H. Tu, W. Han, *Adv. Energy Mater.* **2020**, 10, 2070088; g) S. Zhao, X. Tian, Y. Zhou, B. Ma, A. Natarajan, *J. Energy Chem.* **2020**, 46, 22; h) S. Chen, J. Luo, N. Li, X. Han, J. Wang, Q. Deng, Z. Zeng, S. Deng, *Energy Storage Mater.* **2020**, 30, 187.

# ADVANCED FUNCTIONAL MATERIALS

## Supporting Information

for *Adv. Funct. Mater.*, DOI 10.1002/adfm.202305624

Combined Defect and Heterojunction Engineering in ZnTe/CoTe<sub>2</sub>@NC Sulfur Hosts Toward Robust Lithium–Sulfur Batteries

*Chen Huang, Jing Yu, Canhuang Li, Zhibiao Cui, Chaoqi Zhang\*, Chaoyue Zhang\*, Bingfei Nan, Junshan Li, Jordi Arbiol and Andreu Cabot\**

## ***Supporting Information for***

### **Combined Defect and Heterojunction Engineering in ZnTe/CoTe<sub>2</sub>@NC Sulfur Hosts toward Robust Lithium-Sulfur Batteries**

*Chen Huang, Jing Yu, Canhuang Li, Zhibiao Cui, Chaoqi Zhang\*, Chaoyue Zhang\*, Bingfei Nan, Junshan Li, Jordi Arbiol and Andreu Cabot\**

*C. Huang, J. Yu, C. H. Li, C. Q. Zhang, C. Y. Zhang, B. F. Nan, A. Cabot  
Catalonia Institute for Energy Research-IREC  
Sant Adrià de Besòs, Barcelona 08930, Spain  
E-mail: acabot@irec.cat*

*C. Huang, C. H. Li  
Department of Chemistry  
Universitat de Barcelona 08028, Spain*

*J. Yu, J. Arbiol  
Catalan Institute of Nanoscience and Nanotechnology (ICN2), CSIC and BIST, Campus UAB,  
Bellaterra, 08193 Barcelona, Catalonia, Spain.*

*Z.B. Cui  
School of Chemistry, South China Normal University, Guangzhou 510006, PR China*

*C. Q. Zhang  
College of Materials Science and Engineering, Fuzhou University  
No.2, Xueyuan Road, Minhou County, Fuzhou City, Fujian Province  
350108, China  
E-mail: czhang@irec.cat*

*C. Y. Zhang  
Key Laboratory for Magnetism and Magnetic Materials of the Ministry of Education & School  
of Physical Science & Technology  
Lanzhou University Lanzhou 730000, China  
E-mail: chzhang@irec.cat*

*J. S. Li  
Institute for Advanced Study  
Chengdu University 610106, Chengdu, China*

## **Experimental section**

### ***Materials***

Cobalt(II) nitrate hexahydrate (analytical reagent, AR,  $\text{Co}(\text{NO}_3)_2 \cdot 6\text{H}_2\text{O}$ ), zinc nitrate hexahydrate (AR,  $\text{Zn}(\text{NO}_3)_2 \cdot 6\text{H}_2\text{O}$ ), tris(hydroxymethyl)-aminomethane (Tris,  $\geq 99.8\%$ ) and 2-methylimidazole (AR,  $\text{C}_4\text{H}_6\text{N}_2$ ) were obtained from Sigma Aldrich. Tellurium powder (AR, Te), methanol (AR,  $\text{CH}_3\text{OH}$ ), polyvinylidene fluoride (PVDF), N-methylpyrrolidone (NMP), 1,3-dioxolane (DOL), 1,2-dimethoxyethane (DME) and dopamine hydrochloride ( $\text{DA} \cdot \text{HCl}$ ) were purchased from Fisher. All chemicals were used as received, without further processing. Deionized water was used for all the water-based experiments.

### ***Synthesis of Zn-MOF (ZIF-8)***

0.873 g  $\text{Zn}(\text{NO}_3)_2 \cdot 6\text{H}_2\text{O}$  was dissolved in 40 mL methanol to form solution A. 1.15 g of 2-methylimidazole was dissolved in 40 mL methanol solution to form solution B. Then solution B was quickly added to solution A under rapid stirring. The obtained mixture was aged for 24 h. The white resulting powder was collected by centrifugation, washed with ethanol three times, and dried in a vacuum oven at 70 °C for 12 h to obtain ZIF-8.

### ***Synthesis of Co-ZIF-67 in the presence of ZIF-8 (ZIF-8/ZIF-67)***

200 mg ZIF-8 was dispersed in 50 mL methanol solution, and then 0.5 g  $\text{Co}(\text{NO}_3)_2 \cdot 6\text{H}_2\text{O}$  was added to the above solution to form solution C. 1.5 g of 2-methylimidazole was dissolved in 50 mL methanol to form solution D. Then, solution D was quickly added to solution C under stirring. The product was washed with ethanol three times and finally centrifuged and dried to obtain the purple solid (ZIF-8/ZIF-67). For comparison, Zn-ZIF-8 and Co-ZIF-67 were synthesized similarly, using  $\text{Zn}(\text{NO}_3)_2 \cdot 6\text{H}_2\text{O}$  and  $\text{Co}(\text{NO}_3)_2 \cdot 6\text{H}_2\text{O}$  as precursors.



### ***Synthesis of ZIF-8/ZIF-67@PDA***

1 mmol tris(hydroxymethyl)-aminomethane (Tris,  $\geq 99.8\%$ ) was dissolved in 100 mL ethanol to form a homogeneous solution. 60 mg of ZIF-8/ZIF-67 was added to the above solution and sonicated for 1 h to form solution E. 60 mg DA·HCl was added to solution E and kept stirring for 6 h. Then, the material was centrifuged and washed with ethanol three times. Finally, the material was centrifuged and dried in a vacuum oven at 70 °C for 10 h to obtain a black solid (ZIF-8/ZIF-67@PDA). ZIF-8@PDA and ZIF-67@PDA were obtained by a similar synthesis process.

### ***Synthesis of ZnTe/CoTe<sub>2</sub>@NC***

ZIF-8/ZIF-67@PDA (100 mg) and tellurium powder (300 mg) were pyrolyzed at 600 °C under Ar for 2 h to obtain ZnTe/CoTe<sub>2</sub>@NC. CoTe<sub>2</sub>@NC and ZnTe@NC were obtained in the same way from ZIF-8@PDA and ZIF-67@PDA.

### ***Synthesis of v-ZnTe/CoTe<sub>2</sub>@NC***

v-ZnTe/CoTe<sub>2</sub>@NC powders were obtained by annealing ZnTe/CoTe<sub>2</sub>@NC powders at 350 °C for 3 h in an Ar/H<sub>2</sub> atmosphere. The vacancy content can be modified by tuning the annealing time and temperature and potentially by adjusting the reducing power of the annealing atmosphere, i.e. controlling the amount of hydrogen. Because the annealing temperature can strongly affect other material parameters and the change of the atmospheric concentration is not convenient in our set-up, we choose to modify the Te vacancy concentration through the annealing time, in the range between 1 h and 5 h.

### ***Synthesis of NC***

The ZIF-8/ZIF-67 @PDA particles are then subjected to thermal annealing in flowing Ar at 900 °C at a ramp rate of 2 °C min<sup>-1</sup>, Zn nanoparticles evaporate under high-temperature conditions, followed by etching away the unstable Co nano particles with H<sub>2</sub>SO<sub>4</sub>. Finally, NC was obtained.

### ***Synthesis of v-ZnTe/CoTe<sub>2</sub>@NC/S, ZnTe/CoTe<sub>2</sub>@NC/S, CoTe<sub>2</sub>@NC/S and ZnTe@NC/S***

v-ZnTe/CoTe<sub>2</sub>@NC, ZnTe/CoTe<sub>2</sub>@NC, CoTe<sub>2</sub>@NC, and ZnTe@NC were grounded with sulfur in a mortar at a mass ratio of 3:7. The obtained material was heated in a tube furnace at 155°C for 12 h, and then at 300°C for 2 h under Ar atmosphere to remove surface sulfur.

### ***Physical characterization***

Crystal structures and crystalline phases were analyzed by X-ray diffraction (XRD) on a Bruker X-ray diffractometer with Cu K $\alpha$  irradiation at 40 kV. The microstructure morphology was observed by scanning electron microscopy (SEM, ZEISS Ultra-55) and transmission electron microscopy (TEM, JEM-2100HR). The N<sub>2</sub> adsorption and desorption curves were used to determine the specific surface area and pore size distribution by Brunauer-Emmett-Teller equation and Barret-Joyner-Halenda (BJH) methods. X-ray photoelectron spectroscopy (XPS, K-Alpha+, Thermo Fisher Scientific) was utilized to determine the surface elemental compositions of the samples. The degree of graphitization of the electrode material was analyzed by Raman spectroscopy. A Perkin Elmer Lambda 950 UV–vis spectrophotometer was used to measure UV–vis absorption spectra. The thermal stability and S loading of the products was characterized by thermogravimetric analysis (TGA, STA209PC). The electronic conductivity of electrodes was tested by the digital four-probe method on samples prepared by pressing electrode material into sheet structure at different pressures at room temperature (Four Probes Tech, RTS-9, China).

### ***Electrochemical characterization***

Cathodes were obtained by the following method: first, the active material (v-ZnTe/CoTe<sub>2</sub>@NC/S, ZnTe/CoTe<sub>2</sub>@NC/S, CoTe<sub>2</sub>@NC/S and ZnTe@NC/S), Super P and polyvinylidene fluoride (PVDF) were mixed and ground at a ratio of 8:1:1. Then, N-

methylpyrrolidone (NMP) was added to the uniformly mixed powder to form a slurry. Finally, the slurry was coated on an aluminum foil and cut into 12 mm raw sheets (the active material S content is about  $1.5 \text{ mg cm}^{-2}$ ) to obtain the working electrode. To test the electrochemical performance of the electrode materials, the working electrode as the cathode, a lithium foil as the anode, and a Celgard 2400 membrane as the separator were assembled into a coin cell. The electrolyte was obtained by dissolving 1.0 M lithium bis(trifluoromethanesulfonyl)imide and 0.2 M  $\text{LiNO}_3$  in a mixture of DOL and DME with a volume ratio of 1:1. The amount of electrolyte was about 20  $\mu\text{L}$  for each coin cell. To test the electrochemical performance at high sulfur loads ( $5.4 \text{ mg cm}^{-2}$ ), additional electrolyte was added to the coin cells. All cells underwent aging to ensure sufficient electrolyte penetration before performing electrochemical tests. Galvanostatic charge/discharge (GCD) tests were performed at a current rate of 0.1C-5C with a voltage window of 1.7 V-2.8 V by using a Neware BTS4. CV tests were studied at scan rates of  $0.1 \text{ mV s}^{-1}$  -  $0.4 \text{ mV s}^{-1}$ . EIS tests were also performed by the same electrochemical workstation.

### ***Synthesis of $\text{Li}_2\text{S}_6$ solution and adsorption test***

S and  $\text{Li}_2\text{S}$  were dissolved into a mixed solution of DME and DOL (V/V=1:1) according to the ratio 5:1, and then stirred overnight at  $80^\circ\text{C}$  to obtain a  $\text{Li}_2\text{S}_6$  solution. For the polysulfide absorption performance test, 25 mg of v-ZnTe/ $\text{CoTe}_2$ @NC, ZnTe/ $\text{CoTe}_2$ @NC,  $\text{CoTe}_2$ @NC and ZnTe@NC was immersed into a 3.0 mL mixture solution and aged overnight.

### ***Synthesis of symmetrical cells and measurements***

The preparation of the symmetrical battery is similar to the preparation of the LSBs but using two identical electrodes (v-ZnTe/ $\text{CoTe}_2$ @NC, ZnTe/ $\text{CoTe}_2$ @NC,  $\text{CoTe}_2$ @NC and ZnTe@NC) as the working and the counter electrode respectively. 40  $\mu\text{L}$  of electrolyte containing 0.5 M  $\text{Li}_2\text{S}_6$  and 1 M LiTFSI dissolved in DOL/DME (V/V= 1:1) was added into the coin cells. The

loading of each electrode is about  $0.5 \text{ mg cm}^{-2}$ . The prepared symmetrical battery was tested at a scan rate of  $5 \text{ mV s}^{-1}$ .

### ***Nucleation experimental test of $\text{Li}_2\text{S}$***

v-ZnTe/CoTe<sub>2</sub>@NC, ZnTe/CoTe<sub>2</sub>@NC, CoTe<sub>2</sub>@NC, and ZnTe@NC were dispersed into ethanol solution, and coated onto carbon paper as working electrodes. Lithium foil was used as the counter electrode. 0.25 M Li<sub>2</sub>S<sub>8</sub> with 1.0 M LiTFSI in tetraethylene glycol dimethyl ether solution and 1.0 M LiTFSI solution without Li<sub>2</sub>S<sub>8</sub> were used as catholyte and anolyte respectively. The prepared battery was first discharged to 2.06 V at 0.1 mA, and then a constant voltage deposition experiment was carried out at a voltage of 2.05 V.

### ***DFT calculations***

All DFT calculations were performed using the Vienna Ab-initio Simulation Package (VASP). The Perdew-Burke-Ernzerhof (PBE) functional for the exchange-correlation term was used with the projector augmented wave (PAW) potentials and a cutoff energy of 400 eV. The convergence of energy and forces were set to  $1 \times 10^{-4} \text{ eV}$  and  $0.05 \text{ eV/\AA}$ , respectively. The heterojunction model was constructed by the CoTe<sub>2</sub> (200) and ZnTe (220). The lattice mismatch was no more than 3% and the vacuum layer was set as 15 Å to avoid the interactions between layers. The adsorption energy  $\Delta E_{ad}$  was calculated as:

$$\Delta E_{ad} = E_{(surf+ad)} - E_{surf} - E_{ad}$$

where  $E_{(surf+ad)}$  is the energy of the LiPS adsorbed on the surface,  $E_{surf}$  is the energy of the clean surface, and  $E_{ad}$  is the energy of the free LiPS.

The formula for calculating the Gibbs free as follow:

$$\Delta G(\text{S}_8\text{-Li}_2\text{S}_8): E_{\text{Li}_2\text{S}_8} - E_{\text{S}_8} - 2E_{\text{Li}^+}$$

$$\Delta G(\text{Li}_2\text{S}_8\text{-Li}_2\text{S}_6): E_{\text{Li}_2\text{S}_6} - E_{\text{Li}_2\text{S}_8} + 0.25E_{\text{S}_8}$$

$$\Delta G(\text{Li}_2\text{S}_6\text{-Li}_2\text{S}_4): E_{\text{Li}_2\text{S}_4} - E_{\text{Li}_2\text{S}_6} + 0.25E_{\text{S}_8}$$

$$\Delta G(\text{Li}_2\text{S}_4\text{-Li}_2\text{S}_2): E_{\text{Li}_2\text{S}_2} - E_{\text{Li}_2\text{S}_4} + 0.25E_{\text{S}_8}$$

$$\Delta G(\text{Li}_2\text{S}_2\text{-Li}_2\text{S}): E_{\text{Li}_2\text{S}} - E_{\text{Li}_2\text{S}_2} + 0.125E_{\text{S}_8}$$

***Pouch cell assembly and measurements:***

The v-ZnTe/CoTe<sub>2</sub>@NC/S cathode and lithium anode were cut into 3×2 cm pieces. The sulfur loading of the cathode in the pouch cell was 1.6 mg cm<sup>-2</sup>. The E/S ratio was about 20 μL mg<sup>-1</sup>, the thickness of the lithium belt anode was 0.4 mm. Separator and electrolyte were sandwiched between the tailored and v-ZnTe/CoTe<sub>2</sub>@NC/S lithium belt.

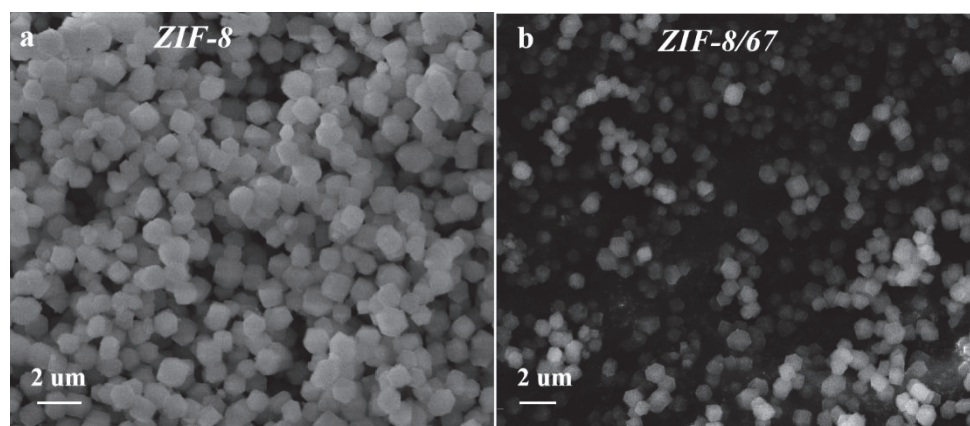


**Figure S1.** SEM images of ZIF-8 (a) and ZIF-8/ZIF-67 (b).

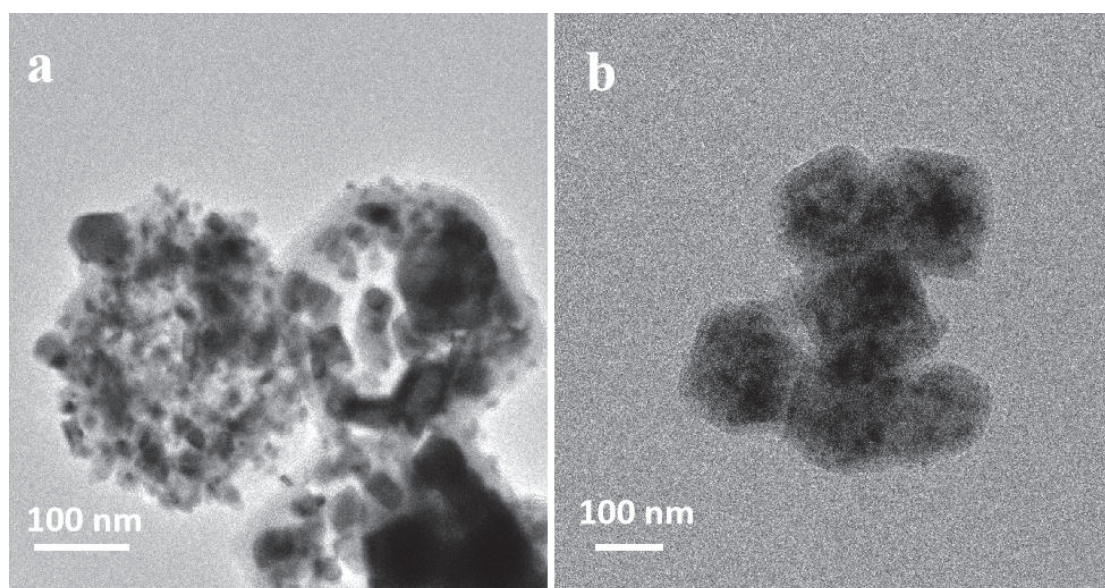


**Figure S2.** TEM images of v-ZnTe/CoTe<sub>2</sub>@NC (a) and v-ZnTe/CoTe<sub>2</sub>@NC/S (b).

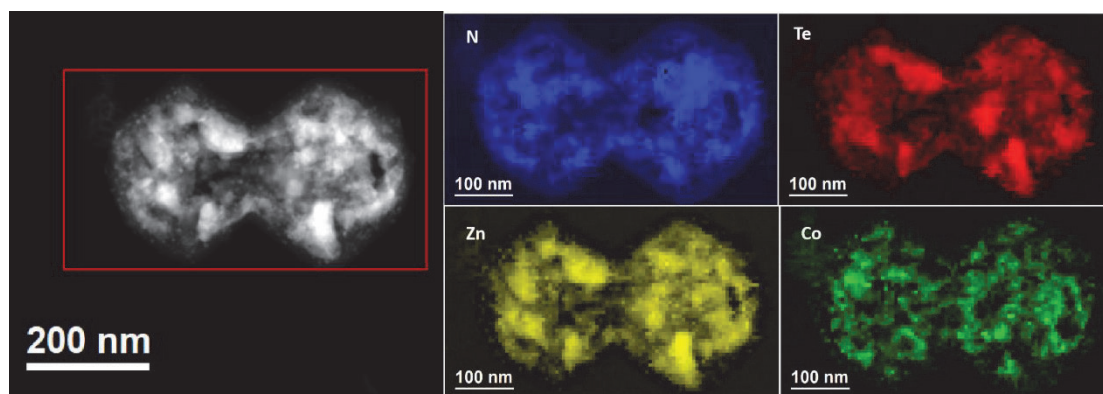


**Figure S3.** STEM micrograph (left) and EELS chemical composition maps of v-ZnTe/CoTe<sub>2</sub>@NC obtained from the red squared area in the STEM micrography.



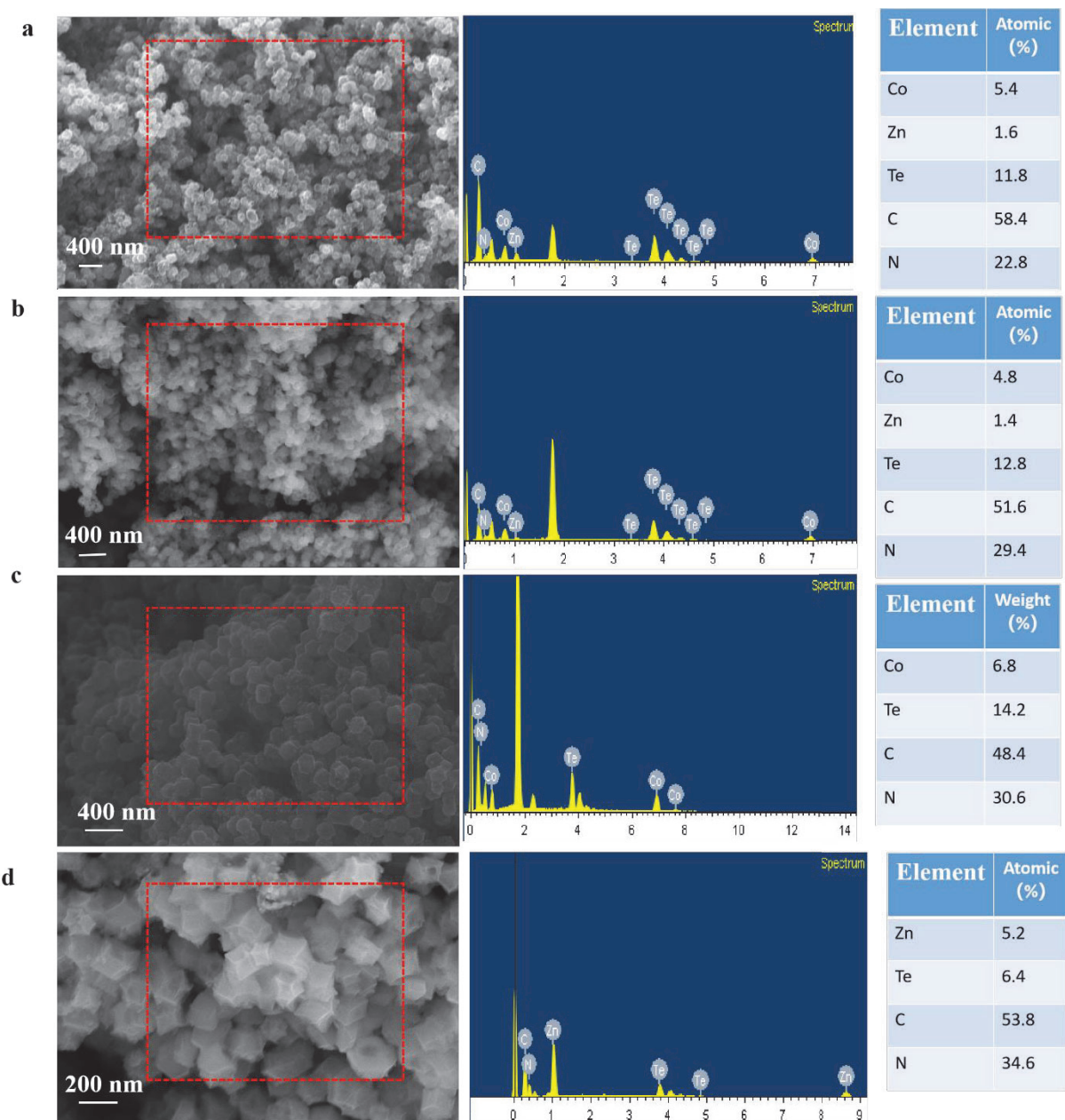


**Figure S4** EDX spectrum of v-ZnTe/CoTe<sub>2</sub>@NC ZnTe/CoTe<sub>2</sub>@NC, CoTe<sub>2</sub>@NC and ZnTe@NC.

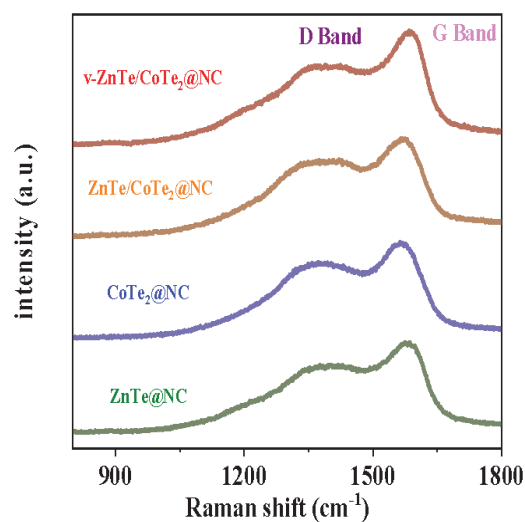


**Figure S5.** Raman spectra of v-ZnTe/CoTe<sub>2</sub>@NC, ZnTe/CoTe<sub>2</sub>@NC, CoTe<sub>2</sub>@NC, and ZnTe@NC.

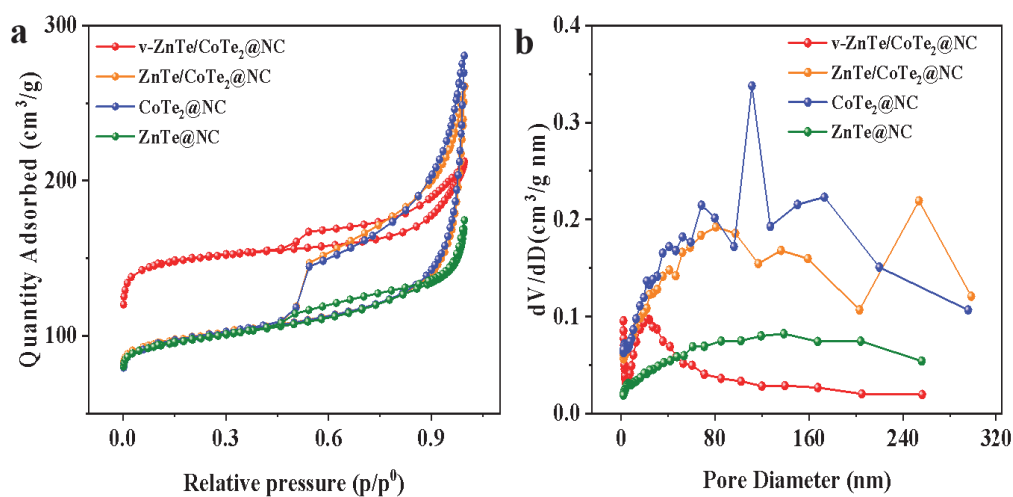


**Figure S6.** (a) Nitrogen adsorption-desorption isotherms and (b) pore size distribution diagram of v-ZnTe/CoTe<sub>2</sub>@NC, ZnTe/CoTe<sub>2</sub>@NC, CoTe<sub>2</sub>@NC, and ZnTe@NC



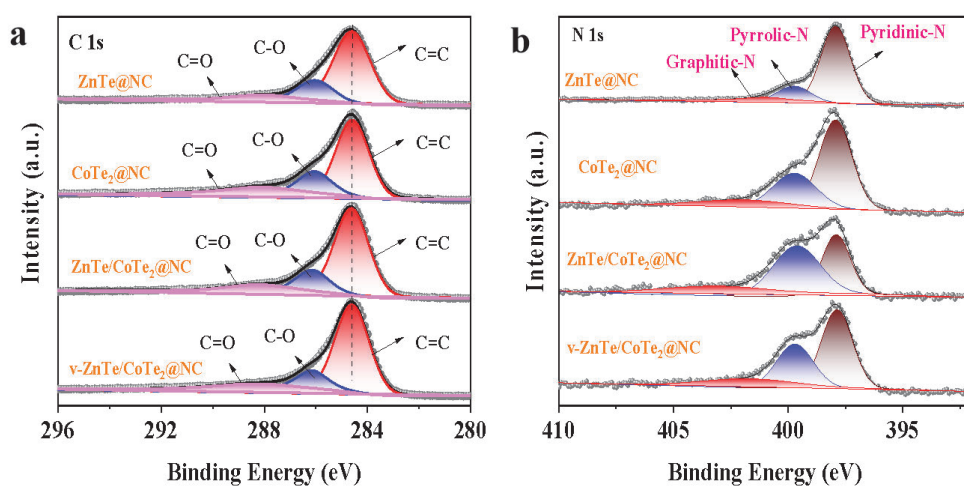


**Figure S7.** (a) C 1s XPS spectra and (b) N 1s XPR spectra of v-ZnTe/CoTe<sub>2</sub>@NC, ZnTe/CoTe<sub>2</sub>@NC, CoTe<sub>2</sub>@NC, and ZnTe@NC.

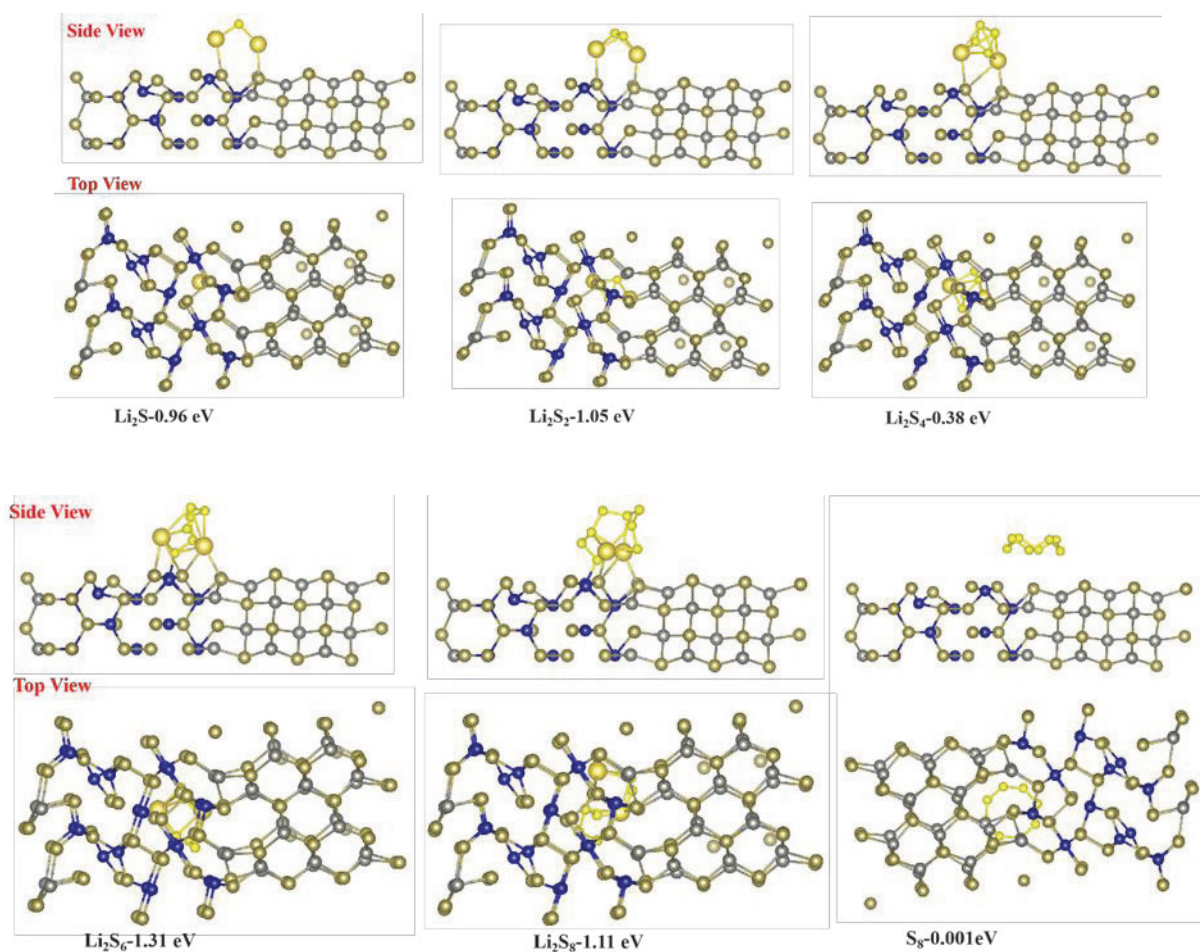


**Figure S8.** DFT-based optimized geometrical configurations of ZnTe/CoTe<sub>2</sub> with LiPSs.

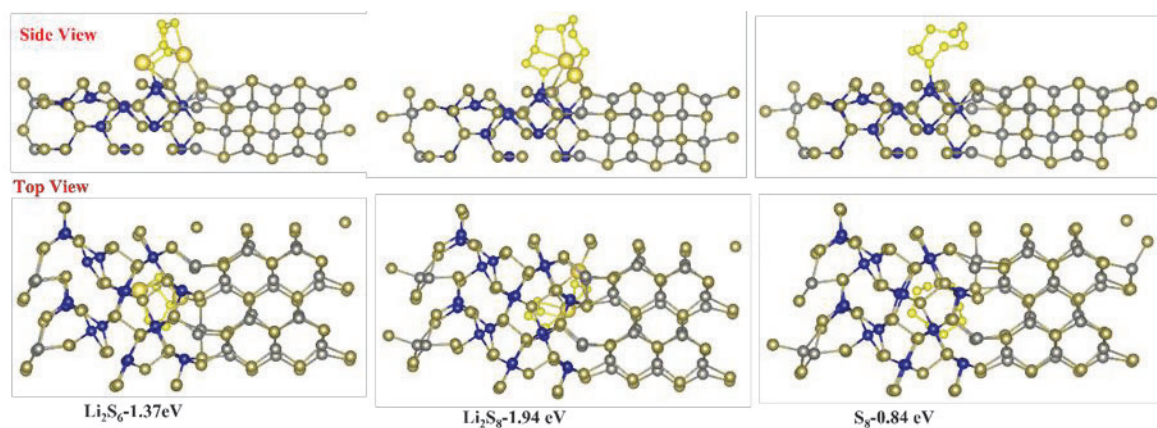
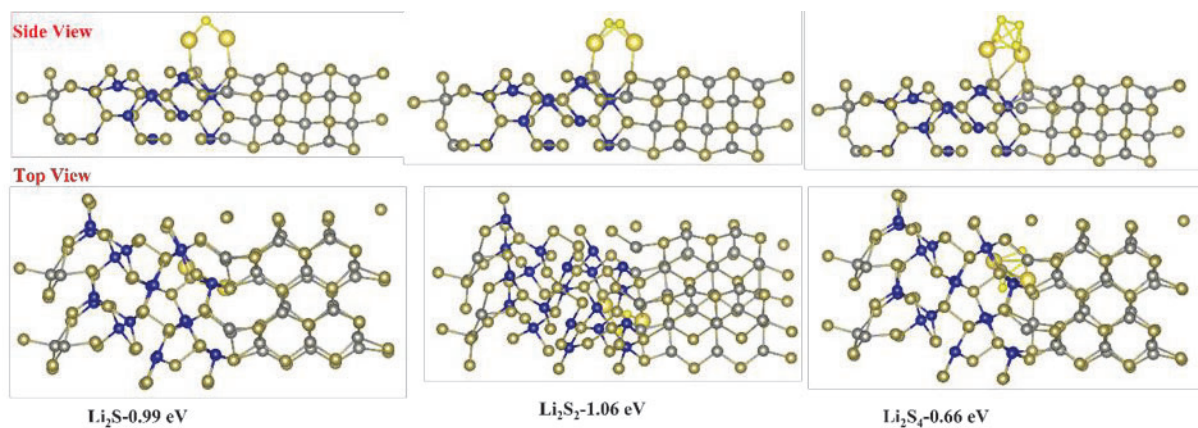


**Figure S9.** DFT-based optimized geometrical configurations of v-ZnTe/CoTe<sub>2</sub> with LiPSs.

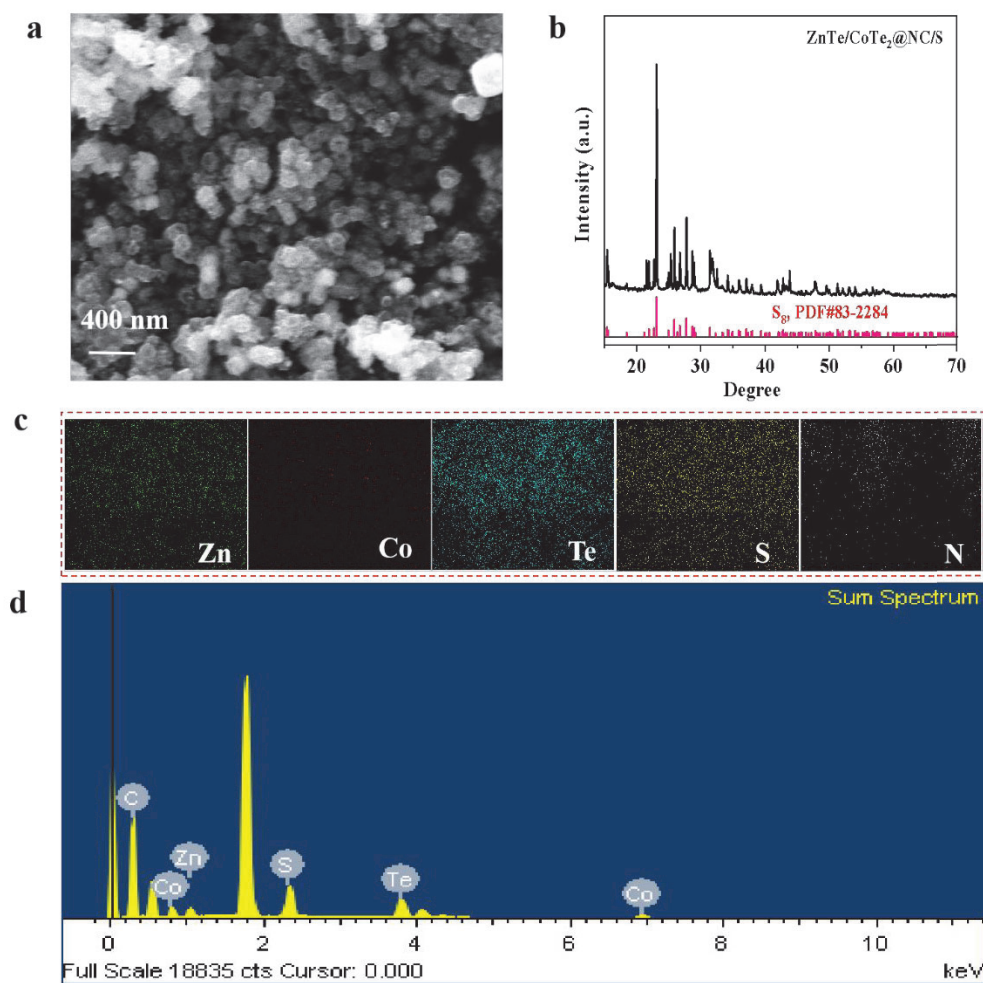


**Figure S10.** (a) SEM image of ZnTe/CoTe<sub>2</sub>@NC/S. (b) XRD pattern of ZnTe/CoTe<sub>2</sub>@NC/S. (c) EDX elemental mapping images: Co, Zn, Te, S, and N. (d) EDX spectrum.

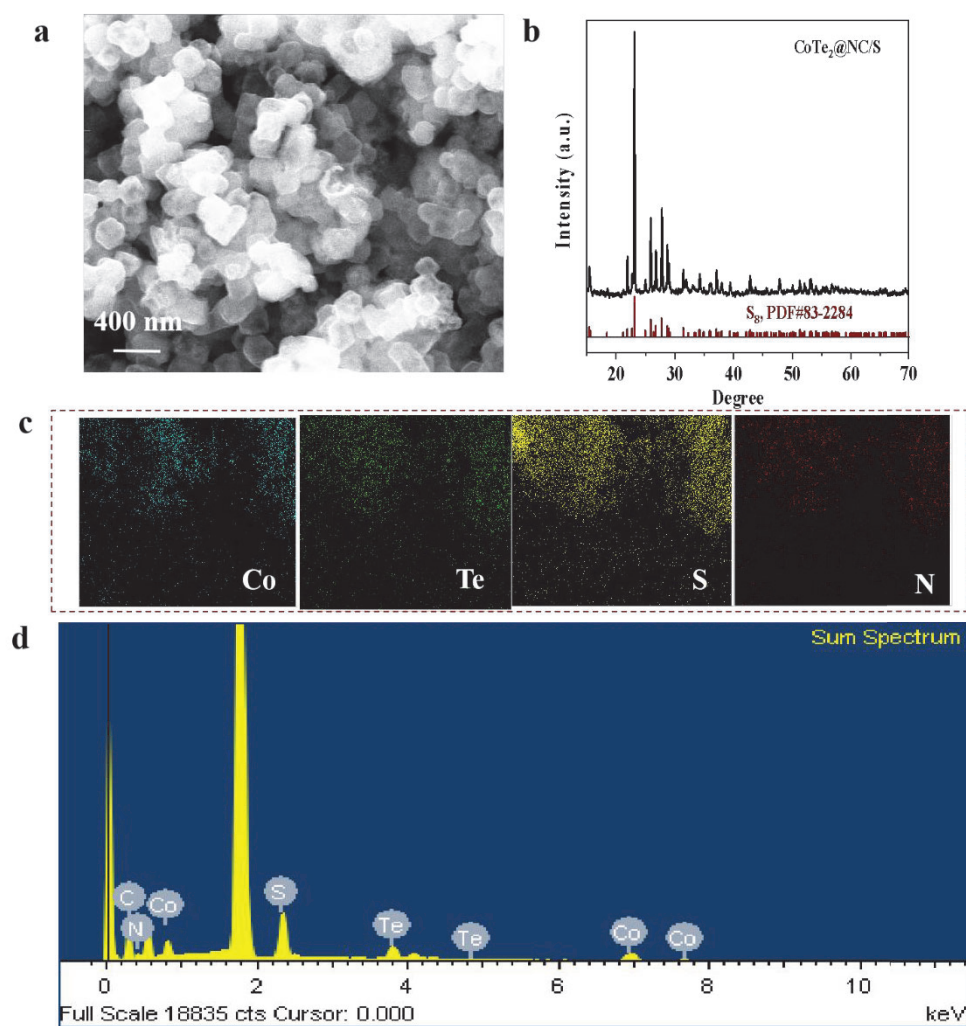


**Figure S11.** (a) SEM image of CoTe<sub>2</sub> @NC/S. (b) XRD pattern of CoTe<sub>2</sub> @NC/S. (c) EDX elemental mapping images: Co, Te, S, and N. (d) EDX spectrum.



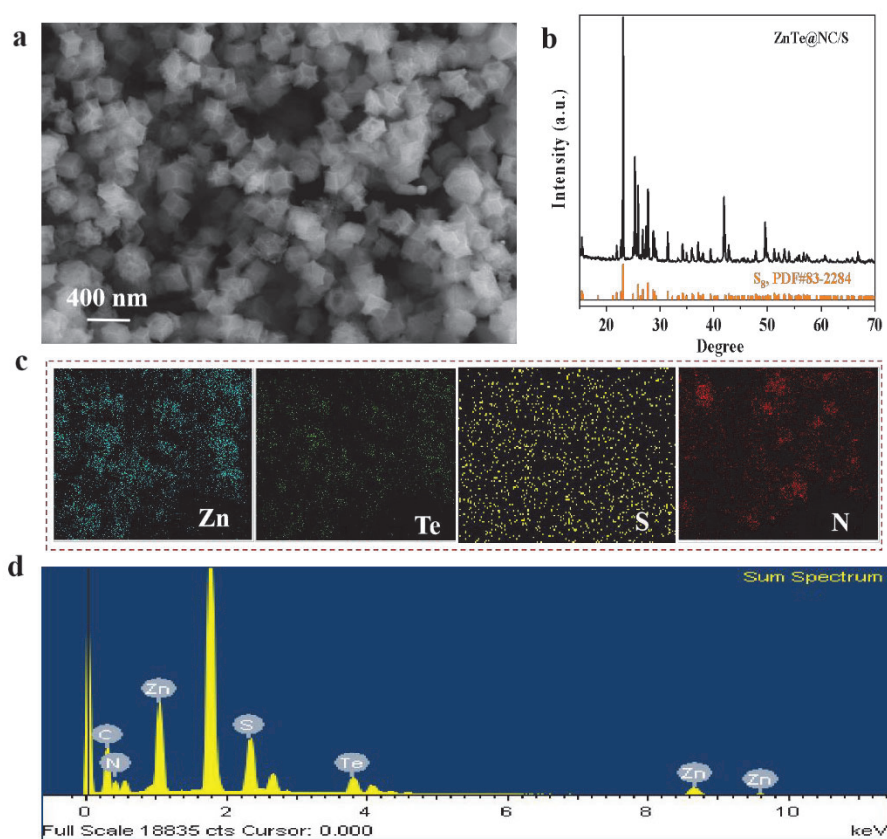


**Figure S12.** (a) SEM image of ZnTe@NC/S. (b) XRD pattern of ZnTe@NC/S. (c) EDX elemental mapping images: Zn, Te, S, and N. (d) EDX spectrum.

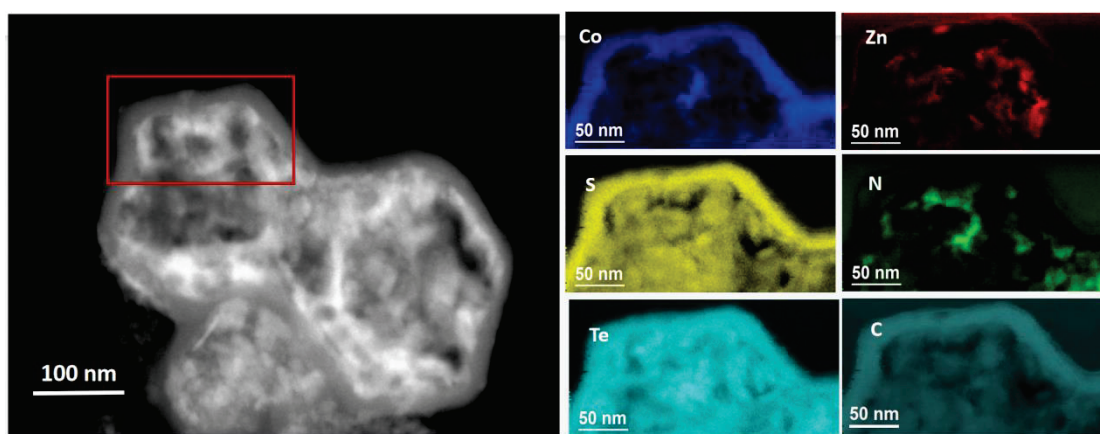


**Figure S13.** STEM micrograph and EELS chemical composition maps of v-ZnTe/CoTe<sub>2</sub>@NC/S obtained from the red squared area in the STEM micrograph.

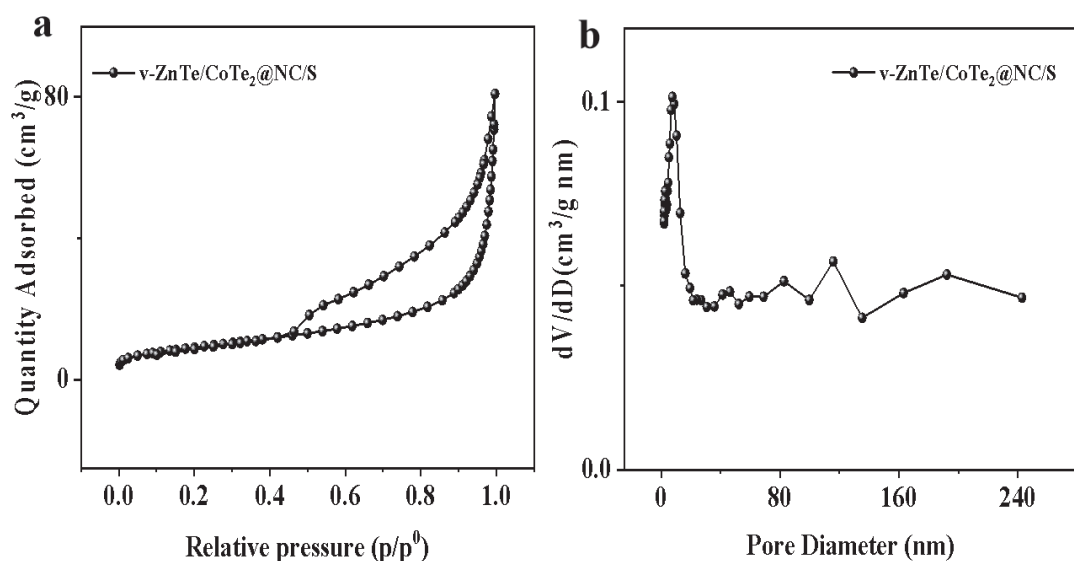


**Figure S14.** Nitrogen adsorption-desorption isotherms, pore size distribution diagram and Pore volume histograms of v-ZnTe/CoTe<sub>2</sub>@NC/S.

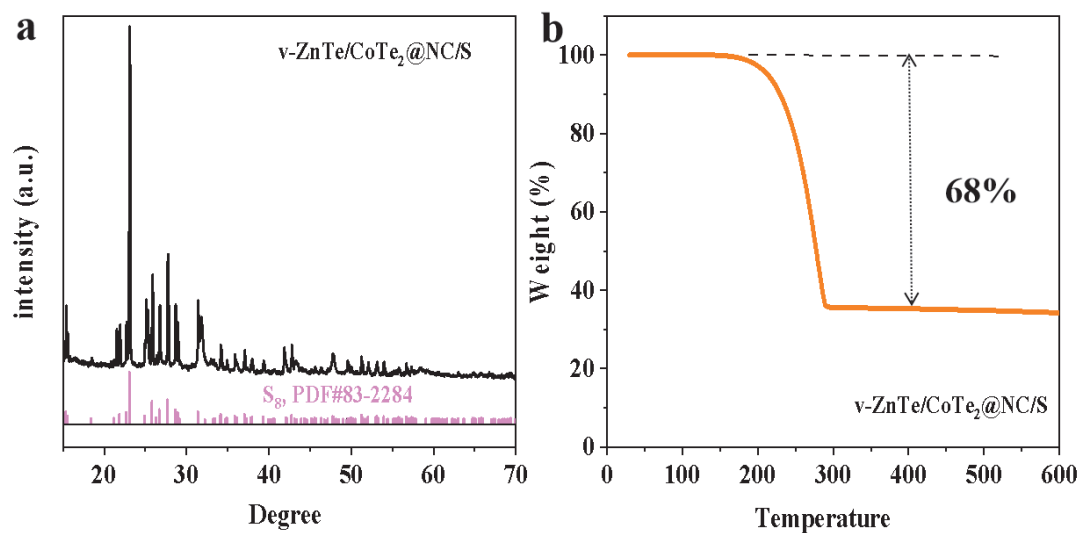


**Figure S15.** XRD pattern (a) and TGA curve (b) of v-ZnTe/CoTe<sub>2</sub>@NC/S.

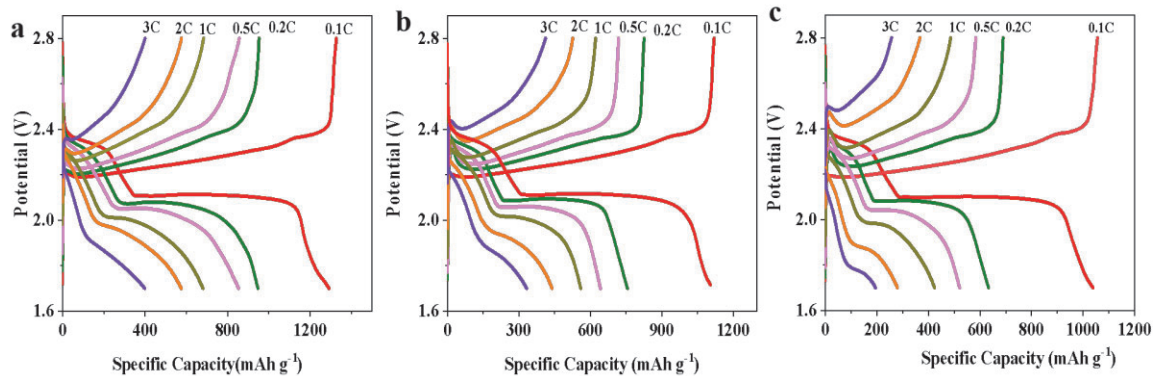


**Figure S16.** GCD curves of cells based on ZnTe/CoTe<sub>2</sub>@NC/S (a), CoTe<sub>2</sub>@NC/S (b), and ZnTe@NC/S (c) at current densities in the range 0.1C-3C.

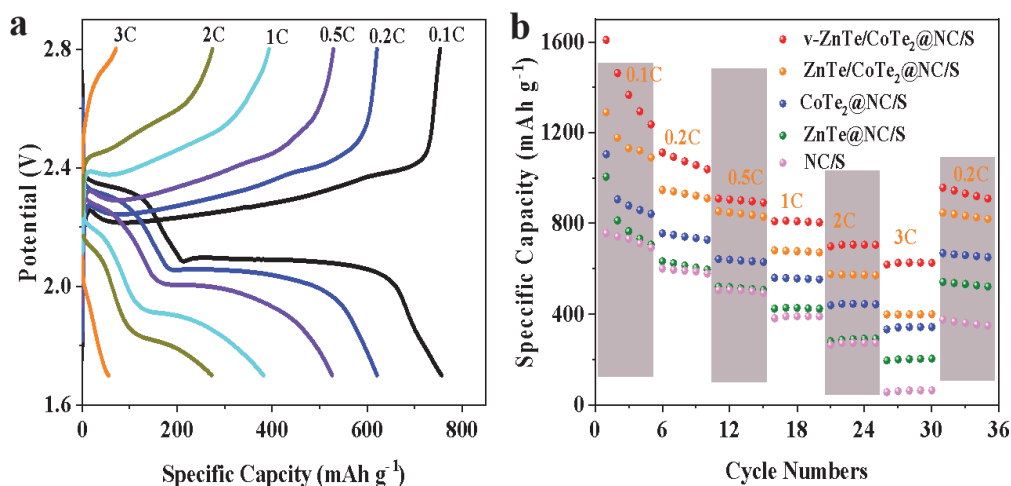


**Figure S17.** (a) GCD curve of NC/S electrode. When the current rate is 0.1C, 0.2C, 0.5C, 1C, 2C, and 3C, the specific capacitances are 757, 621, 526, 381, 264, and 56 mAh g<sup>-1</sup>, respectively. When the current rate returns to 0.2C, the specific capacity of the v-ZnTe/CoTe<sub>2</sub>@NC/S electrode recovers to 379 mAh g<sup>-1</sup>. (b) Rate performance curve. The specific capacity of NC/S decreases with the increase of the current rate. further demonstrating that the formation of NC/S has moderate electrochemical performance.

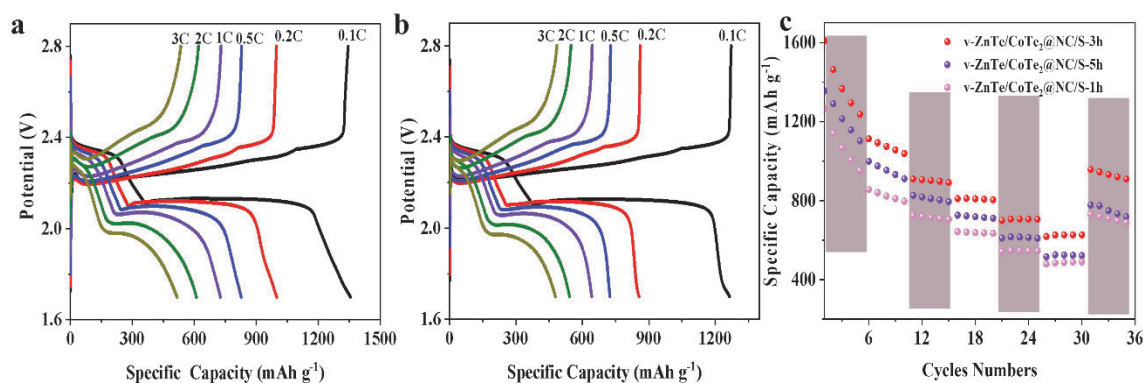


**Figure S18.** (a,b) GCD curve of v-ZnTe/CoTe<sub>2</sub>@NC/S-5h (a) and v-ZnTe/CoTe<sub>2</sub>@NC/S-1h (b), (c) Rate performance of the different electrodes.

Compared with v-ZnTe/CoTe<sub>2</sub>@NC/S-5h (1355 mAh g<sup>-1</sup> at 0.1C) and v-ZnTe/CoTe<sub>2</sub>@NC/S-1h (1265 mAh g<sup>-1</sup> at 0.1C), v-ZnTe/CoTe<sub>2</sub>@NC/S-3h (1608 mAh g<sup>-1</sup> at 0.1C) exhibits higher initial specific capacitance and excellent rate performance, indicating that the content of vacancies can affect the electrochemical performance of electrode materials.



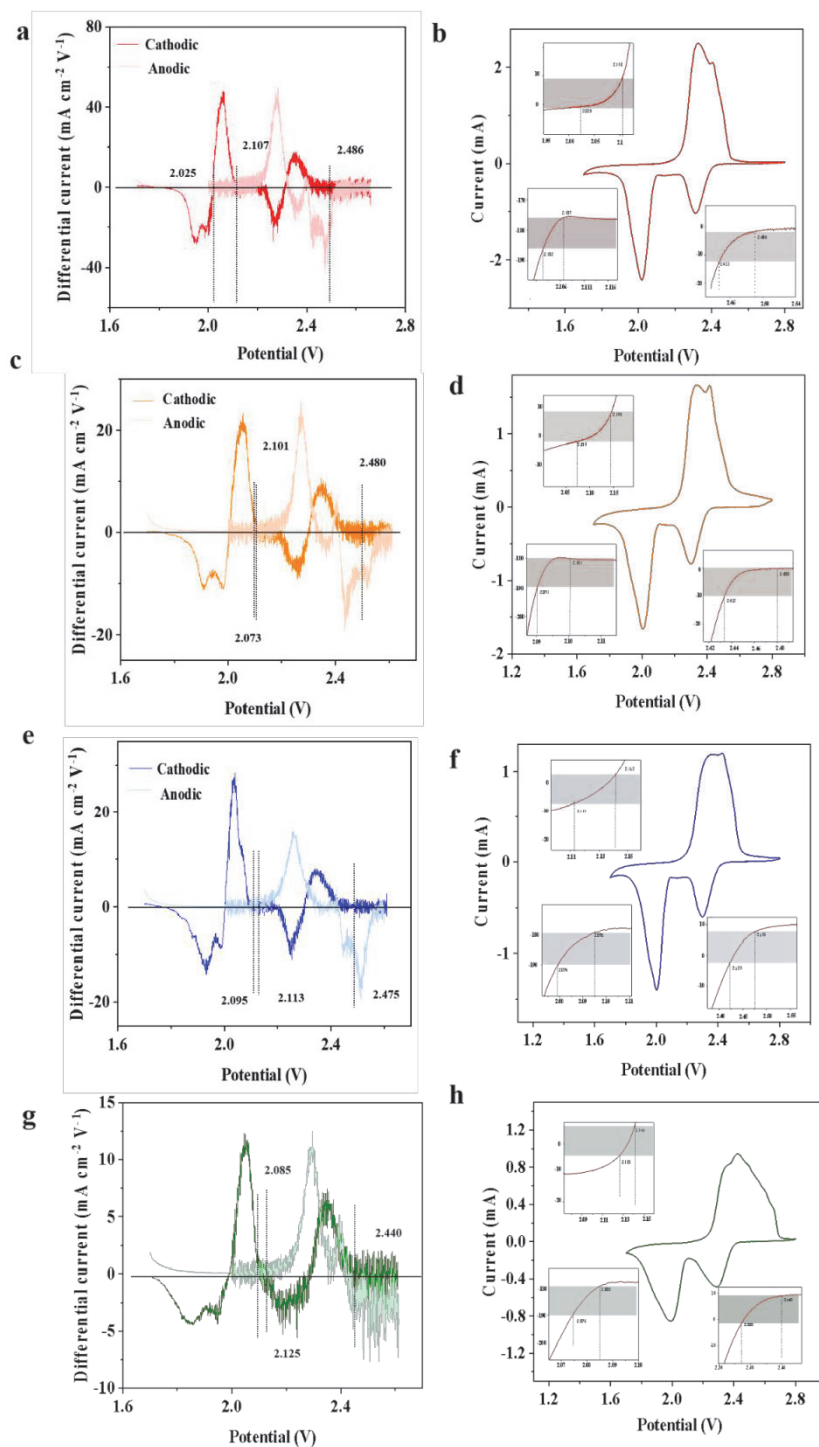


**Figure S19.** Onset potentials for Li-S redox reactions. (a, c, e and g) Differential CV curves of (a) v-ZnTe/CoTe<sub>2</sub>@NC/S, (c) ZnTe/CoTe<sub>2</sub>@NC/S, (e) CoTe<sub>2</sub>@NC/S and (g) ZnTe @NC/S. (b, d, f and h) CV curves and corresponding onset potentials of redox peaks A, C<sub>1</sub>, and C<sub>2</sub> (inset): (b) v-ZnTe/CoTe<sub>2</sub>@NC/S, (d) ZnTe/CoTe<sub>2</sub>@NC/S, (f) CoTe<sub>2</sub>@NC/S and (h) ZnTe@NC/S.

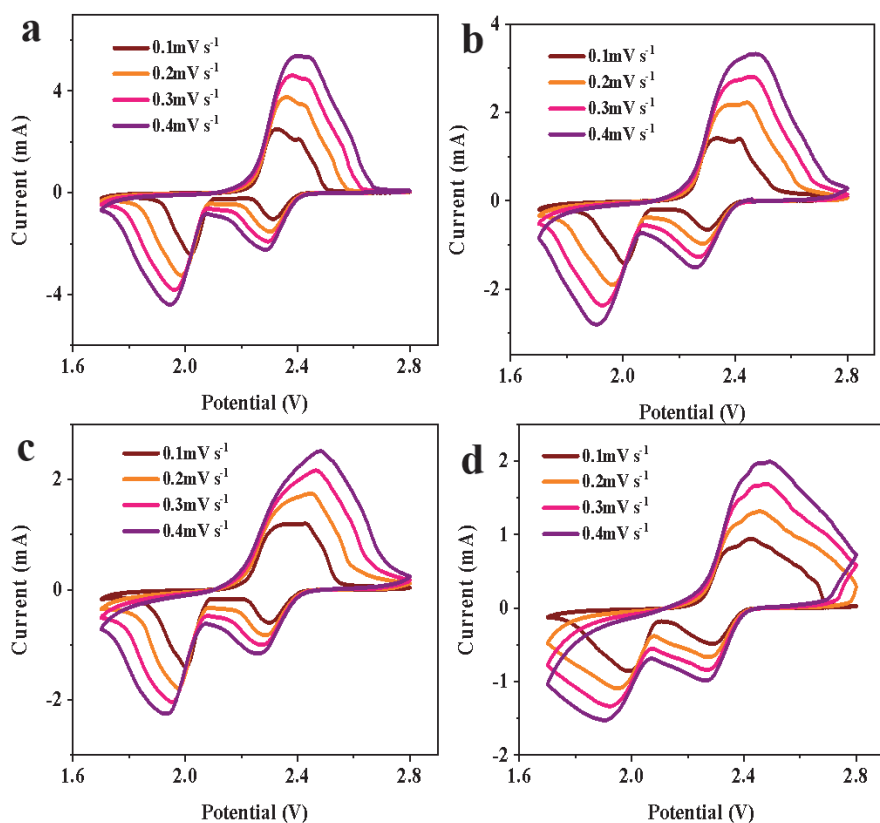


**Figure S20.** CV curves of cells based on v-ZnTe/CoTe<sub>2</sub>@NC/S, ZnTe/CoTe<sub>2</sub>@NC/S, CoTe<sub>2</sub>@NC/S, and ZnTe@NC/S electrodes at scan rates in the range 0.1 mV s<sup>-1</sup>-0.4 mV s<sup>-1</sup>.

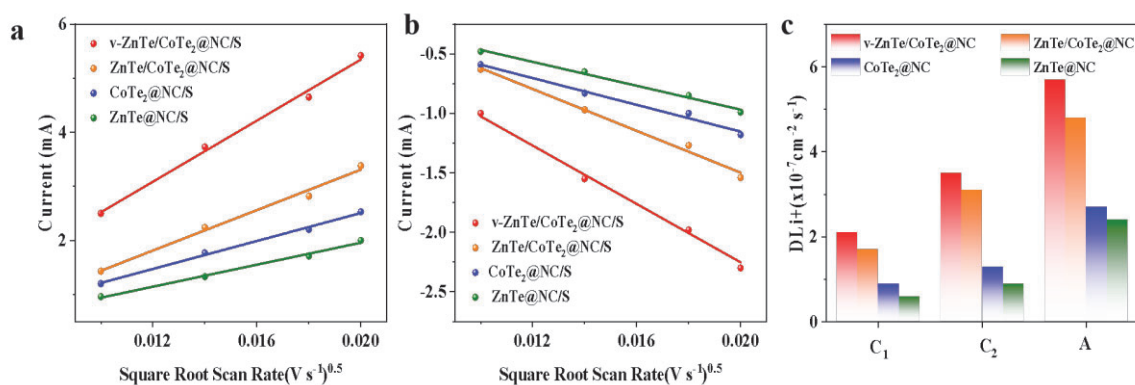


**Figure S21.** Peak current vs. square root of scan rate for different cathodes, v-ZnTe/CoTe<sub>2</sub>@NC/S, ZnTe/CoTe<sub>2</sub>@NC/S, CoTe<sub>2</sub>@NC/S and ZnTe@NC/S. a) A oxidation peak. b) C1 reduction peak. (c) Li<sup>+</sup> diffusion coefficient calculated from the CV redox peaks according to the Randles-Sevcik equation

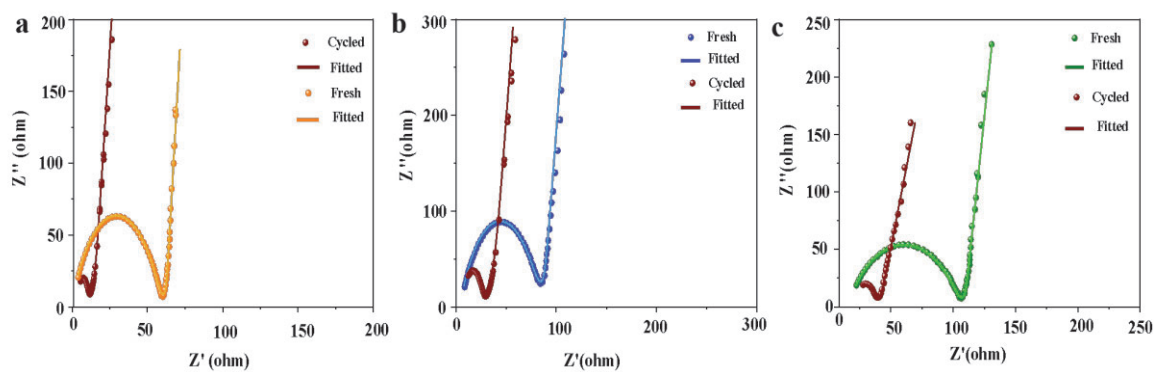


**Figure S22.** EIS spectra of (a) ZnTe/CoTe<sub>2</sub>@NC/S, (b) CoTe<sub>2</sub>@NC/S (c) ZnTe@NC/S coin cells before and after cycling.

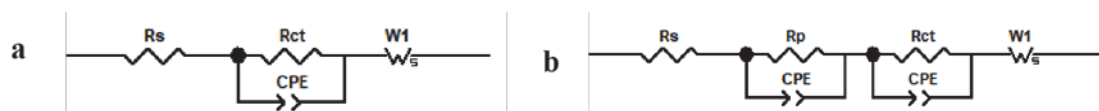


**Figure S23.** Equivalent circuits used to fit the EIS spectra of the assembled coin batteries before (a) and after (b) cycling

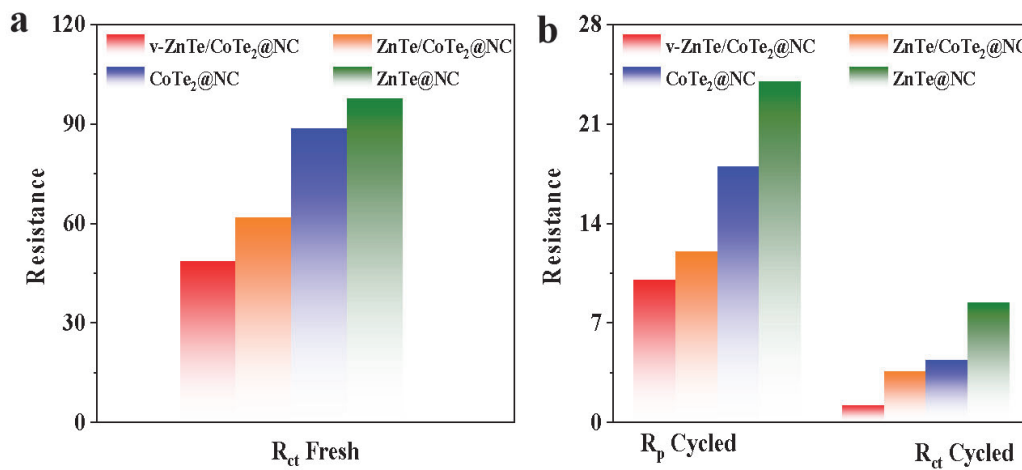


**Figure S24.** Resistances of the four coin cells as obtained from the fitting of the EIS spectra using the equivalent circuits.



**Figure S25.** Optical photographs of v-ZnTe/CoTe<sub>2</sub>@NC/S, ZnTe/CoTe<sub>2</sub>@NC/S, CoTe<sub>2</sub>@NC/S and ZnTe@NC/S electrodes and membranes after 100 cycles.

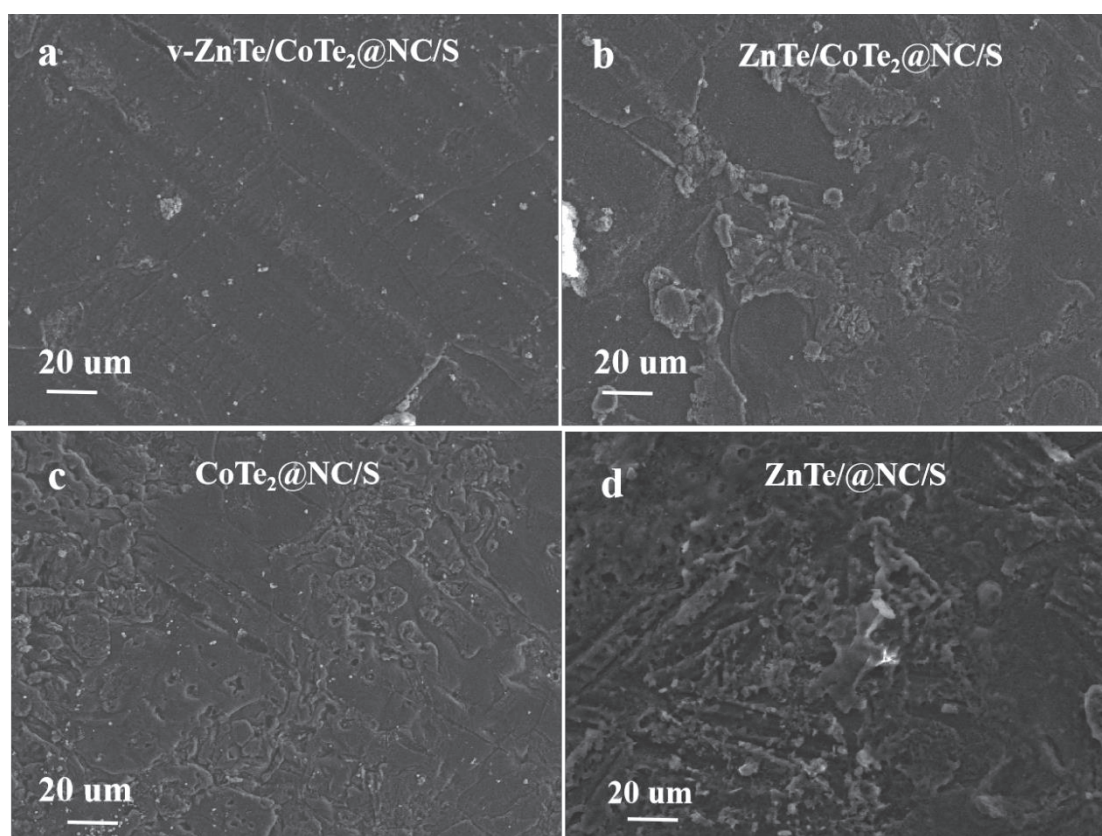


**Figure S26.** SEM images of the Li-anodes of the cycled cells based on v-ZnTe/CoTe<sub>2</sub>@NC/S (a), ZnTe/CoTe<sub>2</sub>@NC/S (b), CoTe<sub>2</sub>@NC/S (c), and ZnTe@NC/S (d) cathodes.

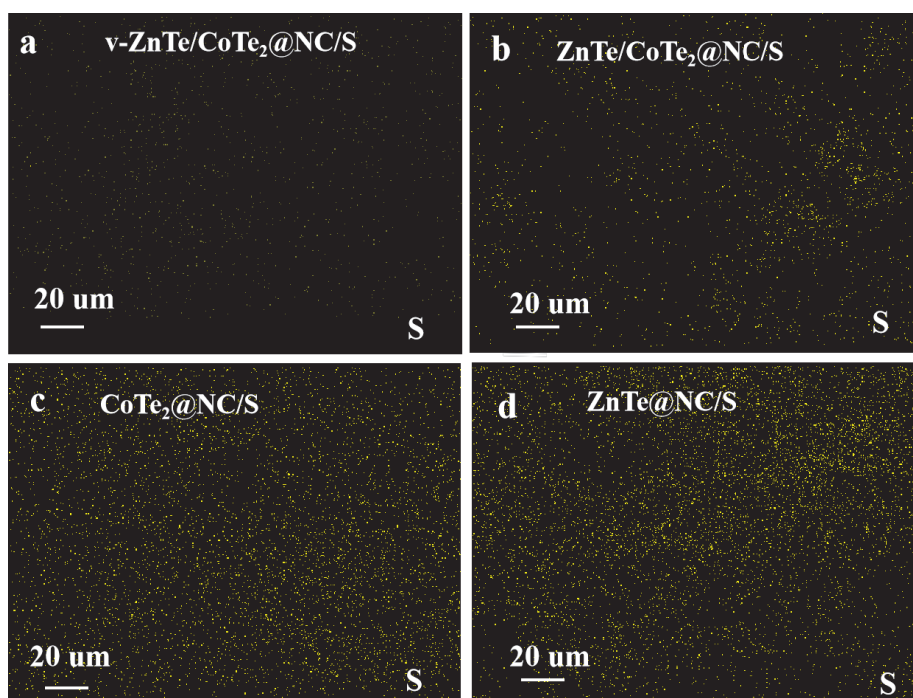


**Figure S27.** EDS mapping image of Li anode showing sulfur signal of the cycled cells based on v-ZnTe/CoTe<sub>2</sub>@NC/S (a), ZnTe/CoTe<sub>2</sub>@NC/S (b), CoTe<sub>2</sub>@NC/S (c), and ZnTe@NC/S (d) cathodes.

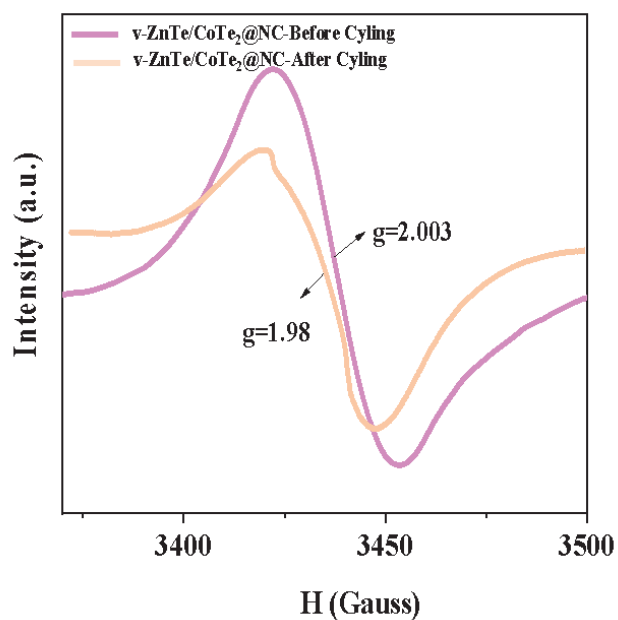


**Figure S28.** EPR spectrum of v-ZnTe/CoTe<sub>2</sub>@NC before and after cycling.

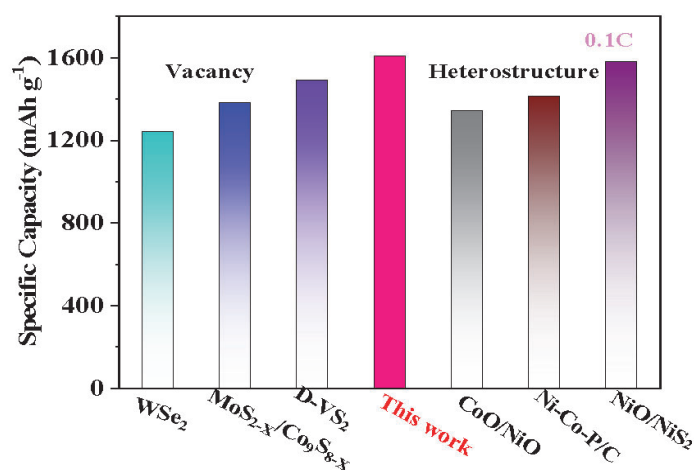


**Figure S29.** Comparison of the capacity obtained with the v-ZnTe/CoTe<sub>2</sub>@NC/S cathode with specific capacities of previously reported vacancy and heterostructure-based electrodes at a current density of 0.1C. References can be found in Table S3.

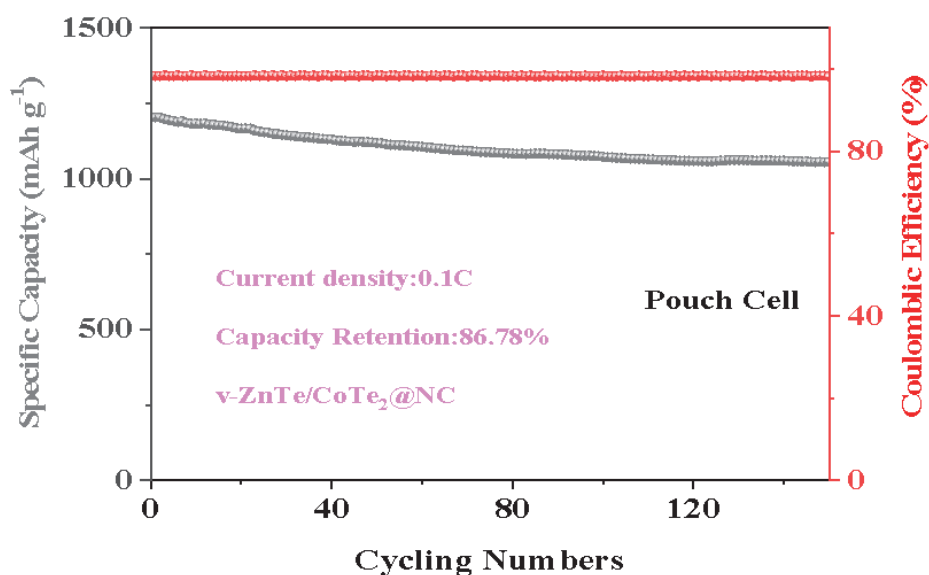


**Figure S30.** Cycle stability of a v-ZnTe/CoTe<sub>2</sub>@NC/S-based pouch cell at 0.1C. Loading: 5.6 mg cm<sup>-2</sup> and 11.2 mg L<sup>-1</sup> electrolyte.



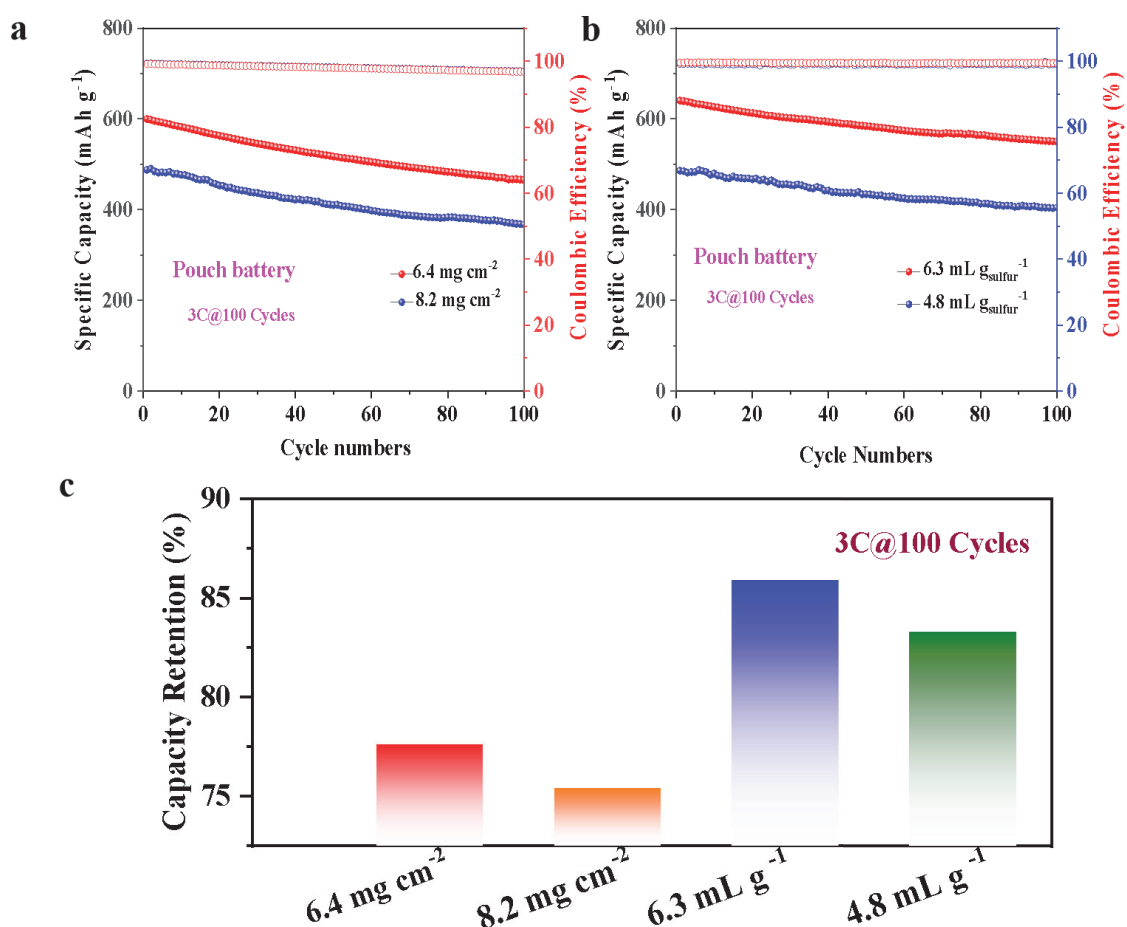


**Figure S31.** (a) Cycling stability of v-ZnTe/CoTe<sub>2</sub>@NC/S-based pouch batteries with different sulfur loading at 3C during 100 cycles. (b) Cycling stability of v-ZnTe/CoTe<sub>2</sub>@NC/S-based pouch batteries with different amounts of electrolyte at 3C during 100 cycles. (c) Capacity retention of the pouch cells under high loading and lean electrolyte.

**Table S1.** I<sub>D</sub>/I<sub>G</sub> value of v-ZnTe/CoTe<sub>2</sub>@NC, ZnTe/CoTe<sub>2</sub>@NC, CoTe<sub>2</sub>@NC, ZnTe @NC.

Sample	I <sub>D</sub> /I <sub>G</sub>
v-ZnTe/CoTe <sub>2</sub> @NC	0.92
ZnTe/CoTe <sub>2</sub> @NC	0.93
CoTe <sub>2</sub> @NC	0.94

ZnTe@NC	0.95
---------	------

**Table S2.** Comparison of the specific capacitance at a current density of 0.1C of v-ZnTe/CoTe<sub>2</sub>@NC/S, ZnTe/CoTe<sub>2</sub>@NC/S, CoTe<sub>2</sub>@NC/S and ZnTe@NC/S.

Sample	Specific capacity (mAh g <sup>-1</sup> )
v-ZnTe/CoTe <sub>2</sub> @NC/S	1608
ZnTe/CoTe <sub>2</sub> @NC/S	1290
CoTe <sub>2</sub> @NC/S	1105
ZnTe/@NC/S	1005

**Table S3.** Electrochemical performance comparisons of v-ZnTe/CoTe<sub>2</sub>@NC/S with similar materials reported previously.

Sample	Specific capacitance (mAh /g)	Current Density (C)	Ref.
WSe <sub>1.5</sub> [1]	1241.5	0.1	[1]
MoS <sub>2-X</sub> /Co <sub>9</sub> S <sub>8-X</sub> [2]	1382.5	0.1	[2]
D-VS <sub>2</sub> [3]	1492.2	0.1	[3]
CoO/NiO [4]	1343	0.1	[4]
Ni-Co-P/C [5]	1412.6	0.1	[5]
NiO/NiS <sub>2</sub> [6]	1580	0.1	[6]
v-ZnTe/CoTe <sub>2</sub> @NC	1608	0.1	This work



**Table S4** Energy density comparison of different electrodes.

Sample	Specific capacitance (mAh /g)	S loading (mg cm <sup>-2</sup> )	Energy density (Wh kg <sup>-1</sup> )	Ref.
Co <sub>3</sub> Se <sub>4</sub> @NC/S <sup>[2]</sup>	1438	1.5	901	[7]
WSe <sub>1.5</sub> /S <sup>[3]</sup>	1241.5	1.5	869	[1]
Co <sub>9</sub> S <sub>8</sub> /MWCNTs/S <sup>[4]</sup>	1154	1.5	832	[8]
LDH/Co <sub>9</sub> S <sub>8</sub> /S <sup>[5]</sup>	1339	1.5	1070	[9]
v-ZnTe/CoTe <sub>2</sub> @NC/S	1608	1.5	1115	This work

## References

- [1] H.-J. Li, K. Xi, W. Wang, S. Liu, G.-R. Li, X.-P. Gao, *Energy Storage Mater.* **2022**, 45, 1229.
- [2] H. Song, T. Li, T. He, Z. Wang, D. Fang, Y. Wang, X. L. Li, D. Zhang, J. Hu, S. Huang, *Chem. Eng. J.* **2022**, 450, 138115.
- [3] G. Liu, Q. Zeng, Z. Fan, S. Tian, X. Li, X. Lv, W. Zhang, K. Tao, E. Xie, Z. Zhang, *Chem. Eng. J.* **2022**, 448, 137683.
- [4] L. Wu, J. Hu, X. Yang, Z. Liang, S. Chen, L. Liu, H. Hou, J. Yang, *J. Mater. Chem. A* **2022**, 10, 23811.
- [5] Z. Wu, S. Chen, L. Wang, Q. Deng, Z. Zeng, J. Wang, S. Deng, *Energy Stor. Mater.* **2021**, 38, 381.
- [6] C. Jin, P. Zhai, J. Tang, L. Huo, Q. He, Y. Ye, L. Qiu, K. Jiang, L. Shang, Y. Li, Y. Gong, Z. Hu, J. Chu, *Energy Environ. Mater.* **2022**, n/a, e12491.
- [7] D. Cai, B. Liu, D. Zhu, D. Chen, M. Lu, J. Cao, Y. Wang, W. Huang, Y. Shao, H. Tu, W. Han, *Adv. Energy Mater.* **2020**, 10, 1904273.
- [8] S. Zhao, X. Tian, Y. Zhou, B. Ma, A. Natarajan, *J. Energy Chem.* **2020**, 46, 22.
- [9] S. Chen, J. Luo, N. Li, X. Han, J. Wang, Q. Deng, Z. Zeng, S. Deng, *Energy Stor. Mater.* **2020**, 30, 187.

# **Chapter 5**

## **Electronic Spin Alignment within Homologous NiS<sub>2</sub>/NiSe<sub>2</sub> Heterostructures to Promote Sulfur Redox Kinetics in Lithium-Sulfur Batteries**

## 5. Electronic Spin Alignment within Homologous NiS<sub>2</sub>/NiSe<sub>2</sub> Heterostructures to Promote Sulfur Redox Kinetics in Lithium-Sulfur Batteries

### Key Findings

1. A homogeneous heterostructure composed of NiS<sub>2</sub>/NiSe<sub>2</sub> was successfully synthesized using a Ni-MOF precursor, exhibiting uniform morphology and strong structural integration.
2. The NiS<sub>2</sub>/NiSe<sub>2</sub> heterostructure facilitated spin splitting of the Ni<sup>3+</sup> 3d orbitals, inducing a low-spin to high-spin state transition that increased the number of unpaired electrons and activated the electronic structure.
3. Enhanced electron transfer and optimized polysulfide adsorption energy were observed in the heterostructure, which significantly lowered the energy barrier for polysulfide redox conversion.
4. The NiS<sub>2</sub>/NiSe<sub>2</sub>@NC/S cathode delivered excellent electrochemical performance in Li-S batteries, including a high initial capacity of 1458 mAh g<sup>-1</sup> at 0.1C, superior rate capability (572 mAh g<sup>-1</sup> at 5C), and long-term cycling stability with only 0.025% capacity decay per cycle over 500 cycles at 1C. Even at a high sulfur loading of 6.2 mg cm<sup>-2</sup>, a capacity of 1058 mAh g<sup>-1</sup> was retained after 300 cycles.

### Introduction

The performance limitations of LSBs are largely attributed to sulfur's inherent electrical insulation, the dissolution and migration of LiPSs, and significant volumetric changes during cycling. To mitigate these challenges, the design of advanced sulfur host materials with high conductivity, strong chemical adsorption, and catalytic capability is essential.

Transition metal chalcogenides, particularly sulfides and selenides, have attracted attention for their exceptional electronic properties, electrocatalytic activity, and ability to interact chemically with LiPSs. Among them, nickel-based compounds, such as NiS<sub>2</sub> and NiSe<sub>2</sub>, show promise due to their conductive nature and catalytic potential.

## Purpose and Background

This chapter explores the use of a homogeneous heterostructure composed of NiS<sub>2</sub> and NiSe<sub>2</sub> as a sulfur host material. While previous studies primarily focused on heterogeneous systems involving different metal elements, we hypothesized that combining different anions (S and Se) with the same metal cation (Ni) could achieve strong lattice compatibility and introduce favorable electronic modulation.

The motivation for selecting this system includes:

Enhanced conductivity: Transition metal sulfides/selenides improve charge transport.

Strong LiPSs adsorption: Polar surfaces form chemical interactions with LiPSs, reducing their mobility and mitigating the shuttle effect.

Catalytic activity: These materials can catalyze the redox conversion of sulfur species, accelerating reaction kinetics.

Structural stability: Their rigid frameworks help buffer volume changes and improve long-term mechanical stability.

### Study Design and Experimental Methods

We designed a synthesis route starting with Ni-based MOFs as precursors. The procedure involved:

Synthesis of Ni-MOF: Prepared via solvothermal reaction using ethanol, trimesic acid (H<sub>3</sub>BTC), Ni(NO<sub>3</sub>)<sub>2</sub>·6H<sub>2</sub>O, and PVP.

Formation of Ni/NC: The Ni-MOF was annealed at 500 °C under an Ar atmosphere, reducing Ni<sup>2+</sup> to metallic Ni while converting organic ligands into NC.

Heterostructure generation: Equal masses of elemental sulfur and selenium were introduced to obtain the NiS<sub>2</sub>/NiSe<sub>2</sub>@NC composite via sulfurization and selenization.

Sulfur loading: Sulfur was incorporated through melt-infiltration to yield the final NiS<sub>2</sub>/NiSe<sub>2</sub>@NC/S cathode.

Magnetic and EPR characterizations were conducted to probe the electronic state transitions and spin configuration in the heterostructure.

## Results and Discussion

### Structural and Electronic Properties

The NiS<sub>2</sub>/NiSe<sub>2</sub> composite formed a homogeneous heterostructure with hollow morphology, ensuring a high surface area and efficient polysulfide interaction. Magnetic characterization indicated stronger magnetic behavior compared to NiS<sub>2</sub> and NiSe<sub>2</sub> alone. EPR results showed more unpaired electrons in NiS<sub>2</sub>/NiSe<sub>2</sub>@NC, confirming enhanced spin state activity.

The transition from low-spin to high-spin  $\text{Ni}^{3+}$  states led to an increased density of active sites and improved catalytic performance, facilitating better electron transport and lower overpotential for polysulfide conversion.

#### Electrochemical Performance

At 0.1C, the initial capacity reached  $1458 \text{ mAh g}^{-1}$ , showcasing high sulfur utilization. At high rates (5C), the cathode still delivered  $572 \text{ mAh g}^{-1}$ , indicating excellent rate capability.

Over 500 cycles at 1C, the capacity fade rate remained low at 0.025% per cycle, illustrating outstanding durability.

Under a high sulfur loading of  $6.2 \text{ mg cm}^{-2}$ , the material achieved a practical areal capacity of  $7.27 \text{ mAh cm}^{-2}$ , retaining  $1058 \text{ mAh g}^{-1}$  after 300 cycles.

These results validate that the homogeneous heterostructure effectively balances conductivity, catalytic activity, and mechanical stability.

#### Conclusion

The design of a  $\text{NiS}_2/\text{NiSe}_2$  homogeneous heterostructure based on MOF-derived synthesis offers a highly effective approach for enhancing the electrochemical performance of LSBs. The synergistic effects of spin-state modulation, improved electronic structure, and stable architecture contribute to both high capacity and long-term cycling stability. This study further supports the potential of tailored anion engineering in developing next-generation sulfur host materials.

# Electronic Spin Alignment within Homologous NiS<sub>2</sub>/NiSe<sub>2</sub> Heterostructures to Promote Sulfur Redox Kinetics in Lithium-Sulfur Batteries

Chen Huang, Jing Yu, Chao Yue Zhang,\* Zhibiao Cui, Jiakun Chen, Wei-Hong Lai, Yao-Jie Lei,\* Bingfei Nan, Xuan Lu, Ren He, Li Gong, Junshan Li, Canhuang Li, Xuede Qi, Qian Xue, Jin Yuan Zhou, Xueqiang Qi, Lluís Balcells, Jordi Arbiol, and Andreu Cabot\*

The catalytic activation of the Li-S reaction is fundamental to maximize the capacity and stability of Li-S batteries (LSBs). Current research on Li-S catalysts mainly focuses on optimizing the energy levels to promote adsorption and catalytic conversion, while frequently overlooking the electronic spin state influence on charge transfer and orbital interactions. Here, hollow NiS<sub>2</sub>/NiSe<sub>2</sub> heterostructures encapsulated in a nitrogen-doped carbon matrix (NiS<sub>2</sub>/NiSe<sub>2</sub>@NC) are synthesized and used as a catalytic additive in sulfur cathodes. The NiS<sub>2</sub>/NiSe<sub>2</sub> heterostructure promotes the spin splitting of the 3d orbital, driving the Ni<sup>3+</sup> transformation from low to high spin. This high spin configuration raises the electronic energy level and activates the electronic state. This accelerates the charge transfer and optimizes the adsorption energy, lowering the reaction energy barrier of the polysulfides conversion. Benefiting from these characteristics, LSBs based on NiS<sub>2</sub>/NiSe<sub>2</sub>@NC/S cathodes exhibit high initial capacity (1458 mAh·g<sup>-1</sup> at 0.1C), excellent rate capability (572 mAh·g<sup>-1</sup> at 5C), and stable cycling with an average capacity decay rate of only 0.025% per cycle at 1C during 500 cycles. Even at high sulfur loadings (6.2 mg·cm<sup>-2</sup>), high initial capacities of 1173 mAh·g<sup>-1</sup> (7.27 mAh·cm<sup>-2</sup>) are measured at 0.1C, and 1058 mAh·g<sup>-1</sup> is retained after 300 cycles.

## 1. Introduction

Lithium-sulfur batteries (LSBs) hold great potential for the development of future energy storage systems for mobility and stationary applications due to their high energy density and abundant sulfur resources. However, their commercialization is currently hampered by several challenges, including<sup>[1]</sup>: 1) the migration of lithium polysulfides (LiPSs) that progressively reduce the amount of cathode active material while decreasing the electrolyte ion mobility and degrading the anode surface; 2) a poor conductivity of sulfur and lithium sulfides (Li<sub>2</sub>S<sub>2</sub>/Li<sub>2</sub>S), which increase the system internal resistance and limits active material utilization, particularly at high sulfur loadings; 3) slow Li-S redox reaction kinetics that limits the rate performance and also the amount of active material participating in each cycle; and 4) the severe volume changes during charge/discharge that reduce the LSB cycling stability.<sup>[2]</sup>

C. Huang, J. Yu, B. Nan, X. Lu, R. He, L. Gong, C. Li, A. Cabot  
Catalonia Institute for Energy Research-IREC  
Sant Adrià de Besòs  
Barcelona 08930, Spain  
E-mail: [acabot@irec.cat](mailto:acabot@irec.cat)  
C. Huang, L. Gong, C. Li  
Department of Chemistry  
University of Barcelona  
Barcelona 08028, Spain  
J. Yu, J. Arbiol  
Catalan Institute of Nanoscience and Nanotechnology (ICN2)  
CSIC and BIST  
Campus UAB  
Bellaterra  
Barcelona, Catalonia 08193, Spain

C. Y. Zhang, J. Y. Zhou  
Key Laboratory for Magnetism and Magnetic Materials of the Ministry of Education & School of Physical Science & Technology  
Lanzhou University  
Lanzhou 730000, China  
E-mail: [zhangchy2020@lzu.edu.cn](mailto:zhangchy2020@lzu.edu.cn)  
Z. Cui  
School of Chemistry  
South China Normal University  
Guangzhou 510006, P. R. China  
J. Chen  
Analysis and Testing Center  
South China Normal University  
Guangzhou 510006, China

The ORCID identification number(s) for the author(s) of this article can be found under <https://doi.org/10.1002/adma.202400810>

DOI: 10.1002/adma.202400810

Various strategies have been proposed to address these limitations, including the use of multifunctional separators<sup>[3]</sup> and particularly the incorporation of host materials and additives within the sulfur cathode.<sup>[4]</sup>

High surface area and porous carbon materials are fundamental as sulfur hosts in LSB cathodes, contributing to the physical trapping of the LiPSs, the damping of the volume changes, and especially to facilitate charge transport within the electrode.<sup>[5]</sup> However, the weak chemical interaction between the nonpolar carbon surface and polar polysulfides falls short of completely inhibiting the migration of LiPS, posing a challenge in achieving stable long-term cycling.<sup>[6]</sup> Such carbon hosts are also inefficient in accelerating the Li-S redox reaction.

Polar inorganic additives can be used to promote LiPS trapping and catalyze the Li-S reaction. Among the vast array of potential catalysts, nickel-based compounds stand out due to their exceptional performance, even at low doses, which stems from nickel's notable high activity and versatility.<sup>[7]</sup> Nickel is also the fifth most abundant element on Earth, which results in a moderate cost, four orders of magnitude lower than that of platinum-group metals. Ni also offers additional oxidation states over Pt and Pd, which allows both to catalyze single electron reactions and form more diverse catalytic phases. In this direction, the redox  $\text{Ni}^{2+}/\text{Ni}^{3+}$  shows particularly high activity compared to other metal-based compounds. Besides, nickel facilitates hemolytic bond cleavage, has a strong affinity to unsaturated systems and coordination of multiple bonds, and is highly nucleophilic on account of its relatively small size, which makes it a privileged reagent for cross-coupling. On top of this, nickel shows notable electrical conductivity and resistance to bulk oxidation, which allows it to maintain good electrical conductivity under operation conditions.

Compared with oxides, chalcogenides show a lower energy gap between the bonding and antibonding orbitals, which is regulated by the chalcogen P-band.<sup>[8]</sup> At the same time, the reduced electronegativity difference between the metal and the chalcogen decreases the electron-pull effect leading to an increase in the en-

ergy of the bonding state that can enhance the interfacial  $\text{S}_6^{2-}/\text{S}^{2-}$  redox kinetics.<sup>[9]</sup>

Based on the above advantages, Ni-based chalcogenides exhibit great potential as catalytic additive to activate the Li-S reaction in LSB cathodes. In this direction, nickel sulfide displays particularly high polysulfide adsorption capability,<sup>[10]</sup> but its moderate electrical conductivity limits the electrode performance and thus calls for an additional phase. In this regard, several heterostructured systems have been demonstrated effective in regulating the surface state of electrode materials, potentially improving both charge transport and transfer, e.g.  $\text{NiS}_2/\text{WS}_2$ ,<sup>[11]</sup>  $\text{NiS}_2/\text{ZnS}$ ,<sup>[12]</sup>  $\text{MoS}_2/\text{NiS}_2$ ,<sup>[13]</sup> and  $\text{MnS}/\text{NiS}_2/\text{MoS}_2$ .<sup>[14]</sup> However, most previous works had focused on composites comprised of different metals, a strategy that unfortunately tends to limit both the performance and especially the stability of the resultant materials. This limitation arises from the introduction of defects, which detrimentally impact the charge transport. Furthermore, these defects and stresses can adversely affect the structural and mechanical integrity of the material, leading to a progressive performance deterioration.

Both  $\text{NiS}_2$  and  $\text{NiSe}_2$  exhibit a pyrite structure wherein  $\text{Ni}^{2+}$  ions are surrounded by six  $\text{X}_2^{2-}$  units. Despite this structural similarity, they display distinct d-electron configurations. This difference endows  $\text{NiSe}_2$  with superior electrical conductivity, attributed to its more favorable electron mobility. In contrast,  $\text{NiS}_2$  is characterized by a faster charge transfer capability.<sup>[15]</sup> These contrasting electronic properties can be synergistically integrated within homologous composites. In this direction, the versatility of nickel chalcogenides emerges as particularly advantageous. This is primarily due to the flexible valence states exhibited by nickel and the ability of chalcogenides to concatenate. As a result, it becomes feasible to engineer materials encompassing a variety of Ni/chalcogen ratios. This compositional flexibility allows for the fine-tuning of the electrochemical properties of these composites, enabling tailored optimization to meet specific performance criteria in various electrochemical applications.

While extensive research has focused on the relationship between electronic energy levels and catalytic properties, the role of electron spins in this dynamic has often been overlooked. Investigating the role of spin states of electrons, particularly in transition metal catalysts, could reveal new insights into reaction mechanisms. Furthermore, understanding spin-related phenomena could lead to the development of novel catalytic materials designed with spin considerations in mind, potentially opening new pathways in green chemistry and sustainable energy solutions. Indeed, the spin state configuration of 3d transition metals is a key factor influencing the catalyst's electronic structure and determining its orbital occupation, activity, and selectivity.<sup>[16]</sup> This spin state can be effectively adjusted through external or internal magnetic fields, the use of ligands, or stresses.<sup>[16g,17]</sup> As an example, we recently reported that transition Co atoms experienced a spin transformation from low spin to high spin under an external magnetic field, thereby generating more unpaired electrons to promote charge transfer within LSBs.<sup>[17c]</sup> Also within the framework of LSBs, Li et al. revealed improved catalytic activity of bimetallic phosphorus sulfides associated with their composition-determined spin state.<sup>[18]</sup>

An innovative and effective approach for manipulating the spin state of materials involves the utilization of heterointerfaces.

W.-H. Lai, Y.-J. Lei  
Institute for Superconducting and Electronic Materials  
Australian Institute of Innovative Materials  
Innovation Campus  
University of Wollongong  
Wollongong, NSW 2500, Australia  
E-mail: yl876@uowmail.edu.au

J. Li  
Institute for Advanced Study  
Chengdu University  
Chengdu 610106, China

X. Qi, Q. Xue, X. Qi  
College of Chemistry and Chemical Engineering  
Chongqing University of Technology  
Chongqing 400054, China

L. Balcells  
Institut de Ciència de Materials de Barcelona  
Campus de la UAB  
Bellaterra, Catalonia 08193, Spain

J. Arbiol, A. Cabot  
ICREA Pg. Lluís Companys  
Barcelona, Catalonia 08010, Spain



The interface of semiconductor heterostructures is characterized by a charge redistribution that results in an internal electric field and an electronic band bending.<sup>[19]</sup> This is linked to a rise in the energy level of the 3d orbitals, thereby altering the metal-LiPS adsorption strength. In addition, the heterostructure can split the metal central orbital, thereby changing the electronic configuration from a low-spin state to a high-spin state. This transition can produce more unpaired electrons and active electronic states in the 3d orbital. This strategy offers an excellent opportunity to design catalysts with optimized catalytic performances, properly defining their spin state by combining two dissimilar materials. Despite the potential of heterointerfaces to tune spin states and particularly their role in catalytic performance, few studies have been reported in this direction, and all in the paradigmatic case of the oxygen evolution reaction.<sup>[20]</sup>

Beyond composition, the structural architecture of the sulfur host material also plays a fundamental role in determining the LSB cathode electrochemical performance. A proper three-dimensional (3D) organization of the different components is essential to maximize the cathode performance, especially with the challenging high sulfur loadings. Hollow materials are particularly effective in alleviating volume changes during cycling while at the same time providing high surface areas, which makes them widely used in the fields of Li-ion batteries,<sup>[21]</sup> supercapacitors,<sup>[22]</sup> and electrocatalysis.<sup>[23]</sup> The internal volume of hollow structures and their large surfaces also allow the loading of large amounts of sulfur.<sup>[24]</sup> Besides, hollow sulfur hosts can physically lock polysulfides, thus reducing their migration.<sup>[25]</sup>

Taking into account all these considerations, herein, hollow homologous heterostructure  $\text{NiS}_2/\text{NiSe}_2@\text{NC}$  particles are synthesized using a Ni-based metal-organic framework (MOF) as a sacrificial template. The electronic structure and spin state of the developed material are thoroughly characterized both experimentally and using density functional theory (DFT) calculations.  $\text{NiS}_2/\text{NiSe}_2@\text{NC}$  is used as the sulfur host to assemble coin- and pouch-type LSBs, whose performance is extensively tested even under high sulfur loading ( $6.2 \text{ mg cm}^{-2}$ ) and lean electrolyte conditions.

## 2. Results and Discussions

**Figure 1a** illustrates the synthesis of the  $\text{NiS}_2/\text{NiSe}_2@\text{NC}/\text{S}$  cathode material. The synthesis details can be found in the Experimental section within the Supporting Information (SI). Briefly, to produce  $\text{NiS}_2/\text{NiSe}_2@\text{NC}$ , first Ni-based hollow precursors (Ni-MOF) were prepared by a solvothermal method using ethanol as solvent, trimesic acid ( $\text{H}_3\text{BTC}$ ) as organic ligands, nickel (II) nitrate as the metal source and polyvinylpyrrolidone (PVP) as a stabilizer.<sup>[26]</sup> Subsequently, the Ni-MOF was heated to  $500^\circ\text{C}$  under an Ar atmosphere to reduce the  $\text{Ni}^{2+}$  to metallic nickel and carbonize the organic ligands into nitrogen-doped carbon.<sup>[27]</sup> The obtained Ni/NC was then simultaneously sulfurized and selenized, using equal mass amounts of S and Se, to form the  $\text{NiS}_2/\text{NiSe}_2@\text{NC}$  composite. Finally,  $\text{NiS}_2/\text{NiSe}_2@\text{NC}/\text{S}$  was produced by introducing S through a melt-infiltration process.

Scanning electron microscopy (SEM) analysis revealed that the precursor Ni-MOF is comprised of  $\approx 2 \mu\text{m}$  spherical particles characterized by their smooth surfaces and a hollow internal structure (Figure S1a, Supporting Information). The hollow

nature of these particles was inferred from the incidental observation of a small number of particles that had fortuitously broken, thereby providing a glimpse into their internal structure. To elucidate the formation mechanism of the hollow structure, the particle evolution during the solvothermal reaction process was examined. Transmission electron microscopy (TEM) images show how the structure of Ni-MOF particles gradually evolves from a solid porous sphere to a partially hollow structure with a crystalline shell, and eventually a fully hollow and crystalline structure (Figure S2, Supporting Information). We associate this evolution with the onset of the Ni-MOF crystallization at the solid-liquid interface of preformed, low-density, amorphous Ni-based particles.<sup>[28]</sup> As the crystallization proceeds, the denser crystalline shell grows at the expense of the low-density amorphous precursor within the particle's core. The organization of the material into a denser shell results in a void inside the particles.

After carbonization, the obtained  $\text{Ni}@\text{NC}$  particles maintained the spherical and hollow architecture, but they significantly shrank to an average diameter of  $\approx 500 \text{ nm}$ , due to the decomposition of the organic ligands (Figure S1b, Supporting Information). After sulfuration and selenization,  $\text{NiS}_2/\text{NiSe}_2@\text{NC}$  retains the  $\text{Ni}@\text{NC}$  hollow morphology and size (Figure 1b). Energy-dispersive X-ray (EDX) spectroscopy combined with SEM imaging and electron energy loss spectroscopy (EELS) combined with high-angle annular dark field (HAADF) scanning transmission electron microscopy (STEM) show the different elements to be homogeneously distributed within the  $\text{NiS}_2/\text{NiSe}_2@\text{NC}$  composite at the  $100 \text{ nm}$  scale (Figure 1c,d). EDX spectra showed the  $\text{NiS}_2/\text{NiSe}_2@\text{NC}$  atomic elemental ratio to be  $\text{Ni/S/Se/N} = 28/50/19/3$  (Figure S3, Supporting Information). High-resolution TEM (HRTEM) characterization of  $\text{NiS}_2/\text{NiSe}_2@\text{NC}$  shows the  $\text{NiS}_2/\text{NiSe}_2@\text{NC}$  particles to be polycrystalline, formed by  $\approx 20 \text{ nm}$  crystallites of both the  $\text{NiS}_2$  and  $\text{NiSe}_2$  phases (Figure 1e).

Additional  $\text{NiSe}_2@\text{NC}$  and  $\text{NiS}_2@\text{NC}$  reference samples were produced by just selenizing or sulfurizing the Ni/NC (see details in the SI). EDX compositional maps of these reference samples also show a homogeneous distribution of the different elements at the  $100 \text{ nm}$  scale (Figures S4 and S5, Supporting Information).

**Figure 2a** shows the X-ray diffraction (XRD) patterns of  $\text{NiS}_2/\text{NiSe}_2@\text{NC}$ ,  $\text{NiSe}_2@\text{NC}$  and  $\text{NiS}_2@\text{NC}$ . The diffraction peaks at  $31^\circ$ ,  $34.7^\circ$ ,  $38.0^\circ$ ,  $44.3^\circ$ , and  $52.6^\circ$ , are attributed to (200), (210), (211), (220), and (311) planes of  $\text{NiS}_2$  (PDF #89-3058). The diffraction peaks at  $30.4^\circ$ ,  $34.1^\circ$ ,  $37.4^\circ$ ,  $43.5^\circ$ , and  $51.5^\circ$  are assigned to the (200), (210), (211), (220), and (311) planes of  $\text{NiSe}_2$  (PDF #88-1711). XRD data confirms the presence of both phases, as observed by HRTEM imaging, but shows the amount of  $\text{NiS}_2$  phase to be notably higher than that of  $\text{NiSe}_2$ . Using the Scherrer equation (Figure S6a, Supporting Information), the size of the crystallites was estimated at  $\approx 20 \text{ nm}$ , which is consistent with HRTEM results. Compared with  $\text{NiS}_2@\text{NC}$ , the peaks corresponding to the  $\text{NiS}_2$  phase in the  $\text{NiS}_2/\text{NiSe}_2@\text{NC}$  XRD pattern are slightly shifted to lower angles (Figure S6b, Supporting Information). At the same time, compared with  $\text{NiSe}_2@\text{NC}$ , the peaks corresponding to the  $\text{NiSe}_2$  phase in the  $\text{NiS}_2/\text{NiSe}_2@\text{NC}$  XRD pattern are slightly shifted to higher angles. These shifts are consistent with the different ionic radii of Se and S and denote a substantial Se and S doping within the  $\text{NiS}_2$  and  $\text{NiSe}_2$  lattices, respectively. Using Vegard's law (Figure S6c, Supporting

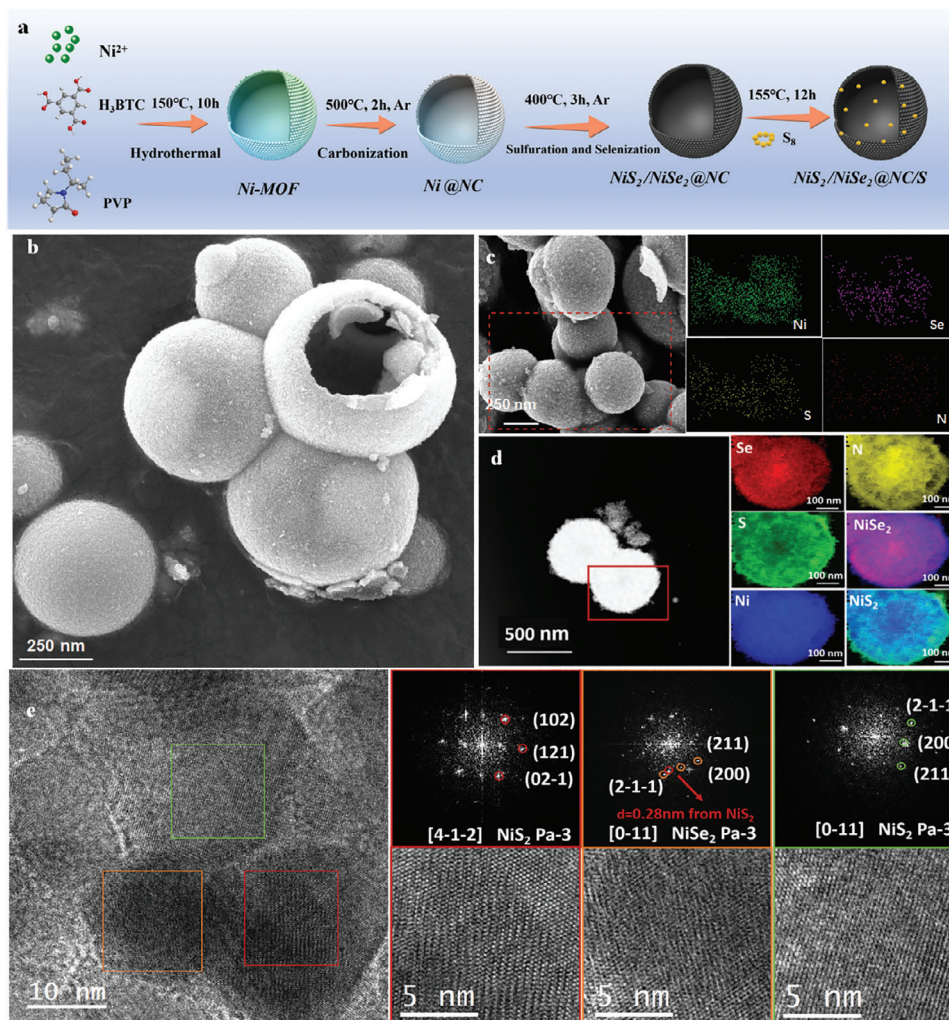


**Figure 1.** a) Schematic diagram of the synthesis of the  $\text{NiS}_2/\text{NiSe}_2@\text{NC}/\text{S}$  cathode material. b) SEM image of  $\text{NiS}_2/\text{NiSe}_2@\text{NC}$ . c) SEM image and SEM-EDX compositional map of  $\text{NiS}_2/\text{NiSe}_2@\text{NC}$ . d) HAADF-STEM image and STEM-EELS composition maps of  $\text{NiS}_2/\text{NiSe}_2@\text{NC}$ . e) HRTEM micrographs from the  $\text{NiS}_2/\text{NiSe}_2@\text{NC}$  sample and the corresponding power spectra. The lattice fringes visualized in the red squared magnified detail correspond to the (102), (121), and (02-1) crystal planes of  $\text{NiS}_2$  visualized along the [4-1-2] zone axis. The lattice spacings shown in the orange squared detail correspond to the (211), (200), and (2-1-1) crystal planes of  $\text{NiSe}_2$  visualized along its [0-11] zone axis. Besides, the lattice fringes visualized in the green squared magnified detail correspond to the (2-1-1), (200), and (211) crystal planes of  $\text{NiS}_2$  visualized along the [0-11] zone axis.

Information), we estimated  $\approx 17\%$  of S in  $\text{NiSe}_2$  and  $\approx 21\%$  Se in  $\text{NiS}_2$  within the  $\text{NiS}_2/\text{NiSe}_2@\text{NC}$ .

The XRD pattern of carbon is not observed due to the good crystallinity of the Ni chalcogenides. Thus, the degree of carbon graphitization was measured using Raman spectroscopy. The Raman peaks centered at  $1350\text{ cm}^{-1}$  and  $1590\text{ cm}^{-1}$  correspond to the D and G bands arising from the disordered structure and bond stretching motion of  $\text{sp}^2$  hybridized carbon, respectively (Figure S7, Supporting Information). Their intensity ratio,  $I_G/I_D$ , for  $\text{NiS}_2/\text{NiSe}_2@\text{NC}$ ,  $\text{NiSe}_2@\text{NC}$ , and  $\text{NiS}_2@\text{NC}$  was 1.02, 1.03, and 1.03, respectively (Table S1, Supporting Information), indicating that carbon is present in both amorphous and graphitized forms. This is convenient for electrochemical applications because while amorphous carbon can provide additional electrochemically active sites, graphitized carbon promotes charge transport.<sup>[22a]</sup>

The specific surface area was determined from  $\text{N}_2$  adsorption/desorption isotherms using the Brunauer-Emmett-Teller (BET) calculation (Figure S8, Supporting Information). The specific surface areas of  $\text{NiS}_2/\text{NiSe}_2@\text{NC}$ ,  $\text{NiSe}_2@\text{NC}$  and  $\text{NiS}_2@\text{NC}$  were  $166.2\text{ m}^2\cdot\text{g}^{-1}$ ,  $132.6\text{ m}^2\cdot\text{g}^{-1}$  and  $108.9\text{ m}^2\cdot\text{g}^{-1}$  respectively. In addition, the Barrett-Joyner-Halenda (BJH) pore size distribution of the three electrode materials showed a main contribution in the micropore size range, 0–50 nm. Such large specific surface area and highly porous structure are associated with the hollow material architecture and the sulfurization/selenization processes that generate additional pores within the structure.

X-ray photoelectron spectroscopy (XPS) shows the surface of  $\text{NiS}_2/\text{NiSe}_2@\text{NC}$  to be chalcogen-rich,  $(\text{S}+\text{Se})/\text{Ni} = 6$  (Table S2, Supporting Information), with S accounting for 76% of the surface chalcogen amount (Figure S9, Supporting Information).



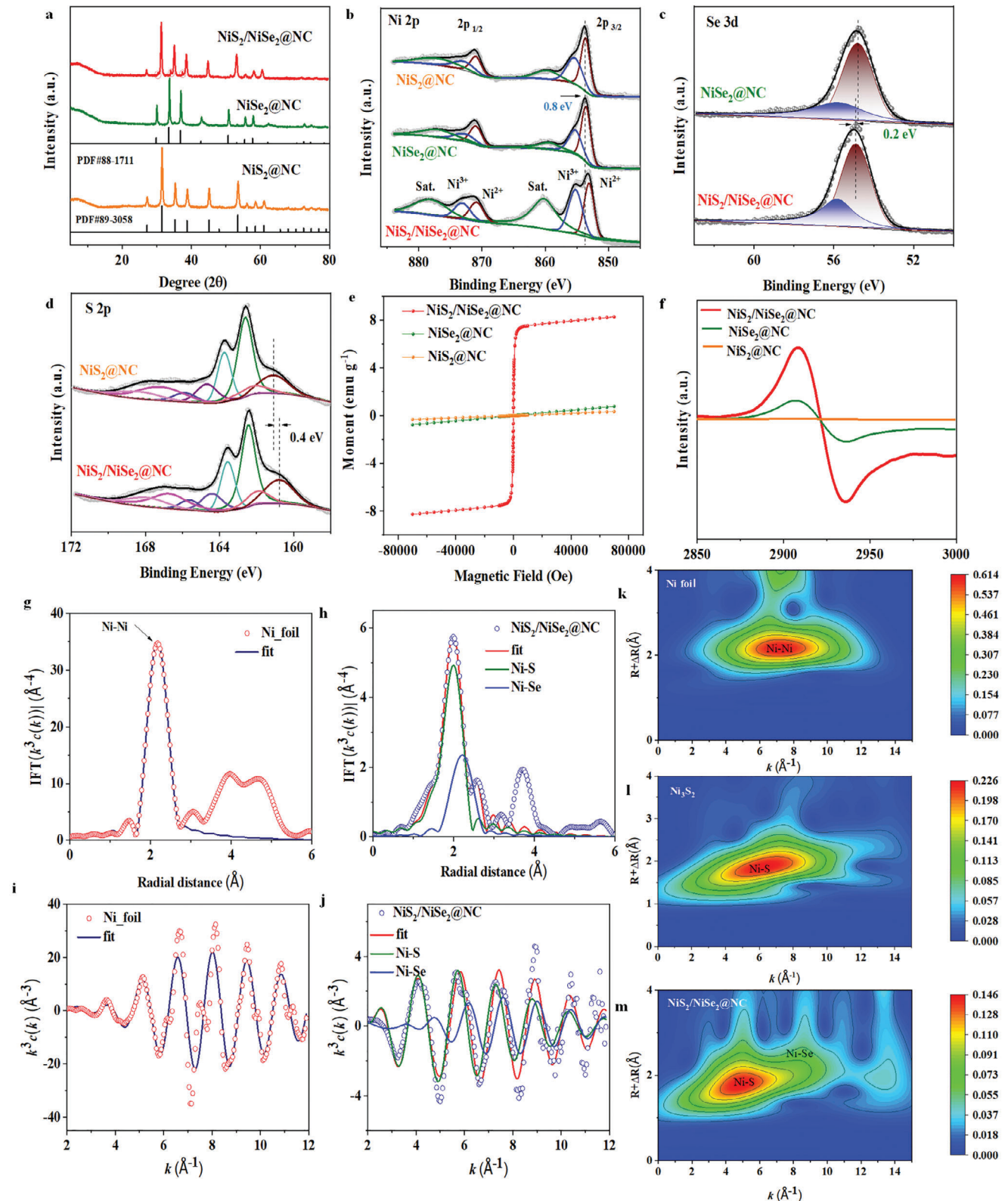


**Figure 2.** Structural and chemical characterization of  $\text{NiSe}_2/\text{NiSe}_2@\text{NC}$ ,  $\text{NiSe}_2@\text{NC}$ , and  $\text{NiS}_2@\text{NC}$ . a) XRD patterns. b–d) High-resolution Ni 2p (b), Se 3d (c), and S 2p (d) XPS spectra. e) Dependences of magnetization on the external magnetic field for  $\text{NiSe}_2/\text{NiSe}_2@\text{NC}$ ,  $\text{NiSe}_2@\text{NC}$ , and  $\text{NiS}_2@\text{NC}$  at room temperature (300 K). f) EPR spectra for  $\text{NiSe}_2/\text{NiSe}_2@\text{NC}$ ,  $\text{NiSe}_2@\text{NC}$  and  $\text{NiS}_2@\text{NC}$ . g) FT-EXAFS fitting curves of Ni K-edge for Ni foil. h) FT-EXAFS fitting curves of Ni K-edge for  $\text{NiSe}_2/\text{NiSe}_2@\text{NC}$ . i) XAFS fitting curves of Ni K-edge for Ni foil ( $K_3$  space). j) XAFS fitting curves of Ni K-edge for  $\text{NiSe}_2/\text{NiSe}_2@\text{NC}$  ( $K_3$  space). k–m) WT contour plots for Ni foil,  $\text{Ni}_2\text{S}_3$ , and  $\text{NiSe}_2/\text{NiSe}_2@\text{NC}$  at R space.

The Ni 2p high-resolution XPS spectrum of NiS<sub>2</sub>/NiSe<sub>2</sub>@NC (Figure 2b) shows two doublets assigned to Ni<sup>2+</sup> (Ni 2p<sub>3/2</sub> = 853.1 eV) and Ni<sup>3+</sup> (Ni 2p<sub>3/2</sub> = 855.3 eV) and two satellite peaks. Compared with NiS<sub>2</sub>@NC and NiSe<sub>2</sub>@NC, the binding energies (BEs) of Ni within NiS<sub>2</sub>/NiSe<sub>2</sub>@NC are red-shifted by ≈0.8 eV. Besides, the Ni satellite peaks of the NiS<sub>2</sub>/NiSe<sub>2</sub>@NC are significantly larger than those of NiSe<sub>2</sub>@NC and NiS<sub>2</sub>@NC (Figures 2e; and S10 and Table S3, Supporting Information). Generally speaking, the greater the relative Ni 2p satellite peak area, the higher its magnetic susceptibility.<sup>[4f,29]</sup> Thus, XPS data point to NiS<sub>2</sub>/NiSe<sub>2</sub>@NC having a larger magnetic susceptibility than NiSe<sub>2</sub>@NC and NiS<sub>2</sub>@NC. The Se 3d spectrum of NiS<sub>2</sub>/NiSe<sub>2</sub>@NC shows one doublet assigned to Se<sup>2-</sup> within a metal selenide chemical environment (Se 3d<sub>5/2</sub> = 55.1 eV, Figure 2c). The doublet is slightly blue-shifted by 0.2 eV with respect to NiSe<sub>2</sub>@NC, which is consistent with both the presence of a significant part of the total Se within the NiS<sub>2</sub> lattice and with some degree of charge transfer from NiSe<sub>2</sub> to NiS<sub>2</sub> within the NiS<sub>2</sub>/NiSe<sub>2</sub> composite.<sup>[30]</sup> On the other hand, the S 2p spectra of the different materials show four doublets that can be assigned to divalent sulfide ions (S<sup>2-</sup>) within the NiSe<sub>2</sub> lattice (S 2p<sub>3/2</sub> = 160.6 eV), S<sup>2-</sup> within the NiS<sub>2</sub> (S 2p<sub>3/2</sub> = 162.4 eV), C-S (S 2p<sub>3/2</sub> = 164.7 eV), and a SO<sub>4</sub><sup>2-</sup> chemical ambient (S 2p<sub>3/2</sub> = 165.8 eV) generated during the surface oxidation of the NiS<sub>2</sub> crystallites when exposed to air during manipulation and transportation (Figure 2d).<sup>[31]</sup> The S<sup>2-</sup> components of NiS<sub>2</sub>/NiSe<sub>2</sub>@NC exhibited a negative shift of ≈0.4 eV compared with NiS<sub>2</sub>@NC, which is also consistent with the presence of large amounts of Se and the charge transfer from NiSe<sub>2</sub> to NiS<sub>2</sub> within the NiS<sub>2</sub>/NiSe<sub>2</sub> composite. The C 1s XPS spectra display peaks at 284.6 eV, 286.2 eV, and 288.4 eV attributed to C = C, C-O, and C = O, respectively (Figure S11a, Supporting Information). In the N 1s high-resolution XPS spectra, three peaks can be fitted at BEs of 398.4 eV, 399.8 eV, and 402.1 eV corresponding to pyridinic-N, pyrrolic-N and graphitic-N, respectively (Figure S11b, Supporting Information). As noted in previous reports, pyridinic-N can effectively increase the electron density and interact with sulfur/polysulfides, while pyrrolic-N and graphitic-N can effectively enhance the affinity of polar atoms to elemental sulfur (S<sub>8</sub>) and polar polysulfides (Li<sub>2</sub>S, Li<sub>2</sub>S<sub>2</sub>, Li<sub>2</sub>S<sub>4</sub>, Li<sub>2</sub>S<sub>6</sub>, and Li<sub>2</sub>S<sub>8</sub>) through strong Lewis acid-base interactions.<sup>[32]</sup>

Figures 2e and Figure S12a (Supporting Information) show the dependence of magnetization on the external magnetic field at 300 K of the different Ni chalcogenides. NiS<sub>2</sub>/NiSe<sub>2</sub>@NC shows a clear hysteresis loop and the largest saturation magnetization among the tested samples, 8.32 emu g<sup>-1</sup> at 100 KOe, indicating magnetic behavior at ambient temperature. The zero-field cooled/field cooled (ZFC/FC) curves of NiS<sub>2</sub>/NiSe<sub>2</sub>@NC (Figure S12b, Supporting Information) indicate a Curie temperature above 300 K, whereas the 1/T increase of magnetization at high field indicates a paramagnetic behavior. Similarly, the magnetic susceptibilities of NiSe<sub>2</sub>@C show a linear behavior with the magnetic field, indicating a paramagnetic behavior coming from Ni ions. Electron paramagnetic resonance (EPR) spectra of the catalysts and control samples were measured at room temperature. The EPR spectra of the Ni chalcogenides show a characteristic feature at g = 2.51 (Figure 2f), associated with unpaired electrons in the Ni 3d orbital. This feature is much more notorious in the NiS<sub>2</sub>/NiSe<sub>2</sub>@NC composite than in NiS<sub>2</sub>@NC and

NiSe<sub>2</sub>@NC pointing to a higher concentration of unpaired electrons in the former. This result suggests an essential contribution of heterostructures in promoting a high-spin state within the catalyst.

X-ray absorption near-edge structure (XANES) and extended X-ray absorption fine structure (EXAFS) spectra were used to analyze the atomic coordination environment and chemical state of NiS<sub>2</sub>/NiSe<sub>2</sub>@NC, NiSe<sub>2</sub>@NC and NiS<sub>2</sub>@NC (Figures S13–15, Supporting Information). The absorption edge position of NiS<sub>2</sub>/NiSe<sub>2</sub>@NC is localized between that of the metallic Ni foil (Ni<sup>0</sup>) and Ni<sub>2</sub>S<sub>3</sub> (Ni<sup>3+</sup>), indicating the positively charged feature of Ni with an intermediate chemical state between 0 and +3.<sup>[33]</sup> The absorption edge of the Ni K-edge in NiS<sub>2</sub>/NiSe<sub>2</sub>@NC is slightly red-shifted compared to NiSe<sub>2</sub>@NC and NiS<sub>2</sub>@NC. This observation confirms that Ni in NiS<sub>2</sub>/NiSe<sub>2</sub>@NC possesses a lower-energy valence state relative to NiSe<sub>2</sub>@NC and NiS<sub>2</sub>@NC (Figure S13a, Supporting Information).<sup>[34]</sup> As depicted in the inset of Figure S13a (Supporting Information), the NiS<sub>2</sub>/NiSe<sub>2</sub>@NC host material exhibits a more intense pre-edge peak relative to the NiSe<sub>2</sub>@NC and NiS<sub>2</sub>@NC pointing at a different coordination environment. The presence of this pre-edge peak (≈8340 eV) in the Ni K-edge spectrum is related to electron transitions from the s orbital to the unoccupied d orbital, which is significantly influenced by the structure geometry and ligand field upon coordination with different species.<sup>[35]</sup> In this case, we hypothesize that the electron transition between NiS<sub>2</sub> and NiSe<sub>2</sub> crystals within the catalyst shifts electrons from a stable ground state to a metastable state. This shift elevates the energy of the catalyst and thus enhances its activity. In particular, this increase in energy lowers the activation energy barrier for the sulfur redox reaction (SRR), thereby promoting the catalytic activity of the catalyst and facilitating the SRR process.

Simultaneously, a weakening in the intensity of the peak ≈8350 eV in the Ni K-edge XANES spectrum is observed for NiS<sub>2</sub>/NiSe<sub>2</sub>@NC (Figure S13a, Supporting Information), which involves an increase in local disorder around the Ni atoms, consistent with the discussed large amount of chalcogen doping and the large density of heterointerphases.<sup>[36]</sup> Besides, the intensity of this peak can also correlated with the spin state of the material. As the peak intensity decreases, the spin state of the electrode material progressively increases.<sup>[37]</sup> Through analysis of the peak intensity, it can be inferred that the heterostructures facilitate the transition of Ni ions from a low spin to a high spin state.

The Fourier transform extended X-ray absorption fine structure (FT-EXAFS) of NiS<sub>2</sub>/NiSe<sub>2</sub>@NC shows characteristic peaks at 2.43 Å and 2.52 Å corresponding to the Ni-S and Ni-Se bonds (Figure S13b, Supporting Information). Specifically, it is observed that the Ni-S bond length in NiS<sub>2</sub>/NiSe<sub>2</sub>@NC is longer compared to that in NiS<sub>2</sub>@NC (2.31 Å). Conversely, the length of the Ni-Se bond in NiS<sub>2</sub>/NiSe<sub>2</sub>@NC is shorter than that in NiSe<sub>2</sub>@NC (2.88 Å) (Table S4, Supporting Information). This discrepancy in bond lengths can be attributed to the variance in electronegativity between S and Se atoms and the fact that Ni binds to both of them, S and Se, in both materials, NiS<sub>2</sub> and NiSe<sub>2</sub>, within NiS<sub>2</sub>/NiSe<sub>2</sub>@NC.<sup>[38]</sup> FT-EXAFS showed a decrease in the intensity of the peak associated with the Ni-S bond in NiS<sub>2</sub>/NiSe<sub>2</sub>@NC compared to NiS<sub>2</sub>@NC (Figure S13c, Supporting Information). This result is also consistent with certain Ni atoms forming bonds not only with S, but also with Se

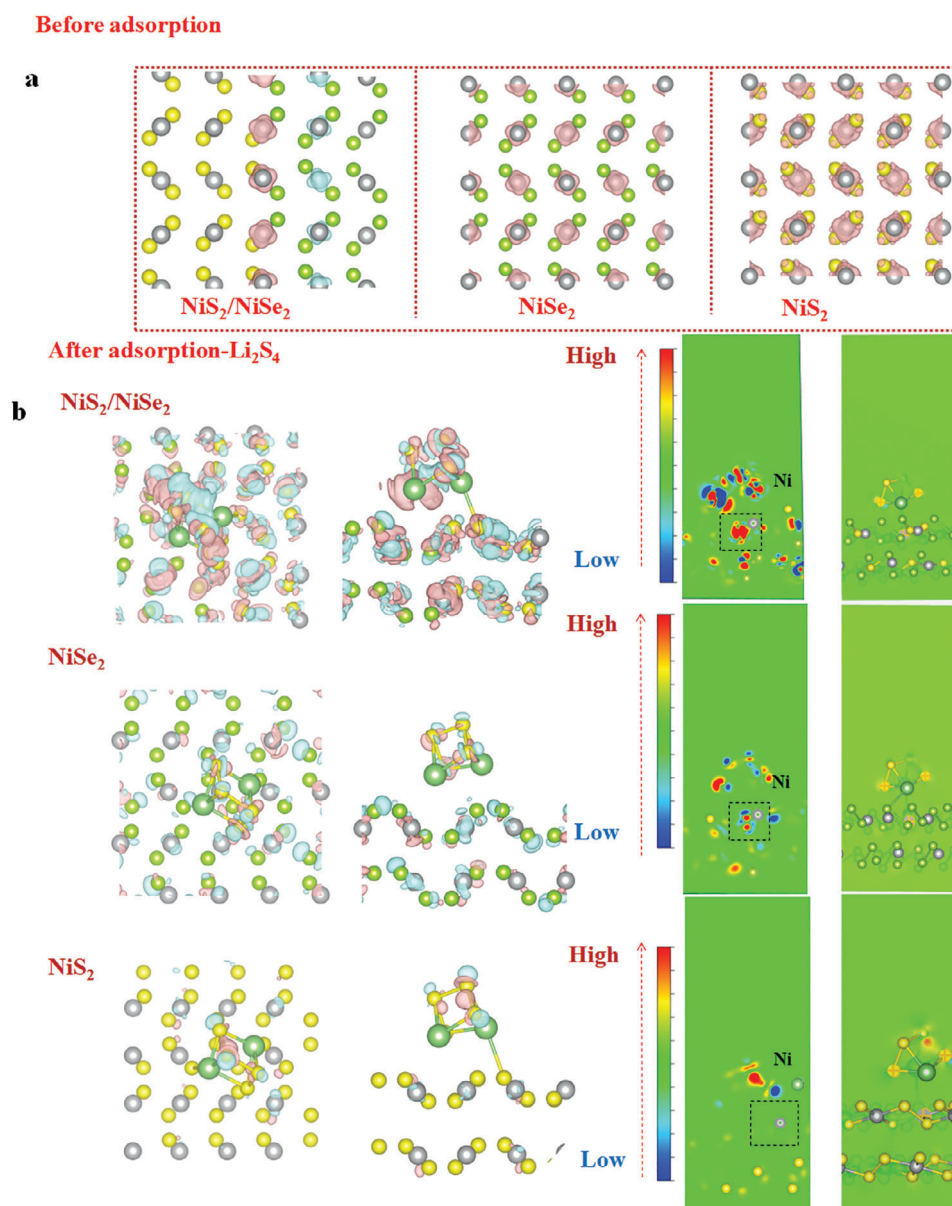


**Figure 3.** a,b) Spin density of  $\text{NiS}_2/\text{NiSe}_2$ ,  $\text{NiSe}_2$ , and  $\text{NiS}_2$  before (a) and after (b) the adsorption of  $\text{Li}_2\text{S}_4$ . Grey = Ni; green = Se; yellow = S; blue = down spin state; and red = up spin state.

atoms inside the  $\text{NiS}_2$  in  $\text{NiS}_2/\text{NiSe}_2@\text{NC}$ .<sup>[39]</sup> The EXAFS fitting curve reveals that the coordination number of Ni is  $\approx 6$  for Ni-S and Ni-Se in  $\text{NiS}_2/\text{NiSe}_2@\text{NC}$  (Figure 2g–j). In addition, the wavelet transform (WT) contours of Ni show a maximum intensity at  $\approx 4 \text{ \AA}^{-1}$  (Figure 2k–m), corresponding to Ni-S and Ni-Se in  $\text{NiS}_2/\text{NiSe}_2@\text{NC}$ .

DFT calculations were used to evaluate the interaction between LiPSs and Ni within each material. First, we calculated the most stable structure of the interphase between  $\text{NiS}_2$  (210) and  $\text{NiSe}_2$  (210). Within this most stable interface, we analyzed the spin state directions before polysulfide adsorption (Figure 3a). The computational results reveal the presence of two distinct electron spin state regions (spin up and spin down) within the  $\text{NiS}_2/\text{NiSe}_2$  host material at the very interface of the two chalcogenides. Upon

introducing the adsorbing polysulfide ( $\text{Li}_2\text{S}_4$ ), a pronounced charge exchange phenomenon is calculated (Figure 3b). Notably, a portion of the electrons at the catalyst surface transfers to the polysulfide. In parallel, the electronic spin within the heterojunction loses its order. Furthermore, an examination of the Ni spin electron density (black dotted frame) reveals  $\text{NiS}_2/\text{NiSe}_2$  to present a much stronger intensity compared with  $\text{NiS}_2$ ,  $\text{NiSe}_2$ , and polysulfides. Thus, we conclude that the spin-charge interaction within the heterostructure is notably higher compared with the pure materials. The strong interaction of Ni ions with polysulfides and the change of electron spin points at Ni as the reaction active sites. Thus, additional DFT calculations to measure the impact of heterostructure on catalytic reactions are focused on them.



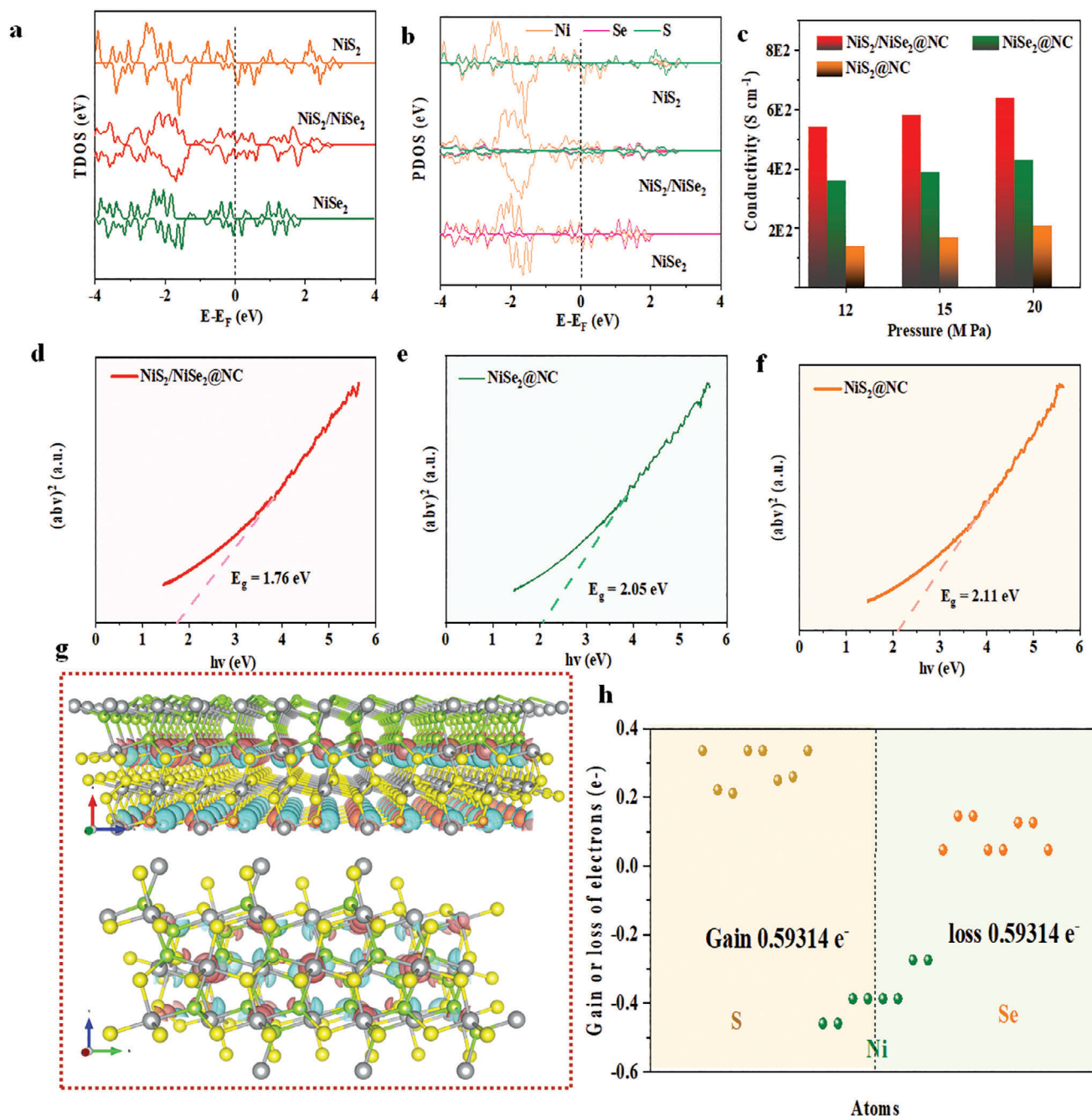


**Figure 4.** a) TDOS and b) partial density of states (PDOS) of NiSe<sub>2</sub>/NiS<sub>2</sub>, NiSe<sub>2</sub>, and NiS<sub>2</sub>. c) Electrical conductivity of NiS<sub>2</sub>/NiSe<sub>2</sub>, NiSe<sub>2</sub>, and NiS<sub>2</sub> tested using four probes at different pressures. d-f) Tauc plots of NiS<sub>2</sub>/NiSe<sub>2</sub>@NC (d), NiSe<sub>2</sub>@NC (e), and NiS<sub>2</sub>@NC (f). g, h) Electron gain/loss of different atoms calculated by Bader charge analysis. Blue and red colors represent the gain and loss of electrons, respectively. Green = Se; Grey = Ni; Yellow = S.

DFT calculations were further used to gain insight into the heterostructure electronic properties and their effects. According to DFT calculations results, the total density of states (TDOS) of NiSe<sub>2</sub>/NiS<sub>2</sub> was more concentrated at the Fermi level compared to NiS<sub>2</sub> and NiSe<sub>2</sub> (Figure 4a,b), indicating promoted charge transport and transfer. While NC plays a dominant role in the charge transport properties of the composites,<sup>[40]</sup> four-point conductivity tests on the printed electrodes showed notable differ-

ences between the chalcogenide composites. NiSe<sub>2</sub>/NiS<sub>2</sub>@NC showed a significantly higher electrical conductivity (Figure 4c), at  $5.4 \times 10^2$  S cm<sup>-1</sup>, than NiSe<sub>2</sub>@NC, at  $3.6 \times 10^2$  S cm<sup>-1</sup>, and particularly NiS<sub>2</sub>@NC, at  $1.4 \times 10^2$  S cm<sup>-1</sup>. These results are consistent with the DFT results. This increase in the TDOS near the Fermi level was also confirmed using UV-vis spectroscopy. Tauc plots from UV-vis absorption spectra are shown in Figure 4d-f. The experimental band gap of the heterostructured

material,  $\text{NiS}_2/\text{NiSe}_2@\text{NC}$  ( $E_g = 1.76$  eV), was lower than that of each of the components,  $\text{NiSe}_2@\text{NC}$  ( $E_g = 2.05$  eV) and  $\text{NiS}_2$  ( $E_g = 2.11$  eV).

The electron gain and loss near the interface were also determined by DFT calculations using theoretical  $\text{NiSe}_2$  and  $\text{NiS}_2$  slab models. As shown in Figure 4g, the differential distribution of charges indicates that electrons are transferred across the heterointerface of  $\text{NiSe}_2$  and  $\text{NiS}_2$ . The charge redistribution on the  $\text{NiS}_2/\text{NiSe}_2$  interface and the electron transfer between different atoms were quantitatively determined by Bader charge analysis (Figure 4h). Bader charge analysis showed the acquisition of 0.59 electrons by the  $\text{NiS}_2$  unit from the  $\text{NiSe}_2$  layer for  $\text{NiS}_2/\text{NiSe}_2$ . The gain of electrons by  $\text{NiS}_2$  coming from  $\text{NiSe}_2$  is consistent with XPS results. Overall, DFT calculations showed the formation of the heterostructure results in a notable charge redistribution between the phases.

To evaluate the potential of sulfur host materials to confine LiPSs, their  $\text{Li}_2\text{S}_6$  adsorption capacity was tested. Optical images of vials containing a 10 mM solution of  $\text{Li}_2\text{S}_6$  and 15 mg of  $\text{NiS}_2/\text{NiSe}_2@\text{NC}$ ,  $\text{NiSe}_2@\text{NC}$ , or  $\text{NiS}_2@\text{NC}$  after overnight adsorption are shown in Figure 5a. Significant color differences were observed between the different vials. In the absence of an adsorber, the  $\text{Li}_2\text{S}_6$  solution exhibits an intense orange color. After overnight adsorption, the solution containing  $\text{NiS}_2/\text{NiSe}_2@\text{NC}$  shows a pale yellow color indicating that most of the  $\text{Li}_2\text{S}_6$  has been adsorbed. In contrast, the solutions containing  $\text{NiSe}_2@\text{NC}$  and  $\text{NiS}_2@\text{NC}$  maintain a strong orange aspect, indicating a moderate  $\text{Li}_2\text{S}_6$  trapping effectiveness. The UV-vis spectra of the supernatants confirmed these results and allowed quantifying the  $\text{Li}_2\text{S}_6$  absorbance by following the light absorption in the 350–400 nm region. The chemical interaction between  $\text{Li}_2\text{S}_6$  and  $\text{NiS}_2/\text{NiSe}_2@\text{NC}$  was further evaluated by XPS analysis (Figure 5b). In the high-resolution Ni 2p XPS spectrum of the material after  $\text{Li}_2\text{S}_6$  adsorption ( $\text{NiS}_2/\text{NiSe}_2@\text{NC}-\text{Li}_2\text{S}_6$ ), the two doublets at 852.9 eV and 854.6 eV ( $2p_{3/2}$ ) are assigned to  $\text{Ni}^{2+}$  and  $\text{Ni}^{3+}$ . The two chemical states appear redshifted when compared to the fresh  $\text{NiS}_2/\text{NiSe}_2@\text{NC}$ . This redshift is attributed to the S/Se-Li bond formation, which reduces the electronegativity of the Ni chemical environment.<sup>[40]</sup> In addition, compared with  $\text{NiS}_2/\text{NiSe}_2@\text{NC}$ , the ratio of the satellite peak area of  $\text{NiS}_2/\text{NiSe}_2@\text{NC}-\text{Li}_2\text{S}_6$  is significantly reduced, which is attributed to the transfer of electrons from the heterointerface to the empty polysulfides orbitals, resulting in a reduced amount of unpaired electrons. Besides, the S 2p XPS spectrum of  $\text{NiS}_2/\text{NiSe}_2@\text{NC}$  after  $\text{Li}_2\text{S}_6$  adsorption shows a 0.3 eV blueshift in BE also consistent with electronic interaction between  $\text{NiS}_2/\text{NiSe}_2@\text{NC}$  and LiPSs.<sup>[41]</sup> (Figure S16, Supporting Information)

DFT calculations were further used to gain an understanding of the LiPS adsorption capacity of the host materials. The adsorption models of  $\text{NiS}_2$ ,  $\text{NiSe}_2$ , and  $\text{NiS}_2/\text{NiSe}_2$  with the different sulfur species ( $\text{Li}_2\text{S}$ ,  $\text{Li}_2\text{S}_2$ ,  $\text{Li}_2\text{S}_4$ ,  $\text{Li}_2\text{S}_6$ ,  $\text{Li}_2\text{S}_8$ , and  $\text{S}_8$ ) are shown in Figures S17–22 (Supporting Information), and Figure 5c, and Table S5 (Supporting Information). DFT results show that the LiPSs BE to  $\text{NiS}_2/\text{NiSe}_2$  is higher than that of  $\text{NiSe}_2$  and  $\text{NiS}_2$ . In particular, the adsorption energy between  $\text{NiS}_2/\text{NiSe}_2$  and  $\text{Li}_2\text{S}_6$  is -0.22 eV, significantly above (in absolute value) that of  $\text{NiSe}_2$ , at -0.17 eV, and  $\text{NiS}_2$ , at -0.03 eV.

To study the electrochemical performance of the different chalcogenide composites, they were infiltrated with S to obtain  $\text{NiS}_2/\text{NiSe}_2@\text{NC}/\text{S}$ ,  $\text{NiSe}_2@\text{NC}/\text{S}$ , and  $\text{NiS}_2@\text{NC}/\text{S}$  (see the SI for details). When sulfur is loaded,  $\text{NiS}_2/\text{NiSe}_2@\text{NC}/\text{S}$  effectively inherits the morphology of  $\text{NiS}_2/\text{NiSe}_2@\text{NC}$  (Figure S23, Supporting Information). Upon the introduction of sulfur, the specific surface area of  $\text{NiS}_2/\text{NiSe}_2@\text{NC}/\text{S}$  is significantly reduced ( $10.3 \text{ m}^2 \text{ g}^{-1}$ ) when compared with that of  $\text{NiS}_2/\text{NiSe}_2@\text{NC}$  ( $166.2 \text{ m}^2 \text{ g}^{-1}$ ), indicating that sulfur is effectively confined in the pores of the host material by the simple melting infiltration strategy used (Figure S24, Supporting Information). In addition, XRD characterization further shows that the crystalline S phase exists within  $\text{NiS}_2/\text{NiSe}_2@\text{NC}/\text{S}$ ,  $\text{NiSe}_2@\text{NC}/\text{S}$ , and  $\text{NiS}_2@\text{NC}/\text{S}$ . Besides, thermogravimetric analysis (TGA) quantified the content of S in  $\text{NiS}_2/\text{NiSe}_2@\text{NC}/\text{S}$ ,  $\text{NiSe}_2@\text{NC}/\text{S}$ , and  $\text{NiS}_2@\text{NC}/\text{S}$  is 73.8%, 71.3%, and 70.1% respectively (Figure S25, Supporting Information).

To investigate the reaction mechanism within the different chalcogenides and particularly the LiPS evolution during charge and discharge processes, in situ synchrotron XRD ( $\lambda = 0.6883 \text{ \AA}$ ) patterns were collected (Figure 5d). From the  $\text{NiS}_2/\text{NiSe}_2@\text{NC}/\text{S}$  electrode, an XRD peak at  $\approx 24.6^\circ$  on the fresh cell was indexed to  $\text{S}_8$ . During discharging,  $\text{S}_8$  disappears while a new peak appears at  $\approx 28.1^\circ$ , coinciding with the formation of long-chain polysulfides. With further discharge, long-chain polysulfides gradually convert into short-chain S species and finally  $\text{Li}_2\text{S}$ , with peaks located at  $30.6^\circ$  and  $24.9^\circ$ , respectively. Upon charging to 2.8 V,  $\text{Li}_2\text{S}$  undergoes a reversible process, gradually being reduced to short-chain polysulfides, long-chain polysulfides, and finally  $\text{S}_8$ , demonstrating the fast sulfur reaction kinetics in  $\text{NiS}_2/\text{NiSe}_2@\text{NC}/\text{S}$  cells. In contrast, for the  $\text{NiSe}_2@\text{NC}/\text{S}$  and  $\text{NiS}_2@\text{NC}/\text{S}$  electrodes, a small amount of  $\text{S}_8$  was detected throughout the entire discharge process, indicating that the catalytic ability of these two electrodes cannot completely convert  $\text{S}_8$  (Figure 5e,f). Besides, after charging, in both electrodes the presence of  $\text{Li}_2\text{S}$  was still detected, indicating that the catalytic ability of the catalyst is not sufficient to fully convert solid  $\text{Li}_2\text{S}$  into S. After long-term cycling, this will cause solid sulfides to slowly accumulate on the surface of the positive electrode, leading to performance decay.

To evaluate the electrocatalytic activity of the chalcogenides, symmetric cells were assembled using a 0.5 M  $\text{Li}_2\text{S}_6$  electrolyte, and the different composite materials in both electrodes. As shown in Figure 6a, the cyclic voltammetry (CV) curves of the symmetric cell based on  $\text{NiS}_2/\text{NiSe}_2@\text{NC}$  electrodes showed the highest peak current densities, suggesting a higher activity toward the polysulfide conversion. When similar experiments were performed on  $\text{NiS}_2/\text{NiSe}_2@\text{NC}$  electrodes without  $\text{Li}_2\text{S}_6$ , the CV curves exhibited a rectangular shape, which was attributed to a purely capacitive behavior, indicating that  $\text{Li}_2\text{S}_6$  was the electro-chemically active species in the system. The CV curves of symmetric cells assembled with different host materials ( $\text{NiS}_2/\text{NiSe}_2@\text{NC}$ ,  $\text{NiSe}_2@\text{NC}$ , and  $\text{NiS}_2@\text{NC}$ ) at various scan rates ( $5 \text{ mV s}^{-1}$ – $20 \text{ mV s}^{-1}$ ) are shown in Figure S26 (Supporting Information). With increasing scan rate, the oxidation-reduction current density of the CV curve gradually increases, indicating diffusion-controlled conversion behavior in the symmetric system.<sup>[42]</sup> In contrast to  $\text{NiSe}_2@\text{NC}$  and  $\text{NiS}_2@\text{NC}$ , the CV curves of  $\text{NiS}_2/\text{NiSe}_2@\text{NC}$  exhibit distinct



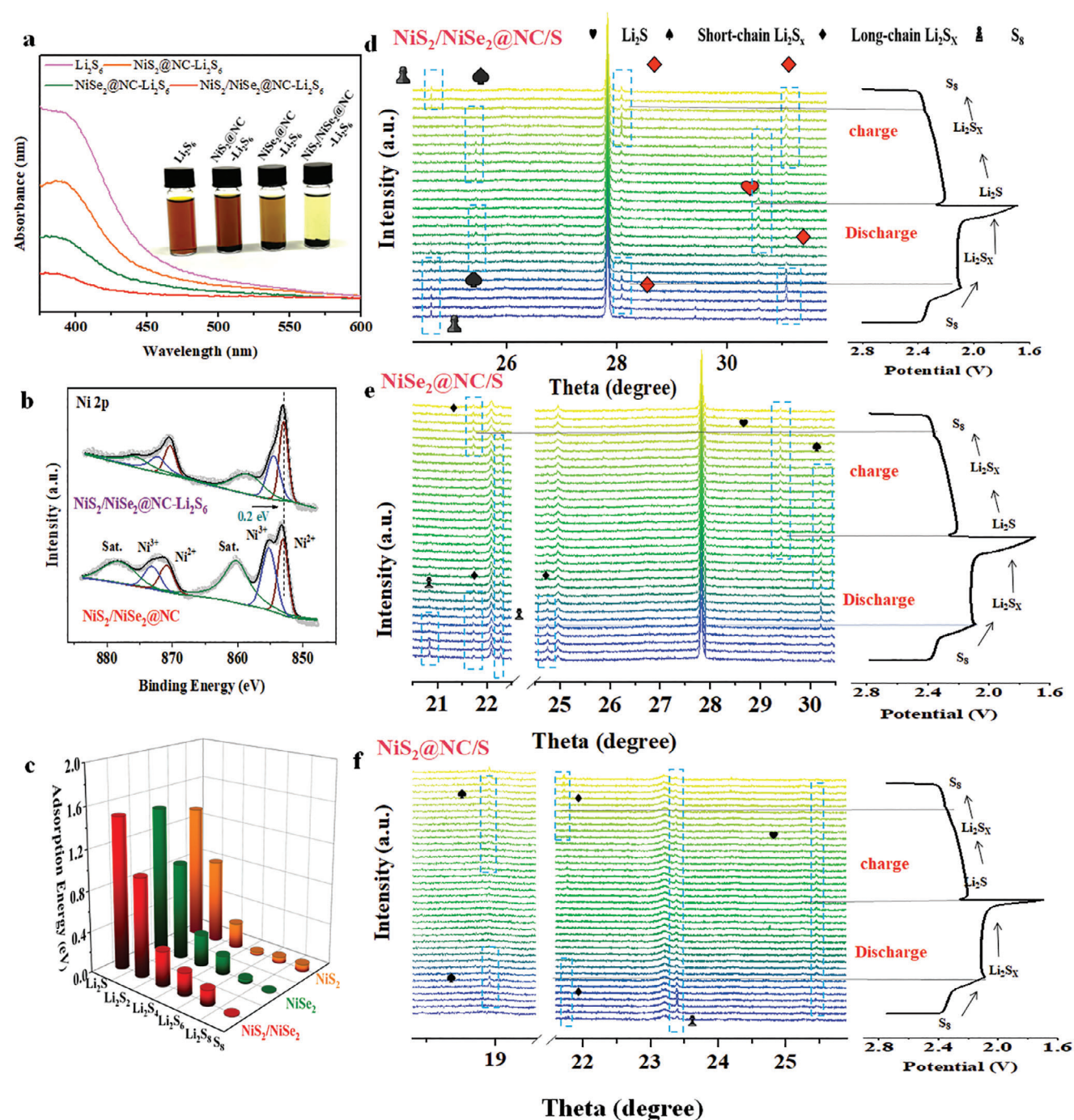


**Figure 5.** a) UV-vis absorption spectra and photographs (inset) of the  $\text{Li}_2\text{S}_6$  solutions containing different adsorbing materials after overnight adsorption. b) High-resolution XPS spectra of Ni 2p before and after  $\text{Li}_2\text{S}_6$  adsorption. c) Adsorption energies of electrode materials with different polysulfides ( $\text{S}_8$ ,  $\text{Li}_2\text{S}_8$ ,  $\text{Li}_2\text{S}_6$ ,  $\text{Li}_2\text{S}_4$ ,  $\text{Li}_2\text{S}_2$ , and  $\text{Li}_2\text{S}$ ). d–f) In situ XRD patterns during charging and discharging of batteries based on  $\text{NiS}_2/\text{NiSe}_2@\text{NC}/\text{S}$  (d),  $\text{NiSe}_2@\text{NC}/\text{S}$  (e), and  $\text{NiS}_2@\text{NC}/\text{S}$  (f) cathodes.

oxidation-reduction peaks even at high scan rates, suggesting rapid oxidation-reduction kinetics. Additionally, the CV curves of the  $\text{NiS}_2/\text{NiSe}_2@\text{NC}$  composite show the highest current density and largest integrated area during all scan rates. These results evidence the significant activity of the heterostructure in facilitating the conversion of polysulfides

Additionally, the electrochemical impedance spectroscopy (EIS) spectra, fitted considering the equiv. circuit diagrams in Figure S27 (Supporting Information), show that the  $\text{NiS}_2/\text{NiSe}_2@\text{NC}$  exhibits the smallest charge transfer resistance during SRR compared, at 9.2  $\Omega$ , compared with the 13.6  $\Omega$  obtained for  $\text{NiSe}_2@\text{NC}$  and the 19.8  $\Omega$  of  $\text{NiS}_2@\text{NC}$ . This

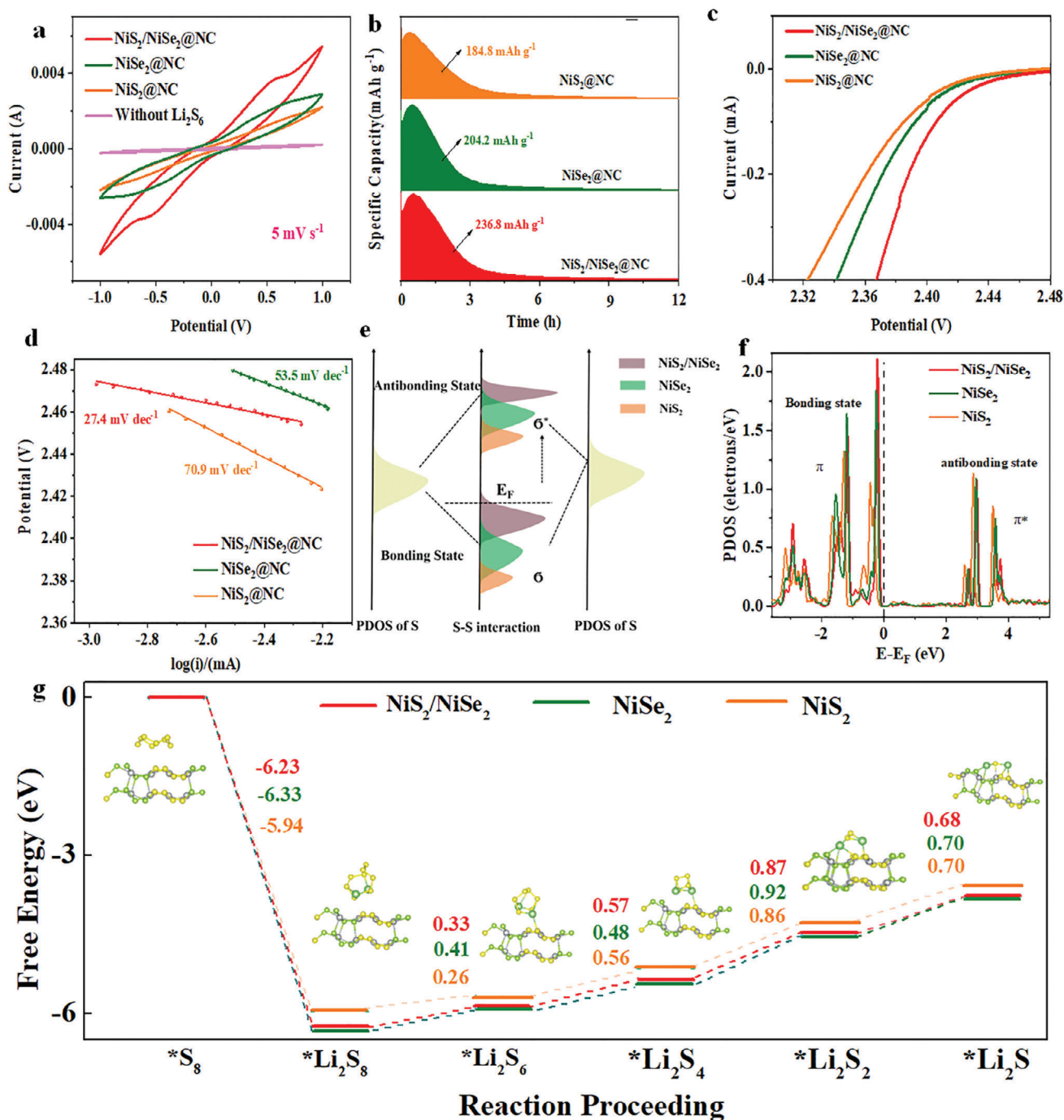


**Figure 6.** a) CV curves of symmetrical cells assembled using two  $\text{NiS}_2/\text{NiSe}_2@\text{NC}$ ,  $\text{NiSe}_2@\text{NC}$  or  $\text{NiS}_2@\text{NC}$ -based electrodes. b) Potentiostatic discharge curves on different electrodes for studying the nucleation kinetics of  $\text{Li}_2\text{S}$ . c) LSV polarization curves  $\text{NiS}_2/\text{NiSe}_2@\text{NC}$ ,  $\text{NiSe}_2@\text{NC}$  and  $\text{NiS}_2@\text{NC}$ . d) Tafel plots of  $\text{NiS}_2/\text{NiSe}_2@\text{NC}$ ,  $\text{NiSe}_2@\text{NC}$  and  $\text{NiS}_2@\text{NC}$ . e, f) Energy level diagram showing orbital hybridization for S-S.  $E_F$  is the Fermi level of the substrate;  $\sigma$  and  $\sigma^*$  represent bonding and antibonding states, respectively. g) Gibbs free energy profiles and optimized adsorption model of LiPS species on  $\text{NiS}_2/\text{NiSe}_2$ ,  $\text{NiSe}_2$ , and  $\text{NiS}_2$ .

result further confirms the superior charge transfer kinetics of the  $\text{NiS}_2/\text{NiSe}_2@\text{NC}$ .

Generally, the performance of LSBs strongly depends on their  $\text{Li}_2\text{S}$  nucleation/deposition process. Thus, the  $\text{Li}_2\text{S}$  deposition process was evaluated by first discharging the cell at a constant

current (0.112 mA) to 2.06 V and then depositing  $\text{Li}_2\text{S}$  at 2.05 V. According to Faraday's law, the capacity ( $Q$ ) of  $\text{Li}_2\text{S}$  deposition was calculated as  $Q = It$ , where  $I$  and  $t$  are the discharge current and time, respectively (Figure 6b). Compared to  $\text{NiSe}_2@\text{NC}$  and  $\text{NiS}_2@\text{NC}$ ,  $\text{NiS}_2/\text{NiSe}_2@\text{NC}$  displayed the fastest  $\text{Li}_2\text{S}$

deposition. More importantly, the deposition capacity of  $\text{Li}_2\text{S}$  on  $\text{NiS}_2/\text{NiSe}_2@\text{NC}$  was the highest, at  $236.8 \text{ mAh g}^{-1}$ , compared to  $\text{NiSe}_2@\text{NC}$  ( $204.2 \text{ mAh g}^{-1}$ ) and  $\text{NiS}_2@\text{NC}$  ( $184.8 \text{ mAh g}^{-1}$ ).

Linear sweep voltammetry (LSV) measurements were employed to investigate the SRR kinetics.<sup>[43]</sup> LSV curves of the polysulfide reduction process (Figure 6c,d) showed the  $\text{NiS}_2/\text{NiSe}_2@\text{NC}$  to display the lowest overpotential. Tafel plot analysis of the polysulfide reduction (Figure 6c,d) further revealed that the  $\text{NiS}_2/\text{NiSe}_2@\text{NC}$  electrode is characterized by the fastest reaction kinetics with a Tafel slope of  $27.4 \text{ mV dec}^{-1}$ , well below that of  $\text{NiSe}_2@\text{NC}$  ( $53.5 \text{ mV dec}^{-1}$ ) and  $\text{NiS}_2@\text{NC}$  ( $70.9 \text{ mV dec}^{-1}$ ). Besides, LSV measurements in the  $\text{Li}_2\text{S}$  oxidation range showed that  $\text{NiS}_2/\text{NiSe}_2@\text{NC}$  exhibits the smallest onset potential compared to  $\text{NiSe}_2@\text{NC}$  and  $\text{NiS}_2@\text{NC}$  (Figure S28, Supporting Information). Additionally, the Tafel slope of  $\text{NiS}_2/\text{NiSe}_2@\text{NC}$ , at  $77 \text{ mV dec}^{-1}$ , is lower than that of  $\text{NiS}_2@\text{NC}$  ( $94 \text{ mV dec}^{-1}$ ) and  $\text{NiSe}_2@\text{NC}$  ( $83 \text{ mV dec}^{-1}$ ), confirming the efficacy of the designed heterostructure.

DFT calculations were further used to study the S-S bond breaking at the surface of the different host materials (Figures 6e,f; and S29, Supporting Information). At the catalyst surface, bonds within adsorbed species are modified, displaying significant changes in the electronic density of the bonding ( $\sigma$ ) and anti-bonding ( $\sigma^*$ ) states around the Fermi level. Compared with  $\text{NiS}_2@\text{NC}$  and  $\text{NiSe}_2@\text{NC}$ , the PDOS of  $\text{NiS}_2/\text{NiSe}_2@\text{NC}$  is shifted upward, thereby reducing the stability of the S-S bond. Thus  $\text{NiS}_2/\text{NiSe}_2@\text{NC}$  facilitates the breakage of S-S bonds and thus promotes the Li-S reaction kinetics.

The Gibbs free energy evolution during the reduction process on the surface of  $\text{NiS}_2/\text{NiSe}_2@\text{NC}$ ,  $\text{NiSe}_2@\text{NC}$ , and  $\text{NiS}_2@\text{NC}$  was further evaluated using DFT calculations. The models and free energy distribution of polysulfide intermediates are shown in the Figure 6g. The lithiation pathway from  $\text{S}_8$  to  $\text{Li}_2\text{S}$  includes several steps. First, two  $\text{Li}^+$  react with  $\text{S}_8$  to generate  $\text{Li}_2\text{S}_8$ . In subsequent steps,  $\text{Li}_2\text{S}_8$  evolves to  $\text{Li}_2\text{S}_6$ ,  $\text{Li}_2\text{S}_4$ ,  $\text{Li}_2\text{S}_2$ , and finally  $\text{Li}_2\text{S}$ . According to previous reports, the solid-state reaction involved in the reduction of  $\text{Li}_2\text{S}_2$  to  $\text{Li}_2\text{S}$  plays a key role in defining the lithiation kinetics and its stability.<sup>[44]</sup> For this step, the Gibbs free energy change calculated on the surface of the  $\text{NiS}_2/\text{NiSe}_2@\text{NC}$  ( $0.68 \text{ eV}$ ) sample is sensibly lower than that of  $\text{NiSe}_2@\text{NC}$  ( $0.70 \text{ eV}$ ) and  $\text{NiS}_2@\text{NC}$  ( $0.70 \text{ eV}$ ).

To study their electrochemical performance, coin-type cells were assembled using a nickel chalcogenide-based sulfur cathode ( $\text{NiS}_2/\text{NiSe}_2@\text{NC}/\text{S}$ ,  $\text{NiSe}_2@\text{NC}/\text{S}$  and  $\text{NiS}_2@\text{NC}/\text{S}$ ), lithium foil as anode, and a solution of 1.0 M lithium bis(trifluoromethanesulfonyl) imide and 0.2 M  $\text{LiNO}_3$  in a mixture of 1,3-dioxolane (DOL) and 1,2-dimethoxyethane (DME) with a volume ratio of 1:1 as electrolyte (see details in Supporting Information). The galvanostatic charge-discharge (GCD) curves of the prepared electrode at 0.1C are shown in Figure 7a. All the discharge curves exhibit two distinct voltage plateaus, corresponding to the transitions  $\text{S}_8 \rightarrow \text{Li}_2\text{S}_6 \rightarrow \text{Li}_2\text{S}_4$  and  $\text{Li}_2\text{S}_4 \rightarrow \text{Li}_2\text{S}_2 \rightarrow \text{Li}_2\text{S}$ . We define the capacity of the first plateau as Q1 and that of the second plateau as Q2. In contrast, only one charging platform is attributed to the polysulfide oxidation to  $\text{S}_8$ .<sup>[40]</sup> Compared with other sulfur cathodes,  $\text{NiS}_2/\text{NiSe}_2@\text{NC}/\text{S}$  exhibits the highest initial specific capacitance ( $1458 \text{ mAh g}^{-1}$ ), well above that of  $\text{NiSe}_2@\text{NC}/\text{S}$  ( $1326 \text{ mAh g}^{-1}$ ),  $\text{NiS}_2@\text{NC}/\text{S}$  ( $1150 \text{ mAh g}^{-1}$ , Table S6, Supporting In-

formation) and most previously reported cathodes (Figure S30 and Table S7, Supporting Information).<sup>[16d,45]</sup> As the current density increases, from 0.1C to 0.2C, 0.5C, 1C, 2C, 3C, and 5C, the specific capacitance of the  $\text{NiS}_2/\text{NiSe}_2@\text{NC}/\text{S}$  cathode decreases from  $1458 \text{ mAh g}^{-1}$  to  $539 \text{ mAh g}^{-1}$  (Figure 7b). Even at 5C, the GCD curve of  $\text{NiS}_2/\text{NiSe}_2@\text{NC}/\text{S}$  maintains two clear discharge plateaus. When the current rate returns to 0.2C, a high specific capacity of  $1050 \text{ mAh g}^{-1}$  can still be obtained. As shown in Figures 7c,d and S31 (Supporting Information), the rate performance of the  $\text{NiS}_2/\text{NiSe}_2@\text{NC}/\text{S}$  cathode is improved over those of  $\text{NiS}_2@\text{NC}/\text{S}$  and  $\text{NiSe}_2@\text{NC}/\text{S}$  electrodes. Besides,  $\text{NiS}_2/\text{NiSe}_2@\text{NC}/\text{S}$  exhibits a smaller polarization voltage, at 131 mV, compared to  $\text{NiSe}_2@\text{NC}/\text{S}$  (173 mV) and  $\text{NiS}_2@\text{NC}/\text{S}$  (183 mV) (Figure 7e). The polarization voltage ( $\Delta E$ ) is here defined as the potential difference between the charge and discharge platforms at 50% charge/discharge capacity.<sup>[46]</sup> The ratio of the capacities of each discharge plateau,  $Q_2/Q_1$ , provides another measure of the catalytic activity of the cathode material toward the LiPSs conversion.  $Q_1$  accounts for the sulfur reaction with  $\text{Li}^+$  ions to soluble high-order LiPSs.<sup>[1a]</sup>  $Q_2$  accounts for the conversion of the soluble LiPS to solid  $\text{Li}_2\text{S}/\text{Li}_2\text{S}_2$ . The theoretical  $Q_2/Q_1$  ratio is 3, but due to the migration of a fraction of the soluble polysulfides and the incomplete  $\text{Li}_2\text{S}_2$  to  $\text{Li}_2\text{S}$  solid-state reaction, experimental  $Q_2/Q_1$  ratios are always below 3. Thus,  $Q_2/Q_1$  provides a measure of the effectiveness of the conversion of S to  $\text{Li}_2\text{S}$ . Consistent with previous results,  $\text{NiS}_2/\text{NiSe}_2@\text{NC}/\text{S}$  exhibits a higher  $Q_2/Q_1$  value (2.68) than  $\text{NiSe}_2@\text{NC}/\text{S}$  (2.47) and  $\text{NiS}_2@\text{NC}/\text{S}$  (2.13). Overall, these results confirm the effective role played by  $\text{NiS}_2/\text{NiSe}_2@\text{NC}$  in promoting the Li-S reaction kinetics for LSBs.

Consistently with the GCD cures, CV curves at  $0.1 \text{ mV s}^{-1}$  display two cathodic peaks,  $C_1$  and  $C_2$ , that account for the reduction of  $\text{S}_8$  to highly soluble LiPSs and precipitated  $\text{Li}_2\text{S}_2/\text{Li}_2\text{S}$ , respectively (Figure 7f). On the other hand, only one broad anodic peak, A, is associated with the oxidation of polysulfides to  $\text{S}_8$ .<sup>[47]</sup> Compared with  $\text{NiSe}_2@\text{NC}/\text{S}$  and  $\text{NiS}_2@\text{NC}/\text{S}$ ,  $\text{NiS}_2/\text{NiSe}_2@\text{NC}/\text{S}$  exhibits the highest peak currents, and the lowest oxidation peak and highest reduction peak potentials. Besides, the  $\text{NiS}_2/\text{NiSe}_2@\text{NC}/\text{S}$  cathode shows the highest cathodic and the lowest anodic peak onset potentials at a current density  $10 \mu\text{A cm}^{-2}$  above the baseline current (Figure S32, Supporting Information; Figure 7g).<sup>[48]</sup>

The CV curves at a scan rate of  $0.1\text{--}0.4 \text{ mV s}^{-1}$  within a voltage window  $1.7\text{--}2.8 \text{ V}$  are shown in Figure S33 (Supporting Information). As the scan rate increases, the current response gradually increases. All the cathodes tested displayed a linear relationship between the peak current ( $I_p$ ) and the square root of the scan rate ( $v$ ), implying a diffusion-limited response (Figure 7h). Thus, the  $\text{Li}^+$  diffusion coefficient ( $D_{\text{Li}^+}$ ) was calculated by the Randles Sevcik equation<sup>[49]</sup>:

$$I_p = 2.69 \times 10^5 n^{1.5} A D_{\text{Li}^+}^{0.5} C_{\text{Li}^+} v^{0.5} \quad (1)$$

where  $n$ ,  $A$ , and  $C_{\text{Li}^+}$  are the number of charges involved in the reaction, the electrode area, and the concentration of  $\text{Li}^+$ , respectively. For the  $\text{NiS}_2/\text{NiSe}_2@\text{NC}/\text{S}$  electrode, the  $D_{\text{Li}^+}$  estimated from the two cathodic peaks and the anodic peak are  $1.89 \times 10^{-7} \text{ cm}^2 \text{ s}^{-1}$ ,  $3.52 \times 10^{-7} \text{ cm}^2 \text{ s}^{-1}$ , and  $5.54 \times 10^{-7} \text{ cm}^2 \text{ s}^{-1}$ , respectively. These values are significantly larger than those



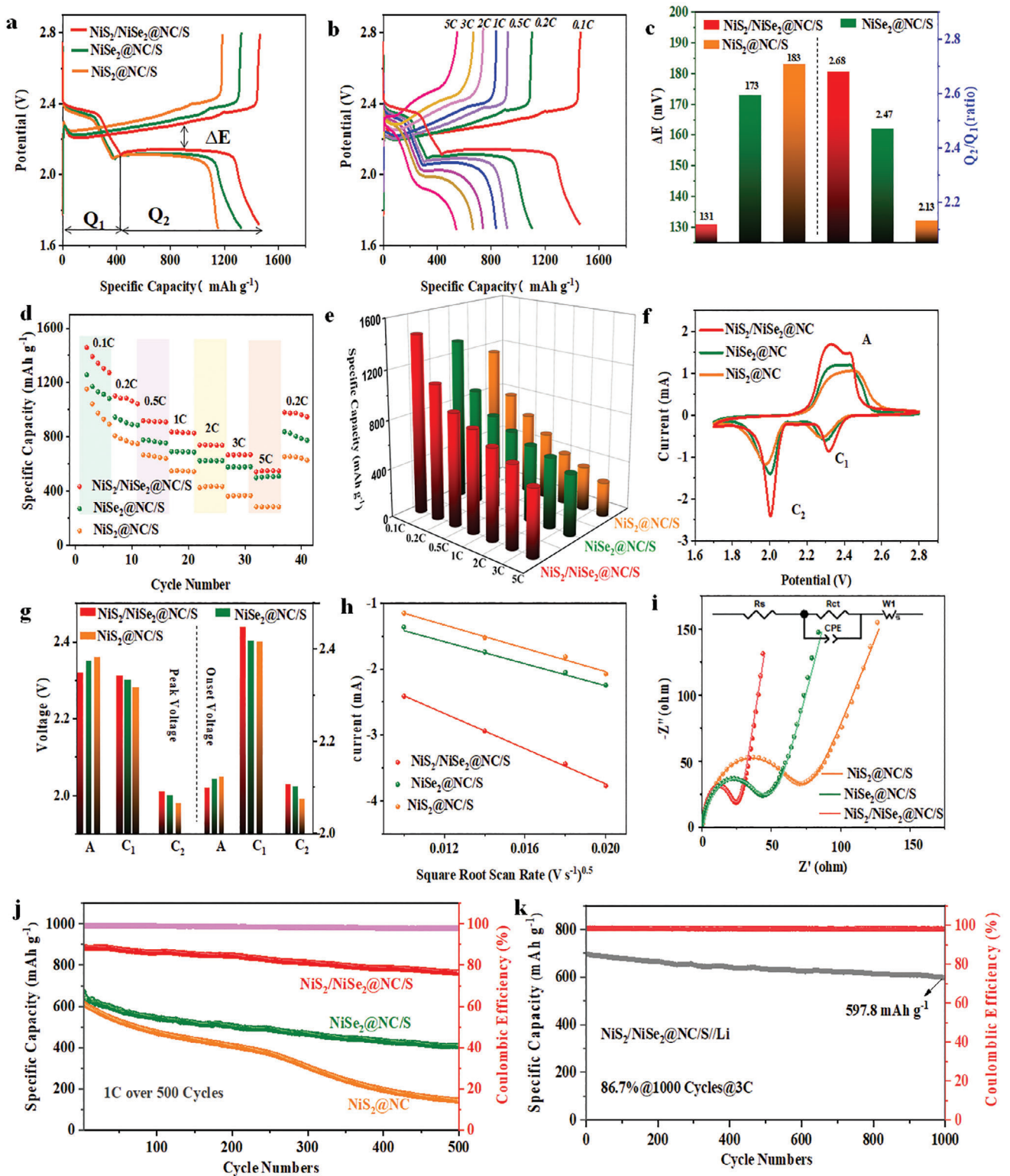


**Figure 7.** Coin cell characterization. a) GCD curves of  $\text{NiS}_2/\text{NiSe}_2@\text{NC}/\text{S}$ ,  $\text{NiSe}_2@\text{NC}/\text{S}$ , and  $\text{NiS}_2@\text{NC}/\text{S}$  cells at a current rate of 0.1C. b) GCD curve of the  $\text{NiS}_2/\text{NiSe}_2@\text{NC}/\text{S}$  cell at current rates in the range from 0.1C to 5C. c)  $\Delta E$  and  $Q_2/Q_1$  values. d, e) Rate performance. f) CV curves of  $\text{NiS}_2/\text{NiSe}_2@\text{NC}/\text{S}$ ,  $\text{NiSe}_2@\text{NC}/\text{S}$ , and  $\text{NiS}_2@\text{NC}/\text{S}$  at 0.1  $\text{mV s}^{-1}$ . g) Peak and onset potentials. h) Peak current vs. square root curve of scan rate. i) Nyquist plot of the EIS spectra. j) Cycle stability at a current rate of 1C. k) Long cycle test of the  $\text{NiS}_2/\text{NiSe}_2@\text{NC}/\text{S}$  cell at 3C.

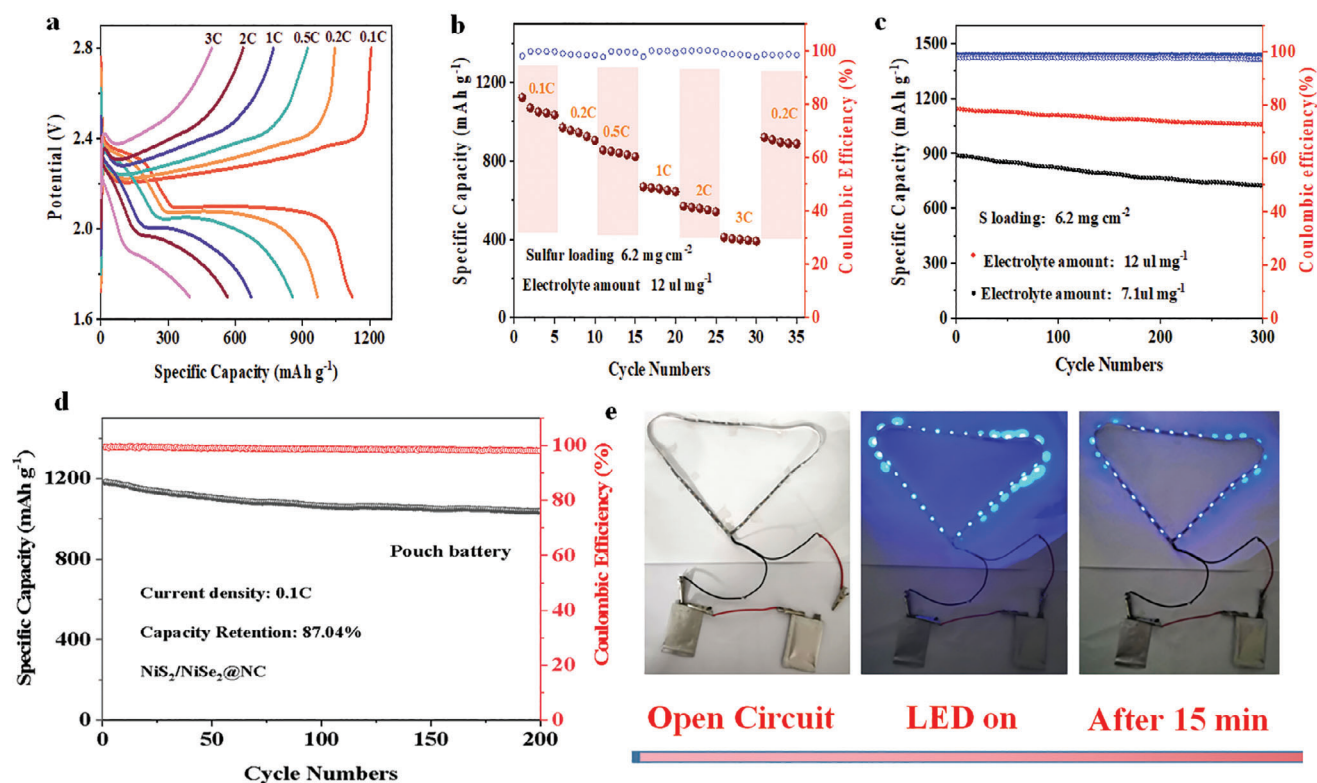


**Figure 8.** a) GCD curve of electrode  $\text{NiS}_2/\text{NiSe}_2@\text{NC}/\text{S}$  at high loadings ( $6.2 \text{ mg cm}^{-2}$ ). b) Rate performance. c) Cyclic stability of  $\text{NiS}_2/\text{NiSe}_2@\text{NC}/\text{S}$  at different amounts of electrolyte (0.1C). d) Long cycle test of pouch cells at 0.1C after 200 cycles. e)  $\text{NiS}_2/\text{NiSe}_2@\text{NC}/\text{S}$ -based pouch cells connected in series light an LED strip for 15 min.

obtained for the other chalcogenide-based cathodes tested (Figure S34, Supporting Information).

As shown in Figure 7i, the Nyquist plot of the EIS spectra of the different cathodes exhibits a semicircle in the high-frequency region and a straight line in the low-frequency region (Table S8, Supporting Information). The semicircle in the high-frequency region accounts for the charge transfer resistance, and the straight line in the low-frequency region is related to the diffusion resistance.<sup>[40,50]</sup> Among the electrodes tested,  $\text{NiS}_2/\text{NiSe}_2@\text{NC}/\text{S}$  was characterized by the smallest semicircle and highest slope in the high and low regions, respectively, indicating the smallest charge transfer and diffusion resistances.

To evaluate the cycling stability of different sulfur cathode materials, 500 continuous GCD cycles were tested at a current density of 1C (Figure 7j).  $\text{NiS}_2/\text{NiSe}_2@\text{NC}/\text{S}$  exhibits a higher initial capacity compared to  $\text{NiSe}_2@\text{NC}/\text{S}$  and  $\text{NiS}_2@\text{NC}$ . Besides,  $\text{NiS}_2/\text{NiSe}_2@\text{NC}/\text{S}$  also exhibits a higher capacity retention, at 87.0%, compared with  $\text{NiSe}_2@\text{NC}/\text{S}$  (60.6%) and  $\text{NiS}_2@\text{NC}/\text{S}$  (23.1%) after 500 cycles (Figure S35, Supporting Information). After 1000 cycles at 3C, the  $\text{NiS}_2/\text{NiSe}_2@\text{NC}$  cell displays a capacity decay rate of just 0.058% per cycle (Figure 7k). Also, after 200 cycles at low current rates (0.1C), the  $\text{NiS}_2/\text{NiSe}_2@\text{NC}/\text{S}$  demonstrates a high capacity retention rate (Figure S36, Supporting Information).

To analyze the stability of the  $\text{NiS}_2/\text{NiSe}_2@\text{NC}$  architecture upon cycling, a coin cell was cycled for 300 cycles at a 3C current rate. Subsequently, the electrodes were disassembled, and

SEM analysis was performed (Figure S37, Supporting Information). SEM images revealed that after cycling, most of the spherical particles remained intact without breaking. Moreover, these particles retained their hollow structure, with only a minor portion exhibiting collapse with the volume expansion during the charge and discharge processes. Overall, the hollow structure of the  $\text{NiS}_2/\text{NiSe}_2@\text{NC}$  particles showed considerable stability even after enduring prolonged cycling at relatively high current rates.

The separation of the postmortem cells was also analyzed after 100 cycles at 1C. Compared with  $\text{NiSe}_2@\text{NC}/\text{S}$  and  $\text{NiS}_2@\text{NC}/\text{S}$ , the separator of the post-mortem  $\text{NiS}_2/\text{NiSe}_2@\text{NC}/\text{S}$  cell was almost transparent, indicating that a minimal amount of LiPS had reached the membrane (Figure S38, Supporting Information). Moreover, the Li anode of the cycled  $\text{NiS}_2/\text{NiSe}_2@\text{NC}/\text{S}$  coin cell exhibited lower corrosion and S concentration, as shown in Figures S39 and S40 (Supporting Information).

The amount of S and electrolyte are key parameters to evaluate the practical application of LSB. The GCD curves at different current densities of a  $\text{NiS}_2/\text{NiSe}_2@\text{NC}/\text{S}$ -based cell with a relatively high sulfur loading,  $6.2 \text{ mg cm}^{-2}$ , and a low electrolyte content,  $12 \text{ ul mg}^{-1}$ , are shown in Figure 8a. All the GCD curves exhibit two discharge plateaus and one charge plateau, demonstrating an excellent rate performance (Figure 8b) and stability (Figure 8c), with a specific capacity of  $1058 \text{ mAh g}^{-1}$  maintained after 300 cycles at 0.1C. Even when further reducing the electrolyte content to  $7.1 \text{ ul mg}^{-1}$ , the  $\text{NiS}_2/\text{NiSe}_2@\text{NC}/\text{S}$  cathode was able to maintain a capacity of  $720.1 \text{ mAh g}^{-1}$  after 300 cycles. Finally, pouch

cells were assembled using the  $\text{NiS}_2/\text{NiSe}_2@\text{NC}/\text{S}$  cathode (see details in SI), and their cycling stability was tested. After 200 cycles, the pouch cells retained above 87% of their initial capacity (Figure 8d,e shows how two  $\text{NiS}_2/\text{NiSe}_2@\text{NC}$ -based pouch cells connected in series can power an LED strip for 15 minutes.).

### 3. Conclusions

In summary, heterostructured  $\text{NiS}_2/\text{NiSe}_2$  particles wrapped within N-doped carbon spheres and displaying a hollow architecture were produced from a Ni-MOF precursor. Magnetic measurements and computational results show the heterostructure to be characterized by  $\text{Ni}^{3+}$  in a high electronic spin state.  $\text{NiS}_2/\text{NiSe}_2@\text{C}$  exhibits orbital spin splitting and possesses a high spin configuration with more unpaired electrons. This high spin state regulates the electronic structure resulting in excellent binding strength and catalytic ability toward LiPS. The porous hollow structure not only effectively confines sulfur, but also provides additional buffer space for the electrochemical reaction.  $\text{NiS}_2/\text{NiSe}_2@\text{NC}$  is used as the host material in the sulfur cathode of LSBs, displaying excellent electrochemical performance. This excellent performance includes a high charge-discharge capacity, excellent rate capability, and long cycle life. This work not only demonstrates the catalytic properties of  $\text{NiS}_2/\text{NiSe}_2$ , but also exemplifies the effect of spin polarization in electrocatalytic reactions.

### Supporting Information

Supporting Information is available from the Wiley Online Library or from the author.

### Acknowledgements

This work was financially supported by the SyDECat project from the Spanish MCIN/AEI/FEDER (PID2022-136883OB-C22), the 2BoSS project of the ERA-MIN3 program with the Spanish grant number PCI2022-132985/AEI/10.13039/501100011033, Generalitat de Catalunya 2021SGR01581 and 2021SGR00457 and European Union Next Generation EU / PRTR. C. H., J. Y., C. Y. Z., and B. F. N. thank the China Scholarship Council for the scholarship support. ICN2 acknowledges the support from the Severo Ochoa Programme (MINECO, grant no. SEV-2017-0706). IREC and ICN2 are both funded by the CERCA Program/Generalitat de Catalunya. This project has received funding from the European Union's Horizon 2020 research and innovation program under grant agreement No 823717-ESTEEM3. These In situ XRD and XAS experiments were performed at the Melbourne Synchrotron, Australia. J. Li is grateful for the project supported by the Natural Science Foundation of Sichuan (2022NS-FSC1229). The authors also greatly acknowledge the support supported by the Supercomputing Center of Lanzhou University, China. This work has received funding from the "Spanish Ministry of Science and Innovation" through "Severo Ochoa" (CEX2019-000917-S) and "OXISOT" (PID2021-128410OB-I00). This study is part of the Advanced Materials program and was supported by MCIN with funding from European Union Next Generation EU (PRTR-C17.11) and by Generalitat de Catalunya. Part of the present work has been performed in the framework of Universitat Autònoma de Barcelona Materials Science PhD program. The authors acknowledge the use of instrumentation as well as the technical advice provided by the Joint Electron Microscopy Center at ALBA (JEMCA). ICN2 acknowledges funding from Grant IU16-014206 (METCAM-FIB) funded by the European Union through the European Regional Development Fund (ERDF), with the support of the Ministry of Research and Universities, Generalitat de Catalunya. ICN2 is a founding member of e-DREAM.

### Conflict of Interest

The authors declare no conflict of interest.

### Data Availability Statement

The data that support the findings of this study are available from the corresponding author upon reasonable request.

### Keywords

hollow particle, homologous heterostructure, lithium-sulfur battery, lithium polysulfides, nickel selenide, nickel sulfide, spin state

Received: January 16, 2024

Revised: March 8, 2024

Published online: April 10, 2024

- [1] a) D. Yang, M. Li, X. Zheng, X. Han, C. Zhang, J. Jacas Biendicho, J. Llorca, J. Wang, H. Hao, J. Li, G. Henkelman, J. Arbiol, J. R. Morante, D. Mitlin, S. Chou, A. Cabot, *ACS Nano* **2022**, *16*, 11102; b) H. Pan, Z. Cheng, Z. Zhou, S. Xie, W. Zhang, N. Han, W. Guo, J. Fransaer, J. Luo, A. Cabot, M. Wübbenhorst, *Nano-Micro Lett.* **2023**, *15*, 165.
- [2] a) L. Peng, M. Zhang, L. Zheng, Q. Yuan, Z. Yu, J. Shen, Y. Chang, Y. Wang, A. Li, *Small Methods* **2022**, *6*, 2200332; b) C. Zhang, R. Du, S. Martí-Sánchez, K. Xiao, D. Yang, C. Zhang, C. Li, G. Zeng, X. Chang, R. He, J. Arbiol, J. Li, J. J. Biendicho, A. Cabot, *Energies* **2023**, *16*, 4545.
- [3] a) X. Lv, T. Lei, B. Wang, W. Chen, Y. Jiao, Y. Hu, Y. Yan, J. Huang, J. Chu, C. Yan, C. Wu, J. Wang, X. Niu, J. Xiong, *Adv. Energy Mater.* **2019**, *9*, 1901800; b) Y. Gong, Y. Wang, Z. Fang, S. Zhao, Y.-s. He, W. Zhang, J. Mu, L. Zhang, Z.-F. Ma, *Chem. Eng. J.* **2022**, *446*, 136943.
- [4] a) C. Zhang, B. Fei, D. Yang, H. Zhan, J. Wang, J. Diao, J. Li, G. Henkelman, D. Cai, J. J. Biendicho, J. R. Morante, A. Cabot, *Adv. Funct. Mater.* **2022**, *32*, 2201322; b) S. Hu, M. Yi, H. Wu, T. Wang, X. Ma, X. Liu, J. Zhang, *Adv. Funct. Mater.* **2021**, *32*, 2111084; c) D. Yang, Z. Liang, C. Zhang, J. J. Biendicho, M. Botifoll, M. C. Spadaro, Q. Chen, M. Li, A. Ramon, A. O. Moghaddam, J. Llorca, J. Wang, J. R. Morante, J. Arbiol, S.-L. Chou, A. Cabot, *Adv. Energy Mater.* **2021**, *11*, 2101250; d) Z. Liang, D. Yang, P. Tang, C. Zhang, J. Jacas Biendicho, Y. Zhang, J. Llorca, X. Wang, J. Li, M. Heggen, J. David, R. E. Dunin-Borkowski, Y. Zhou, J. R. Morante, A. Cabot, J. Arbiol, *Adv. Energy Mater.* **2021**, *11*, 2003507; e) C. Y. Zhang, L. Gong, C. Zhang, X. Cheng, L. Balcells, G. Zeng, J. J. Biendicho, J. Li, G. Z. Sun, J. Y. Zhou, A. Cabot, *Adv. Funct. Mater.* **2023**, *33*, 2305908; f) C. Y. Zhang, X. Lu, X. Han, J. Yu, C. Zhang, C. Huang, L. Balcells, A. G. Manjón, J. Jacas Biendicho, J. Li, J. Arbiol, G. Sun, J. Y. Zhou, A. Cabot, *J. Am. Chem. Soc.* **2023**, *145*, 18992.
- [5] a) L. Guan, H. Hu, L. Li, Y. Pan, Y. Zhu, Q. Li, H. Guo, K. Wang, Y. Huang, M. Zhang, Y. Yan, Z. Li, X. Teng, J. Yang, J. Xiao, Y. Zhang, X. Wang, M. Wu, *ACS Nano* **2020**, *14*, 6222; b) J. Li, C. Chen, Y. Chen, Z. Li, W. Xie, X. Zhang, M. Shao, M. Wei, *Adv. Energy Mater.* **2019**, *9*, 1901935.
- [6] C. Y. Zhang, G. W. Sun, Z. De Shi, Q. Y. Liu, J. L. Pan, Y. C. Wang, H. Zhao, G. Z. Sun, X. P. Gao, X. J. Pan, J. Y. Zhou, *Energy Storage Mater.* **2021**, *43*, 471.
- [7] a) V. P. Ananikov, *ACS Catal.* **2015**, *5*, 1964; b) P. Sabatier, *Catalysis in organic chemistry*, D. Van Nostrand Company, **1922**; c) L. Yang, R. He, X. Wang, T. Yang, T. Zhang, Y. Zuo, X. Lu, Z. Liang, J. Li, J. Arbiol, P. R. Martínez-Alanis, X. Qi, A. Cabot, *Nano Energy* **2023**, *115*, 108714.
- [8] a) Y. Liu, P. Vijayakumar, Q. Liu, T. Sakthivel, F. Chen, Z. Dai, *Nano Lett.* **2022**, *22*, 43; b) J. Li, L. Li, X. Ma, X. Han, C. Xing, X. Qi, R. He, J.



- Arbiol, H. Pan, J. Zhao, J. Deng, Y. Zhang, Y. Yang, A. Cabot, *Adv. Sci.* **2023**, *10*, 2300841.
- [9] J. He, A. Manthiram, *Adv. Energy Mater.* **2020**, *10*, 2002654.
- [10] C. Ye, L. Zhang, C. Guo, D. Li, A. Vasileff, H. Wang, S.-Z. Qiao, *Adv. Funct. Mater.* **2017**, *27*, 1702524.
- [11] J. Wang, L. Zhou, D. Guo, X. Wang, G. Fang, X. a. Chen, S. Wang, *Small* **2023**, *19*, 2206926.
- [12] Z. Jin, T. Lin, H. Jia, B. Liu, Q. Zhang, L. Chen, L. Zhang, L. Li, Z. Su, C. Wang, *Nanoscale* **2020**, *12*, 16201.
- [13] B. Qin, X. Zhao, Q. Wang, W. Yao, Y. Cai, Y. Chen, P. Wang, Y. Zou, J. Cao, X. Zheng, J. Qi, W. Cai, *Energy Storage Mater.* **2023**, *55*, 445.
- [14] T. L. L. Doan, D. C. Nguyen, R. Amaral, N. Y. Dzade, C. S. Kim, C. H. Park, *Appl. Catal., B* **2022**, *319*, 121934.
- [15] X. Han, L. Zhao, Y. Liang, J. Wang, Y. Long, Z. Zhou, Y. Zhang, Y. Li, J. Ma, *Adv. Energy Mater.* **2022**, *12*, 2202747.
- [16] a) Z.-y. Mei, G. Zhao, C. Xia, S. Cai, Q. Jing, X. Sheng, H. Wang, X. Zou, L. Wang, H. Guo, B. Y. Xia, *Angew. Chem., Int. Ed.* **2023**, *62*, e202303871; b) Y. Li, Y. Ji, Y. Zhao, J. Chen, S. Zheng, X. Sang, B. Yang, Z. Li, L. Lei, Z. Wen, X. Feng, Y. Hou, *Adv. Mater.* **2022**, *34*, 2202240; c) Q. Wang, T. Liu, K. Chen, D. Wu, C. Chen, M. Chen, X. Ma, J. Xu, T. Yao, Y. Li, H. Zhou, Y. Wu, *Small* **2022**, *18*, 2204015; d) D. Lu, X. Wang, Y. Hu, L. Yue, Z. Shao, W. Zhou, L. Chen, W. Wang, Y. Li, *Adv. Funct. Mater.* **2023**, *33*, 2212689; e) D. Wu, H.-Q. Yin, Z. Wang, M. Zhou, C. Yu, J. Wu, H. Miao, T. Yamamoto, W. Zhaxi, Z. Huang, L. Liu, W. Huang, W. Zhong, Y. Einaga, J. Jiang, Z.-M. Zhang, *Angew. Chem., Int. Ed.* **2023**, *62*, e202301925; f) T. He, Y. Chen, Q. Liu, B. Lu, X. Song, H. Liu, M. Liu, Y.-N. Liu, Y. Zhang, X. Ouyang, S. Chen, *Angew. Chem., Int. Ed.* **2022**, *61*, e202201007; g) Z. Zhao, M. Hu, T. Nie, W. Zhou, B. Pan, B. Xing, L. Zhu, *Environ. Sci. Technol.* **2023**, *57*, 4556.
- [17] a) Y. Wang, P. Meng, Z. Yang, M. Jiang, J. Yang, H. Li, J. Zhang, B. Sun, C. Fu, *Angew. Chem., Int. Ed.* **2023**, *62*, e202304229; b) Q. Zhang, R. Ao, R. Gao, H. Yang, *Inorg. Chem.* **2022**, *61*, 19780; c) C. Y. Zhang, C. Zhang, G. W. Sun, J. L. Pan, L. Gong, G. Z. Sun, J. J. Biendicho, L. Balcells, X. L. Fan, J. R. Morante, J. Y. Zhou, A. Cabot, *Angew. Chem., Int. Ed.* **2022**, *61*, e202211570.
- [18] H. Li, M. Chuai, X. Xiao, Y. Jia, B. Chen, C. Li, Z. Piao, Z. Lao, M. Zhang, R. Gao, B. Zhang, Z. Han, J. Yang, G. Zhou, *J. Am. Chem. Soc.* **2023**, *145*, 22516.
- [19] M. Li, Y. Liu, Y. Zhang, X. Han, T. Zhang, Y. Zuo, C. Xie, K. Xiao, J. Arbiol, J. Llorca, M. Ibáñez, J. Liu, A. Cabot, *ACS Nano* **2021**, *15*, 4967.
- [20] a) S. Ni, H. Qu, Z. Xu, X. Zhu, L. Chen, H. Xing, X. Wu, H. Liu, L. Yang, *ACS Appl. Mater. Interfaces* **2023**, *15*, 36423; b) R. Liang, C. Shu, A. Hu, M. Li, Z. Ran, R. Zheng, J. Long, *Chem. Eng. J.* **2020**, *393*, 124592.
- [21] J. Zhu, W. Tu, H. Pan, H. Zhang, B. Liu, Y. Cheng, Z. Deng, H. Zhang, *ACS Nano* **2020**, *14*, 5780.
- [22] a) C. Huang, S. Lv, A. Gao, J. Ling, F. Yi, J. Hao, M. Wang, Z. Luo, D. Shu, *Chem. Eng. J.* **2022**, *431*, 134083; b) C. Huang, A. Gao, F. Yi, Y. Wang, D. Shu, Y. Liang, Z. Zhu, J. Ling, J. Hao, *Chem. Eng. J.* **2021**, *419*, 129643.
- [23] a) A. Muthurasu, P. Sampath, T. H. Ko, P. C. Lohani, I. Pathak, D. Acharya, K. Chhetri, D. H. Kim, H. Y. Kim, *Appl. Catal., B* **2023**, *330*, 122523; b) Y. Wang, Y. Wang, H. Gao, Z. Huang, Q. Hao, B. Liu, *Chem. Eng. J.* **2023**, *451*, 138515.
- [24] J. Luo, Y. Liu, H. Xiao, Y. Wang, Y. Mao, Y. Zhang, Y. Su, Y. Xia, S. Chen, Q. Deng, Z. Zeng, S. Deng, J. Wang, *Chem. Eng. J.* **2023**, *451*, 138677.
- [25] F. Zhou, R. Wang, S. He, X. Liu, S. Liu, H. Shao, X. Liu, Z. Xiao, J. Liu, *Adv. Funct. Mater.* **2022**, *33*, 2211124.
- [26] F. Zou, Y.-M. Chen, K. Liu, Z. Yu, W. Liang, S. M. Bhaway, M. Gao, Y. Zhu, *ACS Nano* **2016**, *10*, 377.
- [27] X. Liu, F. Zou, K. Liu, Z. Qiang, C. J. Taubert, P. Ustrian, B. D. Vogt, Y. Zhu, *J. Mater. Chem. A* **2017**, *5*, 11781.
- [28] F.-X. Ma, H. Hu, H. B. Wu, C.-Y. Xu, Z. Xu, L. Zhen, X. W. Lou, *Adv. Mater.* **2015**, *27*, 4097.
- [29] a) S. Jiang, F. Chen, L. Zhu, Z. Yang, Y. Lin, Q. Xu, Y. Wang, *ACS Appl. Mater. Interfaces* **2022**, *14*, 10227; b) N. S. McIntyre, M. G. Cook, *Anal. Chem.* **1975**, *47*, 2208.
- [30] Z. Xue, X. Li, Q. Liu, M. Cai, K. Liu, M. Liu, Z. Ke, X. Liu, G. Li, *Adv. Mater.* **2019**, *31*, 1900430.
- [31] a) Q. Li, R. Deng, Y. Chen, J. Gong, P. Wang, Q. Zheng, Y. Huo, F. Xie, X. Wei, C. Yang, *Small* **2023**, *19*, 2303642; b) H. Deng, L. Yao, Q.-A. Huang, Q. Su, J. Zhang, F. Zhang, G. Du, *RSC Adv.* **2017**, *7*, 9819; c) Z. Li, X. Yu, A. Gu, H. Tang, L. Wang, Z. Lou, *Nanotechnology* **2017**, *28*, 065406; d) S. Srinivasa Rao, D. Punnoose, J.-H. Bae, I. K. Durga, C. V. Thulasi-Varma, B. Naresh, A. Subramanian, V. Raman, H.-J. Kim, *Electrochim. Acta* **2017**, *254*, 269; e) J.-Y. Luo, F.-C. Hu, B.-J. Xi, Q.-W. Han, X.-Q. Wu, Y.-P. Wu, Q. Zhang, R. Chi, D.-S. Li, *Inorg. Chem. Commun.* **2022**, *143*, 109777; f) J. Li, Z. Ding, J. Li, C. Wang, L. Pan, G. Wang, *Chem. Eng. J.* **2021**, *407*, 127199; g) C. Zhou, S. Wan, Y. Chen, L. Fu, H. Chen, C. Kang, Q. Liu, *J. Power Sources* **2021**, *509*, 230401.
- [32] W. Bao, L. Liu, C. Wang, S. Choi, D. Wang, G. Wang, *Adv. Energy Mater.* **2018**, *8*, 1870060.
- [33] L. Ren, J. Liu, Y. Zhao, Y. Wang, X. Lu, M. Zhou, G. Zhang, W. Liu, H. Xu, X. Sun, *Adv. Funct. Mater.* **2023**, *33*, 2210509.
- [34] S. Hu, X. Huang, L. Zhang, G. Li, S. Chen, J. Zhang, X. Liu, *Adv. Funct. Mater.* **2023**, *33*, 2214161.
- [35] a) Z. Zhao, D. Wang, R. Gao, G. Wen, M. Feng, G. Song, J. Zhu, D. Luo, H. Tan, X. Ge, W. Zhang, Y. Zhang, L. Zheng, H. Li, Z. Chen, *Angew. Chem., Int. Ed.* **2021**, *60*, 11910; b) J. Wang, X. Huang, S. Xi, J.-M. Lee, C. Wang, Y. Du, X. Wang, *Angew. Chem., Int. Ed.* **2019**, *58*, 13532; c) J. Song, Z. Chen, X. Cai, X. Zhou, G. Zhan, R. Li, P. Wei, N. Yan, S. Xi, K. P. Loh, *Adv. Mater.* **2022**, *34*, 2204638.
- [36] a) D. Zhang, Y. Li, P. Wang, J. Qu, S. Zhan, Y. Li, *Angew. Chem., Int. Ed.* **2023**, *62*, e202303807; b) C. Zhang, S. Yang, J. Wu, M. Liu, S. Yazdi, M. Ren, J. Sha, J. Zhong, K. Nie, A. S. Jalilov, Z. Li, H. Li, B. I. Yakobson, Q. Wu, E. Ringe, H. Xu, P. M. Ajayan, J. M. Tour, *Adv. Energy Mater.* **2018**, *8*, 1703487.
- [37] M. W. Haverkort, Z. Hu, J. C. Cezar, T. Burnus, H. Hartmann, M. Reuther, C. Zobel, T. Lorenz, A. Tanaka, N. B. Brookes, H. H. Hsieh, H. J. Lin, C. T. Chen, L. H. Tjeng, *Phys. Rev. Lett.* **2006**, *97*, 176405.
- [38] W. Yao, C. Tian, C. Yang, J. Xu, Y. Meng, I. Manke, N. Chen, Z. Wu, L. Zhan, Y. Wang, R. Chen, *Adv. Mater.* **2022**, *34*, 2106370.
- [39] S. Zhang, Q. Zhou, Z. Shen, X. Jin, Y. Zhang, M. Shi, J. Zhou, J. Liu, Z. Lu, Y.-N. Zhou, H. Zhang, *Adv. Funct. Mater.* **2021**, *31*, 2101922.
- [40] C. Huang, J. Yu, C. Li, Z. Cui, C. Zhang, C. Zhang, B. Nan, J. Li, J. Arbiol, A. Cabot, *Adv. Funct. Mater.* **2023**, *31*, 2305624.
- [41] W. Yao, W. Zheng, J. Xu, C. Tian, K. Han, W. Sun, S. Xiao, *ACS Nano* **2021**, *15*, 7114.
- [42] a) J. He, A. Bhargava, A. Manthiram, *Adv. Mater.* **2020**, *32*, 2004741; b) B. Yu, A. Huang, K. Srinivas, X. Zhang, F. Ma, X. Wang, D. Chen, B. Wang, W. Zhang, Z. Wang, J. He, Y. Chen, *ACS Nano* **2021**, *15*, 13279.
- [43] M. Shi, Z. Liu, S. Zhang, S. Liang, Y. Jiang, H. Bai, Z. Jiang, J. Chang, J. Feng, W. Chen, H. Yu, S. Liu, T. Wei, Z. Fan, *Adv. Energy Mater.* **2022**, *12*, 2103657.
- [44] C. Zhang, R. Du, J. J. Biendicho, M. Yi, K. Xiao, D. Yang, T. Zhang, X. Wang, J. Arbiol, J. Llorca, Y. Zhou, J. R. Morante, A. Cabot, *Adv. Energy Mater.* **2021**, *11*, 2100432.
- [45] a) D. Fang, G. Wang, S. Huang, T. C. Li, J. Yu, D. Xiong, D. Yan, X. L. Li, J. Zhang, Y. Von Lim, S. A. Yang, H. Ying Yang, *Chem. Eng. J.* **2021**, *417*, 128546; b) Q. Hao, G. Cui, Y. Zhang, J. Li, Z. Zhang, *Chem. Eng. J.* **2020**, *381*, 122672; c) L. Wu, J. Hu, X. Yang, Z. Liang, S. Chen, L. Liu, H. Hou, J. Yang, *J. Mater. Chem. A* **2022**, *10*, 23811; d) Z. Wu, S. Chen, L. Wang, Q. Deng, Z. Zeng, J. Wang, S. Deng, *Energy Storage Mater.* **2021**, *38*, 381; e) S. Chen, J. Luo, N. Li, X. Han, J. Wang, Q. Deng, Z. Zeng, S. Deng, *Energy Storage Mater.* **2020**, *30*, 187.
- [46] H. Zhang, S. Xin, J. Li, H. Cui, Y. Liu, Y. Yang, M. Wang, *Nano Energy* **2021**, *85*, 106011.

- [47] W. Liu, C. Luo, S. Zhang, B. Zhang, J. Ma, X. Wang, W. Liu, Z. Li, Q.-H. Yang, W. Lv, *ACS Nano* **2021**, *15*, 7491.
- [48] C. Zhang, J. J. Biendicho, T. Zhang, R. Du, J. Li, X. Yang, J. Arbiol, Y. Zhou, J. R. Morante, A. Cabot, *Adv. Funct. Mater.* **2019**, *29*, 1903842.
- [49] R. Chu, T. T. Nguyen, Y. Bai, N. H. Kim, J. H. Lee, *Adv. Energy Mater.* **2022**, *12*, 2102805.
- [50] a) J. He, Y. Chen, W. Lv, K. Wen, C. Xu, W. Zhang, W. Qin, W. He, *ACS Energy Lett.* **2016**, *1*, 820; b) W. Gao, B. Song, Q. Zhang, J. He, Y. Wu, *Small* **2023**, *23* 10225, <https://doi.org/10.1002/sml.202310225>.

# ADVANCED MATERIALS

## Supporting Information

for *Adv. Mater.*, DOI 10.1002/adma.202400810

Electronic Spin Alignment within Homologous NiS<sub>2</sub>/NiSe<sub>2</sub> Heterostructures to Promote Sulfur Redox Kinetics in Lithium-Sulfur Batteries

*Chen Huang, Jing Yu, Chao Yue Zhang\*, Zhibiao Cui, Jiakun Chen, Wei-Hong Lai, Yao-Jie Lei\*, Bingfei Nan, Xuan Lu, Ren He, Li Gong, Junshan Li, Canhuang Li, Xuede Qi, Qian Xue, Jin Yuan Zhou, Xueqiang Qi, Lluís Balcells, Jordi Arbiol and Andreu Cabot\**

## ***Supporting Information for***

### **Electronic Spin Alignment within Homologous NiS<sub>2</sub>/NiSe<sub>2</sub> Heterostructures to Promote Sulfur Redox Kinetics in Lithium-Sulfur Batteries**

*Chen Huang, Jing Yu, Chao Yue Zhang\*, Zhibiao Cui, Jiakun Chen, Wei-Hong Lai, Yao-Jie Lei\*, Bingfei Nan, Xuan Lu, Ren He, Li Gong, Junshan Li, Canhuang Li, Xuede Qi, Qian Xue, Jin Yuan Zhou, Xueqiang Qi, Lluís Balcells, Jordi Arbiol, and Andreu Cabot\**

*C. Huang, J. Yu, B. F. Nan, X. Lu, R. He, L. Gong, C. H. Li, A. Cabot  
Catalonia Institute for Energy Research-IREC  
Sant Adrià de Besòs, Barcelona 08930, Spain  
E-mail: acabot@irec.cat*

*C. Huang, L. Gong, C. H. Li  
Department of Chemistry  
University of Barcelona 08028, Spain*

*C. Y. Zhang, J. Y. Zhou  
Key Laboratory for Magnetism and Magnetic Materials of the Ministry of Education &  
School of Physical Science & Technology  
Lanzhou University Lanzhou 730000, China  
E-mail: zhangchy2020@lzu.edu.cn*

*J. Yu, J. Arbiol  
Catalan Institute of Nanoscience and Nanotechnology (ICN2), CSIC and BIST, Campus UAB,  
Bellaterra, 08193 Barcelona, Catalonia, Spain.*

*Z. B. Cui  
School of Chemistry, South China Normal University, Guangzhou 510006, PR China*

*J. K. Chen  
Analysis and Testing Center, South China Normal University, Guangzhou 510006, China*

*W. H. Lai, Y. J. Lei  
Institute for Superconducting and Electronic Materials  
Australian Institute of Innovative Materials  
Innovation Campus  
University of Wollongong  
Wollongong, NSW, 2500, Australia  
E-mail: yl876@uowmail.edu.au*

*X. D. Qi, Q. Xue, X. Q. Qi  
College of Chemistry and Chemical Engineering  
Chongqing University of Technology, Chongqing, 400054 China*

*J. S. Li  
Institute for Advanced Study*

Chengdu University 610106, Chengdu, China

*L. Balcells*

*Institut de Ciència de Materials de Barcelona,  
Campus de la UAB, 08193 Bellaterra, Catalonia, Spain*

*J. Arbiol and A. Cabot*

*ICREA Pg. Lluís Companys, 08010 Barcelona, Catalonia, Spain*

*\* Corresponding authors*

## **Experimental**

### ***Physical Characterizations***

The crystal structure was tested by X-ray diffraction (XRD). The morphology of the as-prepared samples (NiS<sub>2</sub>/NiSe<sub>2</sub>@NC, NiSe<sub>2</sub>@ NC, and NiS<sub>2</sub>@NC) was characterized by scanning electron microscopy (SEM) and transmission electron microscopy (TEM). The surface composition and chemical state of the host materials were confirmed by X-ray photoelectron spectroscopy (XPS). Thermogravimetric analysis (TGA) was used to measure the S content in the cathode from 50°C to 400°C under a 5°C·min<sup>-1</sup> heating rate in an N<sub>2</sub> atmosphere. UV-vis absorption spectroscopy was used to analyze the adsorption performance of electrode materials on polysulfides. The XAFS data were processed according to the standard procedures using the Athena module implemented in the IFEFFIT software packages. The EXAFS spectra were obtained by subtracting the post-edge background from the overall absorption and then normalizing with respect to the edge-jump step. Subsequently, the  $\chi(k)$  data were Fourier transformed to real (R) space using Hanning windows ( $dk = 1.0 \text{ \AA}^{-1}$ ) to separate the EXAFS contributions from different coordination shells. To obtain the quantitative structural parameters around central atoms, least-squares curve parameter fitting was performed using the ARTEMIS module of the IFEFFIT software packages. The magnetic behavior was performed using SQUID magnetometer.

### ***Electrochemical Measurements***

The prepared electrode material (NiS<sub>2</sub>/NiSe<sub>2</sub>@NC, NiSe<sub>2</sub>@ NC, and NiS<sub>2</sub>@NC), Super P and polyvinylidene fluoride (PVDF) binder were mixed and ground according to 8:1:1, and N-

methylpyrrolidone (NMP) was added during the grinding process to prepare slurry. Then it was evenly coated on the current collector on the aluminum foil, and finally dried at 60 °C for 12 h and cut into 12 mm circular pieces to obtain the working electrode. The sulfur content of the cathode was 2 mg·cm<sup>-2</sup>. To further highlight the practical application of the electrode, the high-loading cathode was prepared by the same method. The prepared sulfur electrode was used as the cathode, the lithium foil was used as the anode, and Celgard 2400 and 1.0 M LiTFSI and 0.1 M LiNO<sub>3</sub> were dissolved in DOL/DME (V:V=1:1) as the separator and electrolyte, respectively, to assemble a 2023 coin battery in argon-filled in the airy glove box. The prepared battery is subjected to CV and GCD tests at a voltage window of 1.7-2.8V, and an EIS test is performed at a frequency of 0.01Hz-100KHz.

### ***Materials***

Nickel Nitrate hexahydrate (AR, Ni(NO<sub>3</sub>)<sub>2</sub> · 6H<sub>2</sub>O) and trimesic acid (AR, H<sub>3</sub>BTC) were purchased from Fisher Chemical Co. All chemicals in the company are used without further processing, the deionized water is used during the experiment.

### ***Synthesis of Ni-MOF***

430 mg Ni (NO<sub>3</sub>)<sub>2</sub> · 6H<sub>2</sub>O, 150 mg trimesic acid and 1.5 g PVP were dissolved in a mixed solution of 60 mL absolute ethanol, deionized water, and DMF (V: V: V =1:1:1). The mixed solution was transferred to an autoclave and kept at 150 °C for 10 h. It was collected by centrifugation, washed five times with ethanol, and then dried at 60 °C to obtain green Ni-MOF.

### ***Synthesis of Ni @NC***

The as-prepared Ni-MOF was calcinated in Ar atmosphere at 500°C for 2 h under 2 °C·min<sup>-1</sup> to obtain Ni@C

### ***Synthesis of NiS<sub>2</sub>/NiSe<sub>2</sub>@NC***

100g sulfur powder and 100g selenium powder were mixed and ground evenly for 15min, placed upstream of the porcelain boat, and the prepared precursor (Ni@NC) was placed downstream of the porcelain boat, and heated at 400°C for 2h under an Ar atmosphere at a heating rate of 1°C·min<sup>-1</sup>. As a comparison, NiSe<sub>2</sub> @NC and NiS<sub>2</sub> @NC samples were also obtained by only adding 100 mg Se or 100 mg S powder via the above same procedure, respectively.



### ***Synthesis of NiS<sub>2</sub>/NiSe<sub>2</sub>@NC/S***

Firstly, the prepared Cathode host material (NiS<sub>2</sub>@NC, NiSe<sub>2</sub>@NC, and NiS<sub>2</sub>/NiSe<sub>2</sub>@NC) and sulfur powder were mixed according to the 1:3 ratio, secondly, after being fully ground in a mortar, kept in a vacuum oven at 155°C for 12 h, and then heated to 300°C to remove surface sulfur, and finally NiS<sub>2</sub>/NiSe<sub>2</sub>@NC/S, NiSe<sub>2</sub>@NC /S and NiS<sub>2</sub>@NC/S were obtained.

### ***Synthesis of Li<sub>2</sub>S<sub>6</sub> Solution and Adsorption Test***

Firstly, S and Li<sub>2</sub>S were dissolved into the mixed solution in DME and DOL according to the ratio of 5:1, and then heated at 80°C overnight to finally obtain the solution of Li<sub>2</sub>S<sub>6</sub>. To measure different sulfur cathode host materials, 15 mg host materials were soaked into the Li<sub>2</sub>S<sub>6</sub> solution, and stood for 12 h to observe the color change.

### ***Synthesis of Symmetrical Cells and Measurements***

Symmetrical cells were fabricated using a similar method as for LSBs. Two identical electrodes (NiS<sub>2</sub>@NC, NiSe<sub>2</sub>@NC, and NiS<sub>2</sub>/NiSe<sub>2</sub>@NC) were used as working and counter electrodes, respectively. 40  $\mu$ L of 0.5 M Li<sub>2</sub>S<sub>6</sub> and 1 M LiTFSI were dissolved in DOL/DME (V/V= 1:1) as the electrolyte. The loading mass of the electrode is about 0.5 mg·cm<sup>-2</sup>. The fabricated symmetric cells were tested at a scan rate of 5 mV·s<sup>-1</sup> by CV test.

### ***Nucleation experimental test of Li<sub>2</sub>S***

First, the prepared sulfur cathode host material (NiS<sub>2</sub>@NC, NiSe<sub>2</sub>@NC and NiS<sub>2</sub>/NiSe<sub>2</sub>@NC) was dissolved in ethanol solution, and then coated on carbon paper as the working electrode, and lithium foil as the counter electrode, 0.25 M Li<sub>2</sub>S<sub>8</sub> with 1.0 M LiTFSI in tetraethylene glycol dimethyl ether solution and 1.0 M LiTFSI solution without Li<sub>2</sub>S<sub>8</sub> were used as catholyte and anolyte respectively, the assembled coin cells were firstly discharged to 2.06V at a constant current, and then subjected to potentiostatic deposition at 2.05V voltage.

### ***DFT calculations***

All DFT calculations were performed using the Vienna Ab-initio Simulation Package (VASP). The Perdew-Burke-Ernzerhof (PBE) functional for the exchange-correlation term was used with the projector augmented wave (PAW) potentials and a cutoff energy of 400 eV. The convergence of energy and forces were set to 1×10<sup>-4</sup> eV and 0.05 eV/Å, respectively. The heterojunction model was constructed by the NiSe<sub>2</sub> and NiS<sub>2</sub>. The lattice mismatch was no more

than 3% and the vacuum layer was set as 15 Å to avoid the interactions between layers. The adsorption energy  $\Delta E_{ad}$  was calculated as:

$$\Delta E_{ad} = E_{(surf+ad)} - E_{surf} - E_{ad}$$

where  $E_{(surf+ad)}$  is the energy of the LiPS adsorbed on the surface,  $E_{surf}$  is the energy of the clean surface, and  $E_{ad}$  is the energy of the free LiPS.

The formula for calculating the Gibbs free as fellow:

$$\Delta G(S_8-Li_2S_8): E_{Li_2S_8} - E_{S_8} - 2E_{Li^+}$$

$$\Delta G(Li_2S_8-Li_2S_6): E_{Li_2S_6} - E_{Li_2S_8} + 0.25E_{S_8}$$

$$\Delta G(Li_2S_6-Li_2S_4): E_{Li_2S_4} - E_{Li_2S_6} + 0.25E_{S_8}$$

$$\Delta G(Li_2S_4-Li_2S_2): E_{Li_2S_2} - E_{Li_2S_4} + 0.25E_{S_8}$$

$$\Delta G(Li_2S_2-Li_2S): E_{Li_2S} - E_{Li_2S_2} + 0.125E_{S_8}$$

#### ***Pouch cell assembly and measurements:***

The NiS<sub>2</sub>/NiSe<sub>2</sub>@NC /S cathode and lithium anode were cut into 4×3 cm pieces. The sulfur loading of the cathode in the pouch cell was 1.8 mg·cm<sup>-2</sup>. The E/S ratio was about 20 μL·mg<sup>-1</sup>, the thickness of the lithium belt anode was 0.4 mm. Separator and electrolyte were sandwiched between the tailored and NiS<sub>2</sub>/NiSe<sub>2</sub>@NC /S lithium belt.

## Supplementary Data

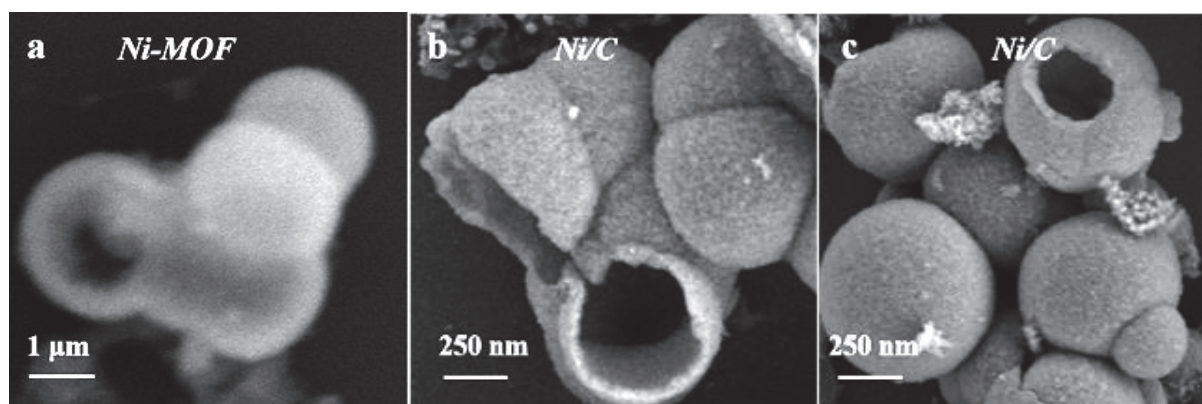


**Figure S1.** (a) SEM images of Ni-MOF (Ni-H<sub>3</sub>BTC) and Ni/NC (b,c).

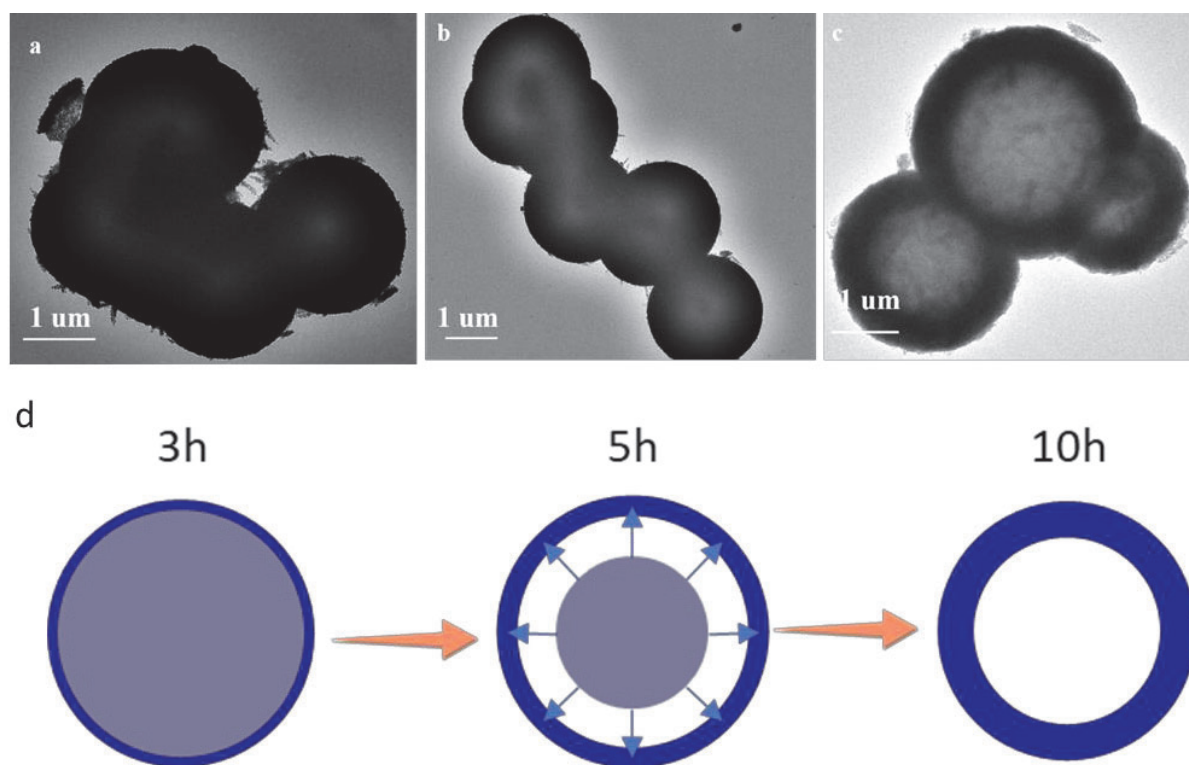


**Figure S2.** (a-c) TEM images of Ni-MOFs prepared with reaction times of (a) 3 h, (b) 5 h, (c) 10 h. (d) The scheme illustrates the mechanism of structure evolution.

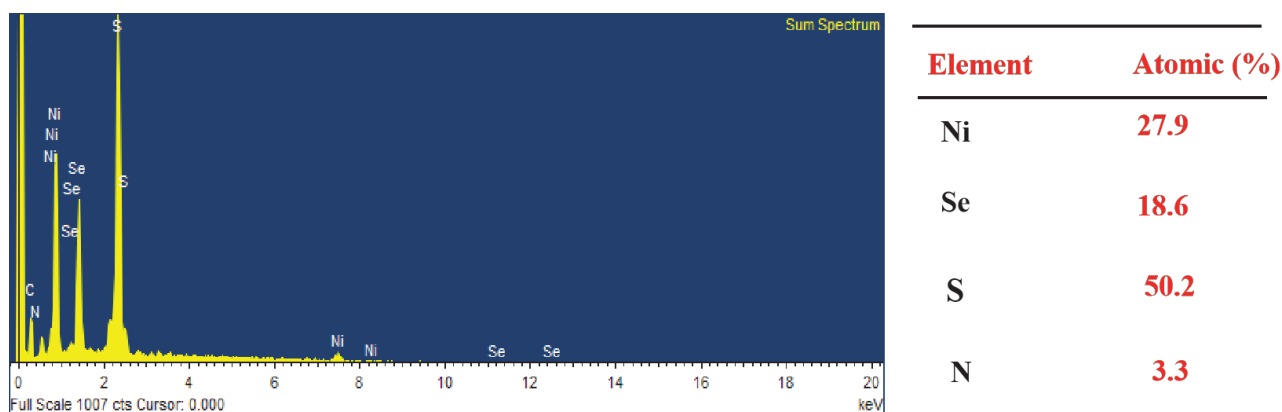


**Figure S3.** EDX spectrum of  $\text{NiS}_2/\text{NiSe}_2@\text{NC}$ , the contents of Ni, Se, S and N are 27.9 %, 18.6 %, 50.2 % and 3.3 % (Atomic %) respectively.

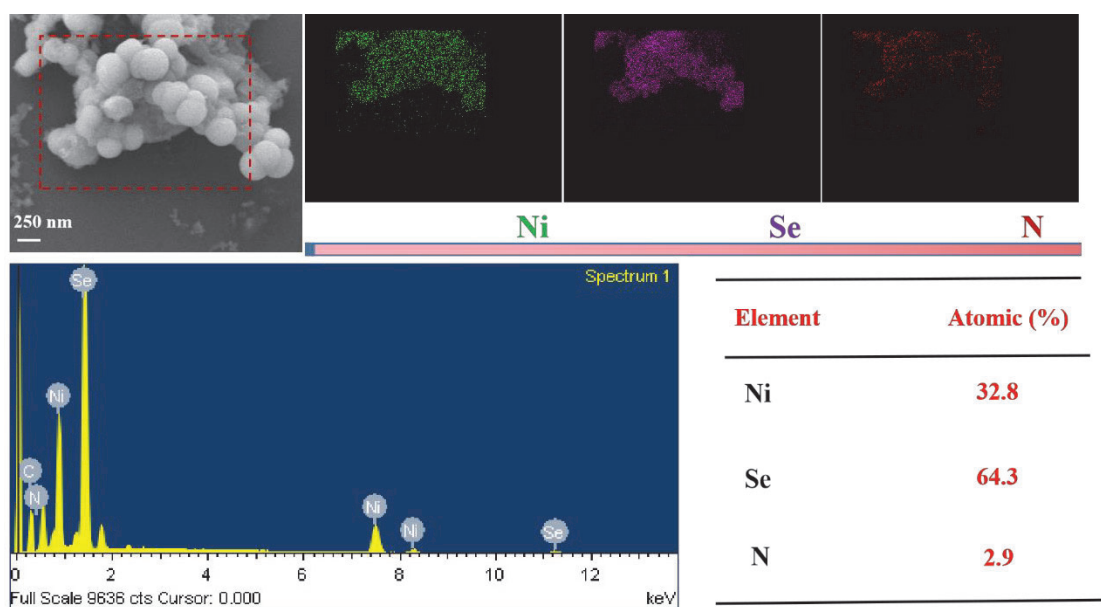


**Figure S4.** SEM image of  $\text{NiSe}_2@\text{NC}$ , EDX elemental mapping images: Ni, Se and N, EDX spectrum of  $\text{NiSe}_2@\text{NC}$ , the contents of Ni, Se and N are 32.8 %, 64.3 % and 2.9 % (Atomic %) respectively.

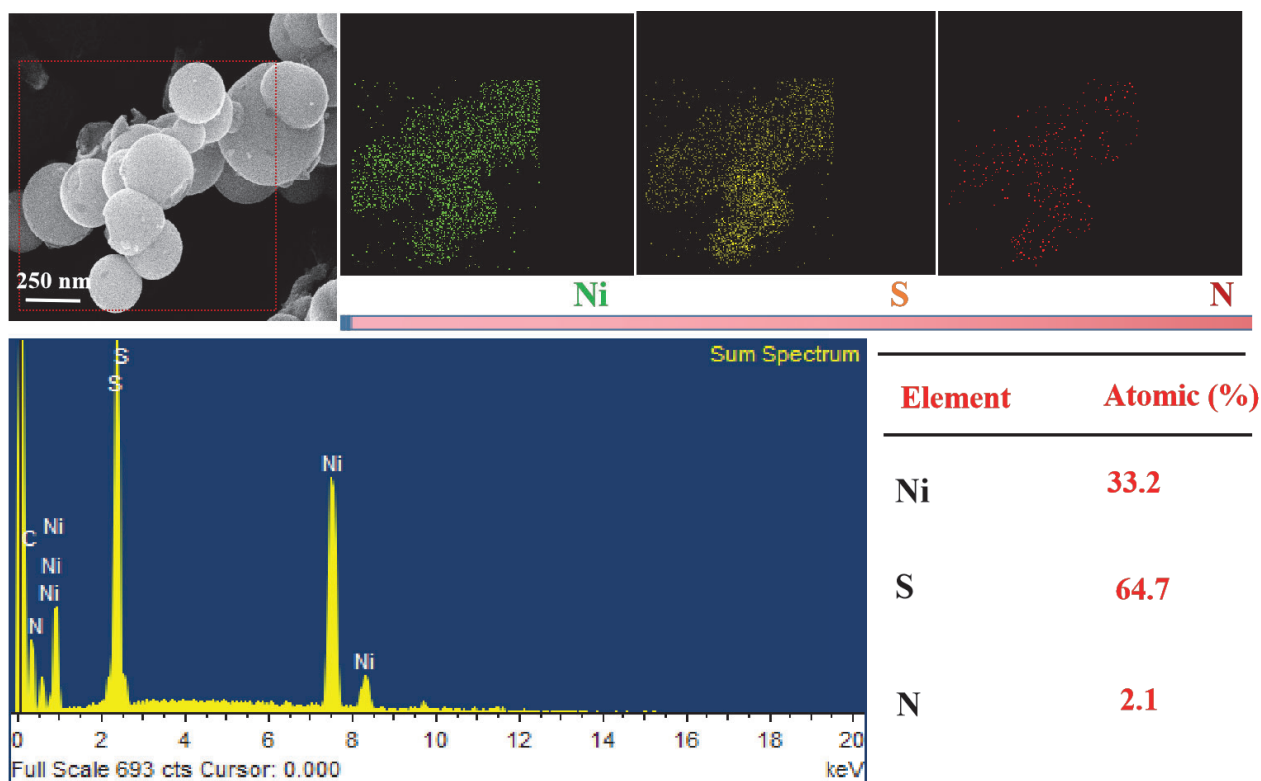


**Figure S5.** SEM image of  $\text{NiS}_2@\text{NC}$ , EDX elemental mapping images: Ni, S and N; EDX spectrum of  $\text{NiS}_2@\text{NC}$ , the contents of Ni, S and N are 33.2 %, 64.7 % and 2.1 % (Atomic %) respectively.

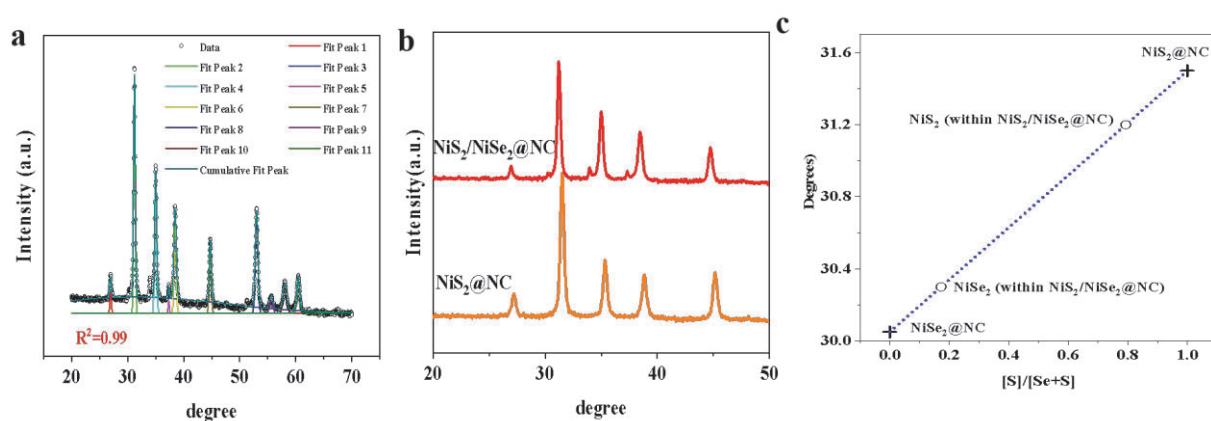


**Figure S6.** Fitting curves of  $\text{NiS}_2/\text{NiSe}_2@\text{NC}$  by Scherrer equation to calculated the particle size based on XRD curves (a) and XRD curves of  $\text{NiSe}_2/\text{NiS}_2@\text{NC}$  and  $\text{NiS}_2@\text{NC}$  (b). The S content in  $\text{NiSe}_2$  and Se within  $\text{NiS}_2$  was obtained by Vergard's law (c).

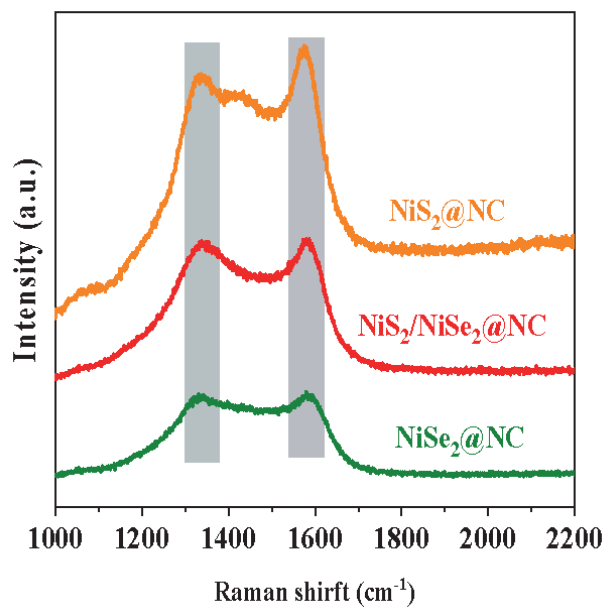


**Figure S7.** Raman spectras of  $\text{NiS}_2/\text{NiSe}_2@\text{NC}$ ,  $\text{NiSe}_2@\text{NC}$  and  $\text{NiS}_2@\text{NC}$ .

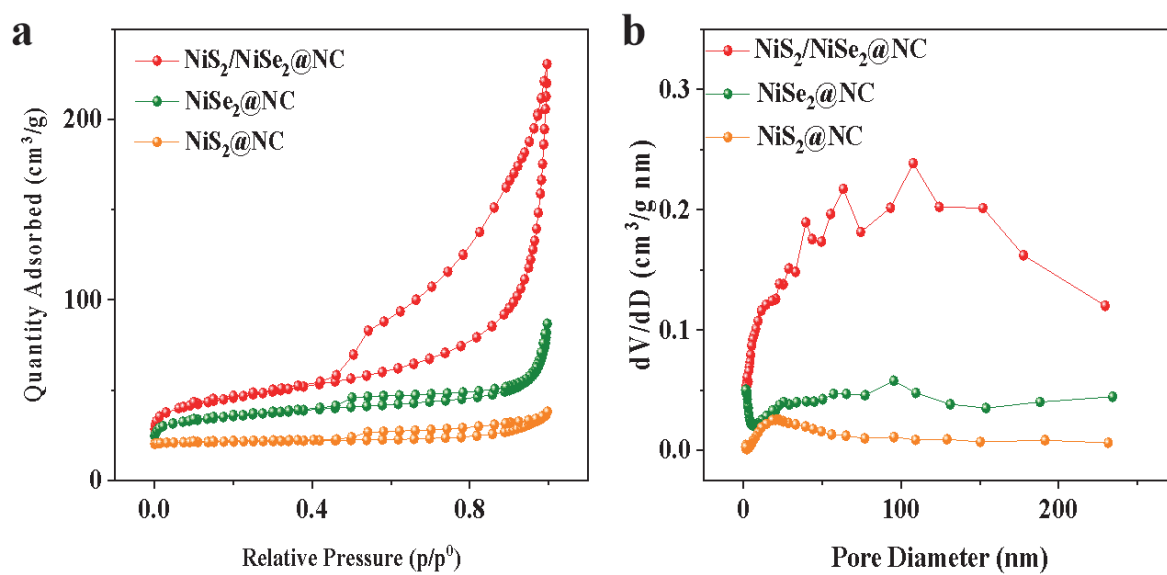


**Figure S8.**  $\text{N}_2$  adsorption/desorption isotherms of  $\text{NiS}_2/\text{NiSe}_2@\text{NC}$ ,  $\text{NiSe}_2@\text{NC}$  and  $\text{NiS}_2@\text{NC}$ .



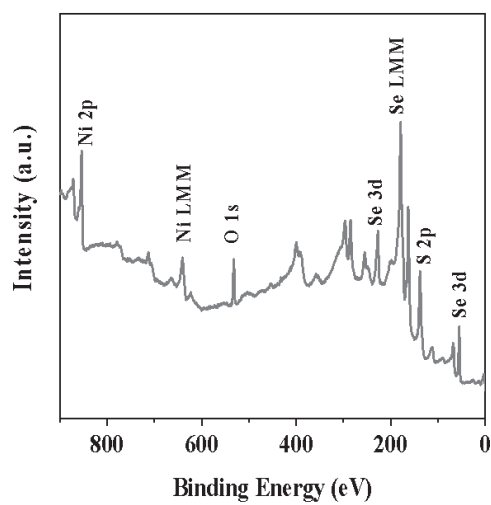


**Figure S9.** XPS full spectra of NiS<sub>2</sub>/NiSe<sub>2</sub>@NC.

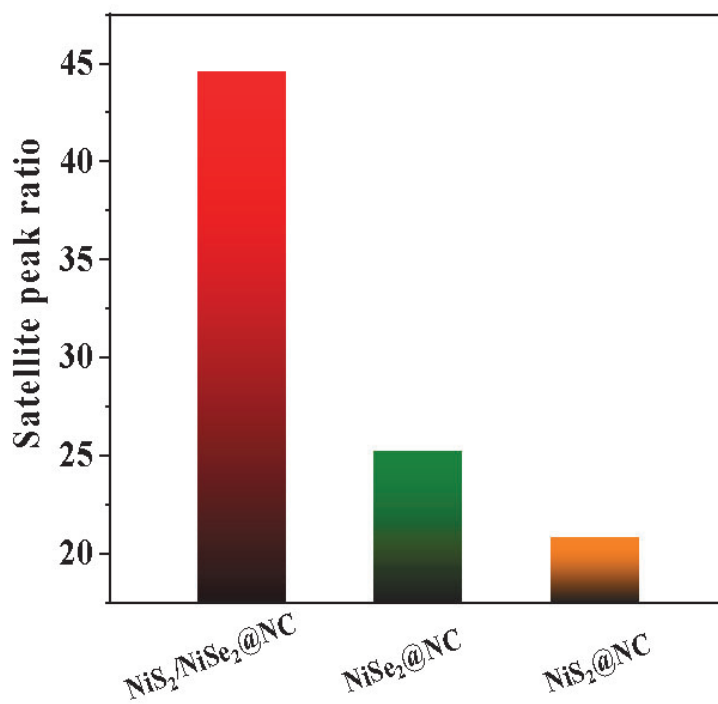


**Figure S10.** Ratio of satellite peaks of different host materials (NiS<sub>2</sub>/NiSe<sub>2</sub>@NC, NiSe<sub>2</sub>@NC, NiS<sub>2</sub>@NC) in XPS spectra.

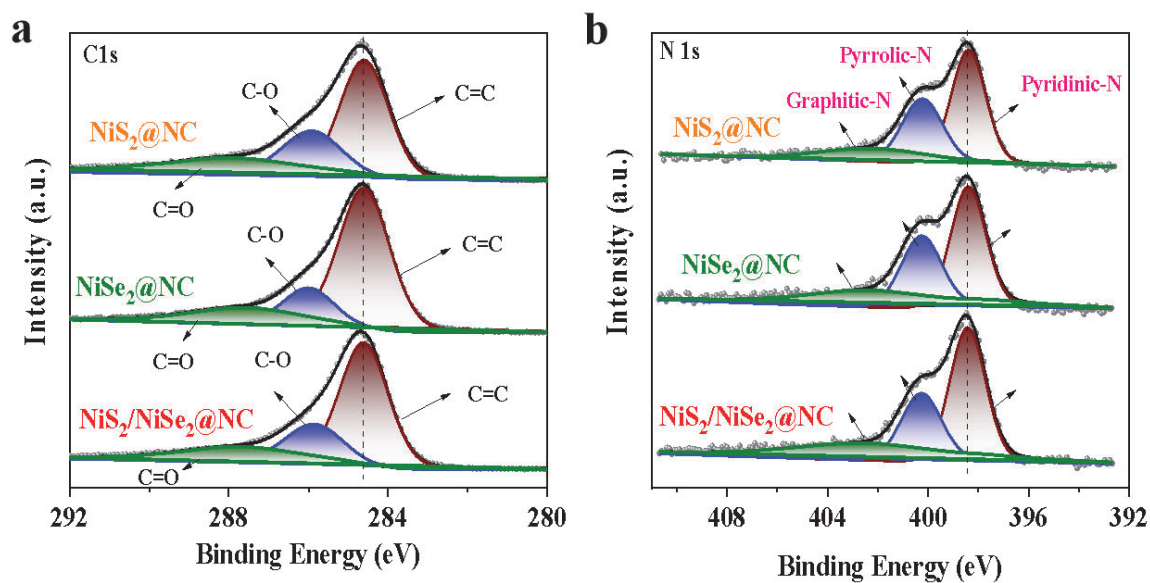


**Figure S11.** High-resolution C 1s (a), and N 1s (b) XPS spectras.

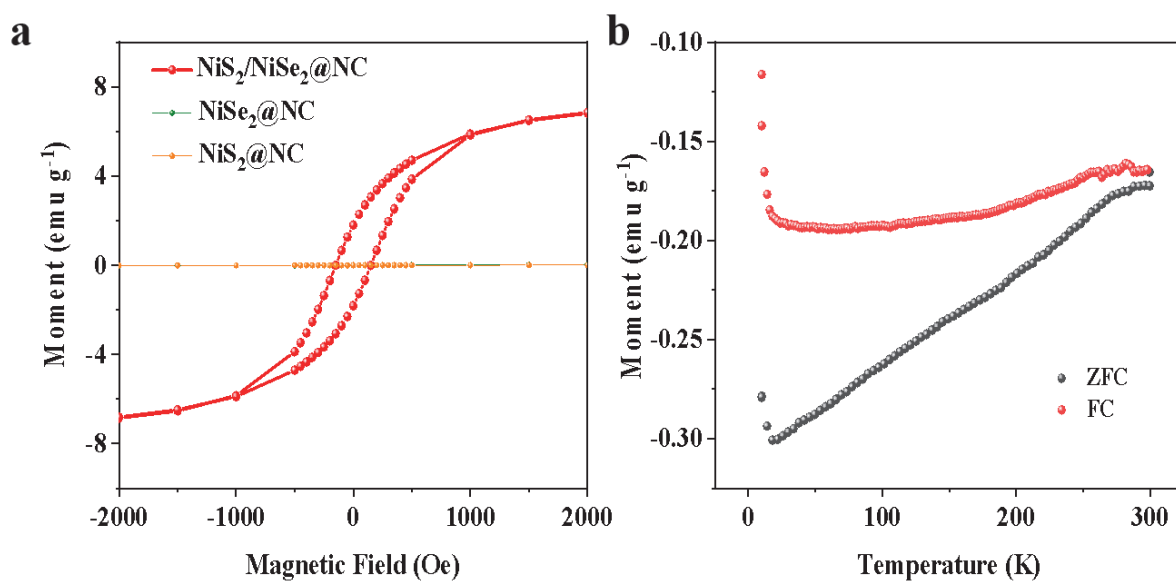


**Figure S12.** (a) Dependences of magnetization on the external magnetic field for  $\text{NiS}_2/\text{NiSe}_2@\text{NC}$ ,  $\text{NiSe}_2@\text{NC}$ , and  $\text{NiS}_2@\text{NC}$  at room temperature (300 K). (b) The ZFC/FC curves of  $\text{NiS}_2/\text{NiSe}_2@\text{NC}$ .

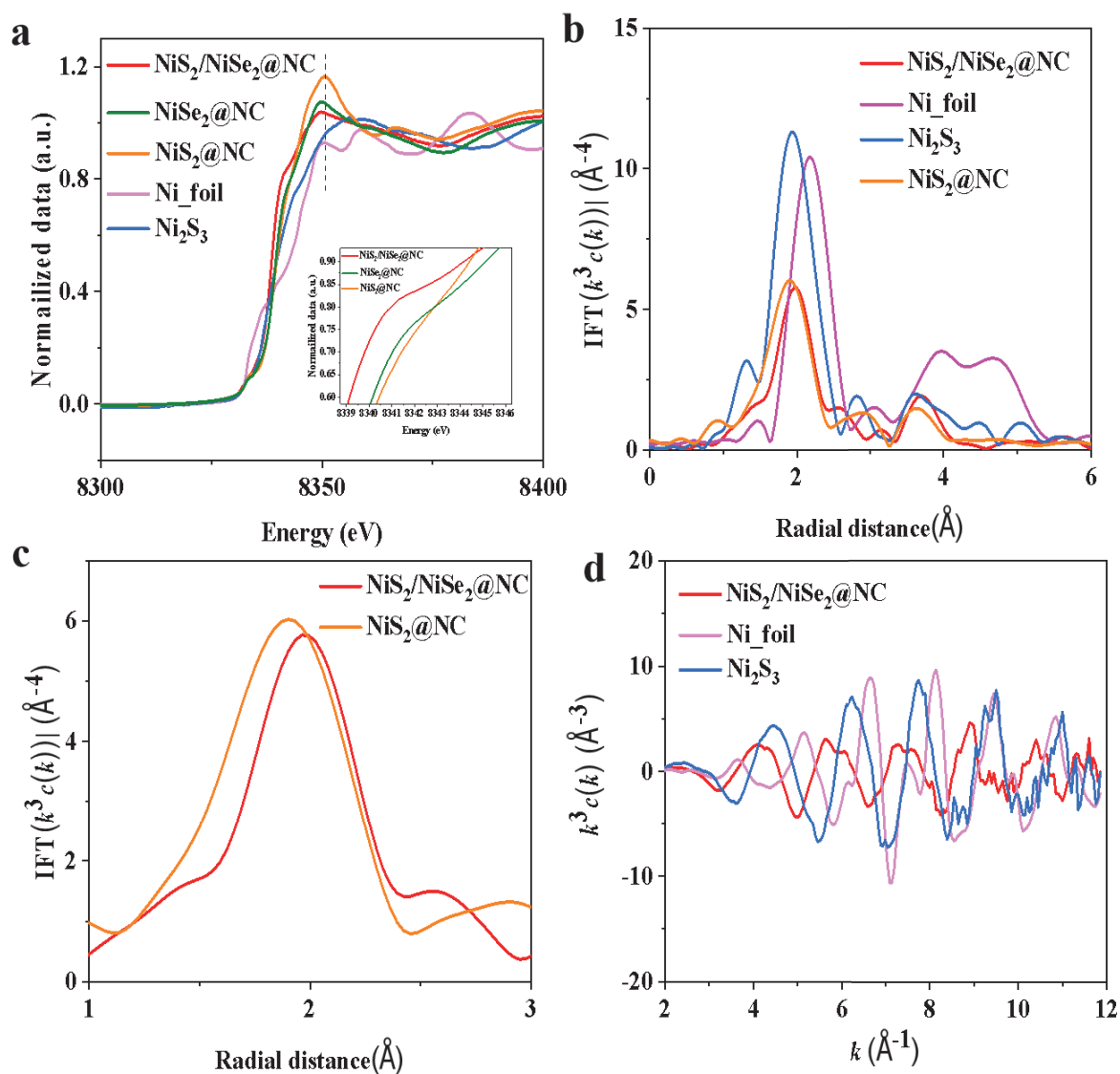


**Figure S13.** (a) Ni K-edge XANES of  $\text{NiS}_2/\text{NiSe}_2@\text{NC}$ , Ni foil,  $\text{Ni}_2\text{S}_3$ ,  $\text{NiSe}_2@\text{NC}$  and  $\text{NiS}_2@\text{NC}$  and (b-c) FT-EXAFS spectra of  $\text{NiS}_2/\text{NiSe}_2@\text{NC}$ ,  $\text{NiS}_2@\text{NC}$ , Ni foil and  $\text{Ni}_2\text{S}_3$ . (d) Ni K-edge XANES of  $\text{NiS}_2/\text{NiSe}_2@\text{NC}$ , Ni foil and  $\text{Ni}_2\text{S}_3$  ( $K_3$  space).

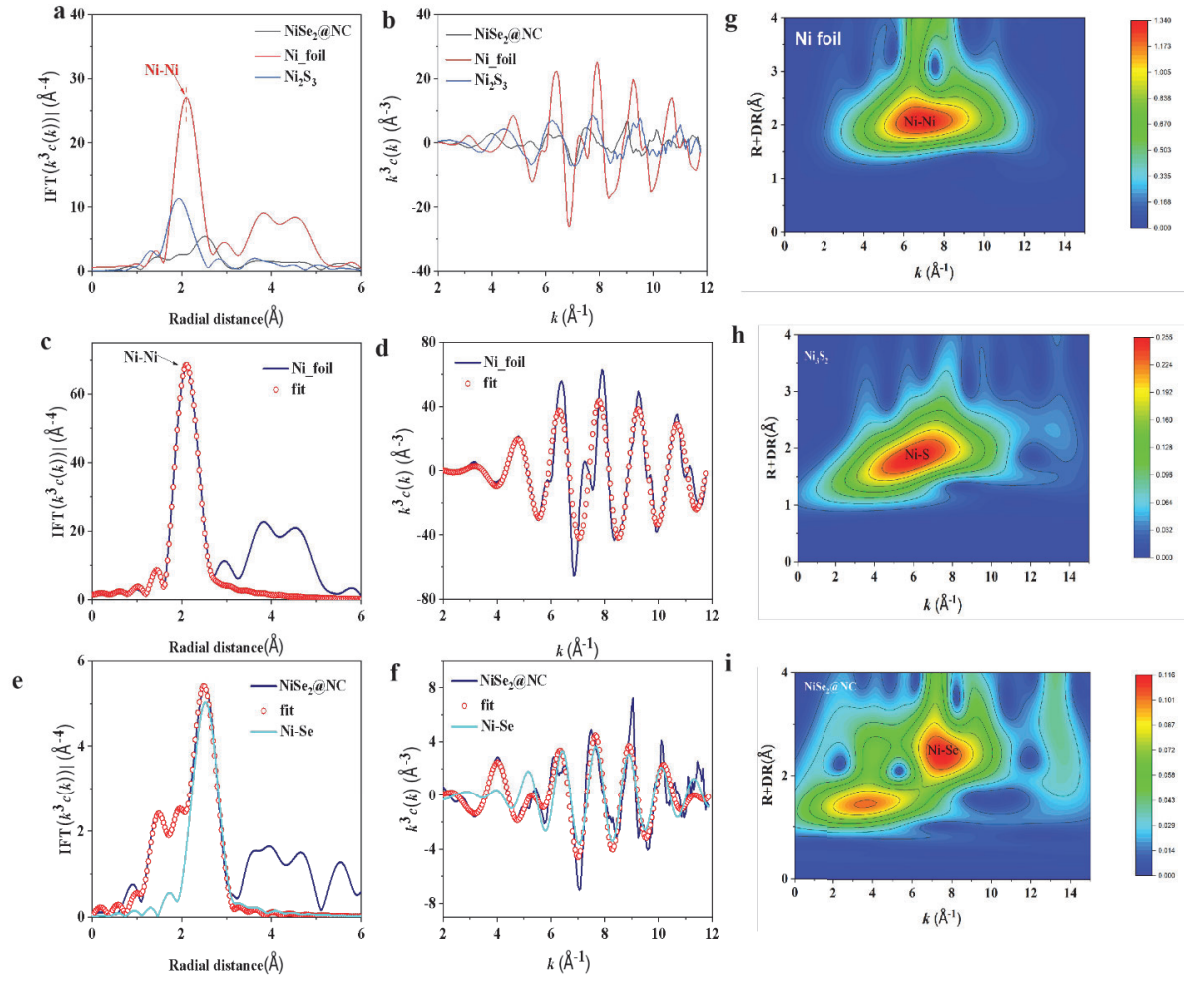


**Figure S14.** (a) FT-EXAFS spectra of NiSe<sub>2</sub>@NC, Ni foil and Ni<sub>2</sub>S<sub>3</sub>, (b) Ni K-edge XANES of NiSe<sub>2</sub>@NC, Ni foil and Ni<sub>2</sub>S<sub>3</sub> ( $K_3$  space), (c) FT-EXAFS fitting curves of Ni K-edge for Ni foil, (d) XAFS fitting curves of Ni K-edge for Ni foil ( $K_3$  space), (e) FT-EXAFS fitting curves of Ni K-edge for NiSe<sub>2</sub>@NC, (f) XAFS fitting curves of Ni K-edge for NiSe<sub>2</sub>@NC ( $K_3$  space), (g-i) WT contour plots for Ni foil, Ni<sub>2</sub>S<sub>3</sub> and NiSe<sub>2</sub>@NC at R space.

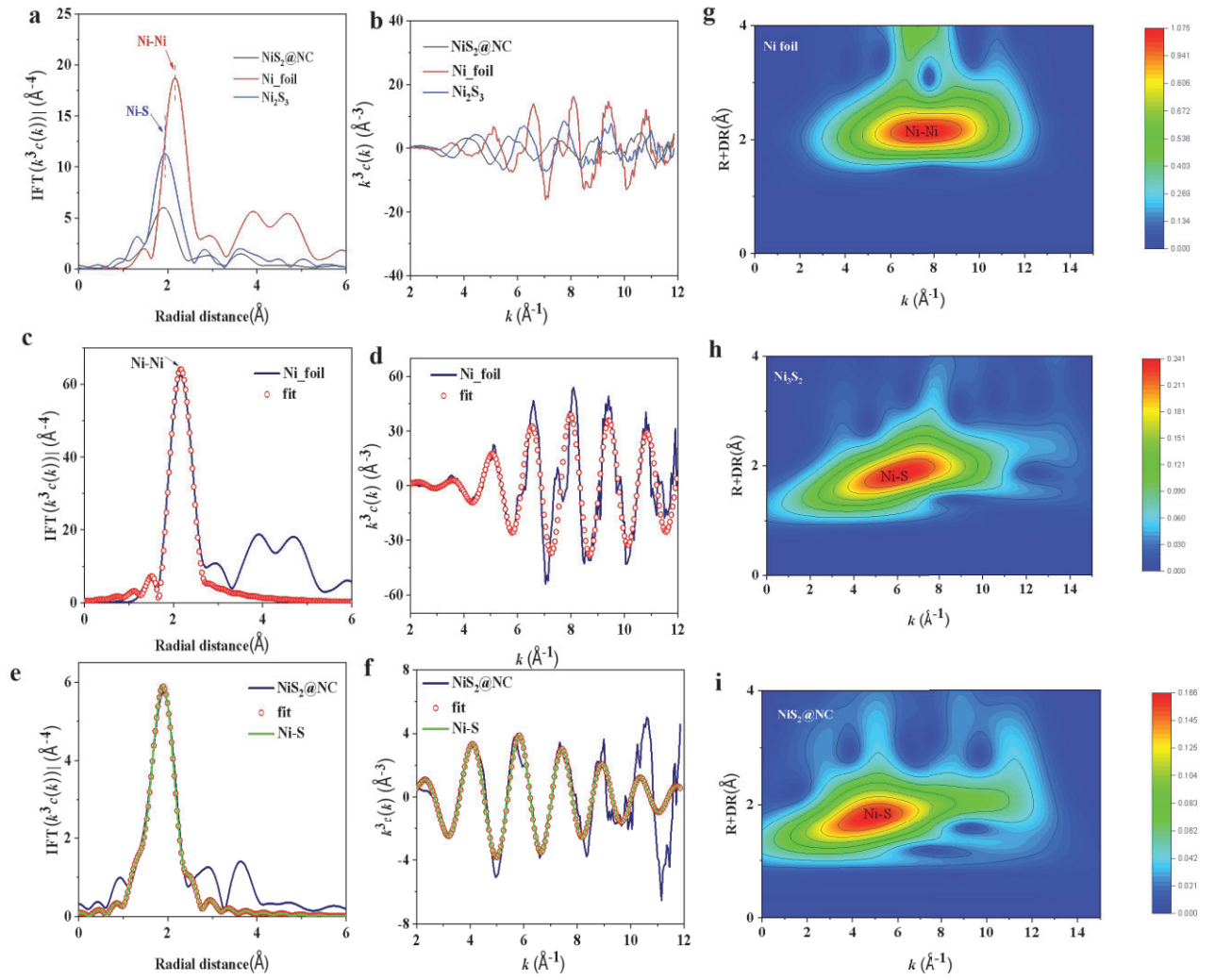


**Figure S15.** (a) FT-EXAFS spectra of NiS<sub>2</sub>@NC, Ni foil and Ni<sub>2</sub>S<sub>3</sub>, (b) Ni K-edge XANES of NiS<sub>2</sub>@NC, Ni foil and Ni<sub>2</sub>S<sub>3</sub> (K<sub>3</sub> space), (c) FT-EXAFS fitting curves of Ni K-edge for Ni foil, (d) XAFS fitting curves of Ni K-edge for Ni foil (K<sub>3</sub> space), (e) FT-EXAFS fitting curves of Ni K-edge for NiS<sub>2</sub>@NC, (f) XAFS fitting curves of Ni K-edge for NiS<sub>2</sub>@NC (K<sub>3</sub> space), (g-i) WT contour plots for Ni foil, Ni<sub>2</sub>S<sub>3</sub> and NiS<sub>2</sub>@NC at R space.

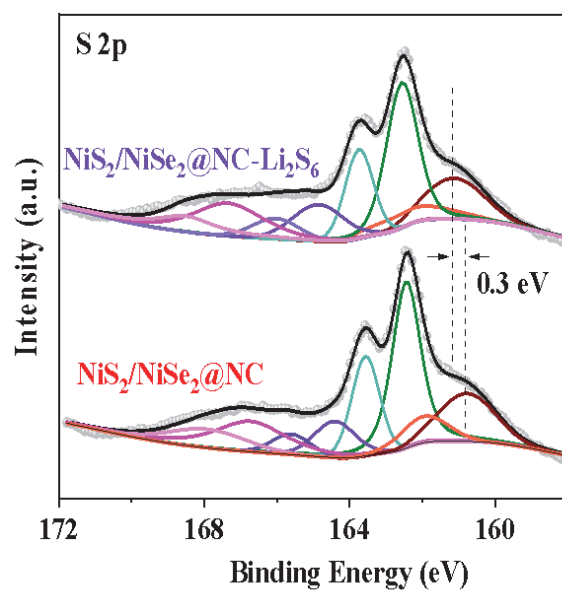


**Figure S16.** High-resolution XPS spectra of S 2p before and after  $\text{Li}_2\text{S}_6$  adsorption for  $\text{NiS}_2/\text{NiSe}_2@\text{NC}$ .

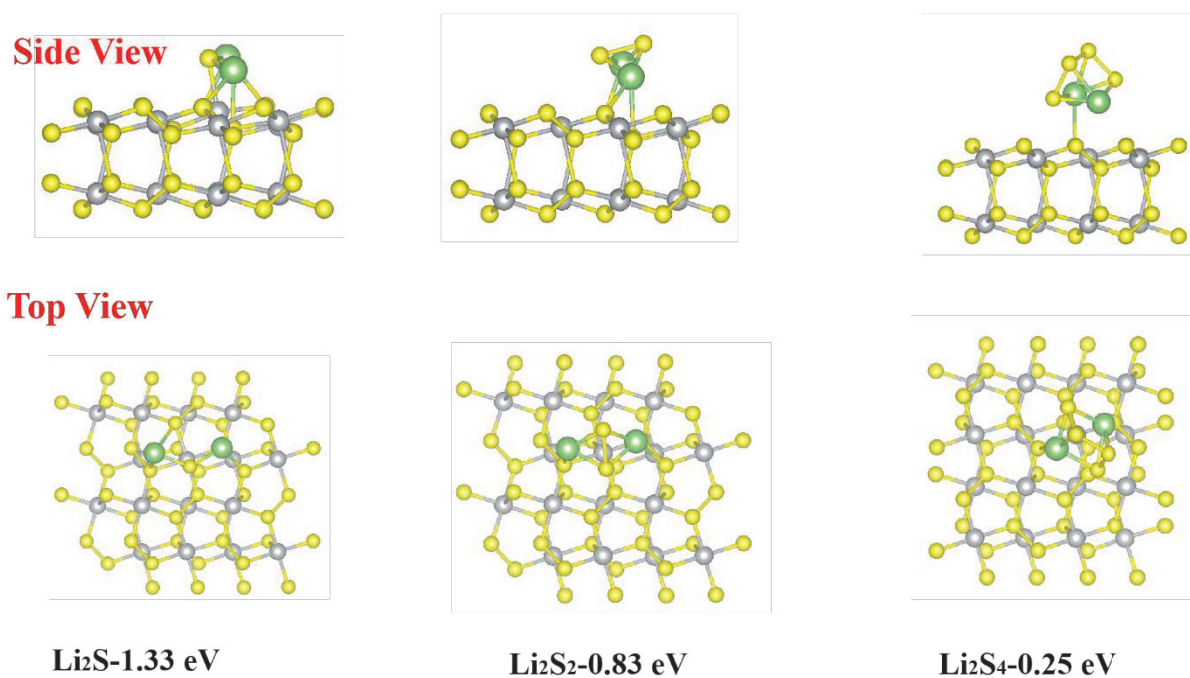
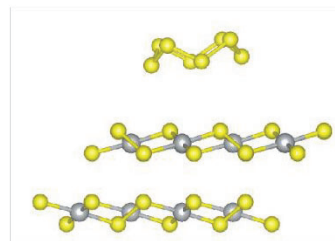
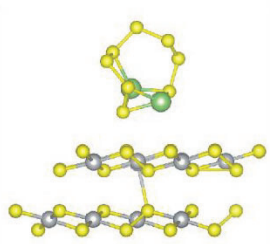
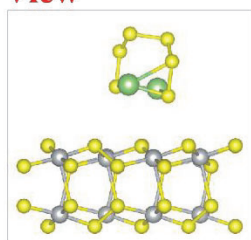


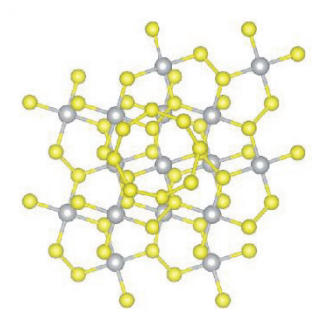
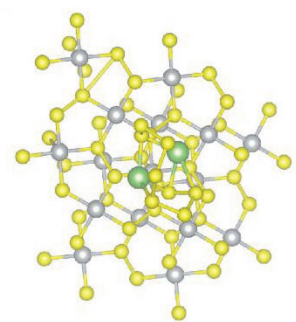
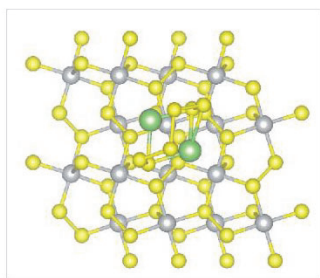
**Figure S17.** DFT-based optimized geometrical configurations of  $\text{NiS}_2$  with LiPSs ( $\text{Li}_2\text{S}$ ,  $\text{Li}_2\text{S}_2$  and  $\text{Li}_2\text{S}_4$ ).



**Side View**



**Top View**



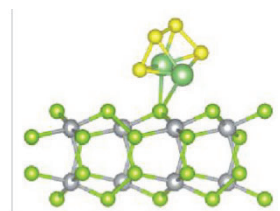
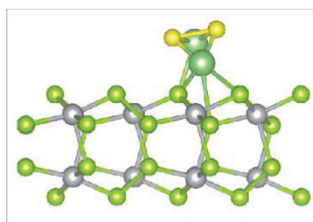
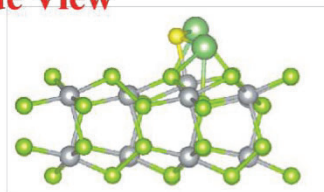
Li<sub>2</sub>S<sub>6</sub>-0.03 eV

Li<sub>2</sub>S<sub>8</sub>-0.06 eV

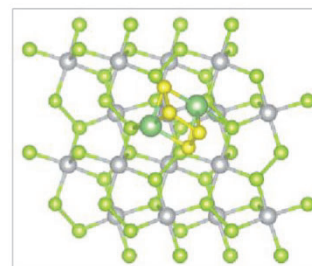
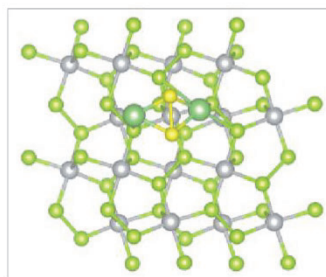
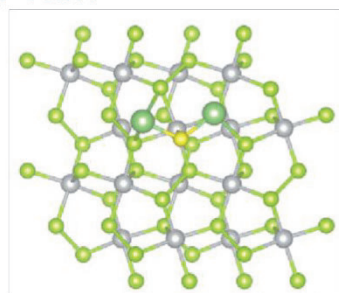
S<sub>8</sub>-0.07 eV

**Figure S18.** DFT-based optimized geometrical configurations of NiS<sub>2</sub> with LiPSs (Li<sub>2</sub>S<sub>6</sub>, Li<sub>2</sub>S<sub>8</sub> and S<sub>8</sub>).

**Side View**



**Top View**



Li<sub>2</sub>S-1.45 eV

Li<sub>2</sub>S<sub>2</sub>-0.95 eV

Li<sub>2</sub>S<sub>4</sub>-0.30eV

**Figure S19.** DFT-based optimized geometrical configurations of NiSe<sub>2</sub> with LiPSs (Li<sub>2</sub>S, Li<sub>2</sub>S<sub>2</sub> and Li<sub>2</sub>S<sub>4</sub>).

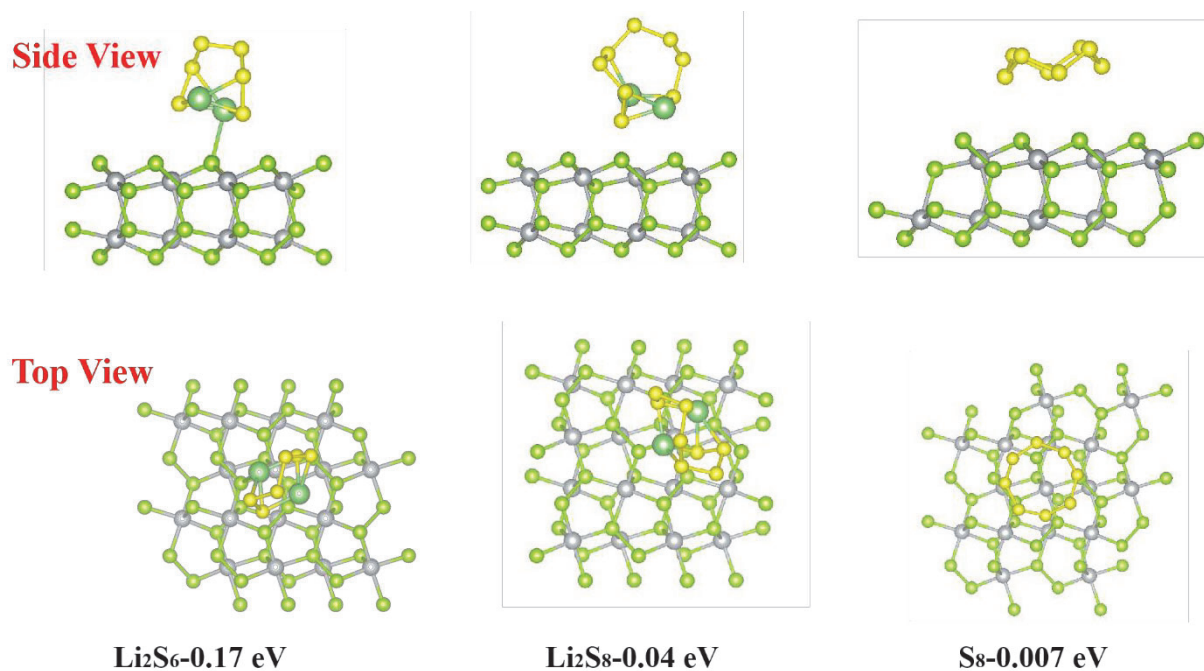


**Figure S20.** DFT-based optimized geometrical configurations of NiSe<sub>2</sub> with LiPSs (Li<sub>2</sub>S<sub>6</sub>, Li<sub>2</sub>S<sub>8</sub> and S<sub>8</sub>).

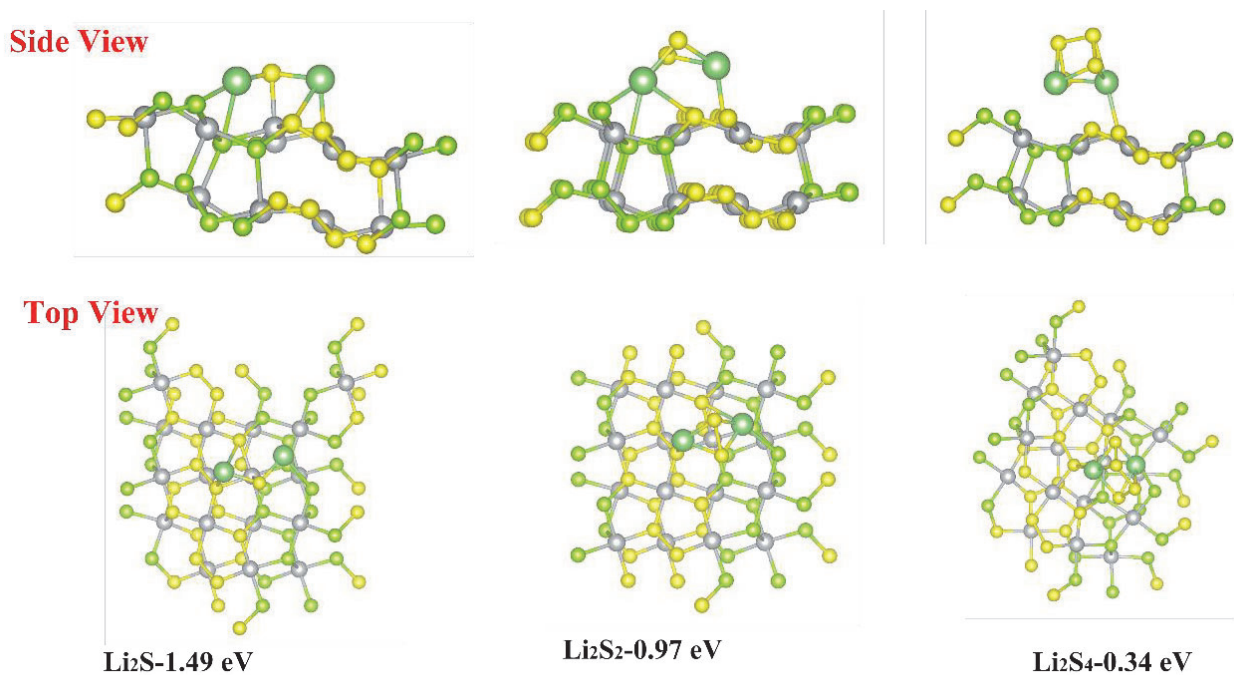


**Figure S21.** DFT-based optimized geometrical configurations of NiS<sub>2</sub>/NiSe<sub>2</sub> with LiPSs (Li<sub>2</sub>S, Li<sub>2</sub>S<sub>2</sub> and Li<sub>2</sub>S<sub>4</sub>).

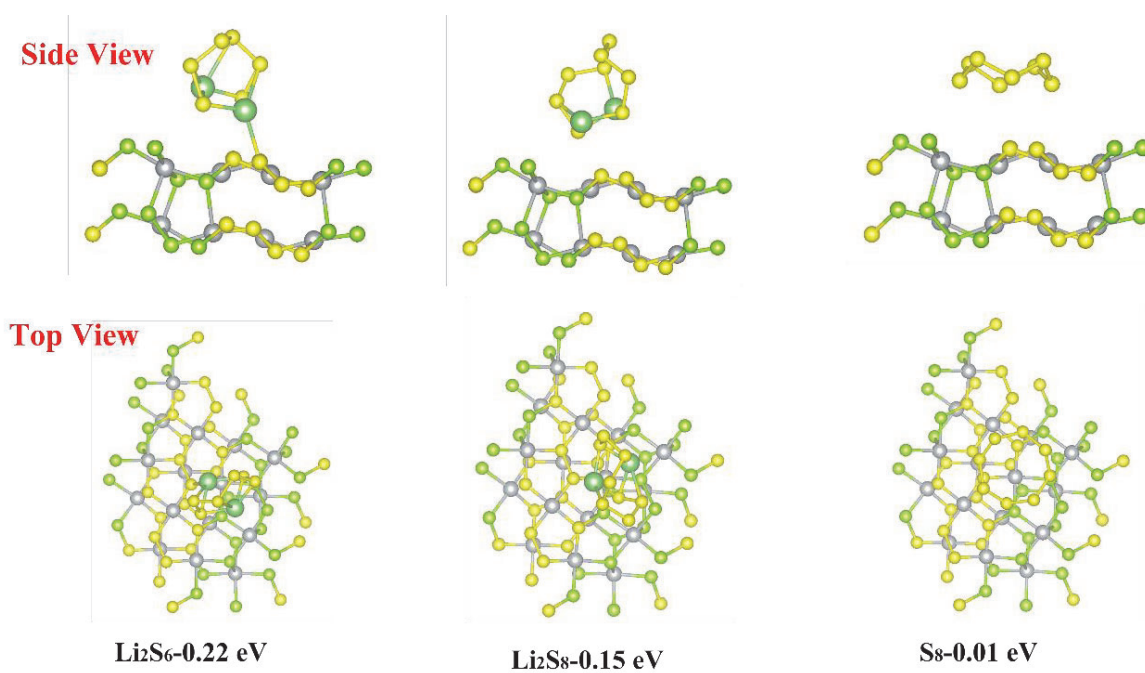


**Figure S22.** DFT-based optimized geometrical configurations of NiS<sub>2</sub>/NiSe<sub>2</sub> with LiPSs (Li<sub>2</sub>S<sub>6</sub>, Li<sub>2</sub>S<sub>8</sub> and S<sub>8</sub>).

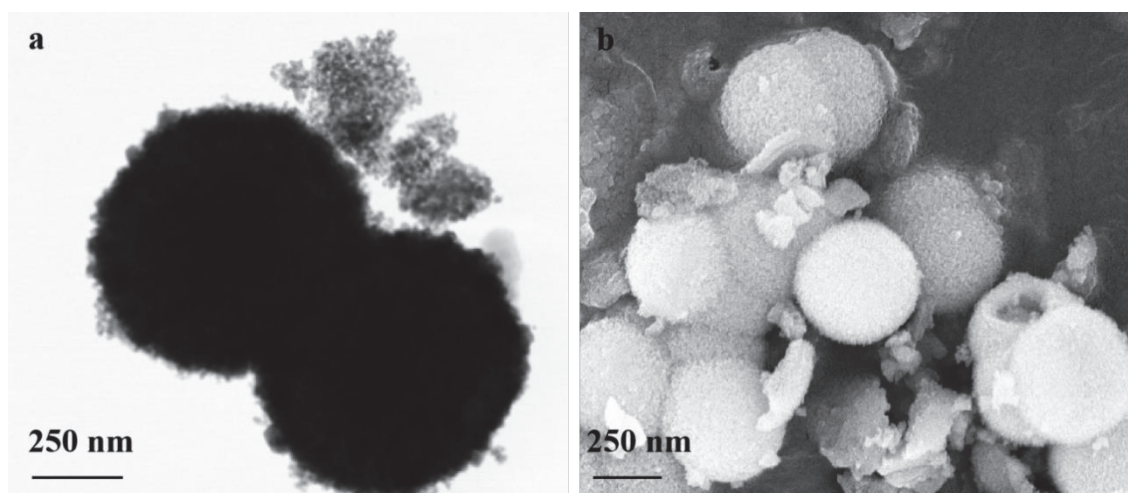


**Figure S23.** TEM (a) and SEM (b) images of NiS<sub>2</sub>/NiSe<sub>2</sub>@NC/S.

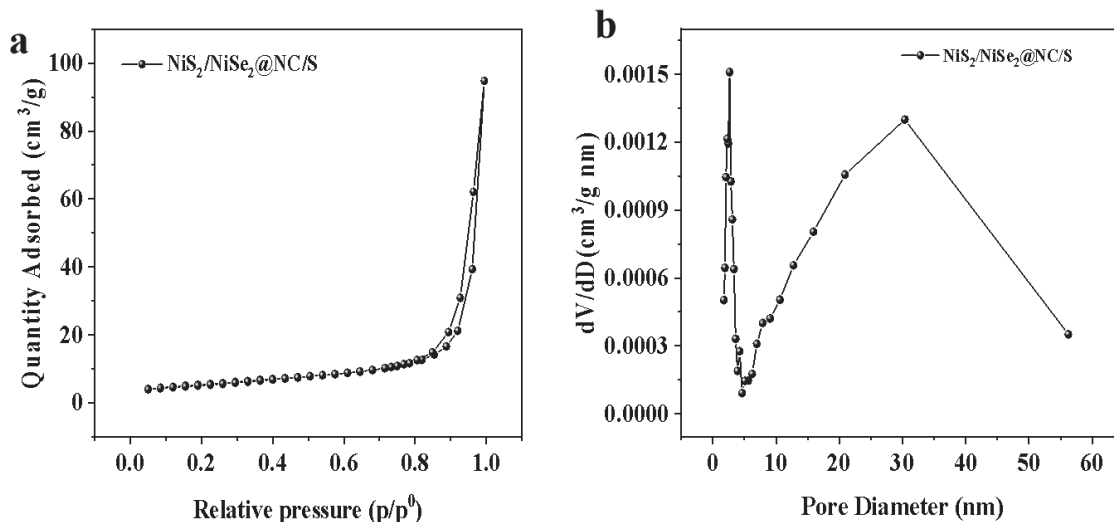


**Figure S24.** Nitrogen adsorption-desorption isotherms, pore size distribution diagram and pore volume histograms of  $\text{NiS}_2/\text{NiSe}_2@\text{NC/S}$ .

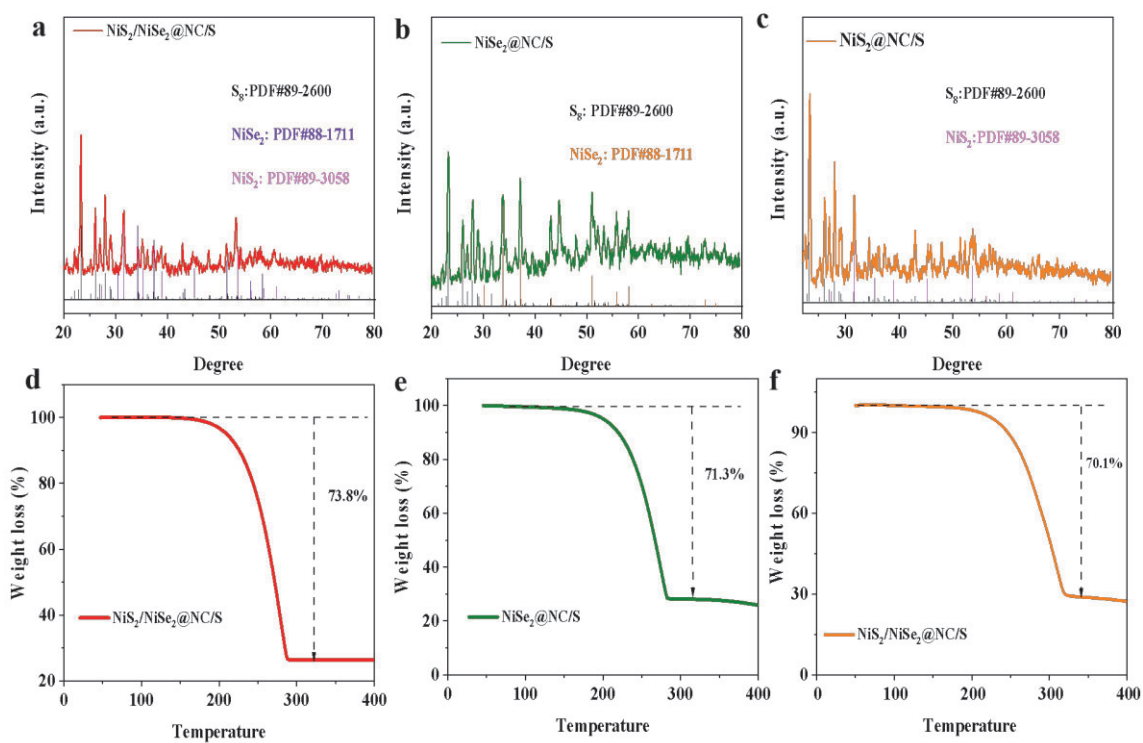


**Figure S25.** XRD curves of  $\text{NiS}_2/\text{NiSe}_2@\text{NC/S}$  (a),  $\text{NiSe}_2@\text{NC/S}$  (b) and  $\text{NiS}_2@\text{NC/S}$  (c), TGA curves of  $\text{NiS}_2/\text{NiSe}_2@\text{NC/S}$  (d),  $\text{NiSe}_2@\text{NC/S}$  (e) and  $\text{NiS}_2@\text{NC/S}$  (f).



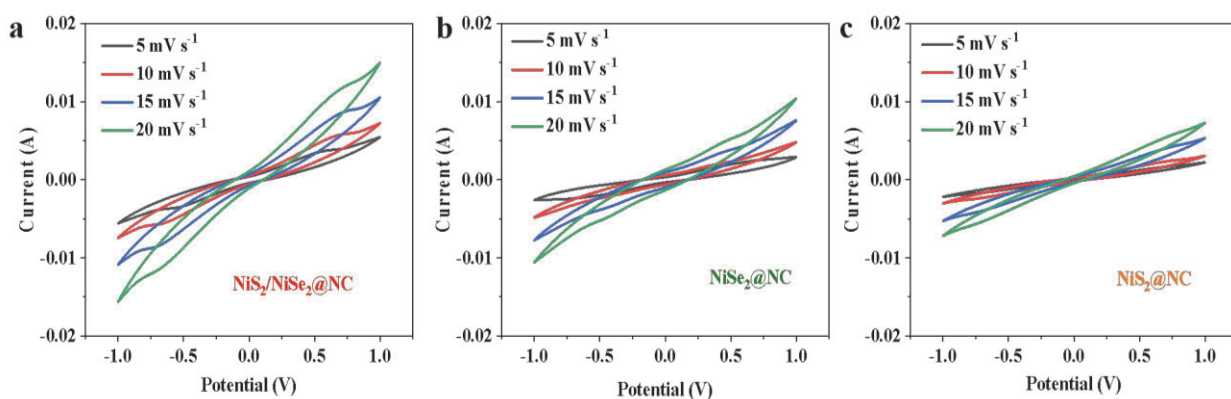


**Figure S26.** CV curves at various scan rate ( $5\text{ mV s}^{-1}$ - $20\text{ mV s}^{-1}$ ) of symmetric cells assembled using two  $\text{NiS}_2/\text{NiSe}_2@\text{NC}$  (a),  $\text{NiSe}_2@\text{NC}$  (b), and  $\text{NiS}_2@\text{NC}$  (c) electrodes.

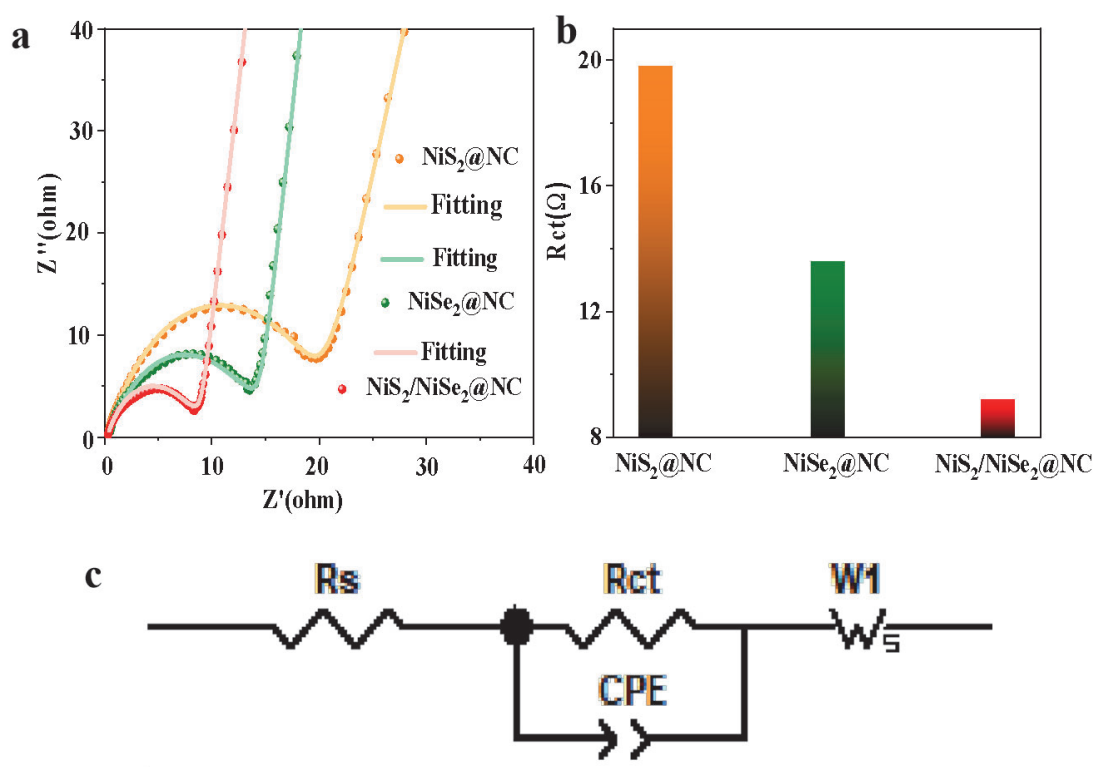


**Figure S27.** EIS spectra (a), fitted data parameters (b), and equivalent circuit (c) of symmetric batteries assembled from different host materials ( $\text{NiS}_2/\text{NiSe}_2@\text{NC}$ ,  $\text{NiSe}_2@\text{NC}$  and  $\text{NiS}_2@\text{NC}$ ).

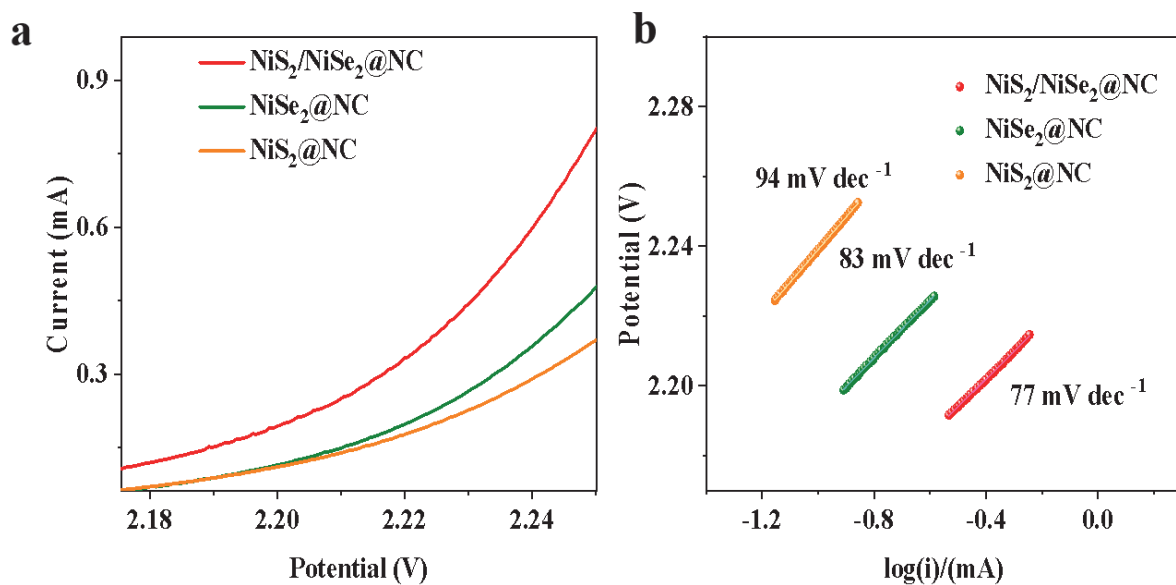


**Figure S28.** LSV plots (a) of  $\text{Li}_2\text{S}$  oxidation and the corresponding Tafel plots (b) obtained from  $\text{NiS}_2/\text{NiSe}_2@\text{NC}$ ,  $\text{NiSe}_2@\text{NC}$ , and  $\text{NiS}_2@\text{NC}$  symmetric cells.

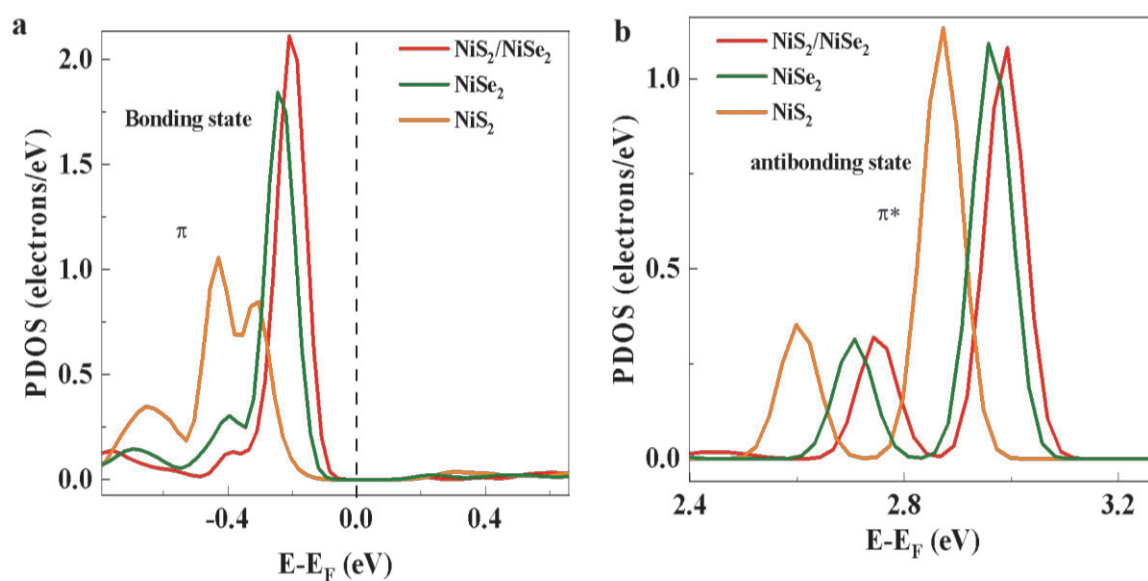


**Figure S29.** DOS curves of  $\text{NiS}_2/\text{NiSe}_2$ ,  $\text{NiSe}_2$  and  $\text{NiS}_2$ .



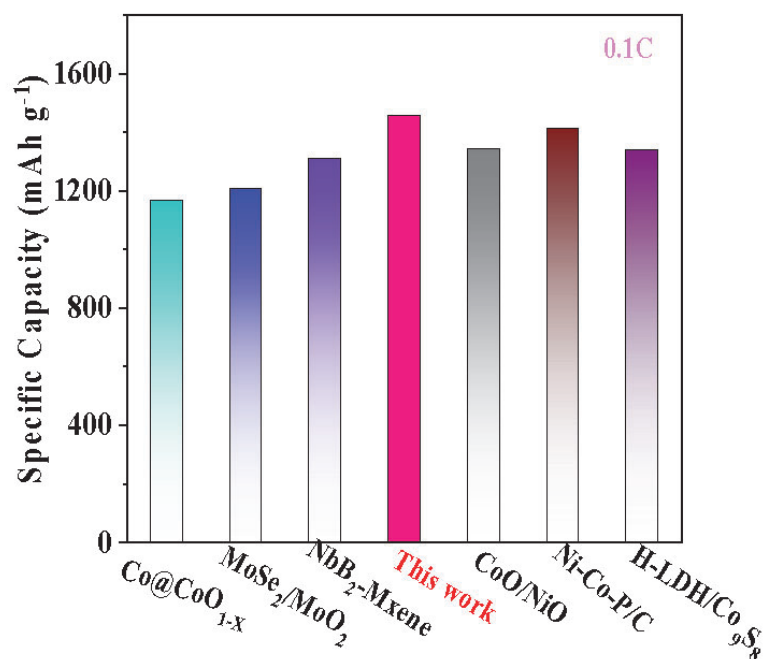


**Figure S30.** Comparison chart of specific capacity of different cathodes at a current rate 0.1C.

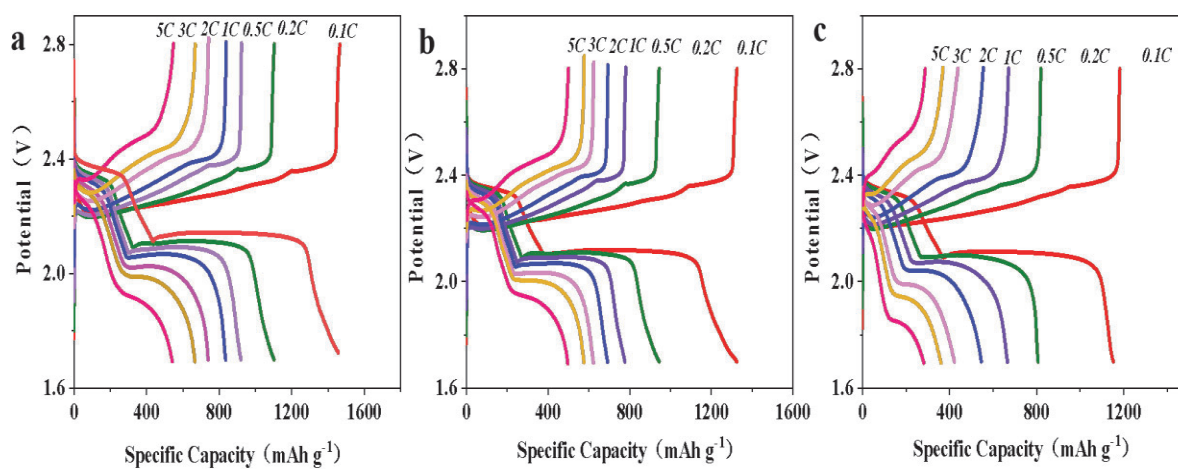


**Figure S31.** GCD curves of cells based on NiS<sub>2</sub>/NiSe<sub>2</sub>@NC/S (a), NiSe<sub>2</sub>@NC/S (b) and NiS<sub>2</sub>@NC/S electrodes at current rate in the range 0.1C-5C.

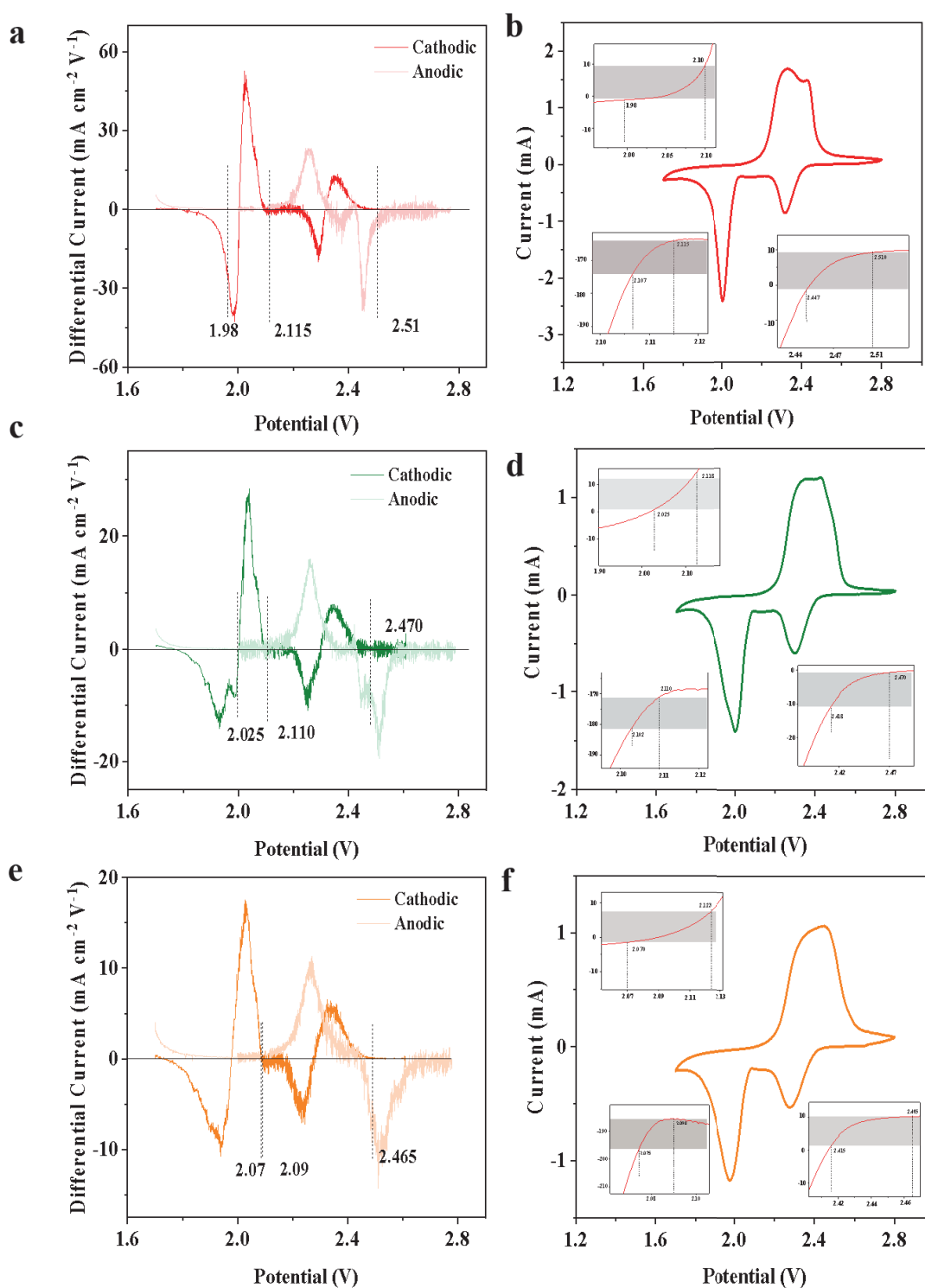


**Figure S32.** Onset potentials for Li-S redox reactions. (a, c and g) Differential CV curves of (a)  $\text{NiS}_2/\text{NiSe}_2@\text{NC}/\text{S}$ , (c)  $\text{NiSe}_2@\text{NC}/\text{S}$  and (e)  $\text{NiS}_2@\text{NC}/\text{S}$ . (b, d and f) CV curves and corresponding onset potentials of redox peaks A, C<sub>1</sub>, and C<sub>2</sub> (inset): (b)  $\text{NiS}_2/\text{NiSe}_2@\text{NC}/\text{S}$ , (d)  $\text{NiSe}_2@\text{NC}/\text{S}$  and (f)  $\text{NiS}_2@\text{NC}/\text{S}$ .

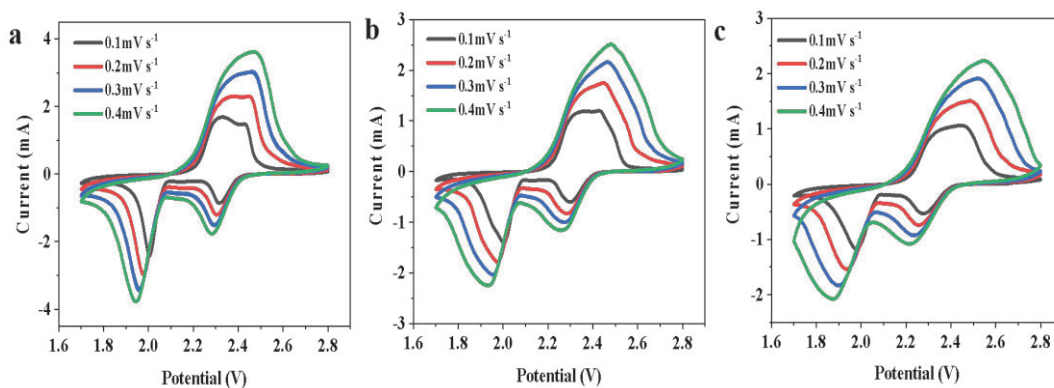


**Figure S33.** CV curves of cells based on  $\text{NiS}_2/\text{NiSe}_2@\text{NC}/\text{S}$ ,  $\text{NiSe}_2@\text{NC}/\text{S}$  and  $\text{NiS}_2@\text{NC}/\text{S}$  electrodes at scan rates in the range  $0.1\text{mV}\cdot\text{s}^{-1}$ - $0.4\text{mV}\cdot\text{s}^{-1}$ .

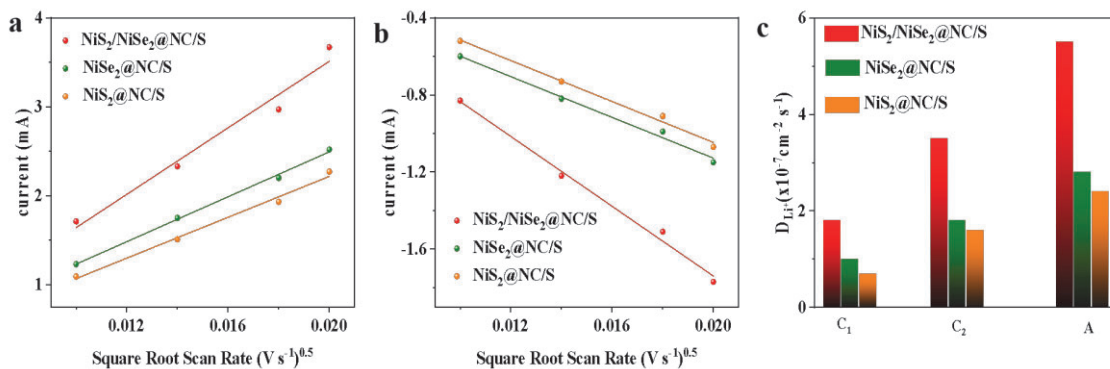


**Figure S34.** Peak current vs. square root of scan rate for different cathodes,  $\text{NiS}_2/\text{NC}/\text{S}$ ,  $\text{NiSe}_2@\text{NC}/\text{S}$  and  $\text{NiS}_2/\text{NiSe}_2@\text{NC}/\text{S}$ . a) A oxidation peak. b)  $\text{C}_1$  reduction peak. c)  $\text{Li}^+$  diffusion coefficient calculated from the CV redox peaks according to the Randles-Sevcik equation.

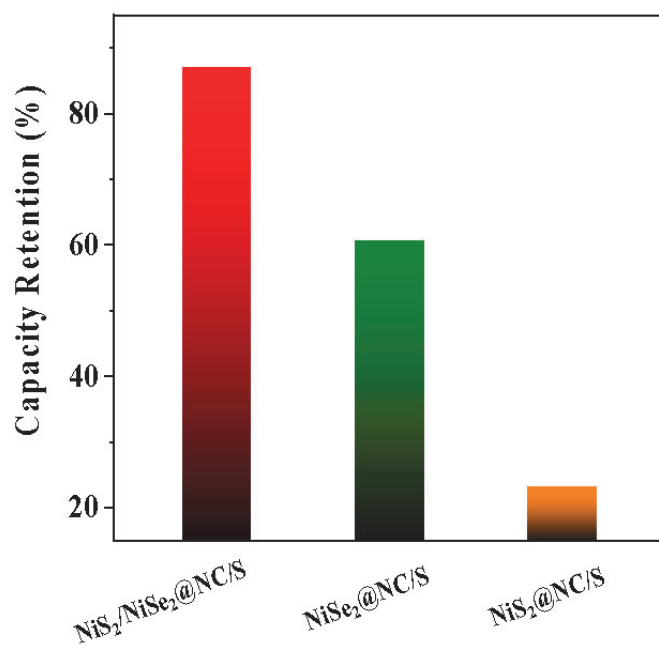


**Figure S35.** The Capacity retention of different electrode (NiS<sub>2</sub>/NiSe<sub>2</sub>@NC/S, NiSe<sub>2</sub>@NC/S and NiS<sub>2</sub>@NC/S) at 1C current rate after 500 cycles.

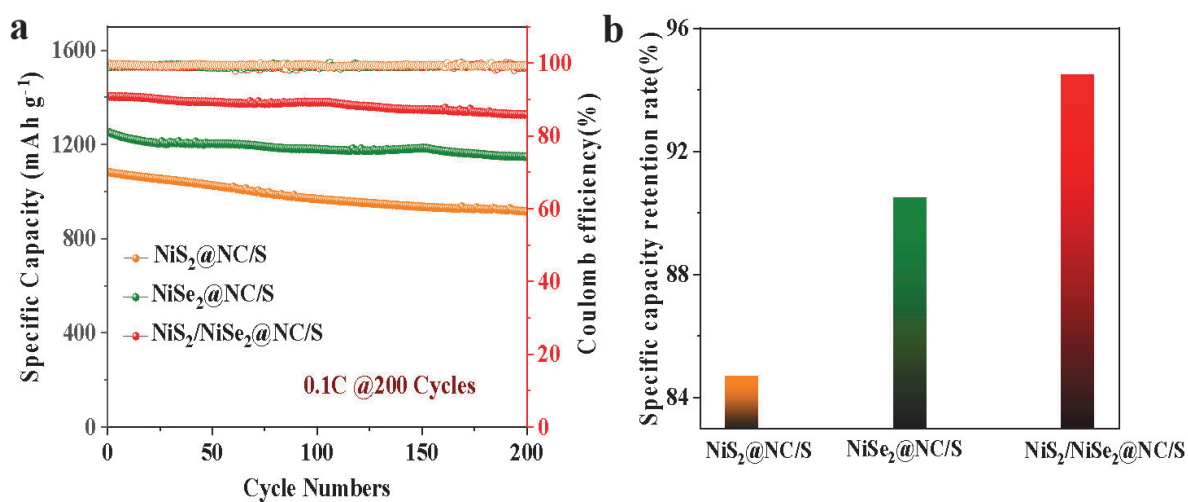


**Figure S36.** (a) Cycling stability of NiS<sub>2</sub>/NiSe<sub>2</sub>@NC/S-, NiSe<sub>2</sub>@NC/S-, and NiS<sub>2</sub>@NC/S-based coin cells at 0.1C during 200 cycles. (b) Capacity retention of the coin cells with different cathodes.

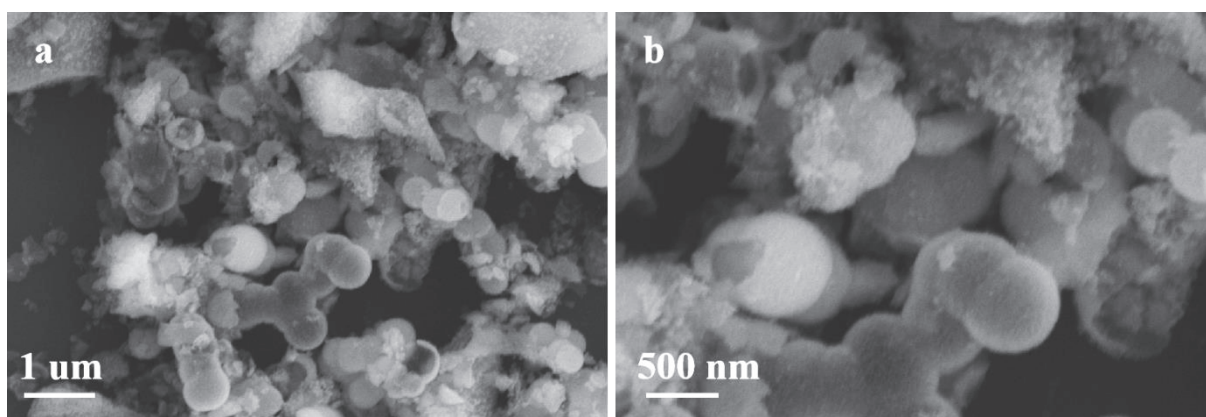


**Figure S37.** Low (a) and high-resolution (b) SEM images of  $\text{NiS}_2/\text{NiSe}_2@\text{NC}/\text{S}$  after 300 cycles at 3C current rate.

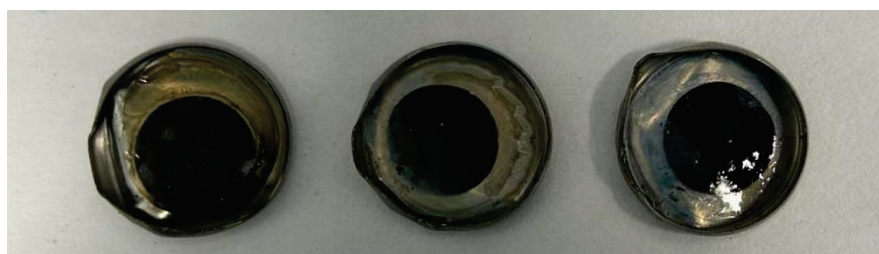


**Figure S38.** Optical photographs of electrodes  $\text{NiS}_2@\text{NC}/\text{S}$ ,  $\text{NiSe}_2@\text{NC}/\text{S}$  and  $\text{NiS}_2/\text{NiSe}_2@\text{NC}/\text{S}$  and membranes after 100 cycles (from left to right).

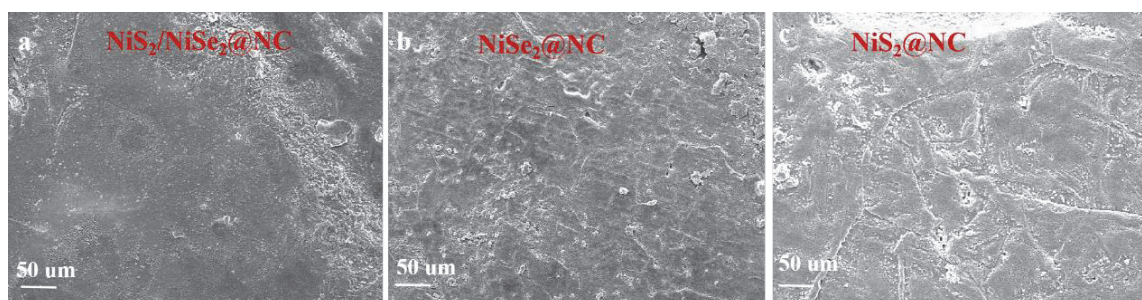


**Figure S39.** SEM images of the Li-anodes of the cycled cells based on  $\text{NiS}_2/\text{NiSe}_2@\text{NC}/\text{S}$ ,  $\text{NiSe}_2@\text{NC}/\text{S}$  and  $\text{NiS}_2@\text{NC}/\text{S}$ .

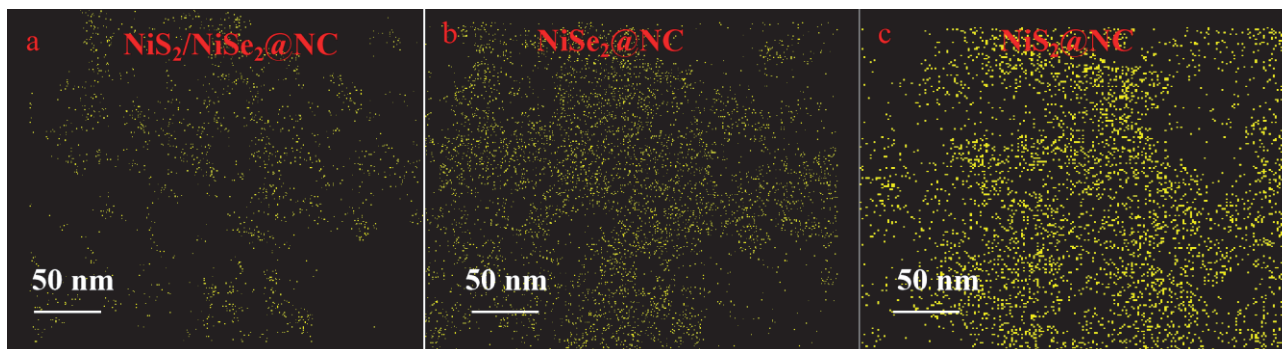


**Figure S40.** EDX mapping image of Li anode showing sulfur signal of the cycled cells based on NiS<sub>2</sub>/NiSe<sub>2</sub>@NC/S, NiSe<sub>2</sub>@NC/S and NiS<sub>2</sub>@NC/S.

**Table S1.** I<sub>D</sub>/I<sub>G</sub> value of NiS<sub>2</sub>/NiSe<sub>2</sub>@NC, NiSe<sub>2</sub>@NC and NiS<sub>2</sub>@NC.

Sample	I <sub>D</sub> /I <sub>G</sub>
NiS <sub>2</sub> /NiSe <sub>2</sub> @NC	1.01
NiSe <sub>2</sub> @NC	1.02
NiS <sub>2</sub> @NC	1.07

**Table S2.** Atomic ratio of Ni, S, Se, N and C in NiS<sub>2</sub>/NiSe<sub>2</sub>@NC by XPS test.

Atomic (%)	Ni	S	Se	N	C
NiS <sub>2</sub> /NiSe <sub>2</sub> @NC	7.28	35.15	11.26	7.69	38.62

**Table S3.** Ratio of satellite peaks of different host materials (NiS<sub>2</sub>/NiSe<sub>2</sub>@NC, NiSe<sub>2</sub>@NC, NiS<sub>2</sub>@NC) in XPS spectra.

Sample	Ratio (%)
NiS <sub>2</sub> /NiSe <sub>2</sub> @NC	44.6
NiSe <sub>2</sub> @NC	25.2
NiS <sub>2</sub> @NC	20.7



**Table S4** Bond lengths of Ni-S and Ni-Se in NiS<sub>2</sub>/NiSe<sub>2</sub>@NC, NiSe<sub>2</sub>@NC and NiS<sub>2</sub>@NC.

Sample	Ni-S	Ni-Se
NiS <sub>2</sub> /NiSe <sub>2</sub> @NC	2.43 Å	2.52 Å
NiSe <sub>2</sub> @NC	/	2.88 Å
NiS <sub>2</sub> @NC	2.31 Å	/

**Table S5.** Adsorption energy of polysulfides by NiS<sub>2</sub>/NiSe<sub>2</sub> and NiSe<sub>2</sub>.

Sample	Li <sub>2</sub> S	Li <sub>2</sub> S <sub>2</sub>	Li <sub>2</sub> S <sub>4</sub>	Li <sub>2</sub> S <sub>6</sub>	Li <sub>2</sub> S <sub>8</sub>	S <sub>8</sub>
NiS <sub>2</sub> /NiSe <sub>2</sub>	-1.49 eV	-0.97 eV	-0.34 eV	-0.22 eV	-0.15 eV	-0.01 eV
NiSe <sub>2</sub>	-1.45 eV	-0.95 eV	-0.30 eV	-0.17 eV	-0.04 eV	-0.007 eV

**Table S6.** Comparison of the specific capacitance at a current density of 0.1C for NiS<sub>2</sub>/NiSe<sub>2</sub>@NC/S, NiSe<sub>2</sub>@NC/S, and NiS<sub>2</sub>@NC/S.

Sample	Specific capacity (mAh g <sup>-1</sup> )
NiS <sub>2</sub> /NiSe <sub>2</sub> @NC/S	1458
NiSe <sub>2</sub> @NC/S	1326
NiS <sub>2</sub> @NC/S	1150

**Table S7.** Electrochemical performance comparisons of NiS<sub>2</sub>/NiSe<sub>2</sub>@NC/S with similar materials reported previously.

Sample	Specific capacitance (mAh /g)	Current Density (C)	Ref.
Co@Co <sub>1-x</sub> [ <sup>1</sup> ]	1241.5	0.1	[1]
MoSe <sub>2</sub> /MoO <sub>2</sub> [ <sup>2</sup> ]	1382.5	0.1	[2]
NBb <sub>2</sub> -Mxene[ <sup>3</sup> ]	1492.2	0.1	[3]
CoO/NiO[ <sup>4</sup> ]	1343	0.1	[4]
Ni-Co-P/C[ <sup>5</sup> ]	1412.6	0.1	[5]
H-LDH/CO <sub>9</sub> S <sub>8</sub> [6]	1580	0.1	[6]
NiS <sub>2</sub> /NiSe <sub>2</sub> @NC	1608	0.1	This work

**Table S8.** Internal and charge transfer resistances of NiS<sub>2</sub>/NiSe<sub>2</sub>@NC/S, NiSe<sub>2</sub>@NC/S, and NiS<sub>2</sub>@NC/S electrodes, as obtained from the fitting of the EIS spectra using the equivalent circuits.

Sample	Rs	Error (%)	Rct	Error (%)
NiS <sub>2</sub> /NiSe <sub>2</sub> @NC/S	0.6	0.33	25.4	0.39
NiSe <sub>2</sub> @NC/S	1.4	0.40	48.6	0.48
NiS <sub>2</sub> @NC/S	3.4	0.65	75.3	0.59

## Reference

- [1] D. Fang, G. Wang, S. Huang, T. Chen Li, J. Yu, D. Xiong, D. Yan, X. Liang Li, J. Zhang, Y. Von Lim, S. A. Yang, H. Ying Yang, *Chem. Eng. J.* **2021**, 411, 128546.
- [2] Q. Hao, G. Cui, Y. Zhang, J. Li, Z. Zhang, *Chem. Eng. J.* **2020**, 381, 122672.
- [3] D. Lu, X. Wang, Y. Hu, L. Yue, Z. Shao, W. Zhou, L. Chen, W. Wang, Y. Li, *Adv. Funct. Mater.* **2023**, 33, 2212689.
- [4] L. Wu, J. Hu, X. Yang, Z. Liang, S. Chen, L. Liu, H. Hou, J. Yang, *J. Mater. Chem. A* **2022**, 10, 23811.
- [5] Z. Wu, S. Chen, L. Wang, Q. Deng, Z. Zeng, J. Wang, S. Deng, *Energy Stor. Mater.* **2021**, 38, 381.
- [6] S. Chen, J. Luo, N. Li, X. Han, J. Wang, Q. Deng, Z. Zeng, S. Deng, *Energy Stor. Mater.* **2020**, 30, 187.

# **Chapter 6**

## **Anionic Doping in Layered Transition Metal Chalcogenides for Robust Lithium-Sulfur Batteries**

## 6. Anionic Doping in Layered Transition Metal Chalcogenides for Robust Lithium-Sulfur Batteries

### Key findings

1. A Te-doped  $\text{Bi}_2\text{Se}_3$  with selenium vacancies supported on carbon ( $\text{Te-Bi}_2\text{Se}_{3-x}\text{@C}$ ) was successfully synthesized via doping and defect engineering strategies.
2. Tellurium doping induced lattice distortion and generated selenium vacancies, thereby altering the local coordination environment of Bi atoms and enhancing catalytic activity toward polysulfide conversion.
3. Selenium vacancies increased the carrier concentration and activated unpaired Bi cations, improving polysulfide adsorption and accelerating sulfur redox kinetics.
4. The  $\text{Te-Bi}_2\text{Se}_{3-x}\text{@C}$  cathode demonstrated excellent electrochemical performance, with a high specific capacity (up to  $1508 \text{ mAh g}^{-1}$  at  $0.1\text{C}$ ), outstanding rate capability, and stable cycling even under high sulfur loading and lean electrolyte conditions.

### Introduction

LSBs are among the most promising next-generation energy storage systems due to their high theoretical energy density and the abundance of sulfur. However, practical application is hindered by several intrinsic issues, including the insulating nature of sulfur, the polysulfide shuttle effect, sluggish redox kinetics, and large volume changes during cycling.

To address these limitations, research has increasingly focused on the design of sulfur host materials with high conductivity, strong chemical adsorption, and catalytic functionality. One emerging direction involves using TMSes, such as  $\text{Bi}_2\text{Se}_3$ , due to their unique physicochemical properties.

### Purpose and background

This chapter investigates the development of a tellurium-doped bismuth selenide with selenium vacancies as a sulfur host material to improve the electrochemical

performance of LSB cathodes.

Why Transition TMSes?

1. High electronic conductivity: Compared to oxides and sulfides, selenides possess superior conductivity, facilitating faster charge transfer.
2. Chemical and structural stability: TMSes maintain integrity in harsh electrochemical environments.
3. High charge storage potential: Layered structures in TMSes can accommodate more  $\text{Li}^+$  ions and mitigate volume expansion.

Why  $\text{Bi}_2\text{Se}_3$  Specifically?

1. Topological insulator properties:  $\text{Bi}_2\text{Se}_3$  exhibits surface-conducting states with spin-momentum locking, enhancing surface charge transport.
2. Catalytic potential: Its structure and chemistry allow it to catalyze sulfur redox reactions effectively while adsorbing polysulfides.
3. Shuttle suppression:  $\text{Bi}_2\text{Se}_3$  can chemically anchor LiPSs, reducing migration and improving cycle life.

### Study design and methods

To construct an enhanced sulfur host material, the following strategy was implemented:

1. Precursor selection: Bi- $\text{H}_3\text{BTC}$  metal-organic framework (MOF) was used as a template.
2. Synthesis of  $\text{Bi}_2\text{Se}_3@\text{C}$ : The precursor was carbonized and selenized to obtain  $\text{Bi}_2\text{Se}_3$  particles anchored on carbon.
3. Tellurium doping: Te atoms were introduced into the  $\text{Bi}_2\text{Se}_3$  lattice, substituting for Se atoms.
4. Defect engineering: Te doping led to the formation of selenium vacancies and local lattice distortion.
5. Characterization: various techniques, including XRD, EPR, and DFT calculations, were used to study structural, electronic, and catalytic properties.
6. Electrochemical testing: Te- $\text{Bi}_2\text{Se}_{3-x}@\text{C}/\text{S}$  cathodes were evaluated under various conditions, including high sulfur loading and lean electrolyte.

### Results and discussion



### **Structural and electronic modification**

Lattice distortion: Te doping altered the local Bi coordination environment, shifting the unit cell's charge center and generating an intrinsic electric field.

Defect creation: Selenium vacancies increased the density of free carriers and unpaired  $\text{Bi}^{3+}$  cations, both acting as active sites for LiPSs adsorption and catalysis.

Improved Charge Transfer: The intrinsic electric field induced by lattice distortion enhanced electron mobility within the host.

### **Catalytic and adsorption effects**

Enhanced adsorption capacity for lithium polysulfides due to surface polarity from doping and vacancies.

Accelerated polysulfide conversion due to increased catalytic activity of distorted Bi sites and improved conductivity.

### **Electrochemical performance**

High capacity:  $1508 \text{ mAh g}^{-1}$  at 0.1C.

Excellent Rate Capability: Stable performance at high current densities.

Long-term stability: Low capacity decay and sustained high capacity under high sulfur loading and lean electrolyte conditions.

### **Conclusion**

This study demonstrates that tellurium doping and selenium vacancy engineering in  $\text{Bi}_2\text{Se}_3@\text{C}$  effectively enhance its electrochemical functionality as a sulfur host material.

The  $\text{Te-Bi}_2\text{Se}_{3-x}@\text{C}$  structure offers multiple synergistic advantages:

- Improved electrical conductivity
- Strong chemical affinity for LiPSs
- Accelerated redox kinetics
- High structural stability under cycling stress

These findings underline the value of combining doping, lattice distortion, and defect engineering to design advanced electrode materials for high-performance LSBs.

## Lithium-Sulfur Batteries

## Anionic Doping in Layered Transition Metal Chalcogenides for Robust Lithium-Sulfur Batteries

Chen Huang, Jing Yu, Chao Yue Zhang, Zhibiao Cui, Ren He, Linlin Yang, Bingfei Nan, Canhuang Li, Xuede Qi, Xueqiang Qi, Junshan Li, Jin Yuan Zhou, Oleg Usoltsev, Laura Simonelli, Jordi Arbiol, Yao-Jie Lei,\* Qing Sun,\* Guoxiu Wang,\* and Andreu Cabot\*

**Abstract:** Lithium-sulfur batteries (LSBs) are among the most promising next-generation energy storage technologies. However, a slow Li–S reaction kinetics at the LSB cathode limit their energy and power densities. To address these challenges, this study introduces an anionic-doped transition metal chalcogenide as an effective catalyst to accelerate the Li–S reaction. Specifically, a tellurium-doped, carbon-supported bismuth selenide with Se vacancies ( $\text{Te–Bi}_2\text{Se}_{3-x}\text{@C}$ ) is prepared and tested as a sulfur host in LSB cathodes. X-ray absorption and in situ X-ray diffraction analyses reveal that Te doping induces lattice distortions and modulates the local coordination environment and electronic structure of Bi atoms to promote the catalytic activity toward the conversion of polysulfides. Additionally, the generated Se vacancies alter the electronic structure around atomic defect sites, increase the carrier concentration, and activate unpaired cations to effectively trap polysulfides. As a result, LSBs based on  $\text{Te–Bi}_2\text{Se}_{3-x}\text{@C/S}$  cathodes demonstrate outstanding specific capacities of  $1508 \text{ mAh}\cdot\text{g}^{-1}$  at 0.1 C, excellent rate performance with  $655 \text{ mAh}\cdot\text{g}^{-1}$  at 5 C, and near-integral cycle stability over 1000 cycles. Furthermore, under high sulfur loading of  $6.4 \text{ mg}\cdot\text{cm}^{-2}$ , a cathode capacity exceeding  $8 \text{ mAh}\cdot\text{cm}^{-2}$  is sustained at 0.1 C current rate, with  $6.4 \text{ mAh}\cdot\text{cm}^{-2}$  retained after 300 cycles under lean electrolyte conditions ( $6.8 \mu\text{L}\cdot\text{mg}^{-1}$ ).

## Introduction

Lithium-sulfur batteries (LSBs) have emerged as a promising alternative to Li-ion batteries, offering high energy density, specific capacity, and environmental benefits. However, the commercial viability of LSBs is significantly hindered by challenges associated with the sulfur cathode and lithium metal anode.<sup>[1]</sup> Key issues include the poor conductivity of sulfur ( $\text{S}_8$ ) and its discharge product,  $\text{Li}_2\text{S}$ ,

which impede electronic and ionic transport during electrochemical reactions in the cathode. Additionally, severe volume expansion and the migration of lithium polysulfides (LiPSs) compromise long-term cycling stability.<sup>[1b,2]</sup> The sluggish Li–S reaction kinetics further limit sulfur utilization and output power, especially under the high sulfur loadings and lean electrolyte conditions<sup>[3]</sup> required for practical applications. On the anode side, lithium metal faces challenges such as uncontrolled dendrite growth and signifi-

[\*] C. Huang, J. Yu, R. He, L. Yang, B. Nan, C. Li, Q. Sun, Prof. A. Cabot  
Catalonia Institute for Energy Research-IREC, Sant Adrià de Besòs,  
Barcelona 08930, Spain  
E-mail: acabot@irec.cat

C. Huang, C. Li  
Department of Chemistry, University of Barcelona 08028, Spain

J. Yu, J. Arbiol  
Catalan Institute of Nanoscience and Nanotechnology (ICN2),  
CSIC and BIST, Campus UAB, Bellaterra, 08193 Barcelona,  
Catalonia, Spain

C. Yue Zhang, J. Yuan Zhou  
School of Physical Science & Technology; Lanzhou University  
Lanzhou 730000, China

Z. Cui  
Shenzhen Key Laboratory of Special Functional Materials &  
Shenzhen Engineering Laboratory for Advance Technology of  
Ceramics, College of Materials Science and Engineering, Shenzhen  
University, Shenzhen 518060, P. R. China

R. He, L. Yang  
Enginyeria Electrònica i Biomèdica Facultat de Física, Universitat de  
Barcelona, 08028, Barcelona, Spain

X. Qi, X. Qi  
College of Chemistry and Chemical Engineering, Chongqing  
University of Technology, Chongqing, 400054, China

J. Li  
Institute for Advanced Study; Chengdu University 610106, Cheng-  
du, China

O. Usoltsev, L. Simonelli  
ALBA Synchrotron Light Facility, Carrer de la Llum 2–26, 08290,  
Cerdanyola del Vallès, Spain

J. Arbiol, Prof. A. Cabot  
ICREA Pg. Lluís Companys, 08010 Barcelona, Catalonia, Spain

Y.-J. Lei, G. Wang  
Centre for Clean Energy Technology, School of Mathematical and  
Physical Sciences, Faculty of Science, University of Technology  
Sydney, Sydney, NSW, 2007, Australia  
E-mail: Yaojie.Lei@uts.edu.au  
guoxiu.wang@uts.edu.au

Q. Sun  
Zhengzhou Research Institute, Harbin Institute of Technology,  
Zhengzhou 450000, China  
E-mail: sunqing@hit.edu.cn

cant volume changes during repeated plating/stripping processes, leading to serious safety concerns and suboptimal cycle performance.<sup>[4]</sup>

To overcome the practical challenges faced by LSB cathodes, several strategies have been proposed, including the development of cathode sulfur hosts,<sup>[3,5]</sup> multifunctional separators,<sup>[6]</sup> and functional binders.<sup>[7]</sup> In the first direction, high surface area porous carbon materials are commonly utilized as sulfur hosts due to their affordability, excellent electrical conductivity, lightweight, and capability to physically confine polysulfides.<sup>[8]</sup> However, their non-polar nature results in a poor affinity for trapping polar polysulfides and facilitating their conversion.<sup>[9]</sup> To enhance the performance of carbon hosts, especially in activating the Li–S reaction and inhibiting polysulfide migration, the incorporation of transition metal compounds, For example, transition metal oxides,<sup>[10]</sup> sulfides,<sup>[11]</sup> selenides,<sup>[12]</sup> tellurides,<sup>[13]</sup> phosphides,<sup>[14]</sup> nitrides,<sup>[15]</sup> and single atom compounds.<sup>[16]</sup> Among them, layered transition metal chalcogenides (LTMCs) have shown considerable promise.<sup>[17]</sup> These materials provide stronger chemical interactions with polysulfides, excellent catalytic properties and superior electrical conductivity significantly improving the electrochemical performance of LSBs. However, despite the typical nanosheet-like morphology of LTMCs, they expose a moderate number of active sites and they are characterized by slow charge transfer kinetics.<sup>[18]</sup> These challenges call for additional optimization of these materials, often through material doping, to fully harness their potential.

To enhance the catalytic performance of LTMCs, various strategies have been proposed,<sup>[17,19]</sup> including heterojunction<sup>[20]</sup> and structural<sup>[21]</sup> engineering. Among them, the introduction of vacancies, especially anionic vacancies, has emerged as a particularly effective approach.<sup>[9a,22]</sup> Anionic vacancies not only inject additional free electrons within the LTMC lattice but also modify the coordination environment of the surrounding metal atoms, activating them to capture more polysulfides, and thus facilitating their conversion.<sup>[22a,23]</sup> Additionally, anionic vacancies can distort the crystal lattice symmetry,<sup>[19c]</sup> shifting the charge center within the unit cell. This displacement generates a built-in electric field that facilitates charge transfer.<sup>[19c,24]</sup> The rational engineering of this lattice strain presents an additional promising strategy to modify the electronic structure of the LTMC, thereby enhancing its catalytic performance.

In this study, we engineer Te-doped Bi<sub>2</sub>Se<sub>3</sub> supported on a nanostructured carbon polyhedral framework (Te–Bi<sub>2</sub>Se<sub>3-x</sub>@C). The incorporation of Te atoms is designed to induce lattice distortion and modify the local structure of the catalyst. Concurrently, because the atomic radius of Te is larger than that of Se, when Se atoms are replaced by Te, this size difference drives the formation of Se vacancy.<sup>[25]</sup> The creation of Se vacancies adjusts the electronic structure around atomic defect sites and increases the number of charge carriers within the crystal. Besides, the higher-energy p orbitals of Te introduce additional energy states that significantly enhance electrical conductivity.<sup>[26]</sup> We evaluate the catalytic performance and LiPS affinity of this material

for its potential use as a sulfur host in the cathode of Li–S batteries. Additionally, LSB coin cells are assembled and tested to assess their performance and stability, including under conditions of high sulfur loading and lean electrolyte.

## Results and Discussions

Te–Bi<sub>2</sub>Se<sub>3-x</sub>@C composites were produced through the annealing of Bi<sub>2</sub>Se<sub>3</sub>@C in a Te-rich atmosphere (see details in the Supporting Information, SI). Initially, Bi<sub>2</sub>Se<sub>3</sub>@C was synthesized by selenizing a Bi@C composite, which itself was derived from the carbonization of a Bi-based metal–organic framework (Bi-MOF) precursor under an argon atmosphere. The Bi-MOF was synthesized via a solvothermal reaction involving bismuth nitrate pentahydrate and trimesic acid in a solvent mixture of dimethylformamide (DMF) and methanol (CH<sub>3</sub>OH), where each Bi<sup>3+</sup> ion coordinated with six trimesic acid (H<sub>3</sub>BTC) molecules.<sup>[27]</sup> The resulting Te–Bi<sub>2</sub>Se<sub>3-x</sub>@C composite was then combined with S to produce Te–Bi<sub>2</sub>Se<sub>3-x</sub>@C/S electrodes using a melt-infiltration process (Figure 1a). The precursor Bi–MOF displayed a 1D rod-like morphology with an average rod size of ca. 2 μm (Figure S1a). Upon calcination at 600 °C in an Ar atmosphere, the Bi–MOF was transformed into carbon rods embedded with Bi@C nanoparticles (Figure S1b). These Bi@C rods and an excess of Se powder were annealed under the Ar atmosphere to produce Bi<sub>2</sub>Se<sub>3</sub>@C structures that preserved the rod-like architecture of the initial Bi@C (Figure S1c). With the addition of Te and the subsequent annealing step, elongated structures containing a large dispersion of nanoparticles on their surface were obtained (Figure S1d). While the different samples retained the original elongated architecture, the progressive increase of the particles on their surface is related to their growth through atomic or ionic diffusion driven by thermal energy.<sup>[28]</sup>

Atomic resolution aberration-corrected (AC) high-angle annular dark field scanning transmission electron microscopy (HAADF STEM) images (Figure 1b) of Te–Bi<sub>2</sub>Se<sub>3-x</sub>@C showed the presence of Bi<sub>2</sub>Se<sub>3</sub> (red and blue border area). These regions primarily consist of a five-layer A–B–A–B–A (Se–Bi–Se–Bi–Se) sequence. Some of the sequences, e.g. the one marked in green, show slightly different contrasts in the outermost Se positions, which we tentatively assign to the presence of Te (Figure 1c). The presence of numerous stacking faults is evidenced by the Se–Bi–Se–Bi–Se–Bi–Se sequence (yellow border area). In contrast, HAADF STEM analysis of Bi<sub>2</sub>Se<sub>3</sub>@C (Figure S2) exhibits no significant stacking faults, with only the Se–Bi–Se–Bi–Se sequence (orange area) visible. Therefore, the defects observed in the Te–Bi<sub>2</sub>Se<sub>3-x</sub>@C sample are likely due to the introduction of Te atoms into the Bi<sub>2</sub>Se<sub>3</sub> lattice, which disrupts the stacking sequence and induces faults during crystal growth. Besides, a subtle lattice distortion is observed in different directions in Te–Bi<sub>2</sub>Se<sub>3-x</sub>@C (Figure 1d–e and S3). This distortion is primarily attributed to three factors: 1) the coulombic interaction localized around Te atoms; 2) Jahn–Teller distortion arising from the



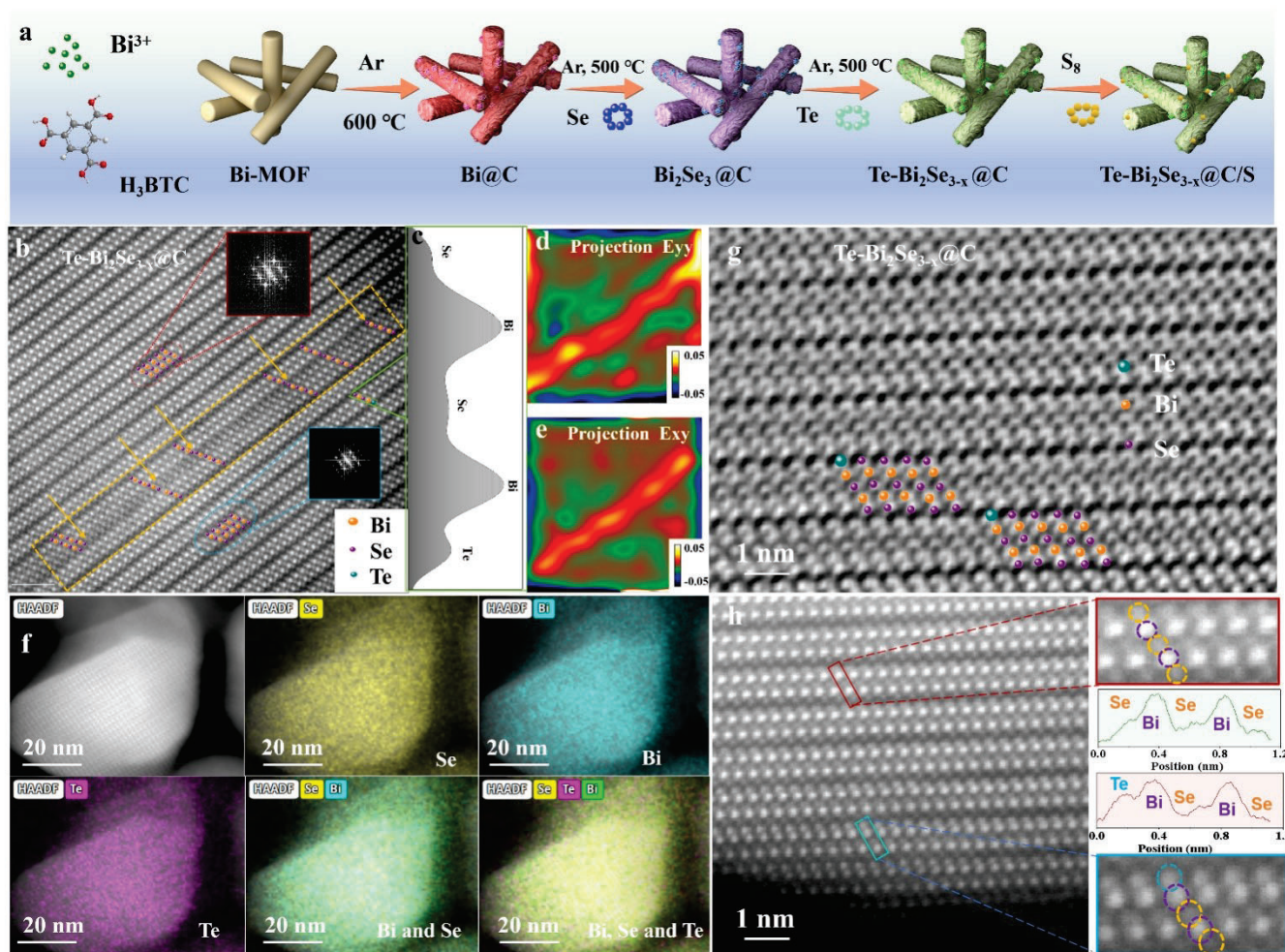


**Figure 1.** (a) Schematic diagram of the synthesis of the  $\text{Te-Bi}_2\text{Se}_{3-x}\text{@C/S}$  cathode material. (b) High-resolution AC HAADF-STEM image of  $\text{Te-Bi}_2\text{Se}_{3-x}\text{@C}$ . (c) Se-Bi-Se-Bi-Te pattern in  $\text{Te-Bi}_2\text{Se}_{3-x}\text{@C}$ . (d,e) Lattice distortion of  $\text{Te-Bi}_2\text{Se}_{3-x}\text{@C}$  in different directions (Eyy and Exy). (f) TEM-EDS spectra of a  $\text{Te-Bi}_2\text{Se}_{3-x}\text{@C}$  particle. (g) iDPC-STEM images of  $\text{Te-Bi}_2\text{Se}_{3-x}\text{@C}$ . (h) HAADF-STEM image of  $\text{Te-Bi}_2\text{Se}_{3-x}\text{@C}$ .

mismatch between Te and Se; and 3) differences in the atomic radius of Te and Se.

Energy dispersive x-ray spectroscopy (EDS) STEM analysis showed a homogeneous distribution of Te, Se, and Bi on  $\text{Te-Bi}_2\text{Se}_{3-x}\text{@C}$  (Figures 1f and S4,5). Inductively coupled plasma mass spectrometry (ICP-MS) analysis yielded the atomic ratio of Te at 3.8 %, well below that of Bi (40.0 %) and Se (56.2 %) (Table S1). Moreover, comparing integrated differential phase contrast (iDPC) and HAADF-STEM images on the samples before ( $\text{Bi}_2\text{Se}_3\text{@C}$ ) and after doping ( $\text{Te-Bi}_2\text{Se}_{3-x}\text{@C}$ ), a distinct increase in intensity was observed in the atomic columns corresponding to Se atoms post-doping (Figures 1g, h and S6). This suggests the substitution of Se atoms with Te, supported by the fact that iDPC STEM intensity is linearly proportional to atomic number (Z), while HAADF STEM is roughly proportional to  $Z^2$ . Since Te has a higher atomic number (52) compared to Se (34), but lower than Bi (83), it is reasonable to speculate that intensity profiles showing an increased intensity at the Se columns in both, iDPC STEM (Figure 1g) and HAADF STEM (Figure 1h), correspond to Te atoms

occupying positions originally held by Se. We also observe that this Se-to-Te substitution predominantly occurs at the edges of the Se-Bi-Se-Bi-Se sequence, where lower interlayer binding energies allow for better accommodation of lattice distortions, facilitating the substitution process.

The XRD patterns of  $\text{Te-Bi}_2\text{Se}_{3-x}\text{@C}$  and  $\text{Bi}_2\text{Se}_3\text{@C}$  match well with the  $\text{Bi}_2\text{Se}_3$  phase, with no secondary phases (Figure 2a).<sup>[29]</sup> While Te doping does not change the crystal structure of  $\text{Bi}_2\text{Se}_3\text{@C}$ , the XRD peaks of  $\text{Te-Bi}_2\text{Se}_{3-x}\text{@C}$  are slightly shifted to lower angles compared to  $\text{Bi}_2\text{Se}_3\text{@C}$  (Figure S7). This shift is primarily attributed to the larger radius of Te atoms compared to Se atoms, resulting in a larger lattice spacing for  $\text{Te-Bi}_2\text{Se}_{3-x}\text{@C}$ . Furthermore, with the introduction of Te atoms, the diffraction peak intensity of  $\text{Te-Bi}_2\text{Se}_{3-x}\text{@C}$  decreases and a wider peak width is observed, indicating lower crystallinity. Overall, these results are consistent with the presence of Te within the  $\text{Bi}_2\text{Se}_3$  lattice at Se sites.<sup>[30]</sup>

The specific surface area and pore size distribution are critical factors influencing a material's adsorption capacity and catalytic performance. Generally, a larger specific sur-

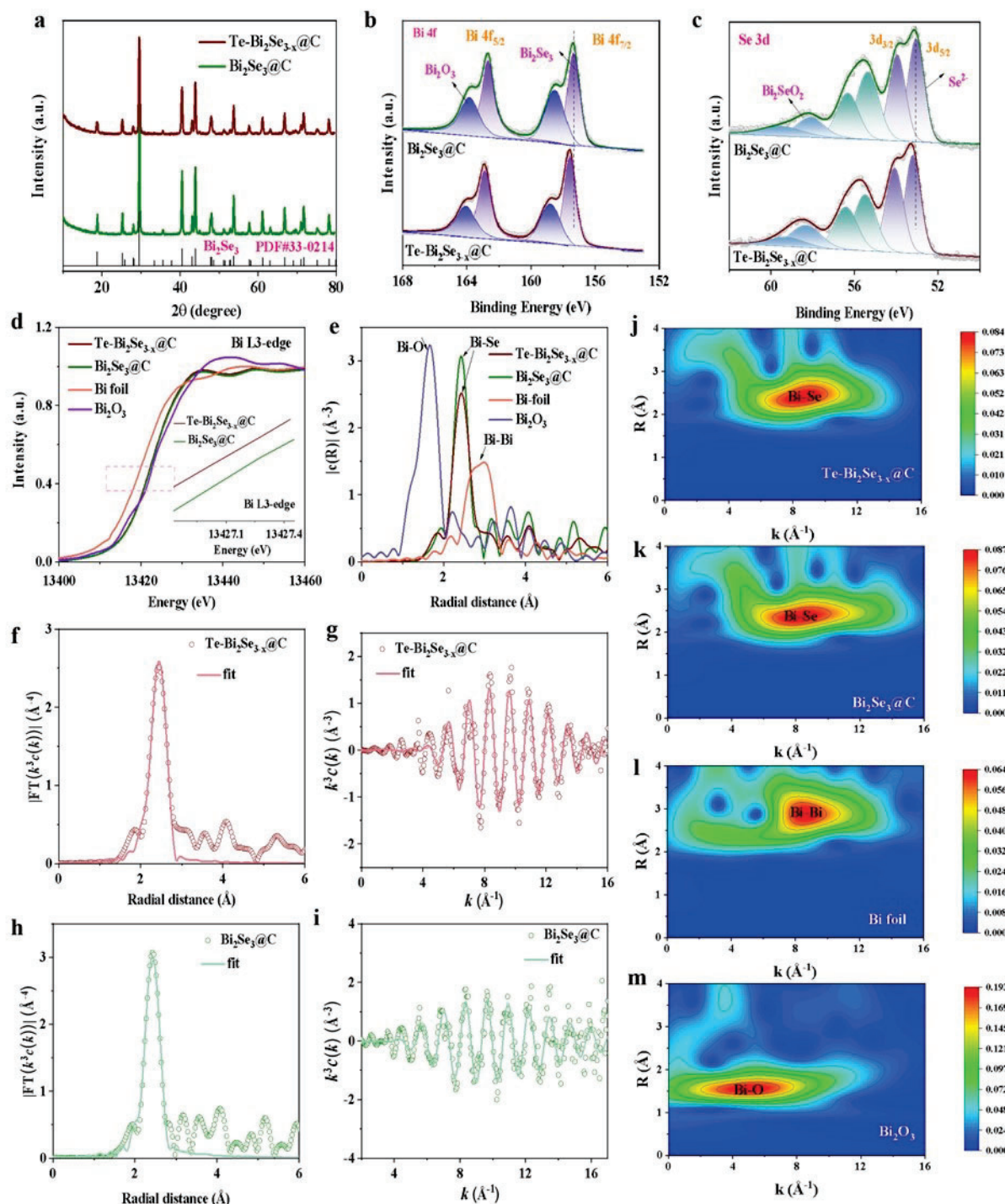


**Figure 2.** (a) XRD patterns of Te-Bi<sub>2</sub>Se<sub>3-x</sub>@C and Bi<sub>2</sub>Se<sub>3</sub>@C. (b, c) High-resolution Bi 4f (b) and Se 3d (c) XPS spectra of Te-Bi<sub>2</sub>Se<sub>3-x</sub>@C and Bi<sub>2</sub>Se<sub>3</sub>@C. (d) Bi L3-edge XANES of Te-Bi<sub>2</sub>Se<sub>3-x</sub>@C, Bi<sub>2</sub>Se<sub>3</sub>@C, Bi foil, and Bi<sub>2</sub>O<sub>3</sub>. (e) FT-EXAFS spectra of Te-Bi<sub>2</sub>Se<sub>3-x</sub>@C, Bi<sub>2</sub>Se<sub>3</sub>@C, Bi foil, and Bi<sub>2</sub>O<sub>3</sub>. (f) FT-EXAFS fitting curves of Bi L3-edge for Te-Bi<sub>2</sub>Se<sub>3-x</sub>@C at R space. (g) FT-EXAFS fitting curves of Bi L3-edge for Te-Bi<sub>2</sub>Se<sub>3-x</sub>@C at k<sub>3</sub> space. (h) FT-EXAFS fitting curves of Bi L3-edge for Bi<sub>2</sub>Se<sub>3</sub>@C at R space. (i) FT-EXAFS fitting curves of Bi L3-edge for Bi<sub>2</sub>Se<sub>3</sub>@C at k<sub>3</sub> space. (j-m) WT contour plots for Te-Bi<sub>2</sub>Se<sub>3-x</sub>@C (j), Bi<sub>2</sub>Se<sub>3</sub>@C (k), Bi foil (l), and Bi<sub>2</sub>O<sub>3</sub> (m).

face area corresponds to enhanced adsorption capacity due to the availability of more active sites, which also boosts catalytic efficiency.<sup>[31]</sup> To evaluate these properties in the synthesized samples, nitrogen (N<sub>2</sub>) adsorption-desorption

isotherms were measured, and Brunauer–Emmett–Teller (BET) analysis was performed. The specific surface areas of Bi<sub>2</sub>Se<sub>3</sub>@C and Te-Bi<sub>2</sub>Se<sub>3-x</sub>@C were determined to be 86 m<sup>2</sup> g<sup>-1</sup> and 94 m<sup>2</sup> g<sup>-1</sup>, respectively (Figure S8 and Ta-



ble S2). Interestingly, despite the larger size of the particles, Te–Bi<sub>2</sub>Se<sub>3-x</sub>@C exhibited a slightly higher specific surface area than Bi<sub>2</sub>Se<sub>3</sub>@C. This increase is attributed to the formation of additional defects on the carbon structures, the larger distribution of particles on the rod surfaces and the additional active sites introduced by Te doping. The incorporation of Te generates Se vacancies in the Bi<sub>2</sub>Se<sub>3</sub> lattice, leading to structural defects and surface depressions that provide more active sites. These structural irregularities and the associated increase in active site density collectively contribute to the enhanced specific surface area of Te–Bi<sub>2</sub>Se<sub>3-x</sub>@C.<sup>[32]</sup> The pore diameters of the materials predominantly fall within the mesoporous range (0–50 nm), which effectively accommodates and disperses sulfur, mitigating its dissolution and the shuttle effect during electrochemical reactions.<sup>[22a]</sup> This diverse pore size distribution plays a crucial role in enhancing the stability and performance of the material in energy applications.

To further explore the structural changes introduced by Te doping, electron paramagnetic resonance (EPR), a highly sensitive technique for detecting and characterizing vacancies in nanomaterials, was employed. EPR provides detailed insights into surface structures and unpaired electron behavior, making it a powerful tool for identifying vacancy signals.<sup>[33]</sup> The presence of Se vacancies in the Te-doped material was confirmed using EPR analysis. As shown in Figure S9a, Te–Bi<sub>2</sub>Se<sub>3-x</sub>@C exhibits a prominent resonance signal at  $g=2.0$ , indicative of unpaired electrons associated with Se vacancies.<sup>[22a,34]</sup> In contrast, Bi<sub>2</sub>Se<sub>3</sub>@C shows no resonance signal under identical conditions, confirming the generation of a significant density of Se vacancies in the Te-doped sample.

The Raman spectra of Te–Bi<sub>2</sub>Se<sub>3-x</sub>@C and Bi<sub>2</sub>Se<sub>3</sub>@C are presented in Figure S9b. The peak at 130 cm<sup>-1</sup> is associated with the E<sub>2g</sub> mode of Bi<sub>2</sub>Se<sub>3</sub>.<sup>[23a,35]</sup> In comparison with Bi<sub>2</sub>Se<sub>3</sub>@C, the Raman peak of Te–Bi<sub>2</sub>Se<sub>3-x</sub>@C shows a noticeable negative shift, aligning with the XRD results. Thermogravimetric analysis (TGA) allowed determining the carbon content in Te–Bi<sub>2</sub>Se<sub>3-x</sub>@C to be about 35.9 % (Figure S10).

The chemical composition and valence state of the elements within the two composites were further analyzed using X-ray photoelectron spectroscopy (XPS). The Te atomic ratio within the Te–Bi<sub>2</sub>Se<sub>3-x</sub>@C sample calculated from the XPS spectra was Te/Bi/Se = 4/36/60 (Table S3), which matches well with ICP data, thus showing no major segregation of Te to the few surface-most layers of the Te–Bi<sub>2</sub>Se<sub>3-x</sub> particles. The high-resolution Bi 4f XPS spectrum of Te–Bi<sub>2</sub>Se<sub>3-x</sub>@C was fitted with two doublets. A first doublet, at binding energies of 157.4 eV (4f<sub>7/2</sub>) and 162.7 eV (4f<sub>5/2</sub>), is associated with Bi<sup>3+</sup> within the selenide lattice (Figure 2b). The second doublet, at 158.5 eV (4f<sub>7/2</sub>) and 163.8 eV (4f<sub>5/2</sub>) in Te–Bi<sub>2</sub>Se<sub>3-x</sub>@C is associated with Bi<sup>3+</sup> in a more electronegative environment, possibly forming Bi<sub>2</sub>O<sub>3</sub>, Bi<sub>2</sub>(SeO<sub>3</sub>)<sub>3</sub>, Bi<sub>2</sub>SeO<sub>2</sub>, or another oxidized form of Bi<sub>2</sub>Se<sub>3</sub>.<sup>[2g,34]</sup> The presence of oxidized components is related to the air exposure of the material during its processing before XPS analysis.<sup>[6a,36]</sup> The same two doublets are obtained for Bi<sub>2</sub>Se<sub>3</sub>@C but both are redshifted with respect to the Bi 4f

XPS spectrum of Te–Bi<sub>2</sub>Se<sub>3-x</sub>@C. The high-resolution Se 3d XPS spectrum of Te–Bi<sub>2</sub>Se<sub>3-x</sub>@C (Figure 2c) displays three distinct doublets, corresponding to Se<sup>2-</sup> in Bi<sub>2</sub>Se<sub>3</sub> at 53.0 eV (Se 3d<sub>5/2</sub>),<sup>[2g,37]</sup> Se<sup>0</sup> at 55.4 eV (Se 3d<sub>5/2</sub>), and SeO<sub>x</sub> (SeO<sub>2</sub>, Bi<sub>2</sub>(SeO<sub>3</sub>)<sub>3</sub>, Bi<sub>2</sub>SeO<sub>2</sub>) at 58.1 eV (Se 3d<sub>5/2</sub>).<sup>[38]</sup> The detection of elemental selenium indicates that not all of the selenium introduced in large excess during the second annealing step fully participated in the formation of the selenide or was evaporated during the process.<sup>[39]</sup> The Se 3d XPS spectrum of Bi<sub>2</sub>Se<sub>3</sub>@C exhibits the same three doublets, though all are redshifted a similar value compared with Te–Bi<sub>2</sub>Se<sub>3-x</sub>@C. The consistent direction and magnitude of the binding energy shifts in both the Se 3d and Bi 4f XPS spectra suggest an upward shift of the Fermi level of Te–Bi<sub>2</sub>Se<sub>3-x</sub>@C relative to Bi<sub>2</sub>Se<sub>3</sub>@C, in agreement with the electronic donor role played by ionized selenium vacancies generated by the introduction of larger Te<sup>2-</sup> ions at Se<sup>2-</sup> sites.<sup>[2g,19a]</sup> The C1s XPS spectra of Te–Bi<sub>2</sub>Se<sub>3-x</sub>@C and Bi<sub>2</sub>Se<sub>3</sub>@C present three characteristic peaks corresponding to C–C, C–O, and C=O at binding energies of 284.6 eV, 286.2 eV, and 288.6 eV, respectively (Figure S11a).<sup>[22a]</sup> The high-resolution Te 3d XPS spectrum of Te–Bi<sub>2</sub>Se<sub>3-x</sub>@C displays two doublets related to Te<sup>2-</sup> within a metal chalcogenide at 574.2 eV (Te 3d<sub>5/2</sub>) and a Te–O chemical environment at 576.1 eV (Te 3d<sub>5/2</sub>) related to the air exposure of the material before XPS analysis (Figure S11b).<sup>[24]</sup> The ratio of oxidized Te is higher than that of oxidized Se. This is related to the electronic structure of Te playing a role in its higher oxidation tendency when exposed to air. Te has a lower ionization energy, making it easier for Te atoms to lose electrons and become oxidized, resulting in Te<sup>+</sup> or Te<sup>2+</sup> states. In contrast, Se has a higher ionization energy, making it less prone to electron loss and therefore less likely to oxidize as extensively as Te. Besides, the preferential location of Te at the edges of the Se–Bi–Se–Bi–Se sequence, due to its larger size, can also promote its relative enhanced oxidation upon air exposure.

The conductivity of Te–Bi<sub>2</sub>Se<sub>3-x</sub>@C samples ( $7.8 \times 10^2$  Scm<sup>-1</sup>) was systematically higher than that of Bi<sub>2</sub>Se<sub>3</sub>@C ( $5.5 \times 10^2$  Scm<sup>-1</sup>) across all pressure conditions, as measured by a four-probe method (Figure S12a). While the main contribution to electronic transport within the composites is primarily from carbon, this improved conductivity is still attributed to the additional carriers introduced by the incorporation of Te.

The total density of states (TDOS) of Bi<sub>2</sub>Se<sub>3</sub>, calculated using density functional theory (DFT), reveals a band gap at the Fermi level, consistent with the semiconductor nature of the material (Figure S12b). In contrast, the electronic structure of Te–Bi<sub>2</sub>Se<sub>3-x</sub> shows the emergence of a distinct hybrid band within the conduction band, leading to a significant increase in TDOS at the Fermi level. This enhanced TDOS at the Fermi level is associated with improved charge transport properties, aligning with the experimentally observed increase in conductivity. It should be noted that the Te–Bi<sub>2</sub>Se<sub>3-x</sub> model included both Se vacancies and structural distortions generated when relaxing the model (see details in the SI).



The chemical state and coordination of Bi atoms were further investigated using X-ray absorption near-edge structure spectroscopy (XANES) and extended X-ray absorption fine structure spectroscopy (EXAFS). The white-line intensity of Te-Bi<sub>2</sub>Se<sub>3-x</sub>@C and Bi<sub>2</sub>Se<sub>3</sub>@C is higher than that of Bi foil, indicating their electronic states are at higher energy than the Bi (0) state in Bi foil. The absorption edges of Te-Bi<sub>2</sub>Se<sub>3-x</sub>@C and Bi<sub>2</sub>Se<sub>3</sub>@C are positioned between the absorption edges of the metallic Bi foil (Bi<sup>0</sup>) and Bi<sub>2</sub>O<sub>3</sub> (Bi<sup>3+</sup>), indicating that Bi exhibits valence between 0 and +3 (Figure 2d).<sup>[40]</sup> Compared to Bi<sub>2</sub>Se<sub>3</sub>@C, Te-Bi<sub>2</sub>Se<sub>3-x</sub>@C exhibit a slight negative shift in the white line intensity, confirming that Bi in Te-Bi<sub>2</sub>Se<sub>3-x</sub>@C has a lower valence state compared to Bi<sub>2</sub>Se<sub>3</sub>@C (inset Figure 2d).<sup>[1b]</sup>

The Fourier-transformed k<sub>3</sub>-weighted EXAFS spectra reveal a reduction in the intensity of the unique shell scattering peak (2.30 Å) corresponding to the Bi-Se bond in Te-Bi<sub>2</sub>Se<sub>3-x</sub>@C (Figure 2e). This reduction primarily stems from the presence of Se vacancies, leading to a decrease in the coordination number of Bi with Se.<sup>[19a]</sup> EXAFS curve fitting and the derived structural parameters (Figure 2f-i and S13-14) show the coordination number of Se and Bi centers in Bi<sub>2</sub>Se<sub>3</sub>@C (N=6.0) is significantly higher than in Te-Bi<sub>2</sub>Se<sub>3-x</sub>@C (N=4.6). This observation suggests that Te atoms are substituting Se atoms within the structure. Additionally, the length of the Bi-Se bond in Te-Bi<sub>2</sub>Se<sub>3-x</sub>@C (2.81 Å) is slightly longer than in Bi<sub>2</sub>Se<sub>3</sub>@C (2.79 Å), a difference that can be attributed to the influence of Se vacancies.

Wavelet transform (WT) analysis (Figure 2j-m) was used to further unveil the structural disorder and charge redistribution around the Bi atoms. In Te-Bi<sub>2</sub>Se<sub>3-x</sub>@C, a slight shift towards a shorter radial distance is observed compared to Bi<sub>2</sub>Se<sub>3</sub>@C. This shift suggests that the alteration in bond length is primarily due to a weakening of Bi-Se coordination. These changes in the coordination environment affect the electron distribution at the surface, which is likely to influence the interaction with polysulfides and alter the kinetics of the catalyzed Li-S reaction.

To assess the LiPSs adsorption capacity of the host materials, they were immersed in a 0.5 mM Li<sub>2</sub>S<sub>6</sub> solution overnight. In all cases, the initial Li<sub>2</sub>S<sub>6</sub> solution appears yellow. After 6 h adsorption, the Li<sub>2</sub>S<sub>6</sub> solution containing only porous carbon (Super P) largely retained its original yellow color, while the solution with Bi<sub>2</sub>Se<sub>3</sub>@C showed a slight lightening (Figure S15). In contrast, the color of the Li<sub>2</sub>S<sub>6</sub> solution containing Te-Bi<sub>2</sub>Se<sub>3-x</sub>@C almost completely vanished, indicating nearly complete adsorption of Li<sub>2</sub>S<sub>6</sub> by the Te-Bi<sub>2</sub>Se<sub>3-x</sub>@C host material. This observation was further confirmed using UV/Vis absorption spectroscopy (Figure 3a).

XPS analysis of the material after the LiPS adsorption test (Te-Bi<sub>2</sub>Se<sub>3-x</sub>@C-Li<sub>2</sub>S<sub>6</sub>) revealed a significant blueshift in the Bi 4f, Se 3d, and Te 3d orbitals compared to the fresh sample (Te-Bi<sub>2</sub>Se<sub>3-x</sub>), suggesting a strong interaction between the sample and the Li<sub>2</sub>S<sub>6</sub> (Figure 3b,c and S16).<sup>[5b,22a]</sup>

DFT calculations were conducted to evaluate the theoretical adsorption capacity of the host materials for polysulfides. Figures S17-20 present the adsorption models for

the various host materials interacting with polysulfides. As noted above, the theoretical calculation model accounted for the effect of vacancies and lattice distortions induced by doping, which are automatically considered during the geometry optimization process. Compared to Bi<sub>2</sub>Se<sub>3</sub>, Te-Bi<sub>2</sub>Se<sub>3-x</sub> exhibits a higher adsorption capacity for LiPSs. Specifically, the adsorption energies of Bi<sub>2</sub>Se<sub>3</sub> and Te-Bi<sub>2</sub>Se<sub>3-x</sub> for Li<sub>2</sub>S<sub>4</sub> are -1.98 eV and -2.81 eV, respectively (Figure 3d).

In situ XRD was used to characterize the evolution of S<sub>8</sub> and Li<sub>2</sub>S during the charge/discharge of a cell (see details in the SI, Figure 3e-g). During the discharge stage, a notable delay is observed in the weakening of the Bragg signal intensity for the α-S<sub>8</sub> phase in the Bi<sub>2</sub>Se<sub>3</sub>@C/S and Super P/S electrodes compared to the Te-Bi<sub>2</sub>Se<sub>3-x</sub>@C/S electrode. The characteristic Bragg signal of the α-S<sub>8</sub> phase persists throughout the discharge process, indicating a relatively slower reaction kinetics within the Bi<sub>2</sub>Se<sub>3</sub>@C and Super P electrodes compared to Te-Bi<sub>2</sub>Se<sub>3-x</sub>@C. As lithiation progresses, in the fully discharged state, the relative intensity of the Li<sub>2</sub>S signal in the Bi<sub>2</sub>Se<sub>3</sub>@C/S and Super P/S cathodes is significantly lower than that in the Te-Bi<sub>2</sub>Se<sub>3-x</sub>@C/S. This suggests insufficient polysulfide conversion during lithiation in the former (Bi<sub>2</sub>Se<sub>3</sub>@C/S and Super P/S), with the α-S<sub>8</sub> phase failing to fully lithiate, consistent with the persistent presence of characteristic signals throughout the characterization process. Upon full charge, during delithiation, all electrodes exhibit characteristic signals corresponding to β-S<sub>8</sub>. However, the β-S<sub>8</sub> signal intensity in the Bi<sub>2</sub>Se<sub>3</sub>@C/S and Super P/S is weak, and a small Bragg signal corresponding to the α-S<sub>8</sub> phase remains from the initial stage. In contrast, the Te-Bi<sub>2</sub>Se<sub>3-x</sub>@C electrode shows negligible α-S<sub>8</sub> phase signal and a strong β-S<sub>8</sub> XRD, suggesting full conversion of S<sub>8</sub> during the charge/discharge cycle.

To assess the catalytic performance of the host materials, 2032 coin-type symmetric cells were assembled using the host materials in both electrodes. These cells were tested without sulfur, utilizing an electrolyte containing Li<sub>2</sub>S<sub>6</sub> (see details in the SI). The cyclic voltammetry (CV) curves of the Te-Bi<sub>2</sub>Se<sub>3-x</sub>@C-based symmetric cells exhibited the highest peak current densities compared to those of Bi<sub>2</sub>Se<sub>3</sub>@C and Super P (Figure 4a). This result suggests that Te doping effectively enhances the LiPS conversion kinetics. Additionally, the CV curves of Te-Bi<sub>2</sub>Se<sub>3-x</sub>@C in a Li<sub>2</sub>S<sub>6</sub>-free electrolyte showed purely capacitive behavior, confirming that the capacity contribution observed in the Li<sub>2</sub>S<sub>6</sub>-containing electrolyte is indeed due to the conversion of polysulfides. Linear sweep voltammetry (LSV) further demonstrated that the Te-Bi<sub>2</sub>Se<sub>3-x</sub>@C electrode exhibited the lowest overpotentials and the lowest Tafel slopes for both the reduction and oxidation of S within polysulfides (Figures 4b, c and S21). This result corroborates that the introduction of Te into Bi<sub>2</sub>Se<sub>3</sub> significantly accelerates the polysulfide conversion kinetics. Additionally, electrochemical impedance spectroscopy (EIS) analyses of the symmetric cells revealed that the Te-Bi<sub>2</sub>Se<sub>3-x</sub>@C electrodes had the lowest charge transfer resistance (10.5 Ω), further suggesting enhanced charge transfer kinetics during the sulfur redox reaction due to the introduction of Te (Figure S22).

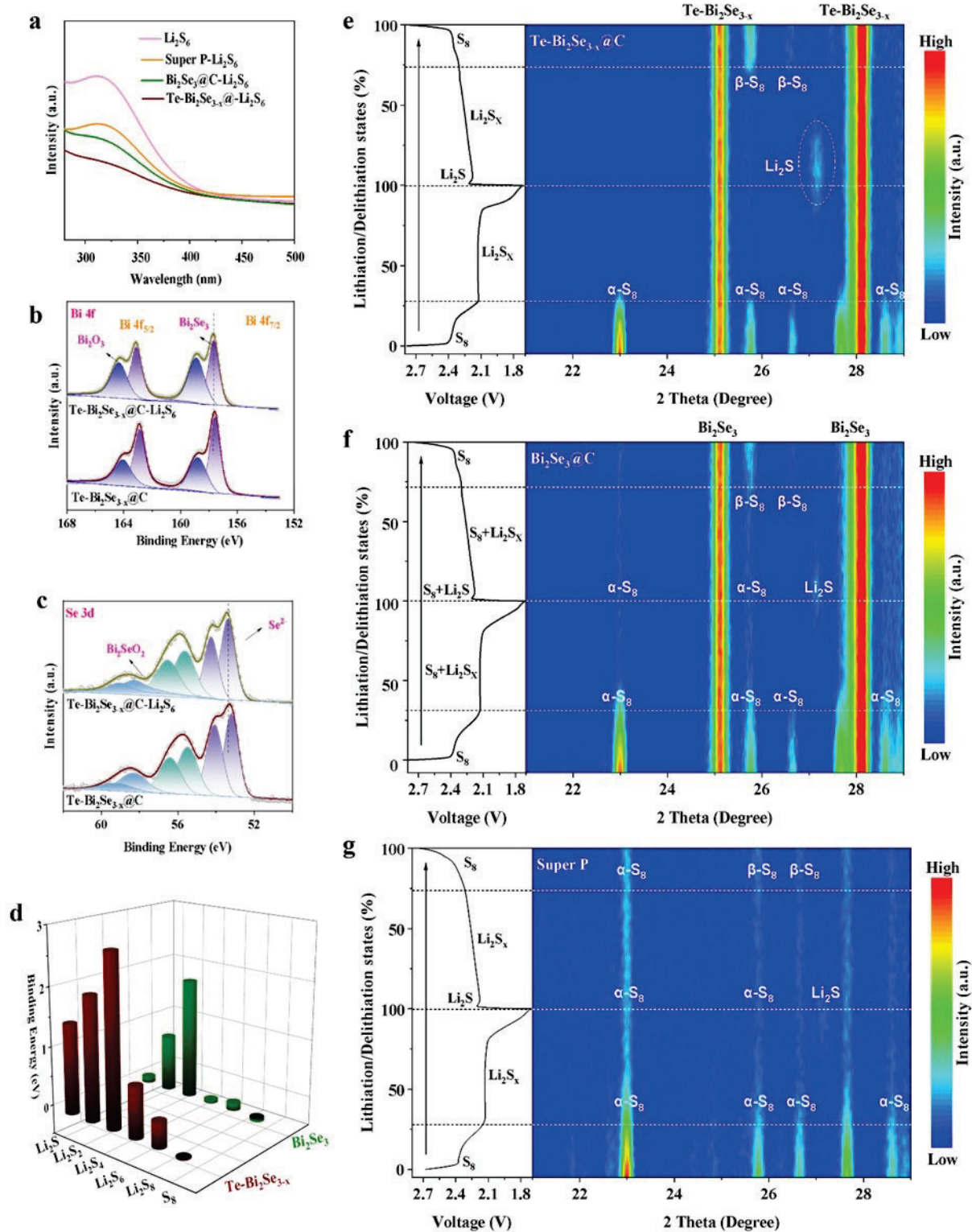


**Figure 3.** (a) UV/Vis absorption spectra and photographs (inset) of  $\text{Li}_2\text{S}_6$  solutions containing different materials after overnight adsorption. (b,c) High-resolution Bi 4f and Se 3d XPS spectra of  $\text{Te-Bi}_2\text{Se}_{3-x}/\text{C}$  before and after  $\text{Li}_2\text{S}_6$  adsorption. (d) DFT-calculated adsorption energies of  $\text{Te-Bi}_2\text{Se}_{3-x}$  and  $\text{Bi}_2\text{Se}_3$  with different polysulfides ( $\text{S}_8$ ,  $\text{Li}_2\text{S}_8$ ,  $\text{Li}_2\text{S}_6$ ,  $\text{Li}_2\text{S}_4$ , and  $\text{Li}_2\text{S}$ ). (e–g) In situ XRD patterns during charging and discharging of cells based on  $\text{Te-Bi}_2\text{Se}_{3-x}/\text{C/S}$ ,  $\text{Bi}_2\text{Se}_3/\text{C/S}$ , and Super P/S cathodes.

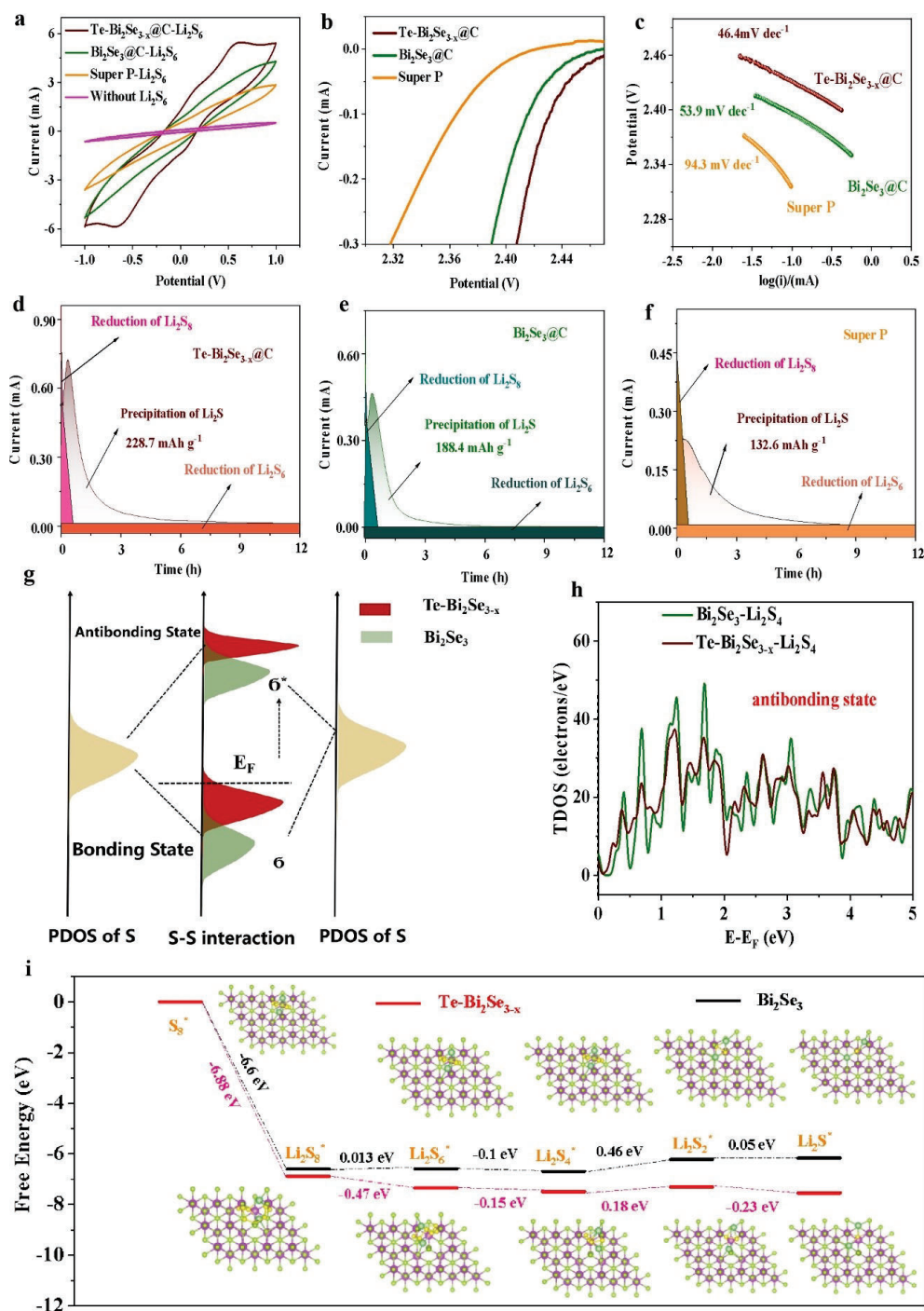


**Figure 4.** (a) CV curves of symmetric cells based on Te-Bi<sub>2</sub>Se<sub>3-x</sub>@C, Bi<sub>2</sub>Se<sub>3</sub>@C, and Super P electrodes at a scan rate of 5 mV s<sup>-1</sup> within the symmetric cells. (b) LSV polarization curves of Te-Bi<sub>2</sub>Se<sub>3-x</sub>@C, Bi<sub>2</sub>Se<sub>3</sub>@C and Super P for LiPSs reduction. (c) Tafel curves of Te-Bi<sub>2</sub>Se<sub>3-x</sub>@C, Bi<sub>2</sub>Se<sub>3</sub>@C and Super P for LiPSs reduction. (d-f) Li<sub>2</sub>S deposition curves of Te-Bi<sub>2</sub>Se<sub>3-x</sub>@C (d), Bi<sub>2</sub>Se<sub>3</sub>@C (e), and Super P (f) at 2.05 V constant voltage. (g) Energy level diagram illustrating orbital hybridization for the S-S bond is depicted below. The Fermi level of the substrate (E<sub>F</sub>) is indicated, with σ and σ\* denoting bonding and antibonding states, respectively. (h) TDOS curves for Bi<sub>2</sub>Se<sub>3</sub> and Te-Bi<sub>2</sub>Se<sub>3-x</sub> after adsorption of Li<sub>2</sub>S<sub>4</sub>. (i) Gibbs free curves and model optimization structure of Te-Bi<sub>2</sub>Se<sub>3-x</sub> and Bi<sub>2</sub>Se<sub>3</sub>.

The analysis of the Li<sub>2</sub>S nucleation step on Te-Bi<sub>2</sub>Se<sub>3-x</sub>@C, Bi<sub>2</sub>Se<sub>3</sub>@C, and Super P revealed that the Te-Bi<sub>2</sub>Se<sub>3-x</sub>@C cathode exhibited the highest current re-

sponse during the 2.05 V potential static test (Figure 4d-f). According to Faraday's law ( $Q=It$ , where  $Q$  is the capacity,  $I$  is the discharge current, and  $t$  is the time), the calculated



capacity of Te-Bi<sub>2</sub>Se<sub>3-x</sub>@C was 229 mAh g<sup>-1</sup>, well above that of Bi<sub>2</sub>Se<sub>3</sub>@C (188 mAh g<sup>-1</sup>) and Super P (133 mAh g<sup>-1</sup>). This indicates that the Te-Bi<sub>2</sub>Se<sub>3-x</sub>@C cathode has a superior ability to facilitate Li<sub>2</sub>S nucleation, contributing to its enhanced electrochemical performance. A similar approach was employed to investigate the dissolution kinetics of Li<sub>2</sub>S (Figure S23). The constant potential charge curve for Te-Bi<sub>2</sub>Se<sub>3-x</sub>@C exhibited a higher current density compared to Bi<sub>2</sub>Se<sub>3</sub>@C and Super P, indicating a lower oxidation overpotential for Li<sub>2</sub>S dissolution. Additionally, the dissolution capacity of Te-Bi<sub>2</sub>Se<sub>3-x</sub>@C (702 mAh g<sup>-1</sup>) significantly surpassed that of Bi<sub>2</sub>Se<sub>3</sub>@C (568 mAh g<sup>-1</sup>) and Super P electrodes (397 mAh g<sup>-1</sup>). These findings collectively confirm that the Te-Bi<sub>2</sub>Se<sub>3-x</sub>@C host demonstrates superior electrocatalytic performance, effectively reducing the polarization of LiPS conversion reactions and enhancing redox kinetics.

In Li-S battery chemistry, the sulfur reduction reaction (SRR) proceeds through a multi-step evolution of LiPSs during the discharge process. Initially, S<sub>8</sub> ring molecules react with Li<sup>+</sup> to form long-chain Li<sub>2</sub>S<sub>8</sub> at approximately 2.7–2.4 V versus the Li/Li<sup>+</sup> electrode. This is followed by the progressive cleavage of S–S bonds, resulting in the sequential formation of shorter-chain polysulfides. These intermediates include Li<sub>2</sub>S<sub>6</sub> at around 2.3 V, Li<sub>2</sub>S<sub>4</sub> at approximately 2.1 V, and finally, the precipitation of insoluble Li<sub>2</sub>S<sub>2</sub> and Li<sub>2</sub>S at 2.1–1.7 V.<sup>[41]</sup>

The initial cleavage of the S<sub>8</sub> ring molecule is generally regarded as a relatively straightforward process. However, the subsequent cleavage into shorter-chain LiPSs becomes progressively more challenging, with the final conversion into insoluble products being notably sluggish.<sup>[42]</sup>

The kinetics of the SRR at each step can be fundamentally described in terms of activation energy ( $E_a$ ). To investigate this, we experimentally measured the  $E_a$  for each stage of the LiPSs conversion process by analyzing the charge transfer resistance ( $R_{ct}$ ) at the corresponding voltages across different temperatures (Figure S24 a–h). By fitting the experimentally measured charge transfer resistances at various temperatures to the Arrhenius equation (Figure S24 i–n).

As depicted in Figure S24 o, the  $E_a$  for the SRR in Te-Bi<sub>2</sub>Se<sub>3-x</sub> is substantially lower than that of Bi<sub>2</sub>Se<sub>3</sub> within the voltage range of 2.7–1.8 V. This is particularly evident during the phase transition from liquid, soluble Li<sub>2</sub>S<sub>x</sub> to solid, insoluble Li<sub>2</sub>S<sub>2</sub>/Li<sub>2</sub>S, which is a crucial step in the overall SRR process due to the significant energy barriers involved in the nucleation and growth of the solid phase.<sup>[43]</sup>

Additionally, we determined the activation energy  $E_a$  for each stage of the reaction at the corresponding voltages. The results (Figure S24p) reveal that  $E_a$  is relatively low at 0.2 eV for the initial conversion of S<sub>8</sub> to Li<sub>2</sub>S<sub>8</sub> at 2.7 V, increases to 0.34 eV in the voltage range of 2.4–2.1 V for the transition from Li<sub>2</sub>S<sub>8</sub> to Li<sub>2</sub>S<sub>6</sub> and Li<sub>2</sub>S<sub>4</sub>, and reaches its highest value of 0.46 eV at 1.8 V, which corresponds to the final step of conversion into insoluble products. These findings underscore that while the transformation of S<sub>8</sub> ring molecules into soluble LiPSs is relatively facile, the subsequent conversion of LiPSs into insoluble end products is

significantly more challenging, making it the rate-limiting step in practical Li-S batteries.

The breaking of the S–S bond of the polysulfides adsorbed on the different surfaces was investigated using DFT calculations (Figure 4g, h and S25). The analysis revealed significant alterations in electron density within bonding and antibonding states near the Fermi level upon polysulfide adsorption onto the host materials. Figure 4j presents the energy level diagram of Li<sub>2</sub>S<sub>x</sub> ( $x=4,6$ ) hybridized with the surface orbitals of Te-Bi<sub>2</sub>Se<sub>3-x</sub> and Bi<sub>2</sub>Se<sub>3</sub>, along with the calculated DOS of polysulfides on the catalyst surface. The diagram illustrates how the bonding of polysulfides on Te-Bi<sub>2</sub>Se<sub>3-x</sub> and Bi<sub>2</sub>Se<sub>3</sub> differently influences the bonding states around the Fermi level of sulfur atoms, with Te-Bi<sub>2</sub>Se<sub>3-x</sub> showing a higher electron density near  $E_F$ . Compared to Bi<sub>2</sub>Se<sub>3</sub>-Li<sub>2</sub>S<sub>x</sub> ( $x=4,6$ ), the TDOS of Te-Bi<sub>2</sub>Se<sub>3-x</sub>-Li<sub>2</sub>S<sub>x</sub> ( $x=4,6$ ) exhibits an upward shift after the absorption of Li<sub>2</sub>S<sub>x</sub> ( $x=4,6$ ), indicating reduced stability of the S–S bond. This reduced stability facilitates the cleavage of S–S bonds, thereby significantly improving the kinetics of the Li-S reaction.

During the reduction of sulfur, S<sub>8</sub> initially reacts with two Li<sup>+</sup> to generate Li<sub>2</sub>S<sub>8</sub>, which is subsequently converted into Li<sub>2</sub>S<sub>6</sub>, Li<sub>2</sub>S<sub>4</sub>, Li<sub>2</sub>S<sub>2</sub>, and ultimately into Li<sub>2</sub>S. DFT calculations of the Gibbs free energy for the entire reaction process on the surface of Te-Bi<sub>2</sub>Se<sub>3-x</sub> and Bi<sub>2</sub>Se<sub>3</sub> (Figure 4i) revealed that the energy barrier on the Te-Bi<sub>2</sub>Se<sub>3-x</sub> surface was significantly lower than that on the Bi<sub>2</sub>Se<sub>3</sub> surface. This reduced energy barrier on the Te-Bi<sub>2</sub>Se<sub>3-x</sub> surface is consistent with the experimental results showing Te-Bi<sub>2</sub>Se<sub>3-x</sub> to promote the entire Li-S reaction process.

To evaluate the electrochemical performance of the host materials within LSB cells, the materials were infiltrated with S (see details in the SI). XRD analysis confirmed the presence of sulfur in the final electrode material (Figure S26). Besides, TGA quantified the sulfur content in Te-Bi<sub>2</sub>Se<sub>3-x</sub>@C/S, Bi<sub>2</sub>Se<sub>3</sub>@C/S, and Super P/S as 69.5 %, 68.3 %, and 66.8 %, respectively (Figure S27). Coin cells were assembled using the sulfur composite electrode as the cathode, lithium foil as the anode, and a solution composed of 1.0 M lithium bis (trifluoromethanesulfonyl) imide and 2 % LiNO<sub>3</sub> in a mixture of 1,3-dioxolane (DOL) and 1,2-dimethoxyethane (DME) in a 1:1 volume ratio as electrolyte. The galvanostatic charge/discharge (GCD) curves of the cells at a 0.1 C current rate are shown in Figure 5a. Two distinct plateaus emerged during the discharge process. The first discharge plateau, with a capacity denoted as Q<sub>1</sub>, was attributed to the conversion of S<sub>8</sub> to long-chain polysulfides (S<sub>8</sub> into Li<sub>2</sub>S<sub>4</sub>).

The second discharge plateau, with a capacity Q<sub>2</sub>, accounted for the solid-solid reaction of polysulfides gaining electrons and reducing to insoluble Li<sub>2</sub>S<sub>2</sub>, and eventually to Li<sub>2</sub>S.<sup>[1a,34]</sup> The unique charging voltage plateau is associated with the complete conversion of polysulfides back to S<sub>8</sub>. Consistent with previous results, the Te-Bi<sub>2</sub>Se<sub>3-x</sub>@C/S cathode demonstrated the highest initial specific capacity (1508 mAh g<sup>-1</sup>), outperforming Bi<sub>2</sub>Se<sub>3</sub>@C/S (1274 mAh g<sup>-1</sup>) and Super P/S (1078 mAh g<sup>-1</sup>, Table S4). Figure S28 illustrates the charging and discharging mechanism of LSBs.

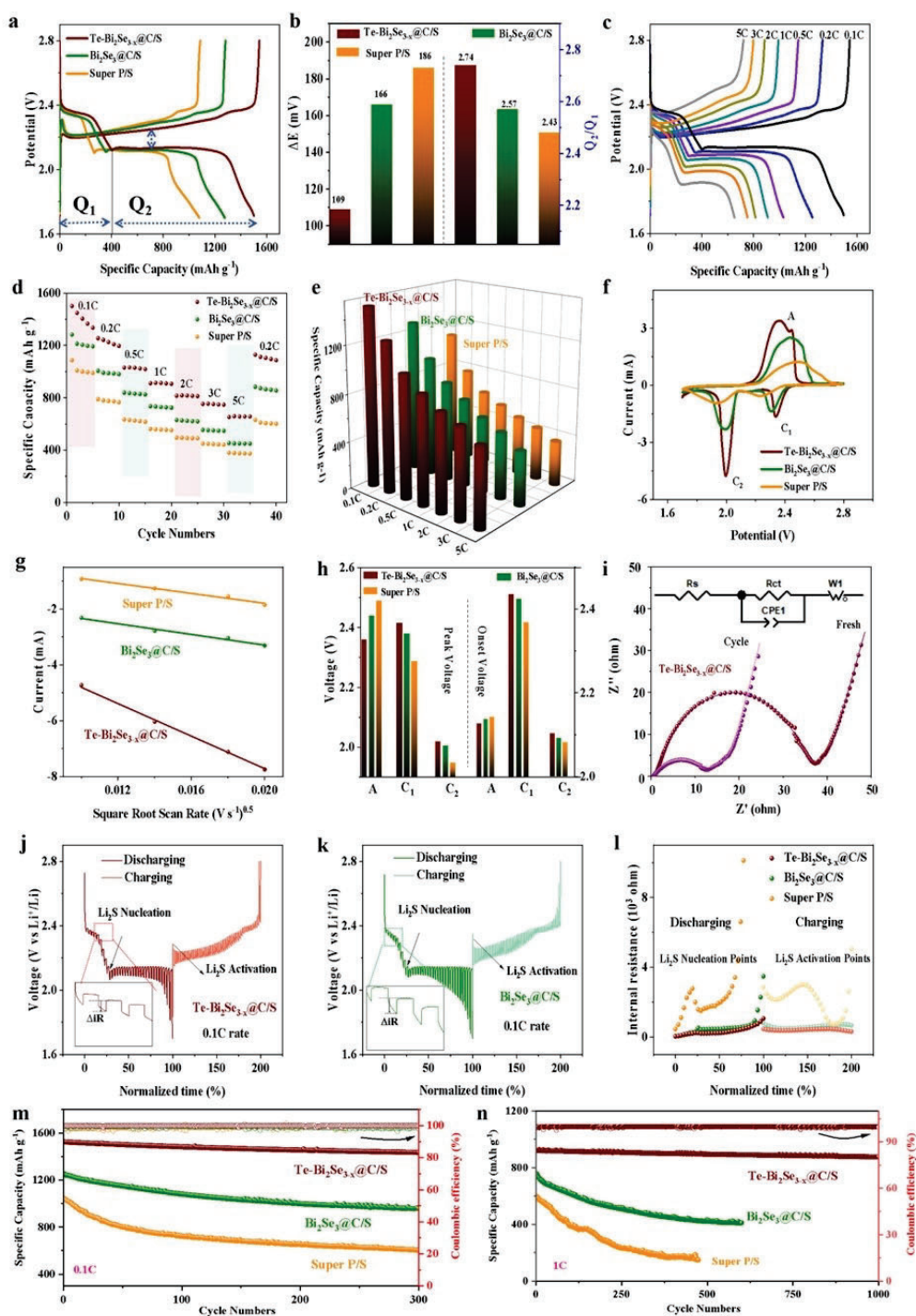


**Figure 5.** (a) GCD curves of different electrodes at a current rate of 0.1 C. (b) Polarization voltage and  $Q_2/Q_1$  ratio for Te-Bi<sub>2</sub>Se<sub>3-x</sub>@C/S, Bi<sub>2</sub>Se<sub>3</sub>@C/S, and Super P/S. (c) GCD curve of Te-Bi<sub>2</sub>Se<sub>3-x</sub> in the voltage window 1.7–2.8 V and current densities from 0.1 C to 5 C. (d, e). Rate performance of different cathodes. (f) CV curves within a voltage window of 1.7–2.8 V at a scan rate of 0.1 mV s<sup>-1</sup>. (g) Peak current vs. the square root of the rate. (h) Peak and onset potentials of Te-Bi<sub>2</sub>Se<sub>3-x</sub>@C/S, Bi<sub>2</sub>Se<sub>3</sub>@C/S, and Super P/S. (i) EIS spectra of Te-Bi<sub>2</sub>Se<sub>3-x</sub>@C/S before and after 100 cycles. The inset displays the equivalent circuit used to fit the data. (j, k) GITT curves on Te-Bi<sub>2</sub>Se<sub>3-x</sub>@C/S (j) and Bi<sub>2</sub>Se<sub>3</sub>@C/S (k). (l) Internal resistances vs. normalized discharge-charge time. (m) Cycling stability at a current density of 0.1 C. (n) Cycling stability at a current rate of 1 C.

We also observed the polarization potential  $\Delta E$  (Figure 5b), defined as the difference between the oxidation platform and the second reduction platform of the Li-S

reaction,<sup>[2f,44]</sup> was significantly lower for Te-Bi<sub>2</sub>Se<sub>3-x</sub>@C/S (109 mV) compared to Bi<sub>2</sub>Se<sub>3</sub>@C/S (166 mV) and Super P/S (186 mV). Additionally, the  $Q_2/Q_1$  ratio was used to quantify

the catalytic activity of the host material toward LiPS conversion (Figure 5b).<sup>[38a,45]</sup> The first plateau involves 4 electrons, while the second plateau involves 12 electrons, leading to a theoretical  $Q_2/Q_1$  ratio of 3 for a complete 16-electron  $S_8$  lithiation process. However, this ratio is typically lower than 3 due to the dissolution of polysulfides that cannot further participate in the reaction and the incomplete reduction from  $Li_2S_4$  to  $Li_2S$  during the second discharge. The closer the  $Q_2/Q_1$  ratio is to 3, the stronger the conversion ability of the host material to convert polysulfides.<sup>[22a]</sup> Experimentally, the  $Q_2/Q_1$  ratio measured for Te- $Bi_2Se_{3-x}@C/S$  (2.74) was significantly higher than that of  $Bi_2Se_3@C/S$  (2.57) and Super P/S (2.43), demonstrating that the Te-doped host material has excellent catalytic ability to accelerate the conversion of polysulfides.

The GCD curves of Te- $Bi_2Se_{3-x}@C/S$ ,  $Bi_2Se_3@C/S$ , and Super P/S at different current rates and the rate performance of the cells are displayed in Figures 5c–e and S29. At current densities of 0.1 C, 0.2 C, 0.5 C, 1 C, 2 C, 3 C, and 5 C, the specific capacity for Te- $Bi_2Se_{3-x}@C/S$  was 1508, 1262, 1033, 923, 815, 756, and 655  $mAh\ g^{-1}$ , respectively. These values are significantly higher than those obtained for the two reference electrodes. Even at the highest current rate tested (5 C), a clear voltage plateau can be observed for Te- $Bi_2Se_{3-x}@C/S$ , indicating a fast conversion of polysulfides in this electrode. Upon returning to a 0.2 C current rate, the specific capacity of the Te- $Bi_2Se_{3-x}@C/S$  electrode reached 1134  $mAh\ g^{-1}$ , demonstrating notable reversibility.

The level of Te doping can significantly influence the electrochemical properties of the material. To test the influence of this parameter, we increased the Te content to 15 mg and 20 mg to prepare samples with higher doping levels, and conducted electrochemical tests to evaluate their performance. The GCD curve of the sample with a Te doping amount of 15 mg is shown in Figure S30a. At current densities of 0.1 C, 0.2 C, 0.5 C, 1 C, 2 C, 3 C, and 5 C, the specific capacities are 1325, 1183, 976, 856, 763, 675, and 614  $mAh\ g^{-1}$ , respectively. For the sample with a Te doping amount of 20 mg, the GCD curves are presented in Figure S30b. At the same current densities, the corresponding specific capacities are 1282, 1025, 866, 764, 670, 617, and 536  $mAh\ g^{-1}$ , respectively. These results indicate that increasing the doping amount leads to a slight decline in electrochemical performance. The observed decline in electrochemical performance with increased Te doping may be attributed to the Lattice mismatch, impaired ion diffusion, reduced polysulfide adsorption capacity and dilution of active sites due to excessive doping.

The CV curves of different electrodes at a scan rate of 0.1  $mVs^{-1}$  within a potential window from 1.7 V to 2.8 V are depicted in Figures 5f and S31. The Te- $Bi_2Se_{3-x}@C/S$ -based cell exhibits distinct dual reduction peaks, corresponding to the conversion of  $S_8$  to  $Li_2S_x$  ( $4 \leq x \leq 8$ ) and insoluble  $Li_2S/Li_2S_2$ , respectively. The oxidation peak is attributed to the conversion between polysulfides and  $S_8$ .<sup>[12c,46]</sup> When compared with other cathodes ( $Bi_2Se_3@C/S$  and Super P/S), Te- $Bi_2Se_{3-x}@C/S$  demonstrates the highest current response and the lowest peak-separation polarization, again consistent with the superior catalytic activity of this material.

The diffusion coefficient of  $Li^+$  was qualitatively evaluated through CV tests at scan rates ranging from 0.1  $mVs^{-1}$  to 0.4  $mVs^{-1}$ . The current of the redox peak displays a linear relationship with the square root of the scan rate (Figure S32). Consequently, the diffusion coefficient of  $Li^+$  ( $D_{Li}$ ) was calculated using the Randles–Sevcik equation.<sup>[23a,47]</sup>

$$I_p = 2.69 \times 10^5 n^{1.5} A D_{Li}^{0.5} C_{Li} v^{0.5}$$

where  $n$  is the number of charges,  $A$  is the geometric area of the electrode, and  $C_{Li}$  represents the concentration of  $Li^+$ .  $D_{Li}$  was obtained from a linear fitting of  $I_p$  vs.  $v^{0.5}$  (Figure 5g). Compared with  $Bi_2Se_3@C/S$  and Super P/S, Te- $Bi_2Se_{3-x}@C/S$  exhibits the steepest slope, i.e. the highest  $D_{Li}$  as obtained from the anodic peak and the two cathodic peaks, at  $6.4 \times 10^{-7} cm^2 s^{-1}$ ,  $3.4 \times 10^{-7} cm^2 s^{-1}$  and  $4.2 \times 10^{-7} cm^2 s^{-1}$ , respectively. These values are significantly higher than those obtained for the other two cathodes.

The electrocatalytic activity of the different sulfur hosts was further analyzed by measuring the onset potential at a current density of 10  $\mu A\ cm^{-2}$  above the baseline current (Figures 5h and S33).<sup>[5a,12c]</sup> Compared to  $Bi_2Se_3@C/S$  and Super P/S, Te- $Bi_2Se_{3-x}@C/S$  exhibited the lowest anodic peak onset and the highest cathodic peak onset potential, indicating superior redox kinetics.

As shown in Figures 5i and S34, the EIS spectrum of Te- $Bi_2Se_{3-x}@C/S$  revealed the smallest semicircle in the high-frequency region, corresponding to the lowest charge transfer resistance ( $R_{ct}$ ) at 38.6  $\Omega$ , compared to  $Bi_2Se_3@C/S$  (79.6  $\Omega$ ) and Super P/S (97.5  $\Omega$ ).<sup>[19d,48]</sup> Additionally, the Te- $Bi_2Se_{3-x}@C/S$  cathode displayed a lower Warburg resistance in the low-frequency region, indicating faster diffusion of  $Li^+$  ions.<sup>[49]</sup> Furthermore, the cycled Te- $Bi_2Se_{3-x}@C/S$  electrode exhibited a smaller diffusion resistance compared to the fresh electrode, which is attributed to the chemical activation of the cathode, involving the dissolution and redistribution of the active species.<sup>[1a]</sup>

The galvanostatic intermittent titration technique (GITT) was employed to examine how the composite layer affects the dynamic changes in internal resistance during the cell discharge-charge cycle. GITT measurements were performed at a 0.1 C current density. The voltage measured after the resting period was identified as the open-circuit voltage ( $V_{oc}$ ), whereas the voltage recorded during the current pulse was denoted as the short-circuit voltage ( $V_{sc}$ ). As illustrated in Figures 5j–k and S35, the Te- $Bi_2Se_{3-x}@C/S$  cell shows a smaller voltage difference between  $V_{oc}$  and  $V_{sc}$  compared to the  $Bi_2Se_3@C/S$  and Super P/S. Using this data, the dynamic internal resistance ( $\Delta iR$ ) was calculated with the following equation.

$$\Delta iR = |V_{oc} - V_{sc}|/I$$

Throughout the entire charge–discharge cycle,  $\Delta iR$  of the Te- $Bi_2Se_{3-x}@C/S$  cell remains significantly below that of  $Bi_2Se_3@C/S$  and Super P/S cells, which is consistent with the enhanced charge transport and reaction kinetics attributed to Te doping (Figure 5l).



To evaluate the cycling stability, repeated GCD tests were conducted at a 0.1 C current rate (Figures 5m and S36). After 300 cycles, the Te-Bi<sub>2</sub>Se<sub>3-x</sub>@C/S cathode demonstrated the highest capacity retention (94.6 %), significantly outperforming Bi<sub>2</sub>Se<sub>3</sub>@C/S (76.2 %) and Super P/S (54.2 %). At a higher current rate of 1 C, Te-Bi<sub>2</sub>Se<sub>3-x</sub>@C/S maintained a capacity retention rate of 91.4 % after 1000 cycles, whereas cells with Bi<sub>2</sub>Se<sub>3</sub>@C/S and Super P/S cathodes failed after approximately 500 cycles (Figure 5n). The performance of the Te-Bi<sub>2</sub>Se<sub>3-x</sub>@C/S electrode was also compared with that of previously reported cathodes (Figure S37 and Table S5). At a current density of 0.1 C, Te-Bi<sub>2</sub>Se<sub>3-x</sub>@C/S exhibited the highest specific capacity, underscoring its exceptional performance among state-of-the-art cathode materials.<sup>[2a,23c,50]</sup>

To evaluate the structural stability of the electrodes, the cells were subjected to 200 cycles at a 3 C current rate. After cycling, the electrodes were disassembled and analyzed using SEM (Figure S38). The results revealed that most of the rod-like structures remained intact, with only minor fragmentation observed, likely caused by volume expansion during charge and discharge cycles. Overall, the rod-like structures developed in this study demonstrated exceptional stability, maintaining their integrity even after prolonged cycling at high current rates.

After 100 cycles at a 1 C current rate, the cells were dismantled, and their separators were examined. Notably, the separator from the Te-Bi<sub>2</sub>Se<sub>3-x</sub>@C/S cell was the most translucent compared to those from Bi<sub>2</sub>Se<sub>3</sub>@C/S and Super P/S cells, indicating minimal penetration of LiPSs into the membrane (Figure S39). Additionally, we cycled the coin cell at 1 C for 100 cycles and subsequently disassembled it for SEM imaging and sulfur concentration analysis of the Li metal. The Li metal surface in Te-Bi<sub>2</sub>Se<sub>3-x</sub>@C/S appeared smoother compared to Bi<sub>2</sub>Se<sub>3</sub>@C/S and Super P/S. Furthermore, analysis of the recovered Li anode from the Te-Bi<sub>2</sub>Se<sub>3-x</sub>@C/S cell revealed a lower sulfur concentration. This finding confirms the effective suppression of LiPS diffusion, highlighting enhanced stability and improved protection of the Li anode (Figure S40).

To evaluate the stability of the sulfur host during cycling, we performed EPR tests on the cycled electrode material. The corresponding data is shown in Figure S41. A strong signal corresponding to Se vacancies is still evident, confirming the retention of these vacancies in the electrode material after cycling. However, the EPR signal intensity decreased and the peak position shifted negatively (from 2.0 to 1.96). This shift is likely due to interactions between the host material and polysulfides, as well as possible sulfur/polysulfide adsorption or incorporation at the Se vacancies.

To gain insight into the role of Bi in the charge and discharge process of Te-Bi<sub>2</sub>Se<sub>3-x</sub>@C, the Bi-L3 XANES spectra were examined ex situ during the discharging and charging of the battery. The XANES spectra at four points during the battery discharging from 2.3 V to 1.7 V are displayed in Figure 6. As the discharge progresses, the position of the white line peak of the Bi-L3 edge shifts significantly to a higher energy (Figure 6a). This shift indicates that Bi gradually loses electrons, increasing the valence state of Bi. This observation suggests a strong

interaction between the Bi atoms in the host material and the S atoms in the polysulfide. During the discharge process, Bi transfers electrons to S and LiPSs, promoting the reduction reaction of S or LiPSs. Conversely, during the charging process, the Bi L3 edge shifts to a lower energy level, indicating that Bi transitions to a lower valence state (Figure 6b). Thus, during charging, Li<sub>2</sub>S/Li<sub>2</sub>S<sub>2</sub>/Li<sub>2</sub>S<sub>4</sub> transfer electrons to Bi, thereby accelerating the oxidation reaction. These results indicate that Bi can serve as an effective electron reservoir to catalyze the redox reaction of S during both discharge and charge through electron transfer.

Additionally, the EXAFS results for Te-Bi<sub>2</sub>Se<sub>3-x</sub>@C/S during the charge and discharge process indicate that the average bond length of the first shells of Bi-Se is 2.3 Å (Figure 6c, d). This suggests that the Te-Bi<sub>2</sub>Se<sub>3-x</sub>@C phase remains stable without undergoing any phase transitions throughout the charge and discharge cycles. As illustrated in Figure 6e-f, the WT of the Te-Bi<sub>2</sub>Se<sub>3-x</sub>@C/S electrode demonstrates that the maximum values at all charge and discharge voltages are concentrated around 7.5 Å. There is no significant energy shift, confirming that Te-Bi<sub>2</sub>Se<sub>3-x</sub>@C remains in a stable state as a catalyst throughout the charge and discharge process.

The adsorption model of Li<sub>2</sub>S<sub>4</sub> on different host materials is illustrated in Figure 6g. Compared to the Bi<sub>2</sub>Se<sub>3</sub>-Li<sub>2</sub>S<sub>4</sub> system, the Te-Bi<sub>2</sub>Se<sub>3-x</sub>-Li<sub>2</sub>S<sub>4</sub> model shows a significant difference in electron distribution. At the interface, the Te doping leads to more pronounced electron sharing between the host material and the polysulfide. This increased electron sharing between Te-Bi<sub>2</sub>Se<sub>3-x</sub> and Li<sub>2</sub>S<sub>4</sub> indicates a stronger electronic coupling between the host and the adsorbed material.

To further elucidate the interaction between the host material and S<sub>8</sub>, Li<sub>2</sub>S and polysulfides during the conversion process, differential charge density DFT analyses were carried out. As shown in Figure S42, when S<sub>8</sub> is adsorbed onto the surfaces of Te-Bi<sub>2</sub>Se<sub>3-x</sub> slabs, the charge density of S<sub>8</sub> is +0.035 eV. This finding reveals that Te-Bi<sub>2</sub>Se<sub>3-x</sub> particles act as electron donors, providing additional electrons to S<sub>8</sub> and thereby accelerating its reduction during the discharge process. During the charging process, the charge density of Li<sub>2</sub>S on the Te-Bi<sub>2</sub>Se<sub>3-x</sub> slabs is -0.66 eV. This indicates that the Te-Bi<sub>2</sub>Se<sub>3-x</sub> slabs can harvest electrons from Li<sub>2</sub>S, enhancing its oxidation reaction. Results from DFT calculations align closely with the ex situ XAS results. The DFT analysis further confirms that the incorporation of Te-Bi<sub>2</sub>Se<sub>3-x</sub> particles facilitates electron redistribution, alters charge densities, and effectively catalyzes the redox reactions of sulfur during charge and discharge cycles.

The loading amount of active material (S) and the amount of electrolyte used are critical parameters for evaluating the practical application of electrode materials. To assess applicability, Te-Bi<sub>2</sub>Se<sub>3-x</sub>@C/S-based cells with a high sulfur loading of 6.4 mg·cm<sup>-2</sup> were assembled. The GCD curves and rate performance of one such high sulfur loading cell are presented in Figure 7a, b. At current densities of 0.1 C, 0.2 C, 0.5 C, 1 C, 2 C, and 3 C, the specific capacities were 1248, 1032, 932, 830, 755, and 632 mAh·g<sup>-1</sup>, respectively. This corresponds to areal capacities of 8.0, 6.6,

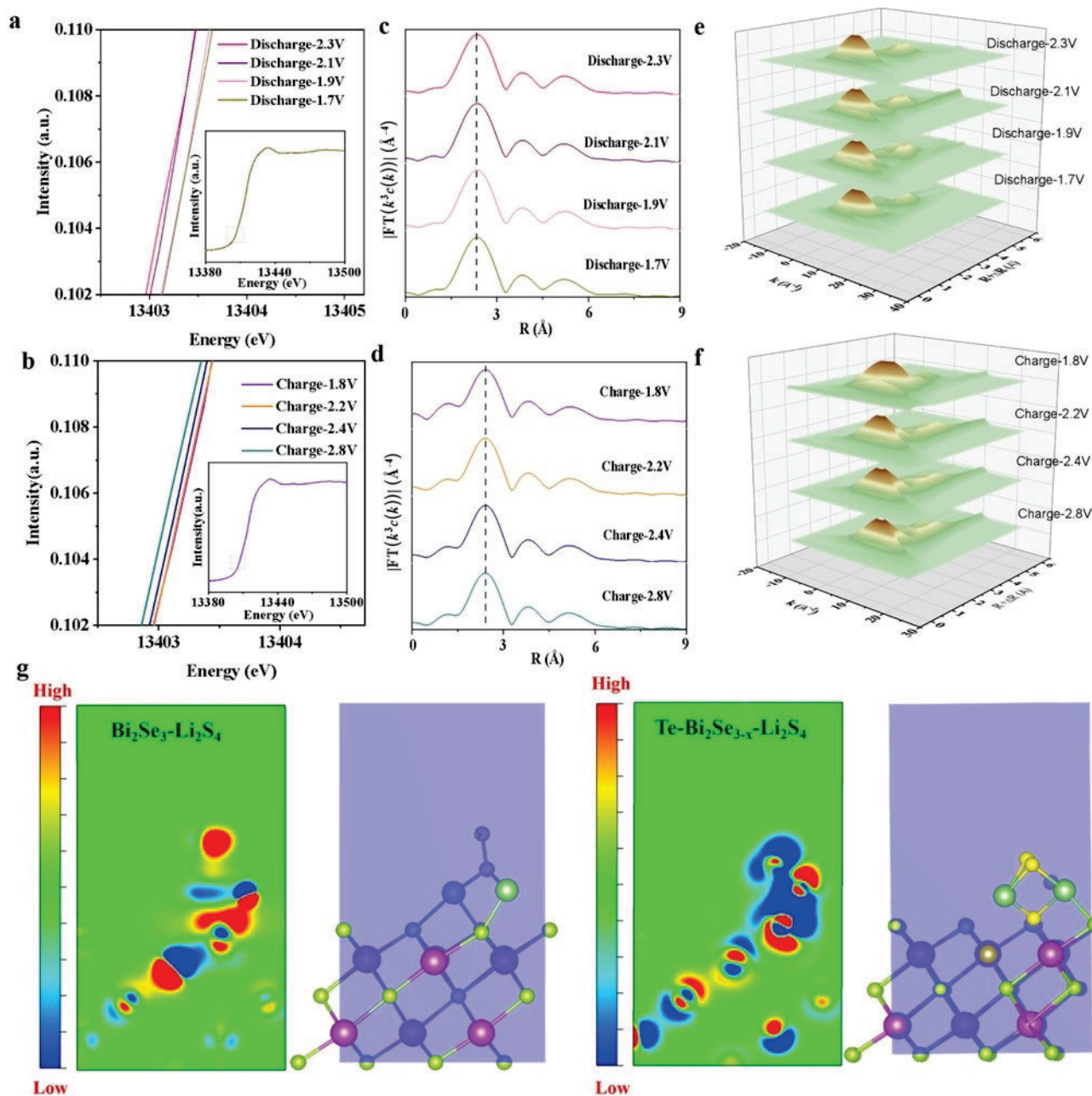


**Figure 6.** (a,b) Enlargements of the shift of the Bi L3-edge from ex situ XANES spectra of the  $\text{Te-Bi}_2\text{Se}_{3-x}$ @C/S sample during the discharge (a) and the charge (b) processes. Insets show the full XANES spectra. (c,d) k<sup>3</sup>-weighted FT-EXAFS curves of  $\text{Te-Bi}_2\text{Se}_{3-x}$ @C/S in R space during discharge and charge processes. (e,f) WT plots of the Bi L3-edge of the  $\text{Te-Bi}_2\text{Se}_{3-x}$ @C/S sample during discharge (e) and charge processes (f). (g) The adsorption models of  $\text{Li}_2\text{S}_4$  on  $\text{Bi}_2\text{Se}_3$  and  $\text{Te-Bi}_2\text{Se}_{3-x}$ .

6.0, 5.3, 4.8, and 4.0  $\text{mAh}\cdot\text{cm}^{-2}$ , all of which exceed the typical values obtained in cathode materials for Li-ion batteries. The cycling stability of the high sulfur loading  $\text{Te-Bi}_2\text{Se}_{3-x}$ @C/S-based cell was further tested under different electrolyte contents. With electrolyte amounts of 10.4  $\mu\text{L}\cdot\text{mg}^{-1}$  and 6.8  $\mu\text{L}\cdot\text{mg}^{-1}$ , the capacity retention after 300 cycles at a 0.1 C current rate was 92.8 % and 90.5 %, respectively (Figure 7c). To further validate the practical application of  $\text{Te-Bi}_2\text{Se}_{3-x}$ @C/S cathodes, pouch-type batteries (3 cm×4 cm) were assembled using the

$\text{Te-Bi}_2\text{Se}_{3-x}$ @C/S cathode. In the pouch cell, the cathode exhibited an initial specific capacity of 1224  $\text{mAh}\cdot\text{g}^{-1}$  at a current density of 0.1 C, retaining 86.7 % of its capacity after 200 cycles (Figure S43). Additionally, Figure 7d demonstrates that two  $\text{Te-Bi}_2\text{Se}_{3-x}$ @C/S pouch cells connected in series were capable of powering an LED strip for over 30 min, showcasing the practical potential of this material in real-world applications. To better demonstrate the battery's performance, we conducted additional cycling tests at a higher rate of 5 C for 500 cycles (Figure S44). Under these

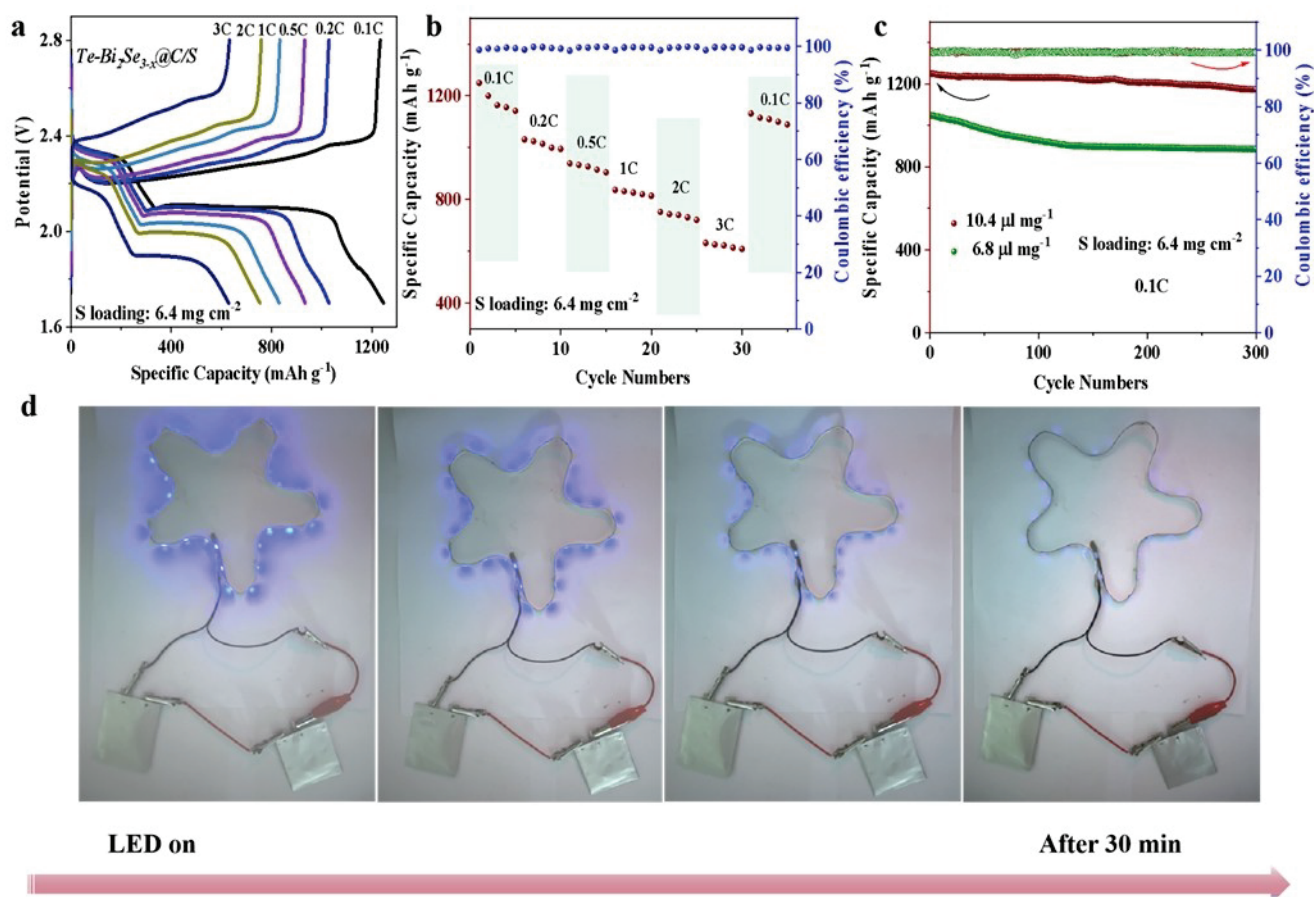


**Figure 7.** (a) GCD curves of  $\text{Te-Bi}_2\text{Se}_{3-x}\text{@C/S}$  cells with a high S loading ( $6.4 \text{ mg cm}^{-2}$ ). (b) Rate performance of the high S loading cell. (c) Cycling stability of  $\text{Te-Bi}_2\text{Se}_{3-x}\text{@C/S}$  at a current density of 0.1 C under different electrolyte contents. (d)  $\text{Te-Bi}_2\text{Se}_{3-x}\text{@C/S}$  based pouch cells powering an LED strip.

conditions, the capacitance retention rate was 75.6 %, highlighting the robust electrochemical stability of the assembled battery. We have also produced and tested a larger pouch battery ( $3 \text{ cm} \times 6 \text{ cm}$ ). The practical applications and cycle stability of this larger-specification pouch battery are shown in Figure S45. These  $\text{Te-Bi}_2\text{Se}_{3-x}\text{@C/S}$ -based pouch cells can power a temperature and humidity monitoring clock, demonstrating the practical applicability of the prepared electrodes. Furthermore, when cycled at 5 C for 500 cycles, the capacitance retention rate reaches 70.2 %, indicating an excellent application potential and cycle stability (Figure S45b).

## Conclusions

In summary, both experimental results and theoretical calculations confirmed the effectiveness of anionic doping in  $\text{Bi}_2\text{Se}_3$  for enhancing the performance of LSBs. Specifically, in Te-doped  $\text{Bi}_2\text{Se}_3$ , Te occupies the Se sites. Due to its larger atomic size, it generates Se vacancies, which leads to an increased concentration of free carriers in the electrode material. Additionally, the increase of unpaired Bi cations provided additional active sites for LiPS adsorption and

catalytic reactions, thereby promoting sulfur conversion kinetics. Simultaneously, Te doping induces lattice distortion within the  $\text{Bi}_2\text{Se}_3$  material, causing a shift in the positive/negative charge center of the unit cell toward the negative direction. This phenomenon generates an intrinsic electric field, facilitating the transfer of charges within the cathode material. By leveraging doping, defects, and lattice distortion engineering, the  $\text{Te-Bi}_2\text{Se}_{3-x}\text{@C}$  cathode exhibited outstanding electrochemical performance, including high specific capacity (up to  $1508 \text{ mAh g}^{-1}$  at 0.1 C), excellent rate capability, and prolonged cycle stability, even under high sulfur loading and lean electrolyte conditions. Overall, this work offers valuable insights into the strategic design of anionically doped layered metal chalcogenide catalysts that enhance both polysulfide adsorption and redox activity in sulfur cathodes for advanced LSBs.

## Acknowledgements

This work was financially supported by the 2BoSS project of the ERA-MIN3 program with the Spanish grant number PCI2022-132985/AEI/10.13039/501100011033, Generalitat de Catalunya 2021SGR01581 and 2021SGR00457 and Euro-



pean Union Next Generation EU/PRTR. C. H., J. Y. thank the China Scholarship Council for the scholarship support. ICN2 is supported by the Severo Ochoa program from Spanish MCIN/AEI (Grant No.: CEX2021-001214-S). IREC and ICN2 are both funded by the CERCA Program/ Generalitat de Catalunya. The authors thank the support from the project AMaDE (PID2023-149158OB-C43), funded by MCIN/AEI/10.13039/501100011033 and by “ERDF A way of making Europe”, by the “European Union”. XAS experiments were performed at CLAES beamline of ALBA Synchrotron with the collaboration of ALBA staff. J. Li is grateful for the project supported by the Natural Science Foundation of Sichuan (2022NSFSC1229). The authors acknowledge the support of the Supercomputing Center of Lanzhou University, China. This work has received funding from the “Spanish Ministry of Science and Innovation” through “Severo Ochoa” (CEX2019-000917-S) and “OXISOT” (PID2021-128410OB-I00). This study is part of the Advanced Materials program and was supported by MCIN with funding from the European Union Next Generation EU (PRTR-C17.I1) and by Generalitat de Catalunya. Part of the present work has been performed in the framework of the Universitat Autònoma de Barcelona Materials Science PhD program. The authors acknowledge the use of instrumentation as well as the technical advice provided by the Joint Electron Microscopy Center at ALBA (JEMCA). ICN2 acknowledges funding from Grant IU16-014206 (METCAM-FIB) funded by the European Union through the European Regional Development Fund (ERDF), with the support of the Ministry of Research and Universities, Generalitat de Catalunya. ICN2 is a founding member of e-DREAM.<sup>[51]</sup>

## Conflict of Interest

The authors declare no conflict of interest.

## Data Availability Statement

The data that support the findings of this study are available from the corresponding author upon reasonable request.

**Keywords:** Bi<sub>2</sub>Se<sub>3</sub> • induced lattice • lithium-sulfur battery • lithium polysulfides • Se vacancies

- [1] a) D. Fang, G. Wang, S. Huang, T. Chen Li, J. Yu, D. Xiong, D. Yan, X. Liang Li, J. Zhang, Y. Von Lim, S. A. Yang, H. Ying Yang, *Chem. Eng. J.* **2021**, *411*, 128546; b) C. Huang, J. Yu, C. Y. Zhang, Z. Cui, J. Chen, W.-H. Lai, Y.-J. Lei, B. Nan, X. Lu, R. He, L. Gong, J. Li, C. Li, X. Qi, Q. Xue, J. Y. Zhou, X. Qi, L. Balcells, J. Arbiol, A. Cabot, *Adv. Mater.* **2024**, *36*, 2400810.
- [2] a) H.-J. Li, K. Xi, W. Wang, S. Liu, G.-R. Li, X.-P. Gao, *Energy Storage Mater.* **2022**, *45*, 1229–1237; b) D. Wang, F. Li, R. Lian, J. Xu, D. Kan, Y. Liu, G. Chen, Y. Gogotsi, Y. Wei, *ACS Nano* **2019**, *13*, 11078–11086; c) S. Li, W. Zhang, J. Zheng, M. Lv, H. Song, L. Du, *Adv. Energy Mater.* **2021**, *11*, 2000779; d) J. He, A. Manthiram, *Adv. Energy Mater.* **2020**, *10*, 2002654; e) D. Liu, C. Zhang, G. Zhou, W. Lv, G. Ling, L. Zhi, Q.-H. Yang, *Adv. Sci.* **2018**, *5*, 1700270; f) D. Zhao, S. Jiang, S. Yu, J. Ren, Z. Zhang, S. Liu, X. Liu, Z. Wang, Y. Wu, Y. Zhang, *Carbon* **2023**, *201*, 864–870; g) M. Li, D. Yang, J. J. Biendicho, X. Han, C. Zhang, K. Liu, J. Diao, J. Li, J. Wang, M. Heggen, R. E. Dunin-Borkowski, J. Wang, G. Henkelman, J. R. Morante, J. Arbiol, S.-L. Chou, A. Cabot, *Adv. Funct. Mater.* **2022**, *32*, 2200529; h) C. Huang, J. Yu, C. Li, Z. Cui, C. Zhang, C. Zhang, B. Nan, J. Li, J. Arbiol, A. Cabot, *Adv. Funct. Mater.* **2023**, *33*, 2305624; i) J. Li, L. Li, J. Wang, A. Cabot, Y. Zhu, *ACS Energy Lett.* **2024**, *9*, 853–879; j) D. Yang, Z. Liang, P. Tang, C. Zhang, M. Tang, Q. Li, J. J. Biendicho, J. Li, M. Heggen, R. E. Dunin-Borkowski, M. Xu, J. Llorca, J. Arbiol, J. R. Morante, S.-L. Chou, A. Cabot, *Adv. Mater.* **2022**, *34*, 2108835.
- [3] H. Pan, Z. Cheng, Z. Zhou, S. Xie, W. Zhang, N. Han, W. Guo, J. Franssaer, J. Luo, A. Cabot, M. Wübbenhorst, *Nano-Micro Lett.* **2023**, *15*, 165.
- [4] B. Hu, J. Xu, Z. Fan, C. Xu, S. Han, J. Zhang, L. Ma, B. Ding, Z. Zhuang, Q. Kang, X. Zhang, *Adv. Energy Mater.* **2023**, *13*, 2203540.
- [5] a) W. Yao, W. Zheng, J. Xu, C. Tian, K. Han, W. Sun, S. Xiao, *ACS Nano* **2021**, *15*, 7114–7130; b) W. Liu, C. Luo, S. Zhang, B. Zhang, J. Ma, X. Wang, W. Liu, Z. Li, Q.-H. Yang, W. Lv, *ACS Nano* **2021**, *15*, 7491–7499; c) C. Zhao, F. Huo, Y. Yang, J. Ruan, F. Chai, H. Xu, Y. Liu, L. Zhang, A. Cabot, Z. Sun, Y. Zhang, *Adv. Funct. Mater.* **2024**, *34*, 2402175.
- [6] a) Y. Gong, Y. Wang, Z. Fang, S. Zhao, Y.-s. He, W. Zhang, J. Mu, L. Zhang, Z.-F. Ma, *Chem. Eng. J.* **2022**, *446*, 136943; b) Y. Li, T. Gao, D. Ni, Y. Zhou, M. Yousaf, Z. Guo, J. Zhou, P. Zhou, Q. Wang, S. Guo, *Adv. Mater.* **2022**, *34*, 2107638; c) Y.-H. Liu, L.-X. Li, A.-Y. Wen, F.-F. Cao, H. Ye, *Energy Storage Mater.* **2023**, *55*, 652–659.
- [7] a) Q. Qi, X. Lv, W. Lv, Q.-H. Yang, *J. Energy Chem.* **2019**, *39*, 88–100; b) M. J. Lacey, F. Jeschull, K. Edström, D. Brandell, *J. Power Sources* **2014**, *264*, 8–14.
- [8] a) M. Zheng, Y. Chi, Q. Hu, H. Tang, X. Jiang, L. Zhang, S. Zhang, H. Pang, Q. Xu, *J. Mater. Chem. A* **2019**, *7*, 17204–17241; b) R. Fang, K. Chen, L. Yin, Z. Sun, F. Li, H.-M. Cheng, *Adv. Mater.* **2019**, *31*, 1800863; c) Y. Xie, J. Ao, L. Zhang, Y. Shao, H. Zhang, S. Cheng, X. Wang, *Chem. Eng. J.* **2023**, *451*, 139017; d) H. Ma, Z. Yu, H. Li, D. Guo, Z. Zhou, H. Jin, L. Wu, X. a Chen, S. Wang, *Adv. Funct. Mater.* **2024**, *34*, 2310301; e) W. Dong, Z. Wu, X. Zhu, D. Shen, M. Zhao, F. Yang, Q. Chang, S. Tang, X. Hong, Z. Dong, S. Yang, *Chem. Eng. J.* **2024**, *488*, 150872; f) J. Yu, I. Pinto-Huguet, C. Y. Zhang, Y. Zhou, Y. Xu, A. Vizintin, J.-J. Velasco-Vélez, X. Qi, X. Pan, G. Oney, A. Olgo, K. Märker, L. M. Da Silva, Y. Luo, Y. Lu, C. Huang, E. Härk, J. Fleming, P. Chenevier, A. Cabot, Y. Bai, M. Botifoll, A. P. Black, Q. An, T. Amietszajew, J. Arbiol, *ACS Energy Lett.* **2024**, *9*, 6178–6214.
- [9] a) Y. Zhang, C. Ma, C. Zhang, L. Ma, S. Zhang, Q. Huang, C. Liang, L. Chen, L. Zhou, W. Wei, *Chem. Eng. J.* **2023**, *452*, 139410; b) J. Pu, W. Gong, Z. Shen, L. Wang, Y. Yao, G. Hong, *Adv. Sci.* **2022**, *9*, 2104375; c) J. Mou, Y. Li, L. Ou, J. Huang, *Energy Storage Mater.* **2022**, *52*, 111–119.
- [10] a) J. Liu, G. Li, D. Luo, J. Li, X. Zhang, Q. Li, H. Li, Y. Zhang, Z. Chen, *Adv. Funct. Mater.* **2024**, *34*, 2303357; b) B. Wang, Y. Ren, Y. Zhu, S. Chen, S. Chang, X. Zhou, P. Wang, H. Sun, X. Meng, S. Tang, *Adv. Sci.* **2023**, *10*, 2300860; c) C. Y. Zhang, C. Zhang, G. W. Sun, J. L. Pan, L. Gong, G. Z. Sun, J. J. Biendicho, L. Balcells, X. L. Fan, J. R. Morante, J. Y. Zhou, A. Cabot, *Angew. Chem. Int. Ed.* **2022**, *61*, e202211570.
- [11] a) X. Dai, G. Lv, Z. Wu, X. Wang, Y. Liu, J. Sun, Q. Wang, X. Xiong, Y. Liu, C. Zhang, S. Xin, Y. Chen, T. Zhou, *Adv. Energy Mater.* **2023**, *13*, 2300452; b) Y. Li, C. Xu, D. Li, Y.

- Zhang, B. Liu, P. Huo, *Chem. Eng. J.* **2024**, *502*, 158151; c) H. Ding, Z. Chen, H. Li, H. Suo, C. Liu, H. Yu, J. Yuan, Z. Sun, Y. Zhu, B. Song, *Nano Lett.* **2024**, *24*, 15118–15126; d) D. Yang, Y. Han, M. Li, C. Li, W. Bi, Q. Gong, J. Zhang, J. Zhang, Y. Zhou, H. Gao, J. Arbiol, Z. Shi, G. Zhou, A. Cabot, *Adv. Funct. Mater.* **2024**, *34*, 2401577.
- [12] a) H. Xu, Q. Jiang, Z. Shu, K. S. Hui, S. Wang, Y. Zheng, X. Liu, H. Xie, W.-F. Ip, C. Zha, Y. Cai, K. N. Hui, *Adv. Sci.* **2024**, *11*, 2307995; b) F. Han, D. Yan, X. Guan, Q. Lu, S. Yin, Y. Yan, H. Zhou, P. Yang, Q. Zhang, S. Zhang, J. Xia, Y. Xing, *Energy Storage Mater.* **2024**, *71*, 103652; c) D. Yang, M. Li, X. Zheng, X. Han, C. Zhang, J. Jacas Biendicho, J. Llorca, J. Wang, H. Hao, J. Li, G. Henkelman, J. Arbiol, J. R. Morante, D. Mitlin, S. Chou, A. Cabot, *ACS Nano* **2022**, *16*, 11102–11114; d) D. Yang, Z. Liang, C. Zhang, J. J. Biendicho, M. Botifoll, M. C. Spadaro, Q. Chen, M. Li, A. Ramon, A. O. Moghaddam, J. Llorca, J. Wang, J. R. Morante, J. Arbiol, S.-L. Chou, A. Cabot, *Adv. Energy Mater.* **2021**, *11*, 2101250.
- [13] a) X. Wu, R. Xie, D. Cai, B. Fei, C. Zhang, Q. Chen, B. Sa, H. Zhan, *Adv. Funct. Mater.* **2024**, *34*, 2315012; b) Q. Gong, D. Yang, H. Yang, K. Wu, J. Zhang, W. Bi, J. Diao, C. Li, J. Yu, C. Y. Zhang, M. Li, G. Henkelman, J. Arbiol, Q. Zhang, A. Cabot, *ACS Nano* **2024**, *18*, 28382–28393.
- [14] a) J. Zhang, D. Yang, C. Li, Q. Gong, W. Bi, X. Zheng, J. Arbiol, S. Li, A. Cabot, *Nano Lett.* **2024**, *24*, 7992–7998; b) H. Mollania, C. Zhang, R. Du, X. Qi, J. Li, S. Horta, M. Ibañez, C. Keller, P. Chenevier, M. Oloomi-Buygi, A. Cabot, *ACS Appl. Mater. Interfaces* **2023**, *15*, 58462–58475.
- [15] B. Fei, C. Zhang, D. Cai, J. Zheng, Q. Chen, Y. Xie, L. Zhu, A. Cabot, H. Zhan, *ACS Nano* **2021**, *15*, 6849–6860.
- [16] a) D. Yang, C. Li, M. Sharma, M. Li, J. Wang, J. Wei, K. Liu, Y. Zhang, J. Li, G. Henkelman, Q. Zhang, A. Cabot, *Energy Storage Mater.* **2024**, *66*, 103240; b) Z. Liang, D. Yang, P. Tang, C. Zhang, J. Jacas Biendicho, Y. Zhang, J. Llorca, X. Wang, J. Li, M. Heggen, J. David, R. E. Dunin-Borkowski, Y. Zhou, J. R. Morante, A. Cabot, J. Arbiol, *Adv. Energy Mater.* **2021**, *11*, 2003507.
- [17] S. Hu, M. Yi, H. Wu, T. Wang, X. Ma, X. Liu, J. Zhang, *Adv. Funct. Mater.* **2022**, *32*, 2111084.
- [18] a) C. Tan, Z. Luo, A. Chaturvedi, Y. Cai, Y. Du, Y. Gong, Y. Huang, Z. Lai, X. Zhang, L. Zheng, X. Qi, M. H. Goh, J. Wang, S. Han, X.-J. Wu, L. Gu, C. Kloc, H. Zhang, *Adv. Mater.* **2018**, *30*, 1705509; b) X. Yu, Y. Ding, J. Sun, *iScience* **2023**, *26*, 107489.
- [19] a) W. Yao, C. Tian, C. Yang, J. Xu, Y. Meng, I. Manke, N. Chen, Z. Wu, L. Zhan, Y. Wang, R. Chen, *Adv. Mater.* **2022**, *34*, 2106370; b) W. Hou, P. Feng, X. Guo, Z. Wang, Z. Bai, Y. Bai, G. Wang, K. Sun, *Adv. Mater.* **2022**, *34*, 2202222; c) Z. Luo, D. Shu, F. Yi, J. Ling, M. Wang, C. Huang, A. Gao, *New J. Chem.* **2021**, *45*, 22748–22757; d) C. Huang, A. Gao, F. Yi, Y. Wang, D. Shu, Y. Liang, Z. Zhu, J. Ling, J. Hao, *Chem. Eng. J.* **2021**, *419*, 129643; e) K. Zhang, G. Zhang, J. Qu, H. Liu, *Small* **2020**, *16*, 1907001.
- [20] a) A. Huang, L. Kong, B. Zhang, X. Liu, L. Wang, L. Li, J. Xu, *ACS Nano* **2024**, *18*, 12795–12807; b) Y. Li, Z. Wang, C. Wei, K. Tian, X. Zhang, S. Xiong, B. Xi, J. Feng, *Chem. Eng. J.* **2024**, *497*, 154658.
- [21] J. Han, P. Wang, H. Zhang, N. Song, X. An, B. Xi, S. Xiong, *Chin Chem Letters* **2024**, *35*, 109543.
- [22] a) C. Huang, J. Yu, C. Li, Z. Cui, C. Zhang, C. Zhang, B. Nan, J. Li, J. Arbiol, A. Cabot, *Adv. Funct. Mater.* **2023**, *33*, 2305624; b) M. Yang, P. Liu, Z. Qu, F. Sun, Y. Tian, X. Ye, X. Wang, X. Liu, H. Li, *Nano Energy* **2022**, *104*, 107922.
- [23] a) K. Zou, X. Chen, W. Jing, X. Dai, P. Wang, Y. Liu, R. Qiao, M. Shi, Y. Chen, J. Sun, Y. Liu, *Energy Storage Mater.* **2022**, *48*, 133–144; b) X. Dai, X. Wang, G. Lv, Z. Wu, Y. Liu, J. Sun, Y. Liu, Y. Chen, *Small* **2023**, *19*, 2302267; c) H. Song, T. Li, T. He, Z. Wang, D. Fang, Y. Wang, X. L. Li, D. Zhang, J. Hu, S. Huang, *Chem. Eng. J.* **2022**, *450*, 138115; d) Z. Ye, Y. Jiang, L. Li, F. Wu, R. Chen, *Adv. Mater.* **2022**, *34*, 2109552; e) Y. Song, H. Li, J. Li, J. An, J.-J. Shao, G. Zhou, *J. Energy Chem.* **2023**, *87*, 51–60.
- [24] B. Wang, L. Wang, D. Ding, Y. Zhai, F. Wang, Z. Jing, X. Yang, Y. Kong, Y. Qian, L. Xu, *Adv. Mater.* **2022**, *34*, 2204403.
- [25] L. Hu, C. Liu, F. Zhang, H. Wang, B. Wang, *Small* **2024**, *20*, 2311079.
- [26] a) K. Xu, X. Liu, J. Liang, J. Cai, K. Zhang, Y. Lu, X. Wu, M. Zhu, Y. Liu, Y. Zhu, G. Wang, Y. Qian, *ACS Energy Lett.* **2018**, *3*, 420–427; b) Y. Zhu, Y. Wu, J. Zhao, X. Zeng, J. Mao, J. Chen, *Nat. Sustain.* **2023**, *15*, 16210.
- [27] Y. Liang, N. Song, Z. Zhang, W. Chen, J. Feng, B. Xi, S. Xiong, *Adv. Mater.* **2022**, *34*, 2202673.
- [28] Y. B. Chan, V. Selvanathan, L.-H. Tey, M. Akhtaruzzaman, F. H. Anur, S. Djearamane, A. Watanabe, M. Aminuzzaman, *Nanomaterials* **2022**, *12*, 3589.
- [29] a) R. He, S. Ou, Y. Liu, Y. Liu, D. Xu, *Chin. J. Catal.* **2022**, *43*, 370–378; b) W. Liang, B. Chen, W. Lin, L. Shao, X. Shi, Z. Sun, *Mater. Lett.* **2023**, *332*, 133542.
- [30] Y. Liao, R. He, W. Pan, Y. Li, Y. Wang, J. Li, Y. Li, *Chem. Eng. J.* **2023**, *464*, 142669.
- [31] J. Yang, L. Fu, F. Wu, X. Chen, C. Wu, Q. Wang, *Catalysts* **2022**, *12*, 1085.
- [32] H. Wang, Q. Ma, F. Sun, Y. Shao, D. Zhang, H. Sun, Z. Li, Q. Wang, J. Qi, B. Wang, *Molecules* **2023**, *28*, 5620.
- [33] Z. Hou, P. Hei, C. Shu, R. Zheng, T. Yang, Q. Zhang, J. Long, *ACS Sustainable Chem. Eng.* **2020**, *8*, 6667–6674.
- [34] X. Ma, Y. Li, X. Long, H.-c. Luo, C. Xu, G. Wang, W. Zhao, *J. Energy Chem.* **2023**, *77*, 227–238.
- [35] J. H. Moon, H. Seong, G. Kim, Y. Jin, W. Nam, H. Yoo, T. Jung, K. Lee, M. Yang, S. Y. Cho, J. Choi, *Appl. Surf. Sci.* **2023**, *638*, 157976.
- [36] a) C. Li, D. Yang, J. Yu, J. Wang, C. Zhang, T. Yang, C. Huang, B. Nan, J. Li, J. Arbiol, Y. Zhou, Q. Zhang, A. Cabot, *Adv. Energy Mater.* **2024**, *14*, 2303551; b) Y. Zhang, B. Zhang, J. Li, J. Liu, X. Huo, F. Kang, *Chem. Eng. J.* **2021**, *403*, 126377.
- [37] a) G.-E. Lee, I.-H. Kim, Y. S. Lim, W.-S. Seo, B.-J. Choi, C.-W. Hwang, *J. Korean Phys. Soc.* **2014**, *65*, 696–701; b) P. H. Le, K. H. Wu, C. W. Luo, J. Leu, *Thin Solid Films* **2013**, *534*, 659–665.
- [38] a) X. Zhao, C. Zhang, G. Yang, Y. Wu, Q. Fu, H. Zhao, Y. Lei, *Inorg. Chem. Front.* **2021**, *8*, 4267–4275; b) Z. Li, H. Pan, W. Wei, A. Dong, K. Zhang, H. Lv, X. He, *Ceram. Int.* **2019**, *45*, 11861–11867; c) T. Yang, J. Liu, D. Yang, Q. Mao, J. Zhong, Y. Yuan, X. Li, X. Zheng, Z. Ji, H. Liu, G. Wang, R. Zheng, *ACS Appl. Energy Mater.* **2020**, *3*, 11073–11081; d) D. Khalafallah, W. Huang, M. Wunn, M. Zhi, Z. Hong, *J. Energy Storage* **2022**, *45*, 103716.
- [39] Y.-C. Yeh, P.-H. Ho, C.-Y. Wen, G.-J. Shu, R. Sankar, F.-C. Chou, C.-W. Chen, *J. Phys. Chem. C* **2016**, *120*, 3314–3318.
- [40] S. Hu, X. Huang, L. Zhang, G. Li, S. Chen, J. Zhang, X. Liu, *Adv. Funct. Mater.* **2023**, *33*, 2214161.
- [41] a) M. Wild, L. O'Neill, T. Zhang, R. Purkayastha, G. Minton, M. Marinescu, G. J. Offer, *Energy Environ. Sci.* **2015**, *8*, 3477–3494; b) L. Peng, Z. Wei, C. Wan, J. Li, Z. Chen, D. Zhu, D. Baumann, H. Liu, C. S. Allen, X. Xu, A. I. Kirkland, I. Shakir, Z. Almutairi, S. Tolbert, B. Dunn, Y. Huang, P. Sautet, X. Duan, *Nat. Catal.* **2020**, *3*, 762–770.
- [42] a) Y.-X. Yin, S. Xin, Y.-G. Guo, L.-J. Wan, *Angew. Chem. Int. Ed.* **2013**, *52*, 13186–13200; b) L. Wang, T. Zhang, S. Yang, F. Cheng, J. Liang, J. Chen, *J. Energy Chem.* **2013**, *22*, 72–77.
- [43] J. Yu, C. Huang, O. Usoltsev, A. P. Black, K. Gupta, M. C. Spadaro, I. Pinto-Huguet, M. Botifoll, C. Li, J. Herrero-Martín, J. Zhou, A. Ponrouch, R. Zhao, L. Balcells, C. Y. Zhang, A. Cabot, J. Arbiol, *ACS Nano* **2024**, *18*, 19268–19282.

- [44] C. Dong, C. Zhou, M. Wu, Y. Yu, K. Yu, K. Yan, C. Shen, J. Gu, M. Yan, C. Sun, L. Mai, X. Xu, *Adv. Energy Mater.* **2023**, *13*, 2301505.
- [45] D. Yang, C. Zhang, J. J. Biendicho, X. Han, Z. Liang, R. Du, M. Li, J. Li, J. Arbiol, J. Llorca, Y. Zhou, J. R. Morante, A. Cabot, *ACS Nano* **2020**, *14*, 15492–15504.
- [46] C. Zhang, J. J. Biendicho, T. Zhang, R. Du, J. Li, X. Yang, J. Arbiol, Y. Zhou, J. R. Morante, A. Cabot, *Adv. Funct. Mater.* **2019**, *29*, 1903842.
- [47] a) M. J. Theibault, C. Chandler, I. Dabo, H. D. Abruña, *ACS Catal.* **2023**, *13*, 3684–3691; b) E. Ghasemiestahbanati, A. Shehzad, K. Konstantas, C. J. Setter, L. A. O'Dell, M. Shaibani, M. Majumder, M. R. Hill, *J. Mater. Chem. A* **2022**, *10*, 902–911.
- [48] C. Huang, S. Lv, A. Gao, J. Ling, F. Yi, J. Hao, M. Wang, Z. Luo, D. Shu, *Chem. Eng. J.* **2022**, *431*, 134083.
- [49] R. Chu, T. T. Nguyen, Y. Bai, N. H. Kim, J. H. Lee, *Adv. Energy Mater.* **2022**, *12*, 2102805.
- [50] a) J. Cho, S. Ryu, Y. J. Gong, S. Pyo, H. Yun, H. Kim, J. Lee, J. Yoo, Y. S. Kim, *Chem. Eng. J.* **2022**, *439*, 135568; b) M. Guo, S. Gu, R. Zhou, Z. Zhang, S. Xu, Y. Wang, G. Zhou, *Chem. Eng. J.* **2024**, *484*, 149500; c) X. Zeng, Y. Tang, L. Liu, Y. Zhang, M. Qian, Y. Gao, *ACS Sustainable Chem. Eng.* **2021**, *9*, 15830–15838; d) L. Zhan, X. Ning, X. Zhou, J. Luo, X. Fan, *Adv. Powder Technol.* **2022**, *33*, 103521.
- [51] R. Ciancio, R. E. Dunin-Borkowski, E. Snoeck, M. Kociak, R. Holmestad, J. Verbeeck, A. I. Kirkland, G. Kothleitner, J. Arbiol, *Microsc. Microanal.* **2022**, *28*, 2900–2902.

Manuscript received: October 22, 2024

Accepted manuscript online: December 17, 2024

Version of record online: January 3, 2025



## Supporting Information

### **Anionic Doping in Layered Transition Metal Chalcogenides for Robust Lithium-Sulfur Batteries**

*C. Huang, J. Yu, C. Yue Zhang, Z. Cui, R. He, L. Yang, B. Nan, C. Li, X. Qi, X. Qi, J. Li, J. Yuan Zhou, O. Usoltsev, L. Simonelli, J. Arbiol, Y.-J. Lei\*, Q. Sun\*, G. Wang\*, A. Cabot\**

## **Anionic Doping in Layered Transition Metal Chalcogenides for Robust Lithium-Sulfur Batteries**

Chen Huang<sup>1,2</sup>, Jing Yu<sup>1,3</sup>, Chao Yue Zhang<sup>4</sup>, Zhibiao Cui<sup>5</sup>, Ren He<sup>1,6</sup>, Linlin Yang<sup>1,6</sup>, Bingfei Nan<sup>1</sup>, Canhuang Li<sup>1,2</sup>, Xuede Qi<sup>7</sup>, Xueqiang Qi<sup>7</sup>, Junshan Li<sup>8</sup>, Jin Yuan Zhou<sup>4</sup>, Oleg Usoltsev<sup>9</sup>, Laura Simonelli<sup>9</sup>, Jordi Arbiol<sup>3,10</sup>, Yao-Jie Lei<sup>\*11</sup>, Qing Sun<sup>\*1,12</sup>, Guoxiu Wang<sup>\*11</sup> and Andreu Cabot<sup>\*1,10</sup>

1. C. Huang, J. Yu, R. He, L. L. Yang, B. F. Nan, C. H. Li, Q. Sun, A. Cabot  
Catalonia Institute for Energy Research-IREC, Sant Adrià de Besòs, Barcelona 08930, Spain  
E-mail: acabot@irec.cat
2. C. Huang, C. H. Li  
Department of Chemistry, University of Barcelona 08028, Spain
3. J. Yu, J. Arbiol  
Catalan Institute of Nanoscience and Nanotechnology (ICN2), CSIC and BIST, Campus UAB, Bellaterra, 08193 Barcelona, Catalonia, Spain.
4. C. Y. Zhang, J.Y. Zhou  
School of Physical Science & Technology; Lanzhou University Lanzhou 730000, China.
5. Z. B. Cui  
Shenzhen Key Laboratory of Special Functional Materials & Shenzhen Engineering Laboratory for Advance Technology of Ceramics, College of Materials Science and Engineering, Shenzhen University, Shenzhen 518060, P. R. China.
6. R. He, L.L.Yang  
Enginyeria Electrònica i Biomèdica Facultat de Física, Universitat de Barcelona, 08028, Barcelona, Spain
7. X. D. Qi, X.Q. Qi  
College of Chemistry and Chemical Engineering, Chongqing University of Technology, Chongqing, 400054, China.
8. J. S. Li  
Institute for Advanced Study; Chengdu University 610106, Chengdu, China.
9. O. Usoltsev, L. Simonelli  
ALBA Synchrotron Light Facility, Carrer de la Llum 2-26, 08290, Cerdanyola del Vallès, Spain.
10. J. Arbiol and A. Cabot  
ICREA Pg. Lluís Companys, 08010 Barcelona, Catalonia, Spain
11. Y. J. Lei, G. X. Wang  
Centre for Clean Energy Technology, School of Mathematical and Physical Sciences, Faculty of Science, University of Technology Sydney, Sydney, NSW, 2007, Australia.  
E-mail: Yaojie.Lei@uts.edu.au guoxiu.wang@uts.edu.au
12. Q. Sun  
Zhengzhou Research Institute, Harbin Institute of Technology, Zhengzhou 450000, China  
E-mail: sunqing@hit.edu.cn

Supporting information for this article is given via a link at the end of the document.

## ***Material Synthesis***

**Materials:** Bismuth nitrate pentahydrate (analytical reagent, AR,  $\text{Bi}(\text{NO}_3)_3 \cdot 5\text{H}_2\text{O}$ ), trimesic acid (AR,  $\text{H}_3\text{BTC}$ ) were obtained from Sigma Aldrich. Selenium and tellurium powder (AR, Se and Te), polyvinylidene fluoride (PVDF), N,N-dimethylformamide (DMF), methanol ( $\text{CH}_3\text{OH}$ ), N-methylpyrrolidone (NMP), 1,3-dioxolane (DOL) and 1,2-dimethoxyethane (DME) and Super P were purchased from Fisher. All chemicals were used as received, without further processing. Deionized water was used for all the water-based experiments.

**Synthesis of Bi-MOF (Bi- $\text{H}_3\text{BTC}$ ):** All chemicals and reagents were used directly without further purification. Bi- $\text{H}_3\text{BTC}$  was first prepared by the following simple and economical solvothermal method. 1.94 g  $\text{Bi}(\text{NO}_3)_3 \cdot 5\text{H}_2\text{O}$  and 1.68 g  $\text{H}_3\text{BTC}$  were dissolved in a mixed solution of 30 mL DMF and  $\text{CH}_3\text{OH}$  with constant stirring, then transferred to an autoclave at 120 °C for 24 h, and finally washed with ethanol several times and dried overnight at 60 °C to obtain Bi- $\text{H}_3\text{BTC}$ .

**Synthesis of Bi @C:** The synthesized Bi- $\text{H}_3\text{BTC}$  was carbonized in a tube furnace at 600 °C for 4 h at a heating rate of 5 °C  $\text{min}^{-1}$  in Ar atmosphere.

**Synthesis of  $\text{Bi}_2\text{Se}_3$ @C:** The Bi@C and Se powders were put into the upstream and downstream of the porcelain boat respectively according to the mass ratio of 1: 5, and kept in a tube furnace at 600 °C for 6 h in Ar gas atmosphere with a heating rate of 2 °C  $\text{min}^{-1}$ .

**Synthesis of  $\text{Te-Bi}_2\text{Se}_{3-x}$ @C:** 200 mg of  $\text{Bi}_2\text{Se}_3$ @C and 10 mg of Te powder were put into the downstream and upstream of the porcelain boat, respectively, and kept in a tube furnace at 500 °C for 1 h in an Ar atmosphere at a heating rate of 5 °C  $\text{min}^{-1}$  to obtain  $\text{Te-Bi}_2\text{Se}_{3-x}$ @C.

**Synthesis of  $\text{Te-Bi}_2\text{Se}_{3-x}$ @C/S,  $\text{Bi}_2\text{Se}_3$ @C/S and Super P/S:** Mix the prepared sulfur host material ( $\text{Te-Bi}_2\text{Se}_{3-x}$ @C,  $\text{Bi}_2\text{Se}_3$ @C and Super P) and sulfur powder according to the mass ratio of 3:7, then grind in a mortar for 30 minutes, and finally put the mixed material in an autoclave at 155°C for 12 h, to remove the surface sulfur of the material The electrode material was transferred to a tube furnace at 300 °C for 2 h at heating rate 5°C  $\text{min}^{-1}$ .

## ***Physicochemical Characterizations***

The crystal structure was tested by X-ray diffraction (XRD, Miniflex 600) with Cu K radiation ( $\lambda = 1.5106 \text{ \AA}$ ) operating at 40 kV and 15 mA, The morphology of the as-prepared samples ( $\text{Te-Bi}_2\text{Se}_{3-x}$ @C,  $\text{Bi}_2\text{Se}_3$ @C) was characterized by scanning electron microscopy (SEM) and transmission electron microscopy (TEM) with UC (UniColore) Technology. The surface

composition and chemical state of the host materials were confirmed by X-ray photoelectron spectroscopy (XPS, Thermo Fisher Scientific, ESCALAB 250). Before XPS testing, the sample was exposed to air during handling and transportation. Thermogravimetric analysis (TGA NETZSCH, STA449-F5) was used to measure the S content in the cathode from 50 °C to 400 °C at a heating rate of 5°C/min in an N<sub>2</sub> atmosphere. UV-vis absorption spectroscopy (Lambda 950 UV-Vis-NIR Spectrophotometer, Perkin Elmer) was used to analyze the adsorption performance of electrode materials on polysulfides. XAFS testing is primarily conducted using the Rigaku XAFS-4000 system. The X-ray absorption near-edge structure spectroscopy (XANES) data were processed according to the standard procedures using the Athena module implemented in the IFEFFIT software packages. The extended X-ray absorption fine structure spectroscopy (EXAFS) spectra were obtained by subtracting the post-edge background from the overall absorption and then normalizing with respect to the edge-jump step. Subsequently, the  $\chi(k)$  data were Fourier transformed to real (R) space using a window ( $dk = 1.0 \text{ \AA}^{-1}$ ) to separate the EXAFS contributions from different coordination shells. To obtain the quantitative structural parameters around central atoms, least-squares curve parameter fitting was performed using the ARTEMIS module of IFEFFIT software packages. Atomic resolution aberration-corrected (AC) high-angle annular dark field-scanning transmission electron microscopy (HAADF-STEM) images and energy dispersive X-ray spectroscopy (EDS) were obtained in a double corrected and monochromated Thermo Fisher Spectra 300 microscope operated at 300 kV. Electron paramagnetic resonance (EPR) (JES-FA200) measurements were conducted at a temperature of 300 K and across a magnetic field strength range of 0.3 to 1.5 Tesla (T).

***LiPS Adsorption:*** Li<sub>2</sub>S and sulfur were dissolved in a mixed solution of DME and DOL (V: V=1:1) at a mass ratio of 1:5 and stirred overnight at 80 °C to prepare a Li<sub>2</sub>S<sub>6</sub> solution. Then, soak 20 mg of different sulfur host materials (Te-Bi<sub>2</sub>Se<sub>3-x</sub>@C, Bi<sub>2</sub>Se<sub>3</sub>@C, and Super P) into a 0.5 mM Li<sub>2</sub>S<sub>6</sub> solution stand overnight for polysulfide adsorption test.

### ***Electrochemical Measurements***

The prepared electrode material (Te-Bi<sub>2</sub>Se<sub>3-x</sub>@C, Bi<sub>2</sub>Se<sub>3</sub>@C, and Super P), Super P, and PVDF binder were mixed and ground according to 8:1:1, and NMP as added during the grinding process to prepare slurry. Then it was evenly coated on the current collector on the aluminum foil, and finally dried at 60 °C for 12 h and cut into 12 mm circular pieces to obtain the working electrode. The sulfur content of the cathode was 1.2 mg cm<sup>-2</sup>. For each coin cell, 20  $\mu$ L of electrolyte was used. To further highlight the practical application of the electrode, the high-loading cathode was prepared by the same method. The prepared sulfur electrode was used as

the cathode, the lithium foil was used as the anode, and Celgard 2400 and 1.0 M Lithium Bis(trifluoromethanesulfonyl)imide (LiTFSI) and 0.1 M LiNO<sub>3</sub> were dissolved in DOL/DME (v:v, 1:1) as the separator and electrolyte, respectively, to assemble a 2023 coin battery in argon-filled in the airy glove box. The prepared battery is subjected to cyclic voltammetry (CV) and galvanostatic charge/discharge (GCD) tests at a voltage window of 1.7-2.8 V, and an electrochemical impedance spectroscopy (EIS) test is performed at a frequency of 0.01 Hz-100 KHz. The Galvanostatic Intermittent Titration Technique (GITT) is used to measure the diffusion coefficient and reaction kinetics of battery materials.

**Symmetric Cells Test:** Two identical electrodes were used as working electrodes, 0.5 mM Li<sub>2</sub>S<sub>6</sub> solution was used as the electrolyte, and Celgard 2400 membrane was used as a diaphragm to assemble 2032 coin cells, and CV test was performed at 5 mV s<sup>-1</sup> a scan rate at voltage window of -1.0 V-1.0 V.

**Li<sub>2</sub>S Nucleation Test:** Different samples were coated on carbon cloth as the working electrode, lithium foil was used as the counter electrode, Celgard 2400 was used as the separator, and 0.5 mM Li<sub>2</sub>S<sub>6</sub> solution was used as the electrolyte to assemble coin batteries. Firstly, the coin battery was discharged to 2.06 V at a constant current, and then a constant potential Li<sub>2</sub>S deposition experiment was performed at a voltage of 2.05 V.

### **DFT calculations**

All DFT calculations were performed using the Vienna Ab-initio Simulation Package (VASP). The Perdew-Burke-Ernzerhof (PBE) functional for the exchange-correlation term was used with the projector augmented wave (PAW) potentials and a cutoff energy of 400 eV. The convergence of energy and forces were set to 1×10<sup>-4</sup> eV and 0.05 eV/Å, respectively. The lattice mismatch was no more than 3% and the vacuum layer was set as 15 Å to avoid the interactions between layers. In constructing the computational model, we considered the formation of vacancies. Additionally, after incorporating Te into the structure, we adjusted the lattice parameters through geometry optimization to ensure the system reached its lowest energy state, effectively capturing the lattice distortion induced by Te doping. The adsorption energy  $\Delta E_{ad}$  was calculated as:

$$\Delta E_{ad} = E_{(surf+ad)} - E_{surf} - E_{ad}$$

where  $E_{(surf+ad)}$  is the energy of the LiPS adsorbed on the surface,  $E_{surf}$  is the energy of the clean surface, and  $E_{ad}$  is the energy of the free LiPS.

The formula for calculating the Gibbs free as follow:

$$\Delta G(\text{S}_8\text{-Li}_2\text{S}_8): E_{\text{Li}_2\text{S}_8} - E_{\text{S}_8} - 2E_{\text{Li}^+}$$

$$\Delta G(\text{Li}_2\text{S}_8\text{-Li}_2\text{S}_6): E_{\text{Li}_2\text{S}_6} - E_{\text{Li}_2\text{S}_8} + 0.25E_{\text{S}_8}$$

$$\Delta G(\text{Li}_2\text{S}_6\text{-Li}_2\text{S}_4): E_{\text{Li}_2\text{S}_4} - E_{\text{Li}_2\text{S}_6} + 0.25E_{\text{S}_8}$$

$$\Delta G(\text{Li}_2\text{S}_4\text{-Li}_2\text{S}_2): E_{\text{Li}_2\text{S}_2} - E_{\text{Li}_2\text{S}_4} + 0.25E_{\text{S}_8}$$

$$\Delta G(\text{Li}_2\text{S}_2\text{-Li}_2\text{S}): E_{\text{Li}_2\text{S}} - E_{\text{Li}_2\text{S}_2} + 0.125E_{\text{S}_8}$$

***Pouch cell assembly and measurements:***

The Te-Bi<sub>2</sub>Se<sub>3-x</sub>@C/S cathode and lithium anode were cut into 3×4 cm (width × height) and 3×6 cm (width × height) pieces. The sulfur loading of the cathode in the pouch cell was 1.8 mg·cm<sup>-2</sup>. The E/S ratio was about 20 μL·mg<sup>-1</sup>, the thickness of the lithium belt anode was 0.4 mm. The separator and electrolyte were sandwiched between the tailored and Te-Bi<sub>2</sub>Se<sub>3-x</sub>@C/S lithium belt.



## Supporting Information Data

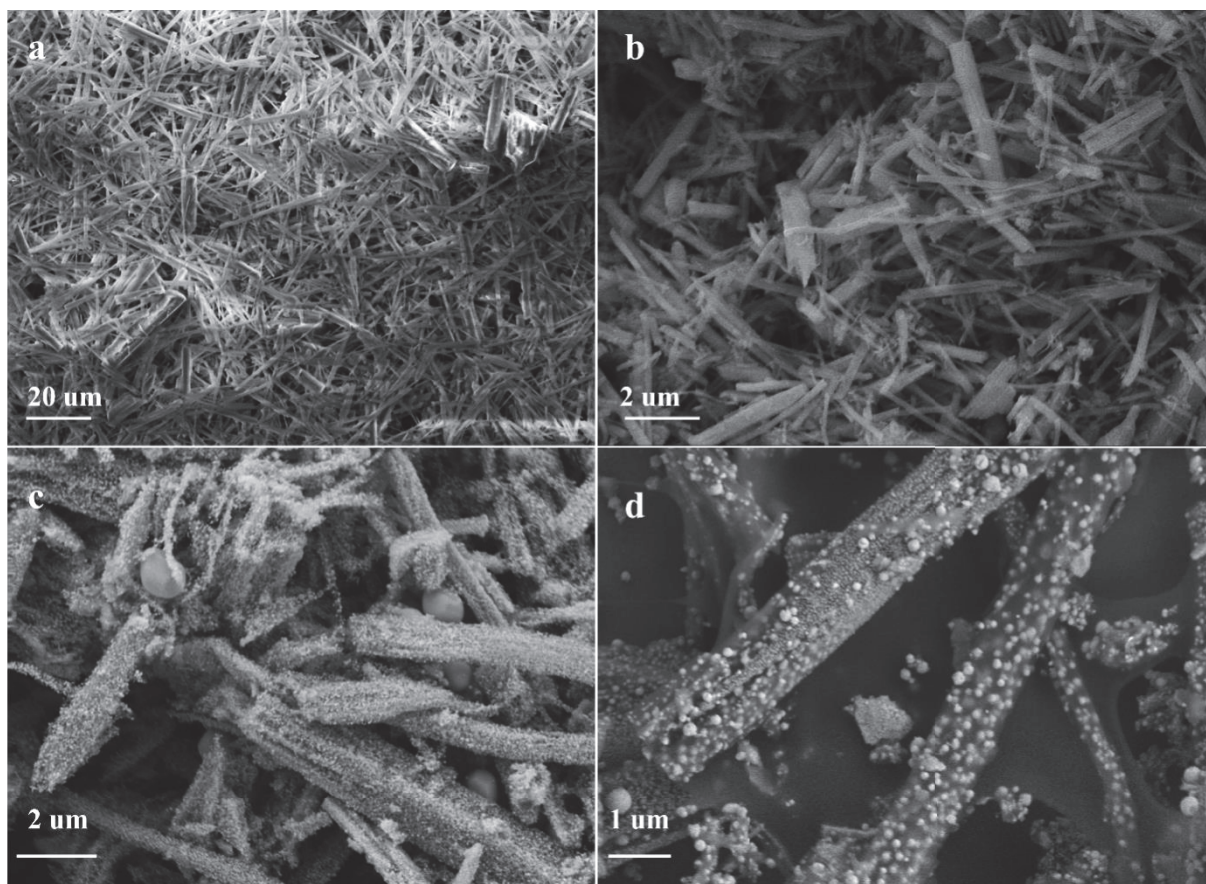


**Figure S1.** SEM images of (a) Bi-MOF, (b) Bi@C, (c)  $\text{Bi}_2\text{Se}_3@\text{C}$ , and (d)  $\text{Te-Bi}_2\text{Se}_{3-x}@\text{C}$ .

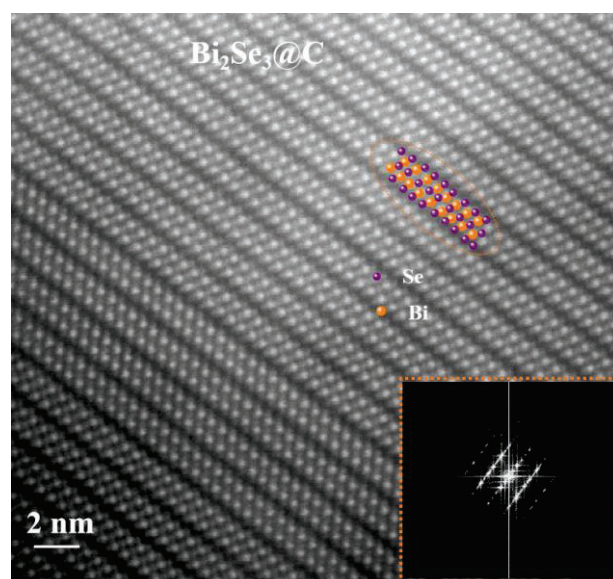


**Figure S2.** Atomic resolution AC HAADF-STEM image of Bi<sub>2</sub>Se<sub>3</sub>@C.

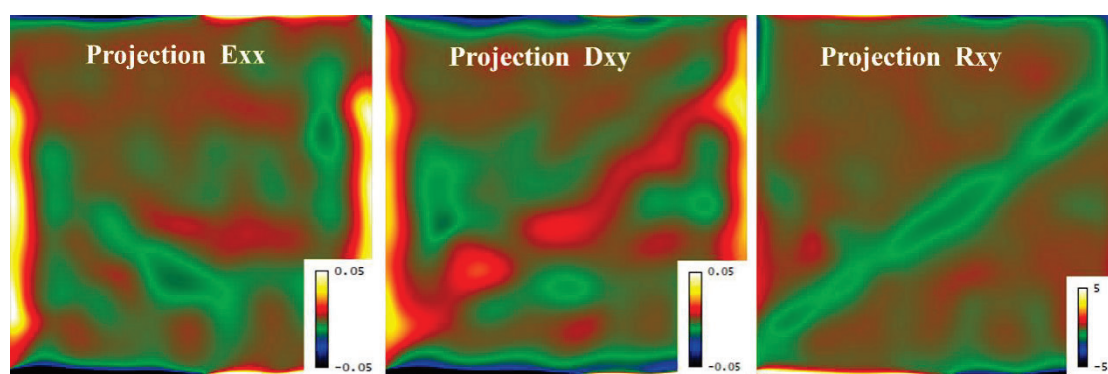


**Figure S3.** Lattice distortion of Te-Bi<sub>2</sub>Se<sub>3-x</sub>@C in different directions (Exx, Dxy and Rxy).

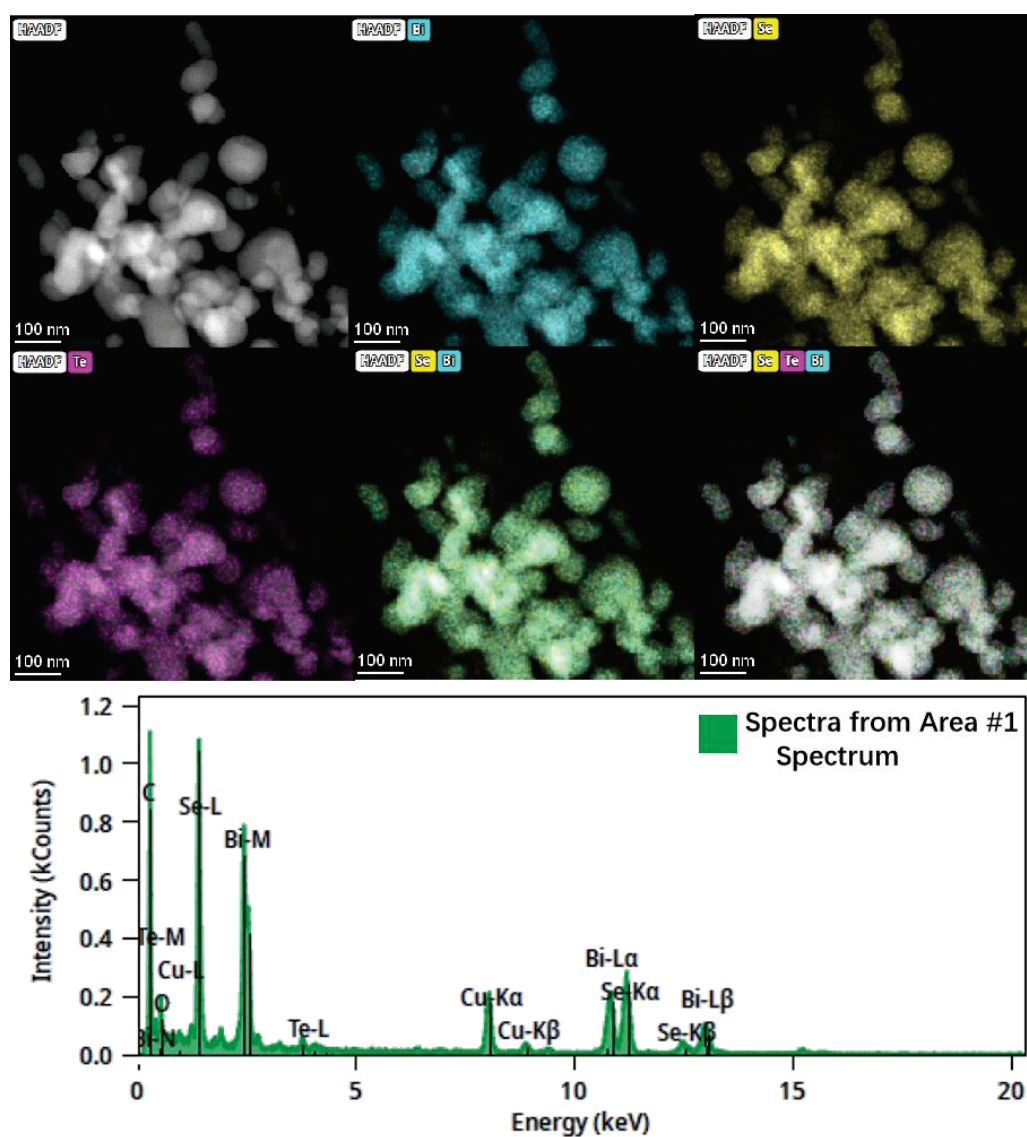


Figure S4. HAADF-STEM image and STEM-EDX composition maps of Te-Bi<sub>2</sub>Se<sub>3-x</sub>@C.

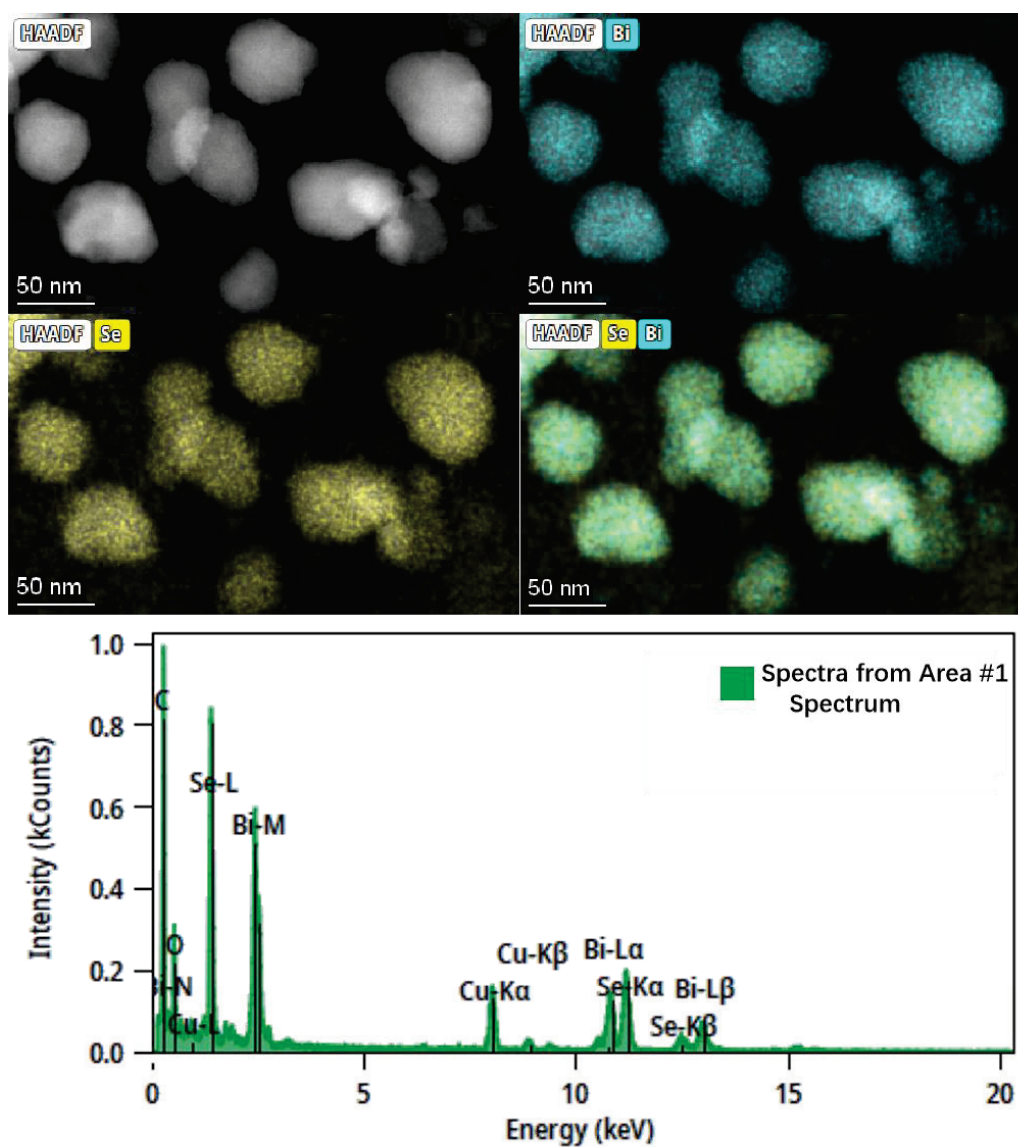
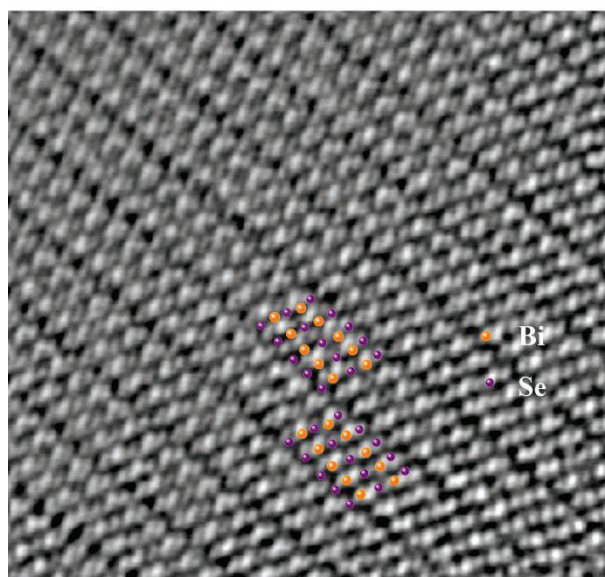
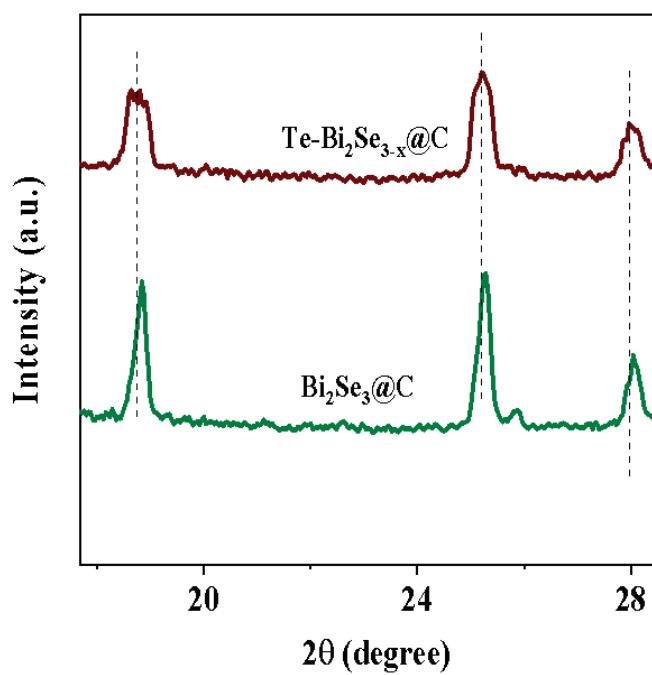


Figure S5. HAADF-STEM image and STEM-EDX composition maps of  $\text{Bi}_2\text{Se}_3@\text{C}$ .





**Figure S6.** iDPC-STEM images of Bi<sub>2</sub>Se<sub>3</sub>@C.



**Figure S7.** XRD patterns of Te-Bi<sub>2</sub>Se<sub>3-x</sub>@C and Bi<sub>2</sub>Se<sub>3</sub>@C.

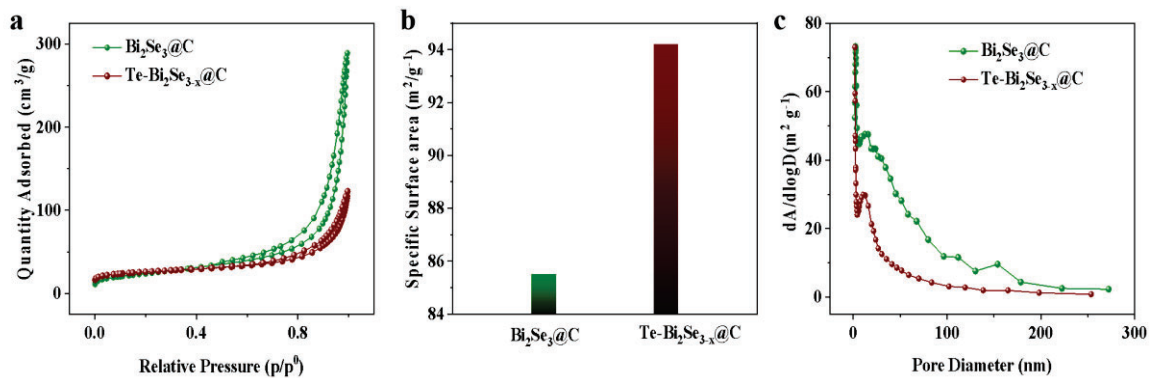


**Figure S8.** Specific surface area and pore volume of different sulfur host materials for Te-Bi<sub>2</sub>Se<sub>3-x</sub>@C and Bi<sub>2</sub>Se<sub>3</sub>@C.

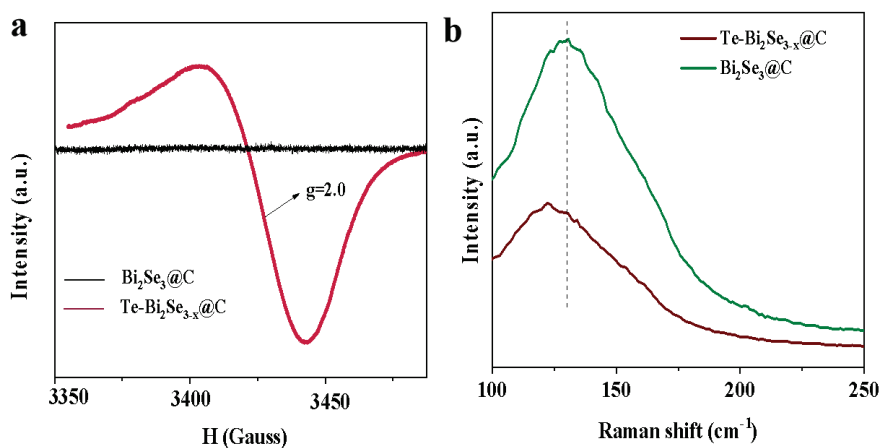


**Figure S9.** (a) EPR curves of Te-Bi<sub>2</sub>Se<sub>3-x</sub>@C and Bi<sub>2</sub>Se<sub>3</sub>@C. (b) Raman spectra of electrode materials.

The carbon content in the Te-Bi<sub>2</sub>Se<sub>3-x</sub>@C composite is calculated based on the transformation of Bi<sub>2</sub>Se<sub>3</sub> into Bi<sub>2</sub>O<sub>3</sub>. We did not consider the Te for this calculation. As shown in Figure S10, the content of C in Te-Bi<sub>2</sub>Se<sub>3-x</sub>@C composite can be calculated based on the following equation.<sup>[1]</sup>



Atomic weight: Bi (209), Se (79), O (16)

$$x + \frac{[(209 \times 2 + 79 \times 3) - (209 \times 2 + 16 \times 3)] \times (1 - x)}{209 \times 2 + 79 \times 3} = 54.5\%$$

$$x = 35.9\%$$

Therefore, the initial C content was calculated to be 35.9%.



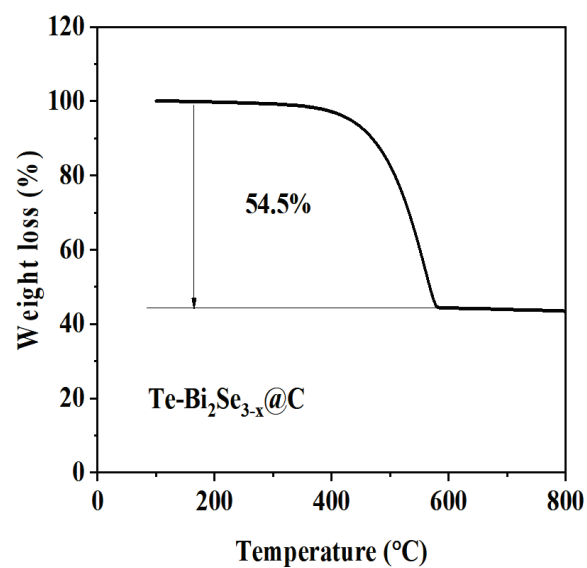


**Figure S10.** TGA curve of  $\text{Te-Bi}_2\text{Se}_{3-x}\text{@C}$  in air atmosphere. Under the air environment, above 400 °C, the mass loss is primarily due to the combustion of carbon and selenium. The carbon content in the  $\text{Te-Bi}_2\text{Se}_{3-x}\text{@C}$  composite is thus about 35.9 %.

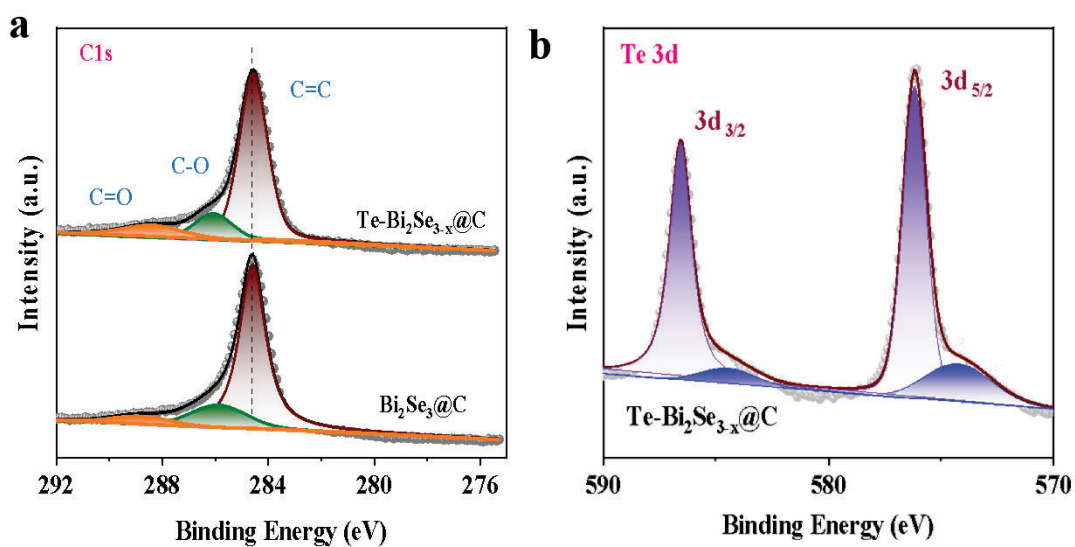


**Figure S11.** (a) C 1s and (b) Te 3d XPS spectra of  $\text{Te-Bi}_2\text{Se}_{3-x}\text{@C}$  and  $\text{Bi}_2\text{Se}_3\text{@C}$ .

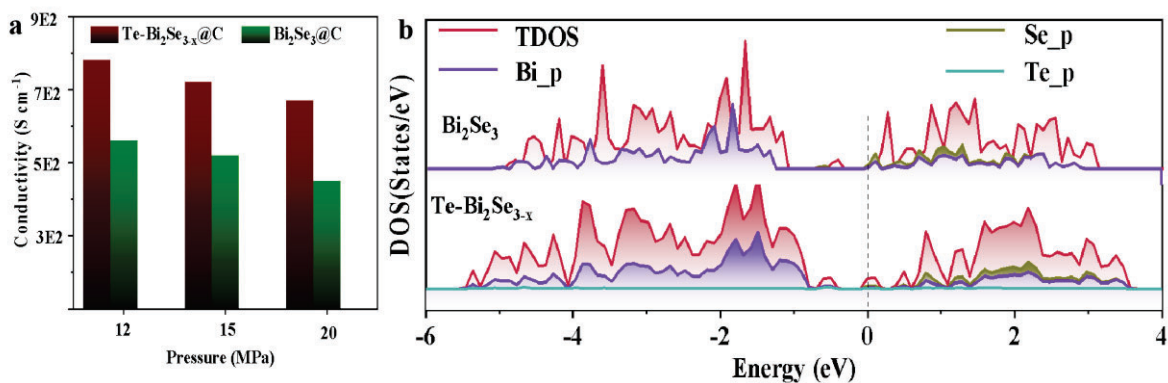


**Figure S12.** Electrical conductivity of Te-Bi<sub>2</sub>Se<sub>3-x</sub>@C and Bi<sub>2</sub>Se<sub>3</sub>@C tested using four probes at different pressures. (b) The density of state (DOS) of Te-Bi<sub>2</sub>Se<sub>3-x</sub> and Bi<sub>2</sub>Se<sub>3</sub>.

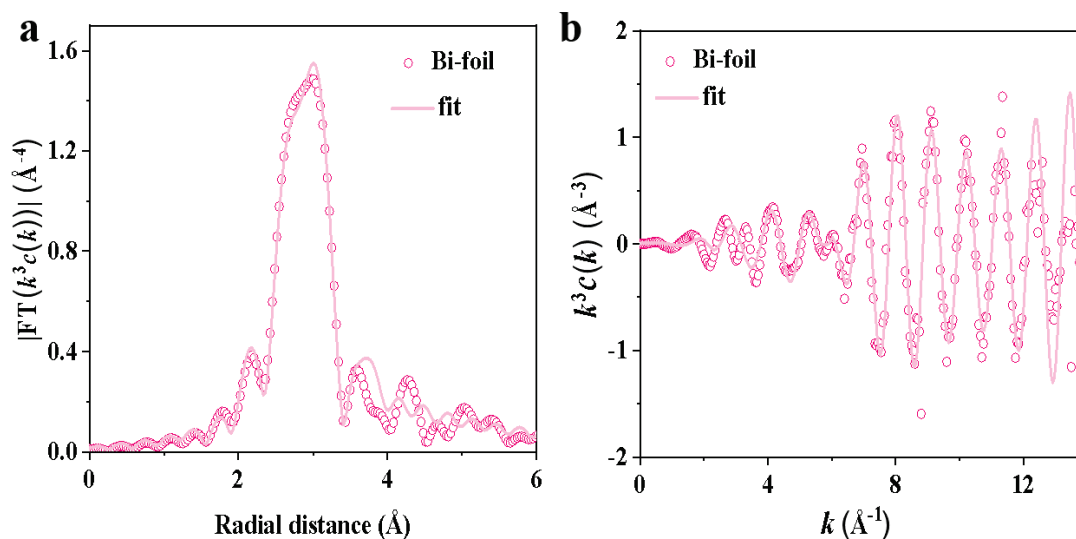


**Figure S13.** (a) Fourier transform extended X-ray absorption fine structure (FT-EXAFS) fitting curves of Bi L3-edge for Bi foil (R space), (b) X-ray absorption fine structure (XAFS) fitting curves of Ni Bi L3-edge for Bi foil (K3 space).

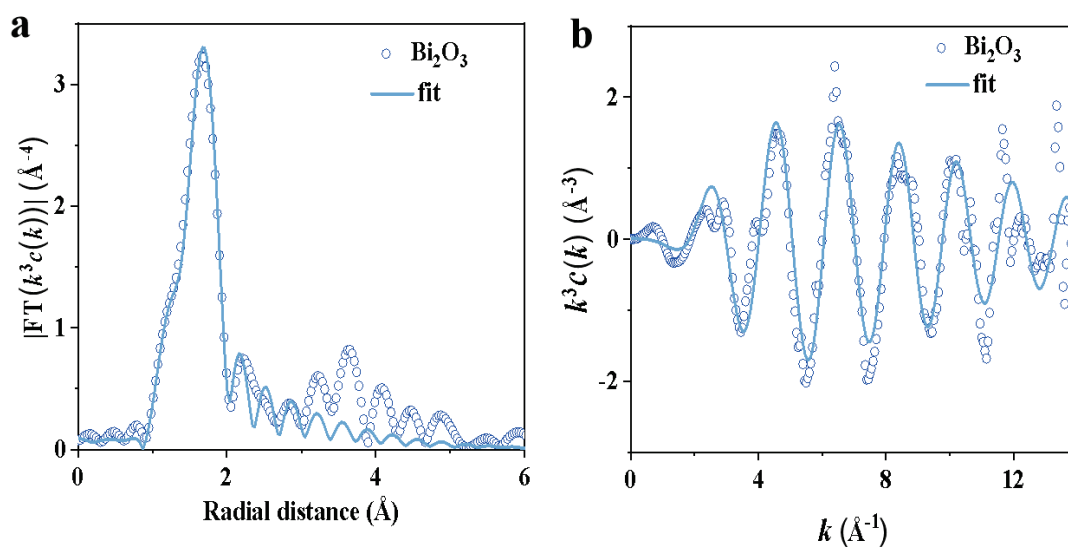


**Figure S14.** (a) FT-EXAFS fitting curves of Bi L3-edge for Bi<sub>2</sub>O<sub>3</sub> (R space), (b) XAFS fitting curves of Ni Bi L3-edge for Bi<sub>2</sub>O<sub>3</sub> (K<sub>3</sub> space).

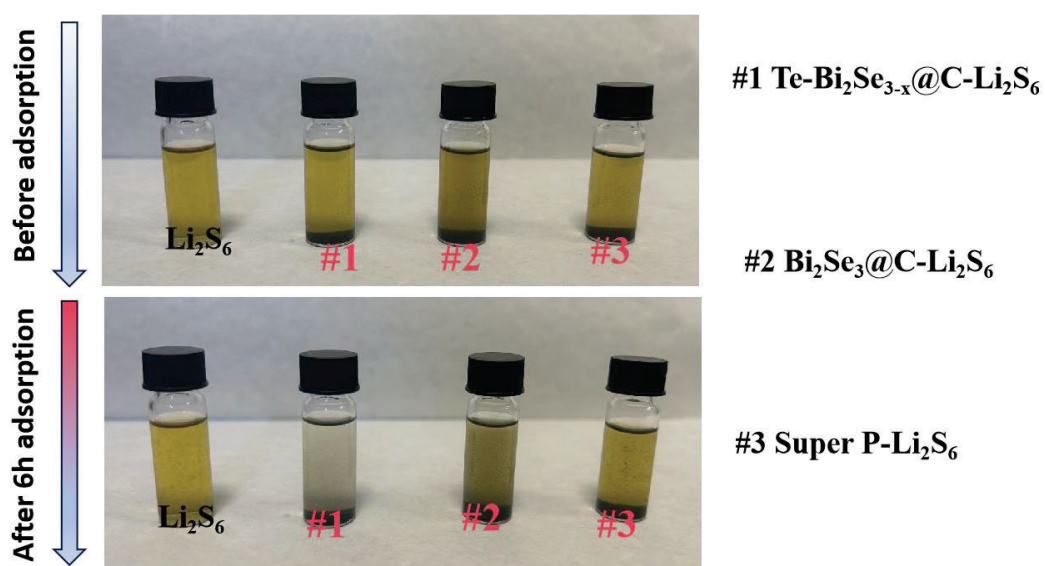


**Figure S15.** Li<sub>2</sub>S<sub>6</sub> solutions containing different materials before adsorption and after 6h adsorption.

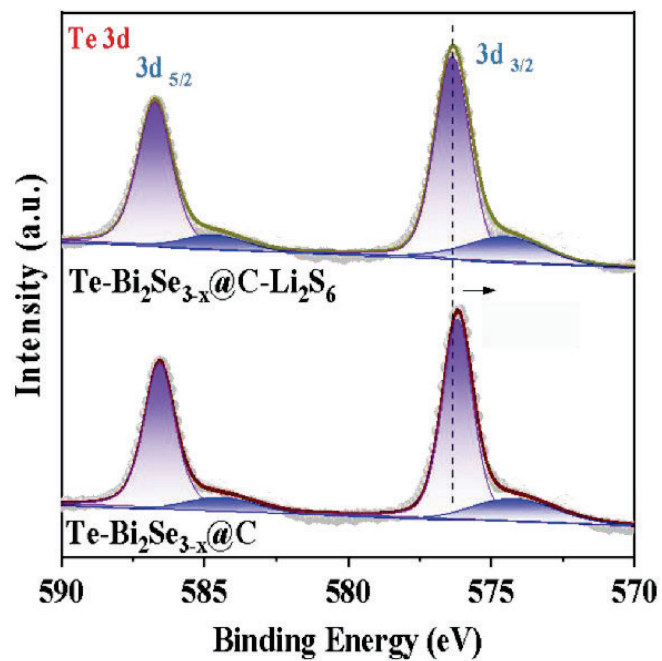


Figure S16 Te 3d XPS spectra before ( $\text{Te-Bi}_2\text{Se}_{3-x}\text{@C}$ ) and after adsorption ( $\text{Te-Bi}_2\text{Se}_{3-x}\text{@C-Li}_2\text{S}_6$ ).

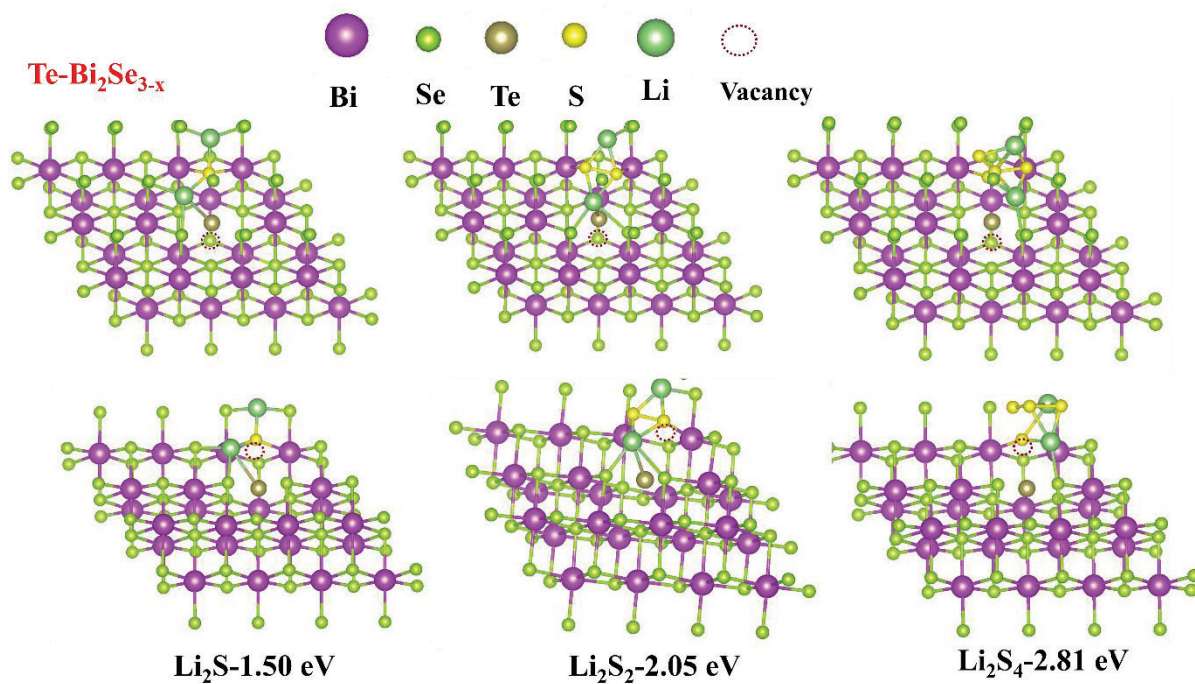
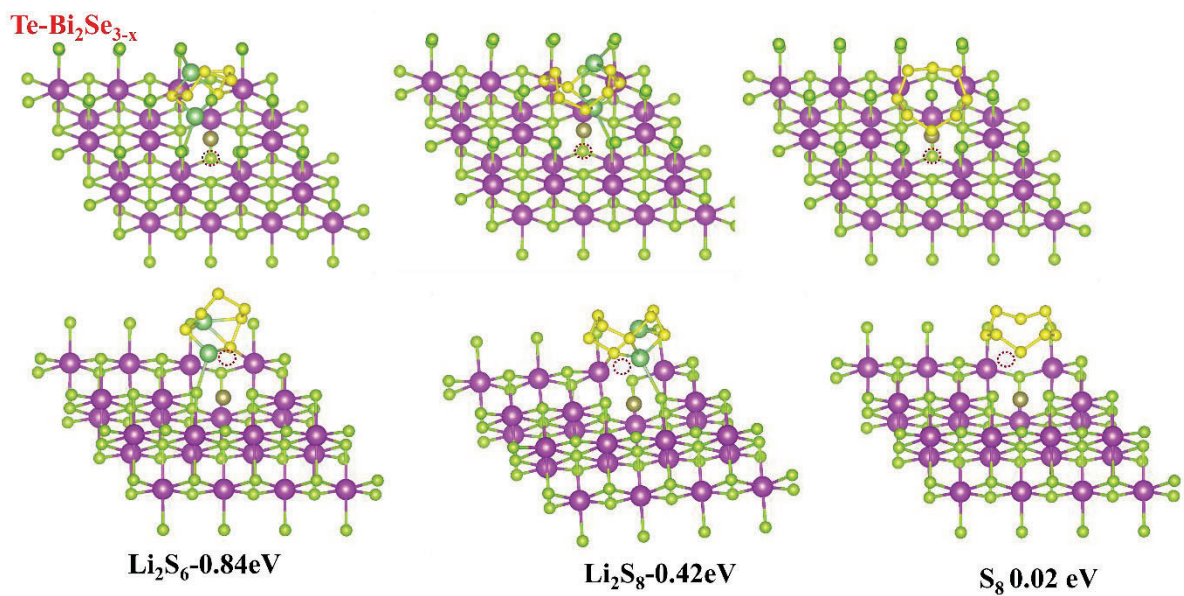
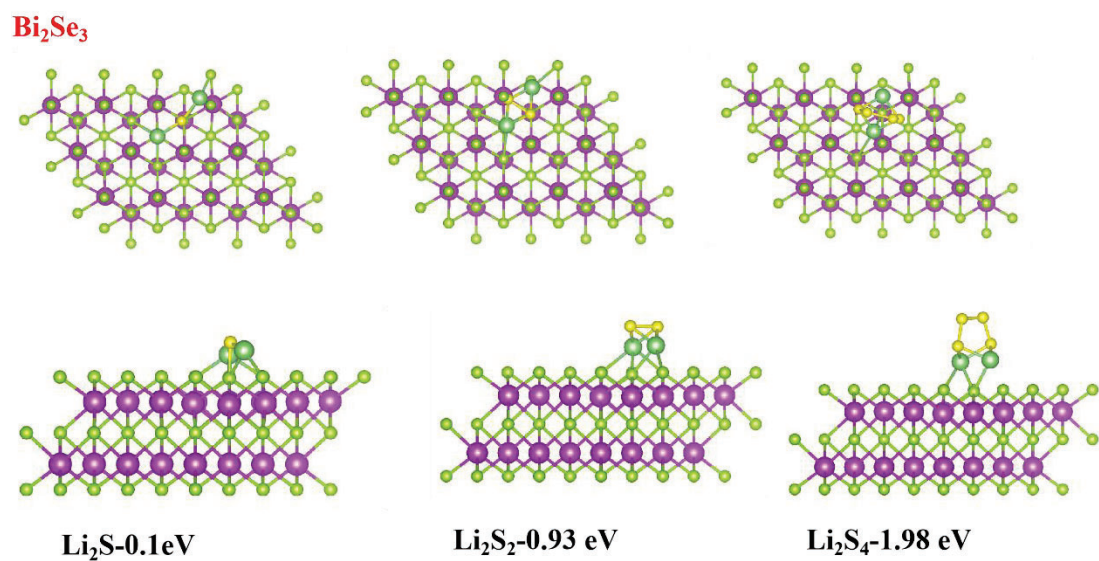


Figure S17. Adsorption model of polysulfides ( $\text{Li}_2\text{S}$ ,  $\text{Li}_2\text{S}_2$  and  $\text{Li}_2\text{S}_4$ ) by host material  $\text{Te-Bi}_2\text{Se}_{3-x}$ .



**Figure S18.** Adsorption model of polysulfides (Li<sub>2</sub>S<sub>6</sub>, Li<sub>2</sub>S<sub>8</sub> and S<sub>8</sub>) by host material Te-Bi<sub>2</sub>Se<sub>3-x</sub>.



**Figure S19.** Adsorption model of polysulfides (Li<sub>2</sub>S, Li<sub>2</sub>S<sub>2</sub> and Li<sub>2</sub>S<sub>4</sub>) by host material Bi<sub>2</sub>Se<sub>3</sub>.



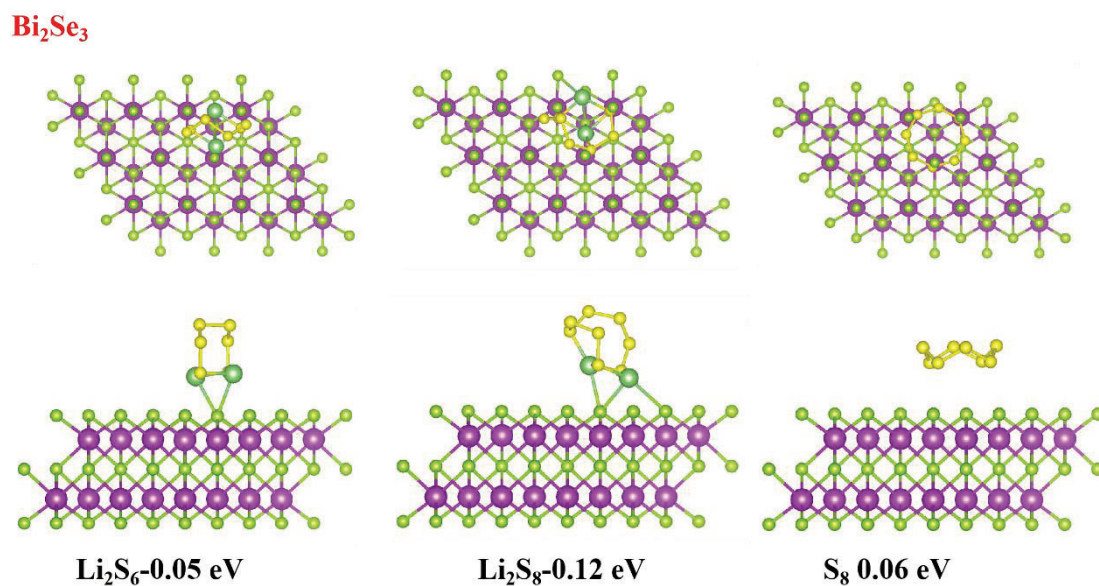


**Figure S20.** Adsorption model of polysulfides (Li<sub>2</sub>S<sub>6</sub>, Li<sub>2</sub>S<sub>8</sub> and S<sub>8</sub>) by host material Bi<sub>2</sub>Se<sub>3</sub>.

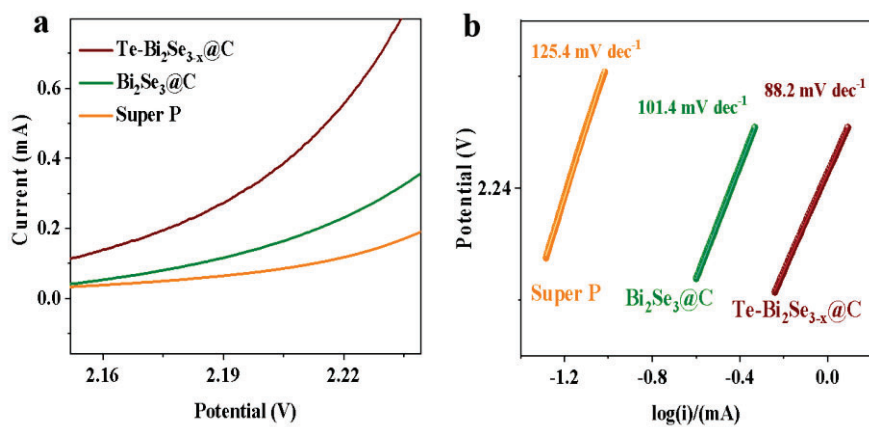


**Figure S21.** LSV and Tafel curves of Te-Bi<sub>2</sub>Se<sub>3-x</sub>@C, Bi<sub>2</sub>Se<sub>3</sub>@C and Super P for Li<sub>2</sub>S oxidation.



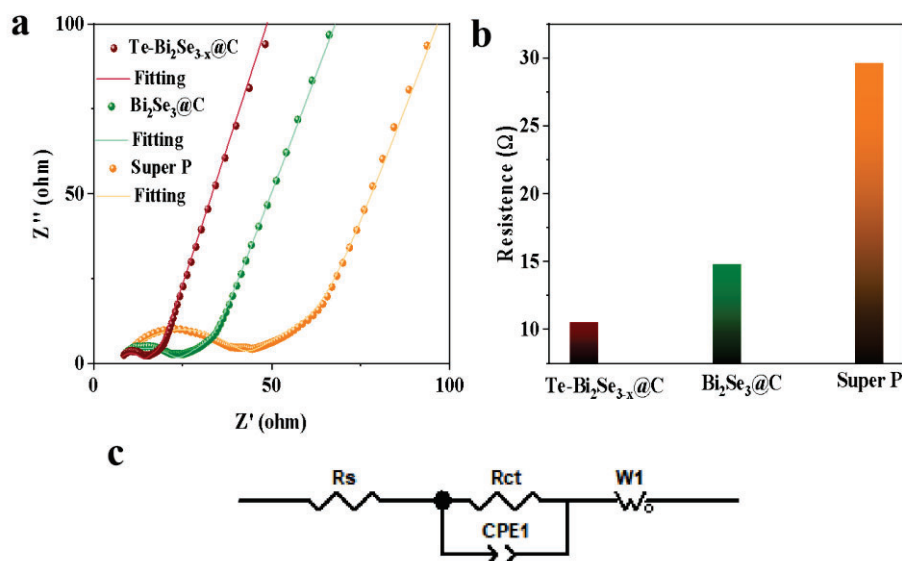


**Figure S22.** EIS spectra of  $\text{Te-Bi}_2\text{Se}_{3-x}\text{@C}$ ,  $\text{Bi}_2\text{Se}_3\text{@C}$  and Super P for Symmetrical cells and the equivalent circuit used to fit the data.

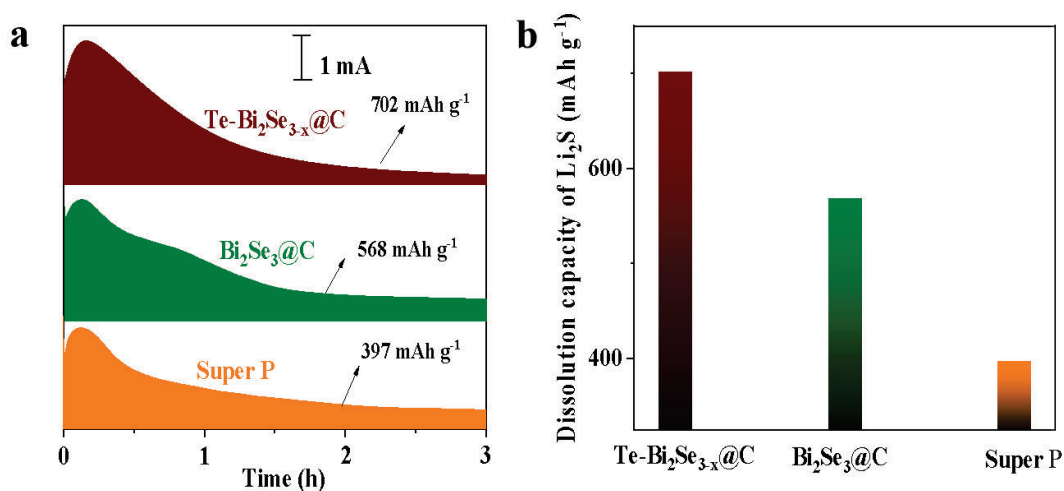


**Figure S23.** Potentiostatic charge profile at 2.40 V for evaluating dissolution kinetics of  $\text{Li}_2\text{S}$ .

The Arrhenius equation is commonly utilized to determine the activation energy ( $E_a$ ), which quantifies the energy required for a reaction to occur, and determines how the reaction rate changes with varying temperatures. The standard representation of the Arrhenius equation is expressed as follows:

$$k = A \times \exp\left(\frac{-E_a}{RT}\right)$$

In this equation,  $k$  represents the reaction rate constant, while  $A$  denotes the pre-exponential factor, which reflects the frequency of reactant collisions leading to a transition state. The term  $E_a$  corresponds to the activation energy, indicating the minimum energy required for the reaction to proceed.  $R$  is the gas constant, and  $T$  represents the absolute temperature in Kelvin. The equation can also be rearranged into an alternative form:

$$\ln k = \frac{-E_a}{RT} + \ln A$$

Experimental studies on LSBs utilize the charge transfer resistance ( $R_{ct}$ ) measured through EIS to evaluate the reaction rate constant ( $k$ ) at various temperatures. The data are then fitted to a log-linear plot based on the Arrhenius equation. From this fitting, the slope corresponds to the negative value of the activation energy ( $\frac{-E_a}{R}$ ), enabling the calculation of the  $E_a$ .

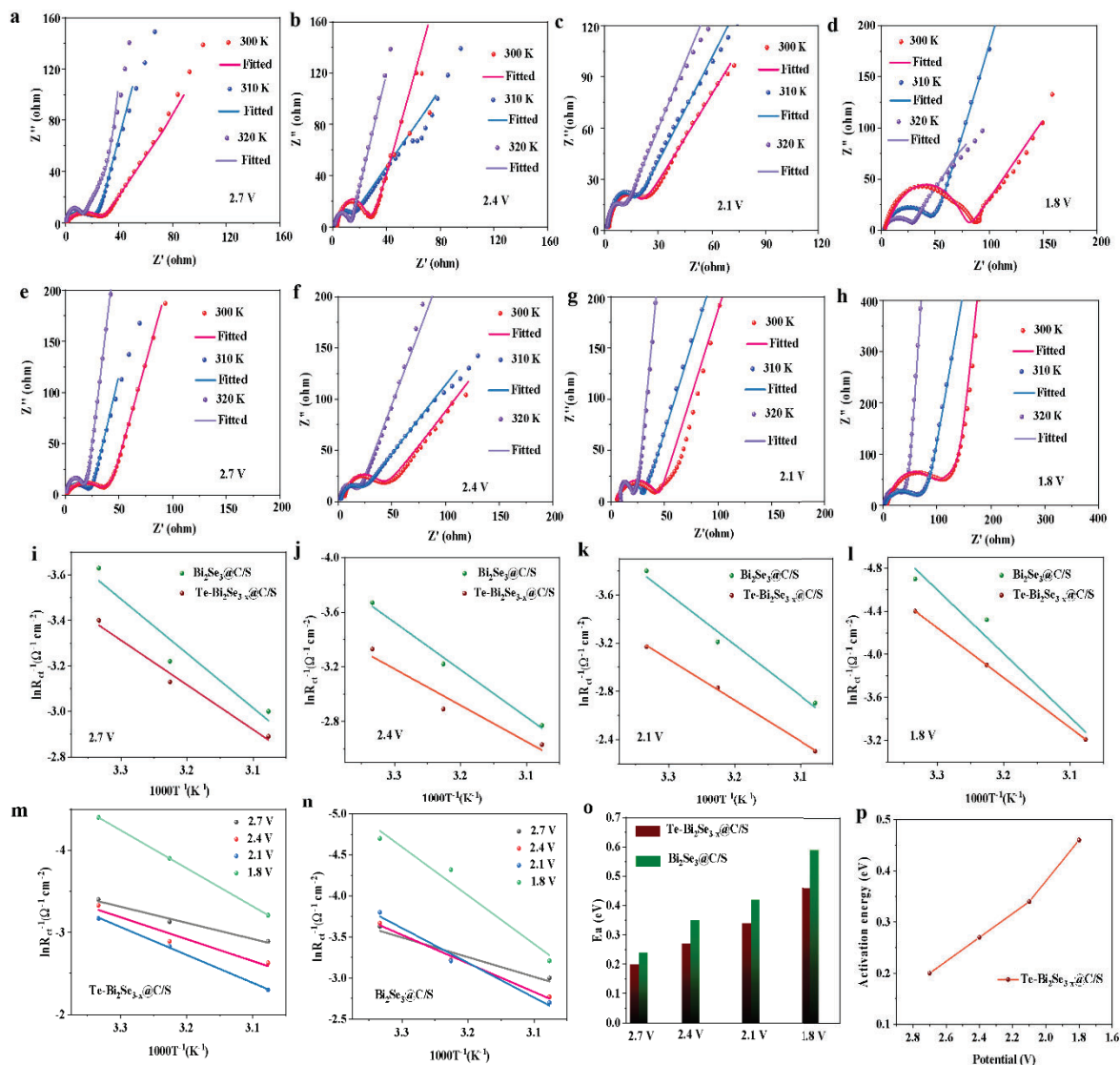


**Figure S24.** (a-d) Nyquist plots of the EIS spectra of the  $\text{Te-Bi}_2\text{Se}_{3-x}\text{@C/S}$  electrodes at various voltages (2.7 V-1.8V) and temperatures (300 K-320 K). (e-h) Nyquist plots of the EIS spectra of the  $\text{Bi}_2\text{Se}_3\text{@C/S}$  electrodes at various voltages (2.7 V-1.8V) and temperatures (300 K-320 K). (i) Arrhenius plot of  $R_{ct}$  calculated from  $\text{Te-Bi}_2\text{Se}_{3-x}\text{@C/S}$  and  $\text{Bi}_2\text{Se}_3\text{@C/S}$  at 2.7 V. (j) Arrhenius plot of  $R_{ct}$  calculated from  $\text{Te-Bi}_2\text{Se}_{3-x}\text{@C/S}$  and  $\text{Bi}_2\text{Se}_3\text{@C/S}$  at 2.4 V. (k) Arrhenius plot of  $R_{ct}$  calculated from  $\text{Te-Bi}_2\text{Se}_{3-x}\text{@C/S}$  (b) and  $\text{Bi}_2\text{Se}_3\text{@C/S}$  at 2.1 V. (l) Arrhenius plot of  $R_{ct}$  calculated from  $\text{Te-Bi}_2\text{Se}_{3-x}\text{@C/S}$  (b) and  $\text{Bi}_2\text{Se}_3\text{@C/S}$  at 1.8 V. (m) Arrhenius plot of  $R_{ct}$  calculated for  $\text{Te-Bi}_2\text{Se}_{3-x}\text{@C/S}$  at different voltage. (n) Arrhenius plot of  $R_{ct}$  calculated for  $\text{Bi}_2\text{Se}_3\text{@C/S}$  at different voltage. (o) Calculated activation energies at different voltage for  $\text{Te-Bi}_2\text{Se}_{3-x}\text{@C/S}$  and  $\text{Bi}_2\text{Se}_3\text{@C/S}$ . (p) Calculated activation energies at different voltage for  $\text{Te-Bi}_2\text{Se}_{3-x}\text{@C/S}$ .

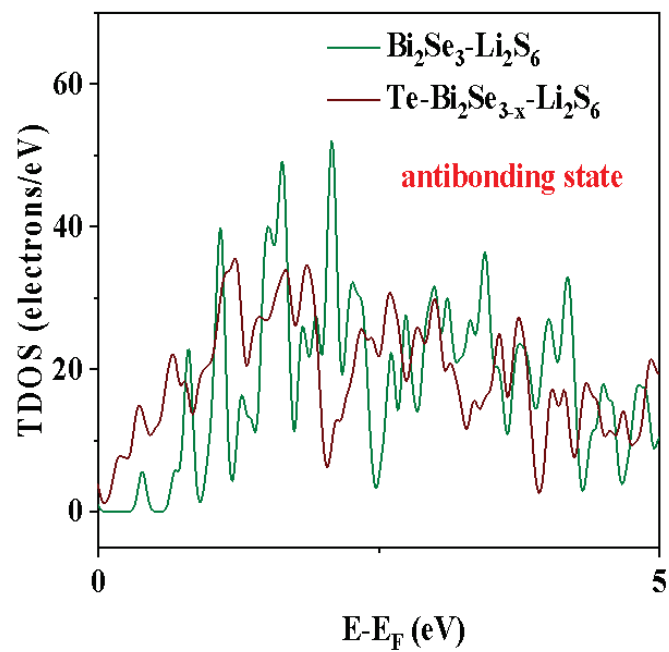


Figure S25. TDOS curves of  $\text{Te-Bi}_2\text{Se}_{3-x}\text{-Li}_2\text{S}_6$  and  $\text{Bi}_2\text{Se}_3\text{-Li}_2\text{S}_6$ .

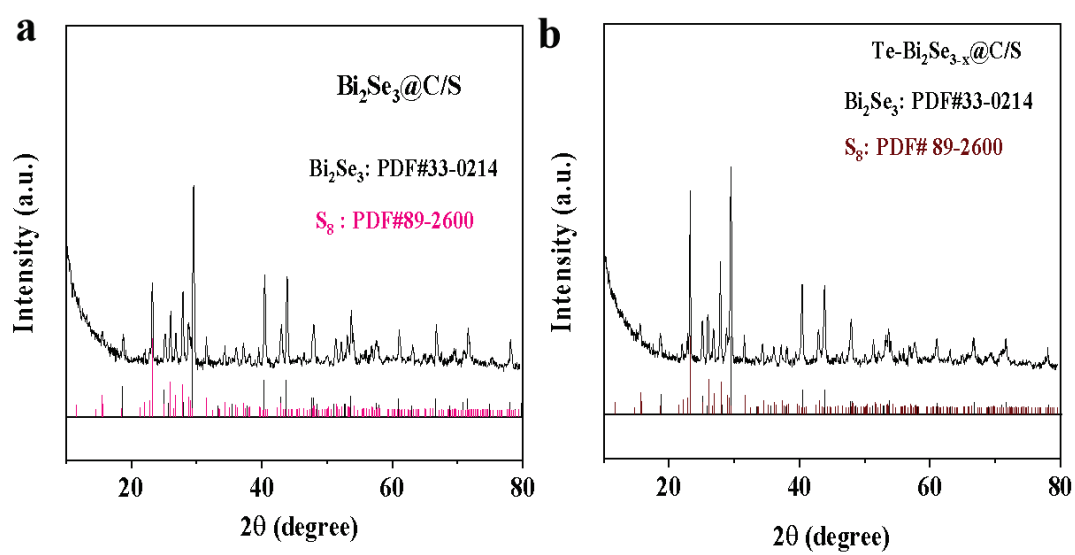
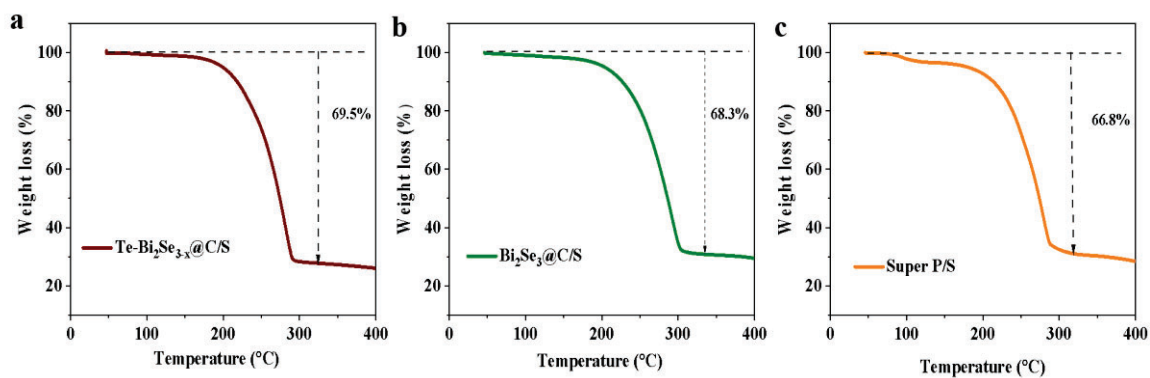
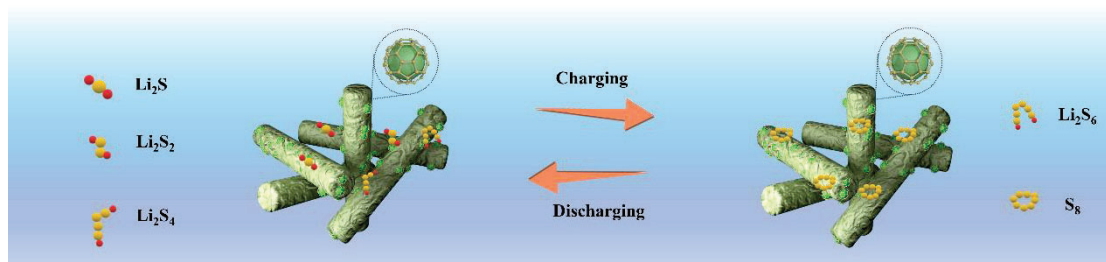


Figure S26. XRD patterns of  $\text{Bi}_2\text{Se}_3\text{@C/S}$  (a) and  $\text{Te-Bi}_2\text{Se}_{3-x}\text{@C/S}$  (b).



**Figure S27.** TGA curves of different electrodes ( $\text{Te-Bi}_2\text{Se}_{3-x}\text{@C/S}$ ,  $\text{Bi}_2\text{Se}_3\text{@C/S}$ , and Super/S).



**Figure S28.** Scheme of the charging and discharging mechanism of cathode electrode materials for LSBs.

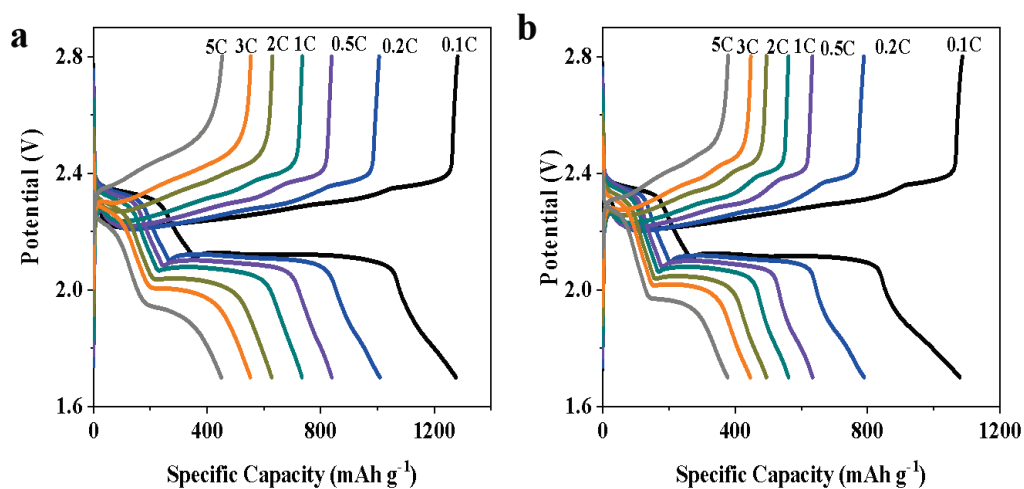


**Figure S29.** GCD curves of  $\text{Bi}_2\text{Se}_3\text{@C/S}$  and Super/S with a voltage window of 1.7 V-2.8 V at current density from 0.1C to 5C.

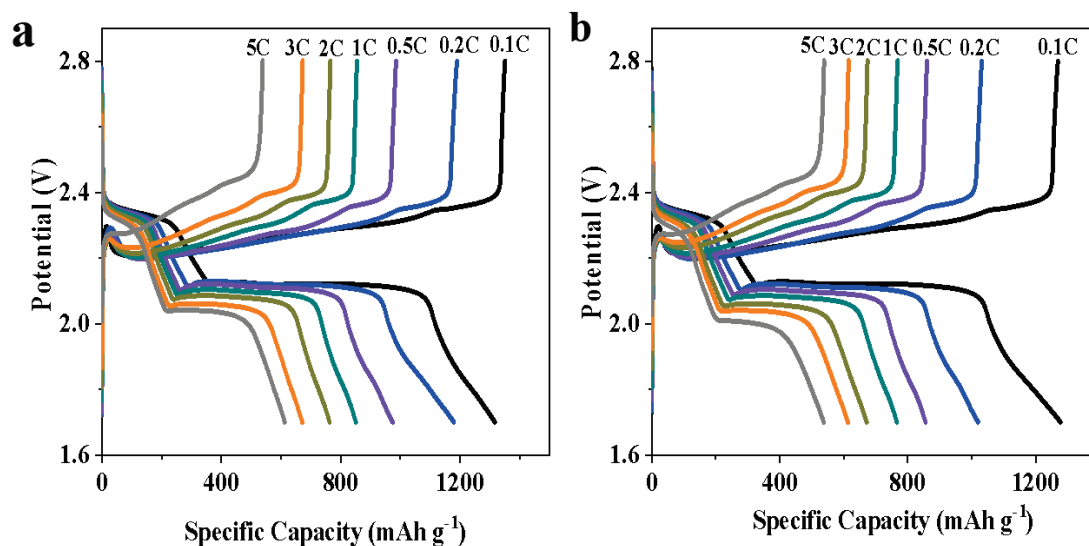


**Figure S30.** GCD curves of the prepared electrode materials with Te doping contents of 15 mg (a) and 20 mg (b).

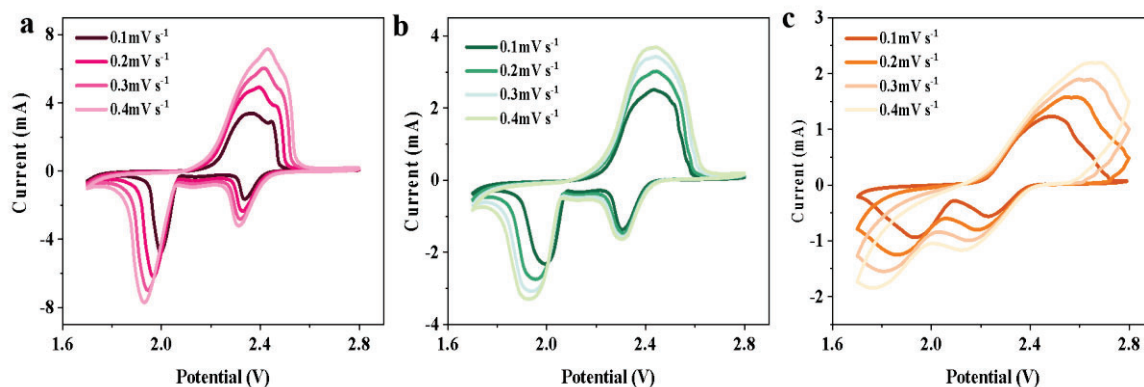


**Figure S31.** CV curves of  $\text{Te-Bi}_2\text{Se}_{3-x}\text{@C/S}$ ,  $\text{Bi}_2\text{Se}_3\text{@C/S}$  and Super/S with a voltage window of 1.7 V-2.8 V and a scan rate from 0.1  $\text{mV s}^{-1}$  to 0.4  $\text{mV s}^{-1}$ .

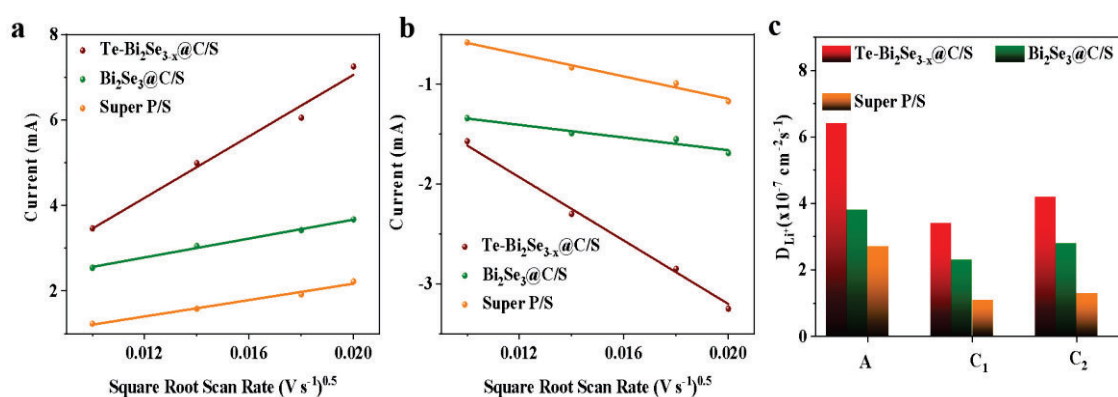


**Figure S32.** Peak current vs. square root of scan rate for different cathodes,  $\text{Te-Bi}_2\text{Se}_{3-x}\text{@C/S}$ ,  $\text{Bi}_2\text{Se}_3\text{@C/S}$  and Super P/S. a) A oxidation peak. b) C1 reduction peak. (c)  $\text{Li}^+$  diffusion coefficient calculated from the CV redox peaks according to the Randles-Sevcik equation.



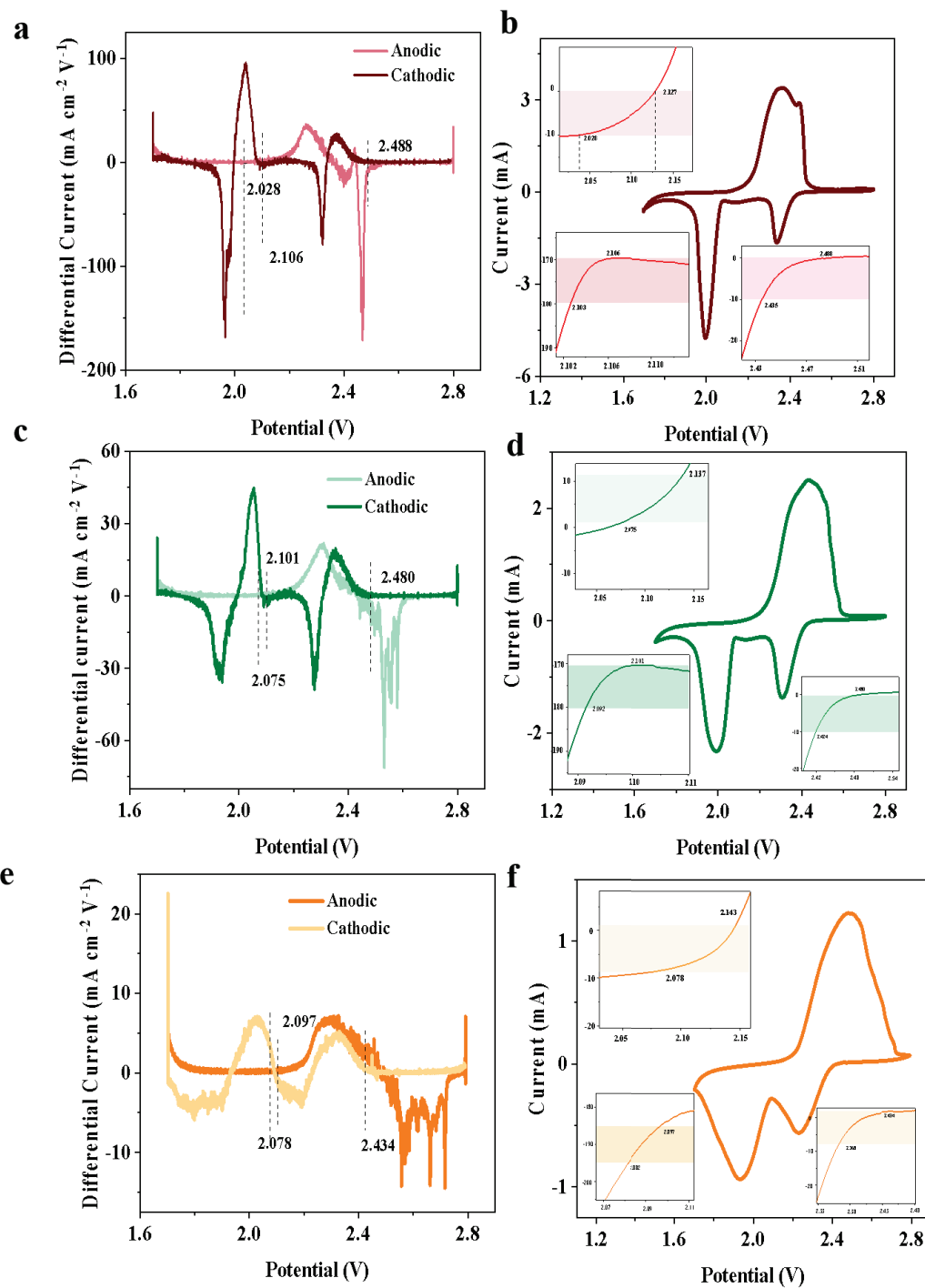


**Figure S33.** Onset potentials for Li-S redox reactions. (a, c and e) Differential CV curves of (a) Te-Bi<sub>2</sub>Se<sub>3-x</sub>@C/S, (c) Bi<sub>2</sub>Se<sub>3</sub>@C/S, (e) Super/S. (b, d and f) CV curves and corresponding onset potentials of redox peaks A, C1, and C2 (inset): (b) Te-Bi<sub>2</sub>Se<sub>3-x</sub>@C/S, (d) Bi<sub>2</sub>Se<sub>3</sub>@C/S, (f) Super/S.

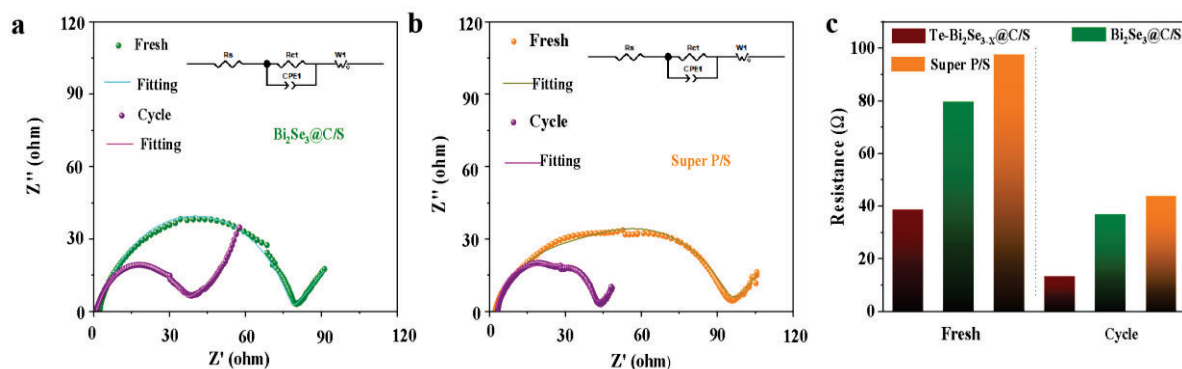


**Figure S34.** EIS spectra and equivalent circuit diagrams of different electrodes ( $\text{Te-Bi}_2\text{Se}_{3-x}@\text{C/S}$ ,  $\text{Bi}_2\text{Se}_3@\text{C/S}$  and Super P/S) and  $R_{ct}$  values of the assembled batteries before and after cycling.

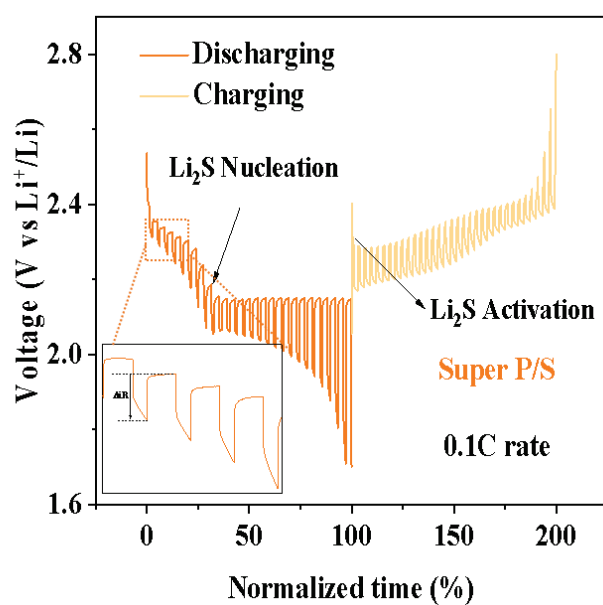


**Figure S35.** GITT curve for Super P/S.

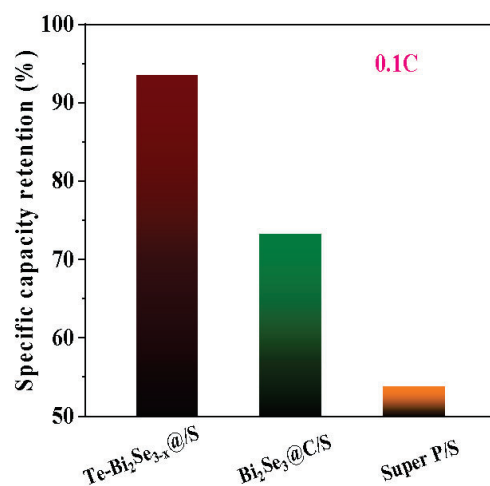


**Figure S36.** Specific Capacity retention of different electrodes at a current density of 0.1C for 300 cycles.

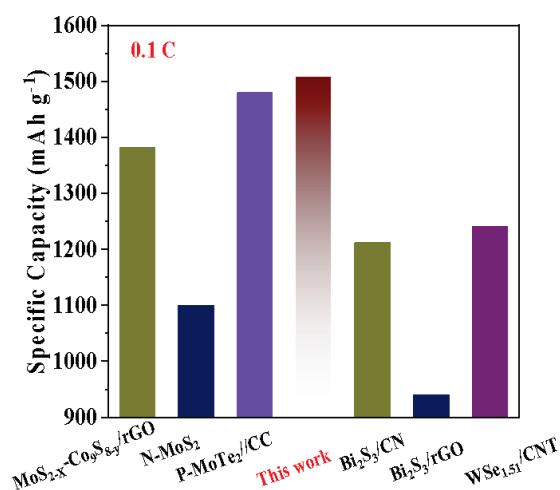


**Figure S37.** Comparison of the capacity obtained with the Te-Bi<sub>2</sub>Se<sub>3-x</sub>@C/S cathode with specific capacities of previously reported vacancy and heterostructure-based electrodes at a current density of 0.1C. References can be found in Table S4.

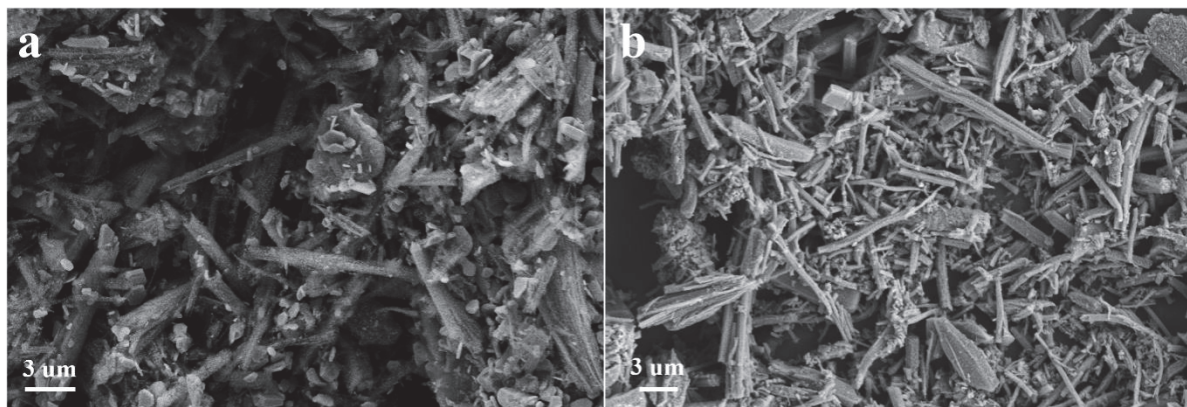


**Figure S38.** SEM images of Te-Bi<sub>2</sub>Se<sub>3-x</sub>@/S before cycling (a) and after 200 cycles at 3C rate (b), respectively.

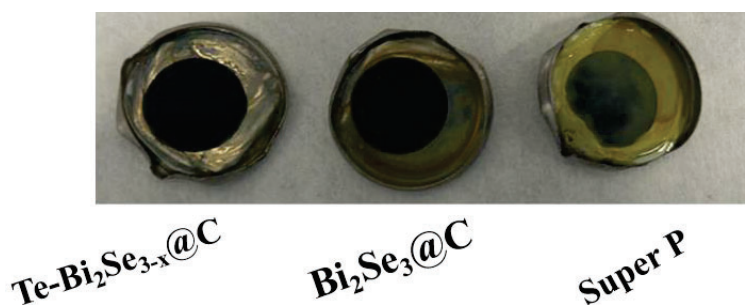


**Figure S39.** Photographs of the separator of disassembled coin batteries: Te-Bi<sub>2</sub>Se<sub>3-x</sub>@C/S, Bi<sub>2</sub>Se<sub>3</sub>@C/S and Super P/S.

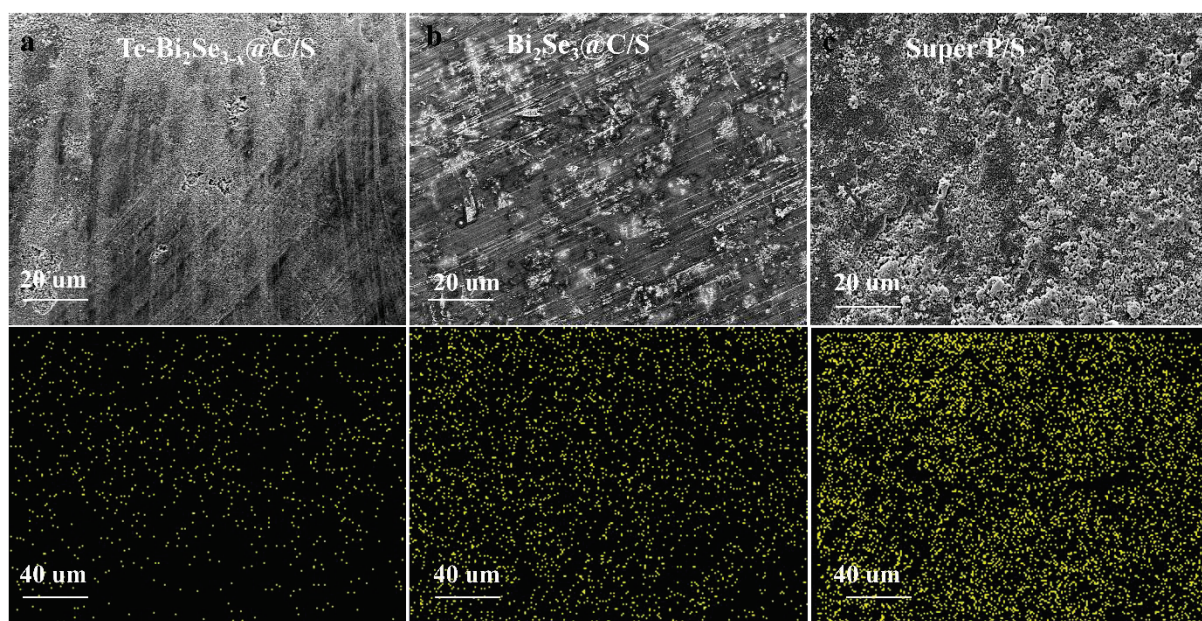


**Figure S40.** SEM and EDS mapping image of Li anode showing sulfur signal of the cycled cells based on Te-Bi<sub>2</sub>Se<sub>3-x</sub>@C/S (a), Bi<sub>2</sub>Se<sub>3</sub>@C/S (b) and Super P/S (c) cathodes.

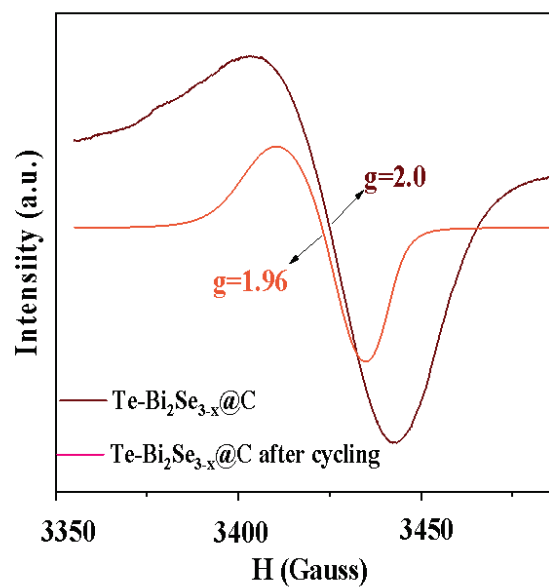


Figure S41. EPR spectrum of  $\text{Te-Bi}_2\text{Se}_{3-x}\text{@C}$  before and after cycling.

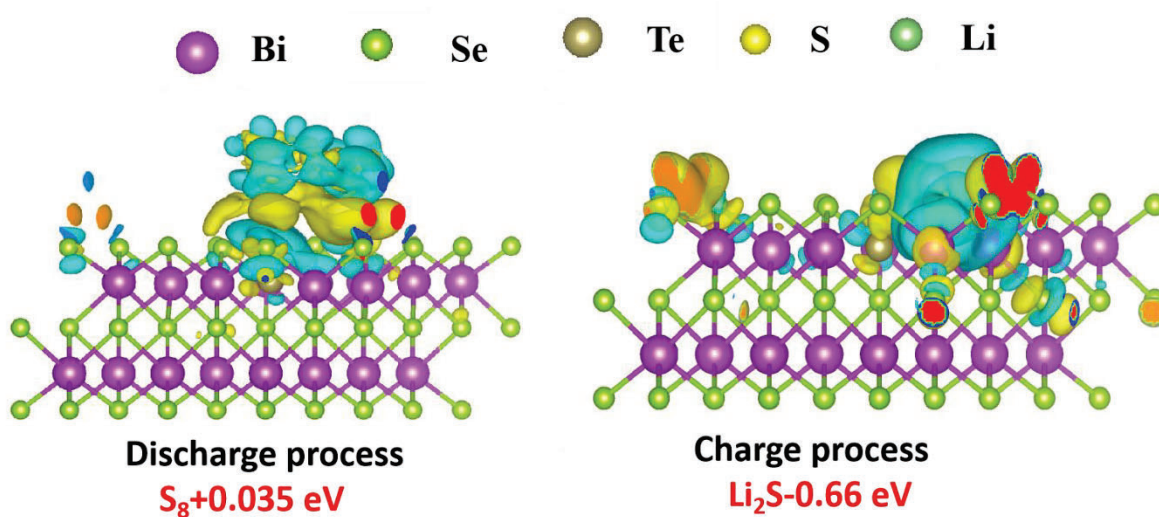
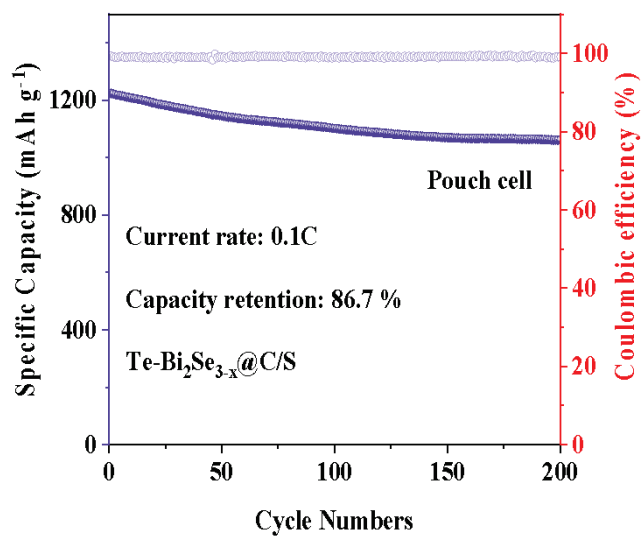
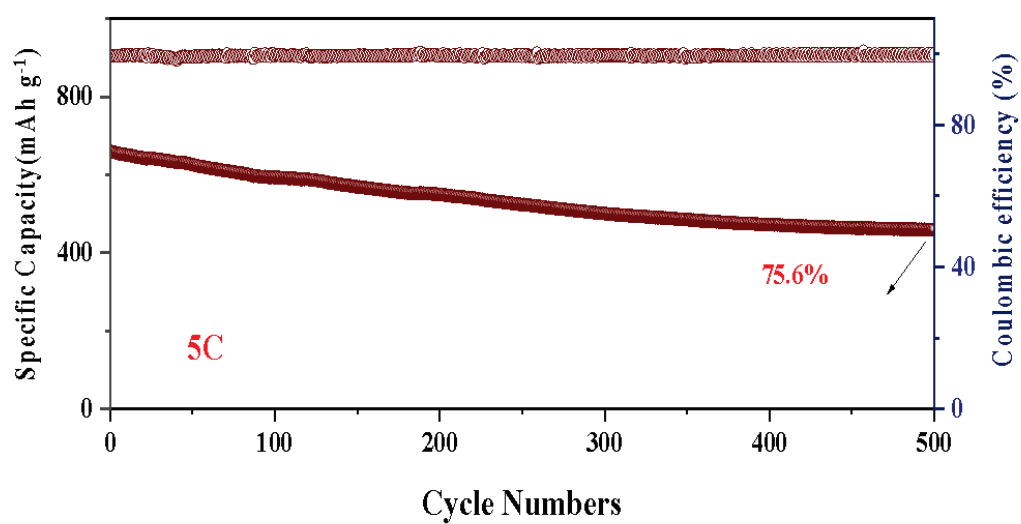


Figure S42. The view of the charge density difference for  $\text{S}_8$  and  $\text{Li}_2\text{S}$  adsorbed on a  $\text{Te-Bi}_2\text{Se}_{3-x}$  slab. Charge depletion and accumulation are presented in blue and yellow, respectively.





**Figure S43.** Cycling stability test of pouch cells based on Te-Bi<sub>2</sub>Se<sub>3-x</sub>@C/S assembled for 200 cycles at a current density of 0.1C.



**Figure S44.** Cycling stability test of pouch cells based on Te-Bi<sub>2</sub>Se<sub>3-x</sub>@C/S assembled for 500 cycles at a current density of 5C.



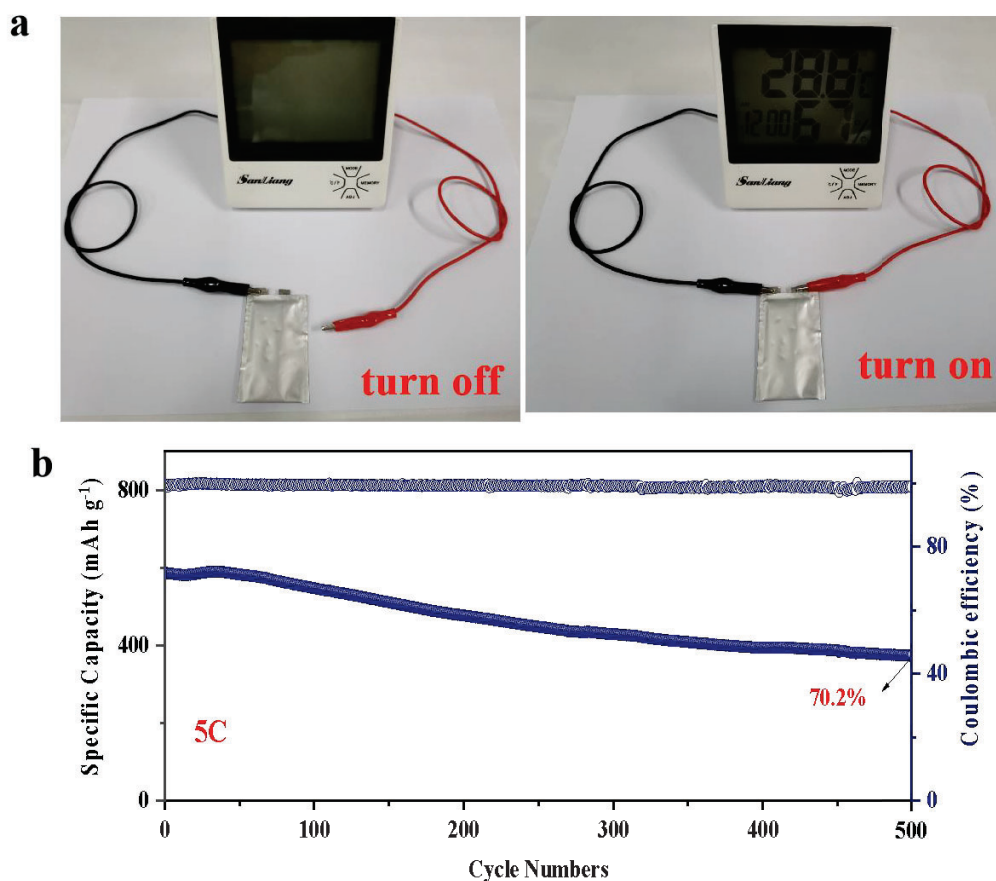


**Figure S45.** (a) Te-Bi<sub>2</sub>Se<sub>3-x</sub>@C/S based larger-specification pouch cells powering a commercial temperature and humidity monitoring clock. (b) Cycling stability test of larger-specification pouch cells based on Te-Bi<sub>2</sub>Se<sub>3-x</sub>@C/S assembled for 500 cycles at a current density of 5C.

**Table S1.** Content of various elements in host material Te-Bi<sub>2</sub>Se<sub>3-x</sub>@C by ICP-MS testing.

Content (atomic ratio)	Te	Bi	Se
	3.8 %	40.0 %	56.2 %

**Table S2.** Specific surface area of Te-Bi<sub>2</sub>Se<sub>3-x</sub>@C and Bi<sub>2</sub>Se<sub>3</sub>@C.

Sample	Specific surface area (m <sup>2</sup> g <sup>-1</sup> )
Te-Bi <sub>2</sub> Se <sub>3-x</sub> @C	94
Bi <sub>2</sub> Se <sub>3</sub> @C	86

**Table S3.** Content of various elements in host material Te-Bi<sub>2</sub>Se<sub>3-x</sub>@C by XPS testing.

Content (atomic ratio)	Te	Bi	Se
	3.6 %	36.2 %	60.2%

**Table S4.** Comparison of the specific capacitance at a current density of 0.1C of Te-Bi<sub>2</sub>Se<sub>3-x</sub>@C/S, Bi<sub>2</sub>Se<sub>3</sub>@C/S and Super P /S.

Sample	Specific capacity (mAh g <sup>-1</sup> )
Te-Bi <sub>2</sub> Se <sub>3-x</sub> @C/S	1508
Bi <sub>2</sub> Se <sub>3</sub> @C/S	1274
Super P /S	1078

**Table S5.** Electrochemical performance comparisons of Te-Bi<sub>2</sub>Se<sub>3-x</sub>@C/S with similar materials reported previously.

Sample	Specific capacitance (mAh /g)	Current Density (C)	Ref.
MoS <sub>2-x</sub> -Co <sub>9</sub> S <sub>8-y</sub> /rGO <sup>[2]</sup>	1382.5	0.1	[2]
N-MoS <sub>2</sub> <sup>[3]</sup>	1100	0.1	[3]
P-MoTe <sub>2</sub> //CC <sup>[4]</sup>	1480	0.1	[4]
Bi <sub>2</sub> S <sub>3</sub> /CN <sup>[5]</sup>	1212	0.1	[5]
Bi <sub>2</sub> S <sub>3</sub> /rGO <sup>[6]</sup>	940	0.1	[6]
WSe <sub>1.51</sub> /CNT <sup>[7]</sup>	1241.5	0.1	[7]
<b>Te-Bi<sub>2</sub>Se<sub>3-x</sub>@C</b>	<b>1508</b>	<b>0.1</b>	<b>This work</b>

## Reference

- [1] a) Y. Liu, W. Zhong, C. Yang, Q. Pan, Y. Li, G. Wang, F. Zheng, X. Xiong, M. Liu, Q. Zhang, *J. Mater. Chem. A* **2018**, 6, 24702; b) C. Huang, A. Gao, F. Yi, Y. Wang, D. Shu, Y. Liang, Z. Zhu, J. Ling, J. Hao, *Chem. Eng. J.* **2021**, 419, 129643.
- [2] H. Song, T. Li, T. He, Z. Wang, D. Fang, Y. Wang, X. L. Li, D. Zhang, J. Hu, S. Huang, *Chem. Eng. J.* **2022**, 450, 138115.
- [3] J. Cho, S. Ryu, Y. J. Gong, S. Pyo, H. Yun, H. Kim, J. Lee, J. Yoo, Y. S. Kim, *Chem. Eng. J.* **2022**, 439, 135568.
- [4] M. Guo, S. Gu, R. Zhou, Z. Zhang, S. Xu, Y. Wang, G. Zhou, *Chem. Eng. J.* **2024**, 484, 149500.
- [5] X. Zeng, Y. Tang, L. Liu, Y. Zhang, M. Qian, Y. Gao, *ACS Sustain. Chem. Eng.* **2021**, 9, 15830.
- [6] L. Zhan, X. Ning, X. Zhou, J. Luo, X. Fan, *Advanced Powder Technology* **2022**, 33, 103521.
- [7] H.-J. Li, K. Xi, W. Wang, S. Liu, G.-R. Li, X.-P. Gao, *Energy Stor. Mater.* **2022**, 45, 1229.

# **Chapter 7**

## **Generation of Unpaired Electrons to Promote Electron Transfer at the Cathode of Room-Temperature Sodium Sulfur Batteries**

## 7.Generation of Unpaired Electrons to Promote Electron Transfer at the Cathode of Room-Temperature Sodium Sulfur Batteries

### Key findings

1. A P-N heterojunction sulfur host material,  $\text{Co}_3\text{O}_4\text{-NC@C}_3\text{N}_4$ , was designed and synthesized for RT-SSBs.
2. The N atoms in  $\text{C}_3\text{N}_4$  donated electrons to Co in  $\text{Co}_3\text{O}_4$ , triggering a spin state transition in  $\text{Co}^{3+}$  from low spin to high spin, thereby increasing the number of unpaired electrons and enhancing catalytic activity.
3. The  $\text{Co}_3\text{O}_4\text{-NC@C}_3\text{N}_4/\text{S}$  cathode demonstrated excellent electrochemical performance, achieving a high reversible capacity ( $1133 \text{ mAh}\cdot\text{g}^{-1}$  at  $0.1\text{C}$ ), strong rate capability ( $575 \text{ mAh}\cdot\text{g}^{-1}$  at  $5\text{C}$ ), and outstanding cycling stability (87.3% capacity retention after 1000 cycles at  $1\text{C}$ ).
4. This study reveals how the engineered P–N heterojunction facilitates charge redistribution and spin state modulation to accelerate sulfur redox kinetics in RT-SSBs.

### Introduction

LSBs have been extensively studied due to their high theoretical energy density and cost-effective raw materials. However, issues such as polysulfide shuttle effects, volume changes, and safety concerns hinder their practical deployment. As global demand for sustainable and affordable energy storage grows, alternative systems like RT-SSBs are gaining interest due to the abundant availability and lower cost of sodium. Although RT-SSBs and LSBs operate on similar electrochemical principles, differences in ionic radius, redox potential, and reactivity necessitate distinct material designs and performance strategies. As lithium and sodium share chemical similarities, insights from LSBs can be adapted to guide RT-SSB development, particularly in cathode design.

## **Purpose and background**

The goal of this study is to extend the strategies developed for LSBs to RT-SSBs by designing a multifunctional sulfur host material that addresses the following key challenges:

Poor electron/ion conductivity in sulfur cathodes

Polysulfide dissolution and shuttle effect

Sluggish redox reaction kinetics

## **Why RT-SSBs?**

**Abundant Resources:** Sodium is more abundant and globally distributed than lithium, reducing supply chain risks and production costs.

**Safety:** Sodium exhibits lower chemical reactivity than lithium, decreasing the risk of thermal runaway and improving safety.

**Wider Temperature Tolerance:** RT-SSBs can operate stably across a broader temperature range, ideal for diverse environmental conditions.

## **Study design and methods**

**Material design**

**C<sub>3</sub>N<sub>4</sub>:** An n-type semiconductor with high thermal stability, chemical inertness, and electron-donating nitrogen sites.

**Co<sub>3</sub>O<sub>4</sub>:** A p-type semiconductor rich in Co<sup>3+</sup> sites that facilitate redox reactions.

The two were assembled via electrostatic self-assembly to form a P-N heterojunction (Co<sub>3</sub>O<sub>4</sub>-NC@C<sub>3</sub>N<sub>4</sub>), with Co<sub>3</sub>O<sub>4</sub> nanoparticles coated by a thin layer of NC for enhanced conductivity.

## **Characterization and analysis**

**Theoretical calculations:** DFT was used to investigate charge transfer and spin state changes.

**Magnetic and structural characterization:** Used to analyze Co<sup>3+</sup> spin states and validate electron transfer.

**Electrochemical testing:** RT-SSBs were assembled using the synthesized sulfur host and tested for rate capability, capacity, and cycle stability.



## Results and discussion

### Electron transfer and spin modulation

Electron flow: N atoms in  $\text{C}_3\text{N}_4$  transferred electrons to  $\text{Co}^{3+}$  in  $\text{Co}_3\text{O}_4$ , filling vacant 3d orbitals.

Spin transition: This electron transfer led to a change from low-spin to high-spin  $\text{Co}^{3+}$ , increasing the number of unpaired electrons.

Catalytic enhancement: The high-spin  $\text{Co}^{3+}$  sites offered more active centers for NaPS conversion, accelerating redox kinetics and improving performance.

### Electrochemical performance

Rate capability:  $\text{Co}_3\text{O}_4\text{-NC@C}_3\text{N}_4/\text{S}$  exhibited  $1133 \text{ mAh}\cdot\text{g}^{-1}$  at 0.1C, maintaining  $575 \text{ mAh}\cdot\text{g}^{-1}$  even at 5C.

Cycling stability: Demonstrated 87.3% capacity retention after 1000 cycles at 1C, indicating strong structural integrity and suppressed shuttle effect.

Synergistic Effects: The p–n heterojunction created a built-in electric field that facilitated directional charge transport and enhanced sulfur redox reaction dynamics.

## Conclusion

This work demonstrates a rational strategy to adapt lithium-based cathode engineering approaches to sodium-based energy systems. By constructing a p-n heterojunction sulfur host ( $\text{Co}_3\text{O}_4\text{-NC@C}_3\text{N}_4$ ), the study successfully enhances electron transfer, modulates spin states, and boosts catalytic activity for polysulfide conversion in RT-SSBs.

Key contributions include:

Introducing spin modulation via heterojunction-induced electron transfer.

Providing insights into the electronic interaction mechanisms at the host interface.

Offering a high-performance and stable sulfur cathode design for RT-SSBs.

This work lays a foundation for further exploration of heterostructure and spin engineering in sodium-based electrochemical energy storage systems.



# Generation of unpaired electrons to promote electron transfer at the cathode of room-temperature sodium sulfur batteries

Chen Huang<sup>a,b</sup>, Jing Yu<sup>a,c,\*</sup>, Yao-Jie Lei<sup>d</sup>, Oleg Usoltsev<sup>e</sup>, Li Gong<sup>a,b</sup>, Zhibiao Cui<sup>f</sup>, Junshan Li<sup>g</sup>, Canhuang Li<sup>a,b</sup>, Bingfei Nan<sup>a</sup>, Xuan Lu<sup>a</sup>, Ren He<sup>a</sup>, Xuede Qi<sup>a,h</sup>, Qian Xue<sup>a,h</sup>, Jiali Chai<sup>a</sup>, Yuchuan Ren<sup>a</sup>, Xiaoyu Bi<sup>a</sup>, Yapeng Cheng<sup>a</sup>, Jin Yuan Zhou<sup>i</sup>, Alina Skorynina<sup>e</sup>, Aram Bugaev<sup>j</sup>, Paulina R. Martínez-Alanis<sup>a</sup>, Lluís Balcells<sup>k</sup>, Jordi Arbiol<sup>c,l,\*</sup>, Chao Yue Zhang<sup>i,\*</sup>, Andreu Cabot<sup>a,l,\*</sup>

<sup>a</sup> Catalonia Institute for Energy Research-IREC, Sant Adrià de Besòs, Barcelona 08930 Spain

<sup>b</sup> Department of Chemistry, University of Barcelona 08028 Spain

<sup>c</sup> Catalan Institute of Nanoscience and Nanotechnology (ICN2), CSIC and BIST, Campus UAB, Bellaterra, 08193 Barcelona, Catalonia, Spain

<sup>d</sup> Institute for Superconducting and Electronic Materials, Australian Institute of Innovative Materials, Innovation Campus, University of Wollongong, Wollongong, NSW 2500, Australia

<sup>e</sup> ALBA Synchrotron, Carrer de la Llum, 2, 26, 08290 Cerdanyola del Vallès, Barcelona, Catalonia, Spain

<sup>f</sup> School of Chemistry, South China Normal University, Guangzhou 510006, China

<sup>g</sup> Institute for Advanced Study, Chengdu University 610106 Chengdu, China

<sup>h</sup> College of Chemistry and Chemical Engineering, Chongqing University of Technology, Chongqing 400054 China

<sup>i</sup> School of Physical Science & Technology, Lanzhou University, Lanzhou 730000, China

<sup>j</sup> Center for Photon Science, Paul Scherrer Institut, Forschungsstrasse 111, Villigen 5232, Switzerland

<sup>k</sup> Institut de Ciència de Materials de Barcelona, Campus de la UAB, 08193 Bellaterra, Catalonia, Spain

<sup>l</sup> ICREA Pg. Lluís Companys, 08010 Barcelona, Catalonia, Spain

## ARTICLE INFO

### Keywords:

Room temperature sodium-sulfur battery

Co<sub>3</sub>O<sub>4</sub>

C<sub>3</sub>N<sub>4</sub>

Spin catalysis

Sodium polysulfide

## ABSTRACT

Room-temperature sodium-sulfur batteries offer significant potential for energy storage, but they are hindered by slow Na-S reaction kinetics. While trial and error screening shows cobalt-based sulfur hosts to effectively activate this reaction, this study aims to enable a more rational catalyst design by exploring how cobalt's electronic configuration within the cathode composite affects its activity and how this configuration can be adjusted through charge injection from neighboring atoms. Cobalt oxide nanoparticles coated with carbon nitride serve as a model system for this purpose, where N atoms in C<sub>3</sub>N<sub>4</sub> donate electrons to Co, generating additional unpaired Co 3d electrons, that are then transferred to sodium polysulfides with a reduced kinetic barrier. Experimental and theoretical analyses reveal that this activated electronic state boosts charge transfer, while the adjusted d-band center improves adsorption energy, lowering the reaction energy barrier for the polysulfide conversion rate-determining step.

## 1. Introduction

Room temperature sodium-sulfur batteries (SSBs) are a promising cost-effective, high-density energy storage solution. However, they face challenges with cathode materials, including volume expansion, poor conductivity, sodium polysulfide (SPS) dissolution, and sluggish sulfur reduction reaction (SRR) kinetics [1–7]. To address these issues, sulfur hosts must improve conductivity, withstand volume changes, and

enhance polysulfide trapping and conversion [8–17]. This can be achieved using composite materials that combine metal-based single atoms or particles supported on porous carbon structures [4,18–22]. Within these composites, the support/catalyst interphase tunes the electronic structure, modulating the charge transfer processes, aligning electronic bands, and potentially enhancing surface reactivity. At this interphase, a plethora of singularities such as stress/strain, charge accumulation/depletion, structural and atomic defects, and electric fields arise, which

\* Corresponding authors.

E-mail addresses: [Jing.yu@icn2.cat](mailto:Jing.yu@icn2.cat) (J. Yu), [arbiol@icrea.cat](mailto:arbiol@icrea.cat) (J. Arbiol), [zhangchy2020@lzu.edu.cn](mailto:zhangchy2020@lzu.edu.cn) (C.Y. Zhang), [acabot@irec.cat](mailto:acabot@irec.cat) (A. Cabot).

<https://doi.org/10.1016/j.cej.2025.160146>

Received 18 October 2024; Received in revised form 25 December 2024; Accepted 31 January 2025

Available online 1 February 2025

1385-8947/© 2025 Elsevier B.V. All rights are reserved, including those for text and data mining, AI training, and similar technologies.

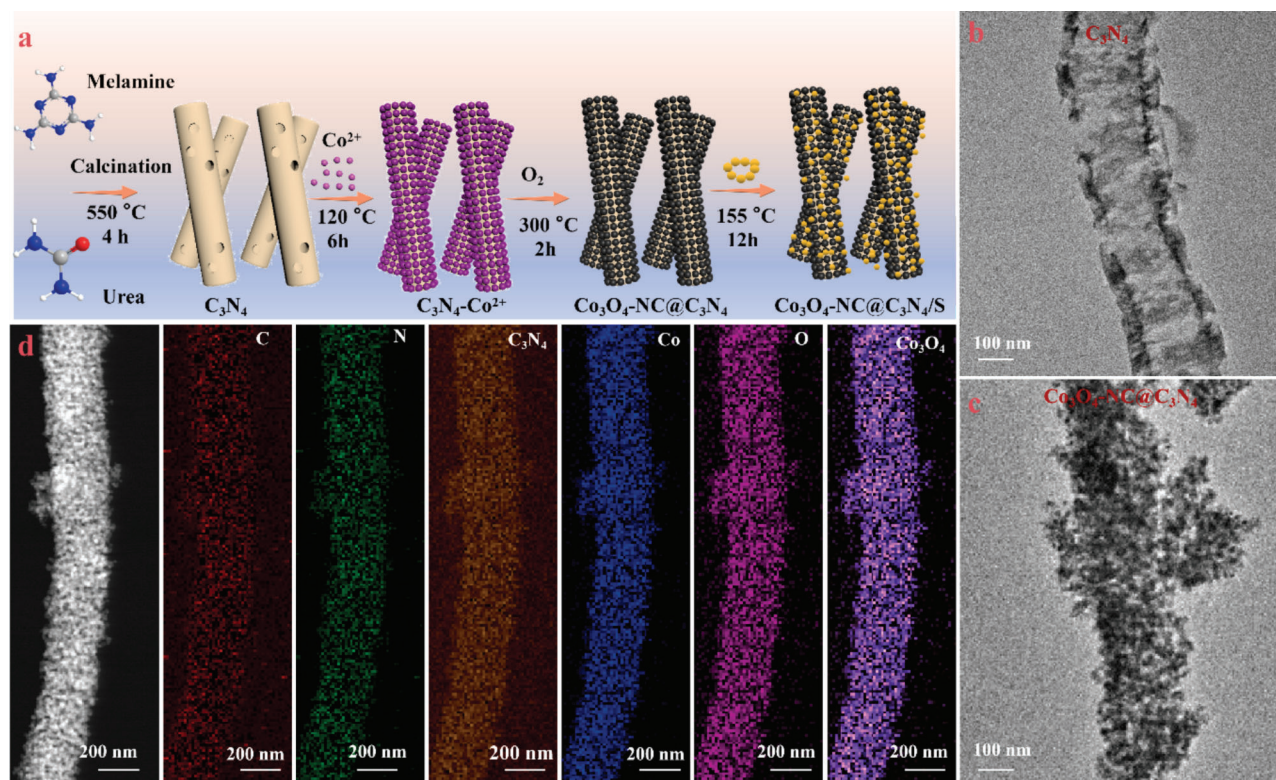


**Fig. 1.** (a) Scheme of the synthesis process used to produce Co<sub>3</sub>O<sub>4</sub>-NC@C<sub>3</sub>N<sub>4</sub>/S. (b,c) TEM images of C<sub>3</sub>N<sub>4</sub> and Co<sub>3</sub>O<sub>4</sub>-NC@C<sub>3</sub>N<sub>4</sub>. (d) EELS elemental composition maps obtained from the HAADF STEM micrograph of Co<sub>3</sub>O<sub>4</sub>-NC@C<sub>3</sub>N<sub>4</sub>.

are critical in facilitating the diffusion of ions and electrons, thereby influencing transformation reactions. While most research on heterojunctions focuses on analyzing electronic structures, electron flow directions, and the generated built-in electric fields [22–26], the electronic state occupation and spin state are crucial yet often neglected factors in determining the relationship between electronic energy levels and catalytic performance. The density of unpaired electrons can be manipulated through various methods, including the application of external magnetic fields, the use of specific ligands, and the application of stress [27–30]. Introducing additional unpaired electrons through the design of heterostructures offers an effective, attractive, and innovative approach. The interface of these heterostructures is characterized by a redistribution of charges, which impacts electronic structure and orbital occupancy [27,28,31–35].

In this work, we investigate the impact of heterostructures and the role of unpaired electrons on SRR catalytic activity using Co<sub>3</sub>O<sub>4</sub>@C<sub>3</sub>N<sub>4</sub> composites as a model system. Our findings reveal that heterostructures induce splitting of the metal central orbitals, generating additional unpaired electrons within the 3d orbitals. This transition from a low-spin to a high-spin active electronic state enhances charge transfer, thereby significantly promoting catalytic activity.

## 2. Results and discussion

### 2.1. Cathode material synthesis and physicochemical properties

Co<sub>3</sub>O<sub>4</sub> particles combined with N-doped carbon (NC), supported on C<sub>3</sub>N<sub>4</sub> nanotubes (Co<sub>3</sub>O<sub>4</sub>-NC@C<sub>3</sub>N<sub>4</sub>) and loaded with sulfur (Co<sub>3</sub>O<sub>4</sub>-NC@C<sub>3</sub>N<sub>4</sub>/S) were produced in three steps (Fig. 1a, see details in the Experimental section). Initially, urea-derived tubular C<sub>3</sub>N<sub>4</sub> (Fig. 1b, S1, and S2a,b) is dispersed into a cobalt (II) nitrate methanol solution containing PVP through ultrasonication and hydrothermal treatment. In this process, Co<sup>2+</sup> ions are immobilized on the negatively charged g-C<sub>3</sub>N<sub>4</sub> surface [25,36]. The obtained powder is annealed at 300 °C under

air to produce Co<sub>3</sub>O<sub>4</sub> nanoparticles supported on the tubular C<sub>3</sub>N<sub>4</sub>, as observed by transmission electron microscopy (TEM) and Electron Energy Loss Spectroscopy (EELS) (Fig. 1c, d) [37]. The low-temperature annealing does not affect the C<sub>3</sub>N<sub>4</sub> framework but decomposes the PVP to generate N-doped carbon (NC) intertwined with the Co<sub>3</sub>O<sub>4</sub> nanoparticles (Fig. S2c) [38–40].

The N content derived from PVP is approximately 0.8 % by mass (Table S1). It is incorporated into the carbon structure improving the overall electronic properties of the electrode material.

Energy dispersive X-ray (EDX) spectra show the Co<sub>3</sub>O<sub>4</sub>-NC@C<sub>3</sub>N<sub>4</sub> atomic elemental ratio to be Co/O/N/C = 16/21/36/27 (Fig. S3). In the last step, the resulting host material is infiltrated by melted sulfur powder, yielding the Co<sub>3</sub>O<sub>4</sub>-NC@C<sub>3</sub>N<sub>4</sub>/S cathode material. Reference Co<sub>3</sub>O<sub>4</sub>-NC/S and C<sub>3</sub>N<sub>4</sub>/S cathode materials were prepared in the same way but without adding C<sub>3</sub>N<sub>4</sub> in the former and Co<sup>2+</sup> ions and PVP in the latter (Experimental section in Supporting information). Thermogravimetric analysis (TGA) showed the sulfur content in Co<sub>3</sub>O<sub>4</sub>-NC@C<sub>3</sub>N<sub>4</sub>/S, Co<sub>3</sub>O<sub>4</sub>-NC/S, and C<sub>3</sub>N<sub>4</sub>/S to be 58.6 %, 56.4 %, and 54.6 %, respectively (Fig. S4).

X-ray diffraction (XRD) analysis (Fig. 2a) confirms Co<sub>3</sub>O<sub>4</sub>-NC and Co<sub>3</sub>O<sub>4</sub>-NC@C<sub>3</sub>N<sub>4</sub> to contain the Co<sub>3</sub>O<sub>4</sub> crystal structure (PDF#76–1802) [41]. Compared to Co<sub>3</sub>O<sub>4</sub>-NC, Co<sub>3</sub>O<sub>4</sub>-NC@C<sub>3</sub>N<sub>4</sub> displays an additional distinct peak at 27.4°, which is attributed to the (002) crystal plane of C<sub>3</sub>N<sub>4</sub> [42]. The Brunauer-Emmett-Teller (BET) specific surface areas calculated from the N<sub>2</sub> adsorption/desorption hysteresis curves of Co<sub>3</sub>O<sub>4</sub>-NC and Co<sub>3</sub>O<sub>4</sub>-NC@C<sub>3</sub>N<sub>4</sub> are 52.6 m<sup>2</sup> g<sup>−1</sup> and 64.9 m<sup>2</sup> g<sup>−1</sup>, respectively (Fig. 2b, S5 and Table S2). As expected, the Co<sub>3</sub>O<sub>4</sub>-NC@C<sub>3</sub>N<sub>4</sub> exhibits a larger specific surface and also a larger pore volume than Co<sub>3</sub>O<sub>4</sub>-NC, associated with the presence of the C<sub>3</sub>N<sub>4</sub> support. X-ray photoelectron spectroscopy (XPS) analysis (Fig. S6 and S7) shows the presence of Co<sup>3+</sup> and Co<sup>2+</sup> chemical environments [43]. The Co 2p XPS spectrum of Co<sub>3</sub>O<sub>4</sub> supported on C<sub>3</sub>N<sub>4</sub> is redshifted compared to that of unsupported Co<sub>3</sub>O<sub>4</sub>, which is attributed to the injection of electrons from the C<sub>3</sub>N<sub>4</sub> to the Co<sub>3</sub>O<sub>4</sub>. Besides, in the Co<sub>3</sub>O<sub>4</sub>-NC@C<sub>3</sub>N<sub>4</sub> composite,



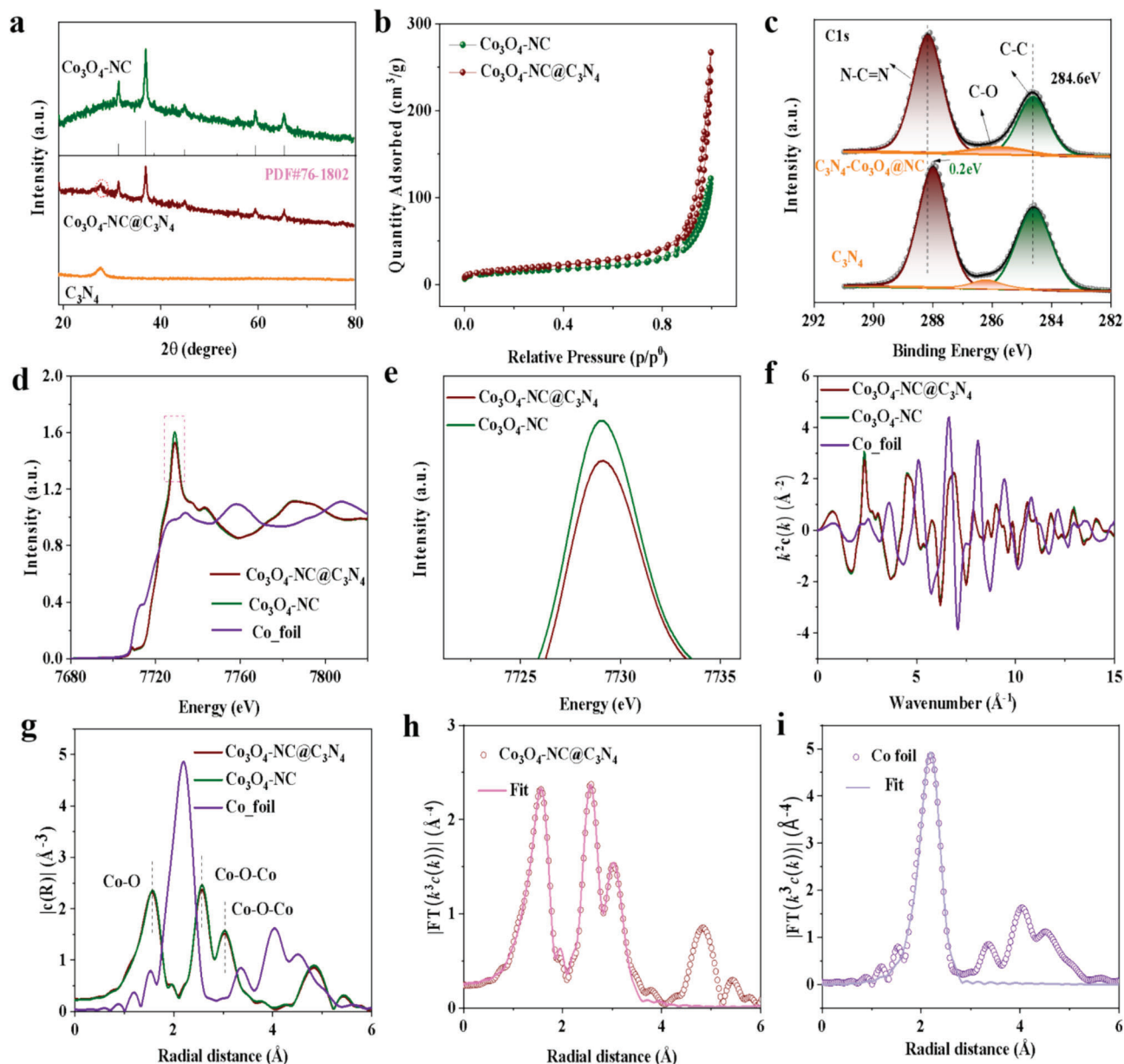


**Fig. 2.** (a) XRD patterns of different electrode materials (Co<sub>3</sub>O<sub>4</sub>-NC@C<sub>3</sub>N<sub>4</sub>, Co<sub>3</sub>O<sub>4</sub>-NC, and C<sub>3</sub>N<sub>4</sub>). (b) Specific surface area curves of different host materials (Co<sub>3</sub>O<sub>4</sub>-NC@C<sub>3</sub>N<sub>4</sub>, Co<sub>3</sub>O<sub>4</sub>-NC). (c) High-resolution N 1s XPS spectra of Co<sub>3</sub>O<sub>4</sub>-NC@C<sub>3</sub>N<sub>4</sub> and C<sub>3</sub>N<sub>4</sub>. (d) Co K-edge XANES of Co<sub>3</sub>O<sub>4</sub>-NC@C<sub>3</sub>N<sub>4</sub>, Co<sub>3</sub>O<sub>4</sub>-NC, and Co foil. (e) Magnified area of the pink curve of Co<sub>3</sub>O<sub>4</sub>-NC@C<sub>3</sub>N<sub>4</sub>, Co<sub>3</sub>O<sub>4</sub>-NC, and Co foil for Co K-edge XANES. (f) k<sup>2</sup> weighted Co K-edge EXAFS spectra of C<sub>3</sub>N<sub>4</sub>-Co<sub>3</sub>O<sub>4</sub>@NC, Co<sub>3</sub>O<sub>4</sub>@NC, and Co foil. (g) FT-EXAFS spectra of Co<sub>3</sub>O<sub>4</sub>-NC@C<sub>3</sub>N<sub>4</sub>, Co<sub>3</sub>O<sub>4</sub>-NC, and Co foil. (h-i) FT-EXAFS fitting curves of Co K-edge for Co<sub>3</sub>O<sub>4</sub>-NC@C<sub>3</sub>N<sub>4</sub> and Co foil. (For interpretation of the references to colour in this figure legend, the reader is referred to the web version of this article.)

the N=C=N binding energy undergoes a significant blueshift with respect to C<sub>3</sub>N<sub>4</sub> (Fig. 2c), which is associated with the electron loss of C<sub>3</sub>N<sub>4</sub> upon contact with Co<sub>3</sub>O<sub>4</sub> [42].

The Co K-edge X-ray absorption near-edge structure (XANES) spectrum of Co<sub>3</sub>O<sub>4</sub>-NC@C<sub>3</sub>N<sub>4</sub> exhibits a slight redshift compared with Co<sub>3</sub>O<sub>4</sub>-NC, denoting a higher electronic concentration, consistent with XPS results (Fig. 2d). A weakening in the white line peak intensity, at around 7730 eV (Fig. 2e), points at the intensity of the white line is related to the spin state and coordination environment [44,45]. Specifically, a higher spin state of the metal ions within Co<sub>3</sub>O<sub>4</sub>-NC@C<sub>3</sub>N<sub>4</sub> than within Co<sub>3</sub>O<sub>4</sub>-NC [46]. The Fourier-transformed extended X-ray absorption fine structure (FT-EXAFS) of Co<sub>3</sub>O<sub>4</sub>-NC@C<sub>3</sub>N<sub>4</sub> shows peaks at 1.91 Å, 2.86 Å, and 3.03 Å (phase uncorrected) attributed to the Co-O, and two different Co-O-Co bonds, respectively (Fig. 2f-g). A slight decrease in the intensity of the Co-O peak at 1.91 Å for Co<sub>3</sub>O<sub>4</sub>-NC@C<sub>3</sub>N<sub>4</sub>

compared with Co<sub>3</sub>O<sub>4</sub>-NC (Fig. S8a) indicates a smaller coordination number (CN) that is likely associated with the change of spin state in the Co<sub>3</sub>O<sub>4</sub>-NC@C<sub>3</sub>N<sub>4</sub>. The standard 3 shells Fourier analysis of EXAFS spectra for Co<sub>3</sub>O<sub>4</sub>-NC@C<sub>3</sub>N<sub>4</sub> indicates a coordination number of around 4.9 and interatomic distance Co-O R = 1.9165 Å (Fig. 2h-i and S8b), slightly higher than that of CN = 4.7 of Co<sub>3</sub>O<sub>4</sub>-NC (with interatomic distance R = 1.9151 Å), which is again associated with the increase oxidation state of Co and the formation of Co-N bonds at the interphase of C<sub>3</sub>N<sub>4</sub> and Co<sub>3</sub>O<sub>4</sub>, thus increasing the Co coordination number (Table S3, S4).

## 2.2. Electrochemical performance of Co<sub>3</sub>O<sub>4</sub>-NC@C<sub>3</sub>N<sub>4</sub>/S

Coin-type Na-S cells were assembled using the prepared electrodes (Co<sub>3</sub>O<sub>4</sub>-NC@C<sub>3</sub>N<sub>4</sub>/S, Co<sub>3</sub>O<sub>4</sub>-NC/S, and C<sub>3</sub>N<sub>4</sub>/S) as the cathode, Na foil

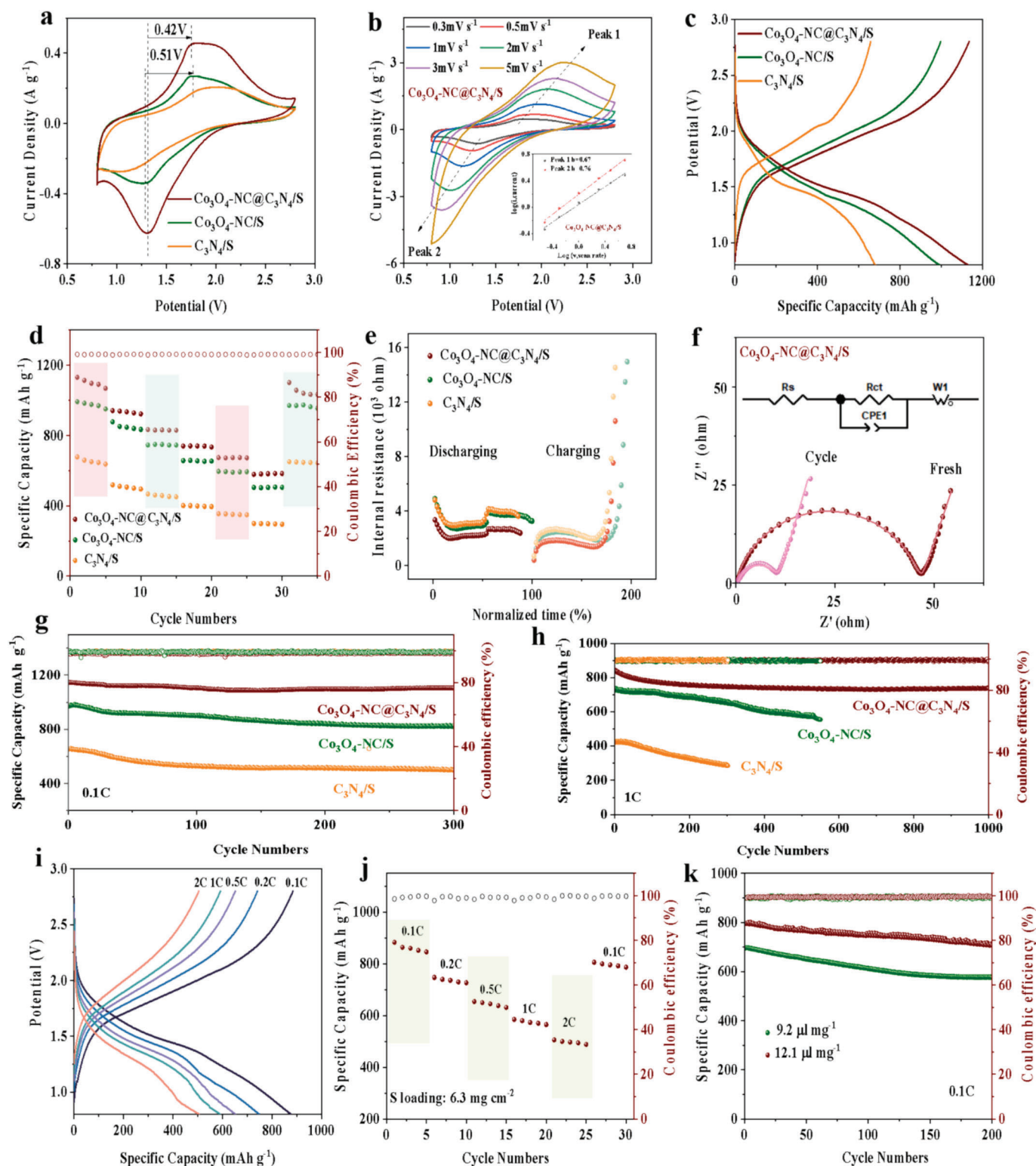


**Fig. 3.** (a) CV curves of different cathodes at  $0.3 \text{ mV s}^{-1}$  scan rate and  $0.8 \text{ V}$ – $2.8 \text{ V}$  voltage window. (b) The CV curve of  $\text{Co}_3\text{O}_4\text{-NC}/\text{C}_3\text{N}_4/\text{S}$  at  $0.3$ – $5 \text{ mV s}^{-1}$  scan rate (logarithmic curve of scan rate versus current density, inset b). (c) GCD curves of different cathodes at a current rate of  $0.1\text{C}$ . (d) Rate performance of different cathodes ( $\text{Co}_3\text{O}_4\text{-NC}/\text{C}_3\text{N}_4/\text{S}$ ,  $\text{Co}_3\text{O}_4\text{-NC}/\text{S}$ , and  $\text{C}_3\text{N}_4/\text{S}$ ). (e) Internal resistances and normalized discharge–charge time. (f) EIS curve of  $\text{Co}_3\text{O}_4\text{-NC}/\text{C}_3\text{N}_4/\text{S}$ . (g) Cycle stability curves of different cathodes cycled for 300 cycles at  $0.1\text{C}$  current rate. (h) Cycle stability curves of  $\text{Co}_3\text{O}_4\text{-NC}/\text{C}_3\text{N}_4/\text{S}$ ,  $\text{Co}_3\text{O}_4\text{-NC}/\text{S}$ , and  $\text{C}_3\text{N}_4/\text{S}$  at  $1\text{C}$  current rate after 1000 cycles. (i) GCD curves of  $\text{Co}_3\text{O}_4\text{-NC}/\text{C}_3\text{N}_4/\text{S}$  at high loading ( $6.3 \text{ mg cm}^{-2}$ ), (j) Rate performance and Coulombic efficiency, (k) Cycling stability curves under different electrolyte contents.

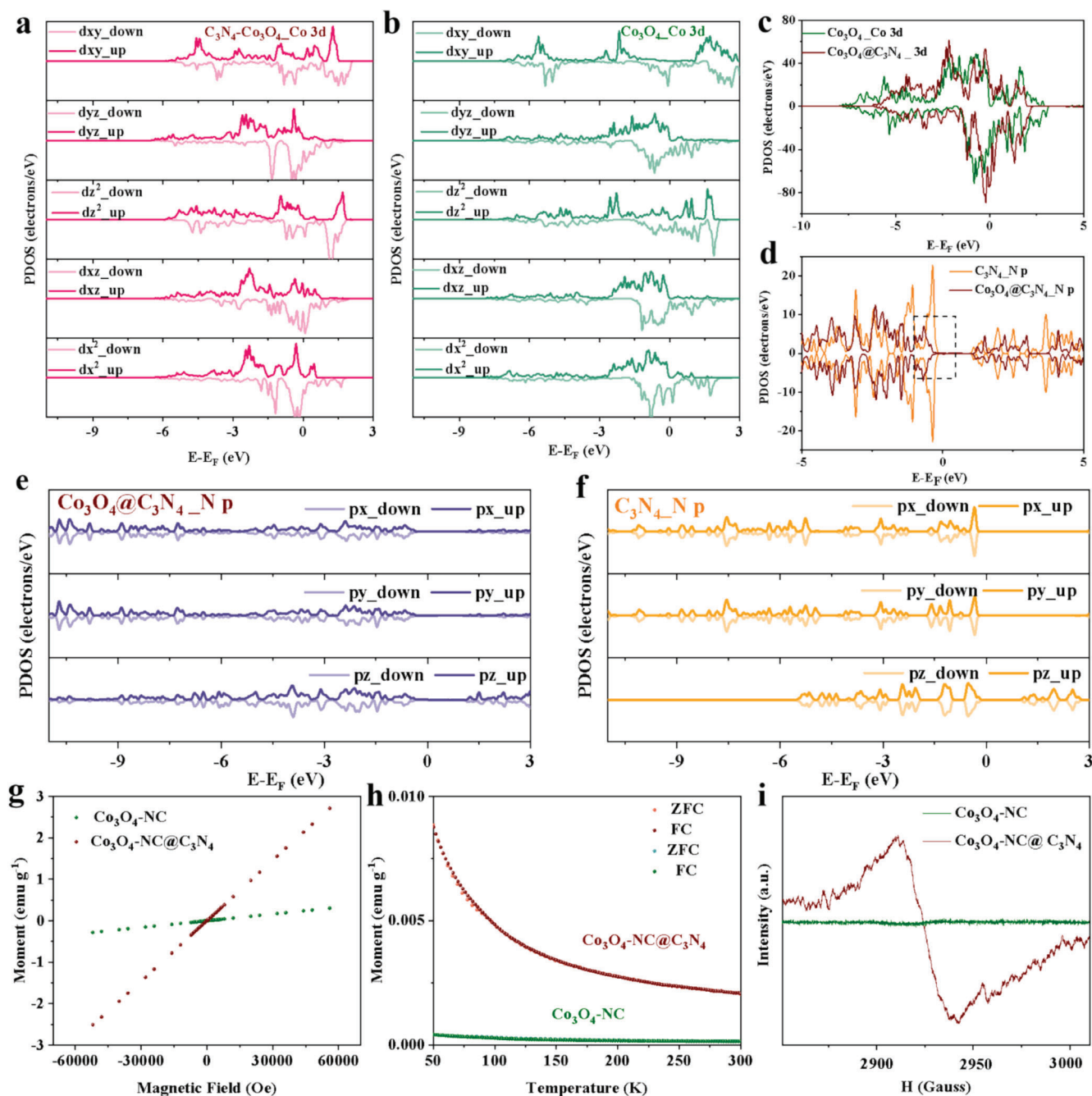


Fig. 4. (a-c) PDOS and TDOS curves of Co<sub>3</sub>O<sub>4</sub>@C<sub>3</sub>N<sub>4</sub> and Co<sub>3</sub>O<sub>4</sub> for Co 3d. (d-f) PDOS and TDOS curves of Co<sub>3</sub>O<sub>4</sub>@C<sub>3</sub>N<sub>4</sub> and C<sub>3</sub>N<sub>4</sub> for N p. (g-h) ZFC/FC curves of Co<sub>3</sub>O<sub>4</sub>-NC@C<sub>3</sub>N<sub>4</sub> and Co<sub>3</sub>O<sub>4</sub>-NC. (i) EPR spectra for Co<sub>3</sub>O<sub>4</sub>-NC@C<sub>3</sub>N<sub>4</sub> and Co<sub>3</sub>O<sub>4</sub>-NC.

as the anode, 1 M NaClO<sub>4</sub> in a mixture of dimethyl carbonate (DEC) and ethylene carbonate (EC) in a 1:1 ratio, with 5 wt% fluoroethylene carbonate (FEC) added as the electrolyte. Fig. 3a displays the Cyclic voltammetry (CV) curves of Co<sub>3</sub>O<sub>4</sub>-NC@C<sub>3</sub>N<sub>4</sub>/S, Co<sub>3</sub>O<sub>4</sub>-NC/S, and C<sub>3</sub>N<sub>4</sub>/S at 0.3 mV·s<sup>-1</sup> scan rate within the 0.8–2.8 V voltage window. The reduction peak centered at 1.32 V accounts for the conversion from S<sub>8</sub> to Na<sub>2</sub>S<sub>x</sub> (4 < x ≤ 8) and further to Na<sub>2</sub>S<sub>2</sub> and Na<sub>2</sub>S, respectively. The oxidation peak at 1.81 V corresponds to the reversible process from Na<sub>2</sub>S<sub>2</sub> and Na<sub>2</sub>S to S<sub>8</sub> [47].

Compared to Co<sub>3</sub>O<sub>4</sub>-NC/S and C<sub>3</sub>N<sub>4</sub>/S, Co<sub>3</sub>O<sub>4</sub>-NC@C<sub>3</sub>N<sub>4</sub>/S demonstrates the lowest anodic peak voltage and the smallest difference in cathodic peak potential, indicating minimal electrochemical polarization. At higher scan rates, up to 5 mV·s<sup>-1</sup>, (Fig. 3b and S9), CV profiles display a minimal shift in the peak position, suggesting minimal

polarization in the electrode. A linear dependence was obtained between the logarithm of the current and the scan rate ((i = av<sup>b</sup>, inset in Fig. 3b and S10) with b values for peak 1 and peak 2 in the Co<sub>3</sub>O<sub>4</sub>-NC@C<sub>3</sub>N<sub>4</sub>/S cathode of 0.67 and 0.75, respectively, which suggest the presence of both ion diffusion and adsorption phenomena during the electrochemical process [47].

Galvanostatic charge–discharge (GCD) curves (Fig. 3c and S11, S12 and Table S5) show the Co<sub>3</sub>O<sub>4</sub>-NC@C<sub>3</sub>N<sub>4</sub>/S to have the highest capacity and rate performance (Fig. 3d and S13 among the tested cathodes). As a reference, the specific capacities of the pure host material (Co<sub>3</sub>O<sub>4</sub>-NC@C<sub>3</sub>N<sub>4</sub>) at 0.1C, 0.5C, 1C, 2C, 3C, and 5C were 51.6, 27.7, 12.4, 2.8, 0.15 and 0.06 mAh g<sup>-1</sup>, respectively (Fig. S14). These capacities are clearly below those obtained after sulfur loading, indicating that the conversion of polysulfides plays a primary role in the entire



electrochemical reaction process.

As an additional reference, Fe-based catalysts were also prepared and evaluated. The XRD patterns of  $\text{Fe}_3\text{O}_4\text{-NC@C}_3\text{N}_4$  and  $\text{Fe}_3\text{O}_4\text{-NC}$  (Fig. S15) indicate the successful synthesis of these materials with the  $\text{Fe}_3\text{O}_4$  crystal structure (PDF#75-0033) [48]. Compared to  $\text{Fe}_3\text{O}_4\text{-NC}$ ,  $\text{Fe}_3\text{O}_4\text{-NC@C}_3\text{N}_4$  displays an additional distinct peak at  $27.4^\circ$ , which is attributed to the (002) crystal plane of  $\text{C}_3\text{N}_4$  [42]. By mixing the host material with sulfur using the melt infiltration process,  $\text{Fe}_3\text{O}_4\text{-NC@C}_3\text{N}_4/\text{S}$  and  $\text{Fe}_3\text{O}_4\text{-NC/S}$  were produced, and their electrochemical performance was evaluated (Fig. S16). For  $\text{Fe}_3\text{O}_4\text{-NC@C}_3\text{N}_4/\text{S}$ , the specific capacities at current densities of 0.1, 0.5, 1, 2, 3, and 5C were 1044, 881, 781, 701, 647, and 516  $\text{mAh g}^{-1}$ , respectively. Under the same conditions,  $\text{Fe}_3\text{O}_4\text{-NC/S}$  delivered specific capacities of 975, 818, 729, 644, 576, and 466  $\text{mAh g}^{-1}$ , respectively. These are significant capacities and rate performances, but slightly below those obtained with the Co-based catalyst. This data also shows that the presence of  $\text{C}_3\text{N}_4$  promotes capacity also in this system. To further investigate the mechanism by which  $\text{C}_3\text{N}_4$  improves electrochemical performance, we performed electron paramagnetic resonance (EPR) tests on  $\text{Fe}_3\text{O}_4\text{-NC@C}_3\text{N}_4$  and  $\text{Fe}_3\text{O}_4\text{-NC}$  (Fig. S17). The EPR spectra of  $\text{Fe}_3\text{O}_4\text{-NC@C}_3\text{N}_4$  exhibited a higher g-value response compared to  $\text{Fe}_3\text{O}_4\text{-NC}$ , indicating the presence of more unpaired electrons in  $\text{Fe}_3\text{O}_4\text{-NC@C}_3\text{N}_4$ . This suggests that the formation of a heterostructure via the introduction of  $\text{C}_3\text{N}_4$  facilitates electron transfer between  $\text{C}_3\text{N}_4$  and  $\text{Fe}_3\text{O}_4$  as well.

Galvanostatic intermittent titration technique (GITT) tests were carried out at a current density of 0.1C. The voltage recorded after the resting period was defined as the open-circuit voltage ( $V_{\text{OC}}$ ), while the voltage measured during the current pulse was defined as the short-circuit voltage ( $V_{\text{SC}}$ ). As shown in Fig. 3e and S18, throughout the entire charge–discharge process, the dynamic internal resistance ( $\Delta iR = |V_{\text{OC}} - V_{\text{SC}}|/I$ ) of the  $\text{Co}_3\text{O}_4\text{-NC@C}_3\text{N}_4/\text{S}$  cell remains consistently lower than that of the  $\text{Co}_3\text{O}_4\text{-NC/S}$  and  $\text{C}_3\text{N}_4/\text{S}$  cells (Fig. 3e).

Electrochemical impedance spectroscopy (EIS) spectra of all electrodes display a semicircle in the high-frequency region and a straight line in the low-frequency region, associated with the charge transfer resistance ( $R_{\text{ct}}$ ) and  $\text{Na}^+$  diffusion resistance, respectively (Fig. 3f and S19) [37,49]. When compared to  $\text{Co}_3\text{O}_4\text{-NC/S}$  and  $\text{C}_3\text{N}_4/\text{S}$ , the fresh  $\text{Co}_3\text{O}_4\text{-NC@C}_3\text{N}_4/\text{S}$  battery exhibits the lowest  $R_{\text{ct}}$  in the high-frequency region. After the charge–discharge cycle, the charge-transfer resistance value notably decreases compared to the fresh electrodes for all cells, which is linked to the chemical activation process involving the dissolution and redistribution of active species [42]. During the initial charge–discharge cycles, the repeated insertion and extraction of  $\text{Na}^+$  enhance the active surface area of the electrode material. This process improves the electrode's interaction with the electrolyte, leading to lower resistance for charge transfer. Furthermore, the discharge products of the reaction of sulfur and sodium,  $\text{Na}_2\text{S}_x$  ( $x = 2-8$ ), become progressively more uniformly distributed during cycling. This process facilitates the formation of a more stable conductive network, thereby minimizing the resistance to electron and ion transport. Meanwhile, the redistribution and chemical immobilization of active materials like  $\text{Na}_2\text{S}_x$  ( $x = 2-8$ ) create a more uniform and conductive electrode surface. This also mitigates the polysulfide shuttle effect and enhances reaction kinetics over time [50–52].

After 300 cycles at 0.1C current rate, the capacity retention rates for  $\text{Co}_3\text{O}_4\text{-NC@C}_3\text{N}_4/\text{S}$ ,  $\text{Co}_3\text{O}_4\text{-NC/S}$ , and  $\text{C}_3\text{N}_4/\text{S}$  were 96.4 %, 84.6 %, and 76.8 %, respectively (Fig. 3g and S20). At 1C,  $\text{Co}_3\text{O}_4\text{-NC@C}_3\text{N}_4/\text{S}$  retained a high reversible specific capacity of 737.2  $\text{mAh g}^{-1}$  after 1000 cycles, with capacity retention exceeding 87.3 % (Fig. 3h). In contrast,  $\text{Co}_3\text{O}_4\text{-NC/S}$  and  $\text{C}_3\text{N}_4/\text{S}$  experienced a significant capacity drop after 600 and 300 cycles, respectively, at the same current rate (1C). As shown in Fig. S21 and Table S6,  $\text{Co}_3\text{O}_4\text{-NC@C}_3\text{N}_4/\text{S}$  exhibits outstanding performance not only compared with  $\text{Co}_3\text{O}_4\text{-NC/S}$  and  $\text{C}_3\text{N}_4/\text{S}$ , but also with previously Co-based reported cathodes [53–59]. To emphasize the advantages of the host material synthesized in this study in terms of cycling performance, we compared its cycling stability

with that of previously reported Co-based sulfur host materials (Table S7). Our results demonstrate that the capacity loss per cycle for the material developed in this work is significantly lower than that of sulfur-based cathode materials reported in earlier studies [3,53,57,60–63].

Increasing the sulfur loading to 6.3  $\text{mg cm}^{-2}$  specific capacities of 5.52, 4.71, 4.05, 3.70, and 3.13  $\text{mAh cm}^{-2}$  at 0.1C, 0.2C, 0.5C, 1C and 2C were obtained for the  $\text{Co}_3\text{O}_4\text{-NC@C}_3\text{N}_4/\text{S}$  cell (Fig. 3i–j). At this high sulfur loading and with a low content of electrolyte of 12.1  $\mu\text{L mg}^{-1}$ , the electrode can still maintain a 706  $\text{mAh g}^{-1}$  after 200 cycles at 0.1C, which represents a capacity decay per cycle of 0.056 %. When further reducing the electrolyte content to 9.2  $\mu\text{L mg}^{-1}$ , a capacity of 576.6  $\text{mAh g}^{-1}$  with a decay rate per cycle of 0.086 % was achieved after 200 cycles at 0.1C (Fig. 3k). Besides, pouch batteries based on  $\text{Co}_3\text{O}_4\text{-NC@C}_3\text{N}_4/\text{S}$  cathodes showed a capacity of 682.2  $\text{mAh g}^{-1}$  and retention of 88.7 % after 200 cycles at 0.1C (Fig. S22).

### 2.3. Electrochemical enhancement mechanism within $\text{Co}_3\text{O}_4\text{-NC@C}_3\text{N}_4$

The projected density of states (PDOS) for the Co 3d and N p orbitals in  $\text{C}_3\text{N}_4$ ,  $\text{Co}_3\text{O}_4$ , and  $\text{Co}_3\text{O}_4\text{-NC@C}_3\text{N}_4$  were evaluated using DFT calculations (Fig. 4a–f). The Co 3d PDOS intensity in  $\text{Co}_3\text{O}_4\text{-NC@C}_3\text{N}_4$  is higher than in  $\text{Co}_3\text{O}_4$ , indicating a greater electron cloud density around Co atoms in the  $\text{Co}_3\text{O}_4\text{-NC@C}_3\text{N}_4$  composite (Fig. 4a–c). Additionally, the N p PDOS in  $\text{C}_3\text{N}_4$  shows higher intensity compared to  $\text{Co}_3\text{O}_4\text{-NC@C}_3\text{N}_4$ , revealing a denser electron cloud density around N atoms in  $\text{C}_3\text{N}_4$  (Fig. 4d–f). This analysis suggests electron transfer between the N atoms in  $\text{C}_3\text{N}_4$  and the Co atoms in  $\text{Co}_3\text{O}_4$  within the  $\text{Co}_3\text{O}_4\text{-NC@C}_3\text{N}_4$  composite. Specifically, electrons from the N atoms in  $\text{C}_3\text{N}_4$  are transferred to the Co atoms in  $\text{Co}_3\text{O}_4$ , increasing the Co 3d unpaired electrons. These additional electrons facilitate further interaction with polysulfides, in agreement with the differential charge density analysis.

To corroborate the increase of the unpaired electrons, susceptible to spin alignment, the magnetization ( $M-H$ ) curves of  $\text{Co}_3\text{O}_4\text{-NC@C}_3\text{N}_4$  and  $\text{Co}_3\text{O}_4\text{-NC}$  at room temperature are depicted in Fig. 4g. We observe both materials to display characteristic paramagnetic behavior, with  $\text{Co}_3\text{O}_4\text{-NC@C}_3\text{N}_4$  displaying a much larger magnetic moment compared to  $\text{Co}_3\text{O}_4\text{-NC}$ , which is potentially associated to the extra charge injected from the  $\text{C}_3\text{N}_4$  to the  $\text{Co}_3\text{O}_4$ . This higher magnetic moment is confirmed by the dependence of the magnetic moment on temperature, both after zero field and field cooling (ZFC/FC), as shown in Fig. 4h. Additionally, electron paramagnetic resonance (EPR) spectra (Fig. 4i) reveal  $\text{Co}_3\text{O}_4\text{-NC@C}_3\text{N}_4$  exhibits a significantly enhanced signal at  $g = 2.48$  compared with  $\text{Co}_3\text{O}_4\text{-NC}$ , confirming the higher concentration of unpaired electrons within  $\text{Co}_3\text{O}_4\text{-NC@C}_3\text{N}_4$ .

DFT calculations reproduced the discontinuous band gap at the Fermi level within the total DOS (TDOS) of  $\text{Co}_3\text{O}_4$  (Fig. S23). In contrast,  $\text{Co}_3\text{O}_4\text{-NC@C}_3\text{N}_4$  exhibits evident hybridization bands at the Fermi level, suggesting that the formation of heterostructures facilitates charge transfer and enhances the electrical conductivity of the composite material. Four probe tests under varying pressures experimentally confirmed that the electrical conductivity of  $\text{Co}_3\text{O}_4\text{-NC@C}_3\text{N}_4$  is significantly larger than that of  $\text{Co}_3\text{O}_4\text{-NC}$  (Fig. S24). Besides, UV–vis absorption spectra show that the presence of the  $\text{C}_3\text{N}_4$  decreases the band gap of the material, from  $E_g = 1.83$  eV for  $\text{Co}_3\text{O}_4\text{-NC}$  to  $E_g = 1.74$  eV for  $\text{Co}_3\text{O}_4\text{-NC@C}_3\text{N}_4$  (Fig. S25). According to the d-band theory, the shift of the center of the d-band towards the Fermi level in metal atoms increases the likelihood of electron filling in the anti-bonding orbitals between the metal and adsorbed molecules [64]. This is expected to strengthen the metal's adsorption ability for SPSS.

The affinity between sulfur host materials ( $\text{C}_3\text{N}_4$ ,  $\text{Co}_3\text{O}_4$  and  $\text{Co}_3\text{O}_4\text{-NC@C}_3\text{N}_4$ ) and various SPSS ( $\text{Na}_2\text{S}$ ,  $\text{Na}_2\text{S}_2$ ,  $\text{Na}_2\text{S}_4$ ,  $\text{Na}_2\text{S}_6$ ,  $\text{Na}_2\text{S}_8$ , and  $\text{S}_8$ ) was also evaluated through DFT calculations (Fig. S26–32). As an example, for  $\text{Na}_2\text{S}_6$ , the adsorption energies of the host materials  $\text{C}_3\text{N}_4$ ,  $\text{Co}_3\text{O}_4$ , and  $\text{Co}_3\text{O}_4\text{-NC@C}_3\text{N}_4$  are  $-0.05$  eV,  $-1.36$  eV, and  $-2.42$  eV, respectively. The stronger chemical adsorption of SPSS by  $\text{Co}_3\text{O}_4$ -

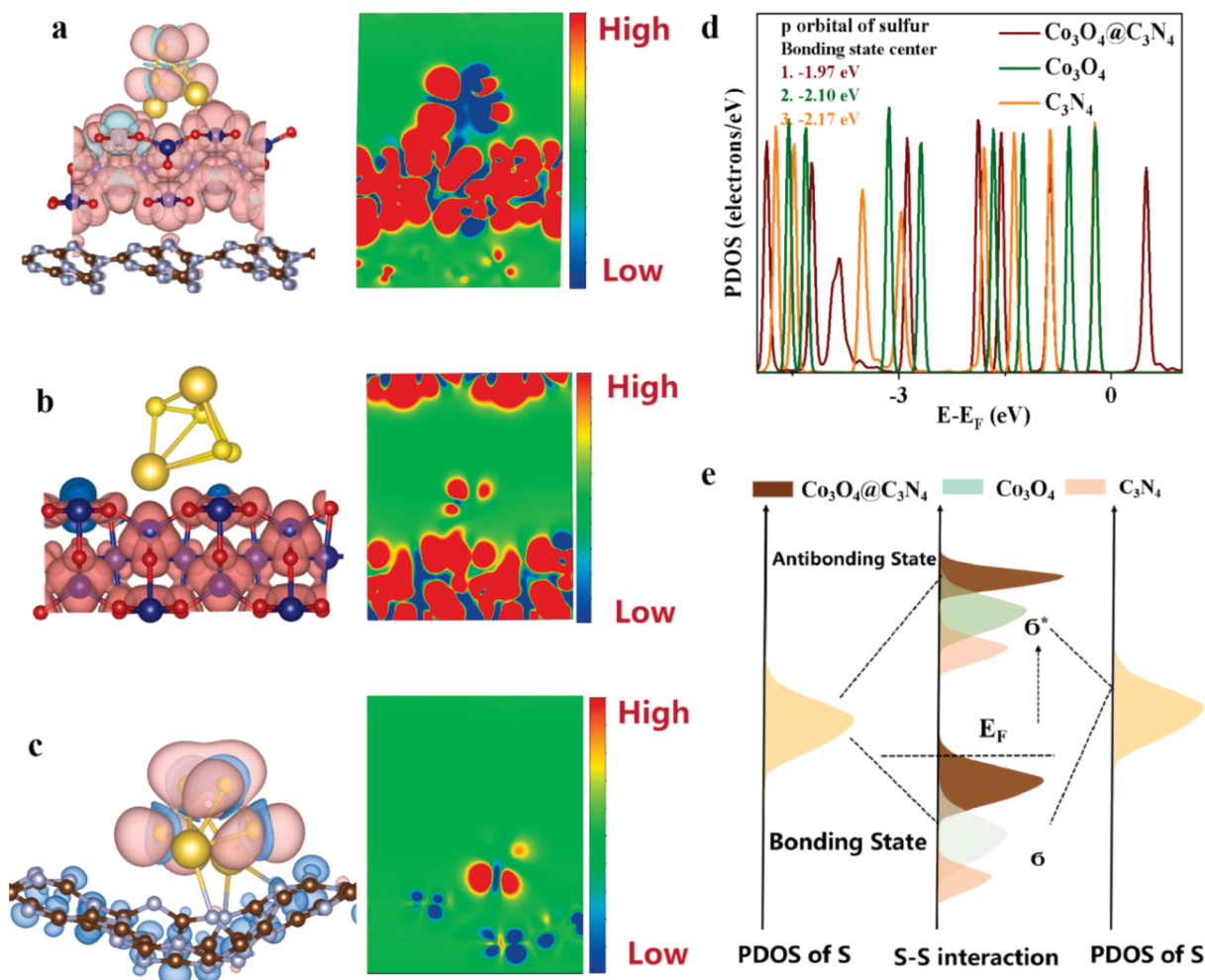


**Fig. 5.** (a-c) Spin density of  $\text{Co}_3\text{O}_4@/\text{C}_3\text{N}_4\text{-Na}_2\text{S}_4$ ,  $\text{Co}_3\text{O}_4\text{-Na}_2\text{S}_4$ , and  $\text{C}_3\text{N}_4\text{-Na}_2\text{S}_4$ . (d-e) Energy level diagram showing orbital hybridization for S-S.  $E_F$  is the Fermi level of the substrate;  $\sigma$  and  $\sigma^*$  represent bonding and antibonding states, respectively.

$\text{NC}@/\text{C}_3\text{N}_4$  primarily stems from the chemical bond formed between  $\text{Co}^{\delta+}$  atoms in  $\text{Co}_3\text{O}_4\text{-NC}@/\text{C}_3\text{N}_4$  and  $\text{S}^{\delta-}$  in the SPS. This theoretical result was experimentally confirmed through  $\text{Na}_2\text{S}_6$  adsorption tests, showing  $\text{Co}_3\text{O}_4\text{-NC}@/\text{C}_3\text{N}_4$  to exhibit a stronger interaction with SPSs than  $\text{Co}_3\text{O}_4\text{-NC}@/\text{C}_3\text{N}_4$  and  $\text{C}_3\text{N}_4$  (see details in the SI, Fig. S33a). Additionally, XPS analysis of the samples after SPS adsorption revealed a negative shift in the high-resolution Co 2p XPS spectrum confirming the interaction between the active sites of metal Co and S atoms in SPS (Fig. S33b)[17].

The adsorption models of  $\text{Na}_2\text{S}_4$  on various host materials are illustrated in Fig. 5a-c, with red representing spin up and blue representing spin down. A comparison of the  $\text{Co}_3\text{O}_4\text{-Na}_2\text{S}_4$ ,  $\text{C}_3\text{N}_4\text{-Na}_2\text{S}_4$ , and  $\text{Co}_3\text{O}_4@/\text{C}_3\text{N}_4\text{-Na}_2\text{S}_4$  adsorption models reveals significant differences in electronic distributions. In the  $\text{Co}_3\text{O}_4\text{-Na}_2\text{S}_4$  and  $\text{C}_3\text{N}_4\text{-Na}_2\text{S}_4$  systems, the electron clouds remain largely confined to the host material and  $\text{Na}_2\text{S}_4$ , showing limited interaction between the two. However, in the  $\text{Co}_3\text{O}_4@/\text{C}_3\text{N}_4\text{-Na}_2\text{S}_4$  model, there is a pronounced electron sharing between the  $\text{Co}_3\text{O}_4@/\text{C}_3\text{N}_4$  and  $\text{Na}_2\text{S}_4$ , indicating stronger electronic coupling between the host and the adsorbed species.

DFT calculations for  $\text{Na}_2\text{S}_4$  adsorption on different host materials indicate that the bonding states of the P orbital in the S center occur at -1.97 eV, -2.10 eV, and -2.17 eV for  $\text{Co}_3\text{O}_4@/\text{C}_3\text{N}_4$ ,  $\text{Co}_3\text{O}_4$ , and  $\text{C}_3\text{N}_4$ , respectively (Fig. 5d-e). Compared to  $\text{Co}_3\text{O}_4$  and  $\text{C}_3\text{N}_4$ , the DOS profile for  $\text{Co}_3\text{O}_4@/\text{C}_3\text{N}_4$  is more closely aligned with the Fermi level, suggesting enhanced SRR catalytic activity. This closer alignment promotes more efficient charge transfer, which facilitates the breaking of S-S bonds,

contributing to the observed improved catalytic performance. Fig. 5e presents the energy level diagram illustrating the hybridization of  $\text{Na}_2\text{S}_4$  with the surface orbitals of  $\text{Co}_3\text{O}_4@/\text{C}_3\text{N}_4$ ,  $\text{Co}_3\text{O}_4$ , and  $\text{C}_3\text{N}_4$ . The diagram demonstrates how polysulfide bonding on  $\text{Co}_3\text{O}_4@/\text{C}_3\text{N}_4$ ,  $\text{Co}_3\text{O}_4$ , and  $\text{C}_3\text{N}_4$  influences the bonding state around the Fermi level of sulfur atoms in distinct ways. Notably,  $\text{Co}_3\text{O}_4@/\text{C}_3\text{N}_4$  exhibits a higher electron density near the Fermi level ( $E_F$ ), and the total density of states (TDOS) of  $\text{Co}_3\text{O}_4@/\text{C}_3\text{N}_4\text{-Na}_2\text{S}_4$  shifts upward after absorbing  $\text{Na}_2\text{S}_4$ , compared to  $\text{Co}_3\text{O}_4\text{-Na}_2\text{S}_4$  and  $\text{C}_3\text{N}_4\text{-Na}_2\text{S}_4$ . This upward shift indicates reduced stability of the S-S bond, which facilitates its cleavage. Consequently, the kinetics of the Na-S reaction is significantly enhanced.

As shown in Fig. 6a, upon contact with  $\text{Na}_2\text{S}_4$ , the DOS of  $\text{Co}_3\text{O}_4@/\text{C}_3\text{N}_4\text{-Na}_2\text{S}_4$  at the Fermi level exhibits a higher peak intensity compared to  $\text{Co}_3\text{O}_4\text{-Na}_2\text{S}_4$ , pointing at an easier electron transfer between the host material and the SPS. Fig. 6b illustrates the highest occupied molecular orbital (HOMO) and lowest unoccupied molecular orbital (LUMO) of  $\text{Na}_2\text{S}_4$  after adsorption onto the different host materials. The energy gaps ( $E_g$ ) between the LUMO and HOMO orbitals of  $\text{Na}_2\text{S}_4$  adsorbed by  $\text{C}_3\text{N}_4$ ,  $\text{Co}_3\text{O}_4$ , and  $\text{Co}_3\text{O}_4@/\text{C}_3\text{N}_4$  are 1.03 eV, 1.82 eV, and 0.44 eV, respectively. Thus, the  $\text{Co}_3\text{O}_4@/\text{C}_3\text{N}_4$  heterostructure introduces additional electrons that result in a reduction of the LUMO and HOMO gap of  $\text{Na}_2\text{S}_4$ . This narrower energy gap implies that electrons can more readily transition from the HOMO to the LUMO, promoting electron transfer and accelerating the SRR kinetics. Using the (110) crystal plane of  $\text{Co}_3\text{O}_4$  and the single-layer plate structure of  $\text{C}_3\text{N}_4$ , the Bader charge analysis revealed a gain of 0.09 electrons by the  $\text{Co}_3\text{O}_4$  unit

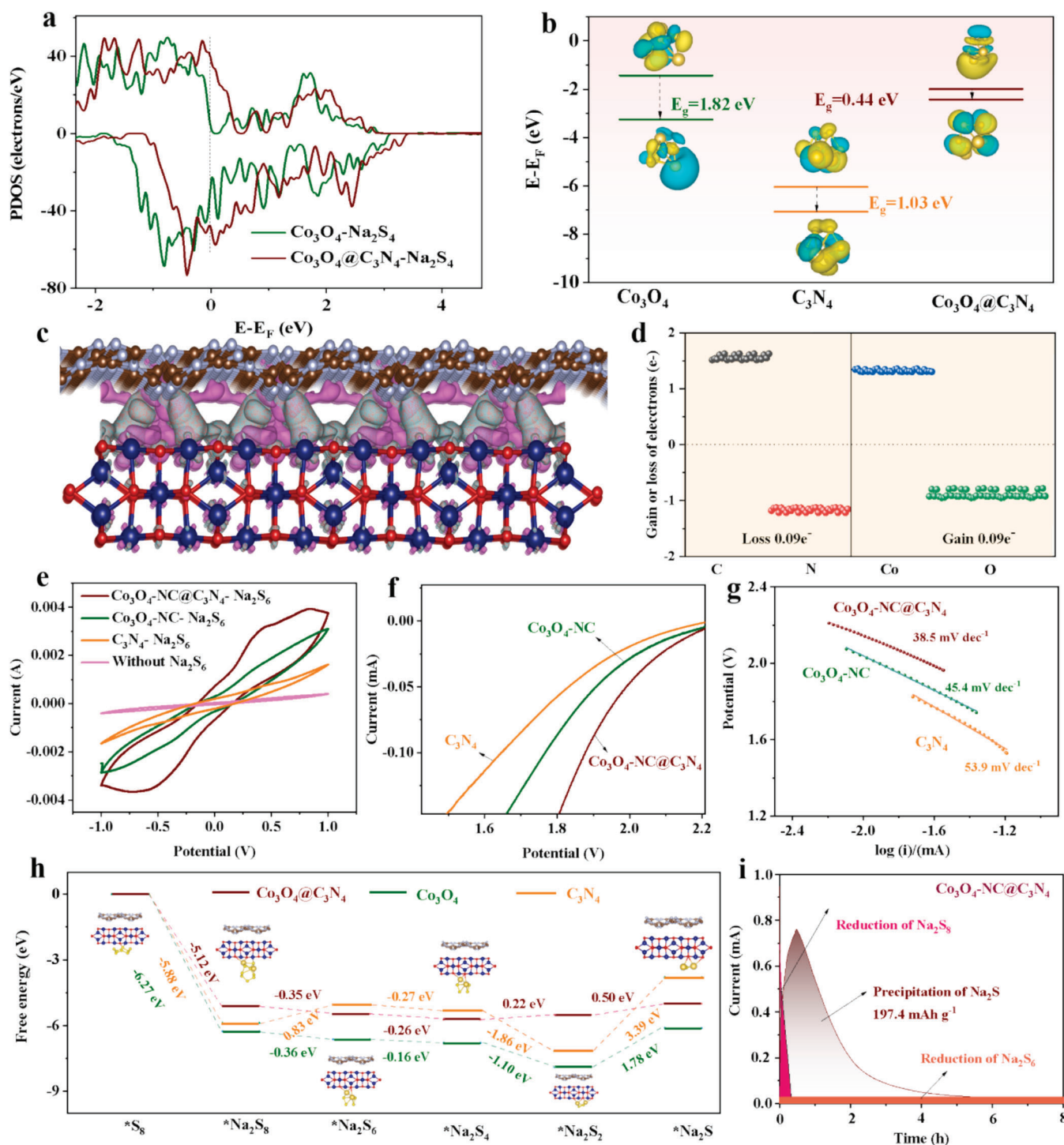


**Fig. 6.** (a) PDOS of  $\text{Co}_3\text{O}_4@\text{C}_3\text{N}_4\text{-Na}_2\text{S}_4$  and  $\text{Co}_3\text{O}_4\text{-Na}_2\text{S}_4$ . (b) Model diagram of HOMO and LUMO of  $\text{Na}_2\text{S}_4$  after adsorption by different host materials and the band gap between HOMO and LUMO. (c, d) Electron gain/loss for different atoms as obtained by Bader charge analysis. (e) Symmetrical batteries assembled from different host materials ( $\text{Co}_3\text{O}_4\text{-NC}@C_3\text{N}_4$ ,  $\text{Co}_3\text{O}_4\text{-NC}$ ,  $\text{C}_3\text{N}_4$ ). (f-g) LSV polarization curves and Tafel plots. (h) Gibbs free energy profiles and optimized adsorption model towards SPSS species on  $\text{C}_3\text{N}_4$ ,  $\text{Co}_3\text{O}_4$ , and  $\text{Co}_3\text{O}_4@\text{C}_3\text{N}_4$ . (i)  $\text{Na}_2\text{S}$  deposition experiment test for  $\text{Co}_3\text{O}_4\text{-NC}@C_3\text{N}_4$ .

from the  $\text{C}_3\text{N}_4$  layer in the  $\text{Co}_3\text{O}_4@\text{C}_3\text{N}_4$  system (Fig. 6c, d).

To experimentally corroborate the improved charge transfer and catalytic activity theoretically predicted, CV and LSV analysis of symmetrical cells was carried out. CV at 5 mV·s<sup>-1</sup> scan rate of  $\text{Co}_3\text{O}_4\text{-NC}@C_3\text{N}_4//\text{Co}_3\text{O}_4\text{-NC}@C_3\text{N}_4$  symmetrical cells with a  $\text{Na}_2\text{S}_6$  electrolyte showed higher current densities and more distinct redox peaks compared with  $\text{Co}_3\text{O}_4\text{-NC}$ , and  $\text{C}_3\text{N}_4$  cells (see details in the Experimental section, Fig. 6e). Additionally, LSV measurements show the

$\text{Co}_3\text{O}_4\text{-NC}@C_3\text{N}_4$  cathode displays the smallest Tafel slope (Fig. 6f-g).

In addition, the performance of Co-based and Fe-based catalysts was assessed using CV and EIS in symmetric cells. As illustrated in Fig. S34a, compared to  $\text{Fe}_3\text{O}_4\text{-NC}@C_3\text{N}_4$ ,  $\text{Co}_3\text{O}_4\text{-NC}@C_3\text{N}_4$  demonstrates a higher peak current, a larger enclosed area, and more distinct redox peaks in the CV profiles, suggesting that  $\text{Co}_3\text{O}_4\text{-NC}@C_3\text{N}_4$  exhibits superior catalytic activity. Additionally, the EIS spectra, fitted using the equivalent circuit diagrams shown in Fig. S34 b,c, reveal that  $\text{Co}_3\text{O}_4\text{-NC}@C_3\text{N}_4$  is



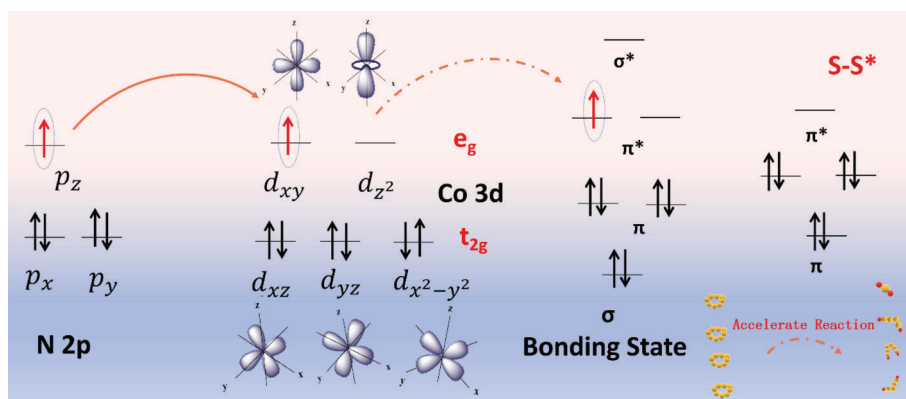


**Fig. 7.** Schematic configurations for high spin (HS) and low spin (LS) states of Co<sup>3+</sup> and the chemical bond formation between the reactive surface and S-S bond.

characterized by the lowest charge transfer resistance during the SRR, with a value of 26.8 Ω. This is significantly lower than the 48.6 Ω observed for Fe<sub>3</sub>O<sub>4</sub>-NC@C<sub>3</sub>N<sub>4</sub>. These results further validate the superior charge transfer kinetics of Co<sub>3</sub>O<sub>4</sub>-NC@C<sub>3</sub>N<sub>4</sub>, highlighting its enhanced catalytic performance in facilitating sulfur conversion reactions.

The Gibbs free energy of the various steps during the reduction of SPSs is displayed in Fig. 6h. The rate-determining step, the one exhibiting the largest Gibbs energy barrier, is the transformation from Na<sub>2</sub>S<sub>2</sub> to solid Na<sub>2</sub>S. For this step, Co<sub>3</sub>O<sub>4</sub>@C<sub>3</sub>N<sub>4</sub> displays the smallest Gibbs energy barrier (0.50 eV) when compared with Co<sub>3</sub>O<sub>4</sub> (1.78 eV) and C<sub>3</sub>N<sub>4</sub> (3.39 eV). This result is consistent with Na<sub>2</sub>S precipitation experiments, showing the capacity of Co<sub>3</sub>O<sub>4</sub>-NC@C<sub>3</sub>N<sub>4</sub> clearly surpassed that of Co<sub>3</sub>O<sub>4</sub>-NC and C<sub>3</sub>N<sub>4</sub> (Fig. 6i and S35).

Fig. 7 illustrates the proposed electron transfer mechanism responsible for the enhanced SRR activity and improved cell performance of Co<sub>3</sub>O<sub>4</sub>-NC@C<sub>3</sub>N<sub>4</sub>. The mechanism involves electron transfer from the N atoms in C<sub>3</sub>N<sub>4</sub> to the vacant orbitals of Co<sup>3+</sup> in Co<sub>3</sub>O<sub>4</sub>. Compared to pure Co<sub>3</sub>O<sub>4</sub>-NC, the formation of the Co<sub>3</sub>O<sub>4</sub>-NC@C<sub>3</sub>N<sub>4</sub> heterostructure facilitates electron transfer from N atoms in C<sub>3</sub>N<sub>4</sub> to Co<sup>3+</sup> in Co<sub>3</sub>O<sub>4</sub>. This process introduces an additional unpaired electron into the high-energy e<sub>g</sub> orbital of Co<sup>3+</sup>, generating a high spin state. The unpaired electron then moves to occupy the newly formed interaction bond between S-S\* and Co<sup>3+</sup>. This results in the formation of an antibonding state with higher energy, which destabilizes the S-S\* bond on Co<sup>3+</sup> and facilitates its decomposition. This electron transfer mechanism is key to improving SRR activity and overall cell performance in the Co<sub>3</sub>O<sub>4</sub>-NC@C<sub>3</sub>N<sub>4</sub> system.

### 3. Conclusion

In summary, a Co-based composite was presented and tested as a sulfur host in the cathode of SSBs. Within these composites, the hollow tubular C<sub>3</sub>N<sub>4</sub> provides enough space to disperse the catalyst, facilitates Na<sup>+</sup> ion diffusion, and alleviates the volume change during the reaction. Most importantly, within the composite, electrons are transferred from N atoms in C<sub>3</sub>N<sub>4</sub> to Co atoms in Co<sub>3</sub>O<sub>4</sub>, resulting in additional unpaired electrons in the 3d orbital of Co<sup>3+</sup> that induce a change in the spin state of the Co ion to high spin. Additionally, the generated unpaired electrons facilitate transfer between the host material and the polysulfides, thereby significantly improving polysulfide adsorption and accelerating its catalytic conversion. Therefore, Co<sub>3</sub>O<sub>4</sub>-NC@C<sub>3</sub>N<sub>4</sub>/S cathodes exhibit excellent rate capability and long cycle life in SSBs, even at high load, in lean electrolyte conditions, and at the pouch cell level.

### CRediT authorship contribution statement

**Chen Huang:** Writing – original draft, Methodology, Investigation,

Formal analysis, Data curation, Conceptualization. **Jing Yu:** Supervision, Methodology, Formal analysis, Data curation. **Yao-Jie Lei:** Methodology, Investigation. **Oleg Usoltsev:** Supervision, Resources. **Li Gong:** Investigation, Formal analysis. **Zhibiao Cui:** Formal analysis, Data curation. **Junshan Li:** Formal analysis, Data curation. **Canhuang Li:** Investigation, Data curation. **Bingfei Nan:** Investigation, Data curation. **Xuan Lu:** Methodology, Investigation. **Ren He:** Investigation, Data curation. **Xuede Qi:** Investigation, Formal analysis. **Qian Xue:** Investigation, Formal analysis. **Jiali Chai:** Investigation, Data curation. **Yuchuan Ren:** Investigation, Data curation. **Xiaoyu Bi:** Investigation, Data curation. **Yapeng Cheng:** Supervision, Methodology. **Jin Yuan Zhou:** Supervision, Resources. **Alina Skorynina:** Supervision, Resources. **Aram Bugaev:** Supervision, Resources. **Paulina R. Martínez-Alanis:** Investigation, Data curation. **Lluís Balcells:** Supervision, Resources. **Jordi Arbiol:** Visualization, Supervision, Resources, Funding acquisition. **Chao Yue Zhang:** Supervision, Resources, Funding acquisition. **Andreu Cabot:** Writing – review & editing, Visualization, Supervision, Resources, Funding acquisition, Conceptualization.

### Declaration of competing interest

The authors declare that they have no known competing financial interests or personal relationships that could have appeared to influence the work reported in this paper.

### Acknowledgements

This work was financially supported by the SyDECat and AMaDE projects from the Spanish MCIN/AEI/FEDER (PID2022-136883OB-C22 and PID2023-149158OB-C43, respectively), the 2BoSS project of the ERA-MIN3 program with the Spanish grant number PCI2022-132985 /AEI /10.13039 /501100011033, Generalitat de Catalunya 2021SGR01581 and 2021SGR00457 and Next Generation EU / PRTR-C17.I1. C. H., J. Y., C.Y. Z., and B. F. N thank the China Scholarship Council for the scholarship support. ICN2 acknowledges the support from the Severo Ochoa Program from Spanish MCIN / AEI (Grant No.: CEX2021-001214-S). IREC and ICN2 are both funded by the CERCA Program/Generalitat de Catalunya. J. Li is grateful for the project supported by the Natural Science Foundation of Sichuan (2022NSFSC1229). The authors also greatly acknowledge the support supported by the Supercomputing Center of Lanzhou University, China. This work has received funding from the “Spanish Ministry of Science and Innovation” through “Severo Ochoa” (CEX2019-000917-S) and “OXISOT” (PID2021-128410OB-I00). This study is part of the Advanced Materials program and was supported by MCIN with funding from the European Union Next Generation EU (PRTR-C17.I1) and by Generalitat de Catalunya. Part of the present work has been performed in the framework of Universitat Autònoma de Barcelona Materials Science PhD

program. The authors acknowledge the use of instrumentation as well as the technical advice provided by the Joint Electron Microscopy Center at ALBA (JEMCA). ICN2 acknowledges funding from Grant IU16-014206 (METCAM-FIB) funded by the European Union through the European Regional Development Fund (ERDF), with the support of the Ministry of Research and Universities, Generalitat de Catalunya. ICN2 is a founding member of e-DREAM[65].

## Appendix A. Supplementary data

Supplementary data to this article can be found online at <https://doi.org/10.1016/j.cej.2025.160146>.

## Data availability

Data will be made available on request.

## References

- [1] X. Xu, D. Zhou, X. Qin, K. Lin, F. Kang, B. Li, D. Shanmukaraj, T. Rojo, M. Armand, G. Wang, A room-temperature sodium-sulfur battery with high capacity and stable cycling performance, *Nat. Commun.* 9 (2018) 3870.
- [2] B.-W. Zhang, L. Cao, C. Tang, C. Tan, N. Cheng, W.-H. Lai, Y.-X. Wang, Z.-X. Cheng, J. Dong, Y. Kong, S.-X. Dou, S. Zhao, Atomically Dispersed Dual-Site Cathode with a Record High Sulfur Mass Loading for High-Performance Room-Temperature Sodium-Sulfur Batteries, *Adv. Mater.* 35 (2023) 2206828.
- [3] J. Mou, Y. Li, T. Liu, W. Zhang, M. Li, Y. Xu, L. Zhong, W. Pan, C. Yang, J. Huang, M. Liu, Metal-Organic Frameworks-Derived Nitrogen-Doped Porous Carbon Nanocubes with Embedded Co Nanoparticles as Efficient Sulfur Immobilizers for Room Temperature Sodium-Sulfur Batteries, *Small Methods* 5 (2021) 2100455.
- [4] Z. Yan, J. Xiao, W. Lai, L. Wang, F. Gebert, Y. Wang, Q. Gu, H. Liu, S.-L. Chou, H. Liu, S.-X. Dou, Nickel sulfide nanocrystals on nitrogen-doped porous carbon nanotubes with high-efficiency electrocatalysis for room-temperature sodium-sulfur batteries, *Nat. Commun.* 10 (2019) 4793.
- [5] J. Yu, I. Pinto-Huguet, C.Y. Zhang, Y. Zhou, Y. Xu, A. Vizintin, J.-J. Velasco-Vélez, X. Qi, X. Pan, G. Oney, A. Olgo, K. Märker, L.M. Da Silva, Y. Luo, Y. Lu, C. Huang, E. Härk, J. Fleming, P. Chenevier, A. Cabot, Y. Bai, M. Botifoll, A.P. Black, Q. An, T. Amietszajew, J. Arbiol, Mechanistic Insights and Technical Challenges in Sulfur-Based Batteries: A Comprehensive In Situ/Operando Monitoring Toolbox, *ACS Energy Lett.* 9 (2024) 6178–6214.
- [6] D. Yang, Y. Han, M. Li, C. Li, W. Bi, Q. Gong, J. Zhang, J. Zhang, Y. Zhou, H. Gao, J. Arbiol, Z. Shi, G. Zhou, A. Cabot, Highly Conductive Quasi-1D Hexagonal Chalcogenide Perovskite  $\text{Sr}_2\text{Ti}_2\text{S}_{21}$  with Efficient Polysulfide Regulation in Lithium-Sulfur Batteries, *Adv. Funct. Mater.* 34 (2024) 2401577.
- [7] H. Pan, Z. Cheng, Z. Zhou, S. Xie, W. Zhang, N. Han, W. Guo, J. Franssaer, J. Luo, A. Cabot, M. Wübbenhorst, Boosting Lean Electrolyte Lithium-Sulfur Battery Performance with Transition Metals: A Comprehensive Review, *Nanomicro Lett* 15 (2023) 165.
- [8] L. Zhao, Y. Tao, Y. Zhang, Y. Lei, W.-H. Lai, S. Chou, H.-K. Liu, S.-X. Dou, Y.-X. Wang, A Critical Review on Room-Temperature Sodium-Sulfur Batteries: From Research Advances to Practical Perspectives, *Adv. Mater.* 36 (2024) 2402337.
- [9] Y. Wang, Y. Lai, J. Chu, Z. Yan, Y.-X. Wang, S.-L. Chou, H.-K. Liu, S.-X. Dou, X. Ai, H. Yang, Y. Cao, Tunable Electrocatalytic Behavior of Sodioted  $\text{MoS}_2$  Active Sites toward Efficient Sulfur Redox Reactions in Room-Temperature Na-S Batteries, *Adv. Mater.* 33 (2021) 2100229.
- [10] X. Zhou, Z. Yu, Y. Yao, Y. Jiang, S. Rui, J. Liu, Y. Yu, A High-Efficiency  $\text{Mo}_2\text{C}$  Electrocatalyst Promoting the Polysulfide Redox Kinetics for Na-S Batteries, *Adv. Mater.* 34 (2022) 2200479.
- [11] Q. Gong, D. Yang, H. Yang, K. Wu, J. Zhang, W. Bi, J. Diaol, C. Li, J. Yu, C.Y. Zhang, M. Li, G. Henkelman, J. Arbiol, Q. Zhang, A. Cabot, Cobalt Telluride Meets Tellurium Vacancy: An Efficient Catalyst as a Multifunctional Polysulfide Mediator toward Robust Lithium-Sulfur Batteries, *ACS Nano* 18 (2024) 28382–28393.
- [12] C. Li, J. Yu, C. Zhang, D. Yang, J. Wang, H. Li, C. Huang, K. Xiao, Y. Cheng, Y. Ren, X. Qi, T. Yang, J. Li, J. Wang, G. Henkelman, J. Arbiol, J. Nan, A. Cabot, Tungsten phosphide on nitrogen and phosphorus-doped carbon as a functional membrane coating enabling robust lithium-sulfur batteries, *J. Colloid Interface Sci.* 670 (2024) 61–72.
- [13] C. Li, D. Yang, J. Yu, J. Wang, C. Zhang, T. Yang, C. Huang, B. Nan, J. Li, J. Arbiol, Y. Zhou, Q. Zhang, A. Cabot, Three Birds with One Stone: Multifunctional Separators Based on  $\text{SnSe}$  Nanosheets Enable High-Performance Li-, Na- and K-Sulfur Batteries, *Adv. Energy Mater.* 14 (2024) 2303551.
- [14] J. Zhang, D. Yang, C. Li, Q. Gong, W. Bi, X. Zheng, J. Arbiol, S. Li, A. Cabot, Two-Dimensional Transition Metal Phosphides As Cathode Additive in Robust Lithium-Sulfur Batteries, *Nano Lett.* 24 (2024) 7992–7998.
- [15] C.Y. Zhang, L. Gong, C. Zhang, X. Cheng, L. Balcells, G. Zeng, J.J. Biendicho, J. Li, G.Z. Sun, J.Y. Zhou, A. Cabot, Sodium-Sulfur Batteries with Unprecedented Capacity, Cycling Stability and Operation Temperature Range Enabled by a  $\text{CoFe}_2\text{O}_4$  Catalytic Additive Under an External Magnetic Field, *Adv. Funct. Mater.* 33 (2023) 2305908.
- [16] C.Y. Zhang, X. Lu, X. Han, J. Yu, C. Zhang, C. Huang, L. Balcells, A.G. Manjón, J. Jacas Biendicho, J. Li, J. Arbiol, G. Sun, J.Y. Zhou, A. Cabot, Identifying the Role of the Cationic Geometric Configuration in Spinel Catalysts for Polysulfide Conversion in Sodium-Sulfur Batteries, *J. Am. Chem. Soc.* 145 (2023) 18992–19004.
- [17] C. Huang, J. Yu, C. Li, Z. Cui, C. Zhang, C. Zhang, B. Nan, J. Li, J. Arbiol, A. Cabot, Combined Defect and Heterojunction Engineering in  $\text{ZnTe}/\text{CoTe}_2$ @NC Sulfur Hosts Toward Robust Lithium-Sulfur Batteries, *Adv. Funct. Mater.* 33 (2023) 2305624.
- [18] J. Jacas Biendicho, P. Mazaira, H. Avireddy, C. Zhang, P. Tang, A. Missyul, L. Trilla, J. Arbiol, J.R. Morante, A. Cabot,  $\text{FeS}_2$ -Decorated Carbon NanoFiber as Solid Phase Conversion-Type Cathode for Li-S Batteries, *Energies* (2023).
- [19] M.K. Aslam, I.D. Seymour, N. Katyal, S. Li, T. Yang, S.-J. Bao, G. Henkelman, M. Xu, Metal chalcogenide hollow polar bipyramid prisms as efficient sulfur hosts for Na-S batteries, *Nat. Commun.* 11 (2020) 5242.
- [20] D. Yang, J. Wang, C. Lou, M. Li, C. Zhang, A. Ramon, C. Li, M. Tang, G. Henkelman, M. Xu, J. Li, J. Llorca, J. Arbiol, D. Mitlin, G. Zhou, A. Cabot, Single-Atom Catalysts with Unsaturated Co- $\text{N}_2$  Active Sites Based on a  $\text{C}_2\text{N}$  2D-Organic Framework for Efficient Sulfur Redox Reaction, *ACS Energy Lett.* 9 (2024) 2083–2091.
- [21] C. Zhao, F. Huo, Y. Yang, J. Ruan, F. Chai, H. Xu, Y. Liu, L. Zhang, A. Cabot, Z. Sun, Y. Zhang, Development of Synergistically Efficient Ni-Co Pair Catalytic Sites for Enhanced Polysulfide Conversion in Lithium-Sulfur Batteries, *Adv. Funct. Mater.* 34 (2024) 2402175.
- [22] D. Yang, C. Li, M. Sharma, M. Li, J. Wang, J. Wei, K. Liu, Y. Zhang, J. Li, G. Henkelman, Q. Zhang, A. Cabot, Three birds with one arrow: Multifunctional single-atom catalysts enable efficient lithium-sulfur batteries, *Energy Stor. Mater.* 66 (2024) 103240.
- [23] H. Zhang, Z. Zhao, Y.-N. Hou, Y. Tang, J. Liang, X. Liu, Z. Zhang, X. Wang, J. Qiu, Highly stable lithium-sulfur batteries based on p-n heterojunctions embedded on hollow sheath carbon propelling polysulfides conversion, *J. Mater. Chem. A* 7 (2019) 9230–9240.
- [24] L. Yue, W. Song, Z. Wu, W. Zhao, L. Zhang, Y. Luo, D. Zheng, B. Zhong, Q. Liu, S. Sun, X. Guo, X. Sun, Constructing  $\text{FeS}_2/\text{TiO}_2$  p-n heterostructure encapsulated in one-dimensional carbon nanofibers for achieving highly stable sodium-ion battery, *Chem. Eng. J.* 455 (2023) 140824.
- [25] R. Ren, G. Liu, J.Y. Kim, R.E.A. Ardhi, M.X. Tran, W. Yang, J.K. Lee, Photoactive  $\text{g-C}_3\text{N}_4/\text{CuZIF-67}$  bifunctional electrocatalyst with staggered p-n heterojunction for rechargeable Zn-air batteries, *Appl. Catal. B* 306 (2022) 121096.
- [26] C. Huang, J. Yu, C.Y. Zhang, Z. Cui, J. Chen, W.-H. Lai, Y.-J. Lei, B. Nan, X. Lu, R. He, L. Gong, J. Li, C. Li, X. Qi, Q. Xue, J.Y. Zhou, X. Qi, L. Balcells, J. Arbiol, A. Cabot, Electronic Spin Alignment within Homologous  $\text{NiS}_2/\text{NiSe}_2$  Heterostructures to Promote Sulfur Redox Kinetics in Lithium-Sulfur Batteries, *Adv. Mater.* 36 (2024) 2400810.
- [27] Y. Wang, P. Meng, Z. Yang, M. Jiang, J. Yang, H. Li, J. Zhang, B. Sun, C. Fu, Regulation of Atomic Fe-Spin State by Crystal Field and Magnetic Field for Enhanced Oxygen Electrocatalysis in Rechargeable Zinc-Air Batteries, *Angew. Chem. Int. Ed.* 62 (2023) e202304229.
- [28] Z. Zhao, M. Hu, T. Nie, W. Zhou, B. Pan, B. Xing, L. Zhu, Improved Electronic Structure from Spin-State Reconstruction of a Heteronuclear Fe-Co Diatomic Pair to Boost the Fenton-like Reaction, *Environ. Sci. Technol.* 57 (2023) 4556–4567.
- [29] Q. Zhang, R. Ao, R. Gao, H. Yang, Manipulating the Spin State of Fe Sites via Fe-O-Si Bridge Bonds for Enhanced Polysulfide Redox Kinetics in the Li-S Battery, *Inorg. Chem.* 61 (2022) 19780–19789.
- [30] C.Y. Zhang, C. Zhang, G.W. Sun, J.L. Pan, L. Gong, G.Z. Sun, J.J. Biendicho, L. Balcells, X.L. Fan, J.R. Morante, J.Y. Zhou, A. Cabot, Spin Effect to Promote Reaction Kinetics and Overall Performance of Lithium-Sulfur Batteries under External Magnetic Field, *Angew. Chem. Int. Ed.* 61 (2022) e202211570.
- [31] Z.-Y. Mei, G. Zhao, C. Xia, S. Cai, Q. Jing, X. Sheng, H. Wang, X. Zou, L. Wang, H. Guo, B.Y. Xia, Regulated High-Spin State and Constrained Charge Behavior of Active Cobalt Sites in Covalent Organic Frameworks for Promoting Electrocatalytic Oxygen Reduction, *Angew. Chem. Int. Ed.* 62 (2023) e202303871.
- [32] Z. Ye, Y. Jiang, L. Li, F. Wu, R. Chen, Synergetic Anion Vacancies and Dense Heterointerfaces into Bimetal Chalcogenide Nanosheet Arrays for Boosting Electrocatalysis Sulfur Conversion, *Adv. Mater.* 34 (2022) 2109552.
- [33] Q. Wang, T. Liu, K. Chen, D. Wu, C. Chen, M. Chen, X. Ma, J. Xu, T. Yao, Y. Li, H. Zhou, Y. Wu, Precise Regulation of Iron Spin States in Single Fe- $\text{N}_4$  Sites for Efficient Peroxidase-Mimicking Catalysis, *Small* 18 (2022) 2204015.
- [34] D. Wu, H.-Q. Yin, Z. Wang, M. Zhou, C. Yu, J. Wu, H. Miao, T. Yamamoto, W. Zhaxi, Z. Huang, L. Liu, W. Huang, W. Zhong, Y. Einaga, J. Jiang, Z.-M. Zhang, Spin Manipulation in a Metal-Organic Layer through Mechanical Exfoliation for Highly Selective  $\text{CO}_2$  Photoreduction, *Angew. Chem. Int. Ed.* 62 (2023) e202301925.
- [35] T. He, Y. Chen, Q. Liu, B. Lu, X. Song, H. Liu, M. Liu, Y.-N. Liu, Y. Zhang, X. Ouyang, S. Chen, Theory-Guided Regulation of  $\text{FeN}_4$  Spin State by Neighboring Cu Atoms for Enhanced Oxygen Reduction Electrocatalysis in Flexible Metal-Air Batteries, *Angew. Chem. Int. Ed.* 61 (2022) e202201007.
- [36] D. Liu, D. Chen, N. Li, Q. Xu, H. Li, J. He, J. Lu, ZIF-67-Derived 3D Hollow Mesoporous Crystalline  $\text{Co}_3\text{O}_4$  Wrapped by 2D  $\text{g-C}_3\text{N}_4$  Nanosheets for Photocatalytic Removal of Nitric Oxide, *Small* 15 (2019) 1902291.
- [37] C. Huang, S. Lv, A. Gao, J. Ling, F. Yi, J. Hao, M. Wang, Z. Luo, D. Shu, Boosting the energy density of supercapacitors by designing both hollow  $\text{NiO}$  nanoparticles/ nitrogen-doped carbon cathode and nitrogen-doped carbon anode from the same precursor, *Chem. Eng. J.* 431 (2022) 134083.
- [38] S.A. Al Kiey, H.N. Abdelhamid, Metal-organic frameworks (MOFs)-derived  $\text{Co}_3\text{O}_4$ @N-doped carbon as an electrode materials for supercapacitor, *J. Energy Storage* 55 (2022) 105449.

- [39] X. Ding, X. Ge, C. Xing, Y. Liu, T. Li, X. Li, T. Ma, R. Shen, E. Liang, H. Cao, B. Li,  $\text{Co}_3\text{O}_4$ -C yolk-shell hollow spheres derived from ZIF-12-PVP@GO for superior anode performance in lithium-ion batteries, *J. Mater. Sci.* 58 (2023) 355–368.
- [40] C. Young, J. Kim, Y.V. Kaneti, Y. Yamauchi, One-Step Synthetic Strategy of Hybrid Materials from Bimetallic Metal–Organic Frameworks for Supercapacitor Applications, *ACS Appl. Energy Mater.* 1 (2018) 2007–2015.
- [41] H. Wang, W. Li, D. Liu, G. Liu, X. An, J. Liu, C. Zhou, H. Zhang, G. Wang, Application of  $\text{Co}_3\text{O}_4$ /Nitrogen-doped carbon composite electrode material derived from Zeolitic imidazolate frameworks-67 in supercapacitors, *J. Electroanal. Chem.* 930 (2023) 117152.
- [42] C. Zhang, R. Du, J.J. Biendicho, M. Yi, K. Xiao, D. Yang, T. Zhang, X. Wang, J. Arbiol, J. Llorca, Y. Zhou, J.R. Morante, A. Cabot, Tubular  $\text{CoFeP@CN}$  as a Mott–Schottky Catalyst with Multiple Adsorption Sites for Robust Lithium–Sulfur Batteries, *Adv. Energy Mater.* 11 (2021) 2100432.
- [43] L. Luo, X. Wang, S. Yang, J. Dai, D. Li, L. Xia, C. Chi, A. Cabot, Y. Xu, L. Dai,  $\text{PPy/PANI@MoS}_2$  Composites with a Dual-Channel Architecture for Advanced Asymmetric Supercapacitors, *ACS Appl. Energy Mater.* 6 (2023) 5940–5951.
- [44] D. Zhang, Y. Li, P. Wang, J. Qu, S. Zhan, Y. Li, Regulating Spin Polarization through Cationic Vacancy Defects in  $\text{Bi}_4\text{Ti}_3\text{O}_{12}$  for Enhanced Molecular Oxygen Activation, *Angew. Chem. Int. Ed.* 62 (2023) e202303807.
- [45] Z. Han, C. Choi, S. Hong, T.-S. Wu, Y.-L. Soo, Y. Jung, J. Qiu, Z. Sun, Activated  $\text{TiO}_2$  with tuned vacancy for efficient electrochemical nitrogen reduction, *Appl. Catal. B* 257 (2019) 117896.
- [46] M.W. Haverkort, Z. Hu, J.C. Cezar, T. Burnus, H. Hartmann, M. Reuther, C. Zobel, T. Lorenz, A. Tanaka, N.B. Brookes, H.H. Hsieh, H.J. Lin, C.T. Chen, L.H. Tjeng, Spin State Transition in  $\text{LaCoO}_3$  Studied Using Soft X-ray Absorption Spectroscopy and Magnetic Circular Dichroism, *Phys. Rev. Lett.* 97 (2006) 176405.
- [47] D. Fang, G. Wang, S. Huang, T. Chen Li, J. Yu, D. Xiong, D. Yan, X. Liang Li, J. Zhang, Y. Von Lim, S.A. Yang, H., Ying Yang, Combination of heterostructure with oxygen vacancies in  $\text{Co@CoO}_{1-x}$  nanosheets array for high-performance lithium sulfur batteries, *Chem. Eng. J.* 411 (2021) 128546.
- [48] G. Liu, K. Feng, H. Cui, J. Li, Y. Liu, M. Wang, MOF derived in-situ carbon-encapsulated  $\text{Fe}_3\text{O}_4/\text{C}$  to mediate polysulfides redox for ultrastable Lithium-sulfur batteries, *Chem. Eng. J.* 381 (2020) 122652.
- [49] C. Huang, A. Gao, F. Yi, Y. Wang, D. Shu, Y. Liang, Z. Zhu, J. Ling, J. Hao, Metal organic framework derived hollow  $\text{NiS@C}$  with S-vacancies to boost high-performance supercapacitors, *Chem. Eng. J.* 419 (2021) 129643.
- [50] A.K. Haridas, C. Huang, Advances in Strategic Inhibition of Polysulfide Shuttle in Room-Temperature Sodium-Sulfur Batteries via Electrode and Interface Engineering, *Batteries* 9 (2023) 223.
- [51] H. Kim, M.K. Sadan, C. Kim, J. Jo, M. Seong, K.-K. Cho, K.-W. Kim, J.-H. Ahn, H.-J. Ahn, Enhanced reversible capacity of sulfurized polyacrylonitrile cathode for room-temperature Na/S batteries by electrochemical activation, *Chem. Eng. J.* 426 (2021) 130787.
- [52] H. Liu, W.-H. Lai, Y. Lei, H. Yang, N. Wang, S. Chou, H.K. Liu, S.X. Dou, Y.-X. Wang, Electrolytes/Interphases: Enabling Distinguishable Sulfur Redox Processes in Room-Temperature Sodium-Sulfur Batteries, *Adv. Energy Mater.* 12 (2022) 2103304.
- [53] H. Wang, Y. Qi, F. Xiao, P. Liu, Y. Li, S.-J. Bao, M. Xu, Tesselated N-doped carbon/ $\text{CoSe}_2$  as trap-catalyst sulfur hosts for room-temperature sodium–sulfur batteries, *Inorg. Chem. Front.* 9 (2022) 1743–1751.
- [54] F. Xiao, H. Wang, T. Yao, X. Zhao, X. Yang, D.Y.W. Yu, A.L. Rogach, MOF-Derived  $\text{CoS}_2$ /N-Doped Carbon Composite to Induce Short-Chain Sulfur Molecule Generation for Enhanced Sodium–Sulfur Battery Performance, *ACS Appl. Mater. Interfaces* 13 (2021) 18010–18020.
- [55] Y. Lei, C. Wu, X. Lu, W. Hua, S. Li, Y. Liang, H. Liu, W.-H. Lai, Q. Gu, X. Cai, N. Wang, Y.-X. Wang, S.-L. Chou, H.-K. Liu, G. Wang, S.-X. Dou, Streamline Sulfur Redox Reactions to Achieve Efficient Room-Temperature Sodium–Sulfur Batteries, *Angew. Chem. Int. Ed.* 61 (2022) e202200384.
- [56] K. Tang, X. Peng, Z. Zhang, G. Li, J. Wang, Y. Wang, C. Chen, N. Zhang, X. Xie, Z. Wu, A Highly Dispersed Cobalt Electrocatalyst with Electron-Deficient Centers Induced by Boron toward Enhanced Adsorption and Electrocatalysis for Room-Temperature Sodium–Sulfur Batteries, *Small* 20 (2024) 2311151.
- [57] G. Qin, Y. Liu, P. Han, S. Cao, X. Guo, Z. Guo, High performance room temperature Na-S batteries based on FCNT modified  $\text{Co}_3\text{C-Co}$  nanocubes, *Chem. Eng. J.* 396 (2020) 125295.
- [58] Q. Ma, J. Ai, H. Zou, H. He, Z. Li, J. Mujtaba, Z. Fang, Gallate-MOF derived  $\text{CoS}_2/\text{C}$  composites as an accelerated catalyst for room-temperature sodium–sulfur batteries, *ChemComm* 58 (2022) 13612–13615.
- [59] Z. Yan, Y. Liang, W. Hua, X.-G. Zhang, W. Lai, Z. Hu, W. Wang, J. Peng, S. Indris, Y. Wang, S.-L. Chou, H. Liu, S.-X. Dou, Multiregion Janus-Featured Cobalt Phosphide-Cobalt Composite for Highly Reversible Room-Temperature Sodium-Sulfur Batteries, *ACS Nano* 14 (2020) 10284–10293.
- [60] J. Wu, Z. Yu, Y. Yao, L. Wang, Y. Wu, X. Cheng, Z. Ali, Y. Yu, Bifunctional Catalyst for Liquid–Solid Redox Conversion in Room-Temperature Sodium–Sulfur Batteries, *Small Struct.* 3 (2022) 2200020.
- [61] H. Liu, W. Pei, W.-H. Lai, Z. Yan, H. Yang, Y. Lei, Y.-X. Wang, Q. Gu, S. Zhou, S. Chou, H.K. Liu, S.X. Dou, Electrocatalyzing S Cathodes via Multisulfophilic Sites for Superior Room-Temperature Sodium–Sulfur Batteries, *ACS Nano* 14 (2020) 7259–7268.
- [62] T. Mei, X. Li, X. Lin, L. Bai, M. Xu, Y. Qi, Cobalt Catalytic Regulation Engineering in Room-Temperature Sodium–Sulfur Batteries: Facilitating Rapid Polysulfides Conversion and Delicate  $\text{Na}_2\text{S}$  Nucleation, *Adv. Funct. Mater.* 2418126 (2024).
- [63] Q. Ma, G. Du, B. Guo, W. Tang, Y. Li, M. Xu, C. Li, Carbon-wrapped cobalt nanoparticles on graphene aerogel for solid-state room-temperature sodium-sulfur batteries, *Chem. Eng. J.* 388 (2020) 124210.
- [64] S. Feng, Z.-H. Fu, X. Chen, Q. Zhang, A review on theoretical models for lithium-sulfur battery cathodes, *InfoMat* 4 (2022) e12304.
- [65] R. Ciancio, R.E. Dunin-Borkowski, E. Snoeck, M. Kociak, R. Holmestad, J. Verbeeck, A.I. Kirkland, G. Kothleitner, J. Arbiol, e-DREAM: the European Distributed Research Infrastructure for Advanced Electron Microscopy, *Microscopy and Microanalysis* 28 (2022) 2900–2902.



## *Supporting Information for*

### **Generation of unpaired electrons to promote electron transfer at the cathode of room-temperature sodium sulfur batteries**

Chen Huang <sup>a,b</sup>, Jing Yu<sup>\*a,c</sup>, Yao-Jie Lei <sup>d</sup>, Oleg Usoltsev <sup>e</sup>, Li Gong <sup>a,b</sup>, Zhibiao Cui <sup>f</sup>, Junshan Li <sup>g</sup>, Canhuang Li <sup>a,b</sup>, Bingfei Nan <sup>a</sup>, Xuan Lu <sup>a</sup>, Ren He <sup>a</sup>, Xuede Qi <sup>h</sup>, Qian Xue <sup>h</sup>, Jiali Chai <sup>a</sup>, Yuchuan Ren <sup>a</sup>, Xiaoyu Bi <sup>a</sup>, Yapeng Cheng <sup>a</sup>, Jin Yuan Zhou <sup>i</sup>, Alina Skorynina <sup>e</sup>, Aram Bugaev <sup>j</sup>, Paulina R. Martínez-Alanis <sup>a</sup>, Lluís Balcells <sup>k</sup>, Jordi Arbiol<sup>\*c,l</sup>, Chao Yue Zhang<sup>\*i</sup> and Andreu Cabot<sup>\*a,l</sup>

<sup>a</sup> Catalonia Institute for Energy Research-IREC, Sant Adrià de Besòs, Barcelona 08930, Spain

<sup>b</sup> Department of Chemistry, University of Barcelona 08028, Spain

<sup>c</sup> Catalan Institute of Nanoscience and Nanotechnology (ICN2), CSIC and BIST, Campus UAB, Bellaterra, 08193 Barcelona, Catalonia, Spain

<sup>d</sup> Institute for Superconducting and Electronic Materials, Australian Institute of Innovative Materials, Innovation Campus, University of Wollongong Wollongong, NSW, 2500, Australia

<sup>e</sup> ALBA Synchrotron, Carrer de la Llum, 2, 26, 08290 Cerdanyola del Vallès, Barcelona, Catalonia, Spain

<sup>f</sup> School of Chemistry, South China Normal University, Guangzhou 510006, PR China

<sup>g</sup> Institute for Advanced Study, Chengdu University 610106, Chengdu, China

<sup>h</sup> College of Chemistry and Chemical Engineering, Chongqing University of Technology, Chongqing, 400054 China

<sup>i</sup> School of Physical Science & Technology, Lanzhou University Lanzhou 730000, China

<sup>j</sup> Paul Scherrer Institute Forschungsstrasse 111, Villigen 5232, Switzerland

<sup>k</sup> Institut de Ciència de Materials de Barcelona

Campus de la UAB, 08193 Bellaterra, Catalonia, Spain

<sup>l</sup> ICREA Pg. Lluís Companys, 08010 Barcelona, Catalonia, Spain

Corresponding Author: acabot@irec.cat, arbiol@icrea.cat, zhangchy2020@lzu.edu.cn, Jing.yu@icn2.cat

## Experimental

**Materials:** Cobalt(II) nitrate hexahydrate (AR,  $\text{Co}(\text{NO}_3)_2 \cdot 6\text{H}_2\text{O}$ ), urea ( $\text{CH}_4\text{N}_2\text{O}$ ), melamine ( $\text{C}_3\text{H}_6\text{N}_6$ ), and polyvinylpyrrolidone (AR, PVP) were purchased from Sigma Aldrich. Polyvinylidene fluoride (PVDF), methanol ( $\text{CH}_3\text{OH}$ ), N-methyl-2-pyrrolidone (NMP), dimethyl carbonate (DEC), ethylene carbonate (EC), Super P, and sulfur powder were purchased from Fisher. 1 M  $\text{NaClO}_4$  in a mixture of DEC and EC in a 1:1 ratio, with 5 wt% fluoroethylene carbonate (FEC) and Na foil were from Canrud, China. All chemicals were used without further processing.

**Synthesis of  $\text{C}_3\text{N}_4$ :** In a typical synthesis procedure, 10 g of urea and 3 g of melamine were placed in a crucible within a tube furnace. The furnace was heated to 550 °C at a rate of 5 °C  $\text{min}^{-1}$ , and the temperature was held for 4 h. The resulting yellow product ( $\text{C}_3\text{N}_4$ ) was collected and finely ground into powder.

**Synthesis of  $\text{Co}_3\text{O}_4\text{-NC@C}_3\text{N}_4$ :** 100 mg of  $\text{C}_3\text{N}_4$  was dispersed in 15 mL of  $\text{CH}_3\text{OH}$  and ultrasonicated for 30 minutes. Next, 5 mL of  $\text{Co}(\text{NO}_3)_2 \cdot 6\text{H}_2\text{O}$  methanol solution (12 mg  $\text{mL}^{-1}$ ) and 0.5 g of PVP were added to the mixture. The resulting solution was transferred to a 30 mL high-pressure reactor and heated at 120 °C for 6 h. The product was washed three times with ethanol and then dried in a vacuum oven. Subsequently, the material was annealed at 300 °C for 2 h, with a heating rate of 2 °C  $\text{min}^{-1}$  in air, to produce  $\text{Co}_3\text{O}_4\text{-NC@C}_3\text{N}_4$ . A reference  $\text{Co}_3\text{O}_4\text{-NC}$  sample was prepared by adding no  $\text{C}_3\text{N}_4$  to the initial reaction mixture.

**Preparation of  $\text{Co}_3\text{O}_4\text{-NC@C}_3\text{N}_4/\text{S}$ ,  $\text{Co}_3\text{O}_4\text{-NC/S}$ , and  $\text{C}_3\text{N}_4/\text{S}$ :**  $\text{Co}_3\text{O}_4\text{-NC@C}_3\text{N}_4$ ,  $\text{Co}_3\text{O}_4\text{-NC}$ , and  $\text{C}_3\text{N}_4$  were mixed with sulfur in a mortar at a mass ratio of 3:7. The resulting mixture was heated in a tube furnace at 155 °C for 12 h, followed by an additional heating step at 300 °C for 2 h under argon (Ar) atmosphere to eliminate unbonded sulfur.

**Physical characterizations:** The sulfur content in the cathode was measured through thermogravimetric analysis (TGA NETZSCH, STA449-F5) under a nitrogen ( $\text{N}_2$ ) atmosphere over a temperature range of 50 °C to 400 °C. The crystal structure of the prepared samples ( $\text{Co}_3\text{O}_4\text{-NC@C}_3\text{N}_4$ ,  $\text{Co}_3\text{O}_4\text{-NC}$ , and  $\text{C}_3\text{N}_4$ ) was analyzed using X-ray diffraction (XRD, Miniflex 600) with a Rigaku Smart Lab instrument, operating with Cu  $\text{K}\alpha$  radiation ( $\lambda = 1.5418$  Å). The morphology and compositions of the electrode materials were characterized by scanning electron microscopy (SEM), transmission electron microscopy (TEM) and Electron Energy Loss Spectroscopy (EELS) with UC (UniColore) Technology. The physical properties,

including specific surface area, total pore volume, and pore size distribution, were determined from nitrogen adsorption isotherms using an ASAP 2460 instrument. X-ray photoelectron spectroscopy (XPS, Thermo Fisher Scientific, ESCALAB 250) was used to analyze the chemical composition and valence states of the elements. UV-vis absorption spectra were collected with a PerkinElmer LAMBDA 950 UV-vis spectrophotometer, and the bandgap of the electrode materials was determined using UV-vis spectroscopy using the following equation.

$$(ah\nu)^n = A(h\nu - E_g)$$

where  $a$ ,  $h\nu$ ,  $A$ , and  $E_g$  represent the absorption coefficient, the light energy, a constant, and the optical band gap energy, respectively.

XAFS testing is primarily conducted using the Rigaku XAFS-4000 system. The X-ray absorption near-edge structure spectroscopy (XANES) data were processed according to the standard procedures using the Athena module implemented in the IFEFFIT software packages. The extended X-ray absorption fine structure spectroscopy (EXAFS) spectra were obtained by subtracting the post-edge background from the overall absorption and then normalizing with respect to the edge-jump step. Subsequently, the  $\chi(k)$  data were Fourier transformed to real (R) space using a window ( $dk = 1.0 \text{ \AA}^{-1}$ ) to separate the EXAFS contributions from different coordination shells. To obtain the quantitative structural parameters around central atoms, least-squares curve parameter fitting was performed using the ARTEMIS module of IFEFFIT software packages. Electron paramagnetic resonance (EPR) (JES-FA200) measurements were conducted at a temperature of 300 K and across a magnetic field strength range of 0.3 to 1.5 Tesla (T).

**Electrochemical characterizations:** A slurry was first prepared by dispersing 80 wt % of the active materials ( $\text{Co}_3\text{O}_4\text{-NC}@C_3\text{N}_4/\text{S}$ ,  $\text{Co}_3\text{O}_4\text{-NC}/\text{S}$ , and  $\text{C}_3\text{N}_4/\text{S}$ ), 10 wt% Super P, and 10 wt% PVDF in NMP. This slurry was then coated onto an aluminum foil current collector, which was subsequently cut into 12 mm discs to be used as the working electrode. For electrochemical measurements, the sulfur loading was controlled at approximately  $1.5 \text{ mg cm}^{-2}$ . Additionally, a higher sulfur loading of  $\sim 6 \text{ mg cm}^{-2}$  was prepared to evaluate the practical application potential of the electrode materials. The 2032 coin cells were assembled using 40  $\mu\text{L}$  of 1 M  $\text{NaClO}_4$  in a 1:1 mixture of DEC and EC, with 5 wt% FEC as the electrolyte additive. A glass fiber separator was used. Galvanostatic charge-discharge (GCD) measurements were conducted within a voltage range of 0.8 V to 2.8 V. Cyclic voltammetry (CV) measurements were performed at scan rates between  $0.3 \text{ mV s}^{-1}$  and  $5 \text{ mV s}^{-1}$ , while electrochemical impedance

spectroscopy (EIS) was carried out using a CHI 660E electrochemical workstation over a frequency range of 0.01 Hz to 10 kHz.

***Na<sub>2</sub>S<sub>6</sub> solution and adsorption test:*** Sulfur and Na<sub>2</sub>S were dissolved in a mixed solution of EC and DEC at a 1:1 volume ratio, maintaining a 5:1 sulfur-to-Na<sub>2</sub>S ratio. The solution was stirred overnight at 80 °C to form a Na<sub>2</sub>S<sub>6</sub> solution. To evaluate the polysulfide adsorption performance, 20 mg of Co<sub>3</sub>O<sub>4</sub>-NC @C<sub>3</sub>N<sub>4</sub>, Co<sub>3</sub>O<sub>4</sub>-NC, and C<sub>3</sub>N<sub>4</sub> were each immersed in 3.0 mL of the Na<sub>2</sub>S<sub>6</sub> solution and left to age overnight.

***Assembly of symmetrical cells and measurements:*** The fabrication of the symmetrical battery follows the same procedure as for the coin cells, with the key difference being the use of two identical electrodes (Co<sub>3</sub>O<sub>4</sub>-NC@C<sub>3</sub>N<sub>4</sub>, Co<sub>3</sub>O<sub>4</sub>-NC, and C<sub>3</sub>N<sub>4</sub>) as both the working and counter electrodes. Next, 40 µL of electrolyte containing 0.5 M Na<sub>2</sub>S<sub>6</sub> dissolved in 1 M NaClO<sub>4</sub> in EC and DEC is added to the coin cells. The electrode loading is kept at approximately 0.5 mg cm<sup>-2</sup> per electrode. The symmetrical battery is then tested at a scan rate of 5 mV s<sup>-1</sup>.

***Na<sub>2</sub>S precipitation experiments:*** To conduct Na<sub>2</sub>S deposition experiments, 2032 coin cells were assembled using glass fiber as the separator, sodium as the anode, and Co<sub>3</sub>O<sub>4</sub>-NC@C<sub>3</sub>N<sub>4</sub>, Co<sub>3</sub>O<sub>4</sub>-NC, and C<sub>3</sub>N<sub>4</sub> as the cathode. To prepare the Na<sub>2</sub>S<sub>6</sub> solution, Na<sub>2</sub>S, and sulfur were dissolved in EC and DEC at 80 °C for 12 h, yielding a 0.5 mol L<sup>-1</sup> Na<sub>2</sub>S<sub>6</sub> solution. A 50 µL Na<sub>2</sub>S<sub>6</sub> solution was applied to the cathode, while 50 µL of Na<sub>2</sub>S<sub>6</sub>-free EC/DEC electrolyte was added to the anode. The battery was initially discharged to 1.30 V at 0.112 mA, followed by a constant-voltage deposition experiment performed at 1.25 V.

***Theoretical calculations:*** Density functional theory (DFT) calculations were carried out using the Vienna Ab-initio Simulation Package (VASP). The Perdew-Burke-Ernzerhof (PBE) functional was employed for the exchange-correlation term, [1]utilizing projector-augmented wave (PAW) potentials with a cutoff energy of 400 eV.[2] The energy and force convergence criteria were set to 1×10<sup>-4</sup> eV and 0.05 eV/Å, respectively. The calculation parameters are as follows: K-point 2 × 2 × 2, and the isosurface level ranging from -0.001 to 0.001. The heterojunction model was constructed using C<sub>3</sub>N<sub>4</sub> and Co<sub>3</sub>O<sub>4</sub>, with a vacuum layer of 15 Å applied to prevent interactions between layers. The adsorption energy ΔE<sub>ad</sub> was calculated as:

$$\Delta E_{ad} = E_{(surf+ad)} - E_{sur} - E_{ad}$$

where E<sub>(surf+ad)</sub> is the energy of the SPS adsorbed on the surface, E<sub>sur</sub> is the energy of the clean surface, and E<sub>ad</sub> is the energy of the free SPS.

$$\begin{aligned}
133 \quad \Delta G(\text{S}_8\text{-Na}_2\text{S}_8): & \quad E_{\text{Na}_2\text{S}_8} - E_{\text{S}_8} - 2E_{\text{Na}^+} \\
134 \quad \Delta G(\text{Na}_2\text{S}_8\text{-Na}_2\text{S}_6): & \quad E_{\text{Na}_2\text{S}_6} - E_{\text{Na}_2\text{S}_8} + 0.25E_{\text{S}_8} \\
135 \quad \Delta G(\text{Na}_2\text{S}_6\text{-Na}_2\text{S}_4): & \quad E_{\text{Na}_2\text{S}_4} - E_{\text{Na}_2\text{S}_6} + 0.25E_{\text{S}_8} \\
136 \quad \Delta G(\text{Na}_2\text{S}_4\text{-Na}_2\text{S}_2): & \quad E_{\text{Na}_2\text{S}_2} - E_{\text{Na}_2\text{S}_4} + 0.25E_{\text{S}_8} \\
137 \quad \Delta G(\text{Na}_2\text{S}_2\text{-Na}_2\text{S}): & \quad E_{\text{Na}_2\text{S}} - E_{\text{Na}_2\text{S}_2} + 0.125E_{\text{S}_8}
\end{aligned}$$

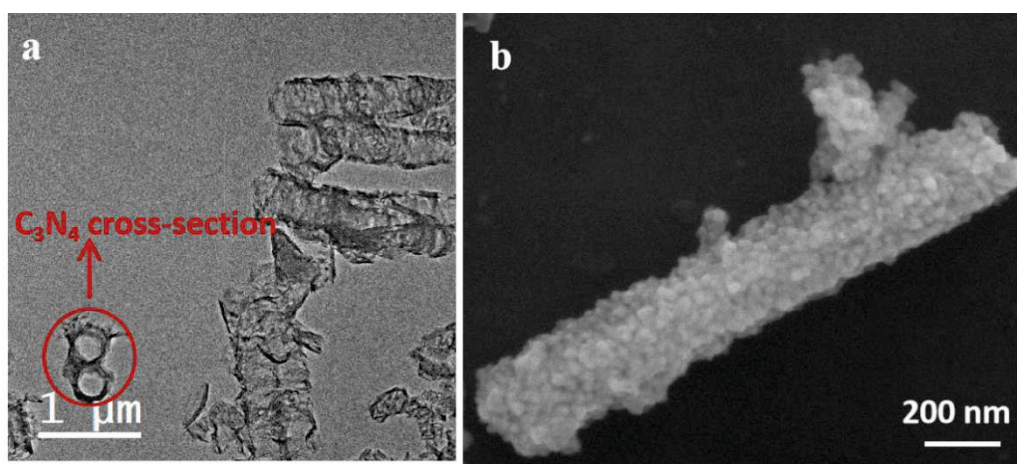


**Fig. S1.** (a) TEM image of  $\text{C}_3\text{N}_4$  and (b) SEM image of  $\text{Co}_3\text{O}_4\text{-NC@C}_3\text{N}_4$ .



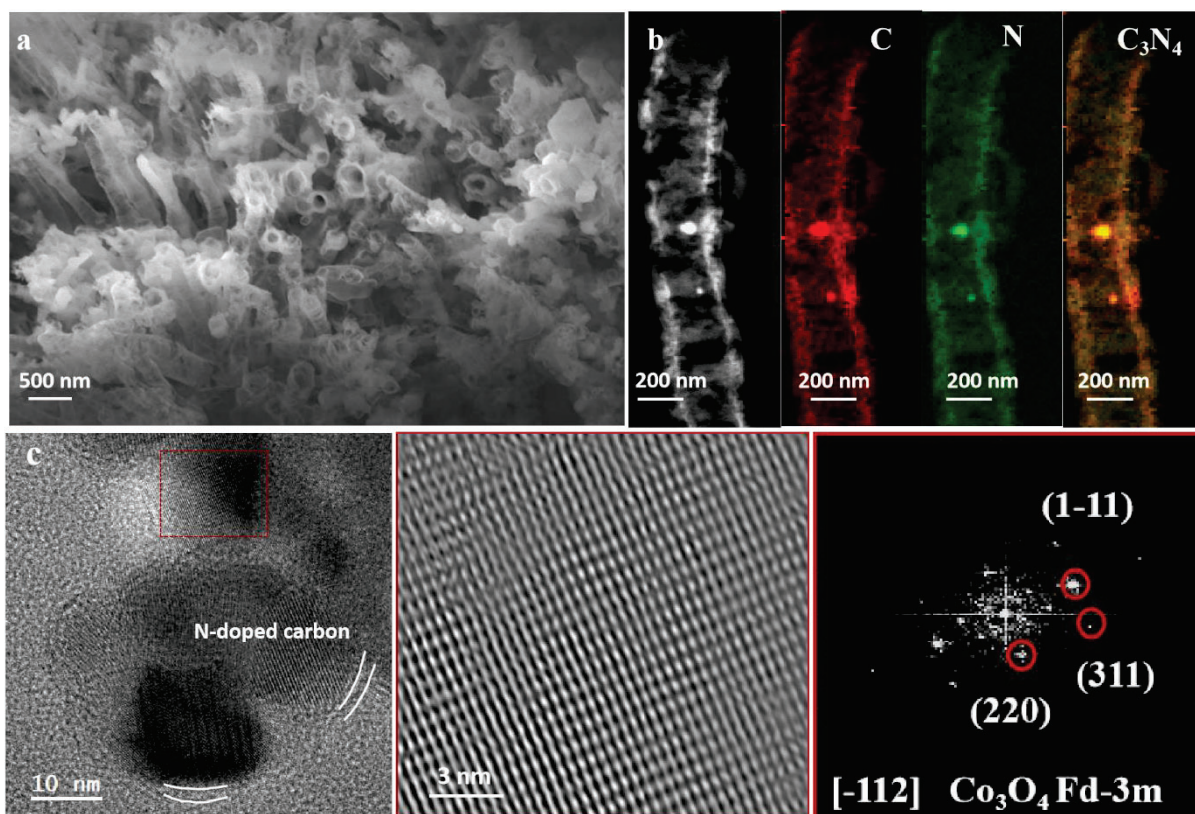
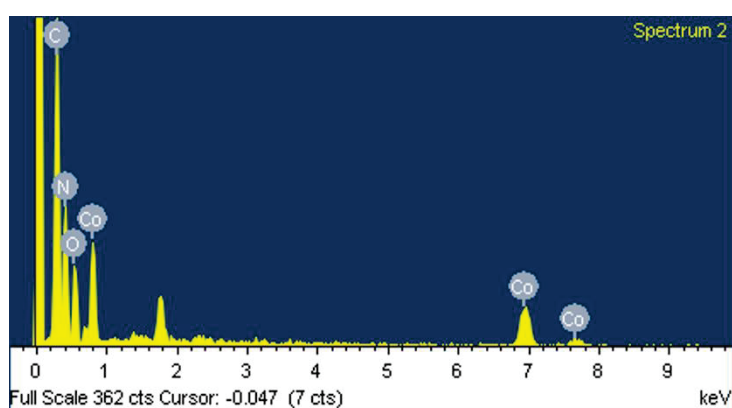


**Fig. S2.** (a) SEM image of  $C_3N_4$ . (b) EELS elemental composition maps obtained from the HAADF STEM micrograph of  $C_3N_4$ . (c) HRTEM micrograph of  $Co_3O_4$ -NC@ $C_3N_4$ . The power spectrum obtained shows that this nanostructure has a crystal phase that can be assigned to the cubic  $Co_3O_4$  (space group = Fd-3m) with  $a=b=c=8.065\text{\AA}$ . The  $Co_3O_4$  lattice fringe distances were determined to be 0.461 nm, 0.282 nm, and 0.245 nm at  $89.45^\circ$  and  $58.08^\circ$ . These values can be interpreted as indicative of the cubic  $Co_3O_4$  phase, visualized along its  $[-112]$  zone axis.



Elements	Atomic (%)
Co	16
O	21
N	36
C	27

**Fig. S3.** EDX spectrum of  $Co_3O_4$ -NC@ $C_3N_4$  and determined atomic composition.



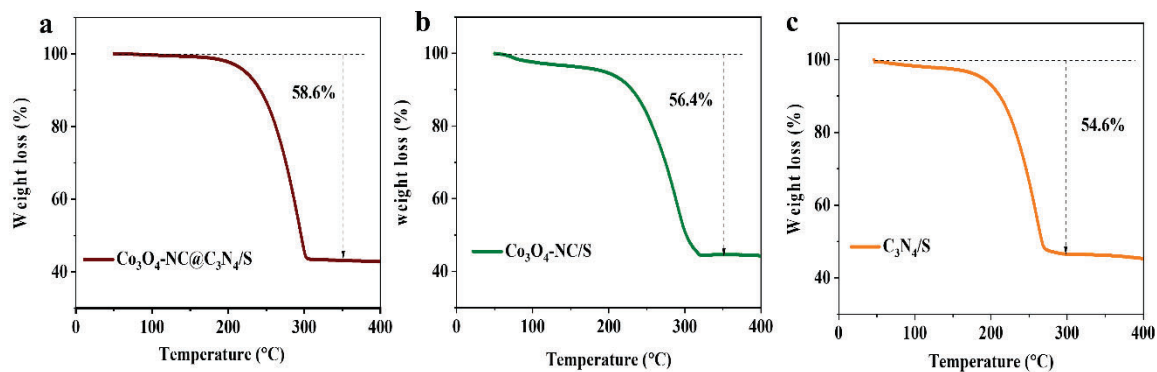


**Fig. S4.** TGA curves for  $\text{Co}_3\text{O}_4\text{-NC@C}_3\text{N}_4/\text{S}$ ,  $\text{Co}_3\text{O}_4\text{-NC/S}$  and  $\text{C}_3\text{N}_4/\text{S}$ .

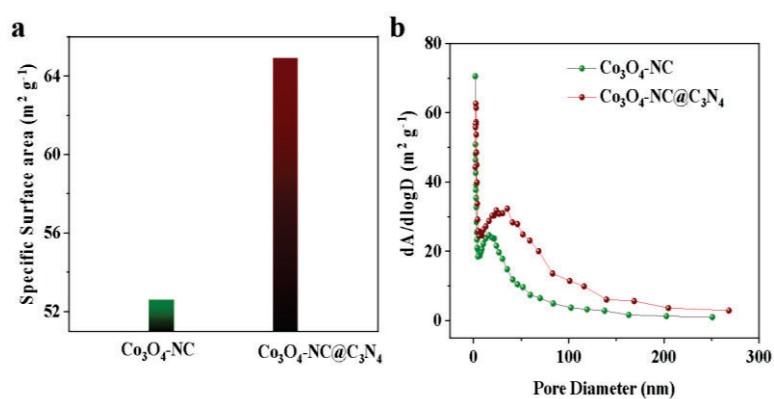


**Fig. S5.** Specific surface area and pore volume curves of different host materials ( $\text{Co}_3\text{O}_4\text{-NC@C}_3\text{N}_4$ ,  $\text{Co}_3\text{O}_4\text{-NC}$ )

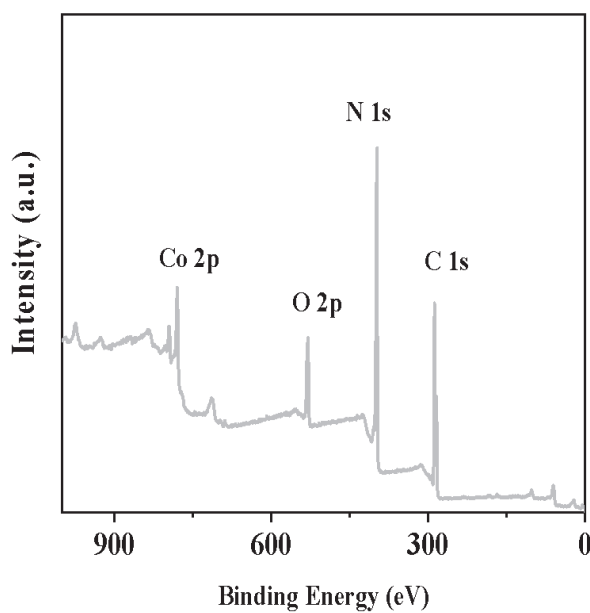


**Fig. S6.** Survey XPS spectrum of  $\text{Co}_3\text{O}_4\text{-NC@C}_3\text{N}_4$ .

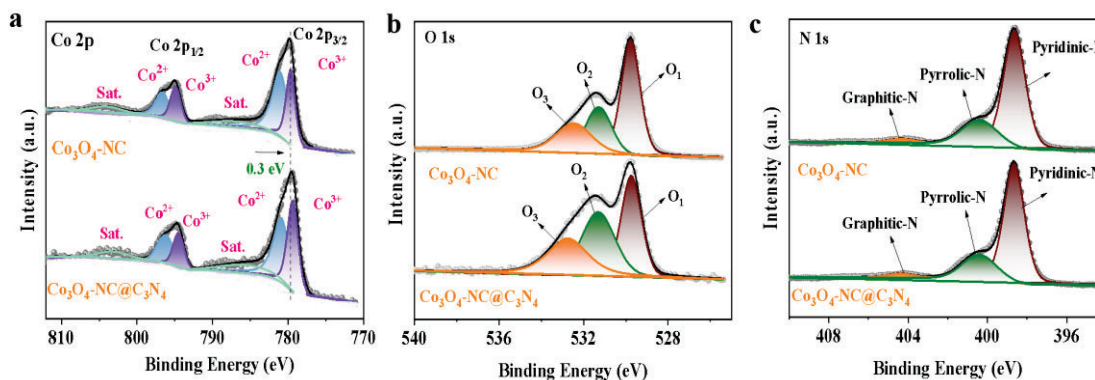


**Fig. S7.** (a-c) High-resolution Co 2p, O 1s and N 1s XPS spectra of Co<sub>3</sub>O<sub>4</sub>-NC@C<sub>3</sub>N<sub>4</sub>, Co<sub>3</sub>O<sub>4</sub>-NC and C<sub>3</sub>N<sub>4</sub>.

The survey XPS spectrum of Co<sub>3</sub>O<sub>4</sub>-NC@C<sub>3</sub>N<sub>4</sub> reveals the presence of Co, O, N, and C, indicating a clean synthesis without major impurities (**Fig. S6**). The O1s XPS spectra of Co<sub>3</sub>O<sub>4</sub>-NC and Co<sub>3</sub>O<sub>4</sub>-NC@C<sub>3</sub>N<sub>4</sub> are illustrated in **Fig. S7b**. The O1 peak at 529.7 eV is assigned to the metal-oxygen bond within Co<sub>3</sub>O<sub>4</sub>, while the peaks at 531.2 eV (O2) and 532.6 eV (O3) correspond to oxygen-containing species and hydroxyl groups adsorbed on the material surface[3-6]. The high-resolution N1s spectra of Co<sub>3</sub>O<sub>4</sub>-NC and Co<sub>3</sub>O<sub>4</sub>-NC@C<sub>3</sub>N<sub>4</sub> can be deconvoluted using three peaks at 398.6, 400.5 and 404.4 eV, corresponding to pyridinic-N, pyrrolic-N and graphitic-N respectively (**Fig. S7c**) [7]. As noted in previous works, pyridinic-N and graphitic-N exhibit superior electron-accepting properties, whereas pyridinic-N and pyrrolic-N can form metal coordination complexes due to the presence of unpaired electrons [8].

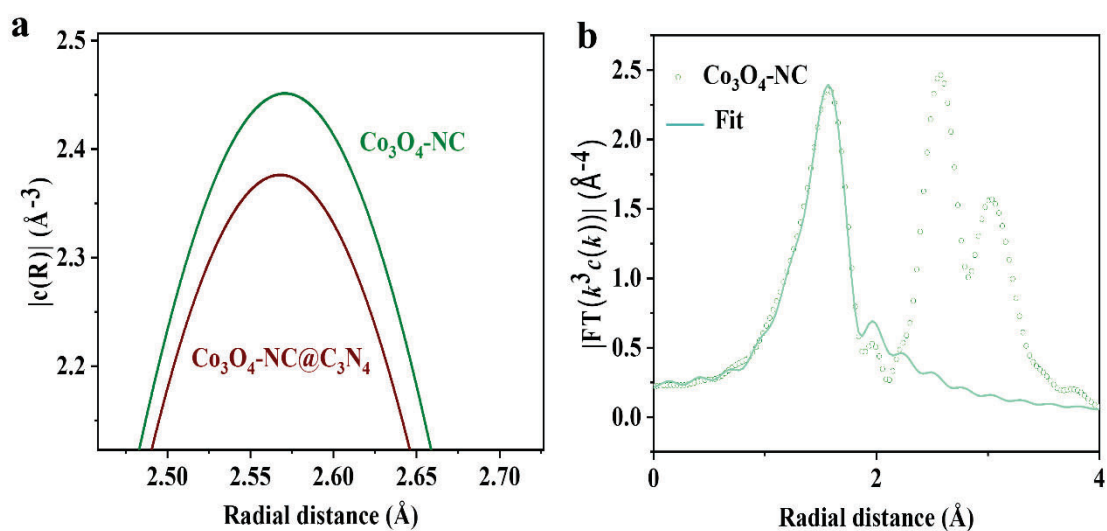


**Fig. S8.** FT-EXAFS (a) plot of  $\text{Co}_3\text{O}_4\text{-NC}$ ,  $\text{Co}_3\text{O}_4\text{-NC@C}_3\text{N}_4$  and FT-EXAFS fitting curves of Co K-edge for  $\text{Co}_3\text{O}_4\text{-NC}$  (b).

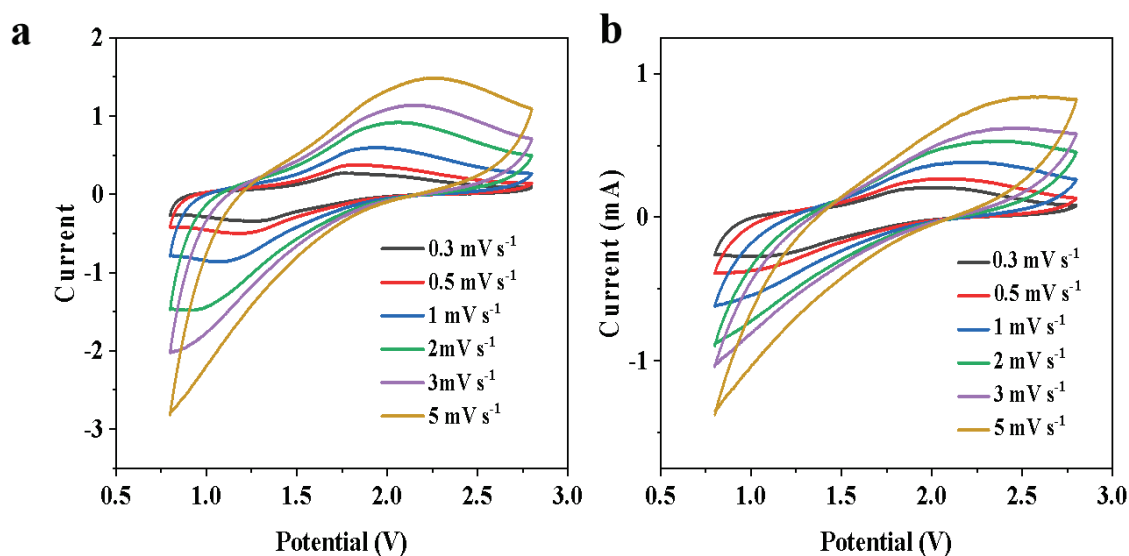


**Fig. S9.** CV curves of  $\text{Co}_3\text{O}_4\text{-NC@C}_3\text{N}_4/\text{S}$  and  $\text{C}_3\text{N}_4/\text{S}$  from 0.8V to 2.8V in the voltage window with scan rate  $0.3\text{mV}^{-1}$  to  $5\text{mV}^{-1}$ .

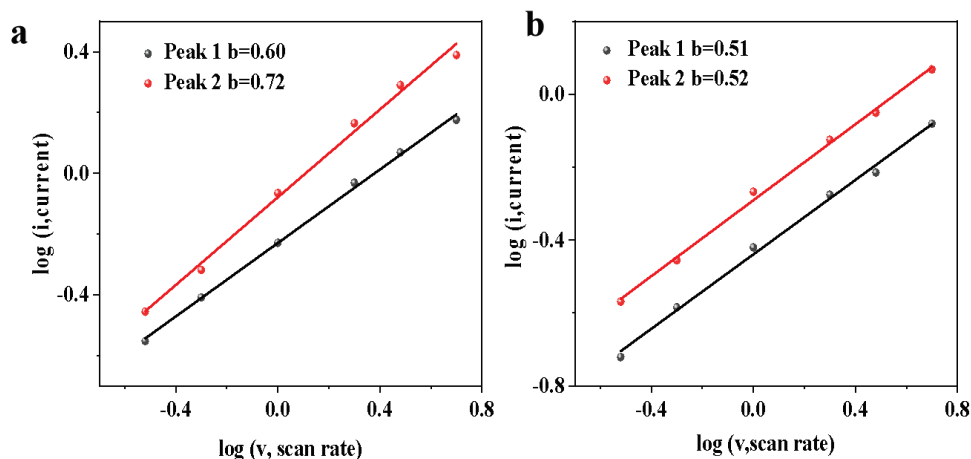


**Fig. S10.** Linear fitting curves ( $\log v / S \log i$ ) for  $\text{Co}_3\text{O}_4\text{-NC@C}_3\text{N}_4/\text{S}$  and  $\text{C}_3\text{N}_4/\text{S}$ .

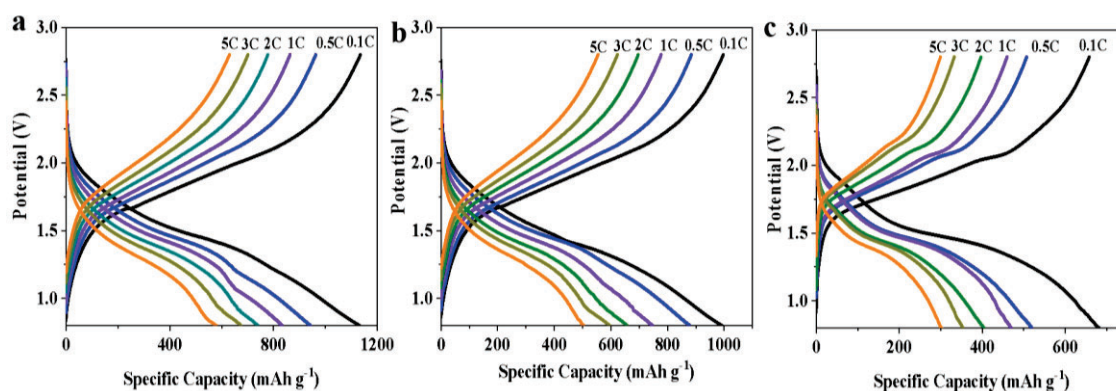


**Fig. S11.** GCD curves of  $\text{Co}_3\text{O}_4\text{-NC@C}_3\text{N}_4/\text{S}$ ,  $\text{Co}_3\text{O}_4\text{-NC/S}$  and  $\text{C}_3\text{N}_4/\text{S}$  at the current rate 0.1C-5C under the potential window is from 0.8 V to 2.8 V.

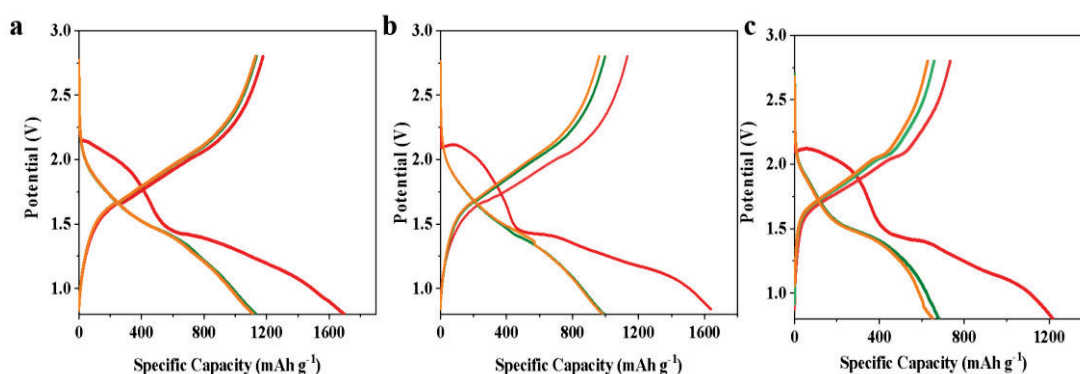


**Fig. S12.** GCD curves of  $\text{Co}_3\text{O}_4\text{-NC@C}_3\text{N}_4/\text{S}$ ,  $\text{Co}_3\text{O}_4\text{-NC/S}$  and  $\text{C}_3\text{N}_4/\text{S}$  (from 1st to 5 th).

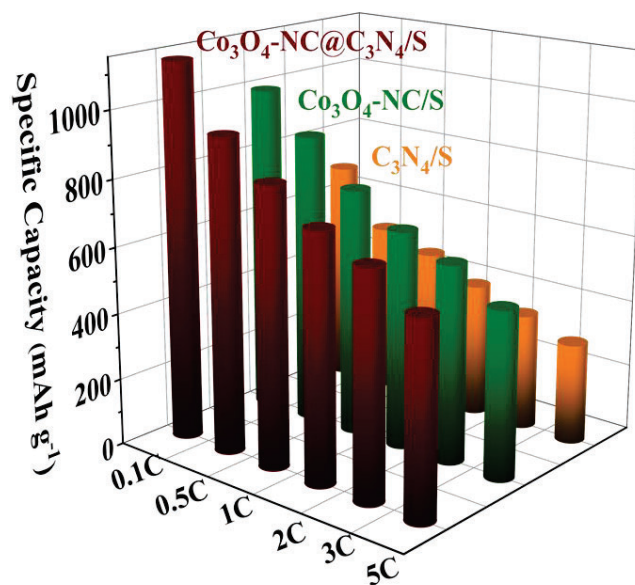


**Fig. S13.** Rate performance of different cathodes (Co<sub>3</sub>O<sub>4</sub>-NC@C<sub>3</sub>N<sub>4</sub>/S, Co<sub>3</sub>O<sub>4</sub>-NC/S and C<sub>3</sub>N<sub>4</sub>/S).

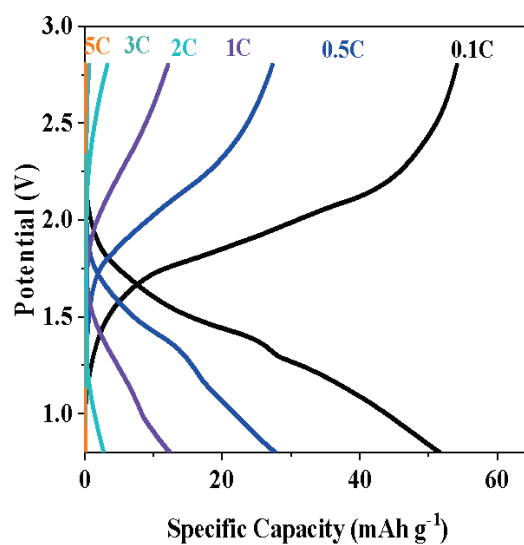


**Fig. S14.** GCD profiles of the pure host (Co<sub>3</sub>O<sub>4</sub>-NC@C<sub>3</sub>N<sub>4</sub>).



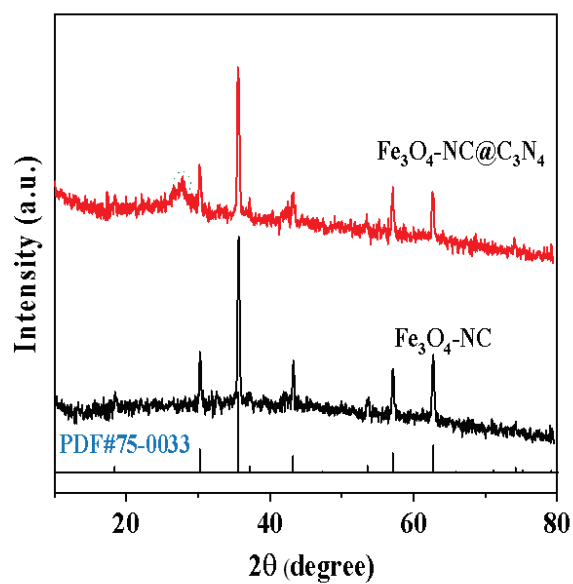


**Fig. S15.** XRD patterns of  $\text{Fe}_3\text{O}_4\text{-NC@C}_3\text{N}_4$  and  $\text{Fe}_3\text{O}_4\text{-NC}$ .

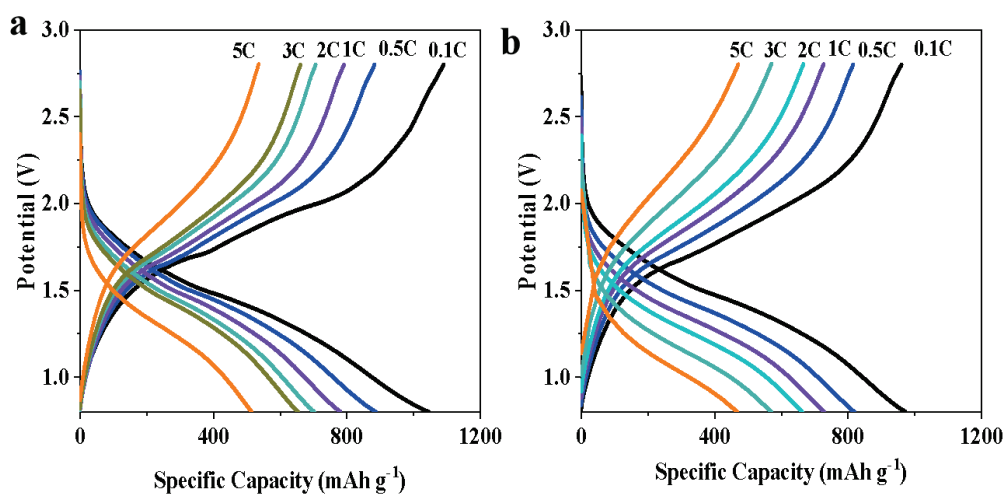


**Fig. S16.** GCD curves of  $\text{Fe}_3\text{O}_4\text{-NC@C}_3\text{N}_4/\text{S}$  (a) and  $\text{Fe}_3\text{O}_4\text{-NC/S}$  (b).

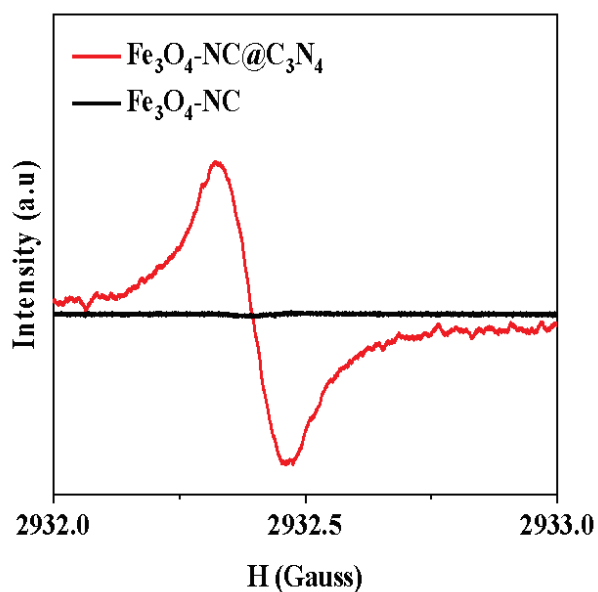


**Fig. S17.** EPR spectra of  $\text{Fe}_3\text{O}_4\text{-NC@C}_3\text{N}_4$  and  $\text{Fe}_3\text{O}_4\text{-NC}$ .

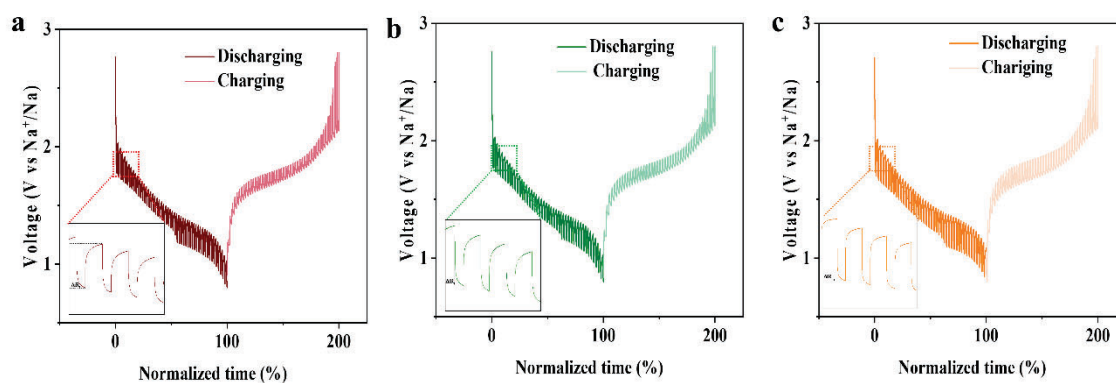


**Fig. S18.** GITT curves for  $\text{Co}_3\text{O}_4\text{-NC@C}_3\text{N}_4/\text{S}$ ,  $\text{Co}_3\text{O}_4\text{-NC/S}$  and  $\text{C}_3\text{N}_4/\text{S}$ .

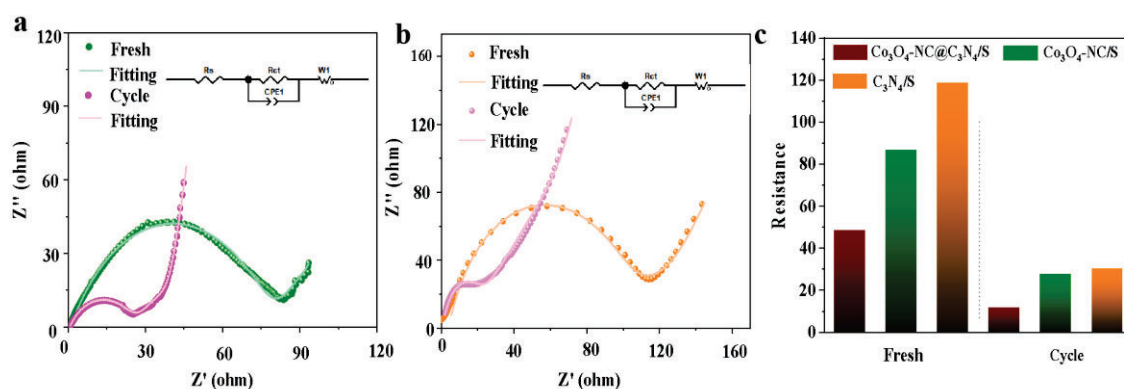


**Fig. S19.** EIS curves and equivalent circuit diagrams of  $\text{Co}_3\text{O}_4\text{-NC/S}$  (a) and  $\text{C}_3\text{N}_4/\text{S}$  (b)  $R_{ct}$  values of different electrodes before and after cycling.

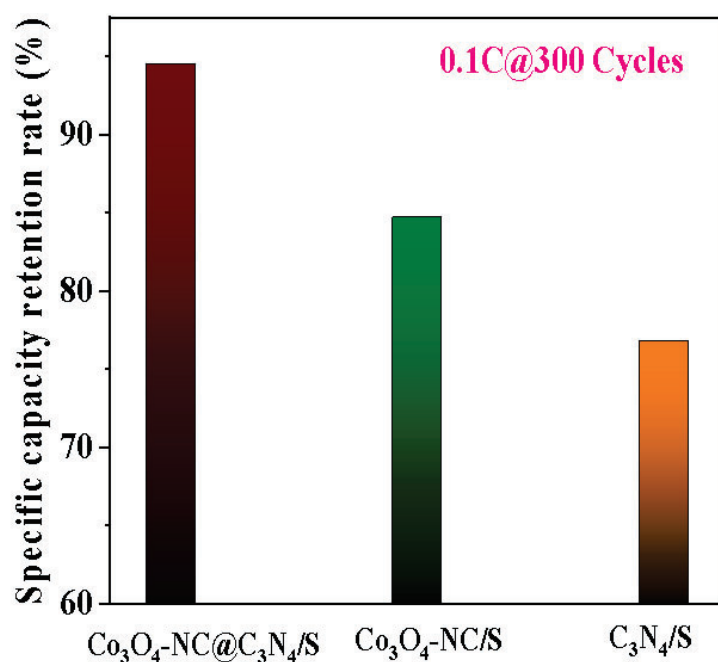


**Fig. S20.** Specific capacity retention rate for  $\text{Co}_3\text{O}_4\text{-NC@C}_3\text{N}_4/\text{S}$ ,  $\text{Co}_3\text{O}_4\text{-NC/S}$  and  $\text{C}_3\text{N}_4/\text{S}$  at 0.1 C current rate after 300 cycles.

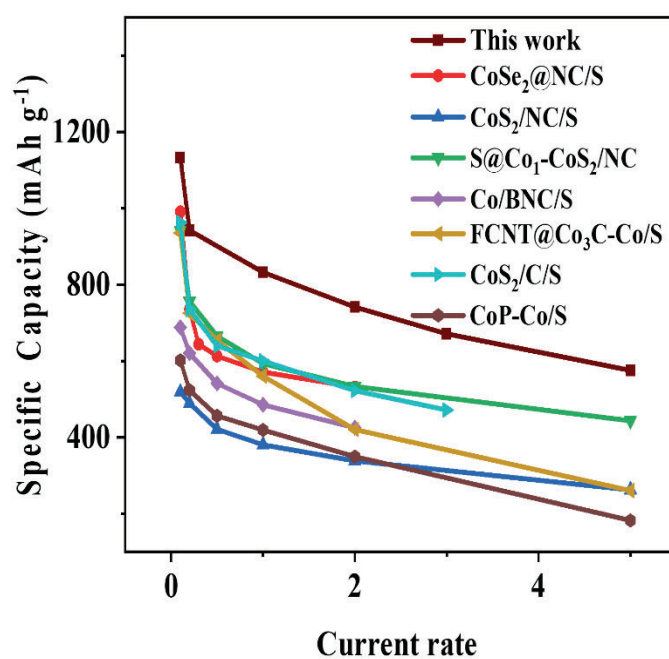


**Fig. S21.** Performance comparison curve between this work and previous works.

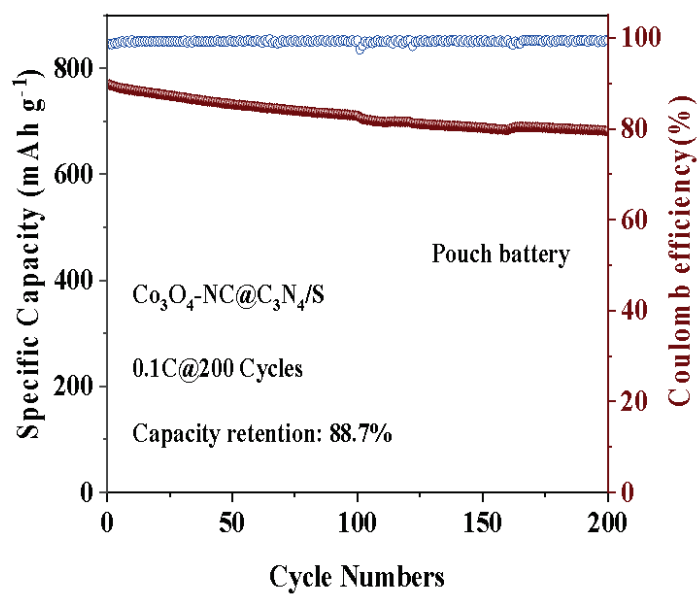


**Fig. S22.** Cycling stability of a pouch cell at 0.1C current rate.

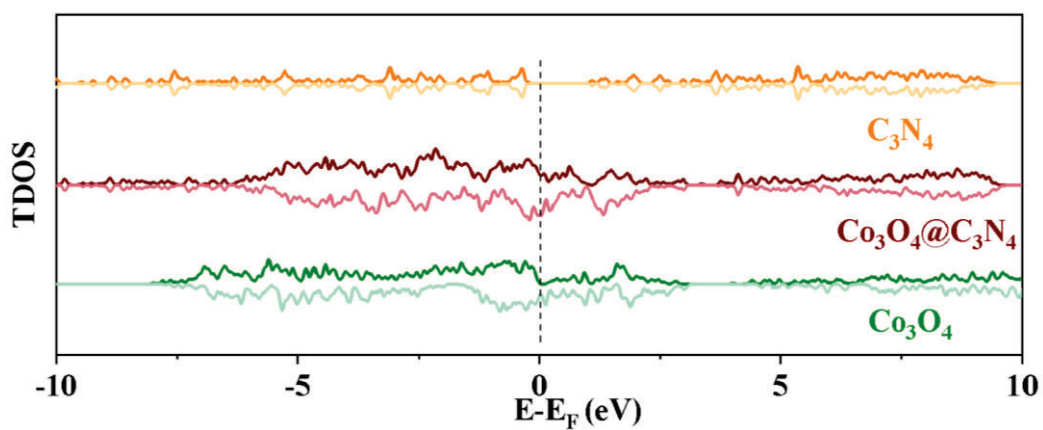


**Fig. S23.** TDOS curves of  $\text{Co}_3\text{O}_4@\text{C}_3\text{N}_4$ ,  $\text{Co}_3\text{O}_4$  and  $\text{C}_3\text{N}_4$ .

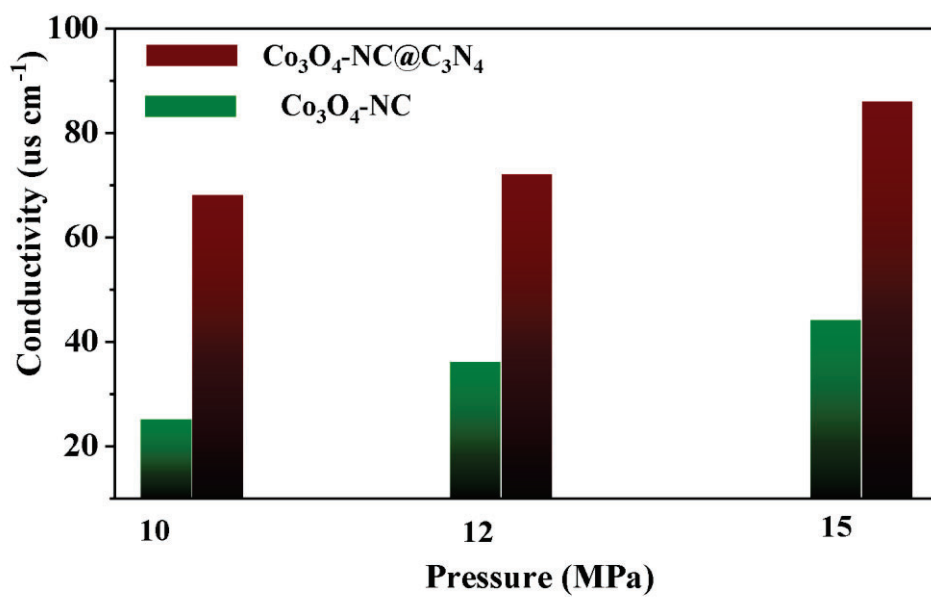


**Fig. S24.** Four-probe electrical conductivity of Co<sub>3</sub>O<sub>4</sub>-NC@C<sub>3</sub>N<sub>4</sub> and Co<sub>3</sub>O<sub>4</sub>-NC.

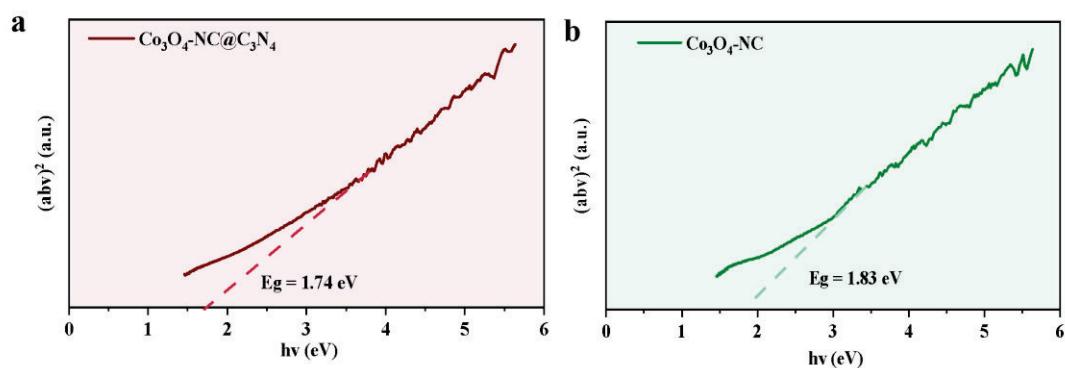


**Fig. S25.** Tauc plots of (a) Co<sub>3</sub>O<sub>4</sub>-NC@C<sub>3</sub>N<sub>4</sub> and (b) Co<sub>3</sub>O<sub>4</sub>-NC.

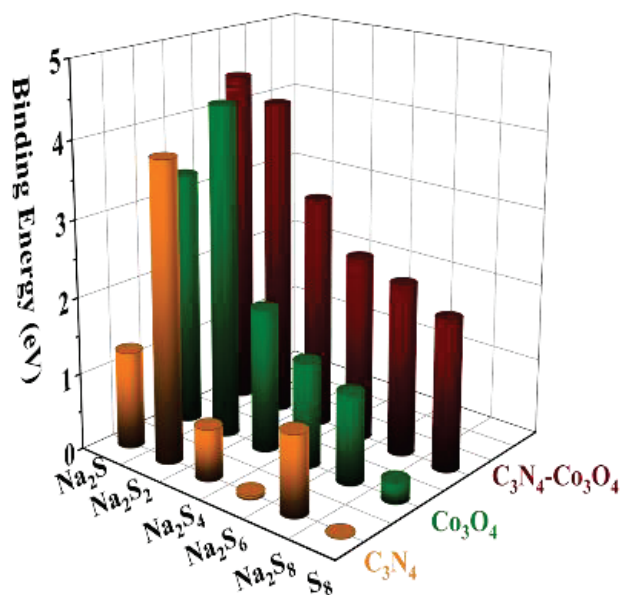


**Fig. S26.** Adsorption energies of C<sub>3</sub>N<sub>4</sub>, Co<sub>3</sub>O<sub>4</sub> and Co<sub>3</sub>O<sub>4</sub>@C<sub>3</sub>N<sub>4</sub> on different sodium polysulfides (S<sub>8</sub>, Na<sub>2</sub>S<sub>8</sub>, Na<sub>2</sub>S<sub>6</sub>, Na<sub>2</sub>S<sub>4</sub>, Na<sub>2</sub>S<sub>2</sub> and Na<sub>2</sub>S)

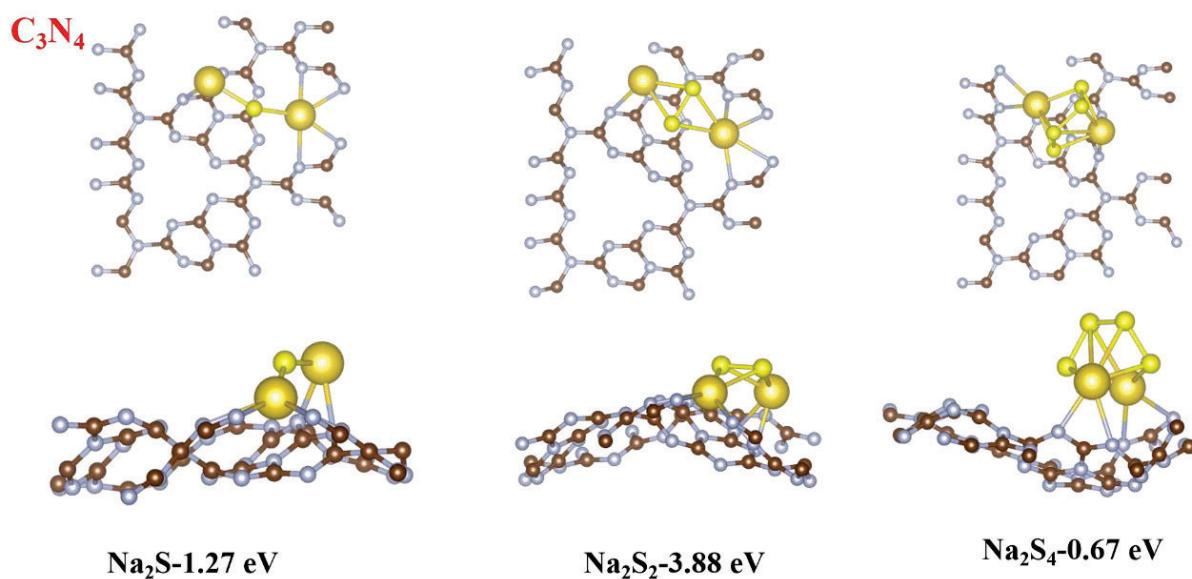


**Fig. S27.** DFT-based optimized geometrical configurations of C<sub>3</sub>N<sub>4</sub> toward Na<sub>2</sub>S, Na<sub>2</sub>S<sub>2</sub> and Na<sub>2</sub>S<sub>4</sub>.



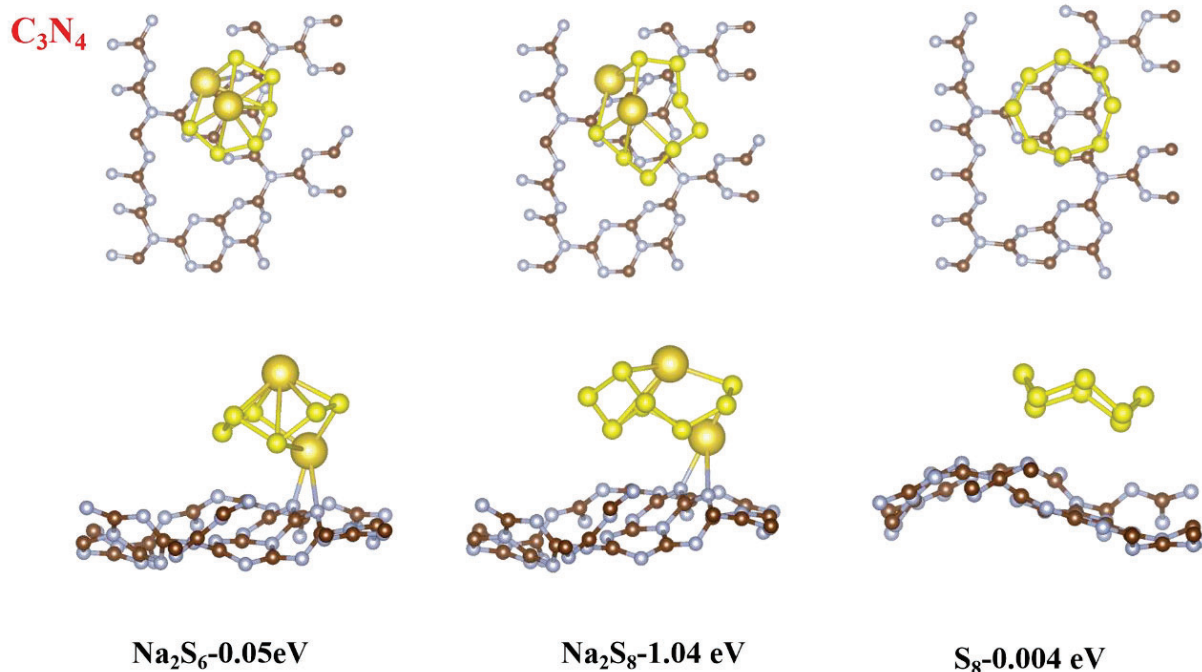


**Fig. S28.** DFT-based optimized geometrical configurations of C<sub>3</sub>N<sub>4</sub> toward Na<sub>2</sub>S<sub>6</sub>, Na<sub>2</sub>S<sub>8</sub> and S<sub>8</sub>.

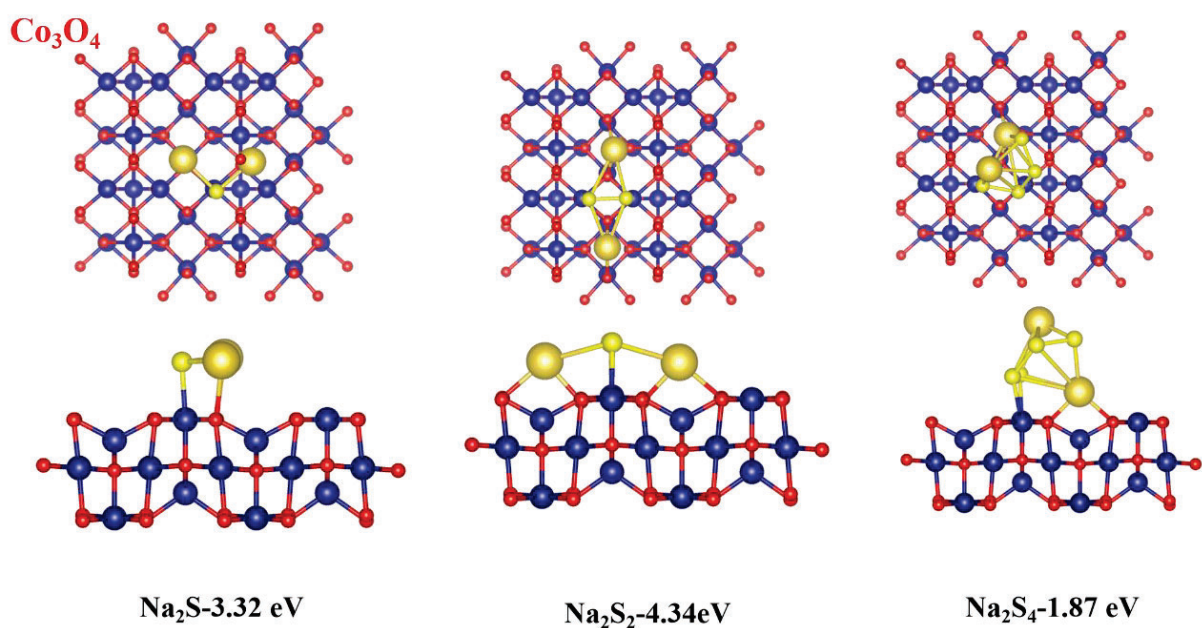


**Fig. S29.** DFT-based optimized geometrical configurations of Co<sub>3</sub>O<sub>4</sub> toward Na<sub>2</sub>S, Na<sub>2</sub>S<sub>2</sub> and Na<sub>2</sub>S<sub>4</sub>.

$\text{Co}_3\text{O}_4$

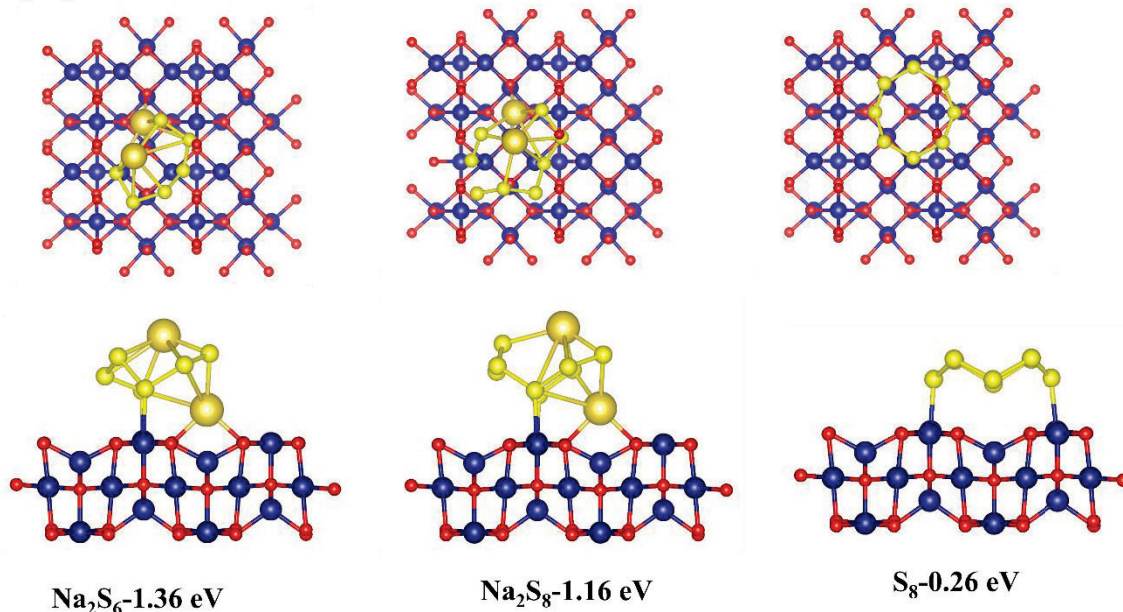


**Fig. S30.** DFT-based optimized geometrical configurations of  $\text{Co}_3\text{O}_4$  toward  $\text{Na}_2\text{S}_6$ ,  $\text{Na}_2\text{S}_8$  and  $\text{S}_8$ .

$\text{Co}_3\text{O}_4@\text{C}_3\text{N}_4$

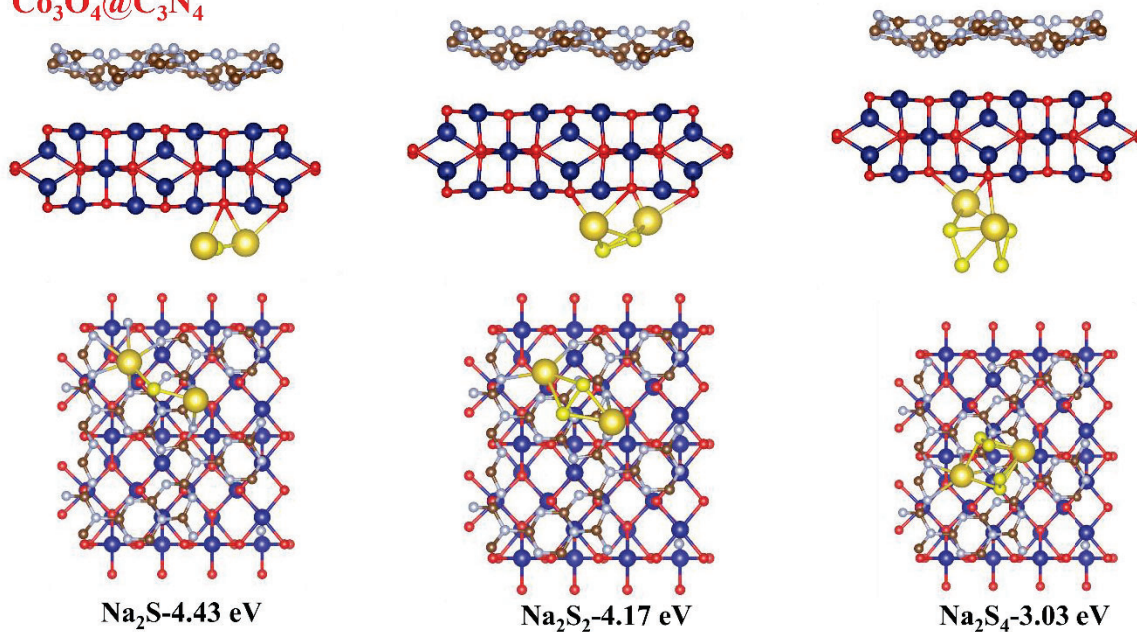


**Fig. S31.** DFT-based optimized geometrical configurations of  $\text{Co}_3\text{O}_4@\text{C}_3\text{N}_4$  toward  $\text{Na}_2\text{S}$ ,  $\text{Na}_2\text{S}_2$  and  $\text{Na}_2\text{S}_4$ .

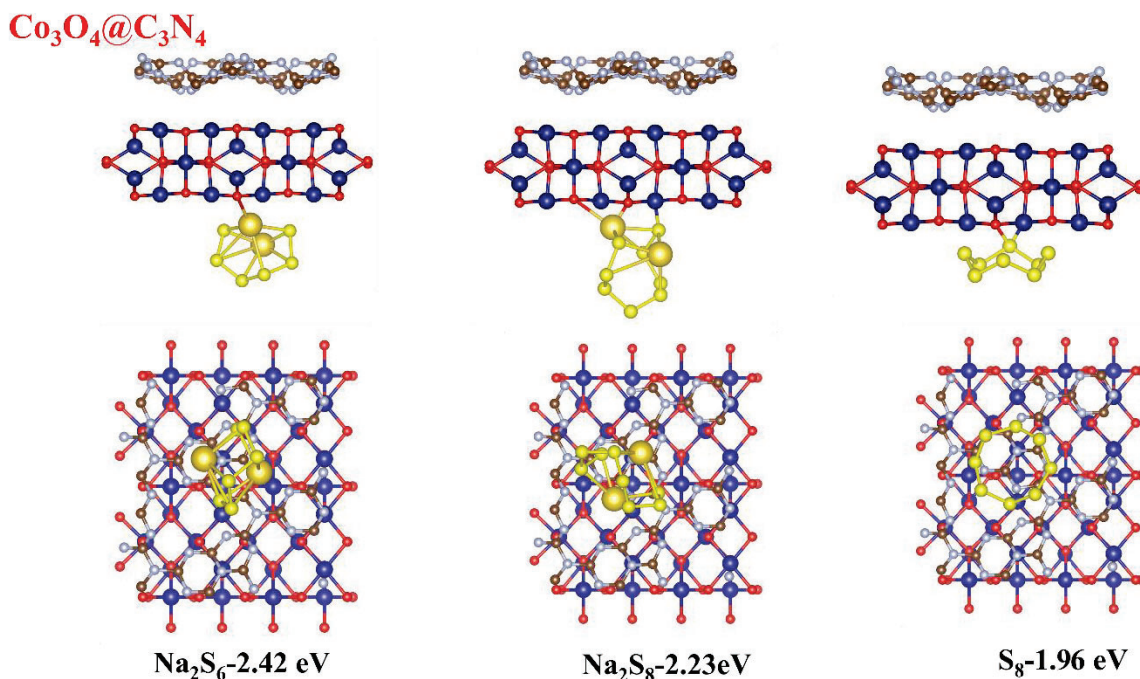


**Fig. S32.** DFT-based optimized geometrical configurations of  $\text{Co}_3\text{O}_4@\text{C}_3\text{N}_4$  toward  $\text{Na}_2\text{S}_6$ ,  $\text{Na}_2\text{S}_8$  and  $\text{S}_8$ .

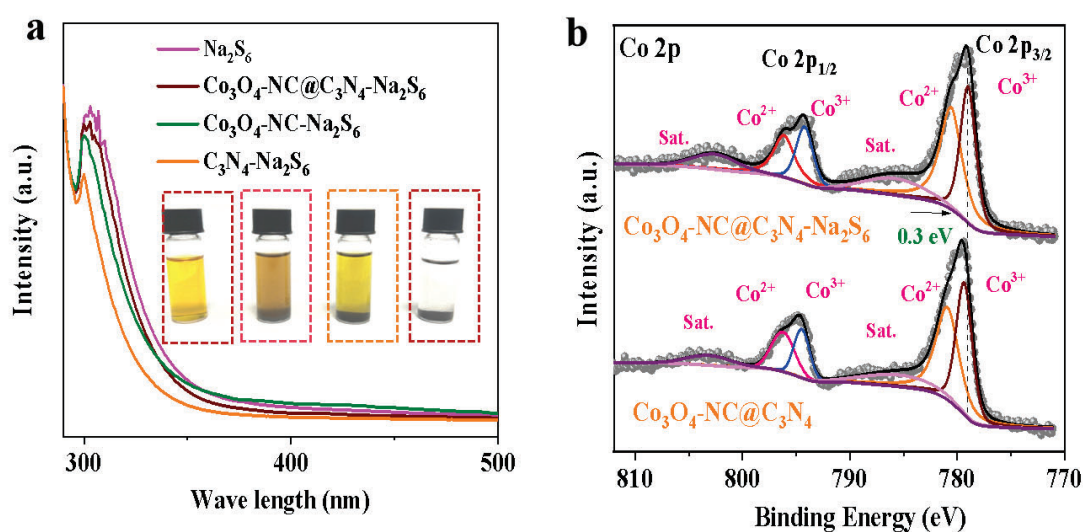


**Fig. S33.** (a) Static adsorption of different host materials ( $\text{Co}_3\text{O}_4\text{-NC@C}_3\text{N}_4$ ,  $\text{Co}_3\text{O}_4\text{-NC}$ ,  $\text{C}_3\text{N}_4$ ). (b) The XPS curves of  $\text{Co}_3\text{O}_4\text{-NC@C}_3\text{N}_4$  after and Adsorption energies of  $\text{C}_3\text{N}_4$ ,  $\text{Co}_3\text{O}_4$  and  $\text{C}_3\text{N}_4\text{-Co}_3\text{O}_4$  on different sodium polysulfides ( $\text{S}_8$ ,  $\text{Na}_2\text{S}_8$ ,  $\text{Na}_2\text{S}_6$ ,  $\text{Na}_2\text{S}_4$ ,  $\text{Na}_2\text{S}_2$  and  $\text{Na}_2\text{S}$ ).

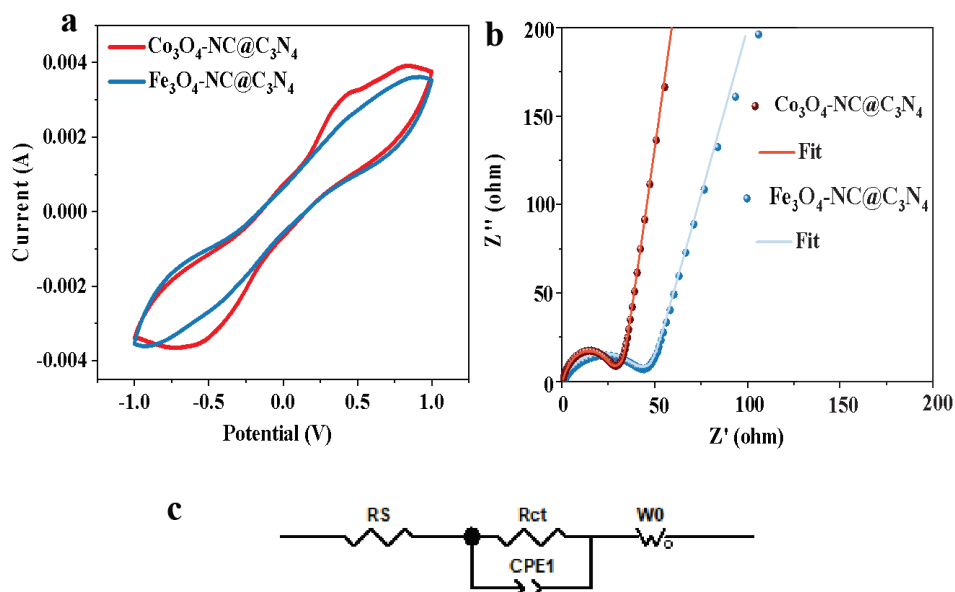


**Fig. S34.** (a) CV profiles, (b) EIS spectra, and (c) equivalent circuit for symmetrical cells assembled with  $\text{Co}_3\text{O}_4\text{-NC@C}_3\text{N}_4$  and  $\text{Fe}_3\text{O}_4\text{-NC@C}_3\text{N}_4$ .

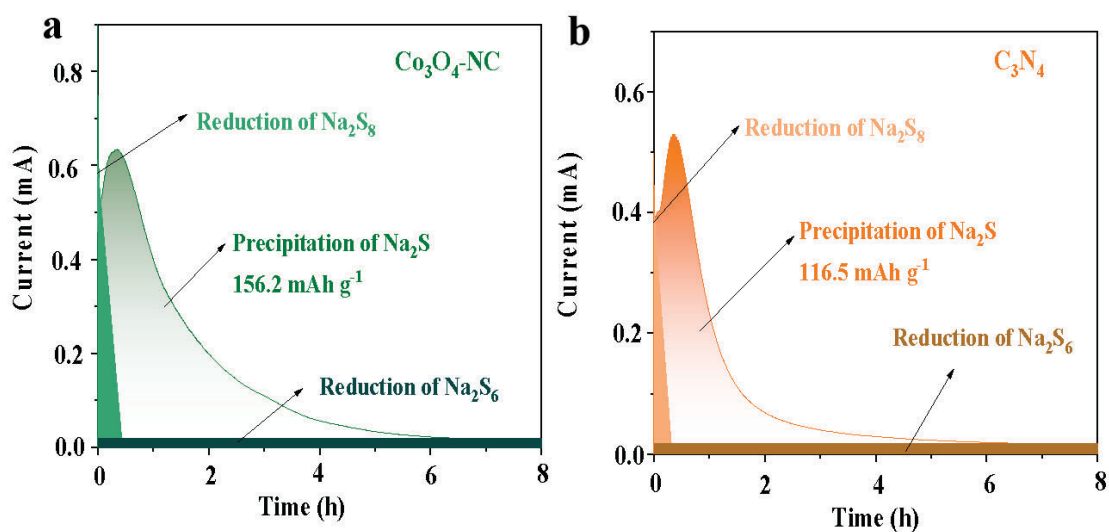


**Fig. S35.**  $\text{Na}_2\text{S}$  deposition experiment test for (a)  $\text{Co}_3\text{O}_4\text{-NC}$  and (b)  $\text{C}_3\text{N}_4$ .



**Table S1** Content ratios of different elements in Co<sub>3</sub>O<sub>4</sub>-NC based on XPS analysis.

Element	Atomic Ratio (%)	Weight Ratio (%)
C	33.8	15
Co	28.8	62.9
N	1.5	0.8
O	35.9	21.3

**Table S2.** Specific surface area of Co<sub>3</sub>O<sub>4</sub>-NC@C<sub>3</sub>N<sub>4</sub> and Co<sub>3</sub>O<sub>4</sub>-NC.

Samples	Specific surface area (m <sup>2</sup> g <sup>-1</sup> )
C <sub>3</sub> N <sub>4</sub> -Co <sub>3</sub> O <sub>4</sub> @NC	64.9
Co <sub>3</sub> O <sub>4</sub> @NC	52.6

**Table S3.** Standard 3 shells Fourier analysis results for Co<sub>3</sub>O<sub>4</sub>-NC samples.

Bonding	R(Å)	R error	N	N error	σ <sup>2</sup>	σ <sup>2</sup> error
	(Å)					
Co-O	1.9151	0.0056	4.730	0.254	0.0033	0.0007
Co-O-Co	2.862	0.0078	3.256	0.592	0.0033	0.0009
Another Co-O-Co	3.344	0.0096	8.234	1.508	0.0070	0.0013

**Table S4.** Standard 3 shells Fourier analysis results for Co<sub>3</sub>O<sub>4</sub>-NC@C<sub>3</sub>N<sub>4</sub> samples.

Bonding	R(Å)	R error	N	N error	σ <sup>2</sup>	σ <sup>2</sup> error
	(Å)					
Co-O	1.9165	0.0057	4.862	0.242	0.0031	0.0006
Co-O-Co	2.8639	0.0072	3.881	0.591	0.0037	0.0008
Another Co-O-Co	3.3469	0.0092	8.095	1.423	0.0069	0.0012

**Table S5.** Comparison of the specific capacity at a current density of 0.1C for Co<sub>3</sub>O<sub>4</sub>-NC@C<sub>3</sub>N<sub>4</sub>/S, Co<sub>3</sub>O<sub>4</sub>-NC/S and C<sub>3</sub>N<sub>4</sub>/S.

Samples	Specific capacity (mAh g <sup>-1</sup> )
Co <sub>3</sub> O <sub>4</sub> -NC@C <sub>3</sub> N <sub>4</sub> /S	1113
Co <sub>3</sub> O <sub>4</sub> -NC/S	995
C <sub>3</sub> N <sub>4</sub> /S	686

**Table S6.** Electrochemical performance comparisons of Co<sub>3</sub>O<sub>4</sub>-NC@C<sub>3</sub>N<sub>4</sub>/S with similar materials reported previously.

Samples	Specific capacitance (mAh /g)	Current Density	Ref.
CoSe <sub>2</sub> @NC/S[9]	990.4	0.1C	[9]
CoS <sub>2</sub> @NC/S[10]	518	0.1 A g <sup>-1</sup>	[10]
S@Co <sub>1</sub> -CoS <sub>2</sub> /NC[11]	941	0.1 A g <sup>-1</sup>	[11]
Co/BNC/S[12]	688	0.1 C	[12]
FCNT@Co <sub>3</sub> C-Co/S[13]	935	0.1 C	[13]
CoS <sub>2</sub> @NC/S[14]	962	0.1 A g <sup>-1</sup>	[14]
CoP-Co/S[15]	601	0.1 A g <sup>-1</sup>	[15]
C <sub>3</sub> N <sub>4</sub> -Co <sub>3</sub> O <sub>4</sub> @NC	1133	0.1 C	This work



**Table S7.** Cycle performance comparisons of Co<sub>3</sub>O<sub>4</sub>-NC@C<sub>3</sub>N<sub>4</sub>/S with similar materials reported previously.

Samples	Capacity loss per cycle (%)	Current Density	Ref.
S@CNTs/Co@NC-0.25[16]	0.068	1C	[16]
S/CoS <sub>2</sub> -CoSe <sub>2</sub> @CNFs[17]	0.073	1C	[17]
ZCS@S[18]	0.028	1 A g <sup>-1</sup>	[18]
NCCS@S[9]	0.044	1C	[9]
Co-NMCN[19]	0.068	0.5C	[19]
S@Co/C/rGO[5]	0.053	0.5C	[5]
FCNT@Co <sub>3</sub> C-Co/S[13]	0.042	2C	[13]
<b>Co<sub>3</sub>O<sub>4</sub>@-NC@ C<sub>3</sub>N<sub>4</sub>/S</b>	<b>1133</b>	<b>0.1 C</b>	<b>This work</b>

## References

- [1] I.A. Pašti, A. Jovanović, A.S. Dobrota, S.V. Mentus, B. Johansson, N.V. Skorodumova, Atomic adsorption on pristine graphene along the Periodic Table of Elements – From PBE to non-local functionals, *Appl. Surf. Sci.*, 436 (2018) 433-440.
- [2] S. Maintz, V.L. Deringer, A.L. Tchougréeff, R. Dronskowski, Analytic projection from plane-wave and PAW wavefunctions and application to chemical-bonding analysis in solids, *J Compu Chem*, 34 (2013) 2557-2567.
- [3] C.Y. Zhang, X. Lu, X. Han, J. Yu, C. Zhang, C. Huang, L. Balcells, A.G. Manjón, J. Jacas Biendicho, J. Li, J. Arbiol, G. Sun, J.Y. Zhou, A. Cabot, Identifying the Role of the Cationic Geometric Configuration in Spinel Catalysts for Polysulfide Conversion in Sodium–Sulfur Batteries, *J. Am. Chem. Soc.*, 145 (2023) 18992-19004.
- [4] C. Huang, S. Lv, A. Gao, J. Ling, F. Yi, J. Hao, M. Wang, Z. Luo, D. Shu, Boosting the energy density of supercapacitors by designing both hollow NiO nanoparticles/nitrogen-doped carbon cathode and nitrogen-doped carbon anode from the same precursor, *Chem. Eng. J.*, 431 (2022) 134083.
- [5] Q. Ma, G. Du, B. Guo, W. Tang, Y. Li, M. Xu, C. Li, Carbon-wrapped cobalt nanoparticles on graphene aerogel for solid-state room-temperature sodium-sulfur batteries, *Chem. Eng. J.*, 388 (2020) 124210.
- [6] L. Yang, R. He, X. Wang, T. Yang, T. Zhang, Y. Zuo, X. Lu, Z. Liang, J. Li, J. Arbiol, P.R. Martínez-Alanis, X. Qi, A. Cabot, Self-supported NiO/CuO electrodes to boost urea oxidation in direct urea fuel cells, *Nano Energy*, 115 (2023) 108714.
- [7] W. Tang, K. Teng, W. Guo, F. Gu, B. Li, R. Qi, R. Liu, Y. Lin, M. Wu, Y. Chen, Defect-Engineered Co<sub>3</sub>O<sub>4</sub>@Nitrogen-Deficient Graphitic Carbon Nitride as an Efficient Bifunctional Electrocatalyst for High-Performance Metal-Air Batteries, *small*, 18 (2022) 2202194.
- [8] C. Huang, J. Yu, C. Li, Z. Cui, C. Zhang, C. Zhang, B. Nan, J. Li, J. Arbiol, A. Cabot, Combined Defect and Heterojunction Engineering in ZnTe/CoTe<sub>2</sub>@NC Sulfur Hosts Toward

- Robust Lithium–Sulfur Batteries, *Adv. Funct. Mater.*, 33 (2023) 2305624.
- [9] H. Wang, Y. Qi, F. Xiao, P. Liu, Y. Li, S.-j. Bao, M. Xu, Tessellated N-doped carbon/CoSe<sub>2</sub> as trap-catalyst sulfur hosts for room-temperature sodium–sulfur batteries, *Inorg. Chem. Front.*, 9 (2022) 1743-1751.
- [10] F. Xiao, H. Wang, T. Yao, X. Zhao, X. Yang, D.Y.W. Yu, A.L. Rogach, MOF-Derived CoS<sub>2</sub>/N-Doped Carbon Composite to Induce Short-Chain Sulfur Molecule Generation for Enhanced Sodium–Sulfur Battery Performance, *ACS Appl. Mater. Interfaces*, 13 (2021) 18010-18020.
- [11] Y. Lei, C. Wu, X. Lu, W. Hua, S. Li, Y. Liang, H. Liu, W.-H. Lai, Q. Gu, X. Cai, N. Wang, Y.-X. Wang, S.-L. Chou, H.-K. Liu, G. Wang, S.-X. Dou, Streamline Sulfur Redox Reactions to Achieve Efficient Room-Temperature Sodium–Sulfur Batteries, *Angew. Chem. Int. Ed.*, 61 (2022) e202200384.
- [12] K. Tang, X. Peng, Z. Zhang, G. Li, J. Wang, Y. Wang, C. Chen, N. Zhang, X. Xie, Z. Wu, A Highly Dispersed Cobalt Electrocatalyst with Electron-Deficient Centers Induced by Boron toward Enhanced Adsorption and Electrocatalysis for Room-Temperature Sodium–Sulfur Batteries, *Small*, 20 (2024) 2311151.
- [13] G. Qin, Y. Liu, P. Han, S. Cao, X. Guo, Z. Guo, High performance room temperature Na-S batteries based on FCNT modified Co<sub>3</sub>C-Co nanocubes, *Chem. Eng. J.*, 396 (2020) 125295.
- [14] Q. Ma, J. Ai, H. Zou, H. He, Z. Li, J. Mujtaba, Z. Fang, Gallate-MOF derived CoS<sub>2</sub>/C composites as an accelerated catalyst for room-temperature sodium–sulfur batteries, *ChemComm*, 58 (2022) 13612-13615.
- [15] Z. Yan, Y. Liang, W. Hua, X.-G. Zhang, W. Lai, Z. Hu, W. Wang, J. Peng, S. Indris, Y. Wang, S.-L. Chou, H. Liu, S.-X. Dou, Multiregion Janus-Featured Cobalt Phosphide-Cobalt Composite for Highly Reversible Room-Temperature Sodium-Sulfur Batteries, *ACS Nano*, 14 (2020) 10284-10293.
- [16] J. Mou, Y. Li, T. Liu, W. Zhang, M. Li, Y. Xu, L. Zhong, W. Pan, C. Yang, J. Huang, M. Liu, Metal–Organic Frameworks-Derived Nitrogen-Doped Porous Carbon Nanocubes with Embedded Co Nanoparticles as Efficient Sulfur Immobilizers for Room Temperature Sodium–Sulfur Batteries, *Small Methods*, 5 (2021) 2100455.
- [17] J. Wu, Z. Yu, Y. Yao, L. Wang, Y. Wu, X. Cheng, Z. Ali, Y. Yu, Bifunctional Catalyst for Liquid–Solid Redox Conversion in Room-Temperature Sodium–Sulfur Batteries, *Small Structures*, 3 (2022) 2200020.
- [18] H. Liu, W. Pei, W.-H. Lai, Z. Yan, H. Yang, Y. Lei, Y.-X. Wang, Q. Gu, S. Zhou, S. Chou, H.K. Liu, S.X. Dou, Electrocatalyzing S Cathodes via Multisulfiphilic Sites for Superior Room-Temperature Sodium–Sulfur Batteries, *ACS Nano*, 14 (2020) 7259-7268.
- [19] T. Mei, X. Li, X. Lin, L. Bai, M. Xu, Y. Qi, Cobalt Catalytic Regulation Engineering in Room-Temperature Sodium–Sulfur Batteries: Facilitating Rapid Polysulfides Conversion and Delicate Na<sub>2</sub>S Nucleation, *Adv. Funct. Mater.*, (2024) 2418126.

# **Chapter 8**

## **Conclusions and Future Work**

## 8. Conclusions and future work

MSBs have gained significant attention as a promising alternative to conventional lithium-ion batteries due to their high theoretical energy density, cost-effectiveness, and environmental benefits. These batteries offer a substantial increase in energy storage capacity compared to traditional systems, making them a compelling choice for applications that require high energy densities, such as electric vehicles (EVs), grid energy storage, and portable electronics.

The fundamental advantage of MSBs lies in their use of sulfur as the cathode material. Sulfur is abundant, low-cost, and environmentally benign, providing a significant advantage over the more expensive and less abundant materials used in conventional lithium/sodium-ion batteries. The theoretical specific capacity of sulfur is approximately  $1675 \text{ mAh g}^{-1}$ , and the theoretical energy density of a Li-S battery can reach up to  $2600 \text{ Wh kg}^{-1}$ , which is significantly higher than that of traditional lithium/sodium-ion batteries. This high energy density is attributed to the conversion reaction mechanism of sulfur, where sulfur is reduced to lithium/sodium sulfides ( $\text{Li}/\text{Na}_2\text{S}_n$ ) during discharge and oxidized back to sulfur during charge.

However, despite their potential, MSBs face several challenges that have hindered their widespread adoption. One major issue is the "shuttle effect," where intermediate polysulfides dissolve into the electrolyte and migrate between the electrodes, leading to a loss of active material and a decrease in cycle life. Additionally, the poor conductivity of sulfur and its large volume change during cycling can negatively impact the battery's performance and longevity.

To address these challenges, extensive research has been directed toward improving the performance of MSBs through various strategies. These include enhancing sulfur conductivity via composite materials, developing advanced electrolytes that mitigate polysulfide dissolution, and designing novel electrode architectures to accommodate volume changes and improve overall stability.

In this thesis, we propose various solutions to address the limitations of host materials in MSBs for practical applications. These strategies include the design of heterostructures, the implementation of defect engineering, the introduction of doping techniques, and the creation

of lattice distortion structures. By employing these approaches, we aim to enhance the electrochemical performance of MSBs, improving their conductivity, catalytic activity, and overall stability, thereby overcoming the challenges faced in real-world applications.

The main conclusions of the thesis are as follows:

1. A sulfur host material based on NC coated with a small amount of a TMT catalyst is proposed to overcome these limitations. The properties of the sulfur redox catalyst are tuned by adjusting the anion vacancy concentration and engineering a ZnTe/CoTe<sub>2</sub> heterostructures. Theoretical calculations and experimental data demonstrate that tellurium vacancies enhance the adsorption of LiPSs, while the formed TMT/TMT and TMT/C heterostructures as well as the overall architecture of the composite simultaneously provide high Li<sup>+</sup> diffusion and fast electron transport. As a result, v-ZnTe/CoTe<sub>2</sub>@NC/S sulfur cathodes show excellent initial capacities up to 1608 mA·h·g<sup>-1</sup> at 0.1C and stable cycling with an average capacity decay rate of 0.022% per cycle at 1C during 500 cycles. Even at a high sulfur loading of 5.4 mg·cm<sup>-2</sup>, a high capacity of 1273 mA·h·g<sup>-1</sup> at 0.1C is retained, and when reducing the electrolyte to 7.5 μL·mg<sup>-1</sup>, v-ZnTe/CoTe<sub>2</sub>@NC/S still maintains a capacity of 890.8 mA·h·g<sup>-1</sup> after 100 cycles at 0.1C.
2. Heterostructured NiS<sub>2</sub>/NiSe<sub>2</sub> particles wrapped within NC spheres and displaying a hollow architecture were produced from a Ni-MOF precursor. Magnetic measurements and computational results show the heterostructure to be characterized by Ni<sup>3+</sup> in a high electronic spin state. NiS<sub>2</sub>/NiSe<sub>2</sub>@C exhibits orbital spin splitting and possesses a high spin configuration with more unpaired electrons. This high spin state regulates the electronic structure resulting in excellent binding strength and catalytic ability toward LiPS. The porous hollow structure not only effectively confines sulfur, but also provides additional buffer space for the electrochemical reaction. NiS<sub>2</sub>/NiSe<sub>2</sub>@NC is used as the host material in the sulfur cathode of LSBs, displaying excellent electrochemical performance. This excellent performance includes a high charge-discharge capacity, excellent rate capability, and long cycle life. This work not only demonstrates the catalytic properties of NiS<sub>2</sub>/NiSe<sub>2</sub> but also exemplifies the effect of spin polarization in electrocatalytic reactions.

3. Both experimental results and theoretical calculations confirmed the effectiveness of anionic doping in  $\text{Bi}_2\text{Se}_3$  for enhancing the performance of LSBs. Specifically, in Te-doped  $\text{Bi}_2\text{Se}_3$ , Te occupies the Se sites. Due to its larger atomic size, it generates Se vacancies, which leads to an increased concentration of free carriers in the electrode material. Additionally, the increase of unpaired Bi cations provided additional active sites for LiPS adsorption and catalytic reactions, thereby promoting sulfur conversion kinetics. Simultaneously, Te doping induces lattice distortion within the  $\text{Bi}_2\text{Se}_3$  material, causing a shift in the positive/negative charge center of the unit cell toward the negative direction. This phenomenon generates an intrinsic electric field, facilitating the transfer of charges within the cathode material. By leveraging doping, defects, and lattice distortion engineering, the  $\text{Te-Bi}_2\text{Se}_{3-x}\text{@C}$  cathode exhibited outstanding electrochemical performance, including high specific capacity (up to  $1508 \text{ mAh}\cdot\text{g}^{-1}$  at  $0.1\text{C}$ ), excellent rate capability, and prolonged cycle stability, even under high sulfur loading and lean electrolyte conditions.

4. The P-N heterostructured sulfur host material based on the combination of hollow tubular  $\text{C}_3\text{N}_4$  and  $\text{Co}_3\text{O}_4$  nanoparticles was produced. When the two materials are combined, electrons are transferred from the N atom in  $\text{C}_3\text{N}_4$  to the Co atom in  $\text{Co}_3\text{O}_4$ , resulting in the generation of additional unpaired electrons in the 3d orbital for  $\text{Co}^{3+}$ . This electron transfer leads to two significant outcomes: Firstly, it induces a change in the spin state of the Co ion. Secondly, the generated unpaired electrons facilitate transfer between the host material and the polysulfides, thereby significantly improving the polysulfides' catalytic and adsorption performance. In addition, the hollow tubular  $\text{C}_3\text{N}_4$  provides enough space to alleviate the volume change of  $\text{Na}^+$  diffusion during the reaction and provide ion transport channels. Therefore, the cathode  $\text{Co}_3\text{O}_4\text{-NC@C}_3\text{N}_4/\text{S}$  exhibits excellent rate capability and long cycle life in RT-SSBs.  $\text{Co}_3\text{O}_4\text{-NC@C}_3\text{N}_4/\text{S}$  also shows satisfactory electrochemical performance even at high load and pouch cell levels.

In summary, the four studies above have addressed key challenges in MSBs by introducing heterostructures, vacancy engineering, doping strategies, and P-N heterojunctions. These innovative approaches have significantly enhanced the adsorption and catalytic processes within MSBs. Consequently, the host materials developed in these studies exhibit exceptional



electrochemical performance, characterized by high specific capacity and long cycle life. Notably, these materials maintain outstanding stability even under high-loading and low-electrolyte conditions, further demonstrating their practical applicability.

## **Future work**

Addressing the shuttle effect of polysulfides in MSBs is crucial for enhancing their electrical performance. To achieve this goal, it is imperative to devise strategies for synthesizing novel host materials that facilitate the conversion of soluble polysulfides into insoluble  $\text{Li}_2\text{S}/\text{Li}_2\text{S}_2$ . This entails leveraging the catalytic properties of TMCs while capitalizing on the high specific surface area to physically confine polysulfides. Moving forward, I am committed to exploring new approaches for designing host materials tailored for use in MSBs. By integrating catalytic functionality with effective polysulfide confinement, we can unlock the full potential of these batteries and contribute to advancements in energy storage technology.

1. **Advanced Host Materials:** Further research should focus on the development of innovative host materials with enhanced properties for MSBs. This includes materials with improved conductivity, higher specific surface area, and enhanced catalytic activity for polysulfide conversion. Exploring new synthesis methods and novel material compositions could lead to host materials that effectively mitigate the shuttle effect and improve overall battery performance.

2. **Nanostructured Electrodes:** Nanostructured electrode architectures offer promising opportunities for enhancing the electrochemical performance of MSBs. Future research should explore the design and fabrication of nanostructured electrodes with tailored morphologies and compositions to optimize sulfur loading, promote ion diffusion, and accommodate volume changes during cycling. Additionally, investigating novel electrode architectures, such as 3D frameworks and hierarchical structures, could further improve battery performance and stability.

3. **Advanced Characterization Techniques:** Advancements in characterization techniques, such as in-situ and operando spectroscopy, microscopy, and diffraction methods, are critical for gaining deeper insights into the fundamental mechanisms governing MSBs. Future research

should leverage these advanced techniques to elucidate the dynamic behavior of MSBs components during charge-discharge cycles, providing valuable information for the design and optimization of next-generation battery systems.

4. Electrolyte Optimization: Investigating electrolyte formulations and additives that can suppress polysulfide dissolution and improve ion transport kinetics is essential for advancing MSBs technology. Research efforts should aim to develop electrolytes with improved stability, high ionic conductivity, and compatibility with various host materials to enhance battery cycling stability and energy density.

## Resum

Les bateries de sofre metàl·lic (MSB) han guanyat una atenció significativa com a alternativa prometedora a les bateries convencionals d'ions de liti gràcies a la seva alta densitat d'energia teòrica, el seu baix cost i els seus beneficis ambientals. Aquestes bateries proporcionen una capacitat d'emmagatzematge d'energia molt superior als sistemes tradicionals, fet que les converteix en una opció atractiva per a aplicacions que requereixen altes densitats d'energia, com els vehicles elèctrics (EV), l'emmagatzematge d'energia a la xarxa i l'electrònica portàtil. L'avantatge fonamental de les bateries de MSB rau en l'ús de sofre com a material de càtode. El sofre és abundant, econòmic i respectuós amb el medi ambient, fet que li confereix un avantatge significatiu respecte als materials més cars i menys abundants emprats en les bateries convencionals d'ions de liti o sodi. La capacitat específica teòrica del sofre és d'aproximadament  $1675 \text{ mAh g}^{-1}$ , i la densitat d'energia teòrica d'una bateria Li-S pot assolir fins a  $2600 \text{ Wh kg}^{-1}$ , superant notablement la de les bateries tradicionals d'ions de liti o sodi. Aquesta alta densitat d'energia s'atribueix al mecanisme de reacció de conversió del sofre, en què el sofre es redueix a sulfurs de liti o sodi ( $\text{Li}/\text{Na}_2\text{S}_n$ ) durant la descàrrega i s'oxida de nou a sofre durant la càrrega.

No obstant això, malgrat el seu potencial, les MSB s'enfronten a diversos reptes que han dificultat la seva adopció generalitzada. Un dels principals inconvenients és l'"efecte llançadora", en què els polisulfurs intermedis es dissolen en l'electròlit i migren entre els elèctrodes, cosa que provoca una pèrdua de material actiu i una reducció de la vida útil del cicle. A més, la baixa conductivitat del sofre i el seu important canvi de volum durant els cicles de càrrega i descàrrega poden afectar negativament tant el rendiment com la durabilitat de la bateria.

Per fer front a aquests desafiaments, s'ha impulsat una intensa recerca per millorar el rendiment de les MSB mitjançant diverses estratègies. Entre aquestes, s'inclou la millora de la conductivitat del sofre mitjançant materials compostos, el desenvolupament d'electròlits avançats que redueixin la dissolució dels polisulfurs i el disseny de noves arquitectures d'elèctrodes capaces d'adaptar-se als canvis de volum i millorar l'estabilitat global del sistema.

En aquesta tesi, proposem diverses solucions per superar les limitacions dels materials hoste en les MSB per a aplicacions pràctiques. Aquestes estratègies inclouen el disseny d'heteroestructures, la implementació d'enginyeria de defectes, la introducció de tècniques de dopatge i la creació d'estructures amb distorsió de xarxa. A través d'aquests enfocaments, aspirem a millorar el rendiment electroquímic de les MSB, incrementant la seva conductivitat, activitat catalítica i estabilitat general, i així superar els desafiaments que dificulten la seva aplicació en el món real.

Les principals conclusions de la tesi són les següents:

1. Es proposa un material hoste de sofre basat en carboni dopat amb nitrogen (NC) recobert amb una petita quantitat d'un catalitzador de tel·lur de metall de transició (TMT) per superar aquestes limitacions. Les propietats del catalitzador redox del sofre es modifiquen ajustant la concentració de vacants d'anions i dissenyant heteroestructures ZnTe/CoTe<sub>2</sub>. Tant els càlculs teòrics com les dades experimentals demostren que les vacants de tel·luri milloren l'adsorció dels polisulfurs de liti (LiPSs), mentre que les heteroestructures TMT/TMT i TMT/C formades, juntament amb l'arquitectura general del compost, permeten simultàniament una alta difusió de Li<sup>+</sup> i un transport ràpid d'electrons. Com a resultat, els càtodes de sofre v-ZnTe/CoTe<sub>2</sub>@NC/S presenten excel·lents capacitats inicials de fins a 1608 mA·h·g<sup>-1</sup> a 0,1C, així com una gran estabilitat cíclica, amb una taxa mitjana de degradació de la capacitat del 0,022% per cicle a 1C durant 500 cicles. Fins i tot amb una alta càrrega de sofre de 5,4 mg·cm<sup>-2</sup>, es manté una capacitat elevada de 1273 mA·h·g<sup>-1</sup> a 0,1C. A més, quan la quantitat d'electròlit es redueix a 7,5 μL·mg<sup>-1</sup>, el material v-ZnTe/CoTe<sub>2</sub>@NC/S encara conserva una capacitat de 890,8 mA·h·g<sup>-1</sup> després de 100 cicles a 0,1C.

2. Les partícules heteroestructurades de NiS<sub>2</sub>/NiSe<sub>2</sub>, encapsulades dins d'esferes de NC i que presenten una arquitectura buida, es van sintetitzar a partir d'un precursor de Ni-MOF. Les mesures magnètiques i els resultats computacionals indiquen que l'heteroestructura es caracteritza per la presència de Ni<sup>3+</sup> en un estat d'espín electrònic alt. NiS<sub>2</sub>/NiSe<sub>2</sub>@NC exhibeix una divisió d'espín orbital i presenta una configuració d'espín alt amb més electrons desaparellats. Aquest estat d'espín elevat regula l'estructura electrònica, cosa que resulta en una excel·lent força d'unió i una alta capacitat catalítica envers els LiPSs. L'estructura buida i porosa no només confina de manera efectiva el sofre, sinó que també proporciona un espai

tampó addicional per a la reacció electroquímica.  $\text{NiS}_2/\text{NiSe}_2@\text{NC}$  s'utilitza com a material hoste en el càtode de sofre de les bateries de liti-sofre (LSBs), demostrant un rendiment electroquímic excel·lent. Aquest rendiment inclou una gran capacitat de càrrega i descàrrega, una excel·lent capacitat de resposta a diferents velocitats i una llarga vida útil. Aquest estudi no només posa en evidència les propietats catalítiques del  $\text{NiS}_2/\text{NiSe}_2$ , sinó que també exemplifica l'efecte de la polarització d'espín en les reaccions electrocatalítiques.

3. Tant els resultats experimentals com els càlculs teòrics van confirmar l'eficàcia del dopatge aniònic en  $\text{Bi}_2\text{Se}_3$  per millorar el rendiment de les LSBs. A causa de la seva major mida atòmica, aquest dopatge genera vacants de Se, fet que condueix a una concentració més elevada de portadors lliures en el material de l'elèctrode. A més, l'augment de cations de Bi desaparellats proporciona llocs actius addicionals per a l'adsorció dels LiPSs i les reaccions catalítiques, afavorint així la cinètica de conversió del sofre. Simultàniament, el dopatge amb Te indueix una distorsió de la xarxa dins del material  $\text{Bi}_2\text{Se}_3$ , provocant un desplaçament en el centre de càrrega positiva/negativa de la cèl·lula unitària cap a la direcció negativa. Aquest fenomen genera un camp elèctric intrínsec, que facilita la transferència de càrregues dins del material del càtode. Aprofitant el dopatge, els defectes i l'enginyeria de distorsió de la xarxa, el càtode  $\text{Te-Bi}_2\text{Se}_{3-x}@\text{C}$  va demostrar un rendiment electroquímic excepcional, incloent-hi una alta capacitat específica (fins a  $1508 \text{ mAh}\cdot\text{g}^{-1}$  a 0,1C), una excel·lent capacitat de resposta a diferents velocitats i una estabilitat cíclica prolongada, fins i tot en condicions d'alta càrrega de sofre i amb quantitats reduïdes d'electròlit.

4. Es va sintetitzar el material hoste de sofre heteroestructurat P-N basat en la combinació de nanopartícules tubulars buides de  $\text{C}_3\text{N}_4$  i  $\text{Co}_3\text{O}_4$ . Quan es combinen aquests dos materials, els electrons es transfereixen de l'àtom de N en  $\text{C}_3\text{N}_4$  a l'àtom de Co en  $\text{Co}_3\text{O}_4$ , donant lloc a la generació d'electrons desaparellats addicionals en l'orbital 3d de  $\text{Co}^{3+}$ . Aquesta transferència d'electrons condueix a dos resultats significatius: en primer lloc, indueix un canvi en l'estat d'espín de l'ió Co. En segon lloc, els electrons desaparellats generats afavoreixen la transferència entre el material hoste i els polisulfurs, millorant així significativament el rendiment catalític i l'adsorció dels polisulfurs. A més, el  $\text{C}_3\text{N}_4$  tubular buit proporciona prou espai per alleujar el canvi de volum associat amb la difusió de  $\text{Na}^+$  durant la reacció i per proporcionar canals de transport d'ions. Per tant, el càtode  $\text{Co}_3\text{O}_4\text{-NC}@\text{C}_3\text{N}_4/\text{S}$  presenta una

excel·lent capacitat de resposta a diferents velocitats i una llarga vida útil en bateries de sofre-sodi a temperatura ambient (RT-SSBs).  $\text{Co}_3\text{O}_4\text{-NC@C}_3\text{N}_4/\text{S}$  també mostra un rendiment electroquímic satisfactori fins i tot a nivells d'alta càrrega i en cel·les de bossa.

En resum, els quatre estudis anteriors han abordat reptes clau en les MSBs mitjançant la introducció d'heteroestructures, enginyeria de vacants, estratègies de dopatge i heterounions P-N. Aquests enfocaments innovadors han millorat significativament els processos d'adsorció i catalítics dins dels MSBs. Com a resultat, els materials hoste desenvolupats en aquests estudis presenten un rendiment electroquímic excepcional, caracteritzat per una gran capacitat específica i una llarga vida útil. En particular, aquests materials mantenen una estabilitat excepcional fins i tot en condicions d'alta càrrega i amb electròlits pobres, demostrant encara més la seva aplicabilitat pràctica.

*paraules clau:* electroquímica, bateria de càtode de sofre, heteroestructura homogènia, vacant, enginyeria de dopatge, heterounió P-N, distorsió de gelosia



# Chen Huang

## Curriculum vitae



1996.06



198 6020 2978



China



chenhuang714@gmail.com

## Google Scholar:

<https://scholar.google.com/citations?user=u2CSk8EAAAAJ&hl=zh-CN>

## Background of education

**2022.09 - 2025.06 PhD, University of Barcelona/ Catalonia Institute for Energy Research  
Electrochemistry Science and Technology**

Research direction: Electronic Structure Engineering for Enhanced Additive Performance in Robust Sulfur Cathodes

**2019.09 - 2022.06 Master South China Normal University  
Physical Chemistry (Electrochemistry)**

Research direction: Metal-organic framework-derived transition metal compounds for high-performance supercapacitors

**2015.09 - 2019.06 Bachelor JiuJang University  
Applied Chemistry**

Score: 87.4/100 (ranked 1/52); CET

## Publications

1. **Chen Huang**, Jing Yu, Chao Yue Zhang, Zhibiao Cui, Bingfei Nan, Ren He, Linlin Yang, Junshan Li, Jordi Arbiol, Yao-Jie Lei\*, Qin Sun\*, Guoxiu Wang\* and Andreu Cabot\*, Anionic Doping in Layered Transition Metal Chalcogenides for Robust Lithium-Sulfur Batteries, *Angew. Chem. Int. Ed.* 2024, e202420488.
2. **Chen Huang**, Jing Yu, Chao Yue Zhang\*, Zhibiao Cui, Jiakun Chen, Wei-Hong Lai, Yao-Jie Lei\*, Bingfei Nan, Xuan Lu, Ren He, Li Gong, Junshan Li, Canhuang Li, Xuede Qi, Qian Xue, Jin Yuan Zhou, Xueqiang Qi, Lluís Balcells, Jordi Arbiol, and Andreu Cabot\*, Electronic Spin Alignment within

Homologous NiS<sub>2</sub>/NiSe<sub>2</sub> Heterostructures to Promote Sulfur Redox Kinetics in Lithium-Sulfur Batteries, *Adv. Mater.* 2024, 36, 2400810.

3. **Chen Huang**, Jing Yu, Canhuang Li, Zhibiao Cui, Chaoqi Zhang\*, Chao Yue Zhang\*, Bingfei Nan, Junshan Li, Jordi Arbiol, and Andreu Cabot\*, Combined Defect and Heterojunction Engineering in ZnTe/CoTe<sub>2</sub>@NC Sulfur Hosts toward Robust Lithium-Sulfur Batteries, *Adv. Funct. Mater.* 2023, 33, 2305624.
4. Chen Huang, Jing Yu\*, Yao-Jie Lei, Oleg Usoltsev, Li Gong, Zhibiao Cui, Junshan Li, Canhuang Li, Bingfei Nan, Xuan Lu, Ren He, Xuede Qi, Qian Xue, Jiali Chai, Yuchuan Ren, Xiaoyu Bi, Yapeng Cheng, Jin Yuan Zhou, Alina Skorynina, Aram Bugaev, Paulina R. Martínez-Alanis, Lluís Balcells, Jordi Arbiol, Chao Yue Zhang\* and Andreu Cabot\*, Generation of unpaired electrons to promote electron transfer at the cathode of room-temperature sodium sulfur batteries, *Chem. Eng. J.* 2025, 506, 160146.
5. **Chen Huang**, Shengyao Lv, Aimei Gao, Jingzhou Ling, Fenyun Yi, Junnan Hao\*, Mengyi Wang, Zhongwei Luo, Dong Shu\*, Boosting the energy density of supercapacitors by designing both hollow NiO nanoparticles/nitrogen-doped carbon cathode and nitrogen-doped carbon anode from the same precursor, *Chem. Eng. J.* 2022, 431, 134083.
6. **Chen Huang**, Aimei Gao, Fenyun Yi, Yicong Wang, Dong Shu\*, Yansheng Liang, Zhenhua Zhu, Jingzhou Ling, Junnan Hao, Metal organic framework derived hollow NiS@C with S-vacancies to boost high-performance supercapacitors, *Chem. Eng. J.* 2021, 419, 129843.
7. **Chen Huang**, Aimei Gao, Zhenhua Zhu, Fenyun Yi, Mengyi Wang, Junnan Hao, Honghong Cheng\*, Jingzhou Ling, Dong Shu\*, Metal organic frameworks derived Ni-doped hierarchical Ni<sub>x</sub>Co<sub>1-x</sub>S@C bundled-like nanostructures for enhanced supercapacitors, *Electrochim. Acta* 2022, 406, 139872.
8. Jing Yu, **Chen Huang**, Oleg Usoltsev, Ashley P. Black, Kapil Gupta, Maria Chiara Spadaro, Ivan Pinto-Huguet, Marc Botifoll, Canhuang Li, Javier Herrero-Martín, Jinyuan Zhou, Alexandre Ponrouch, Ruirui Zhao, Lluís Balcells, Chao Yue Zhang\*, Andreu Cabot\*, and Jordi Arbiol\* Promoting Polysulfide Redox Reactions through Electronic Spin Manipulation, *ACS Nano* 2024, 18(29), 19268-19282.
9. **Chen Huang**, Jing Yu, Qian Xue, Chao Yue Zhang, Zhibiao Cui, Bingfei Nan, Ren He, Linlin Yang, Junshan Li, Jordi Arbiol, Yao-Jie Lei\*, Guoxiu Wang\*, Xueqiang Qi\* and Andreu Cabot\*, Elaborating catalytic behavior of lithium-sulfur batteries by controlling the content of defects based on doping engineering, (*In preparation*).
10. **Chen Huang**, Jing Yu, Chao Yue Zhang, Zhibiao Cui, Bingfei Nan, Junshan Li, Jordi Arbiol, Yao-Jie Lei\*, Guoxiu Wang\*, and Andreu Cabot\*, Optimizing the Spin State of Co<sub>3</sub>O<sub>4</sub> Nanorods by Tungsten Doping Engineering for Promoting Sulfur Redox Kinetics, (*In preparation*).
11. Chao Yue Zhang, Xuan Lu, Xu Han, Jing Yu, Chaoqi Zhang, **Chen Huang**, Lluís Balcells, Alba Garzon Manjon, Jordi Jacas Biendicho, Junshan Li, Jordi Arbiol, Gengzhi Sun, Jin Yuan Zhou\*, Andreu Cabot\*, Identifying the Role of the Cationic Geometric Configuration in Spinel Catalysts for Polysulfide Conversion in Sodium–Sulfur Batteries, *J. Am. Chem. Soc.* 2023, 145(34), 18992-19004.
12. Canhuang Li, Dawei Yang\*, Jing Yu, Jian Wang, Chaoqi Zhang, Tianxiang Yang, **Chen Huang**, Bingfei Nan, Junshan Li, Jordi Arbiol, Yingtang Zhou\*, Qiaobao Zhang\*, Andreu Cabot\* Three Birds with One Stone: Multifunctional Separators Based on SnSe Nanosheets Enable High-Performance Li-, Na-and K-Sulfur Batteries. *Adv. Energy Mater.* 2024, 14(29), 2303551.
13. Canhuang Li, Jing Yu, Chaoqi Zhang\*, Dawei Yang, Jian Wang, Hao Li, **Chen Huang**, Ke Xiao, Yapeng Cheng, Yuchuan Ren, Xuede Qi, Tianxiang Yang, Junshan Li, Jiaao Wang\*, Graeme Henkelman, Jordi Arbiol, Junmin Nan\*, Andreu Cabot\* Tungsten phosphide on nitrogen and phosphorus-doped carbon as a functional membrane coating enabling robust lithium-sulfur batteries. *J. Colloid Interface Sci.* 2024, 670, 61-72.
14. Bingfei Nan, Jing Yu, Mengyao Li, **Chen Huang**, Hongyu Chen, Hao Zhang, Cheng Chang, Junshan Li, Xuan Song, Kai Guo\*, Jordi Arbiol, Andreu Cabot\*, Colloidal Ag<sub>2</sub>SbBiSe<sub>4</sub> nanocrystals as n-type thermoelectric materials, *J. Colloid Interface Sci.*, 2024, 679, 910-920.

## Honor

National Scholarship of China (Top 1% at the master's level);

China Scholarship Council Scholarship (twice);

Excellent graduation thesis (Metal-organic complex-derived nickel-cobalt compound/carbon composites for high-performance supercapacitors);

Triple A Students Jiangxi Province;